Universidad del País Vasco Euskal Herriko Unibertsitatea

AUTORIZACION DEL/LA DIRECTOR/A DE TESIS

PARA SU PRESENTACION

Dr/a. **JESUS UGALDE URIBE-ETXEBARRIA** con N.I.F. **15355621 Q**

como Director/a de la Tesis Doctoral:

COMPUTATIONAL MODELING OF SEMICONDUCTOR NANOSTRUCTURES

realizada en el Departamento **CIENCIA Y TECNOLOGÍA DE POLÍMEROS**

por el Doctorando Don/ña. **ION MIKEL AZPIROZ APECECHEA**,

autorizo la presentación de la citada Tesis Doctoral, dado que reúne las condiciones necesarias para su defensa.

En _____a _____de _____de _____

EL/LA DIRECTOR/A DE LA TESIS

Fdo.: **JESUS UGALDE URIBE-ETXEBARRIA**

Universidad del País Vasco Euskal Herriko Unibertsitatea

CONFORMIDAD DEL DEPARTAMENTO

El Consejo del Departamento de **CIENCIA Y TECNOLOGÍA DE POLÍMEROS** en reunión celebrada el día ____ de _____ de _____ ha acordado dar la conformidad a la admisión a trámite de presentación de la Tesis Doctoral titulada: ***COMPUTATIONAL MODELING OF SEMICONDUCTOR NANOSTRUCTURES*** dirigida por el/la Dr/a. **JESUS UGALDE URIBE-ETXEBARRIA** y presentada por Don/ña. **ION MIKEL AZPIROZ APECECHEA** ante este Departamento.

En _____a _____de _____de _____

Vº Bº DIRECTOR/A DEL DEPARTAMENTO SECRETARIO/A DEL DEPARTAMENTO

Fdo.: **IÑAKI EGUIAZABAL** Fdo.: **AGUSTIN ETXEBERRIA**

Universidad del País Vasco Euskal Herriko Unibertsitatea

ACTA DE GRADO DE DOCTOR O DOCTORA
ACTA DE DEFENSA DE TESIS DOCTORAL

DOCTORANDO/A DON/DÑA. **ION MIKEL AZPIROZ APECECHEA**

TITULO DE LA TESIS:

COMPUTATIONAL MODELING OF SEMICONDUCTOR NANOSTRUCTURES

El Tribunal designado por la Comisión de Postgrado de la UPV/EHU para calificar la Tesis Doctoral arriba indicada y reunido en el día de la fecha, una vez efectuada la defensa por el/la doctorando/a y contestadas las objeciones y/o sugerencias que se le han formulado, ha otorgado por_____la calificación de:

unanimidad ó mayoría

SOBRESALIENTE / NOTABLE / APROBADO / NO APTO

Idioma/s de defensa (en caso de más de un idioma, especificar porcentaje defendido en cada idioma): _____

En _____a _____de _____de _____

EL/LA PRESIDENTE/A, EL/LA SECRETARIO/A,

Fdo.: Fdo.:

Dr/a: _____ Dr/a: _____

VOCAL 1º, VOCAL 2º, VOCAL 3º,

Fdo.: Fdo.: Fdo.:

Dr/a: _____Dr/a:_____Dr/a:_____

EL/LA DOCTORANDO/A,

Fdo.: _____

COMPUTATIONAL MODELING OF SEMICONDUCTOR NANOSTRUCTURES

Jon Mikel Azpiroz

Doctoral Dissertation

Supervisor: Jesus M. Ugalde Uribe-Etxebarria

2014

Eskertzak

Hemen gaude, ta poztutzen naiz...

Lau Teilatu, Itoiz

Eta benetan pozten naiz gainera. Ez da bide erraza izan. Baina zuengatik izan ez balitz, askoz zailagoa izango zatekeen. Eskerrik beroena denoi.

Lehenik eta behin, Jesus, zuri eman nahi nizkizuke eskerrak. 2009a zen, Kimika Teorikoan lankidetza egin nahi nuela jakinarazi nizunean. Esaldia bukatu nuenerako, laborategiko giltzak eskuan zenituen, eta irribarrea ahoan. Eskerrik asko, momentu hartatik bertatik, taldeko ateak irekitzeagatik. Eta eskerrik asko, are gehiago agian, irribarre hura bost urte hauetan ez baitzaizu ezabatu. Baikortasun hori kutsakorra da. Askatasun osoa eman didazu nire ikerketa garatzeko, baina hor egon zara behar izan dudan bakoitzean. Ezer hoberik esan al daiteke tesi zuzendari bati buruz?

`for i in $(seq 1 1000); do echo "esker"; done`.

Bai, Txema, zu zara hurrena. Mila esker zuri ere. Zuregatik izan ez balitz, bost urte hauek hamar izango ziratekeen agian. Beti eduki duzu erantzuna nire galderentzat. Eta beti eduki duzu pazientzia niretzat.

Gainerako taldekideentzat ere, nire eskerrik beroenak. Xabi, gauza asko irakatsi dizkidazu Kimikari buruz. Baina gehiago ditut gogoan, zure etxean egindako afariak, Staafen, ukalondoa barran, hartu ditudan garagardoak, edo Be Bopen erori zaizkizun Gin Tonicak. Txoni, eskerrik asko zuri ere. Askotan joan natzaizu nire arazoekin eta beti aurkitu diezu konponbidea. Handia, Barakaldoko ilehoria!

Für Elise. Eskerrik asko, bihotzez. Benetako lagunak esku bateko behatzekin zenbatzen omen dira. Eta zu horien artean zauzkat. Bizipen asko ditut zurekin, ahaztuko ez ditudanak. Californicationekin hasi, eta Meridan bukatu. Espero dut, nik ere, leku bat edukitzea zure gogoan. Aunque me falten matices.

Ivan, grazie anche a te! Stiamo lavorando duro sui quantum dots e ho imparato moltissimo da te. E tra l'altro, mi hai suggerito tu di andare a Perugia la prima volta!

Eduard, Luca, Mario, Fernando, Joni, Noelia, David, Elena, Jon, Slawek y Andreas. No os querría olvidar. Siempre dispuestos a ayudarme. Os echaré de menos.

Doktoretza Tesiak bidaiatzeko aukera paregabea eskaini dit. Ezin ahaztu, beraz, Perugia eta Merida.

Filippo, grazie di cuore per aver stabilito questa collaborazione insieme a me. Como ti ho detto una volta, non ti potrò mai ringraziare abbastanza. Grazie anche a Simona, Anna, Edoardo e il resto.

Palabras de agradecimiento también para Gabriel. Me hiciste sentir como en casa en México, al otro lado del Atlántico. Un abrazo para ti, para Jessica y para Darío. Y recuerdos para Sigfrido, Maryel, Claudia, Said, Alberto y Mariana.

Kuadrilarentzat ere, pare bat hitz. Zuengatik izan ez balitz, ~~ezin izango nukeen tesia amaitu~~ tesia dezente lehenago bukatuko nukeen. Eta hori ere ez litzateke seinale ona izango. Zorionekoa ni, zuek aurkitu izanagatik. Eskerrik asko zuri bereziki, Kantz. Lan honek, estilo pixkat baldin badu, zuregatik baita.

Bukatzeko, eta bereziki, ama, atte eta Jokin. Eskerrik asko! Tesi honen zati txiki bat, eta naizenaren handi bat, zuei dagokizuelako. Maite zaituztet.

This research was funded by the Spanish Ministry of Education through a FPU fellowship (AP2009-1514).

Technical and human support provided by IZO-SGI, SGIker (UPV/EHU, MICINN, GV/EJ, ERDF and ESF) is gratefully acknowledged.

Contents

1 Laburpena **11**

1.1 Nanoegiturak: Sarrera Orokorra 11

1.1.1 Gainazal efektuak 11

1.1.2 Konfinamendu Kuantikoa 13

1.2 Lan Ildoa 15

1.2.1 DFT Metodoaren Aukeraketa 15

1.2.2 Ligandorik Gabeko Nanoegiturak 15

1.2.3 Ligandodun Nanoegiturak Txikiak 15

1.2.4 Nanoegitura Errealistak 16

1.3 Emaitzen Laburpena 16

1.3.1 DFT Metodoaren Aukeraketa 16

1.3.2 Ligandorik Gabeko Nanoegiturak 16

1.3.3 Ligandodun Nanoegiturak Txikiak 17

1.3.4 Nanoegitura Errealistak 17

2 General Introduction **19**

2.1 Nanotechnology 19

2.2 Nanostructures: Basic Principles 20

2.2.1 Surface Effects 20

2.2.1.1 Introduction 20

2.2.1.2 Defects 21

2.2.1.3 Ligands 22

2.2.2 Quantum Confinement 24

2.2.2.1 Introduction 24

2.2.2.2 Electronic Excitations in Semiconductor Nanostructures . . . 27
2.2.2.3 Luminescence and Blinking . . . 29
2.2.2.4 Auger Recombination . . . 29
2.2.2.5 Electron-Phonon Coupling . . . 29
2.2.2.6 Multiple Exciton Generation . . . 30
2.3 Nanostructures: Colloidal Synthesis . . . 31
2.3.1 Introduction . . . 31
2.3.2 Design of Surface Ligands and Ligand Exchange . . . 32
2.4 Nanostructures: Applications . . . 33
2.4.1 Photocatalysis . . . 33
2.4.2 Optical Sensing . . . 34
2.4.3 Photovoltaics . . . 35
2.4.4 Biology . . . 36
2.5 Scope of the Work . . . 38

3 Methods **41**
3.1 *Ab initio* Methods . . . 42
3.1.1 Born-Oppenheimer Approximation . . . 43
3.1.2 Electronic Wave function . . . 44
3.1.3 Slater Determinant . . . 44
3.1.4 The HF Method . . . 46
3.1.5 Post-HF Methods . . . 49
3.1.5.1 Configuration Interaction (CI) . . . 50
3.1.5.2 Coupled Cluster (CC) . . . 51
3.1.5.3 Rayleigh-Schrödinger Perturbation Theory . . . 52
3.1.5.4 Moller-Plesset Perturbation Theory . . . 55
3.2 DFT . . . 56
3.2.1 Early DFT . . . 56
3.2.1.1 The Thomas-Fermi Model . . . 56
3.2.1.2 The Slater Xα Method . . . 57
3.2.2 Hohenberg-Kohn Theorems . . . 57
3.2.3 Kohn-Sham Approach . . . 59

3.2.4 Approximations to the Exchange-Correlation Energy 62
3.2.4.1 Local Density Approximation (LDA) 62
3.2.4.2 Non Local Approximations 63
3.2.4.3 Hybrid Functionals 66
3.3 Time-Dependent DFT 68
3.3.1 Runge-Gross Theorem 69
3.3.2 Time-Dependent Kohn-Sham Equations 70
3.3.3 Linear Response Theory 71
3.3.4 Quantum Molecular Dynamics 73
3.3.4.1 BO Molecular Dynamics 73
3.3.4.2 Car-Parrinello Molecular Dynamics 74
3.3.5 Basis Sets and Pseudopotentials 75
3.3.5.1 Localized Basis Sets: STOs and GTOs 75
3.3.5.2 Plane Wave Basis Sets 76
3.3.5.3 Pseudopotentials, Effective Core Potentials, and Frozen Cores 78
3.4 QM/MM Methods 79

4 Results **83**

4.1 Benchmark Assessment of Density Functional Methods on Group II–VI MX (M = Zn, Cd; X = S, Se, Te) Quantum Dots 85
4.1.1 Abstract 85
4.1.2 Introduction 85
4.1.3 Computational Methodology 87
4.1.4 Results and Discussions 90
4.1.5 Conclusions and Suggestions 93
4.2 Modeling ZnS and ZnO Nanostructures: Structural, Electronic, and Optical Properties 107
4.2.1 Abstract 107
4.2.2 Introduction 107
4.2.3 Model and Computational Details 110
4.2.4 Results and Discussion 111
4.2.5 Conclusions 114

4.3 A First-Principles Study of II-VI (II = Zn; VI = O, S, Se, Te) Semiconductor Nanostructures . . . 123
4.3.1 Abstract . . . 123
4.3.2 Introduction . . . 123
4.3.3 Model and Method . . . 125
4.3.4 Results and Discussion . . . 127
4.3.5 Summary and Conclusions . . . 134
4.4 Modeling Surface Passivation of ZnS Quantum Dots . . . 149
4.4.1 Abstract . . . 149
4.4.2 Introduction . . . 149
4.4.3 Computational Details . . . 152
4.4.4 Results and Discussion . . . 155
4.4.5 Summary and Conclusions . . . 161
4.5 A DFT/TDDFT Study on the Optoelectronic Properties of the Amine-Capped Magic $(CdSe)_{13}$ Nanocluster . . . 175
4.5.1 Abstract . . . 175
4.5.2 Introduction . . . 175
4.5.3 Model and Method . . . 177
4.5.4 Results and Discussion . . . 179
4.5.5 Summary and Conclusions . . . 186
4.6 Quantum Dot Photoactivation of Pt(IV) Anticancer Agents: Evidence of an Electron Transfer Mechanism Driven by Electronic Coupling . . . 195
4.6.1 Abstract . . . 195
4.6.2 Introduction . . . 195
4.6.3 Computational Section . . . 196
4.6.4 Results and Discussion . . . 197
4.6.5 Conclusions . . . 203
4.7 Effect of Structural Dynamics on the Opto-Electronic Properties of Bare and Hydrated ZnS QDs . . . 211
4.7.1 Abstract . . . 211
4.7.2 Introduction . . . 211
4.7.3 Model and Computational Details . . . 213

4.7.4 Results and Discussion 214
4.7.5 Summary and Conclusions 220
4.8 DFT/TDDFT Study of the Adsorption of N3 and N719 Dyes on ZnO $(10\bar{1}0)$ Surfaces 233
4.8.1 Abstract 233
4.8.2 Introduction 233
4.8.3 Computational Details 235
4.8.4 Results and Discussion 236
4.8.5 Summary and Conclusions 240
4.9 PbS Quantum Dot Sensitized Solar Cells: Insights from First Principles 247
4.9.1 Abstract 247
4.9.2 Introduction 247
4.9.3 Methodology 249
4.9.4 Results and Discussion 250
4.9.5 Conclusions 255

5 Final Conclusions **267**

6 List of Publications **271**

7 Bibliography **275**

Chapter 1

Laburpena

1.1 Nanoegiturak: Sarrera Orokorra

Nanoteknologia, nanoegiturak diseinatu, sintetizatu eta aztertzeaz arduratzen den teknologia da. Nanoteknologiari buruzko lehenengo kontzeptuak Richard P. Feynman Nobel saridunari zor dizkiogu. 1959. urtea zen. Orduz geroztik, nanoteknologiak aparteko garapena bizi izan du, azken urteotako aurrerapen teknikoen eskutik. Aurrerapen hauei esker, zientzialariak materia eskala atomikoan manipulatzeko gai dira. Gaur egun, nanoteknologia zientziaren alor ezberdinetara hedatu da, fisika, kimika, materialen zientzia, ingeniaritza eta medikuntza barne direlarik. Gainera, eguneroko bizitzan gero eta garrantzia handiago du.

Nanoegiturak, izenak berak dioen bezala, nanometro gutxi batzutako tamaina duten egitura ñimiñoak dira. Nanoegitura erdieroaleek, bereziki, fisikarien eta kimikarien interesa piztu dute azken urteotan, euren ezaugarri interesgarriak direla medio. Nanoegitura erdieroaleek bi efektu nagusiri zor dizkiete berezitasunak: gainazalari eta konfinamentu kuantikoari.

1.1.1 Gainazal efektuak

Materialen zientzian jakina denez, gainazaleko atomoak barnekoak baino energetikoagoak dira, euren koordinazio apalagoa dela eta. Material makroskopikoetan, dena den, gainazalak apenas du eraginik, eta egonkortasuna barnealdeko atomoek determinatzen dute. Tamaina txikitu ahala, ordea, gainazal-bolumen erlazioa handitu egiten da eta gainazaleko atomoen eragina nabariagoa bilakatzen da. Ondorioz, materialaren dimentsioak murriztean, hainbat propietate termodinamikotan aldaketa nabarmena antzematen da, urtze tenperaturan eta solido-solido fase trantsizioan, esaterako. Nanoegituretan, zeinetan atomoen proportzion handi bat gainazalean kokatzen den, egonkortasuna gainazalak determinatu ohi du. Nanomaterialen egitura egonkorrena gainazal energia minimizatzen duena da.

Gainazalak paper erabakiorra du nanoegituren propietate elektroniko eta optikoetan. Gainazaleko akatsek (atomo asegabeek, hutsuneek eta dimeroek, esaterako) egoera elektroniko

lokalizatuak eragin ohi dituzte. Egoera hauek, nanoegituraren HOMO-LUMO tartean sartzen direnez, kitzikapen / erlaxazio bide berriak ireki diezazkiekete elektroiei eta zuloei. Sarritan, kanal berri hauek nanoegituren propietateak kaltetzen dituzte. Ondorioz, zientzialariek lanean dihardute gainazaleko akatsen agerpena ekiditeko. Azken aldian, ordea, zenbait aplikaziotarako onuragarriak izan daitezkeela ikusi da.

Ligando eta disolbatzaile molekulek ere, gainazalarekin elkarreragiten duten heinean, nanoegituren egonkortasuna baldintzatzen dituzte. Gainazaleko atomo asegabeei itsatsi ohi zaizkie, gainazal energia apalduz, eta nanoegitura egonkortuz. Sarritan, gainazaleko molekulek nanomaterialen egitura zehazten dute. Ondorioz, kimikariek ligando berrien sintesian dihardute, nanoegiturak apropos sintetizatu ahal izateko.

Egonkortasun termodinamikoa emateaz gain, ligandoek nanoegituraren egitura elektronikoan eragiten dute. Gainazaleko atomo asegabeei lotzean, egoera lokalizatuen agerpena eragozten dute. Dena den, ligando molekulen arteko talka esterikoen eraginez, sarritan atomo asegabeak gelditzen dira gainazalean, eta egoera lokalizatuak ezin dira guztiz saihestu. Ondorioz, nanoegiturak geruza inorganikoekin estali ohi dira maiz. Era honetan osaturiko nanoegiturek, *core@shell* deritzenek, ez dute egoera lokalizaturik pairatzen.

Nanoegituren eta ligandoen egoera elektronikoak egokiro lerratzen direnean, euren artean elektroiak / zuloak truka ditzakete. Zenbait eguzki zelulatan, oxido erdieroalez (TiO_2 edo ZnO) eginiko nanopartikulek Ru(II) konplexuak dituzte gainazalean. Konplexu hauek, eguzki argia absorbatzeko eta kitzikaturiko elektroia nanoegiturara garraitzeko gai dira. Beste zenbait aplikaziotan, nanoegiturak elektroi emale bezala jokatzen du, eta ligandoak hartzaile gisara. CdSe eta CdSe@ZnS nanoegiturek esaterako, argi ikuskorrarekin kitzikatutakoan, gainazaleko Pt(IV) konplexuetara elektroiak transferitzen dituztela ikusi da. Pt(IV) konposatuak erreduzitutakoan Pt(II) konplexuak lortzen dira, minbizia sendatzeko erabilgarri direnak.

Sarritan, zuloak trukatzen dira nanoegituren eta ligandoen artean. Belaunaldi berriko eguzki zeluletan, nanoegitura erdieroleek Ru(II) konplexuen papera betetzen dute, eguzki argia absorbatuz eta kitzikaturiko elektroiak oxidora transferituz. Zenbaitetan, elektroi / zulo elkarrekintza dela eta, elektroiak oinarrizko egoerara itzultzen dira oxidora garraiatu baino lehen. Prozesu hau ekiditze aldera, Ru(II) konplexuak itsatsi dakizkieke nanoegiturei, zuloak harrapatzen baitituzte. Beste zenbait aplikazioatarako, zuloak Ru(II) konplexuetan pilatzea onuragarria izan daiteke, erredukzio / oxidazio erreakzioak kataliza baititzakete. Esaterako, CdS nanoegituren gainazalera loturiko Ru(II) konposatuak ura oxidatzeko erabili dira. Dopamina molekulek ere antzeko jokaera dute. CdSe nanoegituretara itsatsitakoan, zuloak harrapa ditzaketela ikusi da. CdSe nanopartikuletan eraturiko elektroi desparekatuak, gainazalera heldutakoan, espezie erreaktiboak eratzen ditu, minbizi zelulen heriotza eragin dezaketenak.

1.1.2 Konfinamendu Kuantikoa

Nanoegituretan, euren tamaina dela eta, efektu kuantikoek garrantzia dute. Tamaina murriztu ahala, banda elektroniko jarraiak maila elektroniko diskretu bilakatzen dira. Egitura elektronikoa nanoegituraren tamaina eta morfologiaren araberako da gainera. Honek, nanoegituren propietate elektroniko eta optikoak apropos aldatzeko aukera eskaintzen diete zientzialariei, eta gogor dihardute norabide honetan.

Badira, dena den, beste zenbait prozedura nanoegituren propietateak berariaz eraldatzeko. Esaterako, atomo arrotzak gehi dakizkieke. Era honetan sorturiko nanoegitura dopatuek propietate berriak garatzen dituzte. Adibidez, ZnS nanoegituren absortzio eta emisio espektruak UV-tik ikuskorrera lerratzen dira Mn gehitutakoan. Gainera, atomo arrotz hauek nanoegituren fotooxidazioa ekidin dezakete, elektroiak eta zuloak atomo horietan birkonbinatu ohi baitira, gainazalera iritsi baino lehen, non erredox erreakzioetan parte har lezaketen.

Core@shell antolaketak ere oso baliagarriak dira nanoegituren ezaugarriak eraldatzeko. CdSe @ ZnS nanoegiturak adibide klasikoa dira. Era honetako konposatuetan, kitzikapen elektronikoak CdSe muinean gertatzen dira, baina ZnS geruzak CdSe gainazalean gerta litezkeen egoera elektroniko lokalizatuak eta erredox erreakzioak ekiditen ditu. I motako materialak dira hauek, elektroiak eta zuloak barnealdean konfinaturik daudelako. Badira I motako konposatu alderantzizkatuak ere, non elektroiak eta zuloak geruzan barreiatzen diren. Tankera honetako nanoegiturak katalizatzaile gisara erabili ohi dira, erredox erreakzioak eragin baititzakete gainazalean. Dena den, II motako *core@shell* antolaketak dira seguraski interesgarrienak, elektroiak eta zuloak nanoegituraren gune ezberdinetan lokalizatzeko aukera eskaintzen baitute. CdTe@CdSe konposatutean, esaterako, balentzia eta eroankortasun bandak CdTe muinari eta CdSe geruzari dagozkie, hurrenez hurren. Ondorioz, kitzikapen elektronikoa gertatutakoan, elektroiak geruzan barreiatzen dira, zuloak CdTe gunean lagaz. Honela sorturiko elektroi eta zuloen arteko gainezarmen apala dela eta, birkonbinazio prozesua galerazia dago, eta egoera kitzikatuak denboran iraun dezake. II motako *core@shell* nanoegiturek garrantzia handia dute hainbat aplikazio fotovoltaikotan, elektroien eta zuloen banaketak euren garraioa erraz baitezakete. Bestalde, gainazalera zein karga eramaile (elektroiak edo zuloak) heltzen den kontrola daiteke, katalisi aplikaziotarako honek duen garrantziarekin.

Hirugarrenik, indar mekanikoek eragin erabakiorra dute nanoegituren propietateengan. *Core@ shell* nanoegituretan, geruzak tentsio mekanikoak eragin ohi ditu barnealdeko materialean. Honen ondorioz gertatzen diren deformazioek balentzia eta kondukzio bandak lerra ditzakete, nanoegituraren propietate elektroniko eta optikoak eraldatuz.

Dena den, konfinamendu kuantikoa eta nanoegituren egitura elektroniko bereizgarria argiarekin elkarreragitean geratzen dira nabarian. HOMO - LUMO tartearen adinako fotoi bat absorbatutakoan, elektroi bat balentzia bandatik eroankortasun bandara kitzikatzen da. Era honetan, elektroi-zulo parea eratzen da. Lehen egoera kitzikatuaz gain, badira beste zenbait egoera elektroi-zulo parearentzat, fotoiak HOMO - LUMO energia gainditu ahala

eskuragarri daudenak. Zer gertatzen da elektroi-zulo parearekin kitzikapenaren ondoren? Azken urteotan zientzialariak galdera honi erantzuna ematen saihatu dira, prozesu hauek nanoegituren propietate interesgarrien atzean baitaude.

Luminiszentzia (fluoreszentzia edo fosforeszentzia) elektroi-zulo parea lehen egoera kitzikatutik oinarrizko egoerara itzultzen denean gertatzen da, argia igortzen delarik. Zenbait nanoegituratan, argi igorpen hau aldizkakoa da. Berezitasun hau onuragarria izan daiteke zenbaitetan, nanoegituren detekzioa errazten baitu. Bestalde, nanoegituren mugimendua aztertu nahi bada, organismo bizidunetan esaterako, ez da desiragarria izaten. Bi mekanismo proposatu dira nanoegituren aldizkako luminiszentzia azaltzeko. Lehenengoak Auger ionizazioarekin du zerikusia. Zenbaiten ustetan, kitzikapen optikoek elektroien ionizazioa eragin dezakete, elektroi - zulo birkonbinaketa galeraziz. Bigarren mekanismoak gainazaleko egoera lokalizatuak ditu aintzat, karga emaileak harrapatu eta birkonbinaketa eragozten dutenak.

Auger birkonbinaketa konfinamendu kuantikoaren beste ondorioetako bat da. Nanoegituretan, euren tamaina dela eta, elektroien eta zuloen arteako elkarrekintza Coulombikoa apartekoa da. Sarritan, elektroi - zulo birkonbinaketan askaturiko energiak hirugarren karga eramaile bat kitzikatzen du. Zenbaitetan, prozesu honek elektroiak ionizatzen ditu (lehen aipaturiko Auger ionizazioa). Normalean, ordea, elektroia lehen egoera kitzikatura erlaxatzen da, elektroi-fonoi elkarrekintzak direla medio.

Bide batez, eskain diezazkiogun bi hitz elektroi-fonoi akoplamenduari. Material makroskopikoetan, ondoz ondoko maila elektronikoen arteko energia diferentzia txikia denez, kitzikaturiko elektroiek energia soberakina kristalaren bibrazioei (fonoi ere baderitze) eman diezaiekete. Nanoegituretan, ordea, maila elektronikoen arteko tartea 50-200 meV ingurukoa da. Fonoien frekuentzia, berriz, 2-20 meV izan ohi da. Beraz, elektroi-fonoi akoplamendua galerazia legoke. Esperimentalki, ordea, elektroi-fonoi elkarrekintzak gertatzen direla ikusi da. Gertaera hau azaltze aldera, hipotesi ezberdinak plazaratu dira. Lehenengoaren arabera, elektroiek euren energia soberakina zuloei emango liekete, Auger motako birkonbinaketen bidez. Zuloen egoera kuantikoak elektroienak baino hurbilago daude euren artean, eta beraz fonoiekin akoplatzeko aukera lukete. Bigarrenik, argitaratu berri diren esperimentuek, egoera elektronikoen arteko tartea espero zitekeena baino laburragoa dela erakusten dute. Beraz, elektroiak ere gai lirateke fonoiekin elkarrakintza egiteko. Hirugarrenik, gainazaleko egoera elektronikoek ere akoplamenduan parte har lezaketela proposatu da, elektroi eta zuloentzat erlaxazio bide berriak irekiz. Gainazaleko ligandoek ere, euren frekuentzia altuko bibrazioekin, elektroien / zuloen erlaxazioan parte har dezaketela proposatu da.

Konfinamendu kuantikoaren ondorioz, azkenik, elektroi-zulo anitz era daitezke absorbatutako fotoi bakoitzeko, baldin eta fotoi honen energia nanoegituraren HOMO-LUMO tartea baino dezente handiagoa bada (bikoitza gutxienez, bi elektroi-zulo pare sortu ahal izateko). MEG deritzo fenomeno honi (*Multiple Exciton Generation* ingeleraz) eta biziki interesgarria da zenbait aplikaziori begira. Eguzki energiaren esparruan, esaterako, energia altuko fotoiak baliatzeko aukera eskaintzen du.

1.2 Lan Ildoa

Beraz, nanoegitura erdieroaleek zientzialarien interesa piztu dute azken urteotan. Euren propietate erakargarriak ustiatze aldera, esfortzu esperimental eskerga eskaini diete. Dena den, karakterizazio esperimentala zaila da sarritan, nanoegituren tamaina ñimiñoa dela eta. Ondorioz, propietate eta fenomeno askok ezkutuan diraute oraindik. Zentzu honetan, fisikari eta kimikariak ordenagailuez baliatu ohi dira, nanoegiturak *in silico* aztertu ahal izateko. Doktoretza Tesi honek nanoegitura erdieroaleak teorikoki aztertzea du helburu. Horretarako, Den-tsitate Funtzioanalaren Teoriaz baliatu gara (DFT). Lan eskema hierarkiko bati atxiki gatzaizkio.

1.2.1 DFT Metodoaren Aukeraketa

Gaur egun kimikari teoriko batek DFT metodo ezberdinak ditu eskuragarri. Lehenengo pauso batean, DFT metodo ezberdinak aztertu ditugu, gure beharretara hobekien egokitzen dena aukeratu ahal izateko. Erreferentzia gisa, *ab initio* metodo zehatzak erabili ditugu.

1.2.2 Ligandorik Gabeko Nanoegiturak

Behin metodo konputazionala aukeraturik, ligandorik gabeko nanoegituren propietate elektronikoak eta optikoak aztertu ditugu. Bi dira atal honetan sartuko liratekeen lanak:

- Batetik, ZnO eta ZnS nanopartikulak ikertu ditugu. Emaitza teorikoak esperimentuarekin alderatu ahal izateko, eredu errealistak eraiki ditugu.
- Bestetik, eta aurreko puntuko lanari jarraiki, ZnX (O = S, Se, Te) nanoegitura sorta zabal bat aztertu dugu.

1.2.3 Ligandodun Nanoegiturak Txikiak

Behin ligandorik gabeko nanoegiturak karakterizatutakoan, ligandodun ereduak ere aztertu ditugu. Atal hau bi lan nagusitan banatuko litzateke:

- Lehenik, $(ZnS)_6$ nanoegituran eta gainazaleko ligandoen arteko elkarrekintza ikertu dugu.
- Bigarrenik, ligandoek $(CdSe)_{13}$ nanoegiturarengan duten eragina aztertu dugu. Kasu hau bereziki interesgarria da, esperimentalki isolatu baita berriki.

1.2.4 Nanoegitura Errealistak

Aurreko ataletan eskuraturiko esperientzia lagun, eredu errealistak ikertu ditugu, biologian eta aplikazio fotovoltaikoetan duten garrantziarengatik. Biologiari dagokionez, bi gai jorratu ditugu:

- Batetik, CdSe eta CdSe@ZnS nanoegiturak aztertu ditugu. Gainazalean Pt(IV) konplexuak itsatsi dizkiegu, nanoegituraren eta konposatu organometalikoaren arteko elektroi garraioa ikertze aldera, prozesuak terapia fotodinamikorako duen garrantziarengatik.
- Bestetik, ZnS nanoegituren eta ur molekulen arteko elkarrekintza ikertu dugu. Izan ere, nanoegiturak *in vivo* erabili ahal izateko, ingurune urtsuan duten portaera ulertzeak berebiziko garrantzia du.

Aplikazio fotovoltaikoei dagokienez, bi ikerketaren emaitzak bildu ditugu Tesia honetan:

- Lehenik, Ru(II) konplexuen eta ZnO nanoegituren arteko elkarrekintza ikertu dugu, konposatu organometalikoaren eta oxidoaren arteko elektroi transferentzia eguzki energia elektrizitatean bilakatzeko lehen pausoa baita zelda fotovoltaiko askotan.
- Bigarrenik, PbS nanoegiturak erabili ditugu Ru(II) konplexuen ordez, azken belaunaldiko zelda fotovoltaikoetan erabili ohi baitira eguzki energia absorbatzeko.

1.3 Emaitzen Laburpena

1.3.1 DFT Metodoaren Aukeraketa

DFT metodo ezberdinen ikerketari dagokionez, PBE0 da azterturiko 26 funtzionalen artean zehatzena. Beste zenbait funtzional ere erabilgarri suerta daitezke nanoegitura erdieroaleak aztertzeko, baina Hartree-Fock trukea eduki dezaten ezinbestekoa da (funtzional hibridoak). Honek, ordea, kalkuluak garestitu egiten ditu. Kalkulua arintze aldera, GGA eta MGGA funtzionalak erabil daitezke, egitura eta propietate bibrazionalak egokiro deskribatzen baitituzte. Dena den, kitzikapen elektronikoen energiak nabarmenki gutxiesten dituzte. Eragozpen hau erraz konpon daiteke, espektro optikoa *a posteriori* energia handiagoetara lerratuz. Bestalde, oinarrizko egoerak GGA edo MGGA funtzionalekin deskriba daitezke, eta egoera kitzikatuetarako funtzional hibridoak erabili. Oinarri funtzioei dagokienean, def2-SV(P) eta SBKJC deritzenak dira denetan zehatzenak.

1.3.2 Ligandorik Gabeko Nanoegiturak

Behin DFT metodoa aukeratutakoan, ZnX (X = O, S, Se, Te) nanoegiturak aztertu ditugu. Wurtzita kristal egituran eraikiak, optimizatutakoan eraldatu egiten dira, gainazaleko atomo

asega-beak loturak osatzen saiatzen baitira. Eraldaketa hau ekidite aldera, gainazala H^+ (edo Zn^{2+}) eta HX^- (edo X^{2-}) ioiekin estali dugu. Honela, gainazaleko atomoak ase, nanoegituran zeharreko dipoloa ezabatu, eta wurtzita egitura egonkortu egiten direla egiaztatu dugu. Kalkulaturiko kitzikapen energiak bat datoz datu esperimentalekin. Trantsizio elektronikoak LUMO orbitalera gertatzen dira gehienbat, eroankortasun bandako gainerako orbitalak energia handigaoetarantz lerraturik baitaude. Aurkikuntza hau bat dator nanoegituren absortzio espektro zabal eta emisio profil zorrotz bereizgarriekin. X atomoak gainazaletik erauztearekin, egoera elektroniko lokalizatuak agertzen dira nanoegituran, elektroiak / zuloak harrapa ditzaketenak. Honek, ZnX nanoegituretan hain ohikoa den argi ikuskorraren igorpena azalduko luke.

1.3.3 Ligandodun Nanoegiturak Txikiak

Ligandoak, beraz, gainazaleko atomo asegabeetara itsasten dira, nanoegitura egonkortuz. Hau dela eta, nanoegitura-ligando lotura ulertzeak berebiziko garrantzia du. Norabide honetan sakontze aldera, $(ZnS)_6$ kluster ereduaren eta ligando ezberdinen arteko elkarrekintza ere ikertu dugu. Aminak, fosfinak eta fosfina oxidoak gogor itsasten zaizkio nanoegiturari. Lotura alkoholena, tiolena eta selenolena baino dezente sendoagoa da. Gainera, elkarrekintza nanoegiturara loturiko heteroatomoaren biguntasunarekin indartzen da. Bestalde, zenbat eta alkil talde gehiago ligandoan, eta zenbat eta luzeagoak alkil talde hauek, are eta sendoagoa lotura. Elkarrekintzaren naturari dagokionez, elektrostatikoa da gehienbat. Dena den, ekarpen orbitala ere esanguratsua da da, ligandoak itsasterakoan karga transferentzia eta polarizazioa gertatzen direla adieraziz. Nanoegitura-ligando lotura gainazalean itsatsiriko molekula kopuruarekin ahultzen da. Izan ere, ligando kopurua handitu ahala, euren arteko talka esterikoa handitu egiten da batetik, eta nanoegiturak karga onartzeko duen gaitasuna apaldu, bestetik.

Ligandoek ez dute nanoegitura egonkortzen soilik, propietate elektroniko eta optikoetan ere eragin baitezakete. Argi geratu da $(CdSe)_{13}$ nanoegituraren inguruan eginiko kalkuluetan. Amina alifatikoek nanoegituraren kitzikapen elektronikoak urdinerantz lerratzen dituzte. Dena den, ligandoen orbitalak balentzia eta eroankortasun banden sakonean agertzen dira, eta ez dute beraz kitzikapenetan parte hartzen. Amina aromatikoen orbitalak, ordea, nanoegituraren HOMO-LUMO tartetik gertu kokatzen direnez, kitzikapenetan elektronikoetan paper garrantzitsua joka lezakete.

1.3.4 Nanoegitura Errealistak

Izan ere, ligandoen orbitalak nanoegituraren energia mailekin egokiro lerratzen badira, elektroiak / zuloak harrapa ditzakete. Hau da, hain zuzen ere, CdSe (eta CdSe@ZnS) nanoegituren eta gainazalera itsatsiriko *cis,cis,trans* - $[Pt^{IV}(NH_3)_2(Cl)_2(O_2CCH_2CH_2CO_2H)_2]$ konplexuen artean gertatzen dena. Nanoegiturek fotoi bat xurgatutakoan, elektroia LUMO orbitalean kokatu litzateke, eta bertatik Pt(IV) konplexuaren LUMO edo LUMO+1 mailara

hel liteke. Transferentzia LUMO edo LUMO+1 orbitalera gertatu, Pt(IV) konplexuek erreakzio ezberdinak jasango lituzkete. Gure kalkuluen arabera, akoplamendua sendoagoa da LUMO+1 orbitalarekin, eta beraz, *cis,cis,trans* - $[Pt^{IV}(NH_3)_2(Cl)_2(O_2CCH_2CH_2CO_2H)_2]$ konposatua *cis* - $[Pt^{II}(NH_3)_2(Cl)_2]$ (zisplatinoa) bilakatuko litzateke, minbizi zelulak suntsitzeko baliagarria dena.

Beraz, nanoegituren eta ligandoen arteko elektroi trukeak garrantzia du fotokatalisian. Aplikazio fotovoltaikoetara begira ere, berebiziko interesa du. Eguzki zeluletan, esaterako, Ru(II) konplexuek elektroiak transferi diezazkiekete ZnO eta TiO_2 nanopartikulei argia xurgatutakoan. Ondorioz, Ru(II) molekulen (N3 eta N719) eta ZnO nanoegituren arteko elkarrekintza ere ikertu dugu. N3 eta N719 irmo itsasten zaizkio oxidoari. Elkarrekintza bereziki sendoa da konplexuek hiru azido talde erabiltzen badituzte gainazalean finkatzeko. Gure kalkuluen arabera, Ru(II) konplexuak ez lirateke gai ZnO nanopartikulari elektroiak emateko, LUMO orbitala oxidoaren eroankortasun bandatik behera baitute. Esperimentalki, ordea, transferentzia gertatu egiten da. Beraz, emaitza kontraesankor hauek aukeraturiko ereduari eta metodoari egotzi dizkiogu.

Aplikazio fotovoltaikoekin jarraituz, PbS nanopartikulak ere ikertu ditugu, azken belaunaldiko eguzki zeluletan argia absorbatzeko erabiltzen baitira Ru(II) konplexuen ordez. Azterturiko PbS nanoegiturak sendo itsasten zaizkie, (111) aurpegien bitartez, TiO_2 gainazalari. Elkarrekintza bereziki sendoa da TiO_2 (101) gainazalarekin. Maila elektronikoen apropos lerratzen dira elektroi transferentzia PbS nanopartikuletatik oxidora gerta dadin. Dena den, PbS eta TiO_2 gainazalaren orbitalak ez dira gehiegi nahasten. Honen arabera, karga transferentzia ez-adiabatikoki gertatuko litzateke.

Chapter 2

General Introduction

Everything we call real is made of things that cannot be regarded as real.

Niels Bohr

When it comes to atoms, language can be used only as in poetry.

The poet, too, is not nearly so concerned with describing facts as with creating images.

Niels Bohr

There is plenty of room at the bottom.

Richard P. Feynman

2.1 Nanotechnology

Over the last decades new branches of modern research, broadly defined as *nanoscience* and *nanotechnology*, have gained momentum [1, 2]. These new trends deal with the fabrication, characterization, and manipulation of nanosize structures. The first notions about nanotechnology were introduced in 1959 by the Nobel Laureate Richard P. Feynman in his visionary lecture *There's Plenty of Room at the Bottom* [3].

Since then, nanotechnology has grown at at a very fast pace triggered by the recent availability of revolutionary instruments and approaches that allow the investigation and the manipulation of material properties with a resolution close to the atomic level. Nowadays it encompasses a range of techniques rather than a single discipline and stretches across the whole spectrum of science, spanning physics, chemistry, materials science, engineering, and medicine. Nanotechnology is not only among the most active fields in science but it is also being gradually introduced into our daily life.

2.2 Nanostructures: Basic Principles

Nanotechnology deals with the design, development and production of nanostructures, *i.e.* structures sized between 1 and 100 nanometers. In particular, semiconductor nanostructures have gained ground due to their fundamental and technological importance. They exhibit novel properties that differ with respect to those of their bulk counterparts. There are two major effects responsible for the fascinating properties of semiconductor nanomaterials, namely surface effect and quantum confinement [4, 5].

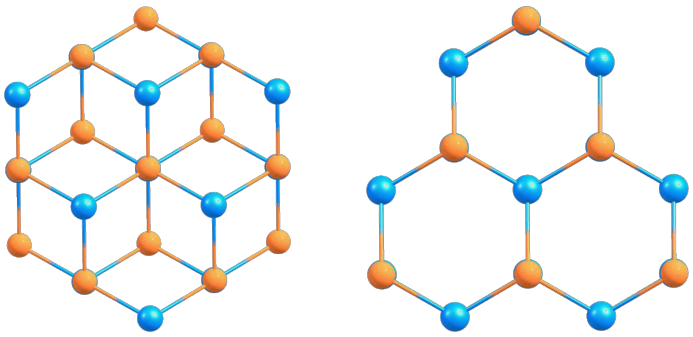
2.2.1 Surface Effects

2.2.1.1 Introduction

In nanostructures the number of atoms forming the surface is a substantial fraction of the total. Due to their lower coordination, surface atoms possess higher energy than the inner ones. In bulk materials, the surface plays a minor role and the stability is governed by the interior. However, with the decreasing size of the material and the increasing surface-to-volume ratio, surface dictates to a large extent the stability of the material. The large changes in thermodynamic properties of nanostructures, including melting temperature depression [6] and solid-solid phase transition elevation [7, 8], can ultimately be traced to this. At the nanoscale, the structure of a given compound is often determined by the minimization of the surface energy [9–11].

For example, zinc-blende structure is the lowest-lying polymorph for a wide variety of II-VI (II = Zn, Cd; VI = S, Se, Te) semiconductor materials in their bulk form. However, as the size of the material approaches the nanoscale, the wurtzite polymorph becomes thermodynamically favored [12] (see Figure 2.1).

Figure 2.1: Crystal structures of the zinc-blende and wurtzite phases.

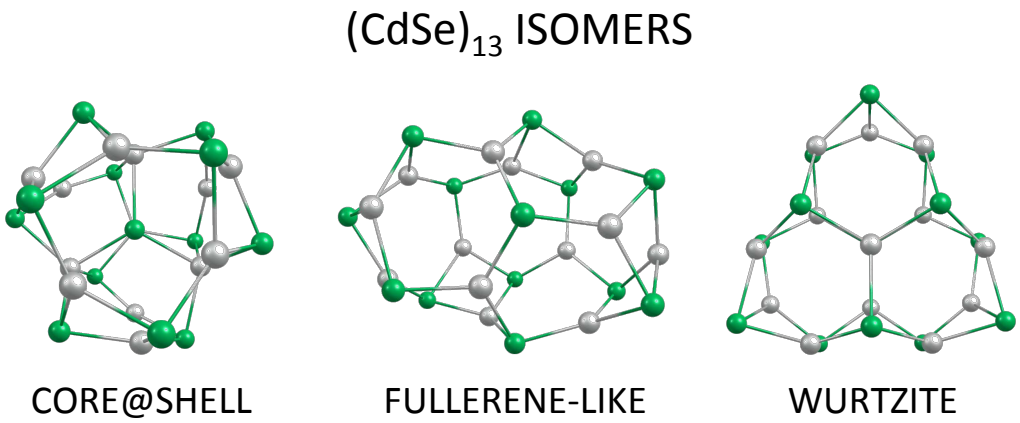


In ultrasmall nanostructures, the surface effects are even more important. Recently, ultrasmall nanostructures have been proven to adopt amorphous geometries [13]. They expe-

rience a drastic transformation relative to the bulk phase, driven by the rearrangement of the surface atoms. The surface reconstruction penetrates deep inside the structure, in such a way that the bulk structure is no longer recognizable. Interestingly, this kind of ultrasmall nanocrystals behave fluxionally [14]. They undergo dynamic structural transformations at room temperature. The geometric changes are reflected on the absorption and emission features, which change over the time.

Nanoclusters comprising a few tens of atoms, typically prepared in the gas phase by laser vaporization [15–17] but recently feasible in solution [18–20], have been predicted to adopt structures hardly conceivable from the bulk [21–25]. Indeed, since there is no clearly identifiable interior in clusters of this size, unique bonding geometries emerge. Among the exotic arrangements reported so far, fullerene-like cages and core@cages clusters are worth mentioning (see Figure 2.2).

Figure 2.2: Core@cage-, fullerene-, and bulk-like isomers of the magic $(CdSe)_{13}$ cluster.



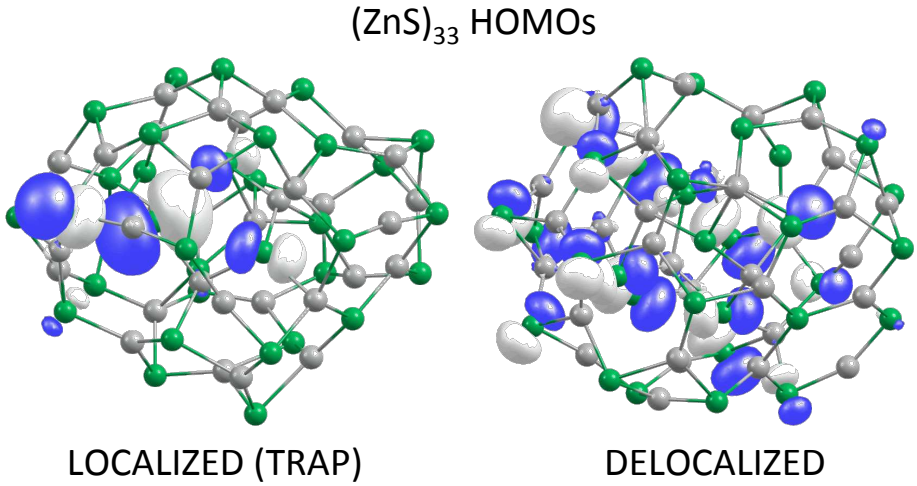
2.2.1.2 Defects

Surface plays an important role on the electronic and optical properties of the nanostructure [26]. Defects on the surface (dangling bonds, vacancies, dimes, etc.) give rise to localized states that intrude into the intrinsic bandgap of the nanostructure. In Figure 2.3 two representative HOMO orbitals are shown, calculated for the $(ZnS)_{33}$ cluster along a Car-Parrinello Molecular Dynamics simulation. The one on the left hand side, which arises from unsaturated atoms on the surface, is localized. The one on the right hand side, instead, is spread over the whole cluster.

Localized states are known to act as trap states for the photogenerated charge carriers (electrons and holes), reducing the overlap between the electron and hole and increasing the probability of nonradiative decay events. Since surface traps degrade the electronic and optical properties of nanostructures, a great deal of research is being devoted to prevent their occurrence. Recently, however, sulfur vacancies have been predicted to favor the electron transfer from PbS Quantum Dots (QDs) to surface attached rhodamine molecules by

increasing the donor-acceptor interaction [27]. Defects seem to be instrumental rather than detrimental to functioning of QD-based photovoltaic devices. This counterintuitive finding generates an unexpected picture on the QD surface chemistry and stimulates new research lines.

Figure 2.3: Localized and delocalized HOMO orbitals of the $(ZnS)_{33}$ cluster, calculated for representative snapshots taken from a Car-Parrinello Molecular Dynamics simulation.



2.2.1.3 Ligands

Due to the large surface-to-volume ratio inherent in nanostructures, the environment exerts a fundamental effect on the structural and optoelectronic properties. Ligands and solvent molecules are known to cap the unsaturated surface atoms, lower the surface energy, and stabilize the whole nanostructure [28–32]. Interestingly, the bonding structure of the nanomaterial depends critically on the nature of the surfactants [33]. This opens up the possibility of manipulating the surface energetics of nanostructures in a controlled fashion. Over the last few years, the development of new capping ligands and the multicomponent mixtures of stabilizing agents have led to a plethora of nanostructural morphologies [34].

From a different perspective, surface ligands determine the solubility of the nanomaterial. Semiconductor QDs are usually synthesized in nonpolar organic solvents, in combination with hydrophobic ligands. To make them soluble in aqueous media, where most of the nanomaterials operate, the native ligands must be replaced by amphiphilic ones. Ligand exchange is also important to decorate the nanoparticle surface with particular molecules that could interact with specific analytes, subcellular structure, electrodes etc. [34].

Apart from imparting thermodynamic stability, modifying solubility, and providing chemical functionalization, surface attached molecules are known to shape the electronic structure of the nanostructure [35]. The saturation of the dangling bonds prevents the appearance of localized midgap states. Unfortunately, the steric interactions between the bulky organic

ligands typically employed in colloidal synthesis prevent the full passivation of the nanostructure. Some of the surface sites are unterminated and the appearance of midgap states is therefore unavoidable. In this respect, inorganic passivation has emerged as an interesting alternative [36]. Embedding the nanostructure in wide-bandgap inorganic material has shown to effectively prevent the appearance of trap states.

However, the chemical functionalization of the nanostructure surface with specific ligands allows the fabrication nanocomposite materials with fascinating properties. In particular, the appropriate alignment of the electronic levels might promote charge transfer processes in the nanocluster-ligand interface upon photoexcitation. This kind of devices have attracted a great deal of interest with a view to their applications in photovoltaics and medicine (see Section 2.4).

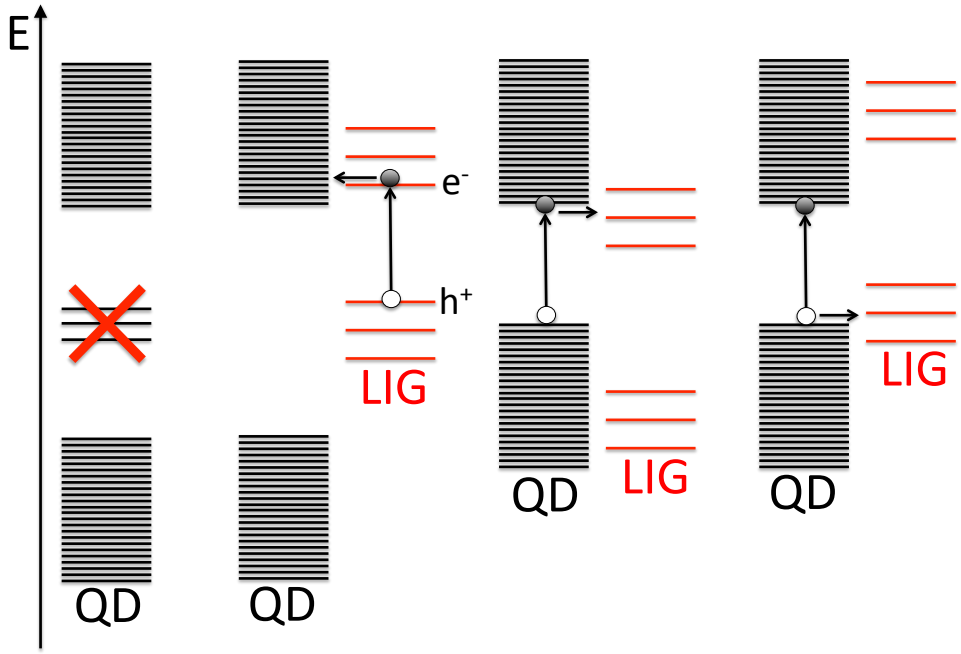
Dye Sensitized Solar Cells (DSSCs), for instance, are composed by a network of sintered semiconductor nanoparticles, grafted with a monolayer of sensitizing dye. This latter absorbs solar radiation and injects the photoexcited electrons into the conduction band of the semiconductor. The concomitant hole is then usually trapped by an electrolyte, closing the circuit [37].

In other kind of nanocomposites, the nanostructure acts as electron donor and the surface ligand as the acceptor. Recently, CdSe and CdSe@ZnS QDs have been shown to photoreduce Pt(IV) complexes and deliver cisplatin-like species. Upon irradiation, electrons are promoted from the valence to the conduction band of the QD and subsequently transferred to the surface adsorbed Pt(IV) species. The electron transfer, driven by electronic coupling, is able to lead to different photoproducts. Such exciting result suggests that it might be possible to control photoreactions and select a specific photochemical pathway among several by tailoring the interaction between the semiconductor nanostructure and the metal complex [38].

In other applications, holes are transferred between the nanostructures and the surface molecules. In QD Sensitized Solar Cells, the QDs play the role of the dye in DSSCs, absorbing solar radiation and injecting the photoexcited electrons into the manifold of unoccupied states of the wide-gap semiconductor [39, 40]. The electron injection competes with charge recombination in the QD, which might lead to an overall diminished conversion efficiency [41]. To prevent recombination events and overcome conversion looses, Ru(II) complexes are being tested to scavenge the photogenerated holes from the QD [42–44]. Likewise, Ru(II) catalyst have been reported to sequester holes from CdS nanorods, followed by electron transfer that restores the system. The latter process is found to be slow, which may provide opportunities for the accumulation of multiple holes at the Ru(II) catalyst, a vital prerequisite for water oxidation [45]. In a similar fashion, dopamine molecules are known to sequester holes from QDs [46]. The as generated dopamine cation might act as oxidant. On the other hand, the unpaired electron in the QD might migrate to the surface and promote reduction reactions. This kind of reactions are known to produce highly reactive species, with potential application for the destruction of cancer cells.

In Figure 2.4 the various effects of the surface ligands on the QD's electronic structure are summarized.

Figure 2.4: Various effects of surface ligands on the QD's electronic structure, including surface state removal, electron injection (both from and to the ligands), and hole sequestering.

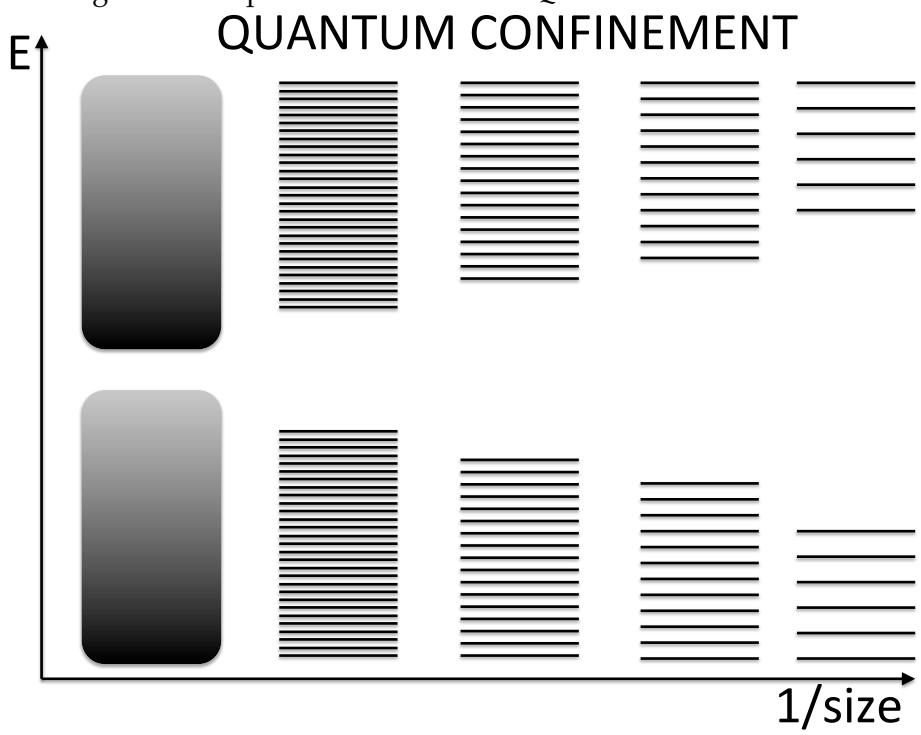


2.2.2 Quantum Confinement

2.2.2.1 Introduction

Regardless of the large surface-to-volume ratio inherent in nanometric materials, semiconductor nanostructures with the same interior bonding geometry as a known macroscopic phase exhibit novel electronic and optical characteristics [4, 5]. With the decreasing size of the material quantum confinement effects arise and charge carriers start behaving as particles in a box. The electronic structure evolves from the limit of the continuous bands in extended solids to the limit of discrete electronic levels in molecules (see Figure 2.5). In this sense, nanostructures represent an interesting paradigm between bulk crystals and small molecules, enabling the exploitation of the useful properties of the former, but displaying the discrete electronic transitions reminiscent from the latter [47]. As the size is reduced, the electronic excitations shift to higher energy, and the oscillator strengths concentrate into just a few transitions. Interestingly, the electronic structure depends critically on the size and the shape of the nanostructure. Such a dependence was discovered independently by the early 1980s in two different materials: in semiconductor doped glasses by Ekimov et al. [48], and in colloidal solutions by Henglein [49]. Since then, the *ad hoc* modification of the electronic and optical properties with the size and the shape has attracted a great deal of research.

Figure 2.5: Impact of the size on the QD's electronic structure.



From a different perspective, impurity doping [50, 51], design of new core@shell nanocomposites [52], and strain tuning [53] are opening new avenues for electronic and optical engineering of semiconductor nanostructures.

Impurity Doping

The on-purpose introduction of impurities aimed at tailoring the electronic and optical properties of bulk semiconductors has lied for long at the heart of many technologies. More recently, doping of nanostructures has earned lots of attention. Dopant atoms with one more valence electron than the host atom (*n*-type doping) donate the extra electron to the nanomaterial, whereas impurities with one less valence electron (*p*-type doping) provide an extra hole. These charge carriers are available to produce electrical current, which is of prime importance for many applications of semiconductor nanostructures [50].

From a different perspective, dopant atoms play a crucial role on the optical properties. For instance, the absorption and emission features of ZnS nanostructures shift from the UV to the Vis upon Mn doping. The resulting nanocomposites are gaining ground in biology against the classical CdSe nanoparticles, due to the toxicity of Cd [54, 55]. Furthermore, doping might protect nanomaterials against photooxidation. The charge carriers generated upon photoexcitation often recombine in the impurity [55], suppressing undesirable redox reactions on the surface [49, 56].

Unfortunately, the field of nanomaterial doping is still in its infancy. The number of impurities per nanostructure is still small, and their location and number vary significantly [57]. This fluctuations lower the performance of the doped material. Consequently, a great deal

of research is being devoted to the understanding of the doping process and to the development of doping strategies. On the latter, the most common route for doping is to include precursors containing the impurity in the synthesis [58]. A second strategy implies the synthesis of semiconductor clusters already containing the impurity, which act as a seed for the nanomaterial's growth [59].

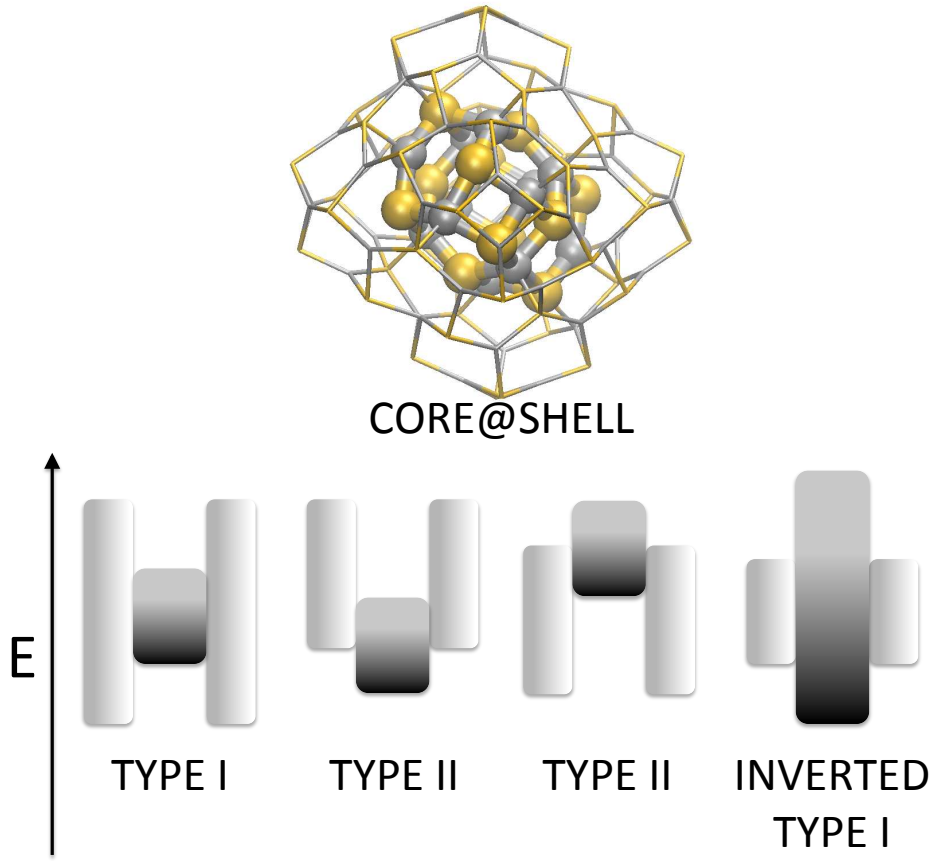
Mn and Co are probably the most widely exploited dopants in the field of semiconductor nanomaterials [57]. Nevertheless, in II-VI compounds they are isovalent with the metal cations for which they substitute and therefore can not provide extra charge carriers. Heterovalent doping is still in its infancy, and progress is still slow. Recent developments include Mn-doped InAs [60], Li-doped ZnO [61], and P- and B-doped Si [62].

Core@Shell Nanocomposites

Core@shell nanocomposites contain at least two semiconductor materials in an onion-like structure (see Figure 2.6, top). The possibility of tailoring the electronic and optical properties of the core by growing a shell of another semiconductor has triggered significant progress in the field [52]. CdSe@ZnS is the classical example of a core@shell nanostructure [36]. In this kind of nanocomposites, where the band alignment is designated as type-I (see Figure 2.6, bottom), the electrons and holes generated upon irradiation are confined in the core material. The shell, with its wider bandgap, electronically passivates the core and prevents photooxidation. Inverted type-I alignments are also possible, allowing the charge carriers to be localized in the shell material [63].

In core@shell nanocomposites with type-II alignment, the valence and conduction bands of the core and shell materials are staggered, resulting in the separation of the charge carriers between the core and the shell [64]. For instance, in CdTe@CdSe nanostructures the valence band edge (and therefore the photogenerated hole) localizes in the core, whereas the conduction band edge (and therefore the photogenerated electron) is spread over the shell. In type-II nanomaterials, during the shell growth the absorption features of the core shift to the red. Furthermore, due to the reduced spatial overlap between the charge carriers, the intensity of the lowest-lying excitations decreases, while the excited state lifetimes increase significantly. Then, the charge recombination occurs across the interface at a lower energy than the bandgap of the constituent materials [53]. Type-II materials have earned lots of attention in photovoltaics, because the segregation of the charge carriers may enhance directional charge transport in electronic devices [65]. Furthermore, they allow controlling which charge carrier is accessible to the surface of the nanocomposite, which is of prime importance for charge transfer applications and catalysis.

Figure 2.6: Archetypical example of a core@shell QD (top). Schematic representation of the energy-level alignment in different core@shell systems (bottom). The upper and lower edges of the rectangles correspond to the positions of the conduction- and valence-band edges of the core (center) and shell materials, respectively.



Strain Tuning

Semiconductor nanomaterials are greatly influenced by structural strain [53]. In core@shell composites, the mismatch in the bond lengths of the constituting materials (12% in the archetypical CdSe@ZnS composites) generates a strain field in the nanostructure. Deviations from the optimal bond length shift the valence and conduction band edges and modify nanomaterials' absorption and emission features. As a rule of thumb, compressive strain shifts the band edges to higher energies, whereas tensile strain moves them downwards.

Apart from the tunability of the electronic structure, quantum confinement effects give rise to novel electronic and optical properties hardly conceivable in the bulk material. They are summarized in the following sections.

2.2.2.2 Electronic Excitations in Semiconductor Nanostructures

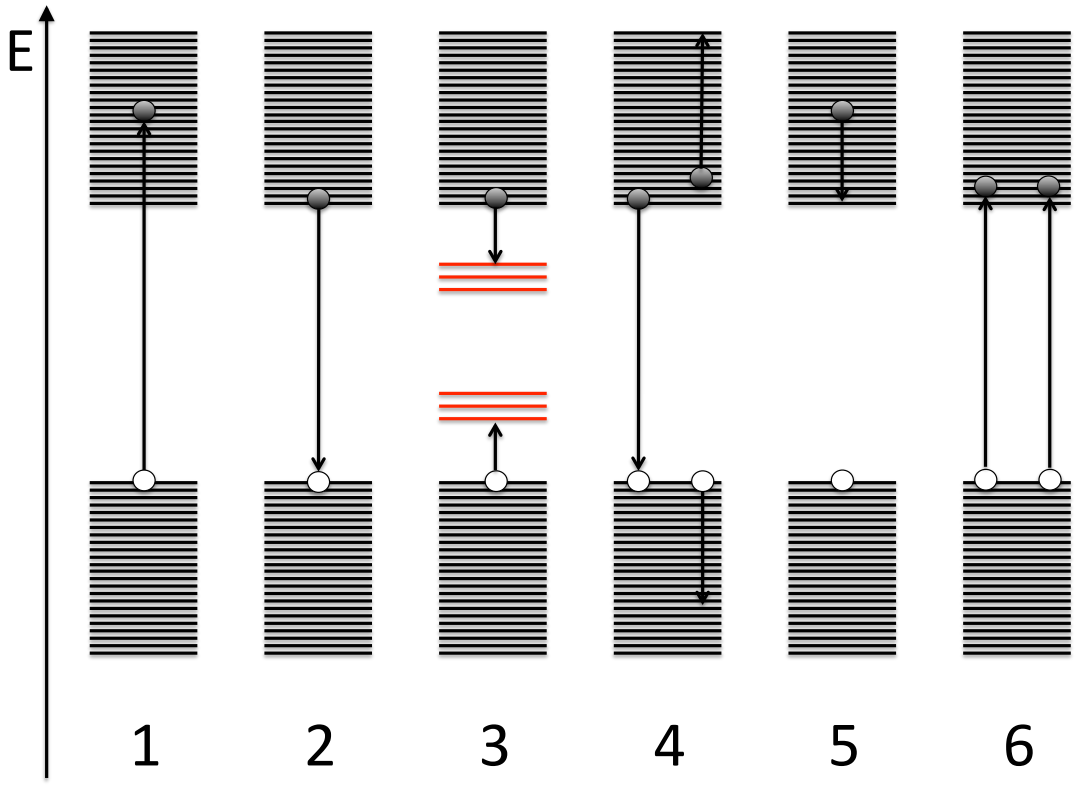
Many of the applications of semiconductor nanomaterials involve interaction with light. As previously stated, the absorption of a photon with an energy equivalent to the bandgap promotes an electron to the conduction band and an electron-hole pair is created, also known as

exciton. Besides the lowest electronic excitation, which implies a transition from the highest occupied to the lowest unoccupied states, there is a dense manifold of excited states available for energies of the incident photon exceeding that of the bandgap. One of the longest standing and most important topics in nanostructure science is the understanding of the complex excitation dynamics following photon absorption [47,66].

Luminescence, be it fluorescence or phosphorescence, implies radiative relaxation from the first excited state to the ground state. With a view to their application as sensors, unveiling the principles governing this kind of processes is of vital importance. Related to this, intermittent emission or ***blinking*** is an intriguing property of semiconductor QDs.

From a different perspective, the relaxation pathways from high-lying excited states to the first excited state have attracted a great deal of theoretical and experimental research. This process, also known as carrier cooling, is a key parameter to improve the performance of nanostructure-based photovoltaic devices. Among the mechanisms proposed to explain the hot exciton relaxation dynamics, ***Auger recombination*** and ***electron-phonon coupling*** are probably the most important ones. From a different perspective, and closely related to the hot exciton dynamics, it is the ***multiple exciton generation***. In the following, the key factors governing the excited state dynamics of semiconductor nanostructures are summarized (see Figure 2.7).

Figure 2.7: Summary of the photoinduced electronic processes in semiconductor QDs. (1) Absorption. (2) Luminescence. (3) Carrier trapping. (4) Auger recombination. (5) Carrier cooling (mainly by means of electron-phonon coupling). (6) Multiple Exciton Generation.



2.2.2.3 Luminescence and Blinking

The emission from single semiconductor nanostructures is often intermittent [67]. This phenomenon, also known as blinking, provides an elegant means to identify single, isolated nanostructures [53]. As a drawback, it has often resulted in problems for tracking the motion of particles in biological environments due to the repeated loss of signal [68]. So far, two main mechanisms have been proposed to explain the on/off behavior of semiconductor nanocrystals. The first one assumes that the nanostructures undergo Auger ionization (*vide infra*), in such a way that radiative electron-hole recombinations are no longer possible. Accordingly, in low dielectric media that poorly solvates the expelled electrons, the off time is expected to diminish [69]. The second hypothesis implies trap states on the surface. Upon photoexcitation, electrons and holes are supposed to get trapped on localized surface sites. The small overlap between the electron and hole wave functions would avoid their radiative recombination. Ligand adsorption removes the trap states and improves the luminesce of the nanostructure [69]. Besides, embedding the nanocrystal in an insulating shell yields deeper and wider potential well, which in turn decreases the off time [70, 71].

2.2.2.4 Auger Recombination

The strong confinement of charge carriers in ultrasmall nanostructures implies a strong Coulomb interaction between electrons and holes. It manifests itself very clearly in Auger recombination and Multiple Exciton Generation processes (*vide infra*). On the former, the excess energy given off by an electron recombining with a hole is given to a third charge carrier. In some cases, the recombination energy produces the ionization of the newly excited electron, which could explain the on/off emission (*vide supra*). Typically, however, the hot electron relaxes back to the edge of the band, often by means of electron-phonon interaction (*vide infra*).

If the electrons and holes densities of states are asymmetric, as it is the case for most nanostructures, rapid Auger energy exchange funnels excitation energy from electrons to holes, due to the denser manifold of states of the latter [72, 73]. Symmetric density of states, as those found in PbS and PbSe nanostructures, renders the Auger channel inefficient, and electron-phonon coupling dominates [73, 74].

2.2.2.5 Electron-Phonon Coupling

In bulk semiconductors, due to the dense manifold of states at the band edges, the electronic states can dissipate energy and cool *via* coupling with phonons. In semiconductor nanostructures, however, the quantization of electronic levels should lead to mismatches between electronic gaps (*ca.* 50-200 meV) and phonon frequencies (*ca.* 2 and 20 meV for acoustic and optical phonons, respectively) [47, 66]. Consequently, a dramatic slowing of electron-phonon relaxation, known as phonon bottleneck, can ensue [75]. With a view to

the application of semiconductor nanostructures as light harvesters, this is an interesting scenario. By slowing electronic energy decay, phonon bottleneck would minimize energy losses in photovoltaic solar cells, enable the extraction of hot electrons/holes, and allow the generation of additional charge carriers [75–78].

Surprisingly, relaxation times show a broad spread from 100 fs to 1 ns [79]. Furthermore, exciton cooling appears to accelerate with decreasing nanostructure size and the increasing electronic energy spacing, in direct opposition to expectations from the phonon bottleneck picture [73,74]. Only under very special conditions slow relaxation rates have been observed [80].

Several hypothesis have been put forward to explain such unexpected findings. Auger-type recombinations have been predicted to break the phonon bottleneck by allowing energy transfer from the excited electrons to holes. In virtue of the higher effective mass of holes and the denser manifold of states at the top of the valence band relative to the conduction band, phonon-mediated relaxation of holes is predicted to occur rapidly [72,81].

Quite recently, state-resolved spectroscopy experiments have proven the electron-phonon coupling to be state-dependent [66]. In line with the experiments, computational simulations have revealed that, except for the lowest excitations energies, electronic energy spacing matches phonon frequencies, explaining the absence of phonon bottleneck [82,83]. For the lowest-lying excited states, *ca.* 0.3-0.6 eV of the electronic energy would be transferred to phonons according to the theoretical results. Alternatively, multiphonon relaxations might also occur.

From a different perspective, nanostructures undergo dynamic transformations under room temperatures. Surface reconstruction and thermal fluctuations break degeneracies inherent in pristine structures and create complex distributions of electronic states [83]. The so generated surface defects could bypass the phonon bottleneck by opening new radiative relaxation pathways for the excited electrons/holes [73,84].

Finally surface attached ligands, by means of their high-frequency vibration modes, have been predicted to play an important role in the relaxation of the hot charge carriers in the nanostructure [85,86].

2.2.2.6 Multiple Exciton Generation

In photovoltaic materials, photons exceeding the energy of the bandgap often create highly excited charge carriers that, when relaxing to their lowest excited state by means of carrier-phonon coupling, dissipate the energy surplus as heat. If the energy lost to heat were used to generate multiple charge carriers, or multiple charge carriers were generate by absorption of a single photon, the efficiency of the device would increase significantly. This property, also known as carrier multiplication (CM) or multiple exciton generation (MEG), is one of the main characteristics of semiconductor nanomaterials. Unlike in their bulk counterparts,

MEG is particularly efficient in semiconductor nanostructures, due to the strong Coulomb interactions and slower nonradiative losses [87].

MEG in semiconductor nanostructures appears within 100 fs of photoexcitation and endures for tens to hundreds of picoseconds [88]. There are two main mechanisms involved in MEG. The ultrafast component arises from the coherent excitation of more than one electron, due to the confinement-enhanced Coulomb interactions and the almost continuous band structure. Due to the dense manifold of electronic states, MEG can also occur by means of incoherent Coulomb scattering, which is slower than coherent MEG. In this process, often found in bulk semiconductors, the highly excited charge carriers relax to their ground and excite new valence electrons across the bandgap [89].

2.3 Nanostructures: Colloidal Synthesis

2.3.1 Introduction

Over the past years several routes have been devised for the production of semiconductor nanostructures. Among them, colloidal techniques have emerged as a new branch of synthetic chemistry. Starting with preparations of simple nanomaterials, the field is now moving towards more and more sophisticated objects where the size, the morphology, and the assembly of multiple parts can be precisely tailored at surprisingly low cost [34].

Colloidal nanomaterials are obtained by reacting the appropriate molecular precursors in solution. The formation of the nanostructure implies the nucleation of the seeds and their subsequent growth. For a narrow size distribution of the products a temporal separation of the nucleation and growth stages is mandatory. The hot-injection technique firstly proposed by Bawendi et al. [90] satisfies this requirement.

Solution phase techniques often require the presence of organic molecules, that dynamically adhere to the surface of the growing material. These surfactant molecules play a key role in modifying the kinetics of the nucleation and growth processes, which in turn determines the size and the shape of the resulting material. Indeed, if the nucleation stage is too fast or too slow with respect to the growth, molecular clusters or bulk crystals will form. The appropriate balance between this two processes is vital for the production of materials with the desired size and shape. This is a challenging problem,which has earned lots of attention [91].

Since the seminal work by Bawendi et al., colloidal routes have undergone a vertiginous development. Nowadays, semiconductor nanostructures with finely tuned properties are routinely produced, based on the appropriate choice of molecular precursors, surfactants, solvent, and reaction conditions. II-VI [90, 92–96], III-V [97–99], and IV-VI [100–106] nanostructures are synthesized at high temperature, in the presence of long-chain alkylphospines, alkylphosphine oxides, alkylphosphonic acids, or alkylamines. Aliphatic are the typical solvents where the reactions are carried out. However, water is gaining ground

as an interesting alternative to the classical organic solvents. Recently, several examples of high-quality semiconductor nanostructures synthesized in aqueous medium have been reported [19, 20, 107–109]. In order to confer hydrosolubility to the nanomaterial, bifunctional ligands are used. Typically, thiol moieties are used to anchor the nanostructure surface and carboxylic/amino groups to confer colloidal stability [107]. The nanomaterials synthesized in water lack of the high monodispersity commonly obtained with organic solvents, but they are very competitive in terms of luminescence efficiency, colloidal stability, and cost [34].

2.3.2 Design of Surface Ligands and Ligand Exchange

As mentioned above, the choice of the surfactant molecules is a critical parameter in the synthesis of colloidal nanostructures. They control not only the nucleation and growth processes, but also impart chemical and colloidal stability to the nanomaterial. Furthermore, they allow the assembly of individual nanoparticles into nanostructured solids. In this respect, the linker molecules determine the interparticle distance and therefore the electronic properties of the assembled material [34].

The typical capping ligands are based on organic hydrocarbon molecules with functional end groups (thio-, amino-, carboxylic, etc.) to anchor the nanostructure surface. Dodecanethiol, oleylamine, hexadecylamine, oleic acid, phosphonic acids, and triocylphosphine oxide (TOPO) are typical examples [110–112]. In spite of being appropriate for colloidal synthesis in organic solvents, they act as insulating barriers [34]. Therefore, they are not amenable for a wide range of applications where charge transport is crucial. From a different perspective, this kind of ligands lack of a second functional group, which could serve to confer water solubility, to facilitate nanostructure assembly, or to enable conjugation with other molecules or surfaces. Exchange of the bulky organic ligands by other capping molecules is a common strategy. However, removing the native ligands often creates surface dangling bonds and midgap states that deteriorate the nanomaterials' properties [113].

The ligand exchange implies the exposure of the native nanomaterial to a large excess of competitive ligand [90, 113, 114]. This procedure results in a partial or a complete exchange of the native molecules, driven by mass action. The exchange is often conducted at low temperature, to prevent the evaporation of ligands such as pyridine [90] or butylamine [115], often used in this operation. The process is favored by the phase separation of the products [116]. The exchange process is typically monitored by means of NMR [113, 117], FTIR [118], or XPS [117, 119].

Ligand exchange reactions are often divided into two groups. The first one comprises exchange for molecules with the same head group. Thiol-for-thiol exchange represents a classical example. In this kind of reactions, the length of the alkyl tail has been reported to play a crucial role in the exchange process, since the molecules have to penetrate through the shell of the native ligands [120]. Combining NMR and FTIR techniques, Hostetler et al. found that the smaller was the tail of the leaving group, the higher was the exchange rate [120]. Phase transfer reactions are used to replace alkylthiols by hydrophilic thiols [116, 121].

The second group involves the use of molecules with different head groups. Pyridine is typically employed to substitute the shell of the native ligands [90]. Pyridine-capped QDs are insoluble in nonpolar aliphatic solvents, but dispersible in more polar solvents. Moreover, pyridine capping often serves as intermediate to achieve the desired functionalization of the QD surface [122,123]. Indeed, pyridine molecules are known to weakly interact with the QD surface. Therefore, they are easily replaced by other molecules or removed by vacuum and/or heat treatments. In some cases, pyridine capping has shown to enhance QD's charge transport and photoconductivity [124].

Ligand exchange is sometimes used to improve the colloidal stability of QDs. The replacement of the original triphenylphosphine ligands with thiol molecules was shown to stabilize Au QDs [125].

The exchange of the original bulky ligands by smaller ones in solution-phase implies the decrease of colloidal stability, which often leads to nanoparticle aggregation. To overcome this drawback, exchange is sometimes applied in QD film or supperlatices. Short-chain molecules have been successfully placed on QD surfaces by this mean [105,126]. Similarly, molecules with two functional ends are often incorporated to QD lattices. This treatment decrease the inteparticle distance and improve the electronic properties of the QD assembly.

In polar solvents, ligands with charged head groups (*i.e.* $RCOO^-$ or $RNH_3{}^+$) ensure the colloidal stability of the QDs. These functional ends repel each other and prevent QD aggregation [107].

To improve the electric properties in QD assembled nanostructures, the native ligands are often substituted by capping molecules that support charge transport. Among them, conductive conjugated polymers and oligomers represent a typical example [127,128].

2.4 Nanostructures: Applications

Semiconductor nanostructures have found application in a wide variety of fields including, among others, photocatalysis, optical sensing, photovoltaics and biology.

2.4.1 Photocatalysis

Electronic excitations in semiconductor QDs result in charge separation. Due to the strong confinement imposed by the small size of QDs, the majority of carriers recombine *via* radiative or nonradiative processes. However, a small fraction (about 10%) of photogenerated electrons and holes migrate to the surface, where redox reactions can take place [129–132].

In order to enhance the photocatalytic activity, semiconductor QDs are often combined with noble metal nanoparticles (Pd, Pt), which largely improve the interfacial charge transfer. They are known to promote charge separation within the QD, discharge electrons across the interface, and provide redox pathways with low overpotential. Furthermore, since metal

nanoparticles collect the photogenerated charges, the semiconductor-metal nanocomposites remain redox-active after dark storage for several hours.

The surface bound metal nanoparticles not only enhance the photocatalytic activity, but also determine product selectivity and greatly stabilize the QD. On the latter, semiconductor QDs often suffer from etching when irradiated, stemming from anion oxidation. Pd/Pt islands on the QD surface prevent this kind of processes by scavenging photogenerated carriers.

2.4.2 Optical Sensing

Organic fluorophores have long been used for the detection of a wide variety of ions and ligands, since their absorption and emission features are modified due to the interaction with the target molecule [133]. Recently, semiconductor QDs have gained ground in the field of sensing and have found application in a wide variety of nanocomposites. For example, QDs can serve as passive carriers for surface attached fluorophores [134–136]. The signal intensity of this kind of heteroestructures is significantly enhanced because each QD bears several fluorophores on its surface. Furthermore, different fluorophores can be coupled to each QD, allowing ratiometric detection. With a view to their application in biology, QDs open new pathways of cellular uptake, compared to those of the free fluorophores.

When the optical features of the QD and the fluorophore overlap, energy transfer from the former to the latter might occur. By means of this process, also known as Förster Resonance Energy Transfer (FRET), QDs are able to tailor the effective fluorescence lifetimes of the fluorophores [137,138].

Owing to their salient emission properties and resistance against photobleaching, QDs by themselves are promising alternatives to organic fluorophores [4, 5]. The fluorescence intensity of QDs is modified when ions or ligands are bound to their surface, allowing their detection [139,140]. For instance, ion-induced generation of surface states have been proven to quench emission. Besides, certain surface coatings are known to sequester charge carriers and dampen the fluorescence signal. In this cases, ion binding prevents charge trapping, abolishes quenching, and restores QD emission [46,141].

In other kind of QD nanocomposites, the actual sensing is performed by surface ligands bearing a quencher. Upon ion binding, ligands undergo conformational changes that alter the distance between the quencher and the QD surface and thus the QD emission [142]. Similarly, QDs have shown to effectively quench the emission of organic fluorophores. This strategy has been successfully exploited for the detection of several metal cations. For instance, He et al., designed pyridyl functionalized Au nanoparticles for Cu^{2+} sensing [143]. Upon Cu^{2+} binding, pyridyl ligands were shown to desorb from the QD surface, so ligand fluorescence was no longer quenched. A similar approach was adopted by Huang and Chan, who designed Au nanoparticles bearing rhodamine B molecules for Hg^{2+} detection [144].

2.4.3 Photovoltaics

Semiconductor QDs have earned lots of attention in the solar cell community due to their paramount technological potential [145–149]. They lie at the heart of several nanostructural architectures for solar energy conversion, including bulk-heterojunction hybrid solar cells [150, 151] and QD sensitized solar cells (QDSSCs) [39, 40].

QDSSCs consist of a mesoporous wide-gap semiconductor, typically TiO_2 or ZnO, grafted with a monolayer of sensitizing QDs, which absorb solar radiation and inject the photoexcited electrons into the manifold of unoccupied states of the oxide. The concomitant hole is then restored by an electrolyte, closing the circuit. QDSSCs have gained ground against the classical DSSCs, due to the ease of their preparation and their lower cost.

QDs possess interesting properties for light harvesting. In particular, the on-purpose modification of the bandgap with the size and the shape allows to span the broad solar spectrum [4, 5]. Modifying the bandgap an appropriate match with the solar spectrum can be attained, but the electron transfer to the wide-gap semiconductor can also be favored, due to a better alignment of the electronic levels. Decreasing the particle size rises the conduction band of the QD and facilitates the charge injection processes by increasing the driving force. Concomitantly, the optical onset shifts to higher energies, which in turn causes relatively poor absorption of incident visible photons. The intricate balance between these two opposing effects determines the overall photocurrent generation in QDSSCs. From a different perspective, high extinction coefficients and large dipole moments, intrinsic to QDs, make them amenable for light absorption [152]. Besides, they provide opportunities to increase solar cell voltage and current, by either extracting hot carriers of taking advantage of the Multiple Carrier Generation [88, 153, 154]. QDDSCs are therefore potentially able to overcome the Shockley-Queisser limit of 33% energy conversion efficiency [155].

Unfortunately, QDSSCs have performed quite disappointingly so far, with reported efficiencies of about 5% for PbS sensitized devices [156]. The field of QDSSCs is still in its infancy and much effort is being devoted to the understanding of the foundations governing their performance.

There are peculiarities inherent to QDs that could explain the poor performance of current QDSSCs nanocomposites. On the one hand, due to their large surface-to-volume ratio, semiconductor QDs usually develop localized surface states that might act as trap states for the photogenerated charge carriers and lower the efficiency of the cell [26, 157, 158]. On the other hand, in QDSSCs the interfacial electron transfer competes with several fast recombination pathways in the QD [41]. Capping the QD with hole scavengers has shown to prevent internal recombination processes and to favor electron injection into the wide-gap oxide [159, 160].

Many other reasons have been put forward to explain the low efficiencies of QDSSCs, among which is the narrow absorption spectrum range of the QDs currently used. In an effort to improve light harvesting over a broad range of wavelengths, QDs of different sizes [161,162]

and compositions [163–165] are combined. On the latter, the co-sensitization of the wide-gap semiconductor with CdS/CdSe [163,164] and CdS/PbS [165] QDs has shown to improve the performance of the cell. A similar strategy implies the combination of QDs and Ru dyes as panchromatic sensitizers. This kind of nanocomposites merge the absorption ranges of both components [40, 166]. Moreover, dye molecules sequester the photogenerated holes from QDs, reducing internal charge recombination and improving electron injection [42–44].

The adsorption of QDs on the semiconductor surface also plays a vital role on the performance of the solar cell. The deposition techniques are often classified into two classes, namely *in situ* and *ex situ* [39]. The *in situ* methods, including chemical bath deposition (CBD) [167] and successive ionic layer absorption and reaction (SILAR) [168,169], imply the growth of the QDs directly on the semiconductor surface. High surface coverage and direct connection between the sensitizer and the semiconductor surface are obtained, but they offer poor control over QD's size, shape, and surface capping. An improper passivation often results in the appearance of surface traps, which in turn favor internal recombination processes and hinder electron injection. *Ex situ* methods, which involve the attachment of ligand-capped QDs on the oxide surface, overcome these drawbacks, because presynthesized QDs are easily controllable in terms of size, shape, and surface passivation [39]. However, lower surface coverages are obtained. Moreover, the long chain organic molecules typical in colloidal synthesis act as an insulating barrier and hinder charge injection [162, 170]. Besides they might also lack of anchoring functional groups. Short-chain bifunctional linkers such as mercaptopropionic acid (MPA) are often used to replace the native ligands, provide stable anchoring of the QDs on the oxide surface, and reduce the donor-acceptor spacing [171]. Nevertheless, since electron injection implies tunneling through the QD-wide gap semiconductor junction, transfer rate is always slower than that of directly adsorbed QDs.

The colloidal stability of QDs is another crucial factor for the solar cell performance. In this sense, many of the semiconductors suffer from photocorrosion when combined with the typical iodide / triiodide (I^- / I_3^-) electrolyte [172, 173]. Therefore, other redox couples are being tested, among which are Co^{2+} / Co^{3+} [168, 174, 175] and S^{2-} / S_x^{2-} [172, 173]. The latter is probably the most promising one because it assists in delivering high open circuit voltage and stability of solar cell operation. As a drawback, sulfur species are known to poison traditional platinum counter electrodes and to reduce QDSSC performance [176]. Moreover, for the classical CdSe@TiO2 nanocomposite, hole transfer to S^{2-} is 2-3 orders of magnitude lower than electro injection [177]. As a consequence, holes accumulate within the QD, therefore increasing the probability of electron-hole recombination.

2.4.4 Biology

Unraveling the intricate cellular processes is one of the main goals of biology. Fluorescent labeling has long been employed to understand the complex spatio-temporal interplay of biomole-cules from the cellular to the integrative level [68]. However, classical organic fluorophores suffer from several drawbacks, including broad absorption/emission spectra and

low photobleaching thresholds, that have limited their effectiveness in long term imaging and multiple sensing [178].

It is only recently, with the vertiginous advent of nanotechnology, that nanostructure materials have been introduced in biology. Their outstanding properties have opened new horizons for researchers. In particular, semiconductor QDs have gained ground for many applications. The tunability of the optical features with the size and the shape have attracted a great deal of interest. Furthermore, semiconductor QDs gather many interesting properties for imaging, labeling, and sensing purposes, including high quantum yield, high molar extinction coefficients, broad absorption and narrow emission spectra, large effective Stokes shifts, and high resistance to photo- and chemical degradation [179–182].

CdSe QDs are probably the most widely exploited fluorophores in biology, because their optical features fall in the Vis. CdSe QDs are often overcoated with a layer of ZnS, to prevent the release of cytotoxic Cd^{2+} cations [52, 183, 184].

As already stated above, the classical colloidal QDs synthesized in organic solvents have no intrinsic aqueous solubility. In order to make them water compatible, the native organic capping molecules are replaced by hydrophilic ligands. Many strategies have been devised to achieve this goal, and are often grouped into three major routes. The first implies the substitution of the original hydrophobic ligands with bifunctional molecules, each combining a functional group to anchor the QD surface and an opposing hydrophilic moiety to confer water solubility [183, 185–187]. The second strategy involves the growth of silica shells on the QD surface, functionalized with polar groups [184, 188]. The third approach employs amphiphilic copolymers to interdigitate the native ligands by means of hydrophobic attraction, while the hydrophilic moieties exposed on the surface ensure aqueous dispersion and permit further derivatization [189–191].

In this sense, the functionalization of semiconductor QDs with biomolecules have earned lots of attention. The resulting inorganic-biological hybrids combine the spectroscopic properties of the QD and the biomolecular fuction of the surface attached ligand [68]. However, there are several requirements that biofunctionalized QDs must fulfill for their application in biology [192]. Firstly, and most important, the bioconjugation should not compromise neither the activity of the biomolecule nor the functionality of the QD. Moreover, the biomolecular orientation should be controlled such that the adhesion of the biomolecule to the QD surface, the distance between the QD and a given moiety of the biomolecule, and the amount of biomolecules per QD are predictable and reproducible. Finally, the hybrid compound should be stable in biological media. Following these prerequisites, peptide-capped QDs have been successfully employed for cellular labeling [193–195]. Due to the QD photobleaching resistance, previously cumbersome cellular processes are now monitored on the single-molecule level [196, 197]. QDs provide an extremely sensitive detection of the target, they are selective, and they offer high spatial resolution. Furthermore, measurements are reproducible, fast, inexpensive, and miniaturized. However, the cellular uptake of this kind of compounds is mediated by the interaction with proteins on the cell surface. Therefore, the delivery of QDs into cells is limited to cells expressing appropriate receptors. Recently,

in vivo application of QDs is being revisited, because concerns about their potential cytotoxicity remain not properly addressed [198,199]. QDs also exhibit other specific disadvantages, including their relatively large size and their instability in biological media [192].

Regarding their applications *in vitro*, surface functionalized QDs are being used for assay detection of DNA, proteins, and other biomolecules. DNA-capped QDs have been employed as DNA labels for *in situ* hybridizations, as probes for human metaphase chromosomes, and in DNA mutation detection [200–202]. Antibody-coated QDs have been shown as sensitive and specific labels for a wide variety of analytes [186,203].

2.5 Scope of the Work

Semiconductor QDs have earned lots of attention triggered by their fascinating properties and their paramount technological potential. In spite of the great experimental efforts devoted to their fabrication and characterization, many of their properties remain elusive, due to their tiny size. In this context, theoretical approaches have emerged as a valuable tool to enlighten some of the otherwise inaccessible features of QDs. This Thesis represents a contribution to this computational endeavor, aimed at calculating, understanding, and predicting QDs' properties.

Over the last years several computational methods have been adopted to model QDs. The foundations of the most important ones are summarized in Chapter 3. Among the theoretical approaches available in a computational chemist toolbox, those rooted on DFT (DFT) are probably the most widely exploited in the nano community. Indeed, most of the results presented in this work are based on DFT calculations. This methodology represents a balanced compromise between accuracy and computational cost and allows rigorous calculations of nanostructure models with hundreds of atoms.

In Chapter 4 the results obtained during the Thesis are presented. First of all, different DFT approaches are assessed, in order to choose the best suited for our purposes. Having the computational scheme set, we adopt a hierarchical work plan, studying nanostructure models of increasing complexity. We start by investigating bare QDs, with particular attention to their structural, electronic, and optical properties. In a second step, we focus on small, ligand-capped QDs, in order to understand the nature of the interaction and the effect of the surface molecules on the properties of QDs. Then we take a step forward in the modeling of QDs, by studying realistic models with important implications in various fields of science, including biology and photovoltaics. On the former, the interaction between QDs and surface attached Pt(IV) complexes is modeled, due to their potential for photodynamic therapy. With view to *in vivo* applications, the effect of hydration on the properties of QDs is also analyzed. Regarding the latter, dye- and QD- sensitized solar cells are studied.

DFT Benchmark

While conceptually simple, DFT depends on several variables that can lead to losses or gains in accuracy. Most of the computational works reported so far are based on a widespread standard combination of DFT functional and basis sets, rather than on their systematic calibration. To set firm ground for the rest of our DFT calculations, in Section 4.1 we present a benchmark assessment of DFT functionals for group II-VI MX (M = Zn, Cd; X = S, Se, Te) QDs.

Bare QD Models

Armed with a sound computational scheme, we investigate the structural, electronic, and optical properties of bare II-VI QDs.

- In Section 4.2 we report on the computational modeling of ZnO and ZnS QDs. To provide a direct comparison with the experiment, realistic wurtzite-like models of 1.5 nm are investigated.
- Section 4.3 represents a natural extension of Section 4.2. We present a systematic study on wurtzite-like 0-, 1-, and 2-dimensional ZnX (X = O, S, Se, Te) clusters, both pristine and with anion vacancies.

Small, Ligand-Capped QD Models

For simplicity, in Sections 4.2 and 4.3 bare models are considered. However, the colloidal approaches often employed QD synthesis leave surfactant molecules on the their surface. Furthermore, many of the applications of QDs nanomaterials imply interaction with capping ligands. To shed light on the interaction between semiconductor QDs and surface molecules, two works on small, ligand-capped QDs are presented.

- In Section 4.4 we report on the computational modeling of the ligand-protected $(ZnS)_6$ QD model, with particular emphasis on the structural and energetic features of the interacting complexes.
- In Section 4.5, we present a theoretical study on the structural, electronic, and optical properties of the amine-capped magic-size $(CdSe)_{13}$ QD, which has been recently isolated experimentally.

Realistic QD Models

In Sections 4.6-4.9 we move a step forward in the characterization of QDs, by investigating realistic models with important implications different fields of science, among which biology and photovoltaics. On the former, two independent works have been carried out:

- Section 4.6 is devoted to the modeling of CdSe and CdSe@ZnS QDs capped with Pt(IV) prodrugs. We pay particular attention to the electron transfer process from the QDs to the surface attached organometalic complexes, which holds potential for photodynamic therapy.
- Section 4.7 deepens on the interaction between ZnS QDs and water molecules, which are ubiquitous in biological media. For a safe application of QDs *in vivo*, their behavior in water solution must be investigated.

With regard to their application in photovoltaics, two other studies are included in this Thesis:

- Section 4.8 reports on the computational modeling of dye sensitized ZnO nanostructures. We try to model the electron injection process from the photoexcited dye to the ZnO, which is of prime importance for the conversion of light into electrical energy.
- Section 4.9 focuses on PbS QD sensitized TiO_2 solar cells, where the QDs act as light harvesters.

Chapter 3

Methods

Your theory is crazy, but it's not crazy enough to be true.

Niels Bohr

What we observe is not nature itself, but nature exposed to our method of questioning.

Werner Heisenberg

I don't like it, and I'm sorry I ever had anything to do with it.

Erwin Schrödinger

If the facts don't fit the theory, change the facts.

Albert Einstein

The theoretical effort aimed at understanding and predicting the properties of semiconductor QDs begun with the effective mass approximation (EMA) [204]. This approach, based on the particle-in-a-box model, provides insight into many of the simplest aspects of QDs, including the fluorescence Stokes shift or the nature of the excitonic transitions in the absorption spectrum. Since the pioneering works by Norris, Bawendi, Efros, and Zunger [205–207], theoretical chemists have taken advantage of more sophisticated atomistic approaches to explain QD intricacies. The empirical pseudopotential methods (EPMs) represented a step forward in the field [208–211]. In spite of being amenable for large systems, they require a careful parametrization for each material. *Ab initio* techniques, instead,

use minimal parametrization and are applicable to most materials across the periodic table, but are computationally more expensive [47].

The Hartree-Fock (HF) approach lies at the heart of *ab initio* methods. It replaces the multi-dimensional wave function with a antisymmetric products of single electron orbitals, which in turn depend on just three spatial variables (four if spin is considered). Therefore, HF implies a great simplification. It incorporates the Pauli exclusion through the exchange interaction. Electron-electron repulsion is also included as mean field, because each electron feels the average potential generated by the remaining electrons. Since orbitals depend on the mean field and the mean field is determined by the orbitals, the HF approach works until self-consistency is achieved.

Although conceptually valuable and useful for many applications, the HF method lacks of electronic correlation effects, which are of prime importance in QDs. The Configuration Interaction (CI) and Coupled Cluster (CC) approaches, built on top of HF, incorporate such effects, but at very high computational expense. Therefore, they are limited to small clusters.

Density Function Theory (DFT) represents an alternative way to incorporate electron correlations indirectly, at a reasonable computational cost. Based on the Hohenberg and Kohn theorems, which show that three-dimensional electron density determines the ground state properties, DFT replaces Coulomb interactions with a density functional. Then, the Kohn-Sham approach establishes a connection between the electron density and a wave function, which is constructed from one electron orbitals. DFT operates until self-consistency is accomplished, as it does HF. The time-dependent version of DFT (TDDFT) describes the response of the system to external perturbations, including electromagnetic fields. This is particularly important with regard to the optical properties of QDs, because it allows the calculation of the electronic excitation energies.

3.1 *Ab initio* Methods

Chemistry is the science dealing with construction, transformation and properties of molecules. Computational Chemistry is an interdisciplinary subfield where mathematical methods are combined with fundamental laws of the Quantum Physics to study atoms, molecules, and processes of chemical relevance by means of computational resources.

Quantum Theory often describes the arrangement of protons, neutrons and electrons with a mathematical function called wave function, Ψ. In principle all the information of a stationary quantum system under study is contained in such wave function. It is obtained solving the so-called time-independent Schrödinger Equation,

$$\hat{H}\Psi_{tot}\left(\{\mathbf{r}_i\},\{\mathbf{R}_\alpha\}\right) = E_{tot}\Psi_{tot}\left(\{\mathbf{r}_i\},\{\mathbf{R}_\alpha\}\right) \tag{3.1}$$

where $\hat{H}$ denotes the Hamiltonian operator and E_{tot} the energy of the system. $\{\mathbf{R}_\alpha\}$ and $\{\mathbf{r}_i\}$ are the set of nuclear and electronic coordinates, respectively. For a system with N_e electrons

and N_N nuclei, the scalar non-relativistic Hamiltonian, in atomic units, would be expressed as follows,

$$\hat{H} = \hat{T}_e + \hat{T}_n + \hat{V}_{ee} + \hat{V}_{en} + \hat{V}_{nn} = -\sum_{i=1}^{N} \frac{\nabla_i^2}{2} - \sum_{A=1}^{M} \frac{\nabla_A^2}{2M_A} + \sum_{i>j}^{N} \frac{1}{r_{ij}} - \sum_{i=1}^{N}\sum_{A=1}^{M} \frac{Z_A}{r_{iA}} + \sum_{A>B}^{M} \frac{Z_A Z_B}{R_{AB}} \quad (3.2)$$

$\hat{T}_e$ and $\hat{T}_N$ represent the kinetic energy of the electrons and nuclei, while $\hat{V}_{ee}$, $\hat{V}_{eN}$ and $\hat{V}_{NN}$ mean the electron-electron, electron-nucleus and nucleus-nucleus interactions, respectively. M_A is the mass of the nucleus A with respect to the mass of an electron, while Z_A and Z_B denote the atomic numbers of nuclei A and B. Finally, r_{ij}, r_{iA} and R_{AB} are the distance between the electrons i and j, electron i and nucleus A, and nuclei A and B, respectively.

3.1.1 Born-Oppenheimer Approximation

Since nuclei are much heavier than electrons, on the time-scale of electron motion nuclei can be considered as stationary objects, fixed at certain positions in space. Accordingly, electrons are assumed to respond instantaneously to any change of the nuclear configuration. Based on this assumptions, the so called Born-Oppenheimer approximation (BO hereafter) [212], decouples the electronic and nuclear motions.

For the electronic motion, the nuclear kinetic term $\hat{T}_n$ can be neglected and the nucleus-nucleus potential energy term $\hat{V}_{nn}$ can be regarded as a constant, since nuclei are considered to be fixed. Therefore, a simplified Schrödinger equation which does not treat nuclear motion is solved for electrons only.

$$\hat{H}_e \Psi_e = \left(\hat{T}_e + \hat{V}_{ee} + \hat{V}_{en} + \hat{V}_{nn}\right) \Psi_e = E_e \Psi_e \quad (3.3)$$

The so-obtained electronic wave function Ψ_e explicitly depends on the electronic coordinates but depends parametrically on the nuclear coordinates:

$$\hat{H}_e \Psi_e \left(\{\mathbf{r}_i\}; \{\mathbf{R}_\alpha\}\right) = E_e \left(\{\mathbf{R}_\alpha\}\right) \Psi_e \left(\{\mathbf{r}_i\}; \{\mathbf{R}_\alpha\}\right) \quad (3.4)$$

Under the same assumptions made to formulate the electronic problem, it is possible to write down the equations for the nuclear motion. As the electrons move much faster than the nuclei, the latter are considered to move in the mean field generated by the former. In other words, the electronic energy E_e, added to the internuclear repulsion $\hat{V}_{nn}$, provides the potential energy surface V_N for the nuclei. Then, the nuclear part of the Schrödinger equation reads as

$$\left(\hat{T}_n + E_e + \hat{V}_{nn}\right) \Psi_n \left(\{\mathbf{R}_\alpha\}\right) = E_{tot} \Psi_n \left(\{\mathbf{R}_\alpha\}\right) \tag{3.5}$$

The potential energy surface of the system represent the central quantity to obtain information about the roto-vibrational levels, equilibrium geometries, and chemical reactivity. However, from now on we will focus on the electronic problem. For simplicity, we will drop the subscript e and the nuclear coordinates $\{\mathbf{R}_\alpha\}$ from $\Psi_e \left(\{\mathbf{R}_\alpha\}\right)$.

3.1.2 Electronic Wave function

The BO approximation reduces the original molecular quantum mechanical problem to a system of interacting electrons under the influence of an external potential due to the nuclei. Unfortunately, due to the two-particle interactions terms in the electron-electron potential contribution, the electronic Schrödinger equation can only be cast into a closed analytical form for one-electron systems. Many mathematical methods have been devised to give an approximate solution to the electronic equation of N-electron systems. In the following, we will try to summarize them.

The electronic Hamiltonian in Eq. 3.4 depends only on the spatial coordinates of the electrons. To completely describe an electron it is mandatory, however, to specify its spin. In the non-relativistic framework, this is accomplished by introducing two spin functions, α and β, corresponding to spin up and down, respectively. Given that the Hamiltonian operator makes no reference to spin, imposing the wave function to depend on spin does not make any difference. A satisfactory theory can be obtained, however, if the following requirement is made on the wave function:

- **Antisymmetry:** A many-electron wave function must be antisymmetric with respect to the interchange of the coordinates (both space and spin) of any two electrons. This requirement, imposed by the fact that electrons are fermions, is a very general statement of the Pauli exclusion principle.

There are two additional conditions that a suitable many-electron wave function must fulfill:

- **Normalization:** Given that $|\Psi|^2$ corresponds to the probability distribution of finding the electron in the space defined by the spatial and the spin coordinates, the wave function has to be normalized to unity.
- **Spin Commutation:** Since the electronic Hamiltonian does not contain any spin operator, it does commute with the spin operators $\hat{S}_z$ and $\hat{S}^2$, *i.e.* $\left[\hat{H}, \hat{S}_z\right] = 0$ and $\left[\hat{H}, \hat{S}^2\right] = 0$.

3.1.3 Slater Determinant

As previously stated, the Schrödinger equation can only be solved analytically for one-electron systems. The resulting mono-electronic wave functions, $\psi_i(\mathbf{r})$, are called *orbitals*.

Recall that for each spatial orbital $\psi(\mathbf{r})$ two different spin orbitals can be formed, *i.e.* $\chi_i(\mathbf{r}) = \alpha \times \psi(\mathbf{r})$ and $\chi_{i+1}(\mathbf{r}) = \beta \times \psi(\mathbf{r})$.

Let us now consider a N-electronic system. The electronic Hamiltonian contains one- and two-electron terms, along with the nuclear repulsion term

$$\hat{H} = \sum_{i=1}^{N} \hat{h}(i) + \sum_{i<j}^{N} \hat{g}(i,j) + \hat{V}_{nn} = \sum_{i=1}^{N} \left(-\frac{1}{2}\nabla_i^2 - \sum_{A=1}^{M} \frac{Z_A}{r_{iA}} \right) + \sum_{i<j}^{N} \frac{1}{r_{ij}} + \hat{V}_{nn} \tag{3.6}$$

Before considering the form of the exact wave function for the fully interacting system, let us first write the Hamiltonian of a system containing N non-interacting electrons ($\sum_{i<j}^{N} \hat{g}(i,j) = \hat{V}_{nn} = 0$ in Eq. 3.6)

$$\hat{H} = \sum_{i=1}^{N} \hat{h}(i) \tag{3.7}$$

In principle, $\hat{h}(i)$ comprises the kinetic energy and the potential energy (due to the nuclei) of electron i. Alternatively, $\hat{h}(i)$ might include the effects of the electron-electron repulsion in some average manner. Anyway, the eigenfunctions of the operator $\hat{h}(i)$

$$\hat{h}(i)\chi_j = \varepsilon_j \chi_j \tag{3.8}$$

constitute a set of spin orbitals $\{\chi_j(x)\}$, where x comprises spatial $\mathbf{r}$ and spin α/β variables. Since $\hat{H}$ is a sum of one-electron operators $\hat{h}(i)$, a simple product of mono-electronic spin orbitals, also known as Hartree product [213],

$$\Psi^{HP}(x_1, x_2, ..., x_N) = \chi_j(x_1)\chi_j(x_2)...\chi_k(x_N) \tag{3.9}$$

is indeed eigenfunction of $\hat{H}$

$$\hat{H}\Psi^{HP} = E\Psi^{HP} \tag{3.10}$$

and the corresponding eigenvalue E is just the sum of the spin orbital energies of each of the spin orbitals appearing in Ψ^{HP}

$$E = \varepsilon_i + \varepsilon_j + ... + \varepsilon_k \tag{3.11}$$

The Hartree product is an uncorrelated wave function. The probability of finding an electron at a given point in space is independent of the position of the other electrons. Assuming independent electrons and a Hamiltonian the form of Eq. 3.7, there is still a deficiency in the Hartree product. As one may notice from Eq. 3.9, the Hartree product does not fulfill the antisymmetry principle and the indistinguishability of the electrons is no longer obeyed. This drawback can easily be overcome by writing the wave function in the form of the Slater determinant [214]

$$\Psi(x_1, x_2, ..., x_N) = (N!)^{1/2} \begin{vmatrix} \chi_i(x_1) & \chi_j(x_1) & ... & \chi_k(x_1) \\ \chi_i(x_2) & \chi_j(x_2) & ... & \chi_k(x_2) \\ ... & ... & & ... \\ \chi_i(x_N) & \chi_j(x_N) & ... & \chi_k(x_N) \end{vmatrix} \tag{3.12}$$

where $(N!)^{1/2}$ is the normalization factor. The permutation of the coordinates of two electrons implies interchanging two rows of the Slater determinant, which changes the sign of Ψ. Thus, the Slater determinant obeys the antisymmetry principle by construction. Furthermore, having two electrons occupying the same spin orbital corresponds to having two columns equal, which makes Ψ zero. Therefore, no more than one electron can occupy the a spin orbital, as stated by the Pauli exclusion principle.

The antisymetrization of the Hartree product introduces exchange effects, so called because they arise from the requirement that $|\Psi|^2$ remains invariant to the exchange of the space and spin coordinates of any two electrons. In particular, the Slater determinant incorporates exchange or Fermi correlation, which means that the motion of two electrons with parallel spin is correlated.

Slater determinants are eigenfunctions of the N-electron spin operator $\hat{S}_z$, with an eigenvalue M_S, equal to one-half the difference between the number of α and β electrons.

$$\hat{S}_z\Psi = M_S\Psi = \frac{1}{2}\left(N_\alpha - N_\beta\right) \tag{3.13}$$

3.1.4 The HF Method

The HF method is central to attempts at providing an approximate solution to the electronic Schrödinger solution [215]. It assumes that the wave function can be represented by a single Slater determinant and finds out the set of spin orbital which variationally minimize the energy. The formulation of the method could be summarized as follows:

1. A N independent particle Schrödinger equation is broken down into separated N independent monoelectronic equations.

2. The approximated wave function Ψ_{HF} is obtained as a single determinant built up from the spin orbitals obtained in the step 1.

3. A trial energy is computed for Ψ_{HF} constructed in step 2.

$$E_0 = \int \Psi^*_{HF} \hat{H} \Psi_{HF} d\tau \tag{3.14}$$

4. The variational principle, which states that the best wave function is the one providing the lowest possible energy, is applied to E_0. By minimizing E_0 with respect to the choice of the spin orbitals, one can derive a set of mono-electronic eigenvalue equations describing the motion of a given electron in the mean field generated by the rest of the $N-1$ electrons. These equations, known as HF equations, determine the optimal spin orbitals and read as

$$\hat{f}(i)\psi(i) = \varepsilon_i \psi(i) \tag{3.15}$$

where $\hat{f}(i)$ is the mono-electronic Fock operator, of the form

$$\hat{f}(i) = -\frac{1}{2}\nabla_i^2 - \sum_{A=1}^{M} \frac{Z_A}{r_{iA}} + v^{HF}(i) \tag{3.16}$$

where $v^{HF}(i)$ is the averaged potential experienced by the ith electron due to the other electrons.

5. Since $v^{HF}(i)$ depends on the spin orbitals of the other electrons, the HF equations 3.15 are nonlinear and have to be solved iteratively, through the self-consistent-field (SCF) procedure, until the $v^{HF}(i)$ no longer change and the spin orbitals used to construct the Fock operator are the same as its eigenfunctions.

One might try to solve the HF equations numerically. In fact, numerical solutions are common in atomic calculations. In the case of molecules, however, no practical recipes are available for obtaining such solutions. Roothaan and Hall overcame this drawback showing that, by introducing a set of known spatial basis functions, the coupled differential equations could be transformed to a set of algebraic equations and solved by standard matrix techniques [216, 217]. Following the recipe proposed by Roothaan and Hall, let us write the unknown molecular orbitals $\{\psi(i)\}$ as a linear combination of K known basis functions $\{\phi_q\}$

$$\psi(i) = \sum_{q=1}^{K} c_{iq}\phi_q \; i = 1, 2, ..., K \tag{3.17}$$

If the set $\{\phi_q\}$ was complete, Eq. 3.17 would be an exact expansion. For practical computational reasons, however, one is always restricted to a finite set of basis functions. Therefore, it is important to choose a set that will deliver, as much as possible, a reasonably accurate expansion for the exact molecular orbitals. Substituting Eq. 3.17 in Eq. 3.15 the Roothaan-Hall are obtained

$$\sum_{q=1}^{K} c_{iq} \left(F_{pq} - S_{pq}\varepsilon_i \right) = 0;\ i = 1, 2, ..., K \tag{3.18}$$

where the overlap matrix **S** having elements

$$S_{pq} = \int \phi_p^*(1)\phi_p(1)dr_1 \tag{3.19}$$

and the Fock matrix **F** having elements

$$F_{pq} = \int \phi_p^*(1)\hat{f}(1)\phi_p(1)dr_1 \tag{3.20}$$

have been introduced. In matricial notation, Eq. 3.18 reads as

$$\mathbf{FC} = \mathbf{SCE} \tag{3.21}$$

where **C** is a $K \times K$ square matrix of the expansion coefficients c_{ij} and **E** is a diagonal matrix of the orbital energies ε_i. The elements of the **F** matrix are

$$F_{pq} = h_{pq} + \sum_r \sum_s P_{rs} \left(\langle pq \mid rs \rangle - \frac{1}{2} \langle ps \mid rq \rangle \right) \tag{3.22}$$

where h_{pq} stands for the mono-electronic integrals

$$h_{pq} = \int \phi_p^*(1)\hat{h}(1)\phi_p(1)dr_1 \tag{3.23}$$

P_{rs} refer to the matrix elements of the so called density matrix **P**

$$P_{rs} = 2\sum_j c_{rj}^* c_{js} \tag{3.24}$$

and $\langle pq \mid rs \rangle$ represents the bi-electronic integrals of the form

$$\langle pq \mid rs \rangle = \int \phi_p^*(1)\phi_q^*(1)\frac{1}{r_{12}}\phi_r(2)\phi_s(2)dr_1dr_2 \tag{3.25}$$

Note that the elements F_{pq} of the Fock matrix depend on the molecular orbital expansion coefficients c_{ij} by means of the density matrix **P**. Thus, once again, the procedure has to be solved iteratively, using an initial guess for the density matrix and repeating the construction and the diagonalization of the Fock matrix until convergence is reached. Summarizing, the Roothaan-HF method comprises the following steps:

1. Evaluation of the mono- and bi-electronic integrals, h_{pq} and $\langle pq \mid rs \rangle$, for all the basis functions in the set $\{\phi_q\}$.
2. Assignment of an initial guess to the expansion coefficients c_{ij} and evaluation of the trial density matrix **P**.
3. Construction of the Fock matrix **F**.
4. Solution of the eigenvalue problem 3.21 to obtain the eigenvalues **C** and the eigenvectors **E**.
5. Convergence check, by comparing the actual density matrix with that of the previous step.
   (a) If the procedure has not converged, return to step 2 with the new density matrix.
   (b) If the procedure has converged, use the resultant solutions to calculate expectation values and other quantities of interest.

3.1.5 Post-HF Methods

The HF approximation, while remarkably successful in many cases, suffers from severe problems when facing a wide variety of chemical problems in which a precise description of the electron correlation is required. The correlation energy E_{corr} is defined as

$$E_{corr} = E_0 - E_{HF} \tag{3.26}$$

where E_0 stands for the exact nonrelavistic energy of the system and E_{HF} refers to the HF energy. Note that, since the HF energy is an upper bound to the exact energy, the correlation energy is negative. Typically E_{HF} represents, in absolute terms, 99% of the E_0. However

the small portion left, E_{corr}, undergoes sizable changes in chemical processes and it is a fundamental term to reproduce and understand the intermolecular interactions.

In spite of its drawback, The HF approximation constitutes a valuable starting point for a number of more accurate *ab initio* methods. These latter approaches, also known as post-HF methods, were conceived to recover the E_{corr}.

In the following, the most important post-HF approaches are briefly introduced.

3.1.5.1 Configuration Interaction (CI)

The CI method is probably the conceptually simplest approach beyond the HF approximation [215]. It breaks up with the orbital model inherent in HF and expresses the wave function of a N-electron system $|\Phi_0\rangle$ as a linear combination of slater determinants. The expansion reads as follows

$$|\Phi_0\rangle = c_0 |\Psi_0\rangle + \sum_{ar} c_a^r |\Psi_a^r\rangle + \sum_{a<b\ r<s} c_{ab}^{rs} |\Psi_{ab}^{rs}\rangle + \sum_{a<b<c\ r<s<t} c_{abc}^{rst} |\Psi_{abc}^{rst}\rangle + ... \tag{3.27}$$

where $|\Psi_0\rangle$ stands for the ground state HF wave function and $|\Psi_a^r\rangle$, $|\Psi_{ab}^{rs}\rangle$, and $|\Psi_{abc}^{rst}\rangle$ refer to singly, doubly, and triply excited configurations, with a, b, and c denoting occupied orbitals and r, s, and t unoccupied ones. Coefficients c_0, c_a^r, c_{ab}^{rs}, c_{abc}^{rst} etc. are variationally optimized. If the basis set was complete, the number of spin orbitals and therefore the number of determinants constructed on their basis would be infinite, and the CI would yield to the exact solution of the electronic Schrödinger equation within the non-relativistic and the BO approximations. Even for finite size basis set, the inclusion of all the possible excited determinants is unfeasible. Only small systems with moderate basis set are tractable with full CI. For larger systems truncated CI expansion are used, where a reduced number of excitations is considered, namely CI Singles (CIS), CI Singles & Doubles (CISD), or CI Singles, Doubles & Triples (CISDT).

All the truncated forms of CI expansion suffer of lack of size-extensivity. However, the truncation is often justified because the vast majority of the excited configurations contribute minimally to wave function and correlation energy. Inspired in this idea, some theoretical methods have been developed to recover the correlation energy, in which the excited configurations are generated amongst the orbitals inside an active space. Electron correlation is often partitioned into dynamical and non-dynamical contributions. The former refers to the instantaneous electron-electron repulsion. The latter arises when multiple determinants are required to cover the coarse electronic structure of a state. That said, we provide a short summary of the active space methods:

1. CASSCF: The Complete Active Space method [218] is based on the concept that in the active orbital space all the possible configurations are obtained by distributing the electrons amongst all the possible active orbitals. Both the expansion coefficients and

the orbitals are optimized, giving a highly flexible wave function that can be used to accurately describe systems where non-dynamic correlation is important. As a drawback, the size of the active space is limited and not all the dynamic correlation energy is recovered.

2. CASPT2: Complete Active Space Second-Order Perturbation Theory [219, 220] employs the multiconfigurational CASSCF wave function as the zeroth-order state to apply second-order perturbation theory, in order to recover dynamic correlation. This method, which is not variational, provides very accurate results and satisfies the size-extensivity requirement.

3. RAS-CI: The Restricted Active Space approach [221] recovers both dynamic and non-dynamic correlation energies. The active orbital space is divided in three different subspaces, namely RAS1, RAS2, and RAS3. RAS1 is the occupied space in which at the most two holes are created; RAS3 is the unoccupied space that receives at mot two electrons from RAS1 and eventually from RAS2; RAS2 is the CAS space in which all the possible excitations are considered and is formed by both occupied and unoccupied orbitals. In spite of not being size-extensive, RAS-CI often provides very accurate results.

3.1.5.2 Coupled Cluster (CC)

Within the CC method [215] the exact wave function of the ground state of a N-electron system $|\Phi_0\rangle$, written in the second quantization language, reads as

$$|\Phi_0\rangle = e^{\hat{T}} |\Psi_0\rangle \tag{3.28}$$

where $|\Psi_0\rangle$ stands for the ground state HF wave function and $\hat{T}$ refers to the cluster operator. This latter comprises several terms

$$\hat{T} = \hat{T}_1 + \hat{T}_2 + \hat{T}_3 + ... \tag{3.29}$$

which, expressed in terms of the creation ($a_r^\dagger$) and annihilation operators (a_a) , have the form

$$\hat{T}_1 = \sum_{a,b} c_a^r a_r^\dagger a_a \tag{3.30}$$

$$\hat{T}_2 = \sum_{a,b} \sum_{r,s} c_{ab}^{rs} a_r^\dagger a_s^\dagger a_a a_b \tag{3.31}$$

where a and b denote occupied and r and s unoccupied ones. Recall that the creation operator $a_r^\dagger$ creates an electron in orbital r included in $|\Psi_0\rangle$, whereas the annihilation operator a_a annihilates an electron in orbital a, in such a way that

$$a_r^\dagger a_a |\Psi_0\rangle = |\Psi_a^r\rangle = |\Psi_1\Psi_2...\Psi_{a-1}\Psi_r\Psi_{a+1}...\Psi_N\rangle \tag{3.32}$$

$$a_r^\dagger a_s^\dagger a_a a_b |\Psi_0\rangle = |\Psi_{ab}^{rs}\rangle = |\Psi_1\Psi_2...\Psi_{a-1}\Psi_r\Psi_{a+1}...\Psi_{b-1}\Psi_s\Psi_{b+1}...\Psi_N\rangle \tag{3.33}$$

The choice of the exponential ansatz is opportune because it introduces high order excitations. For example, the quadruples and the sextuples excitations can be written in term of the doubles. Besides, the exponential form guarantees the size extensivity of the solution as long as a suitable reference function is chosen. As a drawback, the CC method is not variational, so the total energy can be lower than the true total energy. This does not pose a problem because we are usually interested in relative energies and not in absolute values.

The abbreviation of the CC methods begin with CC, followed by the character of the excitations considered in the expansion, namely S (singles), D (doubles), T(triples), or Q (quadruples). CCSD is often employed for benchmark purposes. CCSD(T) poses a further improvement, which includes the triples excitations in a perturbative fashion [222].

The post-HF methods presented up to now are quite demanding computationally and they are amenable a limited set of small systems. Among the *ab initio* methods devised to recover the electronic correlation, MP2 is probably the better suited for large systems such as biomolecules and nanostructures. It is able to capture about 80% of the correlation energy at a lower computational cost than CI and CC methods. Moreover, it is size extensive. To understand the construction of the MP2 approach, the basic notions of the Rayleigh-Schrödinger Perturbation Theory should be given (*vide infra*).

Finally, there are some methods, halfway the CC and perturbational methods, which preserve the accuracy of the CC methods but with a lower computational cost. Among these approaches, CC2 is probably the most popular [223].

3.1.5.3 Rayleigh-Schrödinger Perturbation Theory

Perturbational methods express the Hamiltonian $\hat{H}$ as the sum of an unperturbed model Hamiltonian $\hat{H}_0$ and a perturbation operator $\hat{V}$, *i.e.*

$$\hat{H} = \hat{H}_0 + \lambda\hat{V} \tag{3.34}$$

where λ gives the extent of the perturbation. Assuming to be in a non-degenerate case, the eigenstates $\{|\Psi_i^0\rangle\}$ and the associated eigenvalues $\{E_i^0\}$ of the $\hat{H}_0$ are known

$$\hat{H}_0 \left|\Psi_i^{(0)}\right\rangle = E_i^{(0)} \left|\Psi_i^{(0)}\right\rangle \; i = 0, 1, 2, ... \tag{3.35}$$

Due to the effect of the perturbation, which is however supposed to be small, the eigenfunctions and eigenvalues of $\hat{H}$ will depend on λ. Under the Rayleigh-Schrödinger scheme, they are expanded in a Taylor series of the form

$$E_i = E_i^{(0)} + \lambda E_i^{(1)} + \lambda^2 E_i^{(2)} + ... \tag{3.36}$$

and

$$|\Psi_i\rangle = \left|\Psi_i^{(0)}\right\rangle + \lambda \left|\Psi_i^{(1)}\right\rangle + \lambda^2 \left|\Psi_i^{(2)}\right\rangle + ... \tag{3.37}$$

In order to simplify the derivation, we assume the eigenstates of $\hat{H}_0$ to be normalized

$$\left\langle \Psi_i^{(0)} \middle| \Psi_i^{(0)} \right\rangle = 1 \tag{3.38}$$

and impose the intermediate normalization condition

$$\left\langle \Psi_i^{(0)} \middle| \Psi_i \right\rangle = 1 \tag{3.39}$$

By substitution of Eq. 3.36 and 3.37 into the Schrödinger equation, $\hat{H}\Psi_i = E_i\Psi_i$, we obtain

$$(\hat{H}_0 + \lambda\hat{V})(\left|\Psi_i^{(0)}\right\rangle + \lambda \left|\Psi_i^{(1)}\right\rangle + \lambda^2 \left|\Psi_i^{(2)}\right\rangle + ...) = (E_i^{(0)} + \lambda E_i^{(1)} + \lambda^2 E_i^{(2)} + ...)(\Psi_i^{(0)} + \lambda\Psi_i^{(1)} + \lambda^2\Psi_i^{(2)} + ...) \tag{3.40}$$

Equating λ^n coefficients, we find

$$\hat{H}_0 \left|\Psi_i^{(0)}\right\rangle = E_i^{(0)} \left|\Psi_i^{(0)}\right\rangle \; n = 0 \tag{3.41}$$

$$\hat{H}_0 \left|\Psi_i^{(1)}\right\rangle + \hat{V} \left|\Psi_i^{(0)}\right\rangle = E_i^{(0)} \left|\Psi_i^{(1)}\right\rangle + E_i^{(1)} \left|\Psi_i^{(0)}\right\rangle \; n = 1 \tag{3.42}$$

$$\hat{H}_0 \left|\Psi_i^{(2)}\right\rangle + \hat{V} \left|\Psi_i^{(1)}\right\rangle = E_i^{(0)} \left|\Psi_i^{(2)}\right\rangle + E_i^{(1)} \left|\Psi_i^{(1)}\right\rangle + E_i^{(2)} \left|\Psi_i^{(0)}\right\rangle \; n = 2 \tag{3.43}$$

and so on. Multiplying each of these equations with the $\left\langle \Psi_i^{(0)} \right|$ and using the ortoghonality relation in Eq. 3.39, we get the following expressions for the 0th, 1st, 2nd, and nth order energies

$$E_i^{(0)} = \left\langle \Psi_i^{(0)} \left| \hat{H}_0 \right| \Psi_i^{(0)} \right\rangle \tag{3.44}$$

$$E_i^{(1)} = \left\langle \Psi_i^{(0)} \left| \hat{V} \right| \Psi_i^{(0)} \right\rangle \tag{3.45}$$

$$E_i^{(2)} = \left\langle \Psi_i^{(0)} \left| \hat{V} \right| \Psi_i^{(1)} \right\rangle \tag{3.46}$$

$$E_i^{(n)} = \left\langle \Psi_i^{(0)} \left| \hat{V} \right| \Psi_i^{(n-1)} \right\rangle \tag{3.47}$$

All that remains is to solve the set of Eqs. 3.41-3.43 for $\left|\Psi_i^{(n)}\right\rangle$ and then determine the n-th order energy using Eq. 3.47.

Let us define the resolvent operator R_n

$$R_i = \sum_{k \neq i} \frac{\left|\Psi_k^{(0)}\right\rangle \left\langle \Psi_k^{(0)} \right|}{E_k^{(0)} - E_i^{(0)}} \tag{3.48}$$

and rewrite $\left|\Psi_i^{(1)}\right\rangle$ as

$$\left|\Psi_i^{(1)}\right\rangle = -R_i \hat{V} \left|\Psi_i^{(0)}\right\rangle \tag{3.49}$$

Substituting Eq. 3.49 in 3.46, the 2n order energy reads as

$$E_i^{(2)} = -\sum_{k \neq 0} \frac{\left|\left\langle \Psi_i^{(0)} \left| \hat{V} \right| \Psi_k^{(1)} \right\rangle\right|^2}{E_k^{(0)} - E_i^{(0)}} \tag{3.50}$$

3.1.5.4 Moller-Plesset Perturbation Theory

Within the Moller-Plesset Perturbation Theory [215] the model Hamiltonian $\hat{H}_0$, also called Fockian $\hat{F}$, represents a model of N non-interacting electrons and has the form

$$\hat{F} = \sum_i \left(\hat{h}_i + \hat{J}_i + \hat{K}_i \right) = \sum_i \left(\hat{h}_i + \hat{g}_i \right) \tag{3.51}$$

where $\hat{g}_i$ is the bielectronic operator comprising the Coulomb ($\hat{J}_i$) and exchange ($\hat{K}_i$) operators.

$$\hat{J}_i \psi_j(1) = \int \psi_i^*(2) \frac{1}{r_{12}} \psi_i(2) dr_2 \psi_j(1) \tag{3.52}$$

$$\hat{K}_i \psi_j(1) = \int \psi_i^*(2) \frac{1}{r_{12}} \psi_j(2) dr_2 \psi_i(1) \tag{3.53}$$

The perturbation operator $\hat{V}$, also termed fluctuation potential, is given by the difference

$$\hat{V} = \hat{H} - \hat{F} \tag{3.54}$$

As one may notice from Eq. 3.51, the HF wave function $\Psi_0^{(0)}$ is eigenfunction of $\hat{F}$, and the corresponding eigenvalue $E_0^{(0)}$ is

$$E_0^{(0)} = \left\langle \Psi_0^{(0)} \right| \hat{F} \left| \Psi_0^{(0)} \right\rangle = \sum_a^N \varepsilon_a \tag{3.55}$$

where a runs over the occupied orbitals. Similarly, any other Slater determinant, $\Psi_i^{(0)} = \left\{ \Psi_a^r, \Psi_{ab}^{rs}, ... \right\}$, built up from the HF wave function by substituting occupied molecular orbitals a, b with unoccupied r, s , is also eigenfunction of $\hat{F}$. From Eq. 3.45, it can be easily demonstrated that the first order correction (MP1) delivers the HF energy. Accordingly, the first contribution to the correlation energy comes from the second order term

$$E_0^{(2)} = \left\langle \Psi_0^{(0)} \right| \hat{V} \left| \Psi_0^{(0)} \right\rangle = -\sum_{k \neq 0} \frac{\left| \left\langle \Psi_0^{(0)} \left| \hat{V} \right| \Psi_k^{(1)} \right\rangle \right|^2}{E_k^{(0)} - E_0^{(0)}} \tag{3.56}$$

Only doubly-excited determinants contribute to Eq. 3.56. Singly-excited determinants do not interact with the HF wave function, as stated by Brillouin's theorem [215]. In terms of spin orbitals, the MP2 energy is given by

$$E_0^{(2)} = E_{MP2} = \frac{1}{4}\sum_{a,b}^{N}\sum_{r,s}^{V}\frac{|\langle ab \,||\, rs\rangle|^2}{\varepsilon_a + \varepsilon_b - \varepsilon_r - \varepsilon_s} \tag{3.57}$$

where a, b and r, s stand for the occupied and the unoccupied orbitals, respectively, N refers to the number of electrons, and V means the number of virtual spin orbitals employed to generate the doubly-excited determinants. Integrating over the spin, Eq. 3.57 reads as

$$E_{MP2} = 2\sum_{a,b}^{N/2}\sum_{r,s}^{V/2}\frac{|\langle ab \mid rs\rangle|\,|\langle rs \mid ab\rangle|}{\varepsilon_a + \varepsilon_b - \varepsilon_r - \varepsilon_s} - 2\sum_{r,s}^{N/2}\sum_{r,s}^{V/2}\frac{|\langle ab \mid rs\rangle|\,|\langle rs \mid ba\rangle|}{\varepsilon_a + \varepsilon_b - \varepsilon_r - \varepsilon_s} \tag{3.58}$$

3.2 DFT

The Quantum Theory states that all the properties of an N-electron system lie in the wave function, which is obtained solving the Schrödinger equation for that given system. The wave function based methods, as mentioned above, try to find (approximate) solutions to the electronic Schrödinger equation. The problem here is that the electronic wave function Ψ_e is a 3N-dimensional object (or 4N-dimensional if spin is considered) and its complexity increases exponentially with the number size of the atomic or molecular system in hands. In this framework, the DFT (DFT) emerged as a highly promising method for electronic structure calculations. It replaced the N-electron wave function by the much simpler electron density $\rho(\mathbf{r})$, which is a function of the three spatial variables.

Although not strictly *ab initio*, DFT is nonetheless very closely related to the HF method, but modified in such a way that its accuracy is substantially improved. Indeed, it includes electron correlation effects at the same computational cost of HF. Accordingly, accurate calculations on large systems are affordable with DFT. Therefore, it has gained momentum within the computational chemistry community.

3.2.1 Early DFT

3.2.1.1 The Thomas-Fermi Model

The first attempts to use the electron density rather than the wave function are due to Thomas and Fermi [224, 225]. Central to their approach is a quantum statistical model of electrons which takes into account only the kinetic energy while treating the nuclear-electron and electron-electron contributions by means of classical mechanics. Thomas and Fermi derived the following expression for the kinetic energy based on the uniform electron gas

$$T_{TF}[\rho(\mathbf{r})] = \frac{3}{10}(3\pi^2)^{2/3}\int \rho^{5/3}(\mathbf{r})d\mathbf{r} \tag{3.59}$$

which, added to the classical nucleus-electron and electron-electron potentials, yields the Thomas-Fermi expression for the energy of an atom

$$E_{TF}[\rho(\mathbf{r})] = \frac{3}{10}(3\pi^2)^{2/3}\int \rho^{5/3}(\mathbf{r})d\mathbf{r} - Z\int \frac{\rho(\mathbf{r})}{\mathbf{r}}d\mathbf{r} + \frac{1}{2}\int\int \frac{\rho(\mathbf{r}_1)\rho(\mathbf{r}_2)}{r_{12}}d\mathbf{r}_1 d\mathbf{r}_2 \tag{3.60}$$

The Thomas-Fermi model provides a poor description of the actual atomic and molecular systems, due to the coarse approximation to the true kinetic energy and the lack of the exchange and correlation effects. Nevertheless, since it is the first example of a genuine density functional for the energy, it paved the way for DFT as we know it today. Thomas and Fermi made use of the variational principle to find out the correct density. They assumed that the ground state of the system is connected to the electron density that minimizes Eq. 3.60 under the constraint

$$\int \rho(\mathbf{r})d\mathbf{r} = N \tag{3.61}$$

3.2.1.2 The Slater Xα Method

Slater made a step forward in DFT [226], when he approximated the non-local exchange contribution of the HF method as

$$E_X[\rho(\mathbf{r})] = -\frac{9}{8}\left(\frac{3}{\pi}\right)^{1/3}\alpha\int \rho(\mathbf{r})^{4/3}d\mathbf{r} \tag{3.62}$$

As one may notice from Eq. 3.62, Slater replaced the non-local HF exchange term by a simple expression written in terms of the local electron density. To improve the quality of the approximation, Slater introduced an adjustable parameter α, which ranges between 2/3 and 1 for most of the atoms in the periodic table [227].

The Thomas-Fermi model and the Slater Xα method are viewed as the precursors to modern DFT methods, since they are formulated in terms of the electronic density alone. However, the real breakthrough came with the paper by Hohenberg and Kohn in 1964 [228]. The theorems proven in this work laid the foundations of the currently available DFT methods.

3.2.2 Hohenberg-Kohn Theorems

Theorem 1: *The external potential $\hat{V}_{ext}(\mathbf{r})$ is, to within a constant, a unique functional of the electron density $\rho(\mathbf{r})$. Since $\hat{H}$ is determined by $\hat{V}_{ext}(\mathbf{r})$, the full many particle ground state is a unique*

functional of $\rho(\mathbf{r})$.

This means that the ground state energy and other properties of a system are uniquely defined by $\rho(\mathbf{r})$. Remarkably, such a one-to-one mapping is only possible for the ground state density $\rho_0(\mathbf{r})$. Moreover, we impose the ground state to be non degenerated. However, the first theorem can easily be extended to degenerated states. At this point, we assume $\rho_0(\mathbf{r})$ to be N-representable. This implies that the density stems from an antisymmetric wave function, in such a way that $\tilde{\rho}(\mathbf{r}) \geq 0$ and $\int \tilde{\rho}(\mathbf{r})dr = N$.

Let us write the ground state energy E_0 as a functional of the ground state density $\rho_0(\mathbf{r})$

$$E_0 = E_0\left[\rho_0\right] \tag{3.63}$$

Broken down into its several contributions, E_0 reads as

$$E_0\left[\rho_0\right] = T\left[\rho_0\right] + E_{ee}\left[\rho_0\right] + V_{ext}\left[\rho_0\right] = T\left[\rho_0\right] + E_{ee}\left[\rho_0\right] + E_{Ne}\left[\rho_0\right] \tag{3.64}$$

where T, E_{ee}, and E_{Ne} stand for the kinetic energy, the electron-electron repulsion and the nucleus-electron attraction respectively. Recall that E_{Ne} depends on the actual system, whereas T and E_{ee} are universal. Collecting the system independent terms into the so called Hohenberg-Kohn functional, $F_{HK}[\rho_0]$, Eq. 3.64 reads as

$$E_0\left[\rho_0\right] = F_{HK}[\rho_0] + E_{Ne}\left[\rho_0\right] = F_{HK}[\rho_0] + \int \rho(\mathbf{r})v(\mathbf{r})d\mathbf{r} \tag{3.65}$$

where $v(\mathbf{r})$ is the external potential due to the nuclei, given by

$$v(\mathbf{r}) = -\sum_{\alpha}\frac{Z_\alpha}{r_{1\alpha}} \tag{3.66}$$

The Hohenberg-Kohn functional $F_{HK}[\rho_0]$ is central to DFT. If it were known we would have solved the Schrödinger equation exactly. Furthermore, since it is universal, it applies equally all the imaginable chemical systems. Unfortunately, the explicit form of $T\left[\rho_0\right]$ and $E_{ee}\left[\rho_0\right]$ contained in $F_{HK}[\rho_0]$ remain elusive. At this point, $E_{ee}\left[\rho_0\right]$ is often split in two

$$E_{ee}\left[\rho\right] = J\left[\rho\right] + E_{ncl}\left[\rho\right] \tag{3.67}$$

where $J\left[\rho\right]$ stands for the classical Coulomb part

$$J\left[\rho\right] = \frac{1}{2}\int\int \frac{\rho(\mathbf{r}_1)\rho(\mathbf{r}_2)}{r_{12}}d\mathbf{r}_1 d\mathbf{r}_2 \tag{3.68}$$

and $E_{ncl}[\rho]$ comprises the non-classical contributions to the electron-electron interaction, namely the self-interaction correction, and the exchange and Coulomb correlations.

The first theorem establishes that the ground state density $\rho_0(\mathbf{r})$ is in principle sufficient to obtain all properties of interest. However, it says nothing about the way to follow in order to find out $\rho_0(\mathbf{r})$. At this point, the second theorem of Hohenberg-Kohn comes into play.

Theorem 2: *For any trial density $\tilde{\rho}(\mathbf{r})$, the energy obtained from the Hohenberg-Kohn density functional represents an upper bound for the true ground state energy E_0.*

$$E_0 \leq E[\tilde{\rho}] \tag{3.69}$$

In other words, the Hohenberg-Kohn functional delivers the lowest energy if and only if the input density is the true ground state energy $\rho_0(\mathbf{r})$. This second theorem paves the way to obtain $\rho_0(\mathbf{r})$ variationally. However, there are a couple of requirements that the variational function $\tilde{\rho}(\mathbf{r})$ must fulfill. One the one hand, it has to be associated with some external potential v (v-reprensentability). On the other hand, it must be N-representable.

3.2.3 Kohn-Sham Approach

The Hohenberg-Kohn theorems say nothing about the explicit form of the density functional and do not provide a recipe to calculate the density. In 1965 Kohn and Sham suggested an avenue to approximate the hitherto unknown Hohenberg-Kohn functional [229]. They realized that most of the problems with direct density functional are connected with the kinetic energy. Since the orbital-based approaches as HF perform much better in this respect, they introduced the idea of a non-interacting reference system built from a set of orbitals such that the major part of the kinetic energy can be computed accurately. The residual part is combined with the non-classical contributions to the electron-electron repulsion, which are also unknown.

In the HF approach, the ground state wave function is approximated as a single Slater determinant Ψ_{HF} constructed from N spin orbitals χ_i. Ψ_{HF} can be regarded as the exact wave function of a fictitious system of N non-interacting electrons, moving in the effective potential V_{HF}. The kinetic energy of Ψ_{HF} can be exactly written as

$$T_{HF} = -\frac{1}{2}\sum_{i}^{N} \langle \chi_i | \nabla^2 | \chi_i \rangle \tag{3.70}$$

At this point, it is possible to set up a non-interacting reference system, with a Hamiltonian

$$\hat{H}_S = -\frac{1}{2}\sum_{i}^{N} \nabla_i^2 + \sum_{i}^{N} V_S(\mathbf{r}_i) \tag{3.71}$$

in which we have introduced an effective local potential $V_S(\mathbf{r})$. Since $\hat{H}_S$ does not contain any electron-electron interactions, its ground state wave function can be expressed as a Slater determinant

$$\Psi_S(x_1, x_2, ..., x_N) = (N!)^{1/2} \begin{vmatrix} \varphi_i(x_1) & \varphi_j(x_1) & ... & \varphi_k(x_1) \\ \varphi_i(x_2) & \varphi_j(x_2) & ... & \varphi_k(x_2) \\ ... & ... & & ... \\ \varphi_i(x_N) & \varphi_j(x_N) & ... & \varphi_k(x_N) \end{vmatrix} \tag{3.72}$$

where the Kohn-Sham spin orbitals φ_i , in complete analogy to the HF method, are determined by

$$\hat{f}^{KS}(i)\varphi(i) = \varepsilon_i \varphi(i) \tag{3.73}$$

with the one-electron Kohn-Sham operator defined as

$$\hat{f}^{KS}(i) = -\frac{1}{2}\nabla_i^2 - V_S(i) \tag{3.74}$$

In the Kohn-Sham approach the effective potential $V_S(\mathbf{r})$ is chosen such that the density $\rho_S(\mathbf{r})$ of the non-interacting system, resulting from the orbitals $\{\varphi_i\}$, exactly equals the ground state density $\rho_0(\mathbf{r})$ of the real system of interacting electrons

$$\rho_S(\mathbf{r}) = \sum_i^N \sum_s |\varphi_i(\mathbf{r}, s)|^2 = \rho_0(\mathbf{r}) \tag{3.75}$$

By analogy with the HF approach, the exact kinetic energy of the non-interacting reference system with the same density as the real can be written as

$$T_S = -\frac{1}{2}\sum_i^N \langle \varphi_i | \nabla^2 | \varphi_i \rangle \tag{3.76}$$

Since the non-interacting kinetic energy is not equal to the true kinetic energy of the interacting system, Kohn and Sham rewrote the HK functional as

$$F[\rho(\mathbf{r})] = T_S[\rho(\mathbf{r})] + J[\rho(\mathbf{r})] + E_{XC}[\rho(\mathbf{r})] \tag{3.77}$$

where the exchange-correlation energy E_{XC} is introduced

$$E_{XC}\left[\rho(\mathbf{r})\right] \equiv \left(T\left[\rho(\mathbf{r})\right] - T_S\left[\rho(\mathbf{r})\right]\right) + \left(E_{ee}\left[\rho(\mathbf{r})\right] - J\left[\rho(\mathbf{r})\right]\right) = T_C\left[\rho(\mathbf{r})\right] + E_{ncl}\left[\rho(\mathbf{r})\right] \quad (3.78)$$

E_{XC} gathers the residual part of the true kinetic energy, T_C, and the non-classical electrostatic contributions. Put simply, it contains everything that is unknown.

At this point, how can we define V_S such that it really provides us with a Slater determinant which yields exactly the same density as our real system? To solve this problem, let us write the energy of our interacting system in terms of the quantities defined in Eq. 3.77

$$\begin{aligned} E\left[\rho\right] = &\quad T_S\left[\rho\right] + J\left[\rho\right] + E_{XC}\left[\rho\right] + E_{Ne}\left[\rho\right] \\ = &\quad T_S\left[\rho\right] + \tfrac{1}{2}\int\int \tfrac{\rho(\mathbf{r}_1)\rho(\mathbf{r}_1)}{r_{12}} d\mathbf{r}_1 d\mathbf{r}_2 + E_{XC}\left[\rho\right] + \int V_{Ne}\rho(\mathbf{r}) d\mathbf{r} \\ = &\quad -\tfrac{1}{2}\sum_i^N \left\langle \varphi_i \left| \nabla^2 \right| \varphi_i \right\rangle + \tfrac{1}{2}\sum_i^N\sum_j^N \int\int \left|\varphi_i(\mathbf{r}_1)\right|^2 \tfrac{1}{r_{12}} \left|\varphi_j(\mathbf{r}_2)\right|^2 d\mathbf{r}_1 d\mathbf{r}_2 + E_{XC}\left[\rho(\mathbf{r})\right] - \sum_i^N \int \sum_A^M \tfrac{Z_A}{r_{1A}} \left|\varphi_i(\mathbf{r}_1)\right|^2 d\mathbf{r}_1 \end{aligned} \quad (3.79)$$

The variational minimization of the energy expression 3.79, under the usual constraint of $\left\langle \varphi_i \left| \varphi_j \right\rangle = \delta_{ij}\right.$, yields the following set mono-electronic equations, known as Kohn-Sahm equations

$$\left(-\frac{1}{2}\sum_i^N \nabla^2 + \left[\int \frac{\rho(\mathbf{r}_2)}{r_{12}} d\mathbf{r}_2 + V_{XC}(\mathbf{r}_1) - \sum_A^M \frac{Z_A}{r_{1A}} \right] \right) \varphi_i = \left(-\frac{1}{2}\sum_i^N \nabla^2 + V_{eff}(\mathbf{r}_1) \right) \varphi_i = \varepsilon_i \varphi_i \quad (3.80)$$

If we compare these equations with the one-particle equations from the non-interacting reference system, we conclude that V_{eff} is identical to V_S

$$V_S(\mathbf{r}) \equiv V_{eff}(\mathbf{r}) = \int \frac{\rho(\mathbf{r}_2)}{r_{12}} d\mathbf{r}_2 + V_{XC}(\mathbf{r}_1) - \sum_A^M \frac{Z_A}{r_{1A}} \quad (3.81)$$

V_{XC} in Eq. 3.81 stands for the potential due to the exchange-correlation energy E_{XC}. Since the functional form of E_{XC} is unknown, we also have no clue as to the explicit expression of V_{XC}. It is simply defined as the functional derivative of E_{XC} with respect to ρ

$$V_{XC} \equiv \frac{\delta E_{XC}}{\delta \rho} \quad (3.82)$$

If E_{XC} and V_{XC} were known, the Kohn-Sham approach would lead to the exact energy. Unlike the HF model, the Kohn-Sham approach is in principle exact. The approximations come into play when we have to decide the functional form of E_{XC} and the corresponding V_{XC}. The modern DFT is intended to find out the best approximation for these two terms.

Notice that once V_S known (Eq. 3.81), the orbitals are determined (Eq. 3.74), which in turn dictate the ground state density (Eq. 3.75) and the ground state energy (Eq. 3.79). However, V_S already depends on the density (and thus on the orbitals) through the Coulomb term $J[\rho]$ (Eq. 3.82). Therefore, the Kohn-Sham one-electron equations have to be solved iteratively, just like the HF equations.

The physical significance of the Kohn-Sham orbitals remains a debated issue. Some authors claim that they do not have any meaning other than allowing the exact density to be calculated. Likewise, the Kohn-Sham orbital energies should not be confused with molecular orbital energies. Other authors, however, based on the fact that the exact Kohn-Sham orbital energy for the HOMO is just the negative of ionization potential [230, 231], and due to the fact that the set of Kohn-Sham equations remind us, as in the HF case, the independent particle model, they attribute to the Kohn-Sham orbitals a similar physical significance and legitimacy than to the HF canonical orbitals. Several publications reported the similarity of the Kohn-Sham molecular orbitals and the molecular orbitals obtained from standard Molecular Orbital - Linear Combination of Atomic Orbitals methods (MO-LCAO hereafter) and claimed that useful information can be obtained about molecular systems from analysis of their molecular orbitals even if the density functional methods are used [231, 232].

3.2.4 Approximations to the Exchange-Correlation Energy

As stated previously, the exchange-correlation functional E_{xc} and hence the exchange-correlation potential V_{xc} are unknown. While DFT itself does not give any recipe to construct approximate exchange-correlation functionals, it holds both the promise that the true E_{xc} is an universal functional of the density. Inspired by this challenge, many approximations to the E_{xc} have been developed so far. They are summarized in the following.

3.2.4.1 Local Density Approximation (LDA)

The first approach, the so called Local Density Approximation (LDA hereafter), considers each volume element with local density $\rho(\mathbf{r})$ to be a homogeneous electron gas. This approximation is expected to be accurate if the electron density varies slowly in space. Accordingly, it is a good model for simple metals such as sodium. However, it is pretty far from any

realistic situation in atoms or molecules, where the density varies rapidly. Nevertheless, LDA occupies a prominent place in DFT, since it is the only system for which the form of the exchange-correlation functional is known exactly (or at least to very high accuracy). In LDA, E_{XC} is given by

$$E_{XC}^{LDA}[\rho] = \int \rho(\mathbf{r})\varepsilon_{XC}[\rho]\, d\mathbf{r} \tag{3.83}$$

where $\varepsilon_{XC}[\rho]$ is the exchange plus correlation energy per electron in a homogeneous electron gas with electron density ρ. $\varepsilon_{XC}[\rho]$ can be further broken down into exchange and correlation contributions

$$\varepsilon_{XC}[\rho] = \varepsilon_X[\rho] + \varepsilon_C[\rho] \tag{3.84}$$

The exchange term $\varepsilon_X[\rho]$ is, apart from the prefactor, equal to the form found by Slater in his approximation of the HF exchange

$$\varepsilon_X[\rho] = -\frac{3}{4}\sqrt[3]{\frac{3\rho(r)}{\pi}} \tag{3.85}$$

No such explicit expression is known for the correlation part $\varepsilon_C[\rho]$. However, based on highly accurate numerical simulations of the homogeneous electron gas, analytical expressions have been developed for $\varepsilon_C[\rho]$. The most popular approach is probably the one presented by Vosko, Wilk and Nusair in 1980 [233], while the most recent and probably also most accurate one has been given by Perdew and Wang [234].

3.2.4.2 Non Local Approximations

Even if density varies rapidly in molecules, LDA provides surprisingly nice results for equilibrium geometries, harmonic frequencies and dipole moments, even for transition metals. However, it has shown to be inadequate for the proper description of several chemical systems. LDA approximations often results in errors of about 10% for the exchange energy, and even more for the correlation term. Consequently, a great deal of research has been devoted to the development of more sophisticated formulations of the exchange-correlation functionals.

The derivation of the first successful extension to the purely local approximations in the early eighties represented a significant breakthrough in the field. To account for the non-homogeneity of the true electron density in molecules, the logical first step beyond the LDA was to consider not only the density $\rho(\mathbf{r})$ at a particular point $\mathbf{r}$, but also the gradient of the charge density $\nabla\rho(\mathbf{r})$. Simply put, LDA can be envisioned as the first term of a Taylor expansion of the exchange-correlation functional E_{XC} in terms of the density

$$E_{XC}\left[\rho_\alpha,\rho_\beta\right]=\underbrace{\int\rho\varepsilon_{XC}\left[\rho_\alpha,\rho_\beta\right]d\mathbf{r}}_{E_{XC}^{LDA}}+\underbrace{\sum_{\sigma,\sigma'}\int C_{XC}^{\sigma,\sigma'}\left[\rho_\alpha,\rho_\beta\right]\frac{\nabla\rho_\sigma}{\rho_\sigma^{2/3}}\frac{\nabla\rho_{\sigma'}}{\rho_{\sigma'}^{2/3}}d\mathbf{r}+...}_{E_{XC}^{NL}} \tag{3.86}$$

where σ and σ' indicate α and β spin. Extending the series with the non-local terms E_{XC}^{NL} is expected to provide a better approximation of the E_{XC} functional. However, the functional form Eq. 3.86, termed the Gradient Expansion Approximation (GEA), performs quite disappointingly (often even worst than LDA) when used to solve real molecular problems. The reason behind is that the exchange-correlation hole associated with the functional of Eq. 3.86 lacks of many of the properties which make the LDA hole physically meaningful. To circumvent this drawback, the holes of the GEA functionals were enforced to fulfill the requirements of the true LDA holes. The functionals restored in this manner are known as Generalized Gradient Approximations (GGA). They are generally written as

$$E_{XC}^{GGA}\left[\rho_\alpha,\rho_\beta\right]=\int f\left[\rho_\alpha,\rho_\beta,\nabla\rho_\alpha,\nabla\rho_\beta,\right]d\mathbf{r} \tag{3.87}$$

In practice E_{XC}^{GGA} is usually partitioned into its exchange and correlation terms

$$E_{XC}^{GGA}=E_X^{GGA}+E_C^{GGA} \tag{3.88}$$

Non Local Approximations to Exchange

The exchange term of E_{XC}^{GGA} is often written as

$$E_X^{GGA}=E_X^{LDA}-\sum_\sigma\int F\left(s_\sigma\right)\rho_\sigma^{4/3}\left(\mathbf{r}\right)d\mathbf{r} \tag{3.89}$$

where s_σ, the argument of function F, stands for the reduced density gradient for spin

$$s_\sigma\left(\mathbf{r}\right)=\frac{\left|\nabla\rho_\sigma\left(\mathbf{r}\right)\right|}{\rho_\sigma^{4/3}\left(\mathbf{r}\right)} \tag{3.90}$$

For F two type of realizations have been developed. The first one is inspired on the GGA exchange functional developed by Becke in 1988 [235] and assumes the following form

$$F^B=\frac{\beta s_\sigma^2}{1+6\beta s_\sigma sinh^{-1}s_\sigma} \tag{3.91}$$

where β is an empirical parameter set to 0.0042 to reproduce the exactly known exchange energies of the rare gas atoms. The functional form of Eq. 3.91 was designed to reproduce the appropriate asymptotical behavior of the exchange energy density.

The second class of GGA functionals express F as a rational function of s_σ. Representative examples of this kind of functionals are the early ones by Becke (B86) [236] and Perdew [237] (P86) or the one developed by Perdew, Burke, and Ernzerhof [238] (PBE). In Perdew's 1986 exchange functional, for instance, F looks like

$$F^{P86} = \left(1 + 1.296\left(\frac{s_\sigma}{(24\pi^2)^{1/3}}\right)^2 + 14\left(\frac{s_\sigma}{(24\pi^2)^{1/3}}\right)^4 + 0.2\left(\frac{s_\sigma}{(24\pi^2)^{1/3}}\right)^6\right)^{1/15} \tag{3.92}$$

Non Local Approximations to Correlation

The main problems found in the advance of modern DFT are due to the correct description of electron correlation. Local models tend to overestimate the correlation energy, leading to inaccuracies in the treatment of inhomogeneous systems. Over the last years, many functionals have been devised for the correlation part of E_{XC}^{GGA}. Some of the most important ones are summarized in the following.

Perdew 86 (P86) [237]: It was developed based on the wave vector analysis, in which the correlation energy is broken down into its different wave length components. It was originally derived from the one proposed by Langreth and Mehl. It reads as follows

$$E_C^{P86} = \left[\rho^\alpha, \rho^\beta\right] = \int \rho\left(\mathbf{r}\right)\varepsilon_c\left(\rho^\alpha, \rho^\beta\right)d\mathbf{r} + \int \frac{d^{-1}e^{-\phi}C\left(\rho\right)\left|\nabla\rho\right|^2}{\rho^{4/3}}d\mathbf{r} \tag{3.93}$$

The P86 functional has been widely used and has proven to deliver better results than its predecessor.

Perdew-Wang 91 (PW91) [234]: The PW91 functional was proposed as a modification of the P86 functional, inspired on a new formulation of the correlation energy of the uniform electron gas. An analytic representation for the correlation energy is mandatory for the energy functional to be accurate both in the local and non local approximations. The correlation energy per electron $\varepsilon_C\left(r_s, X\right)$, in the limit of small values of r_s (i.e. high densities), is given by

$$\varepsilon_C\left(r_s, X\right) = c_0\left(X\right)ln\left(r_s\right) - c_1\left(X\right) + c_2\left(X\right)r_s ln\left(r_s\right) - c_3\left(X\right)r_s + ... \tag{3.94}$$

whereas, for large values of (i.e. small densities), it reads as

$$\varepsilon_C\left(r_s, X\right) = -\frac{d_0\left(X\right)}{r_s^p} + -\frac{d_1\left(X\right)}{r_s^{2p-1/2}} + ... \tag{3.95}$$

Lee-Yang-Parr (LYP) [239]: Inspired in the Colle-Salvetti formula [240], the LYP correlation energy correction reads as

$$E_C^{LYP} = -a\int \frac{1}{1+dp^{-1/3}}\left\{\rho_b\rho^{-2/3}\left[C_F\rho^{5/3} - 2t_w + \left(\frac{1}{9}t_w + \frac{1}{18}\nabla^2\rho\right)e^{-c\rho^{-1/3}}\right]d\mathbf{r}\right\} \tag{3.96}$$

It is worth noting that, unlike P86 and PW91, LYP is not based on the uniform electron gas. The constants a, b, c, and d were determined from a fitting procedure on the helium atom, for which an accurate expression of the correlation energy was derived by means of correlated wave function methods.

Closely related to the GGA constructions, we find the meta-GGA functionals, which also include the laplacian of the electron density, *i.e.*, $\varepsilon_{xc} = \varepsilon_{xc}\left(\rho, \nabla\rho, \nabla^2\rho\right)$.

3.2.4.3 Hybrid Functionals

The functionals presented above are the ones rigorously established by DFT. Becke [241] proposed a different approach for the exchange-correlation, which gave rise to the so called hybrid functionals. In this kind of functionals, HF theory and DFT are combined. HF theory is known to provide the exact description of the exchange interactions (the exchange energy of a Slater determinant can be computed exactly), but lacks of electron correlation. On the other hand, DFT methods include correlation effects, in a much easier way than post-HF methods do. However, they often fail in the description of the exchange. Importantly, this latter term is significantly larger in absolute numbers than the corresponding correlation.

The typical exchange-correlation term of an hybrid functional reads as

$$E_{XC} = E_X^{exact} + E_C^{KS} \tag{3.97}$$

where E_X refers to the exchange energy obtained from the Slater determinant built with the Kohn-Sham molecular orbitals and E_C^{KS} stands for the DFT correlation term.

Becke proposed a novel formulation of the exchange-correlation term, based on the so called adiabatic connection, which provides a rigorous definition for the exchange-correlation energy. In this framework, the exchange-correlation term reads as

$$E_{XC} = \int_0^1 U_{XC}^{\lambda} d\lambda \tag{3.98}$$

where U_{XC}^{λ} stands for the non-classical contribution to the electron-electron interaction for different values of the parameter λ. $\lambda = 0$ corresponds to a non-interacting system, where the only non-classical component is due to the antisymmetry of fermion wave function. Accordingly, $U_{XC}^{\lambda=0}$ comprises exchange only. It corresponds to the exchange contribution of the Slater determinant and can be computed exactly. When $\lambda = 1$, we are dealing with a fully interacting system in which the non-classical contributions include both exchange and correlation. The corresponding exchange-correlation energy, $U_{XC}^{\lambda=1}$, is unknown, but can be approximated by any E_{XC} functional. The non-interacting system ($\lambda = 0$) and the fully interacting one ($\lambda = 1$) are connected through a continuum of partially interacting systems, which share the same density ρ, set as the density of the fully interacting system. To exactly evaluate integral 3.98, U_{XC}^{λ} must be known for intermediate values of λ. Unfortunately, this information remains elusive and Eq. 3.98 has to be solved approximately. The simplest approach is to consider U_{XC}^{λ} as a linear function of λ

$$E_{XC} = \int_0^1 U_{XC}^{\lambda} d\lambda = \frac{1}{2} U_{XC}^{\lambda=0} + \frac{1}{2} U_{XC}^{\lambda=1} \tag{3.99}$$

Adopting the LDA exchage-correlation functional for $U_{XC}^{\lambda=1}$, Eq. corresponds to the *half-and-half* combination of the exact exchange and density functional exchange-correlation as introduced by Becke. Later on, a generalization of Eq. 3.99 was proposed, in which two adjustable parameters c_0 and c_1 were introduced.

$$E_{XC} = c_0 U_{XC}^{\lambda=0} + c_1 U_{XC}^{\lambda=1} \tag{3.100}$$

c_0 and c_1 were set to 0.332 and 0.575 to accurately reproduce the thermochemical data of the G1 data base. A step forward was made when Becke relaxed the linear dependence in λ and considered gradient corrections for the exchange and correlation terms. He introduced semiempirical coefficients to determine the weights of the various terms in E_{XC}. Becke's three parameter functional reads as

$$E_{XC}^{B3} = E_{XC}^{LSDA} + a\left(E_{XC}^{\lambda=0} - E_X^{LSDA}\right) + bE_X^B + cE_C^{PW91} \tag{3.101}$$

Parameter a determines the amount of exact exchange in the functional, whereas b and c tailor the contribution of exchange and correlation gradient corrections to the LDA approximation. The semiempirical parameters where chosen $a = 0.20$, $a = 0.72$, and $a = 0.81$ to reproduce the atomization and ionization energies, as well as the proton affinities of the G2 data base. Eq. 3.101 constitutes a model on which various functionals have been built up. This sort of functionals, where a certain amount of exact exchange is included, are known as

hybrid functionals. Eq. 3.101 incorporates the gradient corrections to the exchange and correlation due to the B [242] and PW91 [234] functionals, respectively. However, it is open to different exchange-correlation functionals. B3PW91 and B3LYP, for example, include PW91 and LYP correlation terms, respectively. B3LYP is probably the most popular functional among the hybrid ones.

Recently, new type of functionals have been devised. The so called hybrid meta-GGA functionals combine a meta-GGA functional with the HF exchange. The double-hybrid functionals, in turn, are constructed adding a non-local electron correlation to an hybrid functional. The so named local hybrid functionals combine the portion of HF and DFT exchange depending on the local properties of the given system, in contrast to global hybrid functionals. Finally, Range-Separated Hybrid functionals (RSH hereafter) split the Coulomb operator into its long-range and short range components, which are treated differently.

As mentioned before, since density functional calculations do not use the exact E_{xc} they are not, strictly speaking, *ab initio* calculations. Besides, there is not any systematic way to improve the calculations by applying more and more sophistication. That is why there is an immense sea of functionals where computational chemists try to stay afloat. And the number of functionals increases dizzily. In the end, the quality of a given functional is determined by comparing with respect to experimental results or calculations performed by means of a high level wave function method.

One of the main advantages of DFT methods is that with a similar computational cost to HF methods, they include some kind of electron correlation, even if the correlation effects cannot be sorted out precisely. They are already mixed from the beginning with the uncorrelated solution. In spite of this fact, DFT have been found to yield satisfactory results for ground state properties of various chemical systems, with a quality comparable to MP2 results, or even better in some cases. Due to their relative low computational cost, DFT is the method of choice for large systems, for which the inclusion of electron correlation by MP or CI methods is prohibitive.

3.3 Time-Dependent DFT

Even if the time-independent version of DFT provides precise results non degenerated for ground state properties, it lacks of a proper description of the excited states. In this context, the time-dependent generalization of the DFT formalism (TDDFT hereafter) (see [243–245] for review) comes into play. It extends the basic ideas of ground state DFT and allows the description of several time-dependent phenomena. The original many-body time-dependent Schrödinger equation

$$\begin{aligned} i\tfrac{\partial}{\partial t}\Psi(\mathbf{r},t) &= \hat{H}(\mathbf{r},t)\Psi(\mathbf{r},t) \\ \hat{H}(\mathbf{r},t) &= -\tfrac{1}{2}\sum_{i=1}^{N}\nabla_i^2 + \tfrac{1}{2}\sum_{i<j}^{N}\tfrac{1}{|\mathbf{r}_i-\mathbf{r}_j|} + \hat{V}_{ext}(\mathbf{r},t) \end{aligned} \tag{3.102}$$

is replaced by set of time-dependent single-particle equation whose solutions (orbitals) yield the same time-dependent density. As one may notice from Eq. 3.102, the electrons are under the influence of a generic time-dependent potential $\hat{V}_{ext}(\mathbf{r}, t)$. The most common perturbation of this class is a long-wavelength electric field, with a characteristic oscillation frequency ω. Typically, the perturbation is weak and linear response analysis is able to simulate the optical properties of most of the chemical systems

3.3.1 Runge-Gross Theorem

For any N-electron system subject to a time-dependent potential, it can be shown that all physical observables are uniquely determined if the time-dependent density, on the one hand, and the state of the system at an arbitrary single instant in time, on the other, are known [246]. Runge-Gross theorem proves that densities $\rho(\mathbf{r}, t)$ and $\rho'(\mathbf{r}, t)$ of two systems evolving from the same initial state $\Psi(\mathbf{r}, t_0)$ under the influence of the scalar potentials $v(\mathbf{r}, t)$ and $v'(\mathbf{r}, t)$, both Taylor expandable about t_0 and differing by more than a purely time-dependent function, will always differ. Simply put, it states that for a given initial wave function, there exists a unique mapping between the time-dependent external potential and its time-dependent density. This theorem represents the time-dependent analogue of the first Hohenberg-Kohn Theorem.

From the Runge-Gross theorem, the time-dependent external potential, associated to a certain time-dependent density $\rho(\mathbf{r}, t)$ is unique up to a purely time-dependent function $c(t)$, determining the total time-dependent wave function, which in turn is unique up to a time-dependent phase factor $\alpha(t)$

$$\Psi(t) = e^{-i\alpha(t)}\tilde{\Psi}[\rho](t) \tag{3.103}$$

For an operator $\hat{\mathcal{O}}(t)$, which might be a function of time but contains no derivative or integral operators on t, this phase factor cancels out when computing the expectation value

$$\left\langle \Psi(t) \left| \hat{\mathcal{O}}(t) \right| \Psi(t) \right\rangle = \hat{\mathcal{O}}(t)[\rho](t) \tag{3.104}$$

In this formulation, only scalar potentials are considered. It is worth mentioning, however, that there is an extension of the TDDFT for a complete treatment of magnetic effects, *i.e.* the Time-Dependent Current-DFT (TDCDFT) [247].

3.3.2 Time-Dependent Kohn-Sham Equations

Based on the second Hohenberg-Kohn theorem, the variational minimization of the ground state energy delivers the Kohn-Sham orbitals. In the time-dependent framework of DFT, there is no such a variational principle for the total energy. There exists, however, a quantity analogous to the ground state energy, the so called quantum mechanical action A

$$A = \int_{t_0}^{t_1} \left\langle \Psi(t) \left| i\frac{\partial}{\partial t} - \hat{H}(t) \right| \Psi(t) \right\rangle dt \tag{3.105}$$

which indeed can be expressed in terms of the density since there is a unique mapping between the density and the wave function, *i.e.*, $A\left[\Psi\left(\rho\right)\right] = A\left[\rho\right]$.

$$A\left[\rho(\mathbf{r},t)\right] = \int_{t_0}^{t_1} \left\langle \Psi\left[\rho\right](t) \left| i\frac{\partial}{\partial t} - \hat{H}(t) \right| \Psi\left[\rho\right](t) \right\rangle dt \tag{3.106}$$

The time-dependent density should be the one which makes the action stationary

$$\frac{\delta A\left[\rho\right]}{\delta\rho(\mathbf{r},t)} = 0 \tag{3.107}$$

$A\left[\rho\right]$ can be written as

$$A\left[\rho\right] = B\left[\rho\right] - \int_{t_0}^{t_1} \int v\left(\mathbf{r},t\right)\rho\left(\mathbf{r},t\right) d\mathbf{r}dt \tag{3.108}$$

where the functional $B\left[\rho\right]$ is independent of the external potential. Time-dependent Kohn-Sham equations are derived assuming the existence of a potential $v_{eff}(\mathbf{r},t)$, for an independent particle system, whose orbitals $\psi(r,t)$ yield the charge density $\rho(\mathbf{r},t)$ of the real interacting system

$$\rho(\mathbf{r},t) = \sum_i f_i \left|\psi_i(\mathbf{r},t)\right|^2 \tag{3.109}$$

where f_i refers for the orbital occupation numbers. Considering that such an $v_{eff}(r,t)$ exists, $B\left[\rho\right]$ can be written as

$$B\left[\rho\right] = \sum_i f_i \int_{t_0}^{t_1} \left\langle \Psi\left[\rho\right](t) \left| i\frac{\partial}{\partial t} - \hat{H}(t) \right| \Psi\left[\rho\right](t) \right\rangle dt - \frac{1}{2}\int_{t_0}^{t_1}\int\int \frac{\rho\left(\mathbf{r}_1,t\right)\rho\left(\mathbf{r}_2,t\right)}{\left|\mathbf{r}_1-\mathbf{r}_2\right|} d\mathbf{r}_1 d\mathbf{r}_2 dt - A_{\mathrm{XC}}\left[\rho\right] \tag{3.110}$$

where $A_{XC}[\rho]$ stands for the exchange-correlation functional and plays a role analogous to the exchange-correlation energy in DFT. The time-dependent Kohn-Sham equations read as

$$\left[-\frac{1}{2}\nabla^2 + v_{eff}(\mathbf{r},t)\right]\psi_i(\mathbf{r},t) = i\frac{\partial}{\partial t}\psi_i(\mathbf{r},t) \tag{3.111}$$

where

$$v_{eff}(\mathbf{r},t) = v(\mathbf{r},t) + \int \frac{\rho(\mathbf{r}_1,t)}{|\mathbf{r}_1 - \mathbf{r}'|}d\mathbf{r}' + v_{XC}(\mathbf{r},t) \tag{3.112}$$

Even if $A_{XC}[\rho]$ is unknown, in the limit of a slowly varying external potential, it can be written as

$$A_{XC} = \int_{t_0}^{t_1} E_{XC}[\rho(t)]\,dt \tag{3.113}$$

where E_{XC} is the time-independent exchange correlation functional. This assumption, called the adiabatic approximation, is local in time and has become the standard in TDDFT. Within the adiabatic approximation

$$v_{XC}(\mathbf{r},t) = \frac{\partial A_{XC}[\rho]}{\partial \rho(\mathbf{r},t)} \approx \frac{\partial E_{XC}[\rho]}{\partial \rho_t(\mathbf{r})} = v_{XC}(\mathbf{r},t) = v_{XC}\left[\rho(r)_{\rho=\rho(t)}\right] \tag{3.114}$$

and v_{XC} is simply the exchange-correlation potential of DFT evaluated with the density at a particular time t. By inserting the LDA functional the so called Adiabatic Local Density Approximation (ALDA) is obtained, which assumes that the exchange-correlation potential at point $\mathbf{r}$ and time t is equal to that of the homogeneous electron gas. Even if this potential suffers from all the problems present in LDA, it yields remarkably good excitation energies and is therefore widely used in TDDFT.

Depending on the strength of the time-dependent potential, two different approaches are considered, namely (1) linear response theory (weak potential) and (2) the full solution of the Kohn-Sham equations (strong potential).

3.3.3 Linear Response Theory

In conditions where the external potential is small enough, it is no necessary to solve the full time-dependent Kohn-Sham equations. In stationary DFT the electronic energy is often expanded, up to second order, as follows

$$\begin{aligned}\triangle E = & \left(\frac{\partial E}{\partial N}\right)_v \triangle N + \int \left(\frac{\delta E}{\delta v(\mathbf{r})}\right)_N \triangle v(\mathbf{r}) d\mathbf{r} + \frac{1}{2}\left(\frac{\partial^2 E}{\partial N^2}\right)_v \triangle N^2 \\ & + \frac{1}{2}\int\int \chi\left(\mathbf{r},\mathbf{r}'\right) \triangle v(\mathbf{r}) \triangle v(\mathbf{r}') d\mathbf{r} d\mathbf{r}' + \int \left(\frac{\delta^2 E}{\delta v(\mathbf{r}) \partial N}\right) \triangle N \triangle v(\mathbf{r}) d\mathbf{r}\end{aligned} \tag{3.115}$$

where χ stands for the linear response function

$$\chi\left(\mathbf{r},\mathbf{r}'\right) = \left(\frac{\delta^2 E}{\delta v\left(\mathbf{r}\right) \delta v\left(\mathbf{r}'\right)}\right)_N = \left(\frac{\delta \rho\left(\mathbf{r}\right)}{\delta v\left(\mathbf{r}'\right)}\right)_N \tag{3.116}$$

From Eq. 3.116, $\delta\rho$ can be written as

$$\delta\rho\left(\mathbf{r}\right) = \int \chi\left(\mathbf{r},\mathbf{r}'\right) \delta v\left(\mathbf{r}'\right) d\mathbf{r}' \tag{3.117}$$

In the time-dependent formalism of DFT, $\delta\rho$ reads as

$$\delta\rho\left(\mathbf{r},\omega\right) = \int \chi\left(\mathbf{r},\mathbf{r}',\omega\right) \delta v_{ext}\left(\mathbf{r}',\omega\right) d\mathbf{r}' \tag{3.118}$$

Simply put, if we shake our N-electron system with an external potential v_{ext}, then the response of the system in terms of the density at point $\mathbf{r}$ and time t is modulated by the response function. However, finding good approximations to this linear response function represents a tough challenge. Instead, TDDFT expresses the exact density response $\delta\rho$ by means of the response function χ_S of the non-interacting Kohn-Sham system

$$\delta\rho\left(\mathbf{r},\omega\right) = \int \chi_S\left(\mathbf{r},\mathbf{r}',\omega\right) \delta v_{eff}\left(\mathbf{r}',\omega\right) d\mathbf{r}' \tag{3.119}$$

with

$$\delta v_{eff}\left(\mathbf{r}',\omega\right) = \delta v_{ext}\left(\mathbf{r}',\omega\right) + \int d\mathbf{r}'' \frac{\delta\rho\left(\mathbf{r}'',\omega\right)}{\left|\mathbf{r}'-\mathbf{r}''\right|} \delta v_{XC}\left(\mathbf{r}',\omega\right) \tag{3.120}$$

and where the change in the exchange-correlation potential, δv_{XC}, is given in terms of the Fourier transform of the so called exchange-correlation kernel

$$\delta v_{XC}\left(\mathbf{r}',\omega\right) = \int d\mathbf{r}'' f_{XC}\left(\mathbf{r},\mathbf{r}',\omega\right) \delta\rho\left(\mathbf{r}'',\omega\right) \tag{3.121}$$

The linear response function of the non-interacting Kohn-Sham system reads as

$$\chi_S\left(\mathbf{r},\mathbf{r}',\omega\right) = \sum_i^{occ}\sum_m^{virt} f_i \psi_i\left(\mathbf{r}\right) \psi_m\left(\mathbf{r}\right) \psi_m\left(\mathbf{r}'\right) \psi_i\left(\mathbf{r}'\right) \left(\frac{1}{\left(\varepsilon_i - \varepsilon_m\right) + \omega} + \frac{1}{\left(\varepsilon_i - \varepsilon_m\right) - \omega}\right) \tag{3.122}$$

Eqs. 3.119-3.122 have to be solved self-consistently to get $\delta\rho$. Once the variation of the density is known, the frequency-dependent polarizability α can be computed, which describes the response of the dipole moment to a time-dependent electric field with frequency $\omega(t)$

$$\alpha_{ij}(\omega) = -\frac{2}{E}\int dr\delta\rho(r,\omega)\, r_j \tag{3.123}$$

According to the Sum-over-States (SOS hereafter) relation,

$$\alpha(\omega) = \sum_l \frac{f_l}{\omega_l^2 - \omega^2} \tag{3.124}$$

As one may notice from Eq. 3.124, α diverges at the exact excitation energies of the unperturbed system, ω_l. Therefore, the excitation energies are available from the frequency-dependent polarizabilities. The residues, f_l, determine the corresponding oscillator strengths [244]. It is worth mentioning that there is a more general formulation of TDDFT, based on Dyson equations, where the excitation energies are poles of the response function.

TDDFT in its linear response approach has been successfully applied to a wide variety of systems, *i.e.*, metal compounds [248–250], organic [251–253] or inorganic molecules [254, 255], extended systems [256], becoming a very powerful tool to calculate excitation energies of realistic systems. However, due to the incorrect asymptotic behavior of the approximate exchage-correlation potentials, TDDFT is not able to accurately describe neither Rydberg states [257, 258] nor charge transfer excitations [259]. Recently, several asymptotically corrected potentials have been developed [260, 261] in order to tackle these drawbacks.

Whenever linear response theory is inappropriate (non-linear optical properties or photochemical processes), the TDDFT Kohn-Sham equations have to be solved directly.

3.3.4 Quantum Molecular Dynamics

Molecular Dynamics (MD hereafter) is a kind of computer simulation were the positions of the particles are propagated on time according to the equations of motion. In the framework of Quantum Mechanics, the motion of the particles is determined by the time-dependent Schrödinger equation.

$$i\frac{\partial}{\partial t}\Psi(\{\mathbf{r}_i\},\{\mathbf{R}_\alpha\};t) = \hat{H}\Psi(\{\mathbf{r}_i\},\{\mathbf{R}_\alpha\};t) \tag{3.125}$$

A cheaper approach describes the motion of the particle according to the equation of Classical Mechanics. In Quantum Mechanics the Hamiltonian operator $\hat{H}$ acts on the wave function Ψ in the same way as the Lagrangian operator $\hat{L}$ acts on the position of the particles in the framework of the Classical Mechanics.

3.3.4.1 BO Molecular Dynamics

One convenient approach to include the electronic structure in MD simulations consists in straightforwardly solving the static electronic structure problem in each MD step given the

set of fixed nuclear positions at that instance of time. This is the so called BO Molecular Dynamics (BOMD hereafter) simulations. BOMD follows the adiabatic time evolution of a system, dividing time into series of time steps. In order to solve the equations of motion, electrons are treated quantum mechanically (solving the electronic equation by means of DFT) and nuclei classically. Thus, we solve the static electronic structure problem in each MD step given the set of fixed nuclear positions at that instance of time. Hence, the electronic structure part is reduced to solving a time-independent quantum problem, namely by solving the time-independent Schrödinger equation, followed by the propagation of the nuclei *via* classical MD. The forces acting on the nuclei are calculated as follows

$$\mathbf{F} = -\nabla_\alpha E = M_\alpha \ddot{\mathbf{R}}_\alpha (t) = -\nabla_\alpha \underset{\{\Psi_0\}}{min} \left\{ \left\langle \Psi_0 \left| \hat{H}_e \right| \Psi_0 \right\rangle \right\} \tag{3.126}$$

where the electronic ground state has to be reached in each MD step according to Eq. 3.126. This can be also written according to Lagranges's formalism

$$\hat{L} \equiv \hat{K} - \hat{U} = \frac{1}{2}\sum_\alpha M_\alpha \dot{R}_\alpha^2 - \underset{\{\Psi_0\}}{min} \left\{ \left\langle \Psi_0 \left| \hat{H}_e \right| \Psi_0 \right\rangle \right\} \tag{3.127}$$

If DFT is used to solve the the electronic problem, the ground state energy of the interacting system of electrons with classical nuclei fixed at positions $\{\mathbf{R}_\alpha\}$ can be obtained as the minimum of Kohn-Sham energy

$$\underset{\Psi_0}{min} \left\{ \left\langle \Psi_0 \left| \hat{H}_e \right| \Psi_0 \right\rangle \right\} = \underset{\{\psi_i\}}{min} E^{KS} \left[\{\varphi_i\} \right] \tag{3.128}$$

where the E^{KS} and $\{\varphi_i\}$ stand for the Kohn-Sham energy and orbitals, respectively.

3.3.4.2 Car-Parrinello Molecular Dynamics

A key breakthrough that changed Quantum MD from simply an interesting idea to powerful and useful method was made by R. Car and M. Parrinello [262]. They introduced an algorithm in which the separate tasks of following the motion of nuclei and finding the electronic ground state given the nuclear positions are treated in a unified way through an extended Lagrangian. The central idea of Car-Parrinello Molecular Dynamics (CPMD hereafter) is to define equations of motion for both the nuclei and the electronic degrees of freedom that are simultaneously followed during MD. Car and Parrinello's extended Lagrangian is constructed with nuclear equations of motion similar to Eq. 3.127 and the introduction of the electronic degrees of freedom as fictitious dynamical variables. The extended Lagrangian describing the simultaneous motion of nuclei and electrons can be written as follows

$$\hat{L} = \frac{1}{2}\sum_\alpha M_\alpha \dot{R}_\alpha^2 - \underset{\{\Psi_0\}}{min} \left\{ \left\langle \Psi_0 \left| \hat{H}_e \right| \Psi_0 \right\rangle \right\} + \frac{1}{2}\sum_i \mu_i \left\langle \dot{\varphi}_i \mid \dot{\varphi}_i \right\rangle + \sum_{i,j} \Lambda_{i,j} \left(\left\langle \varphi_i \mid \varphi_i \right\rangle - \delta_{ij} \right) \tag{3.129}$$

The first two terms on the right-hand side are the same as in Eq. 3.127, while the last two terms introduce fictitious degrees of freedom. The third term has the form of kinetic energy. It introduces a fictitious mass μ for the electrons and a time derivative of the one-electron wave functions φ_i . The final term is required to keep the one-electron wave functions orthogonal.

Given that the nuclear and electronic degrees of freedom are propagated simultaneously during CPMD, the total energy calculated at each step does not correspond exactly to the true BO potential energy surface for the nuclear coordinates. It is also important to realize that the equations of motion for the electrons are a mere mathematical device to allow the dynamics of the nuclei to be generated in a numerically efficient way, *i.e.*, the dynamics of the electronic degrees of freedom cannot be interpreted physically as the dynamics of electrons.

CPMD simulations bypass the explicit electronic minimization at each time step. After an initial standard electronic minimization, the fictitious dynamics of the electrons keep them on the electronic ground state corresponding to each new ionic configuration visited along the simulation, thus yielding accurate ionic forces. In order to preserve this adiabaticity condition, the fictitious mass of the electrons is chosen small enough to avoid energy transfer between ionic and electronic degrees of freedom. This condition in turn requires that the equations of motion are integrated using a smaller time step than the one commonly used in BO molecular dynamics.

3.3.5 Basis Sets and Pseudopotentials

3.3.5.1 Localized Basis Sets: STOs and GTOs

How exactly does one represent the wave functions and densities mathematically? As mentioned above, only the hydrogen-like atoms such as H, He^+, and Li^{2+} can have their Schrödinger equation analytically solved. The resulting hydrogen-like wave functions all consist on a spherical harmonic angular part $Y_{l,m}$ and a radial part $R_{n,l}$

$$\phi = Y_{l,m} R_{n,l} \tag{3.130}$$

where the radial part of $R_{n,l}$ is of the Slater type. Slater Type Functions (STF hereafter) are of the kind

$$\phi^{STF} = Y_{l,m} A r^l e^{-\alpha(\mathbf{r}-\mathbf{R})} \tag{3.131}$$

where $\mathbf{r}$ refers to the position of the electron, $\mathbf{R}$ stands for the position of the nucleus, α is a constant that depends on the nuclear charge, l an integer number accounting for the angular momentum and A the normalization constant so that $\int \left|\phi^{STF}\right|^2 d\mathbf{r} = 1$. Each such Slater type function that describes a state of the electron is said to describe an orbital. Therefore, they are also known as Slater Type Orbitals (STO hereafter).

Assuming that in N-electron systems each electron will dwell an orbital that will resemble one of those hydrogen-like wave functions, discrete sets of different hydrogen-like wave functions could be used as basis sets, that is, elements whose proper combination gives rise to a good approximation of the actual wave function orbitals.

Since the three- and four-centre two-electron integrals involving STO can not be performed analytically, in practice, the mathematical operations required to find the coefficients of the proper combination are much more efficiently carried out if Gaussian Type Orbitals (GTO hereafter) are employed. GTOs are similar to STOs, except their exponents are squared

$$\phi^{GTF} = Ar^l e^{-\alpha(\mathbf{r}-\mathbf{R})^2} \tag{3.132}$$

Unfortunately, the square dependence in the exponential makes the GTOs inferior to the STOs in two respects. On the one hand, GTOs have problems representing the proper behavior near the nucleus, since their slope is zero there, in contrast to a STOs which show a cusp (discontinuous derivative). On the other hand, GTOs fall off too rapidly far from the nucleus compared with STOs, and the tail of the wave function is consequently represented poorly.

Both STOs and GTOs can be chosen to form a quality basis, but the above considerations indicate that more GTOs are necessary for achieving a certain accuracy compared with STOs. The increase in the number of GTO basis functions, however, is more than compensated for by the ease of which the required integrals can be calculated. Moreover, modern basis sets consist of functions that are, each of them, a linear combination (contractions) of GTOs (primitives) that resemble singles STOs

$$\phi_\mu^{CGO} = \sum_{i=1}^{L} c_{i\mu}\phi_i^{GTO} \approx \phi_\mu^{STO} \tag{3.133}$$

All-electron basis sets are defined as basis sets in which all the electrons of our system have their orbital described by one or more localized functions. In the case of pseudopotentials, the core electrons are replaced by a model potential, and the valence electrons are treated by regular localized functions. This way, the chemically active valence electrons are considered to move in the potential caused by the chemically inactive core electrons.

3.3.5.2 Plane Wave Basis Sets

Rather than starting with localized basis functions aimed at modeling the atomic orbitals, and forming linear combinations of these to describe orbitals for the whole system, one may use functions aimed directly at the full system. For modeling extended systems, a unit cell with periodic boundary conditions for instance, this suggests the use of functions with an *infinite* range. The outer valence electrons in metals behave almost like free electrons, which lead to the idea of using solutions for the free electron as basis functions. The Schrödinger equation for a free electron in one dimension is written as follows

$$\hat{H}\phi = -\frac{1}{2}\frac{d^2}{dx^2}\phi = E\phi \tag{3.134}$$

which, after rearrangement of terms, results

$$\frac{d^2}{dx^2}\phi = -2E\phi = -k^2\phi \tag{3.135}$$

where $k = \sqrt{2E}$ has been defined. The solution of Eq. 3.135 is a 1D plane wave (PW hereafter)

$$\phi^{PW}(x) = e^{ikx} \tag{3.136}$$

with an associated energy

$$E(k) = \frac{1}{2}k^2 \tag{3.137}$$

By analogy, a 3D PW is the solution of the Schrödinger equation for a free electron in three dimensions

$$\phi^{PW}(\mathbf{r}) = e^{i\mathbf{kr}} \tag{3.138}$$

with an associated energy

$$E(k) = \frac{1}{2}|\mathbf{k}|^2 \tag{3.139}$$

The so called wave vector $\mathbf{k}$ can be thought of as a frequency factor, with high $\mathbf{k}$ values indicating a rapid oscillation. The $\mathbf{k}$ values allowed are given by the unit cell translational vector $\mathbf{t}$, *i.e.*, $\mathbf{k}\cdot\mathbf{t} = 2\pi m$, with m being a positive integer. This leads to a typical spacing between $\mathbf{k}$ vectors of $\sim 0.01eV$, and the size of the basis set is thus characterized by the highest energy $\mathbf{k}$ vector included ($|\mathbf{k}|_{max}$).

PW basis sets tend to be significantly larger than localized basis sets. However, the size of the former depends only on the size of the periodic cell, not on the actual system described within the cell, in contrast to the linear increase with system size for localized functions. Therefore, PW basis sets become more favorable for large systems.

Even if PW basis sets have primarily been used for periodic systems, they can also be employed to describe molecular species by using a supercell approach, where the molecule is placed in a sufficiently large unit cell such that it does not interact with its own replicas in the neighboring cells. In such a way, some of the problems related to the localized basis sets are bypassed:

1. PWs are orthonormal and energy-independent, and they are not biased to any particular atom. Therefore, any region in space is treated on equal footing and calculations require no basis set superposition corrections.

2. PW approach guarantees to converge to the target wave function, while there is no such a guarantee for localized basis sets.

3. Even if the number of basis functions needed for an accurate calculation is an order of magnitude larger than when localized sets are used, the possibility of evaluating many expressions by means of the Fast Fourier Transform (FTT) algorithm largely compensates the PW approach.

PW basis functions are appropriate for describing delocalized slowly varying electron densities, such as the valence bands in a metal. The core electrons, however, are strongly localized around the nuclei, and the valence orbitals have a number of rapid oscillations in the core region to maintain the orthogonality. Therefore, the adequate description of the core region requires a large number of rapidly oscillating functions, *i.e.*, a PW basis with very large $|\mathbf{k}|_{max}$. Besides, since the singularity of the nuclei-electron potential V_{eN} is almost impossible to describe in a PW basis, pseudopotentials are employed for smearing the nuclear charge and modeling the effect of the core electrons.

3.3.5.3 Pseudopotentials, Effective Core Potentials, and Frozen Cores

Systems involving elements from the lower part of the periodic table have a large number of core electrons. Even if, as already mentioned, core electrons are unimportant in a chemical sense, it is necessary to use a large number of basis functions to expand the corresponding orbitals, otherwise the valence orbitals will not be properly described due to a poor description of the electron-electron repulsion. Moreover, in the lower half of the periodic table relativistic effects further complicate matters. These two problems may be tackled simultaneously by modeling the core electrons by a suitable function, while treating only the valence electrons explicitly.

Such function modeling the core electrons is usually called Pseudopotential (PP hereafter) or Effective Core Potential (ECP hereafter). The neglect of an explicit treatment of the core electrons often gives quite good results at a fraction of the cost of a calculation involving all electrons. Besides, the relativistic effects may also be taken care of without having to perform the full relativistic calculation.

Designing a pseudopotential requires four major steps:

1. Generation of a good-quality all-electron wave function for the atom.

2. Replacement of the valence orbitals by a set of nodeless pseudo-orbitals. Such pseudo-orbitals are designed such that they behave correctly in the outer part, but without the nodal structure in the core region.

3. Replacement of the core electrons by a potential parameterized by expansion into a suitable set of analytical functions of the nuclear-electron distance.

4. Fit of the parameters of the potential such that the solutions of the Schrödinger (or Dirac) equation produce pseudo-orbitals matching the all-electron valence orbitals.

Molecular systems have traditionally been described by localized basis sets, while PW have been favored for extended (periodic) systems. Therefore, there are some differences for the corresponding pseudopotentials. When using STFs or GTFs to describe the valence orbitals, it is natural to also use STFs or GTFs to describe the ECP. Since STFs and GTFs are continuous, there is no fixed distance to characterize the extent of the core potential. The quality of the ECP is determined by the number of electrons chosen to be represented by the ECP.

Regarding the PWs, the size of the basis set is given by the highest energy wave. As mentioned before, the singularity of the nuclear potential V_{eN} and the resulting strongly localized core electrons are hardly described by any reasonable-sized PW basis set. Pseudopotentials are employed to smearing the nuclear charge and modeling the core electrons. These potentials are typically characterized by a core radius r_c, *i.e.*, the pseudopotentials used in connection with PW have a finite physical extent. The potential for $r < r_c$ is described by a suitable analytical function and the pseudo-wave function and its first and second derivatives are required to match those of the reference wave function at r_c. Even if a hard (small r_c) pseudopotential will require more PWs for describing the region beyond r_c than a soft (large r_c) one, a too large r_c will deteriorate the quality of the calculated results and also make the pseudopotential less transferable.

The norm-conserving pseudopotentials proposed by Hamann, Schlüter and Chiang satisfy the conservation of the wave function norm [263]. In addition to the above matching conditions at r_c, they require that the integral of the square of the reference and pseudo-wave from 0 to r_c agrees. Since these pseudopotentials are rather hard, they require relatively large basis sets. Therefore, Varderbilt proposed to relax the norm-conserving condition to give the so-called ultrasoft pseudopotentials [264, 265], reducing the necessary number of PW for the expansion of the valence orbitals by a factor of *ca.* 2.

The so called frozen-core approximation has emerged in the chemical community as a valuable alternative to the pseudopotential approach [266,267]. In this framework, the core electrons are included in the treatment but the corresponding orbitals are fixed at their atomic values. In such a way, the full electron-electron interaction is taken into account but the change in the deep-core orbitals due to the molecular environment is neglected.

3.4 QM/MM Methods

Combined Quantum Mechanics / Molecular Mechanics (QM/MM hereafter) approaches are by now established as a valuable tool for the modeling of biomolecular systems, inor-

ganic/organometallic compounds and solid state systems as well as for studying processes in explicit solvent (see [268] for review).

The QM/MM approach models the total system under study by dividing it in two regions: the active site (I), which contains the properties of interest, is computed at full QM level while the reminder of the system (II) is treated using molecular mechanics (MM) [269]. Owing to the QM-MM interactions, the total energy of the entire system E_{TOT} cannot simply be written as the sum of the energies of the subsystems. Therefore

$$E_{TOT} = E^{I}_{QM} + E^{II}_{MM} + E^{I-II}_{MM} \tag{3.140}$$

where coupling terms are included in E^{I-II}_{MM}.

MM is a totally different approach than QM methods. While these latter are based on *a priori* interpretation of the molecular system, which is described by solving the Schrödinger equation, molecular mechanics can be considered as *a posteriori* method, in which the potential energy surface of a the molecular system, E^{II}_{MM}, is divided in a set of simple mathematical functions that are fit to reproduce experiment or high level *ab initio* results.

The specific form of the analytical function E^{II}_{MM} and the corresponding set of parameters used are referred to as the force field. A common pictorial representation of a force field is one in which atoms are represented by spheres and covalent bonds by springs. The value of the energy is calculated as a sum of several terms: i) internal or bonded terms (E_{bond}) and ii) external or nonbonded terms ($E_{nonbond}$). The former describes the covalent bonds, the angular deformations between covalently bound atoms and torsional energies in the molecule. The latter accounts for the interactions between non-covalently bonded atoms or atoms separated by three or more covalent bonds. In particular, the AMBER95 force field [270] describes the potential energy as

$$\begin{aligned} E^{II}_{MM} = &\quad E_{bond} + E_{nonbond} \\ E^{II}_{MM} = &\sum_{r}^{bonds} K_b \left(r - r_0\right)^2 + \sum_{\theta}^{angles} K_\theta \left(\theta - \theta_0\right)^2 + \sum_{n}^{dihedrals} V_n \left(1 + cos\left(n\phi - \gamma\right)\right) + \\ &+ \sum_{i<j}^{atoms} \epsilon \left[\left(\frac{R^*}{r_{ij}}\right)^{12} - 2\left(\frac{R^*}{r_{ij}}\right)^{6}\right] + \sum_{i<j}^{atoms} \frac{q_i q_j}{r_{ij}} \end{aligned} \tag{3.141}$$

where K_b and K_θ represent the bond stretching and the bending force constants, $V_n$is the rotational potential, ϵ and R^* represent the well depth and the van der Waals radius respectively and q_i means the charge on atom i. Recall that polarization effects are neglected in this approach.

Even if the force fields possess the parameters of a wide variety of bond and angle force constants, one can be interested in a system that has not been parametrized yet. Badger's rules [271] enable to compute the bond stretching and bending angle force constants from equilibrium bond distances and angles respectively, which can be taken from the experiment

or from full QM results. Regarding the bond parameters, Badger assumed that two atoms covalently bonded have an effective charge and they are attracted by a Coulombic force and repelled by the Pauli repulsion, which is approximated as linear. Therefore, the term regarding the bonds in Eq. 3.141 can be written as

$$E_b = E_{ob} - Fr_{ij} - G\frac{q_i q_j}{r_{ij}^2} \tag{3.142}$$

where E_{ob} is the unperturbed bonding energy in $\frac{Kcal}{mol}$, F and G are two dimensionless constants to be defined, q_i are the effective charges in a.u. and r_{ij} is the distance between atom i and atom j given in Å. At the equilibrium bond distance r_0, the force constant is

$$K_b = \left(\frac{\partial E_b}{\partial r_{ij}^2}\right)_{r_{ij}=r_0} = 2G\frac{q_i q_j}{r_0^3} \tag{3.143}$$

where $2G = 664.12$ has been set based on empirical data. The charges and equilibrium bond distances are determined from reference systems calculations at pure QM level.

Badger generalized the results obtained for the bonds to calculate the angle bend force constants between the atoms i, j and k. By analogy, the term regarding the angles in Eq. 3.141 can be written as

$$E_\theta = E_{o\theta} - F\theta - M\frac{q_i q_k}{r_{ik}^2} \tag{3.144}$$

where $r_{ik}^2 = r_{ij}^2 + r_{jk}^2 - 2r_{ij}r_{jk}cos\theta$. At the equilibrium configuration θ_0, the force constant is,

$$K_b = 2G\frac{q_i q_k}{r_{ik}^5}\left[3r_{ij}r_{jk}\left(1 - cos^2\theta\right) - r_{ik}^2 cos\theta\right] \tag{3.145}$$

also in this case the bond distance and the angle are computed at high accuracy on QM model systems.

Chapter 4

Results

Never express yourself more clearly than you are able to think.

Niels Bohr

The opposite of a fact is falsehood, but the opposite of one profound truth may very well be another profound truth.

Niels Bohr

A person who never made a mistake never tried anything new.

Albert Einstein

If you can't explain it simply, you don't understand it well enough.

Albert Einstein

Logic will get you from A to B.

Imagination will take you everywhere.

Albert Einstein

Make everything as simple as possible, but not simpler.

Albert Einstein

If I could explain it to the average person, I wouldn't have been worth the Nobel Prize.

Richard P. Feynman

4.1 Benchmark Assessment of Density Functional Methods on Group II–VI MX (M = Zn, Cd; X = S, Se, Te) Quantum Dots

4.1.1 Abstract

In this work, we build a benchmark data set of geometrical parameters, vibrational normal modes, and low-lying excitation energies for MX quantum dots, with M = Cd, Zn, and X = S, Se, Te. The reference database has been constructed by *ab initio* resolution-of-identity second-order approximate CC RI-CC2/def2-TZVPP calculations on $(MX)_6$ model molecules in the wurtzite structure. We have tested 26 exchange-correlation density functionals, ranging from local generalized gradient approximation (GGA) and hybrid GGA to meta-GGA, meta-hybrid, and long-range corrected. The best overall functional is the hybrid PBE0 that outperforms all other functionals, especially for excited state energies, which are of particular relevance for the systems studied here. Among the DFT methodologies with no Hartree–Fock exchange, the M06-L is the best one. Local GGA functionals usually provide satisfactory results for geometrical structures and vibrational frequencies but perform rather poorly for excitation energies. Regarding the CdSe cluster, we also present a test of several basis sets that include relativistic effects *via* effective core potentials (ECPs) or *via* the ZORA approximation. The best basis sets in terms of computational efficiency and accuracy are the SBKJC and def2-SV(P). The LANL2DZ basis set, commonly employed nowadays on these types of nanoclusters, performs very disappointingly. Finally, we also provide some suggestions on how to perform calculations on larger systems keeping a balance between computational load and accuracy.

4.1.2 Introduction

Semiconductor quantum dots (QD) [272] have earned lots of attention in recent years for their application in a wide variety of fields [273] including, among others, photovoltaics [145–149], photocatalysis [129–132], optical sensing [133,274], optoelectronics [275], biotechnology, and medicine [68,192]. Their unique behavior stems from a few main properties: (a) an easily tunable bandgap with the size of the cluster, (b) a high optical extinction coefficient dependent on the large cross sections of these materials, (c) a sharp emission spectrum, (d) the ability to generate more than one photoexcited electron through the phenomenon of carrier multiplication, and (e) a much longer photostability compared to organic photosensible compounds [4,5,47,53].

Despite the great advancements achieved with these nanomaterials, there are still many open questions to be answered. Charge transfer processes involved in the conversion of solar energy into electricity, for example, from a photoexcited QD injecting electrons into a metal oxide semiconductor nanomaterial such as TiO_2, still need to be completely understood [148]. The role of organic ligands attached on the nanocrystal surface or the type of absorption that can occur between the QD and the metal oxide surface, or the effect of trap

states induced, for example, by doping the QD or by an incomplete passivation of the reconstructed surface, are still to be fully elucidated [26]. To enable significant advances in the design of novel more efficient materials, theoretical modeling can deliver a formidable help as it allows for accurate simulations of spectroscopic and structural properties of the complex heterocomposite interfaces constituting the QD surface and its interaction with the environment.

Theoretical methodologies that can be utilized to study these systems vary a lot depending on the accuracy that one wants to achieve and the type of properties to be investigated. Usually, the typical size of these nanocrystals, about 2–5 nm, would allow the application of just semiempirical or tight-binding methods, which provide only a limited level of accuracy. However, the advent of DFT (DFT) and the possibility to reduce the QD size by means of tailored model systems, smaller and more practical, make these compounds much more affordable from a computational standpoint while keeping in any case a satisfactory level of accuracy. The DFT approximations for the exchange-correlation functional currently available fail to describe the strongly correlated regime, as that found in the two-dimensional electrostatic QDs [276]. In this sense, new methods are being developed, such as the symmetry breaking/restoration methods [277] and modified Kohn–Sham approaches [278]. However, for the QD models considered here, standard DFT methodologies already provide reliable results.

In recent years, many theoretical works based on DFT have appeared in the literature dealing with the QDs properties. In particular, most of those focus their attention on the group II–VI type, here denoted as MX, where M stands for a metal belonging to group 12, such as Cd or Zn, and X for a chalcogen atom, like S, Se, and Te. These QDs are very common and are currently employed in many experimental and commercial laboratories. In this article, we will pay attention only to this specific set of compounds. In Table 4.1, we provide a summary of the computational works carried out so far. The eye-catching feature is how the CdSe QDs are the most studied followed by ZnS. This result however reflects the experimental measurements as these two types of nanocrystals are usually considered as prototypical QDs.

While conceptually simple, DFT depends on several variables that need to be taken into account when tackling a given system. The user of this methodology usually faces two critical choices that can lead to losses or gains in accuracy: (i) the choice of the exchange-correlation functional and (ii) the choice of the basis set expansion. In Table 4.1, we have collected the articles that have been written so far on group II–VI QDs sorted by DFT functional and basis set. It is interesting to note that the majority of these works have been carried out using the B3LYP functional, with 27 papers, followed by PBE with 14, and 11 for PW91PW91. Regarding basis sets, the most used is the LANL2DZ, which includes effective potentials in the core to reduce the computational effort, included in a total of 16 articles. A close look at these statistics shows that most of these works are based on a widespread standard combination of DFT functional and basis set, rather than on their systematic calibration. It is worthy to mention, however, that a few works have attempted to compare the performance of a small

set of DFT functionals [279, 280].

Our purpose is to assess the quality of 26 DFT functionals (Table 4.3), including also less used meta-generalized gradient approximation and long-range corrected functionals. Because semiconductor nanocrystals are mostly known for their optoelectronic properties, we paid particular attention to building a benchmark data set that incorporates the most relevant excited states of several types of QDs. To establish a more robust database, we have also added in the data set spectroscopic ground state properties like bond lengths and vibrational frequencies. Although real nanocrystals obviously present larger sizes than those employed in this work, we have constructed $(MX)_6$ model systems (Figure 4.1) that are small enough to be tackled by very accurate *ab initio* methodologies to obtain the best and most accurate estimates of their excited states and geometric parameters. This same benchmark database has been used to evaluate the quality of eight basis sets. The $(MX)_6$ models have been constructed by cutting a wurtzite lattice, whose existence has been proved recently by Schelly [281].

The present work is structured as follows. In section 4.1.3, we provide detailed insights on how we build the benchmark database and the procedure that is used to assess the accuracy of several DFT functionals and basis sets. In section 4.1.4, a description of the results on various nanosize systems is presented. Finally, in section 4.1.5, we conclude our work and provide some hints for future theoretical investigations on II–VI QDs.

4.1.3 Computational Methodology

Benchmark Set

In a first step, we have attempted to employ very accurate methodologies, like coupled-cluster methodology with single and double excitations perturbatively corrected with triple excitations, CCSD(T) [282], or the complete active space with second-order perturbation method, CASPT2 [219], to construct the benchmark database; however we found these approaches impractical for the large computational requirements. We decided thus to switch to approximated CC methodologies like the resolution-of-identity equation of motion second-order approximate CC, RI-EOM-CC2, for excited states [223], while ground state properties have been estimated using second-order perturbation theory, the RI-MP2 method [283]. RI stands for resolution of identity, which is an accelerated algorithm to compute the two-electron coulomb integrals lying in the Hamiltonian [284]. A large def2-TZVPP basis set has been employed to minimize the errors stemming from the finite size of the basis set expansion. Usually, RI-EOM-CC2/def2-TZVPP may suffer from errors in reproducing accurately excited states; therefore we made a preliminary calculation on a selected few low-lying excited states of $(CdSe)_6$ with the CASPT2 method. These results show the satisfactory agreement between CASPT2 and RI-EOM-CC2; therefore we chose the latter throughout the benchmark tackled in this paper.

The main bond distances and bond angles of the optimized $(MX)_6$ model compounds are

shown in Table 4.4, while their vibrational frequencies are presented in Table 4.5. Finally, in Table 4.6 we have listed the most characteristic lowest-lying excitation energies of these species.

Assessment of DFT Methodologies against the Benchmark Database

The reference data set defined in the previous section is used to assess computationally cheaper methodologies and to select those that provide results that are in closer agreement with our best estimates. In this work, we are mostly interested in benchmarking DFT exchange-correlation (XC) functionals; however, this reference set may be used in the future to assess other computational approaches.

Apart from the functionals, DFT calculations depend also on the size of the basis set employed and the choice of relativistic approximations, with the latter being important thanks to the presence of heavy atoms like Cd or Te in the reference compounds. Because of this, we decided to follow a two-step approach to perform our benchmark: (i) first we assessed the performance of several basis sets, core potentials, and relativistic approximations on one specific system; (ii) then we chose the best combination provided by point (i) to assess the contribution of different DFT functionals on a much larger selection of systems.

To establish the fairness of our results, we followed optimized benchmark recipes that have been made available by other authors [285]. A few quantities are of relevance to assess the accuracy of each DFT functional (or basis set): (i) The mean unsigned errors (MUE) provide the magnitude of the deviation of a given DFT exchange-correlation functional, XC (or basis set, BS), MUE[XC(or BS)]$_{type}$ for a specific "type" parameter, for example; bond distance, MUE[XC(or BS)]$_{bond}$; vibrational frequency, MUE[XC(or BS)]$_{vib}$; or excited states, MUE[XC(or BS)]$_{exc}$, from the reference values, independent of the sign. (ii) The average MUE (AMUE$_{type}$) is the average error spread among all DFT methodologies (or basis sets) for a given parameter. (iii) The normalized mean unsigned errors are defined as NMUE[XC(or BS)]$_{type}$ = MUE[XC(or BS)]$_{type}$/AMUE$_{type}$ (type = bond, vib, exc). The NUMEs provide a normalized error value of a given DFT functional (or basis set) for a specific parameter and are independent of the units employed. Finally, (iv) the balanced mean unsigned error, expressed by BMUE[XC(or BS)] = (NMUE[XC(or BS)]$_{bond}$ + NMUE[XC(or BS)]$_{vib}$ + NMUE[XC(or BS)]$_{exc}$) / 3, indicates the overall performance of a DFT functional (or basis set) against all parameters, independently of the units.

Basis Sets, Core Potentials, and Relativistic Approximations

Several types of basis sets have been benchmarked against one reference system, the $(CdSe)_6$, by performing DFT calculations with a selected number of exchange-correlation functionals: PBE, PBE0, M06-L, and CAM-B3LYP. Both Cd and Se are "heavy" atoms showing important relativistic effects that have been taken into account *via* scalar approximations. Spin–orbit (SO) coupling contribution is not considered here, as all QDs of this study are closed shell

systems. Scalar relativity has been tested using two approaches, the effective-core potentials (ECPs) and the all-electron zeroth-order regular approximation (ZORA). ECPs are integrated into the Gaussian basis sets LANL2DZ, SBKJC, def2-SV(P), and def2-TZVPP, which are the main basis sets considered in this benchmark. All-electron Slater type basis sets, namely DZ and TZ2P, have been employed for the calculations based on the ZORA approximation. In the case of DZ, we have also tested the effect of using frozen core approximation, *i.e.*, freezing the atomic orbital coefficients up to 3d (small-core) and 4p (large-core) for Cd and up to 3p (small-core) and 4p (large-core) for Se. Beware that the def2 basis set library is of all-electron type for Zn, O, and S, while it includes ECPs for Cd, Se, and Te by default. This is not the case for SBKJC and LANL2DZ that always include ECPs.

Exchange-Correlation DFT Functionals

The performance of several popular exchange-correlation (xc) functionals has been tested on both the $(ZnX)_6$ and $(CdX)_6$ (X = S, Se, Te) clusters. We divided our density functional test set into five main groups (see also Table 4.3): (i) The first includes "pure" xc functionals constructed from the generalized gradient approximation (GGA); *i.e.*, they are influenced by both the electron density and the gradient of electron density: PBE, BLYP, BPW91, BP86, G96LYP, mPWLYP, and OLYP. (ii) The second group is composed of GGA xc functionals, which also include a given percentage of Hartree–Fock exchange. This set is identified as hybrid GGA (HGGA) and includes the B1LYP, B3LYP, mPW1PW91, O3LYP, B97-2, PBE0, and X3LYP functionals. (iii) The third group is formed by GGA functionals that include a dependence on the kinetic energy densities and are called meta-GGA (MGGA): M06-L, HCTC, and B97D. (iv) The fourth is composed of meta-GGA functionals including a percentage of Hartree–Fock exchange and are identified as meta-HGGAs (MHGGA): M06, M06-HF, M06-2X, M05, M05-2X, and TPSSH. (v) The fifth and last group is determined by those functionals that preserve their identity at short-range but incorporate 100% Hartree–Fock exchange at long-range, in order to correct the distance dependence of charge-transfer excitations. These functionals, also called long-range corrected, or LRC hereafter, have been employed in this benchmark in three flavors: LC-ωPBE, CAM-B3LYP, and ωB97XD.

The basis set chosen for all of these calculations is the def2-SV(P) basis set that incorporates relativistic effects through the Stuttgart relativistic core potentials. As we will see in the text, this basis set represents the best compromise in terms of computational requirements and accuracy for tackling larger systems.

Details on the Program Packages Used

Calculations have been carried out using several computational packages. The reference data set has been collected using Turbomole 6.4(35) as it provides the RI-EOM-CC2 and the RI-MP2 methodologies. All DFT calculations using Gaussian basis sets have been performed with Gaussian 09,(36) while ADF2012.01(37) has been used to calculate the effect of the DZ

and TZ2P basis within the ZORA approximation. All references for the DFT functionals, basis sets, and ECPs are provided in Table 4.3.

4.1.4 Results and Discussions

Benchmark of Basis Sets, Core Potentials, and Relativistic Approximations

As anticipated earlier, the first step is to benchmark a selected number of basis sets, incorporating relativistic approximations with ECP or all-electron ZORA. The quality of a given basis set for a given parameter (bond distances, vibrational frequencies, and excited states) is evaluated with the MUEs. To obtain a more complete statistical set of data, we computed the same properties using different functionals, PBE, PBE0, M06-L, M06-2X, and CAM-B3LYP, each representing a different description of the exchange-correlation term. In Tables 4.4-4.6, we have listed the results of our benchmark by displaying the reference data set computed at the RI-MP2 (for geometry and vibrational frequencies) and EOM-CC2 (for excited states) levels of theory. Figure 4.2 summarizes the performance of the DFT/PBE0 approach. Regarding the bond parameters, the TZ2P in combination with the PBE0 provides the best performance, with a MUE of 0.034 Å and a maximum deviation of 0.057 Å. The next more accurate values are achieved by the def2-TZVPP in combination with M06-L, M06-2X, and CAM-B3LYP, and also by PBE/TZ2P. In general, as expected, the largest basis sets provide the most accurate values. This trend is however changed for the normal modes values where the PBE0/DZ and PBE0/def2-SV(P) are estimated to be closer to the reference values. Regarding the excited states benchmark, it is interesting to note that the best performing basis set varies a lot with the type of DFT functional. In particular, the computationally cheap SBKJC basis set provides surprising results by outperforming, in some cases, larger basis sets. For example, the combination of SBKJC with M06-2X gives a MUE of 0.10 eV, better than 0.17 eV of def2-TZVPP and 0.22 eV of all-electron ZORA TZ2P.

A better view of the overall performance of each basis set is the balanced mean-unsigned error (BMUE), *i.e.*, a unitless term that takes into account the global average effect of bond distances, vibrations, excited states, and different DFT functionals. The results are presented in Figure 4.2d. It is clear that the best performing basis set is the def2-TZVPP, with a BMUE of 0.808 and a balanced maximum error of 0.781. The worst performance is given by the all-electron DZ basis set, in which a large frozen core has been chosen, with a BMUE of 1.333. Most notably, the LANL2DZ basis, which has been widely used in previous works on QDs, performs very unsatisfactorily, being the second worst basis in the benchmark with a BMUE of 1.247. Breaking down the BMUE in terms of its components, the LANL2DZ has its worst behavior with the geometric parameters, while for excited states it performs only slightly better. Usually, the LANL2DZ is employed for its computational efficiency versus a much larger basis set, like def2-TZVPP; however we must warn of the quality of its results. A very good alternative is the SBKJC basis, which has a BMUE of 0.909, only slightly higher than the def2-TZVPP. Moreover, this same basis set, as anticipated earlier, has by far the best performance for excited states, with a NMUE[SBKJC]exc as low as 0.805, much lower than

the second best given by def2-TZVPP with 0.922. Another very promising basis set for its accuracy and computational efficiency is def2-SV(P), which has a BMUE of only 0.861 and has the second overall best behavior.

Among the all-electron Slater basis set, and within the relativistic ZORA approximation, TZ2P provides the lowest, and therefore most accurate, BMUE value (0.892), followed by the all-electron DZ (0.943). Notably, freezing the core orbitals leads to an important deterioration of the results, especially for the large core DZ, which is suggested to be avoided in all cases.

Assessment of Exchange-Correlation DFT Functionals

In Figures 4.3-4.5 we have listed the computed MUEs of several DFT exchange-correlation functionals at the def2-SV(P) level of theory for geometrical parameters, vibrational frequencies, and excited states of Cd and Zn chalcogenide clusters. In Figure 4.6, we have collected the BMUE[XC]$_{type}$ for type = bond, vib, and exc, collected by averaging the results over all nanoclusters employed, *i.e.*, BMUE[XC]$_{type}$ = (NMUE[XC]$_{type}$-ZnS + NMUE[XC]$_{type}$-ZnSe + ... + NMUE[XC]$_{type}$-CdTe)/6 . This provides an outlook of the general performance of each DFT functional for all molecular species. In Figure 4.6d, we also show the overall BMUE averaged against all parameters and all QDs.

Regarding geometrical parameters, the best functional is TPSSH, followed by M06, LC-ωPBE, M05, and PBE0 (Figure 4.6a). All these functionals include a certain degree of HF exchange and usually are computationally expensive for structural optimizations, especially when used for larger systems. A possible valid alternative is the "pure" local PBE functional, which shows a BMUE$_{bond}$ of just 0.608, meaning that it performs better than the majority of the functionals, including some of the hybrid ones. A similar trend can be found in the vibrational parameters, where the best functional is PBE0, which includes 25% of HF exchange and has a BMUE$_{vib}$ of 0.437, followed by M05 and TPSSH. Again, hybrid functionals provide the most accurate values against the reference benchmark. In this case, almost all local GGAs perform worse than the average, with the only exception of PBE, which has BMUE$_{vib}$ of 1.002, even though it is quite close to the median 1.000. Among MGGA functionals, the M06-L represents a sound replacement, with a BMUE$_{vib}$ of 0.785.

More interestingly, the PBE0 functional also provides the most accurate description of the lowest nine excited states with an overall BMUE$_{exc}$ of 0.370. Other highly performing functionals are mPW1PW91, B97-2, TPSSH, and M05. These methods all belong to the hybrid group, with HF exchange contribution varying from 10% to 28%. Pure GGA functionals have very poor performance, and even the best one, BPW91, produces a BMUE$_{exc}$ of 1.204. In terms of absolute energies, for example for the $(CdS)_6$ cluster, this corresponds to a systematic MUE of 0.78 eV, which is not at all satisfactory. This result is somewhat worrying as pure GGAs are more efficient computationally. Also in this case, the M06-L, which has no HF exchange, describes the reference values with a BMUE$_{exc}$ of 0.803. Despite not being the best overall, it might represent a good compromise in terms of accuracy and efficiency for

studying large clusters. The origin of the bad performance of local GGA functionals can be ascribed to the type of excited states involved in these clusters. These excitations are usually exciton-like, with the formation of the so-called hole–electron pair and the consequent shift of charge that traduces into a long-range *1/r* Coulombic attraction between the hole and the electron. The failure of pure TDDFT lies in the lack of the exact HF exchange term that in linear response theory is directly connected to the correct *1/r* asymptotic behavior. Moreover, these charge transfer states are also severely underestimated as a consequence of self-interaction error. In our work, we systematically demonstrate the higher performance of hybrid functionals, which include a given percentage of HF exchange.

Overall, the functional that predicts more accurately all the parameters over all compounds considered here is PBE0, with a $BMUE_{total}$ of 0.437. This is followed closely by mPW1PW91, M05, and TPSSH. As expected, the hybrid functionals HGGA and MHGGA outperform pure GGAs and MGGAs, with the latter being better than pure GGAs.

The results presented so far take into consideration the prediction of xc-functionals over the whole set of compounds. It is however of particular interest to look at their behavior for specific systems. To keep the description simple, in the analysis, we will focus only on the prediction of the excitation energies, as presented in Figure 4.5. The discussion can be easily extended to the other computed properties. For the whole set of cadmium chalcogenides $(CdS)_6$, $(CdSe)_6$, and $(CdTe)_6$, the PBE0 is the overall best functional by providing excited state energies very close to the reference RI-EOMCC2 values and MUEs of 0.120 eV (CdS), 0.090 eV (CdSe), and 0.099 eV (CdTe), respectively. The next best functional is the mPW1PW91, followed by other MHGGA's, like M06-HF and M05. A look at the correlation diagrams in Figure 4.7 indicates that PBE0 predicts an oscillating behavior above and below the reference excitation energies, providing, in any case, an excellent agreement with the benchmark reference. A similar behavior is found for the other best functionals indicated here and for the other CdX compounds. Pure GGAs, however, always underestimate the excitation energies with deviation from the reference values of up to 0.9–1.0 eV for all CdX systems. Among the MGGA functionals, the M06-L behaves much better than pure GGAs. On the other hand, LRC functionals overcorrect the exciton interaction by providing excitation energies systematically larger than the reference of about 0.3 eV (CAM-B3LYP) or up to 0.9 eV (LC-ωPBE).

One of the key findings in moving to the ZnX chalcogenides is that the situation is somewhat changed. The PBE0 still performs well, but less than in the CdX compounds. In particular, for ZnTe, it gives a MUE as high as 0.374 eV, which is still below the median but much lower performing than for CdX (or even ZnS and ZnSe). In all ZnX species, the PBE0 tends to overestimate all the excitation energies (see Figure 4.7) of about 0.3–0.4 eV. This functional has a 25% HF exchange, the same as mPW1PW91, which suffers from the same problems. Notably, reduction of HF exchange leads to better results. Indeed, the TPSSH functional, with only 10% HF exchange, is the best functional for the ZnX series with MUEs of 0.168 eV (ZnS), 0.091 eV (ZnSe), and 0.105 eV (ZnTe). The smaller importance of the exchange term has also the consequence of improving the results of GGA functionals, especially for

the ZnTe cluster, where in some cases they perform better than hybrid functionals.

In the excited state benchmark seen so far, we decided to include in the test set also those electronic excitations that are transparent to light (*i.e.*, with zero oscillator strength) in order to have a statistically more meaningful set of reference data. However, in reality, we are interested only in optically active excited states. An important aspect to assess the performance of a DFT functional is therefore to check how it reproduces the convoluted optical spectrum of the reference data, which is shown in shaded gray in Figure 4.8. In this figure, on the left, we have plotted the convoluted spectra for all DFT functionals for one system, the $(CdSe)_6$ nanocluster. As expected, the best agreement is provided by the hybrid functionals. However, the facets of the reference curve, *i.e.*, a weaker band at lower energies and a more intense one at higher energies, are well reproduced, though with some differences, in all cases. For this reason, we decided to make a rigid shift of all excitation energies for a given DFT functional equivalent to its MUE. In Figure 4.8, on the right, we have collected the new curves after the shift. Notably, the reference curve is very well aligned with most of the DFT functionals. In particular, the poor performing pure DFT functionals are now able to satisfactorily describe the reference optical spectrum at a fraction of the computational cost, also in comparison with the hybrid functionals.

Another problem that can occur in establishing the quality of a DFT functional in describing the excited states is the starting geometry. It is indeed probable that some of the DFT methodologies employed can produce optimized structures that are far from the reference values and, consequently, lead to poor excitation energies. To assess this, we decided to compute the excited states with all DFT functionals at the reference RI-MP2 geometry. In Figure 4.9, we show the trend of the MUE along the series of XC functionals. As expected, at the reference geometry, the overall AMUE, *i.e.*, the average mean unsigned error, is lower than the one computed by optimizing each structure with a given functional. In addition, the trend of the MUE at the RI-MP2 geometry follows roughly that of the DFT geometries, with some notable exceptions. Indeed, the B97-2 and especially the B1LYP reduce drastically their MUE and perform as well as the PBE0 functional.

4.1.5 Conclusions and Suggestions

In this work, we have built a reference database of *ab initio* RICC2/def2-TZVPP ground state parameters like geometries and vibrational frequencies and several excited states for a group of $(MX)_6$ compounds (M = Cd, Zn; X = S, Se, Te). We have tested the accuracy of 26 exchange-correlation functionals and found out that the hybrid PBE0 is the best performing one, showing a BMUE of 0.437. Other well-behaved functionals usually include HF exchange and, in some cases, also the kinetic energy density. In this group, the M05 and TPSSH have BMUEs of 0.471 and 0.472 very close to PBE0. Local GGA functionals are usually good for structures and normal modes, but for excited states they behave rather poorly. Overall, the best GGA is the PBE with a BMUE of 1.002, while within the MGGAs, the M06-L provides a better value of 0.793.

Regarding the $(CdSe)_6$ cluster, we have also tested the efficiency of several basis sets that incorporate relativistic effects by means of ECPs or ZORA approximations. Overall, the def2-TZVPP with ECPs is the best basis set with a BMUE of 0.808, evaluated for the same set of ground and excited state parameters and a set of five exchange-correlation functionals. The def2-TZVPP, however, requires great computational effort even for small systems, therefore better options are the SBKJC and the def2-SV(P), which have BMUEs of 0.909 and 0.861, respectively. In particular, the SBKJC, which is built with fewer basis functions than the def2-SV(P), performs surprisingly well for excited state calculations by outperforming even the def2-TZVPP basis set.

Finally, we can conclude this section by providing some suggestions for future theoretical work on group II–VI nanoclusters. Realistic QDs are usually large molecules of more than 2 nm in diameter that could easily correspond to structures with more than 200–300 atoms (depending on the type of M and X atoms) and more than 2000–3000 basis functions. These structures have to be first optimized to reach a minimum in the potential energy surface and then used to compute spectroscopic properties, most likely for an infrared or an absorption/emission spectrum. TDDFT calculations would usually require a large amount of memory especially because QDs have a dense manifold of molecular orbitals lying in the HOMO region that could participate in the composition of low-lying excited states. In other words, the larger is the QD, the higher is the number of excitations needed to reproduce the experimental spectrum, and the larger will be the computational effort needed. As a consequence, an approach that will use hybrid functionals, for example PBE0, for geometry optimization and excited state calculations will most likely be prohibitive upon increasing the size of the dot. Within this framework, we foresee two possible workarounds:

1. We have shown that GGA functionals provide reasonable geometries, therefore structural optimizations can be carried out using cheaper methods like PBE. Then, on the optimized structures, a single-point TDDFT calculation using a well-performing hybrid functional could be made (PBE0 standing above all others). In this way, such a sound combination of DFT functionals could provide very reliable results with a reduced computational cost. In preliminary calculations, we have seen that excited states are well reproduced even when the starting structure comes from a different functional than the one used to optimize the structure.

2. Another alternative is to use for the DFT ground state calculations a local GGA density functional as in the previous step and using the same local functional to compute the excited states with TDDFT. Then a rigid shift can be performed on the excitation energies of an amount equivalent to the computed MUE for the given functional. This approach, which is less rigorous than the others, could provide, however, reasonable accuracy with a much reduced computational cost.

Table 4.1: List of theoretical papers on II–VI QDs sorted by exchange-correlation functionals. References are also included. # stands for number of articles.

Functional		#	Refs
LDA	SVWN	10	[22,279,286–293]
GGA	PBE	15	[280,292,294–306]
	PW91PW91	11	[83,280,293,307–314]
	BLYP	3	[315–317]
	BP86	2	[318,319]
	OPBE	1	[279]
HGGA	B3LYP	28	[279,280,293,300,302,303,306,307,318,320–338]
	mPW1PW91	2	[339,340]
	PBE0	2	[280,298]
	BHLYP	1	[302]
MGGA	TPSS	1	[280]
LRC	CAM-B3LYP	1	[280]
	LC-ωPBE	1	[280]

Table 4.2: List of theoretical papers on II–VI QDs sorted by basis sets. References are also included. # stands for number of articles. STO = Slater-type orbitals. GTO = Gaussian-type orbitals. PW = plane waves.

Basis Set				#	Refs
Localized	Numerical		DNP	7	[297,307–309,315–317]
	Analytical	STO	DZ	3	[300,303,306]
			TZ2P	1	[304]
		GTO	STO-3G(*)	1	[279]
			DZ(D)P	2	[333,338]
			SDD(*)	2	[279,325]
			LANL2DZ(*)	16	[279,280,293,298,322–324,326–329,331,332,335–337]
			LANL2MB	1	[279]
			SBKJC(*)	6	[306,307,320,321,339,340]
			def2-SVP	4	[300,303,318,333]
			def2-TZVP	6	[280,302,319,333,334,338]
			def2-QZVP	1	[302]
			aug-cc-pVTZ	1	[302]
PWs				16	[17,22,83,280,288,289,291–294,299,305,310–312,314]

Table 4.3: List of DFT functionals and basis sets included in this work and references therein.

Type	Functional	HF X (%)	Refs	Basis Set	Type Core	Refs
GGA	BLYP		[235,239]	LANL2DZ	ECP	[341–343]
	BP86		[235,237]	SBKJC	ECP	[344–346]
	BPW91		[235,347]	def2-SV(P)	ECP	[348,349]
	G96LYP		[350,351]	def2-TZVPP	ECP	[348,349]
	mPWLYP		[352]	DZ	Frozen Core (Large)	[353]
	OLYP		[354,355]	DZ	Frozen Core (Small)	[353]
	PBE		[238]	DZ	All-Electron / ZORA	[353]
				TZ2P	All-Electron / ZORA	[353]
HGGA	B1LYP	25	[356]			
	B3LYP	20	[241]			
	B97-2	21	[357]			
	mPW1PW91	25	[352]			
	O3LYP	11.61	[358]			
	PBE0	25	[359]			
	X3LYP	21.8	[360]			
MGGA	B97-D		[361]			
	HCTC		[362–364]			
	M06-L		[365]			
MHGGA	M05	28	[366]			
	M05-2X	56	[367]			
	M06	27	[368]			
	M06-2X	54	[368]			
	M06-HF	100	[369,370]			
	TPPSH	10	[371]			
LRC	CAM-B3LYP		[372]			
	LC-ωPBE		[373,374]			
	ωB97XD		[375]			

Table 4.4: Computed MX (M = Cd, Zn; X = S, Se, Te) structural parameters at the RI-MP2/def2-TZVPP level of theory. Bond distances are expressed in Å, angles in degrees.

QD	$(ZnS)_6$	$(ZnSe)_6$	$(ZnTe)_6$	$(CdS)_6$	$(CdSe)_6$	$(CdTe)_6$
M-X_1	2.265	2.382	2.571	2.426	2.537	2.715
M-X_2	2.412	2.516	2.680	2.663	2.757	2.904
M-M	2.776	2.823	2.875	3.121	3.156	3.186
X_1-M-X_1	140.0	140.0	138.7	144.9	145.3	144.5
M-X_1-M	94.5	92.3	88.6	102.0	91.1	88.0
X_1-M-X_2	102.6	104.2	107.0	99.0	100.7	103.5

Table 4.5: Computed MX (M = Cd, Zn; X = S, Se, Te) vibrational frequencies at the RI-CC2/def2-TZVPP level of theory. Frequencies are given in cm^{-1}.

QD	$(ZnS)_6$	$(ZnSe)_6$	$(ZnTe)_6$	$(CdS)_6$	$(CdSe)_6$	$(CdTe)_6$
$1e_g$	80	66	48	57	49	39
$1e_u$	86	66	53	58	49	41
$1a_{1g}$	114	95	69	73	66	55
$1a_{2u}$	119	106	90	82	75	59
$2e_g$	127	100	80	86	70	58
$1a_{1u}$	140	102	74	95	75	64
$2e_u$	158	126	104	108	92	75
$2a_{1g}$	167	132	114	119	101	81
$3e_g$	200	151	118	152	113	98
$3e_u$	198	156	140	159	111	96
$3a_{1g}$	225	173	148	190	128	100
$2a_{2u}$	229	146	105	201	133	111
$4e_g$	309	198	164	284	174	131
$4e_u$	316	194	145	289	177	132
$3a_{2u}$	328	236	205	292	192	145
$1a_{2g}$	335	256	214	298	217	180
$4a_{1g}$	336	207	160	310	192	159
$2a_{1u}$	365	273	231	325	230	192
$5e_g$	387	301	258	337	249	212
$5e_u$	391	303	259	342	251	212

Table 4.6: Lowest MX (M = Cd, Zn; X = S, Se, Te) singlet excited states computed at the RI-CC2/def2-TZVPP level of theory. Transition energies and oscillator strengths, in parentheses, given in eV and a.u., respectively.

QD	$(ZnS)_6$	$(ZnSe)_6$	$(ZnTe)_6$	$(CdS)_6$	$(CdSe)_6$	$(CdTe)_6$
$1e_g$	3.45	3.11	2.54	2.89	2.71	2.38
	(0.0000)	(0.0000)	(0.0000)	(0.0000)	(0.0000)	(0.0000)
$1a_{2u}$	3.74	3.41	2.88	3.22	3.02	2.67
	(0.0346)	(0.0200)	(0.0034)	(0.0658)	(0.0468)	(0.0130)
$1e_u$	4.43	4.05	3.38	3.74	3.57	3.19
	(0.0056)	(0.0035)	(0.0002)	(0.0030)	(0.0002)	(0.0004)
$2e_g$	4.36	4.05	3.54	3.83	3.65	3.28
	(0.0000)	(0.0000)	(0.0000)	(0.0000)	(0.0000)	(0.0000)
$1a_{2g}$	4.40	3.93	3.15	3.92	3.63	3.09
	(0.0000)	(0.0000)	(0.0000)	(0.0000)	(0.0000)	(0.0000)
$2e_u$	4.64	4.27	3.58	3.95	3.71	3.22
	(0.0858)	(0.0329)	(0.0287)	(0.0177)	(0.0037)	(0.0221)
$3e_g$	4.83	4.46	3.99	3.97	3.70	3.39
	(0.0000)	(0.0000)	(0.0000)	(0.0000)	(0.0000)	(0.0000)
$3e_u$	4.67	4.34	3.74	4.03	3.84	3.47
	(0.0015)	(0.0311)	(0.0127)	(0.1351)	(0.1145)	(0.0330)
$1a_{1g}$	4.62	4.44	3.80	4.15	3.88	3.37
	(0.0000)	(0.0000)	(0.0000)	(0.0000)	(0.0000)	(0.0000)

Figure 4.1: Prototypical $(MX)_6$ structure shown from two different sides.

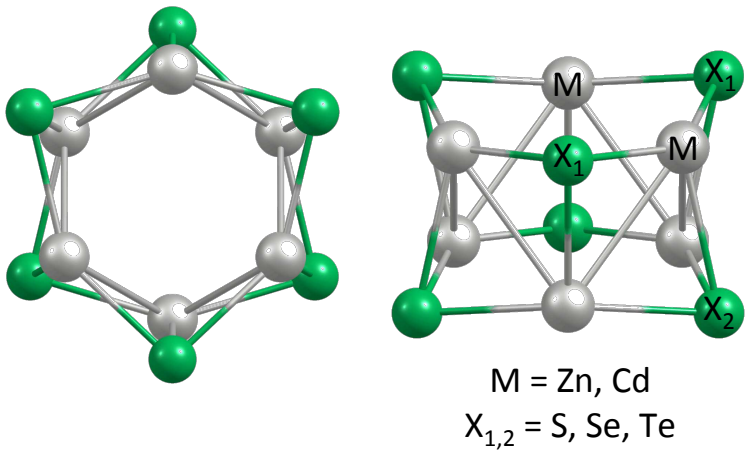


Figure 4.2: Computed mean-unsigned errors (MUEs; in blue) and maximum deviations (MADs; in red) of several basis sets associated with the MX (M = Cd, Zn; X = S, Se, Te) spectroscopic parameters using the PBE0 exchange-correlation functional. (a) bond distances (Å), (b) vibrational frequencies (cm–1), (c) excitation energies (eV). (d) Normalized mean unsigned errors (NMUEs; in blue) and normalized maximum absolute deviations (NMADs; in red) for each parameter (bonds, vibrations, excitations). The balanced mean unsigned errors (BMUEs; in blue) and balanced maximum errors (BMADs; in red) are also computed at the bottom of panel (d) by averaging the errors over all parameters. Note that the normalization step for the computation of BMUEs allows NMUEs to be, in some cases, larger than NMADs.

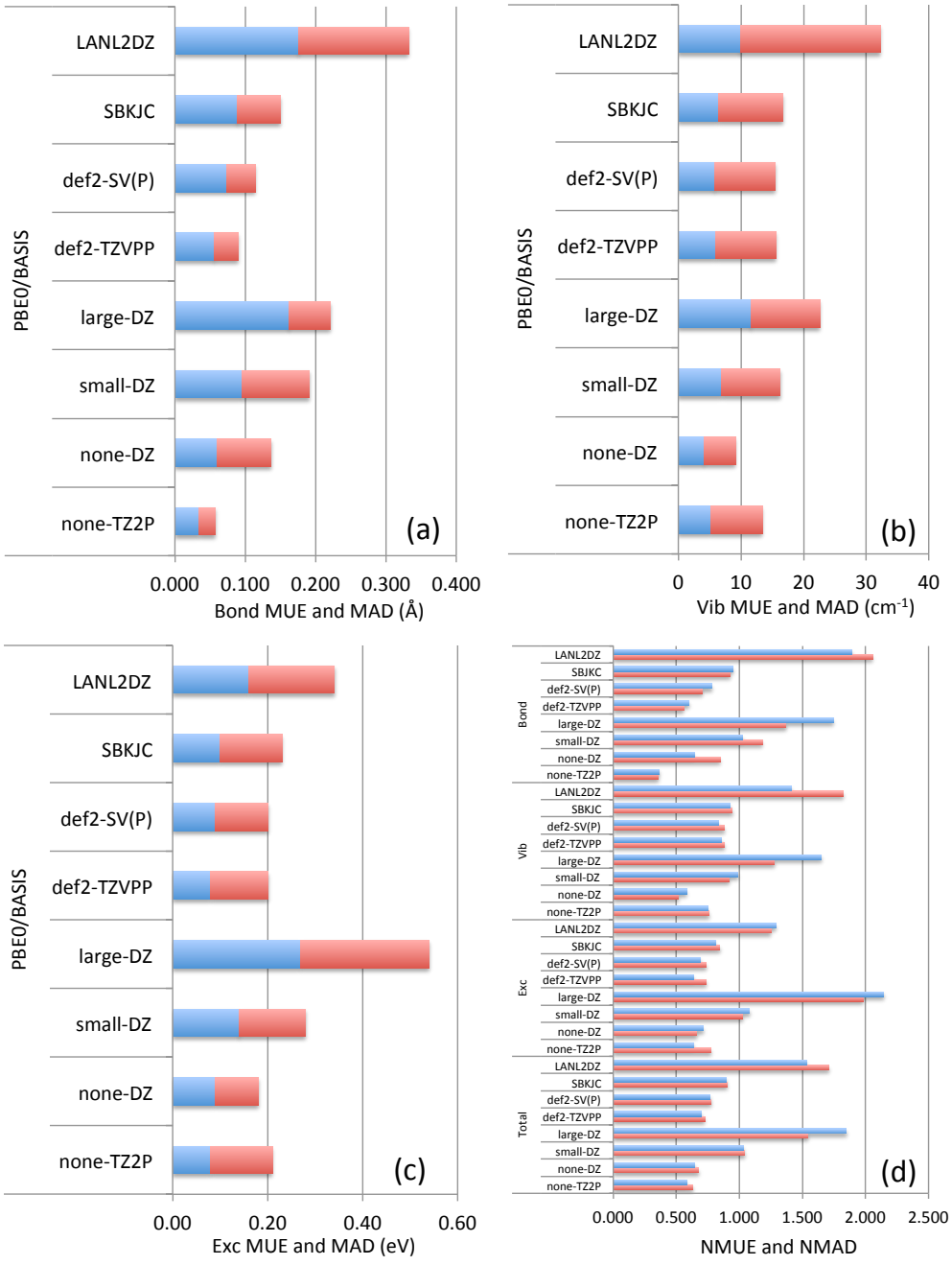


Figure 4.3: Computed mean-unsigned errors (MUEs; in blue) and maximum deviations (MADs; in red) of several exchange-correlation (xc) DFT functionals, in conjunction with the MX (M = Cd, Zn; X = S, Se, Te) bond lengths (in Å). (a) $(ZnS)_6$, (b) $(ZnSe)_6$, (c) $(ZnTe)_6$, (d) $(CdS)_6$, (e) $(CdSe)_6$, and (f) $(CdTe)_6$. The vertical lines indicate average mean unsigned error (AMUE; in blue) and the average maximum absolute deviation (AMD; in red).

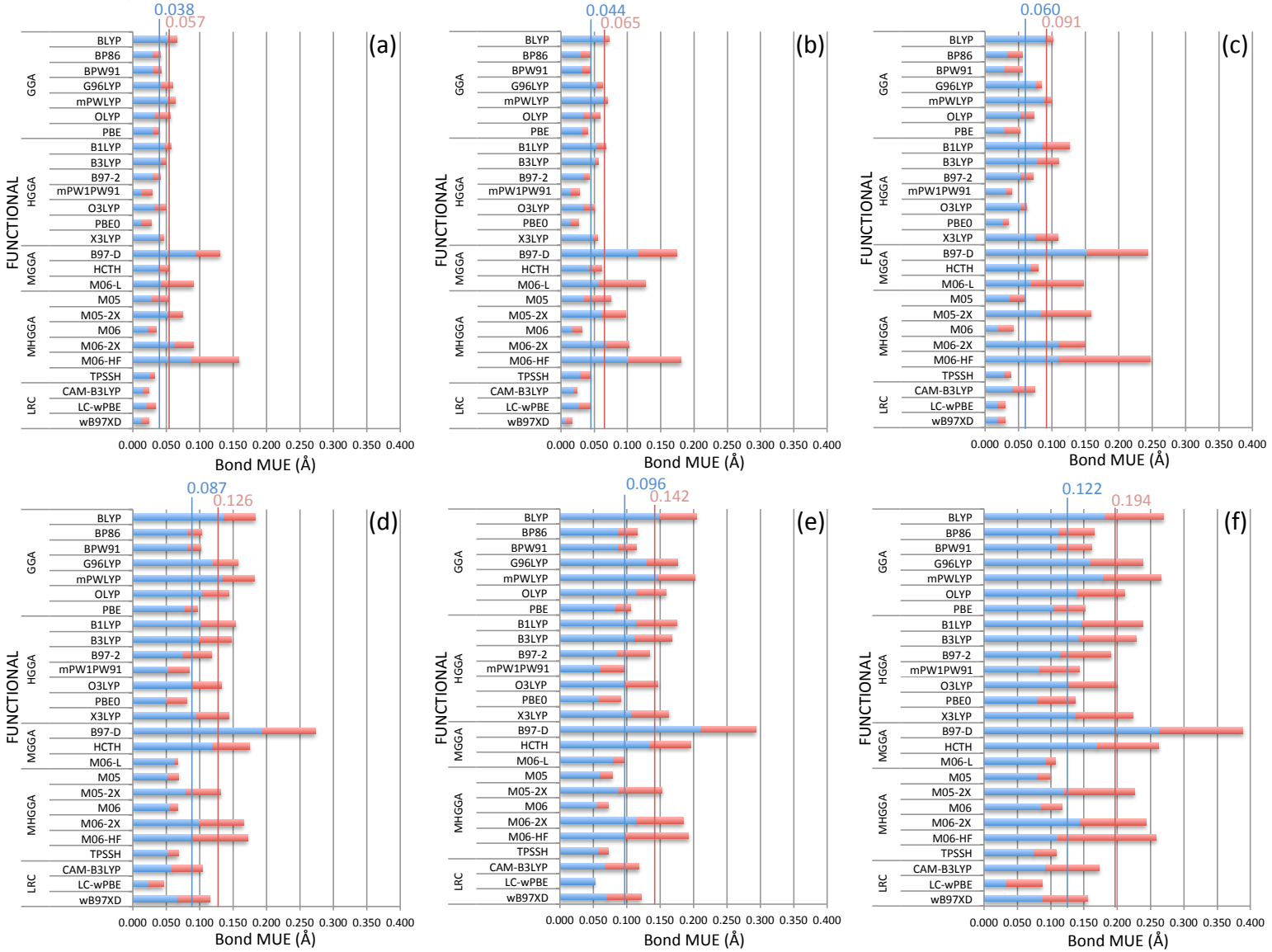


Figure 4.4: Computed mean-unsigned errors (MUEs; in blue) and maximum deviations (MADs; in red) of several exchange-correlation (xc) DFT functionals, in conjunction with the MX (M = Cd, Zn; X = S, Se, Te) normal modes (in cm^{-1}). (a) $(ZnS)_6$, (b) $(ZnSe)_6$, (c) $(ZnTe)_6$, (d) $(CdS)_6$, (e) $(CdSe)_6$, and (f) $(CdTe)_6$. The vertical lines indicate average mean unsigned error (AMUE; in blue) and the average maximum absolute deviation (AMD; in red).

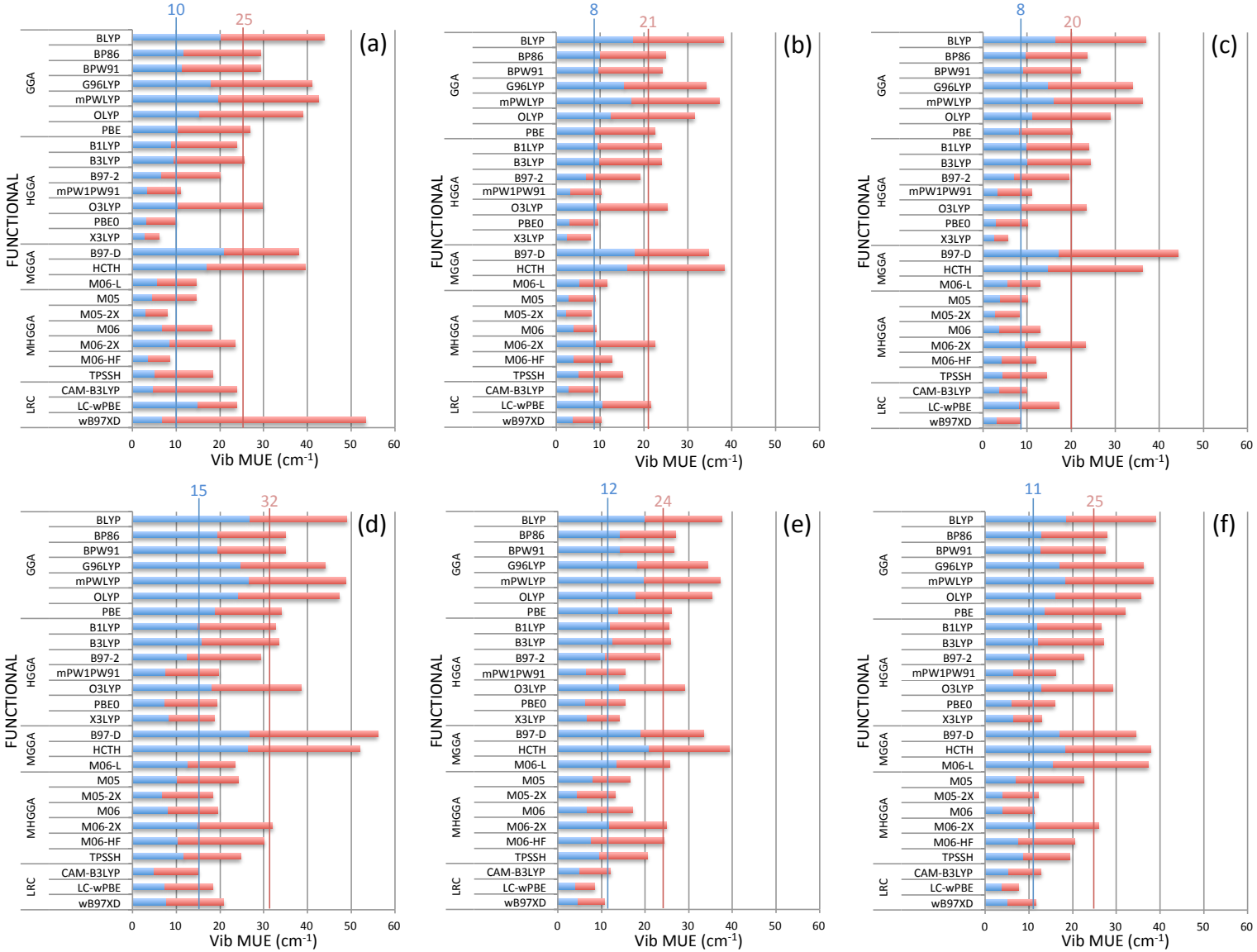


Figure 4.5: Computed mean-unsigned errors (MUEs; in blue) and maximum deviation (MADs; in red) of several exchange-correlation (xc) DFT functionals, in conjunction with the MX (M = Cd, Zn; X = S, Se, Te) excitation energies (in eV). (a) $(ZnS)_6$, (b) $(ZnSe)_6$, (c) $(ZnTe)_6$, (d) $(CdS)_6$, (e) $(CdSe)_6$, and (f) $(CdTe)_6$. The vertical lines indicate average mean unsigned error (AMUE; in blue) and the average maximum absolute deviation (AMD; in red).

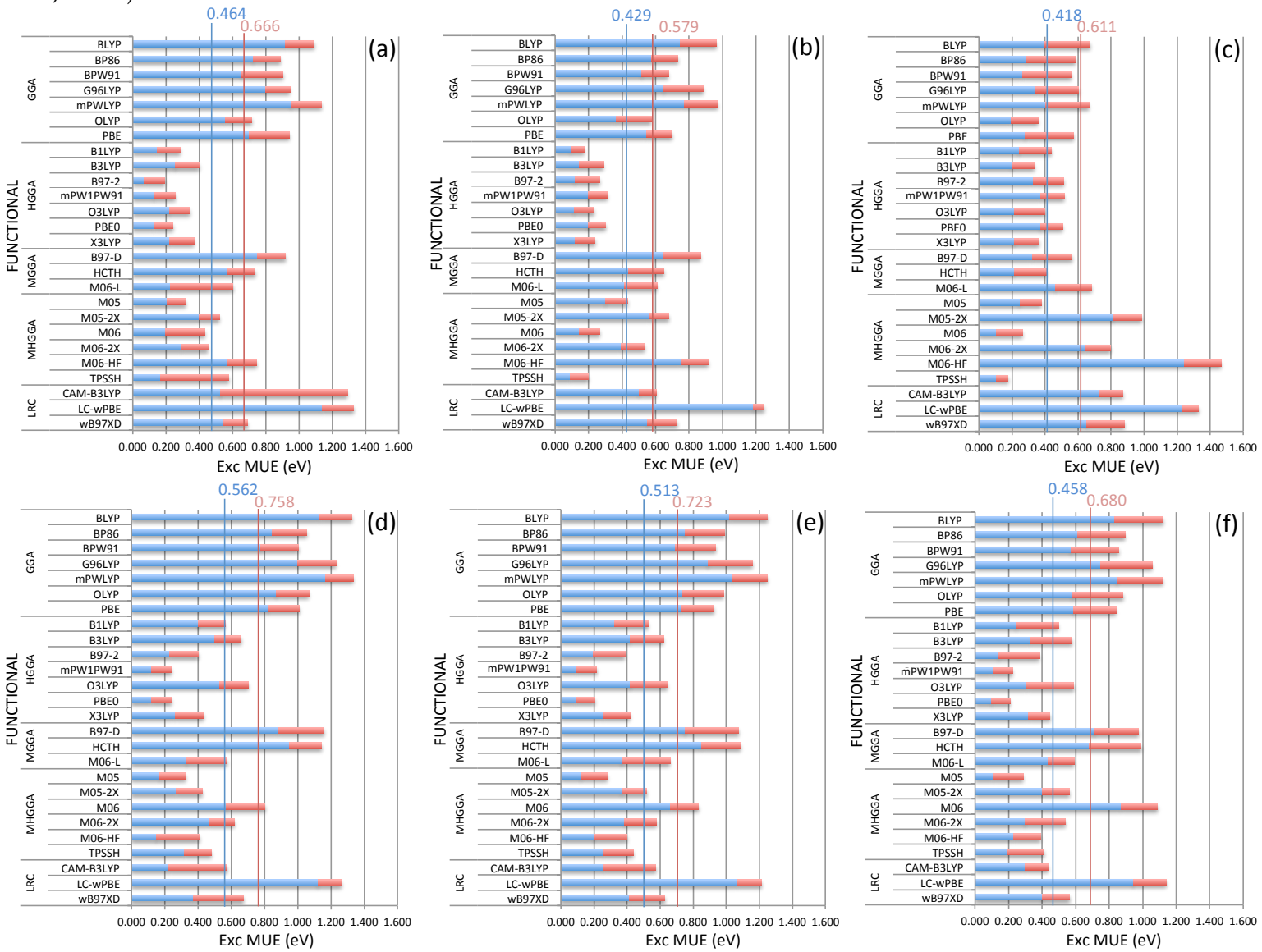


Figure 4.6: BMUEs for (a) bond lengths, (b) vibrational frequencies, and (c) excitation energies averaged over all nanoclusters studied. (d) Total BMUEs averaged over panels (a), (b), and (c).

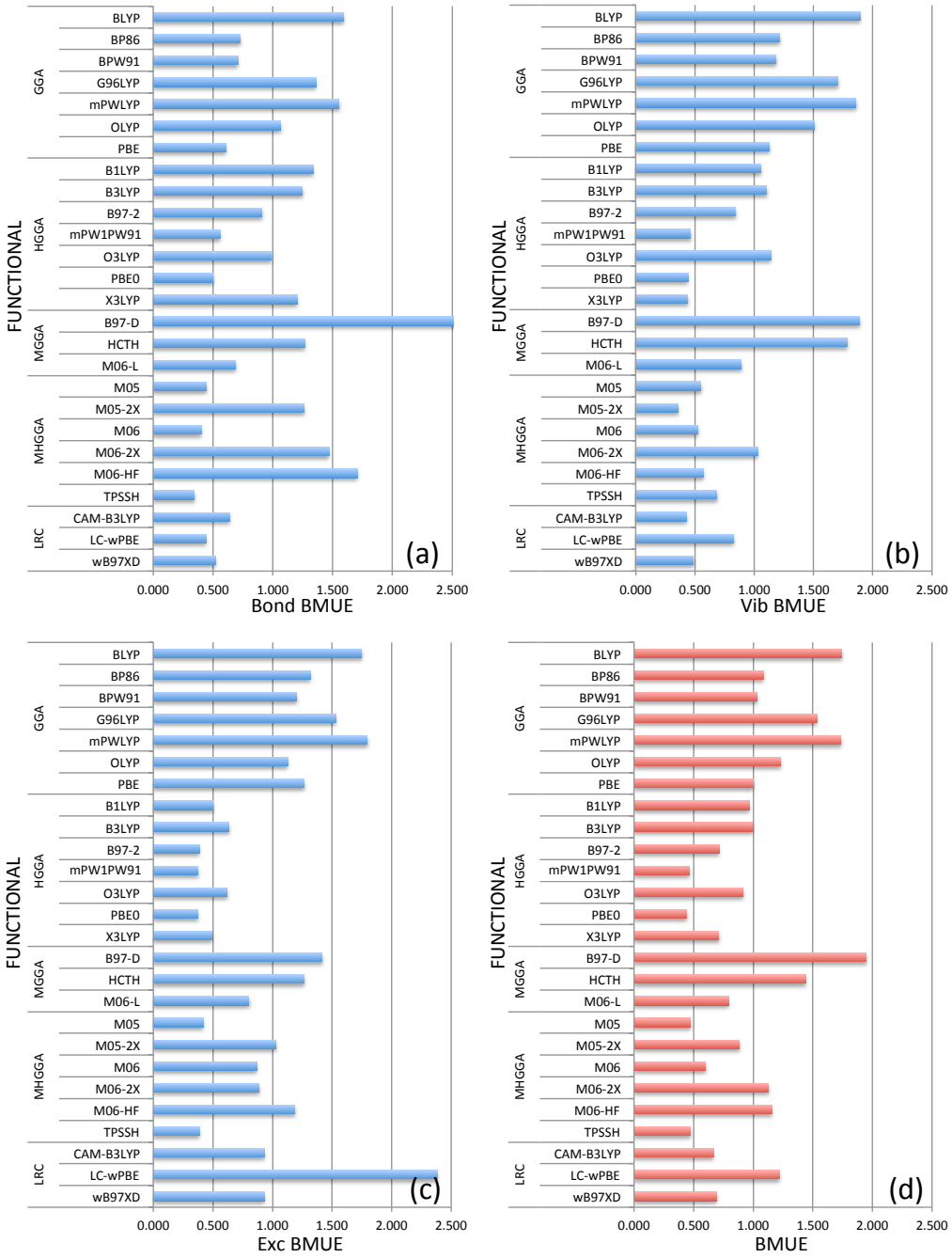


Figure 4.7: Correlation diagrams for the excitation energies computed with a restricted selection of DFT functionals (y axis) against the reference benchmark (x axis). (a) $(ZnS)_6$, (b) $(ZnSe)_6$, (c) $(ZnTe)_6$, (d) $(CdS)_6$, (e) $(CdSe)_6$, and (f) $(CdTe)_6$.

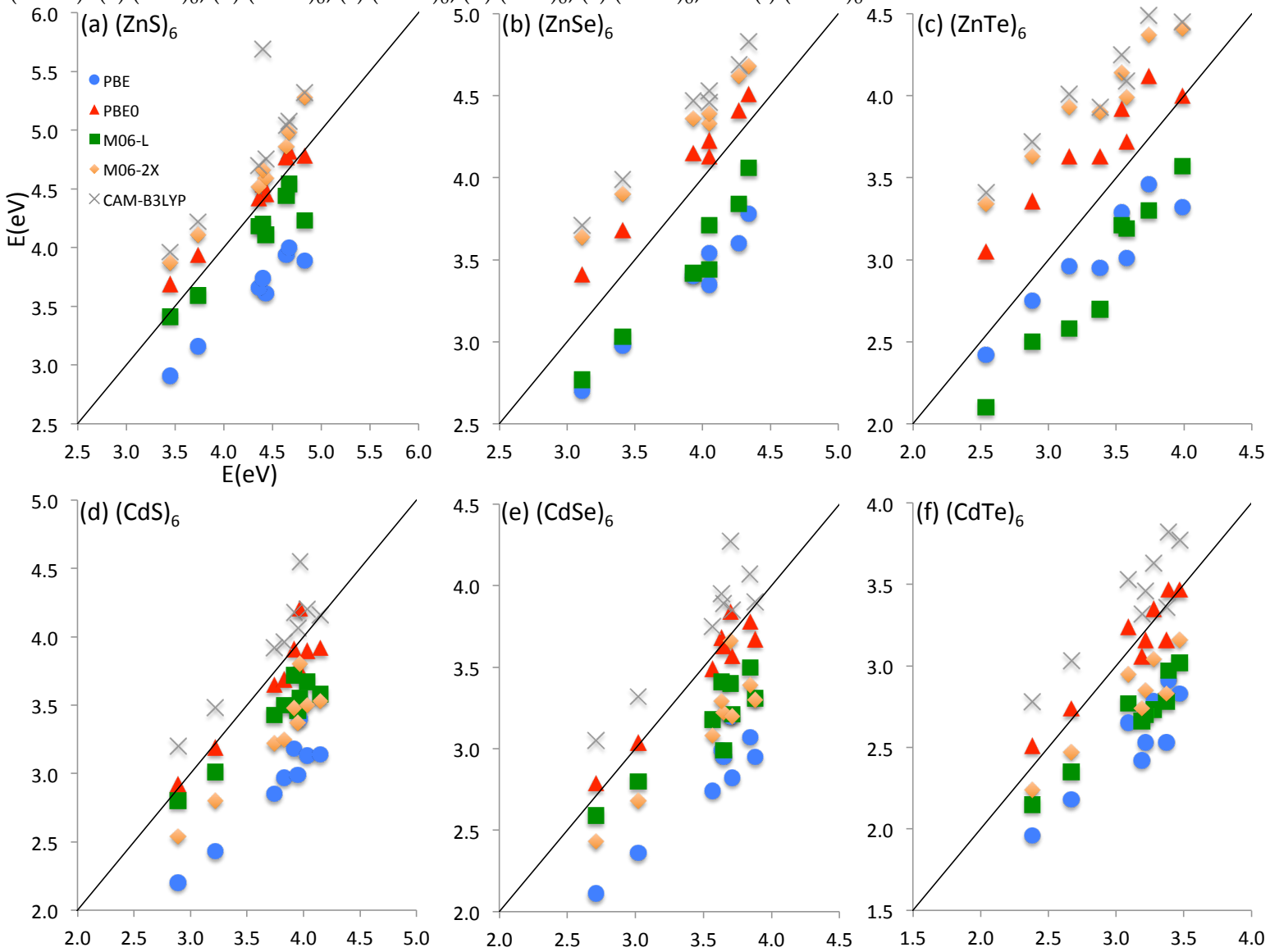


Figure 4.8: (Left) Simulated absorption spectra of the $(CdSe)_6$ cluster, drawn by a Gaussian convolution with FWHM = 3000 cm^{-1}, calculated taking into account the lowest 20 electronic transitions. Results obtained with the def2-SV(P) functional, on top of the geometries optimized with each functional. The reference EOM-RICC2 spectrum is shown in shaded gray. (Right) DFT spectra are shifted rigidly by their MUE value.

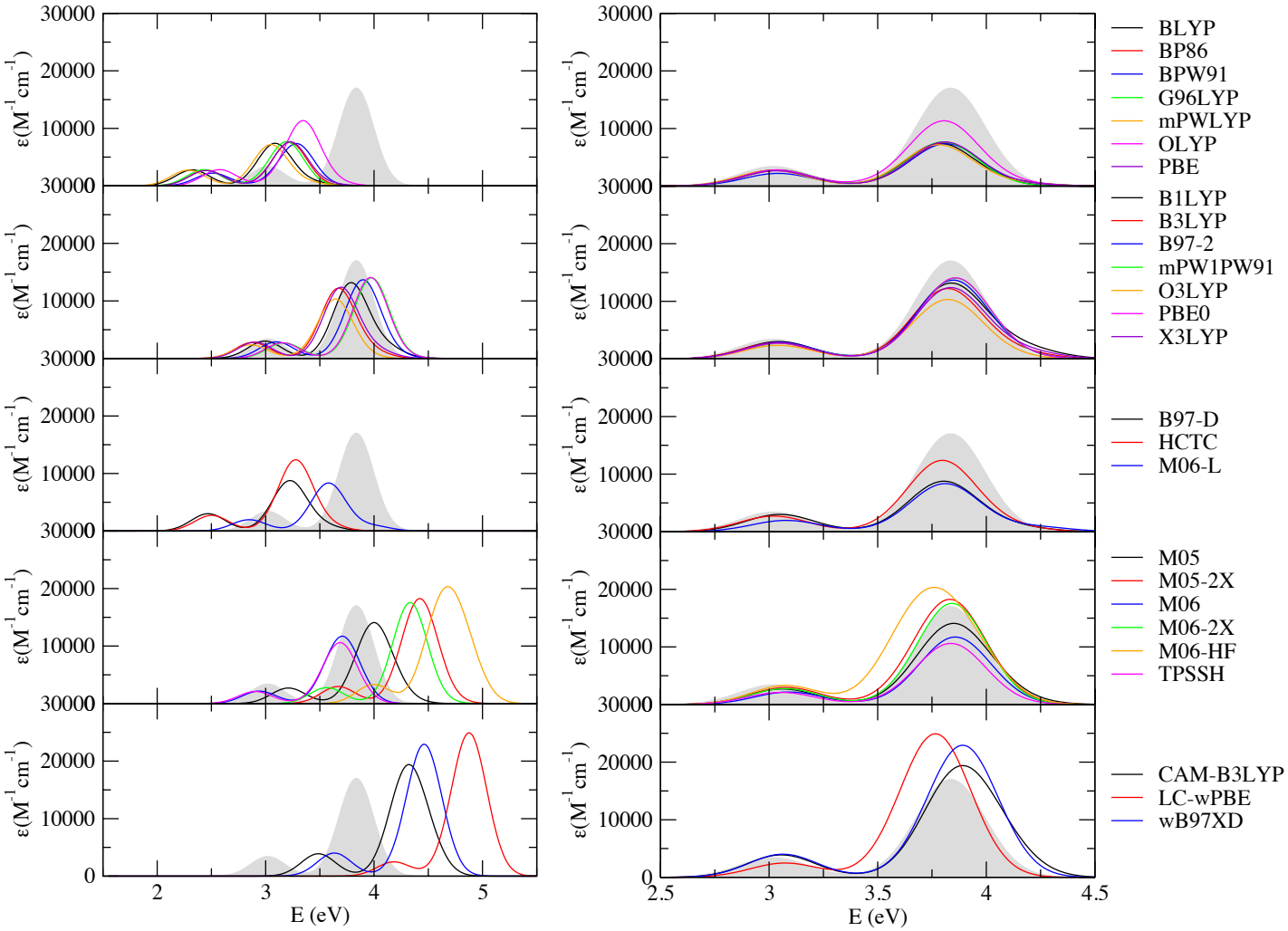
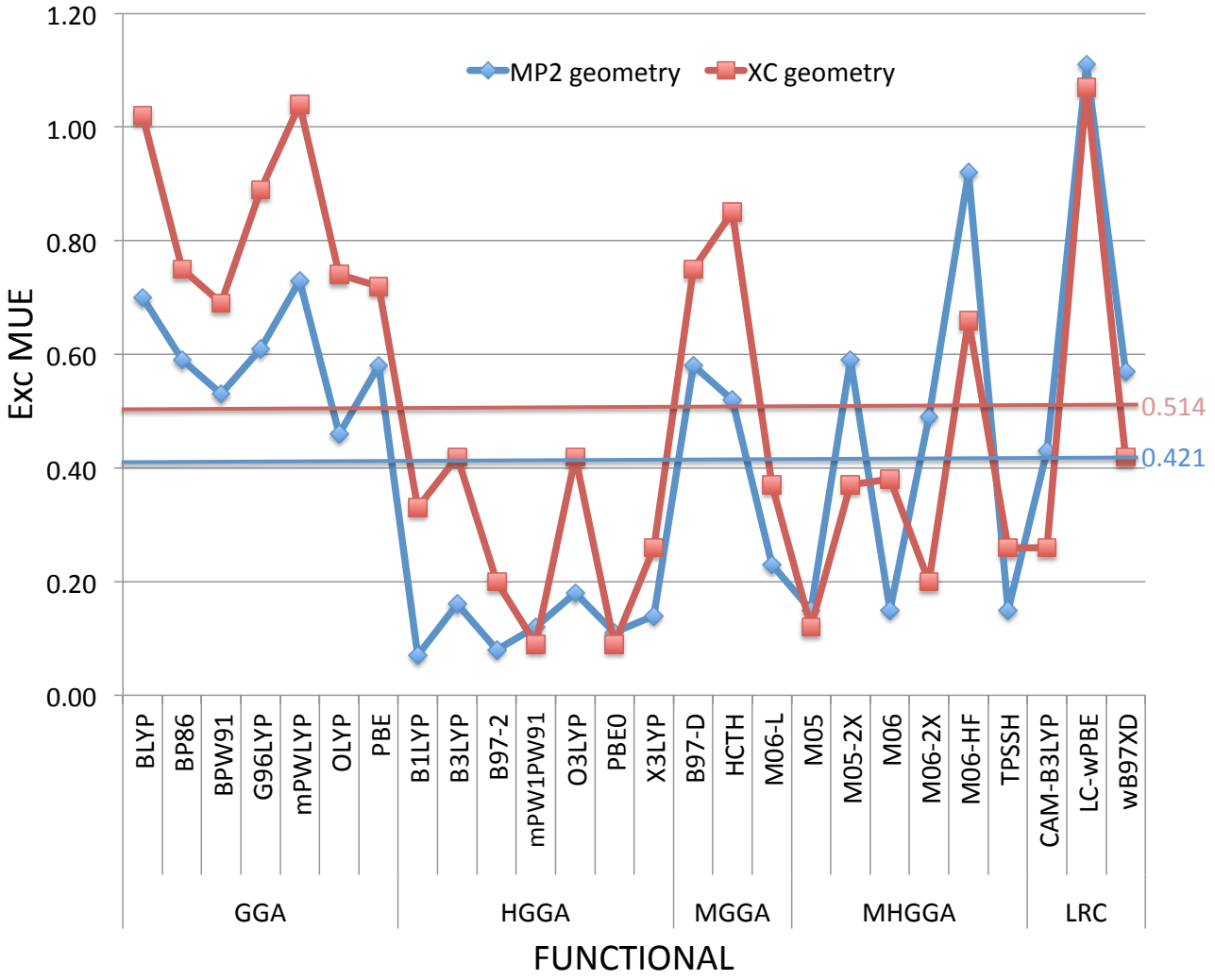


Figure 4.9: MUEs for the excitation energies computed on the $(CdSe)_6$ complex at the RI-MP2 and DFT geometries.



4.2 Modeling ZnS and ZnO Nanostructures: Structural, Electronic, and Optical Properties

4.2.1 Abstract

We report the computational modeling of ZnS and ZnO nanostructures by defining realistic nanoparticle models 1.5 nm sized for each material and investigating their structural, electronic, and optical properties by means of DFT/TDDFT calculations. To provide a direct comparison of calculated data to experimentally characterized nanoparticles, 3D $(ZnX)_{111}$ nanoclusters of prismatic shape have been set up starting from the bulk wurtzite (X = O, S), with two different saturation patterns of the polar surfaces. The investigated models have been optimized by means of Car–Parrinello molecular dynamics and local geometry optimization techniques. The investigated systems exhibit a well-opened HOMO–LUMO energy gap, without any artificial midgap states. TDDFT calculation of the lowest excitation energies are in excellent agreement, within 0.1–0.2 eV, with the experimental absorption onsets reported for similarly sized ZnO and ZnS nanoparticles (3.70 and 4.40 eV, respectively). We have also investigated the electronic structure of the considered nanoparticles, with reference to the valence band structure, finding calculated binding energies for the Zn d-shell to be only slightly displaced toward lower values compared to experimental values, possibly due to quantum confinement effects. This work provides the required computational framework for modeling ZnX and in general II–VI semiconductor nanomaterials, opening the way to simulation of ligand/semiconductor interactions.

4.2.2 Introduction

II–VI semiconductor nanomaterials have been deeply investigated due to their unique photophysical properties, which substantially deviate from those of their bulk counterparts [4]. At the nanoscale, charge carriers are confined to move within regions of the space comparable to their de Broglie wavelength. Such quantum confinement results in a discrete size- and shape- dependent structure of electronic levels and in the appearance of fascinating properties. Promising technological applications of II–VI semiconductor nanomaterials such as photooxidizers and photocatalists [376] [376, 377], photovoltaic solar cells [378–381], quantum devices [382], optical sensitizers [383], and fluorescent probes [68] have been developed due to their wide absorption range, size-tunable emission, high luminescence efficiency, unmatched photostability, and reasonably long photoexcited lifetimes [4].

ZnO and ZnS are among the most studied II–VI compounds. Their wide direct band gaps (3.4 and 3.7 eV respectively) and high exciton binding energies (60 and 40 meV respectively) make ZnO and ZnS particularly suitable for optoelectronic applications [384]. Besides, they are abundant, highly stable, and environmentally friendly materials so that they are amenable also for biomedical applications. Both ZnO and ZnS can adopt three phases, namely, cubic sphalerite (B3), hexagonal wurtzite (B4), or the rarely observed cubic rock salt

(B1). Wurtzite is the most stable polymorph of ZnO at room temperature. On the contrary, ZnS crystallizes in sphalerite under ambient conditions, while wurtzite polymorph is stable above 1020 °C. Nevertheless, with decreasing particle size, the surface-to-volume ratio becomes large enough so that the stability of the two phases is influenced by the surface energy. It has been suggested theoretically that the mean surface energy of a three-dimensional nanoparticle is greater for the sphalerite than for wurtzite [12, 29, 385]. This prediction has found support in recent experimental works reporting the low-temperature synthesis of small wurtzite ZnS nanoparticles [386–391]. Interestingly, the hexagonal wurtzite polymorph exhibits better luminescent properties than the cubic sphalerite phase [392]. It is worth noting, however, that the surface energy and therefore the crystal structure of the nanoparticle strongly depend on the synthesis conditions. A wide range of ZnO and ZnS nanostructures have been obtained by choosing the appropriate temperature, solvent, or coordinating ligands [384]. Moreover, postsynthesis reversible structural transformations at room temperature have been observed by absorption–desorption of methanol and water on the surface of ZnS nanoparticles [28].

Particularly interesting is the size- and shape-dependency of the optical properties of the ZnS and ZnO nanostructures. Due to the quantum confinement mentioned before, a blue-shift of both the absorption and emission spectral onsets is observed with decreasing structural size. The absorption onsets of 0.7–1.5 nm radii ZnO particles appear in the range 3.7–3.8 eV, which are found to red-shift toward the bulk band-gap value of 3.3–3.4 eV upon increasing the particle size [393–395]. The ZnO visible light emission usually falls in the green–yellow region of the spectrum (2.1–2.4 eV), even if blue (2.7–2.8 eV) and orange (1.8–1.9 eV) emissions have also been reported [393–396]. Most of the literature suggests that the green luminescence of ZnO arises from oxygen vacancies, with long-lived visible emission (microsecond range) consistently reported along with a short-lived (nanosecond range) blue luminescence [393–395]. A size-dependent shift of the visible luminescence was also reported [393–395].

ZnS wurtzite nanoparticles of 0.75–2.00 nm radii show absorption onsets in the range 3.9–4.4 eV [387, 397, 398], which are blue-shifted with respect to the bulk band gap of 3.7 eV. With the increasing size of the nanoparticle, the absorption is found to converge toward the bulk value. For particles whose radius is greater than the exciton radius of bulk ZnS (2.5 nm), no quantum confinement effect is observed in the absorption [298, 390, 391].The visible light emission of ZnS has been widely reported in the literature. As in the case of ZnO, the origin of such luminescence remains a debated issue. Kar et al. reported three emission peaks at 3.1, 2.8, and 2.5 eV for wurtzite ZnS nanowires and nanoribbons [399–401]. The first one was suggested to arise from sulfur vacancies and interstitial lattice defects, and the second and the third one were attributed to surface states and zinc vacancies, respectively. Since wurtzite ZnS nanoparticles show similar emission features, their luminescence properties have been explained in the same framework [398]. Tang et al. distinguished three peaks at 3.2, 3.1 and 3.0 eV in the emission spectrum of 3 nm sized sphalerite ZnS nanoparticles [402]. The emission peaks at 3.1 and 3.0 eV were ascribed to surface states and internal

vacancies, respectively. The peak at 3.22 eV may be related to the dangling bonds of the surface-attached ligands.

long with the remarkable amount of experimental investigations, theoretical calculations have contributed to shed light on the structural and electronic properties of ZnO and ZnS. Several works focused on the structural and defective properties of ZnO [403–409]. Most of them addressed the bulk material, and only a few investigations were performed on nanostructure models [291, 410–413]. Due to computational limitations, early theoretical studies of ZnS nanostructures focused on small clusters and on their structural characterization. Global minimization techniques predict that $(ZnS)_n$ clusters with $n \sim 10$–50 adopt hollow spherical structures, where all atoms are three-coordinated [307, 320, 339, 414]. Similar studies by Hamad et al. regarding particles with sizes in the range $n \sim 50$–80 produced core–shell structures in which one spherical cluster was enclosed inside a larger one, with tetrahedral bonding between them [309]. Other theoretical works, however, have suggested that similarly sized bulklike particles are more stable [415]. The optical properties of hollow and core–shell structures have also been studied by Hamad et al. [308]. They predicted the band gap of the hollow clusters to oscillate between 4.4 and 4.7 eV. The gap of core–shell clusters was found to be smaller. Similar sized bulklike clusters exhibit a narrower band gap in the range 3.6–4.0 eV.

Further computational works concerning larger ZnS clusters up to $n \sim 500$ predicted the BCT crystalline structure to be the most stable [309]. It has been proposed that BCT is able to accommodate distortions more easily than bulklike structures. Indeed, wurtzite and sphalerite polymorphs undergo significant rearrangements in order to minimize both the number of dangling bonds in the surface and the net dipole of the structure. Nevertheless, the BCT phase has not been reported experimentally. Moreover, the wurtzite phase was predicted to be only slightly higher in energy than the BCT phase and was expected to be further stabilized in solution. Sphalerite was found to be the least stable out of the three investigated phases. Even if a significant effort has been devoted to the structural elucidation of ZnS nanoparticles with sizes comparable to the experiments, the studies regarding their electronic and optical properties are rather scarce.

The comparison of the optical properties of small ZnO and ZnS clusters with the experimental results is quite difficult since the absorption and luminescence onset shifts with the particle size due to the aforementioned quantum size effect. Thus, the choice of an appropriate model is mandatory. The three-dimensional $(ZnO)_{111}$ cluster saturated by water molecules proposed by some of us [416] has shown to accurately reproduce the experimental optical features of ZnO nanoparticles in the framework of the time-dependent DFT (TDDFT). In the present theoretical work we further progress with the modeling of ZnO and ZnS nanostructures by defining new realistic nanoparticle models for each material and investigating their structural, electronic, and optical properties by means of DFT/TDDFT calculations employing GGA and hybrid functionals. To the best of our knowledge, this is the first time that the optical properties of a realistically large ZnS nanoparticle model are investigated.

4.2.3 Model and Computational Details

To provide a direct comparison of calculated data to experimentally characterized nanoparticles, realistic 3D $(ZnX)_{111}$ nanoclusters have been set up starting from the bulk wurtzite. Such 1.5 nm sized nanoparticles are prismatic in shape, as shown in Figure 4.10. The stability of similar prismatic nanocrystals has been reported for ZnO [411] and ZnS [417]. The dangling bonds in the surface of such bulklike structures lead to artificial surface states that intrude into the band gap. In the particular case of the noncentrosymmetric wurtzite structure, the polarity of the Zn- and X- (X = O, S hereafter) terminated (0001) and $(000\bar{1})$ surfaces establishes an unrealistic net dipole moment along the c axis, which diverges with increasing dimension along this axis, as well as the surface energy [406, 411, 418]. Due to these reasons, the band gap narrows and the nanostructures become metallic, leading to methodological and conceptual troubles. Surface reconstruction and/or proper saturation of unsaturated sites has shown to remove the surface states and decrease the dipole along the c axis, opening the band gap and stabilizing the nanoparticle. Therefore, and in a first step, we saturate the polar surfaces by dissociating H_2X molecules, adsorbing H^+ and HX^- ions on the unsaturated X and Zn sites respectively. The dissociative adsorption of water in the polar surfaces of ZnO has been found to be energetically favorable [406]; thus, we follow the same approach for ZnS. In a second step, we place Zn^{2+} and X^{2-} instead of H^+ and HX^- ions, respectively, to recover stoichiometric clusters composed exclusively of Zn and X.

The investigated models have been fully optimized by means of Car–Parrinello molecular dynamics [262], as implemented in the Quantum-Espresso package [419], employing the GGA-PBE exchange-correlation functional [238] in combination with a plane wave basis set and ultrasoft pseudopotentials [420, 421]. Plane wave basis set cutoffs set for the smooth part of the wave functions and the augmented density are 25 and 200 Ry, respectively. The dimensions of the simulation supercells have been defined by adding 7 Å of vacuo to the largest nanoparticle dimension in each direction. Geometry optimization has been carried out by performing a preliminary dynamic simulation at finite temperature, with an integration time step of 5 au, to explore the potential energy surface of the system. Then we introduce a friction of 0.005 for the electronic degrees of freedom to reach the structural minimum. The fictitious mass used for the electronic degrees of freedom is 500 au, and we set the masses for both S and Zn atoms to 5.0 amu. This setup allows us to perform a rapid nuclear thermalization and to maintain the adiabaticity throughout the simulation. Suitable structures sampled during the dynamics have been further optimized using the PBE functional together with a double-valence set of Slater-type orbitals as implemented in the ADF program package [267].

While satisfactorily reproducing structural parameters, GGA functionals severely underestimate the band gap of II–VI semiconductor materials. Thus, the hybrid B3LYP functional has been employed in conjunction with an SVP basis set to perform TDDFT calculations on the optimized structures. The B3LYP functional has been modified to contain 27.5% Hartree–Fock exchange, as from our previous work [416]. Solvation effects have been in-

cluded by means of the polarizable continuum model (PCM). We chose water as solvent to reproduce the experimental conditions since an increasing number of II–VI nanostructures are synthesized in water solution. This setup has shown to accurately reproduce the absorption properties of ZnO nanostructures [416]. All TDDFT calculations have been performed by the Gaussian09 program package [422].

4.2.4 Results and Discussion

Geometry

As shown in Figure 4.10, all the atoms in the apolar surfaces (see views along x and y axes) of the unrelaxed $(ZnX)_{111}$ structures are threefold coordinated while each polar surface (see view along z axis) bears in our models nine twofold coordinated ions. Thus, following previous works [405, 406, 416], the saturation of the polar surfaces with a variable number of H_2X molecules was studied. Binding of 11 or 12 dissociated H_2X molecules to the polar surfaces of the nanostructures ($[(ZnX)_{111}(H_2X)_{12}]$ model hereafter) led to the saturation of two-coordinated surface atoms and at the same time to the minimization of the dipole along the c axis. In a second step, we substituted H^+ and HX^- with surface Zn^{2+} and X^{2-} ions on the X- and Zn-terminated surfaces, respectively. Proper charge compensation was achieved, by addition of five Zn^{2+} and five X^{2-} ions to the X- and Zn-terminated faces, leading to the $[(ZnX)_{111}(ZnX)_5]$ model. We need to mention here that while for H^+/HX^- saturation a rather straightforward geometry optimization was achieved, for the models saturated with Zn^{2+}/X^{2-} ions we had to perform several Car–Parrinello molecular dynamics simulations, carrying the system at 500 K for 2–3 ps followed by annealing at 0 temperature, to locate a reasonable minimum energy structure.

Bulklike clusters undergo a significant structural rearrangement upon optimization. Such reconstruction has been attributed to the unsaturated atoms on the surface. Since we have saturated the dangling bonds, our models preserve the wurtzite structure (Figure 4.10). It is worth noting that the surface atoms in the relaxed structures remain at least threefold coordinated. However, there is a noticeable deviation from the ideal bulklike structure.

In order to reveal the distortion of the optimized nanoparticles, the average Zn–X bond length of each atom with its neighbors has been calculated. Figure 4.11 shows the variation of such bond lengths as a function of the position of the atom with respect to the center of the cluster. The bonds in the center of the nanoparticle are slightly longer than those experimentally observed in the bulk. The Zn–O bonds in the core of the nanoparticle are 2.05 Å on average, 5% larger compared to the experimental value of 1.95 Å reported for the bulk material. In the case of ZnS, our calculations provide Zn–S bonds of 2.42 Å in the center of the nanoparticle, 3% longer than the value of 2.35 Å observed in the bulk. With the increasing distance with respect to the center of the nanoparticle, the pattern of the bond lengths turns out to be more complicated. Even if some bonds remain as large as those measured in the inner part, most of them show a significant contraction with respect to the

core and tend to converge to the value observed in the bulk, irrespective of ZnO or ZnS and of the model. These findings reveal a surface reconstruction that bring some of the surface ions closer, even in the presence of passivating ligands. The lower coordination of the surface seems to be the driving force of the shrinkage of the bonds in the outer region.

To better characterize the structural reconstruction, the radial distribution function (RDF hereafter) of the relaxed nanoparticles has been calculated. The RDF indicates the number of atoms located at a given distance with respect to a particular point. Figure 4.12 displays the RDFs of the optimized models together with that of the unrelaxed wurtzite structure, taking the center of the cluster as the origin. The core of the optimized nanoparticles resembles the ideal wurtzite structure, with three well-defined shells of atoms. Nevertheless, such inner atoms are slightly shifted outward if compared with the ideal structure, and therefore the bonds are correspondingly longer. Beyond a given radius (5.5 and 6.5 Å from the nanoparticle center for ZnO and ZnS, respectively) the RDF of the optimized nanoparticles substantially deviates from ideal structure, meaning a significant structural reconstruction. Remarkably, in the outermost region of the nanoparticle the X atoms are displaced outward with respect to the Zn atoms. A similar reconstruction has already been reported not only for ZnS [415] but also for CdS and CdSe [286, 287, 423]. Indeed metal atoms prefer a higher coordination, while X atoms, be it oxygen or sulfur, can accommodate a lower coordination environment.

Given the importance of the polar surfaces on the stability of the investigated materials, we performed a closer inspection of the reconstruction of the Zn- and X- terminated surfaces. We realized that the optimized $[(ZnX)_{111}(H_2X)_{12}]$ structures exhibit a more regular geometry than $[(ZnX)_{111}(ZnX)_5]$ structures. While in the ideal wurtzite there are eight clusters of atoms that are symmetrically placed with respect to the center of the plane, for the $[(ZnX)_{111}(ZnX)_5]$ models a more disordered pattern of bond lengths is found, revealing that the atoms are not regularly placed with respect to the center of the polar planes. We thus conclude that $[(ZnX)_{111}\ (ZnX)_5]$ models show a larger reconstruction of the polar surfaces. Indeed, as mentioned before, $[(ZnX)_{111}(H_2X)_{12}]$ nanoparticles were rather straightforwardly optimized, while several Car–Parrinello molecular dynamics simulations had to be carried out to converge the $[(ZnX)_{111}\ (ZnX)_5]$ nanostructures.

Electronic Structure and Absorption Spectra

The investigated ZnO and ZnS model systems exhibit a well-opened HOMO–LUMO energy gap, meaning that the saturation of the polar faces and the surface reconstruction effectively removes the presence of possible artificial midgap states. For sake of comparison the band-gap values of the nanoparticles are shown in Table 4.7, together with the DFT eigenvalues of the frontier Kohn–Sham single-particle molecular orbitals. It is worth noting that ZnS exhibits a wider gap than ZnO (4.77 vs 4.05 eV for the $[(ZnX)_{111}(H_2X)_{12}]$ model and 4.51 vs 4.24 eV for the $[(ZnX)_{111}(ZnX)_5]$ model). As from our previous results on $[(ZnO)_{111}(H_2O)_{12}]$ [416], for all the investigated systems the LUMO is a delocalized conduction band state, which, de-

spite having the same nature of the higher lying orbitals, is quite separated in energy from the rest of the conduction band states; see Table 4.7 and Figure 4.13. The presence of this state is independent from the specific material or saturation pattern and might therefore be an intrinsic property of the considered nanostructures.

Inspection of the energies of the HOMO and the LUMO reveals that the energy of the latter remains relatively similar for ZnO and ZnS, irrespective of the model. Therefore, the wider band gap of ZnS is calculated here to be a consequence of the lower HOMO energy. From these results we thus conclude that both models can be safely employed to determine the systems optical properties, despite $[(ZnO)_{111}(H_2O)_{12}]$ showing a slightly narrower band gap than $[(ZnO)_{111}(ZnO)_5]$, whereas $[(ZnS)_{111}(H_2S)_{12}]$ exhibits a slightly wider gap than $[(ZnS)_{111}(ZnS)_5]$.

Even if the differences of the Kohn–Sham molecular orbital eigenvalues may provide a reasonable approximation to the band-gap transition energies of bulk ZnO and ZnS, the precise description of the excitation energies in confined nanostructures requires a more accurate picture of electron correlation, such as that provided by TDDFT, which takes into account not only the electron–hole interaction and exchange-correlation effects, but also the configurational mixing of single excitations. The TDDFT-calculated electronic transition energies corresponding to the lowest excited states of the nanoparticles studied are given in Table 4.8 along with the calculated oscillator strengths. The energies of the low-lying excited states are in excellent agreement with the experimental absorption onsets reported for 1.5 nm sized ZnO and ZnS nanoparticles (3.70 eV [394] and 4.40 eV [398], respectively). For ZnO and ZnS we calculate lowest excitation energies at, respectively, 3.6 and 3.7 eV and 4.3 and 4.1 eV, for $[(ZnX)_{111}(H_2X)_{12}]$ and $[(ZnX)_{111}(ZnX)_5]$ models, respectively. From the comparison of $[(ZnX)_{111}\ (H_2X)_{12}]$ and $[(ZnX)_{111}\ (ZnX)_5]$ models, we notice, as previously mentioned, that the type of saturation of the polar surfaces does not seem to play a significant role in the excitation energies, with maximum deviations within 0.2 eV. However, the low-lying excitation energies of $[(ZnO)_{111}(H_2O)_{12}]$ are slightly red-shifted with respect to $[(ZnO)_{111}(ZnO)_5]$, while for ZnS the trend is the opposite. This could be predicted from the band-gap values.

In order to get a better understanding of the electronic structure of the investigated nanoparticles, their density of states (DOS hereafter) has been plotted (Figure 4.14 and Figure 4.15) and their valence band structure has been studied. Since all the binary tetrahedrally coordinated semiconductors exhibit a similar valence band structure, the identification of the observed peaks can be rather straightforward. Following the notation proposed in the literature [424] we have labeled the main valence band features as P_I, P_{II}, d, and P_{III}. P_I arises from the valence p orbitals of the X atoms. P_{II} and d are related to the 4s and 3d orbitals of the Zn atoms, respectively. P_{III} has been attributed to the valence s orbitals of X.

The d peak of binary semiconductors has been exhaustively studied by photoelectron spectroscopy and X-ray absorption spectroscopy. In the investigated nanoparticles, the position of the d band with respect to the top of the valence band (valence band maximum, VBM hereafter) is in good agreement with the experimentally reported binding energy differences, which are measured to lie in the range 7.5–10.0 eV for bulk ZnO [424–427] and 9.0

eV for bulk ZnS [424]. Our calculated binding energies are only slightly displaced to lower values. In fact, and depending on the model, our calculations provide binding energies of 7.3–7.5 eV for ZnO and 8.6–8.8 eV for ZnS. A similar underestimate has been observed in recent high-level DFT and GW calculations regarding bulk ZnO [428] and ZnS [429, 430]. Calculated binding energies were reported in the range 6.1–6.9 and 7.1–7.5 eV for ZnO and ZnS, respectively. If the Zn 3*d* orbitals are assumed to be relatively stable with the size of the nanostructure, when moving from the bulk to the nanoscale the VBM supposedly shifts to lower energies due to the quantum confinement effect. Therefore, we speculate that the binding energies are shifted to lower values, in line with our results. In a similar fashion, the binding energies calculated for the other peaks are to some extent underestimated with respect to the corresponding experimental quantities measured for bulk ZnO and ZnS, even though the agreement is quite good. It is worth noting that $[(ZnX)_{111}(H_2X)_{12}]$ and $[(ZnX)_{111}(ZnX)_5]$ models roughly provide the same picture of the valence band structure of both ZnO and ZnS. P_I and P_{II} are slightly closer for ZnO than for ZnS. Indeed, P_{II} is only 2.0–2.2 eV deeper than P_I in the valence band of ZnO, whereas for ZnS the gap is around 2.6 eV. These findings suggest a greater mixing of 2*p* orbitals of O and 4*s* orbitals of Zn in ZnO. Furthermore, the *d* peak is closer to P_{II} in ZnO. In fact, the energy difference between the *d* peak and P_{II} lies in the range 3.8–3.9 eV for ZnO, the gap being around 4.9 eV in the case of ZnS. Finally P_{III} and *d* peak are significantly closer for ZnS than for ZnO, the gaps being 4.1 and 10.6 eV, respectively. This observation means a greater hybridization of 3*d* orbitals of Zn and 3*s* orbitals of S in ZnS.

4.2.5 Conclusions

We have reported on the modeling of ZnO and ZnS nanostructures by defining novel nanoparticle models for each material and investigating their structural, electronic, and optical properties by means of DFT/TDDFT calculations employing a GGA and hybrid functionals. To set up a proper comparison of the optical properties of small ZnO and ZnS clusters with the experimental results, the choice of an appropriate model is mandatory since the absorption and luminescence onsets shift with the particle size due to the quantum size effect. To provide a direct comparison of calculated data to experimentally characterized nanoparticles, realistic 3D $(ZnX)_{111}$ nanoclusters 1.5 nm sized of prismatic shape have been set up starting from the bulk wurtzite (X = O, S). Our modeling strategy followed two lines: (i) we saturated the polar surfaces of ZnX nanoparticles by dissociating H_2X molecules, adsorbing H^+ and HX^- ions on the unsaturated X and Zn sites, respectively; and (ii) we added Zn^{2+} and X^{2-} instead of H^+ and HX^- ions, respectively, to the polar surfaces to recover stoichiometric clusters composed exclusively of Zn and X.

The investigated models were fully optimized by means of Car–Parrinello molecular dynamics and local geometry optimization techniques. While for H^+ / HX^- saturation a rather straightforward geometry optimization was achieved, for the models saturated with Zn^{2+} / X^{2-} ions we had to perform several Car–Parrinello molecular dynamics simulations at

finite temperature, followed by annealing at zero temperature, to locate a reasonable minimum energy structure. Bulklike clusters were found to undergo a significant structural rearrangement upon optimization but preserved the wurtzite structure. Such reconstruction has been attributed to the unsaturated atoms on the surface.

The investigated ZnO and ZnS model systems exhibit a well-opened HOMO–LUMO energy gap, meaning that the saturation of the polar faces and the surface reconstruction effectively remove the presence of possible artificial midgap states. TDDFT calculation of the lowest excitation energies for all studied systems in water solution were in excellent agreement with the experimental absorption onsets reported for 1.5 nm sized ZnO and ZnS nanoparticles (3.70 and 4.40 eV, respectively). For $[(ZnX)_{111}(H_2X)_{12}]$ and $[(ZnX)_{111}(ZnX)_5]$ we calculate lowest excitation energies at, respectively, 3.6 and 4.3 eV and 3.7 and 4.1 eV for X = O and S, respectively. From the comparison of $[(ZnX)_{111}(H_2X)_{12}]$ and $[(ZnX)_{111}(ZnX)_5]$ models we therefore concluded that the type of saturation of the polar surfaces does not seem to play a significant role in determining the excitation energies.

We then investigated the electronic structure of the considered nanoparticles, with reference to the valence band structure, in terms of their density of states. The position of the d band with respect to the top of the valence band maximum was in good agreement with the experimentally reported binding energy differences, which are measured in the range 7.5–10.0 and 9.0 eV for bulk ZnO and ZnS, respectively. Our calculated binding energies are only slightly displaced toward lower values. Our calculations provide binding energies of 7.3–7.5 eV for ZnO and 8.6–8.8 eV for ZnS. The 3*d* orbitals belong to the semicore of the Zn atom, and their position is expected to be relatively stable irrespective of the size of the nanostructure. On the other hand, when moving from the bulk to the nanoscale the valence band maximum supposedly shifts to lower energies due to the quantum confinement effect so that the binding energies are expected to shift to lower values, in line with our results.

In conclusion, we have reported a comprehensive computational modeling investigation of ZnO and ZnS nanostructures, defining realistic models and a highly accurate computational strategy. We believe this work to provide the required computational framework for the investigation of ligand binding to ZnX nanostructures, thus aiding the understanding of the subtle interactions between the ligands and the semiconductor in defining the peculiar optical properties of these systems.

Table 4.7: Energies of the frontier orbitals and band gaps, in eV.

	$[(ZnO)_{111}(H_2O)_{12}]$	$[(ZnO)_{111}(ZnO)_5]$	$[(ZnS)_{111}(H_2S)_{12}]$	$[(ZnS)_{111}(ZnS)_5]$
HOMO-1	–6.33	–6.64	–7.09	–6.81
HOMO	–6.30	–6.56	–7.07	–6.73
LUMO	–2.25	–2.32	–2.29	–2.22
LUMO+1	–1.63	–1.89	–1.88	–1.88
LUMO+1	–1.62	–1.78	–1.70	–1.75
HOMO-LUMO	4.05	4.24	4.77	4.51

Table 4.8: Lowest TDDFT excitation energies, in eV; oscillator strengths in parentheses. Experimental values for ZnO and ZnS are 3.70 and 4.40 eV, respectively, from Refs. (25) and (27).

	$[(ZnO)_{111}(H_2O)_{12}]$	$[(ZnO)_{111}(ZnO)_5]$	$[(ZnS)_{111}(H_2S)_{12}]$	$[(ZnS)_{111}(ZnS)_5]$
1	3.59	3.69	4.26	4.05
	(0.0017)	(0.0426)	(0.0019)	(0.1018)
2	3.62	3.74	4.34	4.09
	(0.0119)	(0.0473)	(0.0651)	(0.0450)

Figure 4.10: Geometrical structures of (a) unrelaxed $(ZnO)_{111}$ cut from the bulk, (b) relaxed $[(ZnO)_{111}(H_2O)_{12}]$, and (c) relaxed $[(ZnO)_{111}(ZnO)_5]$. Similar structures have been obtained for ZnS.

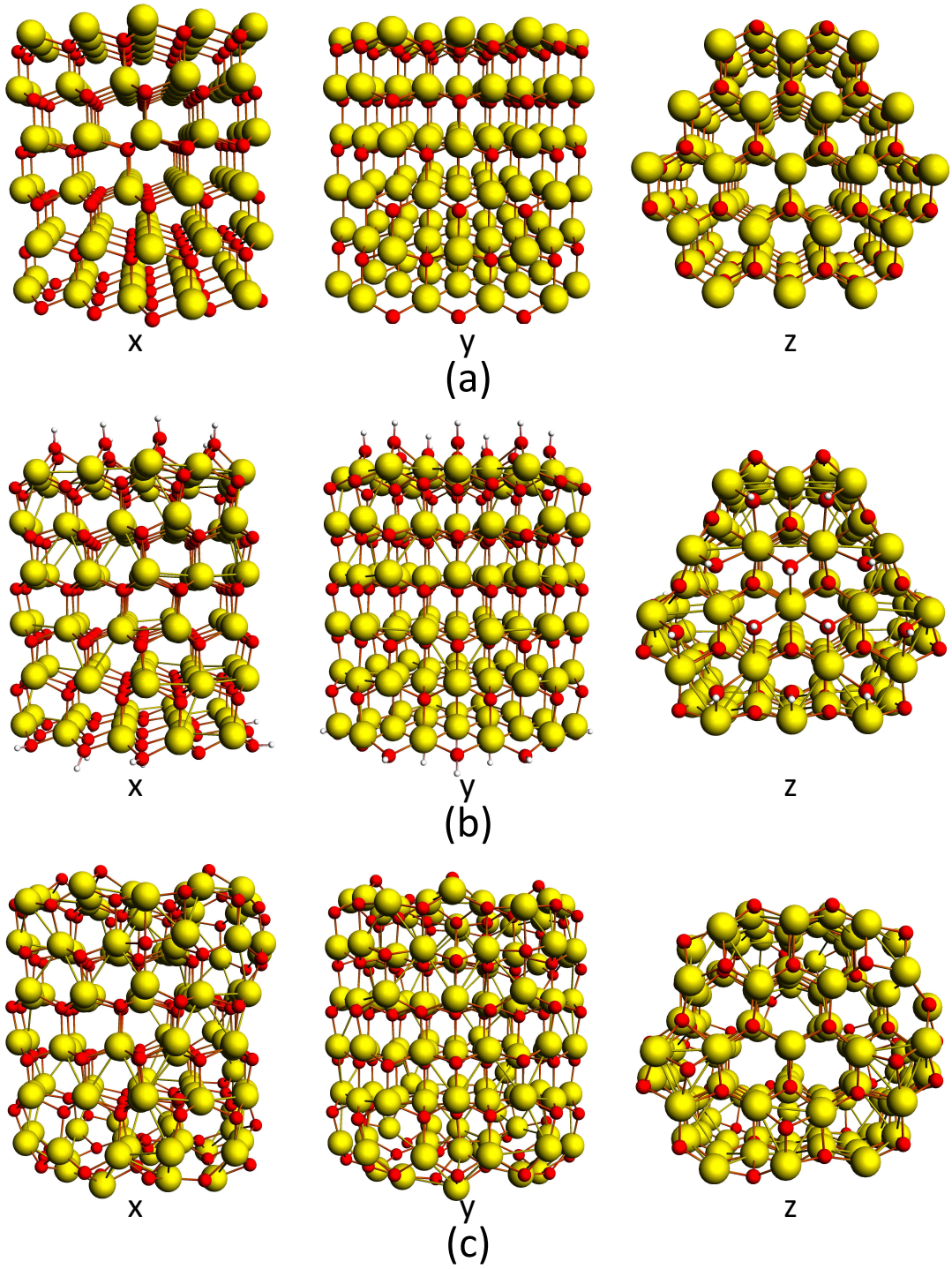


Figure 4.11: Zn–X bond length of each atom with its neighbors as a function of the position of the atom with respect to the center of the cluster. For sake of clarity, surface-attached H2X molecules have not been taken into account in the case of $[(ZnX)_{111}(H_2X)12]$ models. (a) ZnO and (b) ZnS.

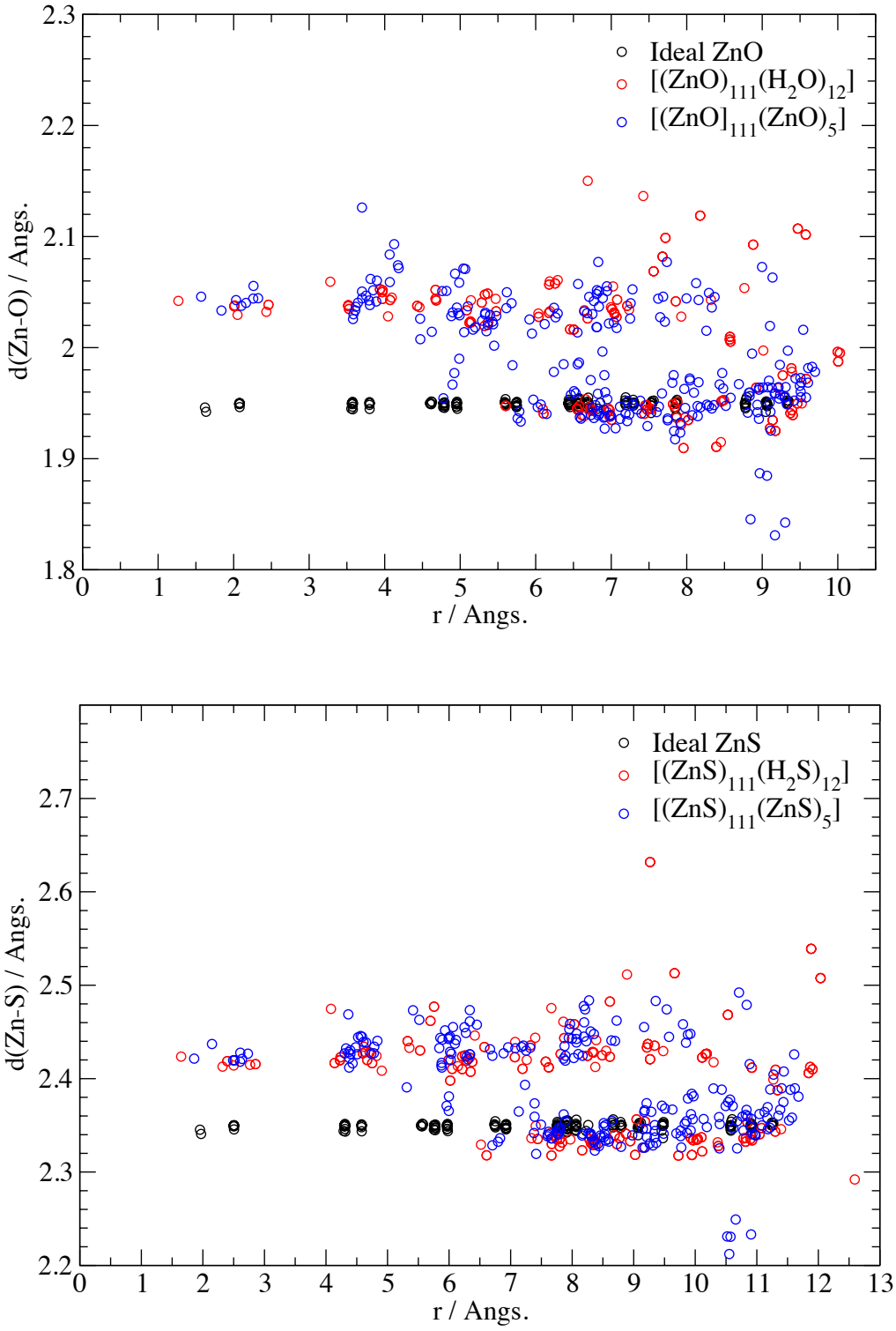


Figure 4.12: Radial distribution function. For sake of clarity, surface-attached H_2X molecules have not been taken into account in the case of $[(ZnX)_{111}(H_2X)_{12}]$ models. (a) ZnO and (b) ZnS.

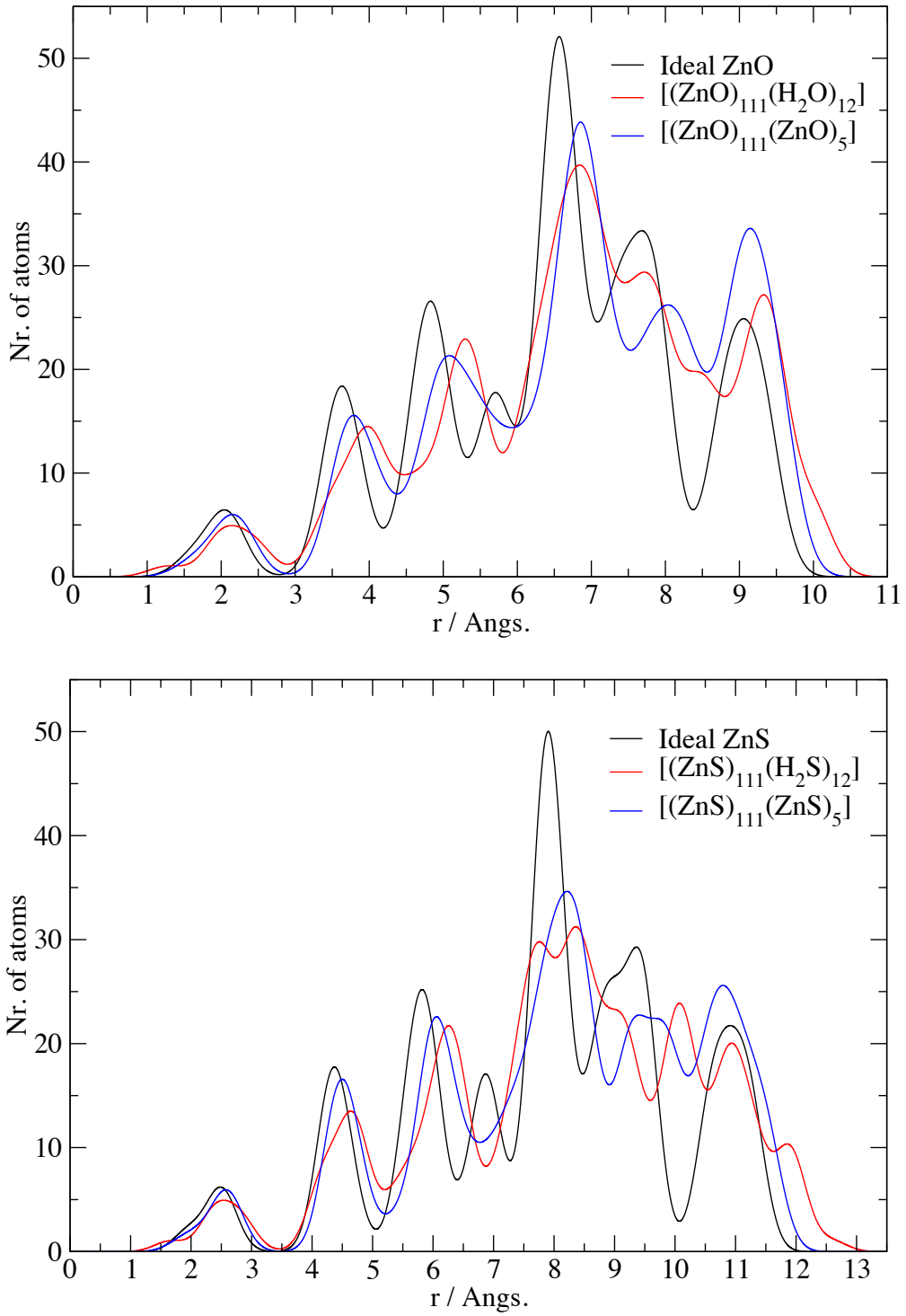
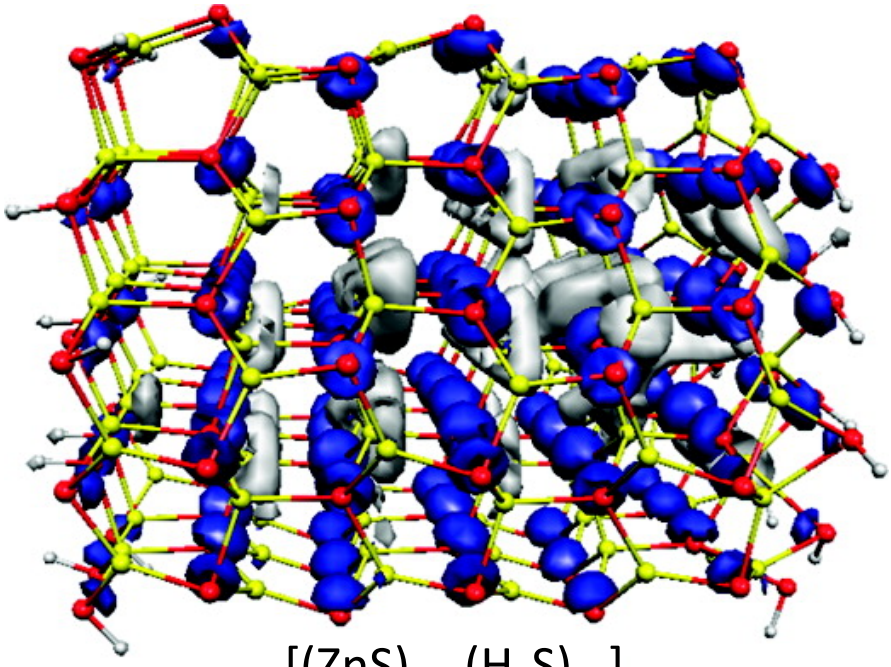


Figure 4.13: Isodensity plots of the LUMO for $[(ZnS)_{111}(H_2S)_{12}]$ (top) and $[(ZnS)_{111}(ZnS)_5]$ (bottom).



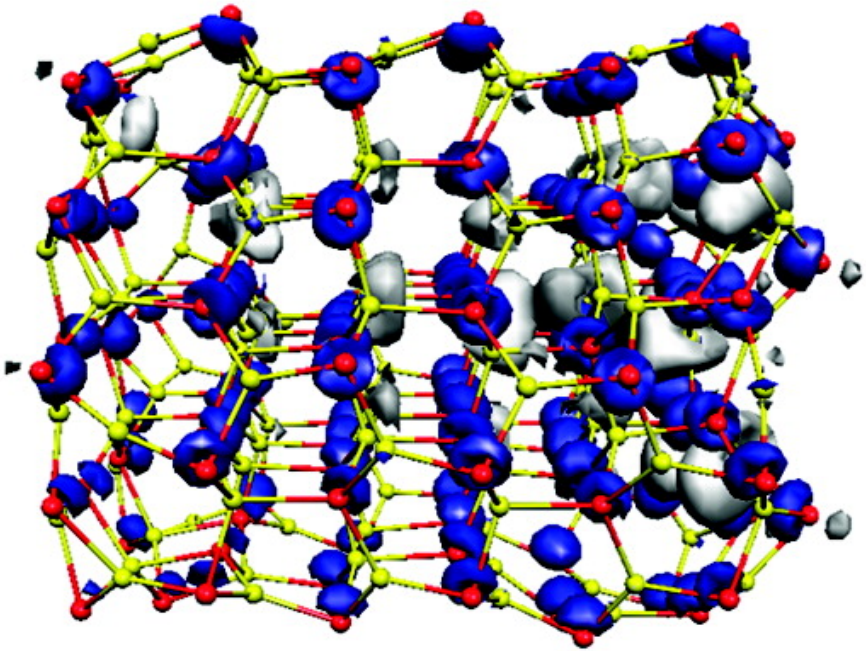


Figure 4.14: Density of states of (a) $[(ZnO)_{111}(H_2O)_{12}]$ and (b) $[(ZnO)_{111}(ZnO)_5]$.

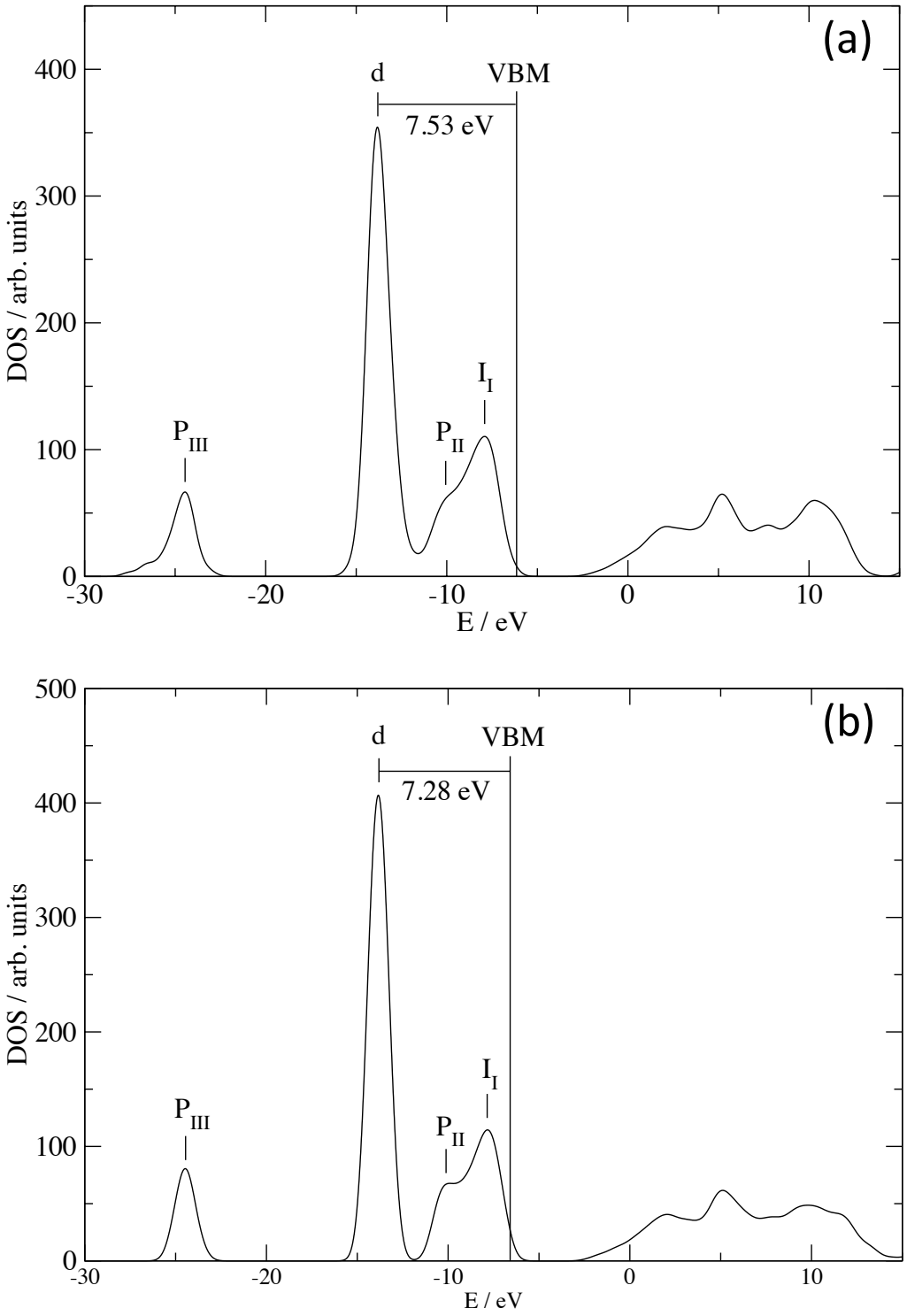
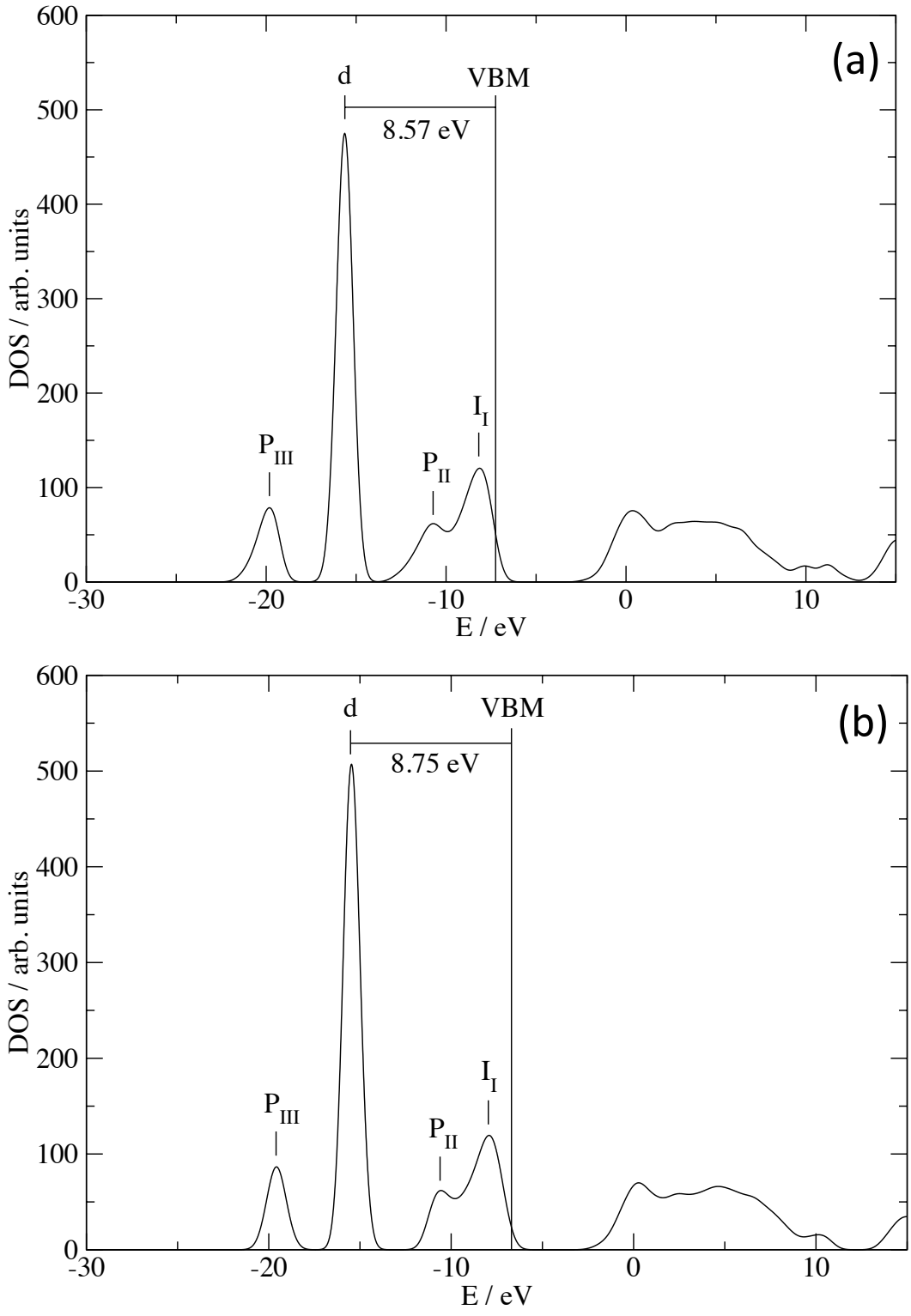


Figure 4.15: Density of states of (a) $[(ZnS)_{111}(H_2S)_{12}]$ and (b) $[(ZnS)_{111}(ZnS)_5]$.



4.3 A First-Principles Study of II-VI (II = Zn; VI = O, S, Se, Te) Semiconductor Nanostructures

4.3.1 Abstract

We present a systematic investigation of the structural, electronic and optical properties of wurtzite-like ZnX (X = O, S, Se, Te) nanostructures at the DFT/TDDFT level of theory. To provide a direct comparison with the experiment, realistic 1.0-1.5 nm size quantum dots have been built up from the bulk. Low-lying computed excitations energies agree well with the available experimental data. In all cases, the LUMO is always the state accepting the excited electron, and is most probably responsible for the broad excitation profiles and narrow emission spectra typical of semiconductor quantum dots. Calculated binding energies for the Zn *3d* shell have been found to be 0.5 eV lower than the corresponding bulk materials. Anion vacancies can explain the visible light emission of ZnX by introducing a trap state in the bandgap of the nanomaterials, in agreement with previous theoretical and experimental works on ZnO. Calculations on rod- and sheet-like prototype clusters pinpoint to a significant quantum confinement effect on the optoelectronic properties of Zn-based nanomaterials.

4.3.2 Introduction

In the last decades, a considerable effort has been devoted to the synthesis and characterization of *bulk* II-VI (II=Zn, VI=O,S,Se,Te) wide-gap materials, mostly for their high stability, high quantum yields and low cytotoxicity. For instance, bulk zinc oxide (ZnO) and zinc sulfide (ZnS), having bandgaps of 3.4 eV and 3.7 eV, respectively, and high exciton binding energies of 60 and 40 meV, play a striking role in electronic industry [384]. Bulk zinc selenide (ZnSe), bandgap of 2.7 eV and exciton binding energy of 20 meV, exhibits a great potential for applications in optoelectronics [431], spintronics [432], and energy upconversion [433]. ZnTe, bandgap of 2.2 eV and an exciton binding energy of 10 meV, is a very attractive material for blue-green emitting diodes [434], optoelectronic detectors [435], photovoltaic solar cells and photocatalysis [317, 436].

More recently, semiconductor *nanomaterials* have attracted much attention for their peculiar size- and shape-dependent properties [4]. Zn-based II-VI semiconductor nanomaterials have been recurrently employed in photooxidation and photocatalysis, photovoltaic solar cells, optical sensitizers, quantum devices, and biology [68, 384, 437]. These nanostructures present two distinct traits that make their properties unique: a.) The high surface-to-volume ratio, which leaves unsaturated atoms on the surface to rearrange their position to minimize the surface energy, ultimately leading to the stabilization of some structures over others [8]; b.) the confinement of charge carriers in a space comparable to their de Broglie wavelength, which results in the discretization of electronic quantum levels, and the appearance of size and shape-dependent properties [438].

Regarding the structure, it is known that *bulk* ZnO, ZnS, ZnSe and ZnTe can adopt three phases: cubic zinc-blende (B3 and ZB hereafter), hexagonal wurtzite (B4 and WZ hereafter) or the rarely observed cubic rocksalt (B1). WZ is the most stable polymorph of ZnO under ambient conditions. On the contrary, ZB is the stable phase of ZnS, ZnSe and ZnTe. In the corresponding *nanomaterials* the lower surface energy and the smaller surface stress of WZ compared to ZB, however, can lead to the the formation of hexagonal ZnS, ZnSe and ZnTe nanostructures that have been theoretically hypothesized [12, 385, 439] and experimentally manufactured. Nearly monodisperse colloidal quantum dots with hexagonal structure are nowadays routinely synthesized [387,398]. Similar solvothermal methods have been exploited for the production of one-dimensional WZ ZnS nanowires [440] and nanotubes [441], and two-dimensional WZ ZnS nanofilms [442], all exhibiting greater luminescent properties than their equivalent ZB phase [392]. Similarly, a wide variety of hexagonal ZnSe [439, 443–447] and ZnTe [448, 449] nanostructures has been synthesized.

Along with the experimental work, a great theoretical effort has been devoted to the modeling of Zn-based II-VI nanostructures. Even if several works on ZnSe and ZnTe nanoclusters have been reported over the years [292, 450], ZnO and ZnS are probably the most studied materials in the ZnX (X = O, S, Se, Te) family. Early computational studies focused on small and medium size $(ZnX)_n$ (X = O, S) clusters and on their structural and electronic properties. Clusters with $n\sim$10-50 have been predicted to adopt hollow spherical and tube-like structures [302, 307, 320, 334, 413, 414, 451, 452] while onion- and bulk- like arrangements have been suggested upon increasing their size [309, 413, 415, 451, 452]. For unsaturated bulk-like nanostructures a transformation from WZ to graphitic phase has been observed for ZnO [319], while formation of a crystalline phase analogous to the zeolite-like BCT structure has been hypothesized for ZnS [309, 319]. In these works, it has been shown that BCT structure is in principle able to accommodate distortions more easily than WZ and ZB polymorphs, which undergo significant rearrangements to minimize the number of dangling bonds on the surface and the net dipole of the bare structure. The existence of the BCT polymorph, however, has not yet been confirmed, most probably because the surface reconstruction is not the only mechanism to stabilize nanostructures bearing dangling bonds. It has been observed that the adsorption of ligands gives rise to a reduction of the distortions on the surface and the inside of the nanostructure, favoring bulk-like structures [28]. In recent theoretical studies, we confirmed this hypothesis showing that the saturation of the Zn- and X- (X = O, S) terminated surfaces with dissociated H_2X molecules stabilizes indeed the WZ polymorph [300, 416].

The main effect of quantum confinement is the characteristic bandgap opening upon decreasing size of the nanomaterial. This has significant consequences on the absorption onsets of the Zn-based II-VI quantum dots. For example, ZnO nanoparticles of 0.7-1.5 nm radii have the main absorption band lying in the range of 3.7-3.8 eV [393–395]. Similar features are encountered also for the other ZnX nanostructures [387, 397, 398, 446, 447, 453, 454]. The intriguing feature of these nanomaterials is however their visible light emission. Along with the band-edge luminescence, several bands in the visible region of the spectrum have been

observed. The typical visible band of ZnO nanostructures lies in the green-yellow region of the spectrum (2.1-2.4 eV), even if blue (2.7-2.8 eV) and orange (1.8-1.9 eV) luminescences have also been reported [393–396]. The origin of these secondary emissions remained unclear until recently, where we have shown how O vacancies were the source of the green luminescence of ZnO [416]. Similarly, visible emission features of ZnS have been recurrently reported in the literature. Blue (2.8-3.1 eV) and green (2.4-2.6 eV) emission bands, attributed to sulfur and zinc vacancies, have been observed in wires [400, 401], ribbons [399, 400] and particles [54, 398, 402, 455, 456]. The more rare orange emission at $\sim$2.0 eV pinpoint to the recombination between interstitial Zn states and Zn vacancies [456]. Somewhat similar features have been observed for ZnSe and ZnTe nanostructures, showing emission bands at 3.0 [446] and 2.2 eV [457], respectively.

In the present computational work we further progress with the characterization of ZnX (X = O, S, Se, Te) nanostructures by defining realistic quantum dot models for each material. We investigated structural, electronic and optical properties using DFT/time-dependent DFT (DFT/TDDFT). Particular attention has been paid to the surface reconstruction and to the absorption features needed to understand the role of anion vacancies in the emission spectra. Finally, we have characterized 1D and 2D model systems of different size to highlight the effect of quantum confinement.

4.3.3 Model and Method

To investigate the role of the morphology on the properties of the ZnX (X = O, S, Se, Te) nanomaterials, we constructed quantum dot (QD), nanorod (NR) and nanosheet (NS) models of WZ type. Figure 4.16 shows the bulk WZ, along with the patterns employed to cut the structures.

Before proceeding with the structural optimizations, we had to consider two effects: a.) The dangling bonds on the surface of the bulk-like nanoclusters lead to localized states that intrude into the energy bandgap; b.) in noncentrosymmetric WZ structures, the polarity of Zn- and X- terminated (0001) and (000$\bar{1}$) surfaces induces a net dipole moment along the *c* axis ([0001]) that diverges with the increasing length of the cluster. [406, 411, 418]. As a consequence of both effects, the bandgap shrinks and the nanostructure becomes metallic, leading to methodological and conceptual troubles.

The structural instability of ZnO [319,411] and ZnS [319] clusters exposing unsaturated polar surfaces, has already been observed, and leads to a phase transition from the WZ to the graphitic structure in ZnO and to a zeolite BCT crystalline phase in ZnS. In some recent theoretical works, we have shown however that the saturation of the Zn- and X- (X = O, S) surfaces stabilizes the WZ polymorph [300, 416]. The optical properties calculated nicely agree with the experimental data measured for similar size hexagonal nanostructures. We believe then that our previous studies provide the required computational framework for the investigation of Zn-based II-VI semiconductor nanostructures presented in this work.

For this reason, we decided first to dissociate H_2X (X = O, S, Se, Te) molecules and then to saturate the polar surface by adsorbing H^+ and HX^- ions on X and Zn, respectively. The number of dissociated H_2X molecules used to saturate the surface is varied until minimization of the energy and of the dipole along the *c* axis is achieved. This work of saturation has been shown to effectively remove artificial intra bandgap states, decrease the dipole moment along the *c* axis and stabilize the nanocluster. Dissociative adsorption of water in the polar surfaces of ZnO has been found to be energetically favorable [406], thus, we have followed the same approach for ZnS, ZnSe and ZnTe. We must stress that the dissociation of H_2X is not only a computational trick. H_2X is indeed routinely employed as X precursor in the synthesis of nanosize ZnX. For other precursors, the formation of H^+ and HX^- ions is a probable scenario, since protic solvents or/and ligands are common in colloidal synthesis of semiconductor nanostructures. We believe thus that ZnX clusters with H^+ and HX^- ions capping surface X and Zn sites are plausible models.

All geometries have been fully optimized using the exchange correlation (xc) Perdew-Burke-Ernzerhof (PBE) [238] functional within the Kohn-Sham framework of DFT (KS-DFT), as implemented in the ADF 2010.01 program [267]. No symmetry constraints have been imposed. A double-valence set (DZ) of Slater-type orbitals (STO) has been added on each atom. For ZnTe, relativistic effects have been included using the Pauli formalism [458].

In our previous works, GGA functionals have shown to satisfactorily reproduce the structural parameters of both bare and passivated Zn-based nanoclusters [300,304,416], at a fraction of the computational cost required by the hybrid functionals.

For simplicity, geometry optimizations have been carried out *in vacuo*. In our small model the inclusion of implicit solvent has been tested using COSMO [459], and only negligible structural changes compared with the vacuum have been noticed. Also the polarity of the medium plays a marginal role.

In spite of reproducing satisfactorily structural parameters, GGA functionals significantly underestimate the bandgap of II-VI semiconductor materials. Thus, the hybrid B3LYP functional with a def2-SVP basis set has been used to compute ground and excited states (TDDFT) on the previously optimized structures. The B3LYP functional has been modified to contain 27.5% HF exchange, following previous works [300, 416]. For computational performance, we decided to switch to the Gaussian09 package [422]. Relativistic Effective Core Potentials have been employed for Te atoms. Solvation effects have been included by the Polarizable Continuum Model (PCM) [460–462], choosing water as the solvent to reproduce the experimental conditions. Recently indeed aqueous-phase synthesis of II-VI semiconductors has emerged as a simple, safe, cheap and environmentally friendly alternative to classical routes carried out in organic solution [19,448,463–465].

4.3.4 Results and Discussion

Quantum Dots

Geometry

Recently, experimental and theoretical works have proven the existence of extremely stable II-VI semiconductor nanoparticles with a well-defined number of constituent atoms [19, 20, 325, 447, 466–470]. These clusters, often referred as magic-size clusters, exhibit high stability and give rise to extremely sharp absorption peaks. We started then our analysis by investigating the magic-size WZ-like $(ZnX)_{48}$ nanoclusters (Figure 4.16 (1)), whose stability has already been reported for ZnTe [454] and CdSe [18, 290] nanoparticles.

Our pristine bulk-like $(ZnX)_{48}$ nanocluster can be envisioned as a $(ZnX)_6$ unit enclosed in a $(ZnX)_{42}$ shell ($(ZnX)_6$ @ $(ZnX)_{42}$). The polar surfaces of this cluster –defined as $[(ZnX)_{48}(H_2X)_7]$ or ZnX-QD from now on– has been saturated with seven dissociated H_2X molecules. This choice leads to the minimization of the dipole along the *c* axis and to the concomitant stabilization of the nanostructure. As an example, the optimized ZnS-QD is displayed in Figure 4.16 (1). Similar structures have been found for ZnO-, ZnSe- and ZnTe-QDs. All the relaxed structures preserve the WZ shape, but with a significant deviation from the ideal bulk-like geometry.

The core of the optimized nanoclusters roughly resembles the unrelaxed WZ structure although an outwards displacement of the atoms is visible, revealing an expansion of the inner part. Experimentally, such increase of the lattice parameters have been reported for magic-size II-VI clusters [467, 471]. For distances from the center of the cluster larger than 4 Å, the RDFs of the relaxed QDs significantly differs from the unrelaxed structures, meaning that the largest reconstruction occurs on the surface of the cluster. In the outermost region, the X atoms are displaced outwards with respect to the Zn atoms. Similar rearrangements have been previously reported not only for ZnS [415] and ZnSe [450] but also for CdS [286] and CdSe [287, 423].

To get a clearer insight into the geometrical reconstruction of these QDs, we computed the average bond length and bond angle of each atom with its neighbors (see Table 4.9). For simplicity in the discussion, we focused on one type of cluster, the ZnO.

Zn-O bonds lying in the core of the nanostructure have distances of 2.082 Å on average, 7% larger than the bulk (1.95Å). On the surface, the bond lengths of the four-fold coordinated atoms –Zn(4)– remain similar to those observed in the core of the quantum dot (2.053 Å on average, only 1% shorter). In contrast, the three-coordinated atoms –Zn(3)– exhibit a significant contraction of the bonds (1.950 Å on average, 6% shorter than the core). Their lower coordination seems to be the driving force for the bond shortening, in agreement with previous theoretical studies on similar size CdSe quantum dots [293, 313] and ZnO and ZnS nanostructures [300]. Finally, on the cation-rich polar surface some of the Zn atoms are in presence of capping HO^- anions, hence they assume five- or six-coordinated (Zn(>4)) . The linkage to HO^- gives rise to a slight elongation of the Zn(>4)-O bonds (2.106 Å on average, 1

% larger the core), presumably because electron density is donated from the capping anions to the Zn(>4)-O [304].

As mentioned earlier, the core atoms of our ZnX-QDs resembles the tetrahedral geometry of the unrelaxed wurtzite structure. The bond angles measured in the inner part of the ZnO-QD cluster, 109.4° on average, are typical of a sp^3 hybridization of the Zn atom. Similarly, the bond angles of the four-fold coordinated surface atoms are also tetrahedral, with a computed 109.3° average angle. On the surface, the three-fold coordinated Zn and O atoms exhibit peculiar geometrical arrangements. Zn(3) atoms are pulled into the plane formed by their three bonded O atoms so that they exhibit a planar trigonal coordination, 122.2°, suggesting a sp^2 hybridization of the metal. A concomitant shortening of the Zn-Zn distances is also observed in the surface. The O(3) atoms are puckered out and assume a 105.0° bond angle on average, indicating a sp^3 hybridization. The repulsion exerted by the lone pair pointing outwards the cluster induces however a shrinkage of the Zn-O(3)-Zn angle, resulting in a coordination that resembles more of a pyramidal geometry. These observations are consistent with the surface reconstruction suggested by the RDF and agree with previous theoretical works regarding other II-VI nanostructures [286–288, 313, 415, 423, 450].

ZnS-, ZnSe- and ZnTe- QDs yield similar patterns of bond lengths and angles as those observed for ZnO (see Table 4.9). The inclusion of relativistic effects in ZnTe though induces a slight shortening of 0.02Å of the Zn-Te bonds, and a negligible effect on the bond angles.

Electronic Structure and Absorption Spectra

For all studied systems, the computed HOMO and LUMO are rather delocalized over the whole cluster (see Figure 4.17), meaning that the saturation of the dangling bonds avoids the occurrence of surface localized trap states. The HOMO is mostly distributed over the chalcogen valence *p* orbitals, while the LUMO is mostly composed of Zn *4s* orbitals.

The computed DFT/B3LYP bandgaps (see Table 4.10) vary in the order of ZnS-QD (4.98 eV) > ZnO-QD (4.73 eV) > ZnSe-QD (4.52 eV) > ZnTe-QD (4.10 eV), in good agreement with the experimental trend of the bulk (ZnS (3.7 eV) > ZnO (3.4 eV) > ZnSe (2.7 eV) > ZnTe (2.2 eV)). As expected, quantum confinement has the effect to blueshift the bandagaps of about ∼1-2 eV. The energies of the HOMO and the LUMO are also coherent with the alignment of the valence and the conduction bands previously calculated for the bulk [52, 472] and nanometric [291] Zn-based II-VI materials. The shortening of the HOMO-LUMO gap from ZnO to ZnS is related to a stabilization of the LUMO, while from ZnS to ZnTe the shortening is attributed to a shift of the HOMO to higher energies.

Another interesting feature is that in all ZnX clusters the HOMO is close in energy to the rest of the valence band orbitals (see Table 4.10), with only 0.02 eV energy difference with the HOMO-1. The LUMO, despite having a similar nature with the upper lying virtual orbitals LUMO+n, is quite separated in energy from the rest of the conduction band states. For example, the LUMO/LUMO+1 energy difference depend on the chalchogenide X atom and decreases constantly from ZnO-QD, 0.66 eV, to ZnTe-QD, 0.37 eV. This observation holds irrespective of the material and agrees not only with our previous works concerning ZnO

[300,416] and ZnS [300] but also with other studies regarding CdSe [313,473], revealing that it might be an intrinsic property of the II-VI semiconductor materials.

Even if the Kohn-Sham molecular orbitals and their eigenvalues may provide a reasonable approximation to the bandgap transitions of bulk II-VI semiconductor materials, TDDFT provides a more accurate description of the excitations in confined systems by taking into account exchange-correlation effects and configurational mixing of single excitations

Figure 4.18 displays the computed TDDFT absorption spectra of the QDs investigated, obtained by a Gaussian convolution of the 20 lowest electronic transitions. Among these low lying transitions, only those with an oscillator strength larger than 0.1 a.u. are reported in Table 4.11. Our lowest excitation energies of 3.97, 4.28, 3.89 and 3.52 eV calculated for ZnO-, ZnS-, ZnSe- and ZnTe- QDs respectively, agree nicely with the absorption onsets experimentally measured for QDs of similar size (see Table 4.10), and are in much better agreement than the energy bandgaps computed by taking the simple HOMO-LUMO energy difference.

From Table 4.11 we can see that all low-lying excited states are composed of transitions from high-lying occupied orbitals to the LUMO. As explained before, this is attributed mostly to the wide gap between the LUMO and the LUMO+1 and to a dense valence band edge. Based on these features, these clusters present broad absorption bands, and, because holes relax to the HOMO by phonon coupling more rapidly than the radiative recombination, narrow LUMO to HOMO emissions.

The Density of States (DOS hereafter) and the valence band of ZnX-QD have been also throughly investigated. All the binary tetrahedrally coordinated semiconductor materials exhibit a similar valence band structure [424], consisting in each case of four peaks, P_I, P_{II}, d and P_{III}. The P_I peak, which is located at the top of the occupied band, arises from the chalogenide (anion) valence *np* orbitals; deeper in the valence band, P_{II} and d are composed mostly of the *4s* and *3d* orbitals of the Zn atoms, respectively; while, the P_{III} peak emerges from the anion valence *ns* orbitals.

To assign unambiguously the peaks observed, the Projected Density of States (PDOS) on Zn and X atoms has been also calculated. Figure 4.19 displays the DOS and PDOS of the ZnX-QDs systems.

The first two bands deep inside the valence band, P_{III} and d, are common to all ZnX clusters. In particular, the first of the P_{III} peaks, $P_{III,b}$, is composed of orbitals localized on surface calchogen atoms, with an important contribution of the capping ligands. The second peak, $P_{III,a}$, arises from molecular orbitals delocalized over the whole nanocluster. The intense peak emerging at about -15 eV corresponds to the Zn *3d* orbitals (d) and is common to all ZnX species. The uppermost occupied bands, between -12.5 and -5.0 eV, assume different shape depending on the chalcogen atom. For ZnO-QD, the P_{II} is located at -9.75 eV, while the P_I lies at slightly higher energies and significantly overlap to P_{II}. On the other hand, for ZnS-, ZnSe- and ZnTe-QDs, three well separated bands are recognizable near the edge of the valence band. The peak lying in the range between -12.0 and -10.0 eV, $P_{I,b}$, arises from

the anion atoms placed in the $(000\bar{1})$ polar surfaces, with a noticeable contribution of the capping H atoms. The band centered at -7.0 eV, $P_{I,a}$, is usually delocalized over the whole cluster. The P_{II} peak lies between these two bands and is related to the overlap of the Zn *4s* orbitals and the np orbital of the anion.

Regarding the conduction band, the low-lying unoccupied orbitals are mainly composed of Zn 4*s* orbitals. This is important when ligands are employed to passivate or/and functionalize the surface of II-VI materials [304]. Indeed, organic ligands are commonly bound to Zn atoms, and are expected to significantly change the electronic and optical properties of the nanostructure by shifting the LUMO energy. The effect of the ligand should decrease when moving from ZnO to ZnTe, because the weight of the chalcogen p orbitals increases from 39% in ZnO-QD to 53% in ZnTe-QD (see Table 4.15), and concomitantly, the percentage of the Zn 4*s* orbitals is reduced from 59% to 45%.

The binding energies of the d band can be calculated as $\triangle_d = E_{HOMO} - E_d$. The binding energy of ZnO-QD is 7.0 eV, consistent with the experimental binding energies measured by X-Ray Photoemission Spectroscopy, which lie in the range 7.5-10.0 eV for bulk ZnO [424–427]. Our calculations provide binding energies of 8.3, 8.7 and 9.3 eV for ZnS-, ZnSe- and ZnTe-QDs, in quite good agreement with the experimental values of 9.0, 9.2 and 9.8 eV measured for their bulk counterparts [424]. The computed values are systematically red-shifted of $\sim$0.5 eV. Similar trends can be found for the other bands, which are to some extent consistently underestimated with respect to the experiment (see Table 4.12).

The energy gap between $P_{I,a}$ and P_{II} ($\triangle_{P_{I,a},P_{II}}$) slightly increases with the atomic number of the anion (ZnO-QD (2.56 eV) $\approx$ ZnS-QD (2.54 eV) $<$ ZnSe-QD (2.68 eV) $<$ ZnTe-QD (2.72 eV)), suggesting that the mixing between the anion valence p orbitals and Zn *4s* orbitals decreases as we move down in the VI group from O to Te. On the contrary, the mix between the anion valence *s* orbitals and the Zn *3d* orbitals shrinks the gap between $P_{III,a}$ and d ($\triangle_{d,P_{III,a}}$) along the chalcogen series. Assuming that the P_{II} and d, localized on the Zn atoms, remain quite unchanged when going from O to Te, the widening of $\triangle_{P_{I,a},P_{II}}$ and the shortening of $\triangle_{d,P_{III,a}}$ can be attributed to the upward shift of $P_{I,a}$ and $P_{III,a}$

All these findings are consistent with spectroscopic measurements on bulk materials (See Table 4.12).

Anion Vacancies

It is well known that structural defects introduce, in the HOMO-LUMO band gap, localized states (or midgap sates) that are responsible of secondary peaks in the ZnX emission spectrum. Recently, we demonstrated that O vacancies were involved in the green-yellow emission of 1.5 nm [$(ZnO)_{111}(H_2O)_{12}$] cluster [416], as suggested also by several experiments [393–396]. In this work we have focused on anion vacancies of neutral chalcogen atoms, since the doubly charged anion vacancies were shown to absorb in the UV region. All the structures have been optimized for the ground state closed shell singlet (S0) state.

Given the propensity of ZnX to generate vacancies localized on the surface, we have limited our attention only to surface defects. Figure 4.20 (a) shows the position of the oxygen va-

cancy in non-defective ZnO-QD. The removal of the oxygen atom move the three Zn atoms, to which the missing atom was bound, at a closer distance, shortening the Zn-Zn bond of about ∼0.7 Å (see Table 4.13). The contraction of the Zn-Zn distances is accompanied by a slight elongation of ∼0.02 Å of the corresponding Zn-O bonds. This geometrical reconstruction is in quantitative agreement with that observed for larger $[(ZnO)_{111}(H_2O)_{12}]$ QD [416], and is found also in ZnS-QD, ZnSe-QD and ZnTe-QD nanoclusters.

As mentioned earlier, removal of a neutral X atom inserts an occupied state into the bandgap of non-defective QDs. The energy difference between the edge of the valence band and such defect state is 1.50 eV in ZnO-QD Figure 4.20 (b) and is shortened along the chalcogen series: 1.23 eV (ZnS-QD), 0.96 eV (ZnSe-QD) and 0.62 eV (ZnTe-QD). This state is essentially constituted by the overlap of the sp^3 orbitals of all Zn atoms surrounding the vacancy, similarly to what was found in bulk ZnO [407], and its energy remain substantially unaffected by the chalcogen atom. Hence, the gap with the trap state is shortened by an upward shift of the HOMO-1, which is mostly composed of the anion np orbitals.

The presence of surface localized state substantially reduces the bandgap, by shifting the lowest singlet-singlet and singlet-triplet transitions of ZnO-QD to 2.83 and 2.70 eV, respectively. This results nicely agree with the green emission of similarly small ZnO nanoparticles, measured at 2.3-2.4 eV [393–396] and assigned to relaxation from a long-lived triplet state [407]. The lowest transitions for the defective ZnS-QD is computed at 3.29 eV, for the S0 → S1 excitation, and 2.92, for the S0 → T1 excitation, in good agreement with the blue emission reported for a wide variety of ZnS nanostructures, observed at 2.8-3.1 eV [54,398–402,455,456]. For ZnSe-QD, our calculations provide gaps of 2.70 (S0→T1) and 3.05 eV (S0 → S1), in line with the blue luminescence of 1 nm size ZnSe nanocrystals, measured at 3.0 eV [446]. Finally, the singlet-triplet gap of 2.24 eV calculated for the defective ZnTe-QD matches well with the green emission reported for nanosize wires and ribbons [457].

Our results suggest that defect-state recombination could explain the visible emission of Zn-based nanostructures

As one may notice from Table 4.14, the singlet-triplet excitations are 0.1, 0.3, 0.3 and 0.6 eV lower in energy than the singlet-singlet transitions for ZnO, ZnS, ZnSe and ZnTe respectively. In general, triplet states are more stable than open-shell singlet states when the exchange energy contribution is more favorable. The stabilization of the excited triplet states is associated to the overlap between the states involved in the transition. The trend observed in our models could therefore be roughly explained analyzing the composition of the frontier orbitals involved in the transitions. As shown in Table 4.15, the contribution of the Zn atoms involved in the Zn-triangle to the defect-like state (the HOMO) decreases markedly from ZnO to ZnTe. The weight of the rest of the Zn atoms is diminished as well. Concomitantly, a larger participation of the anion valence orbitals is observed. Similarly, the contribution of the Zn atoms to the LUMO diminishes and the weight of the anion valence orbitals increases. In this framework, the stabilization of the singlet-triplet excitation compared to the singlet-singlet when going from ZnO to ZnTe could be attributed to the greater overlap between the HOMO and the LUMO, due to the increased anion character found for

both orbitals.

Nanorods

One-dimensional (1D) II-VI semiconductor nanostructures, called also nanorods (NRs), have attracted great interest in the electronic, optoelectronic, electrochemical industry [474–477]. Moreover, they are considered as ideal systems for exploring a large number of novel phenomena at the nanoscale size.

According to experimental findings [441,478], 1D nanoclusters oriented along the *c* axis have been built. Here we restrict our investigation to the smallest NRs that preserve the wurtzite structure. With an approximate diameter of $\sim$0.5 nm, similar shape wires have already been theoretically studied for Zn-based materials such as ZnO [412, 416] and ZnS [297, 340]. To explore the effect of the size on the structural, electronic and optical properties, five clusters, denoted as NR1, NR2 , NR3, NR4 and NR5, of increasing length along the *c* axis have been set up. Two dissociated H_2X molecules have been used to passivate the polar surfaces to minimize the dipole moment and stabilize the rod.

In this section we focus mostly on ZnX-NRs (X = S, Se, Te), because the ZnO-NRs were already studied in a previous work [416]. Figure 4.21 (a) shows the relaxed geometries of ZnS-NRs. The smallest NR1 wire has roughly the same length along the *c* axis as the ZnS-QD, approximately 1.2 nm. NR2, NR3, NR4 and NR5 are 1.8, 2.4, 3.0 and 3.7 nm long, respectively. As observed for ZnS-QD, the unsaturation induces a reconstruction that leads to a closer positioning of the ions. From Figure 4.21 (a), the pulling in of the Zn atoms and the puckering out of the S atoms are noticeable, resulting in a relative radial displacement between Zn and S atoms on the apolar sides perpendicular to *c*. Similar structural relaxations have been observed for ZnSe- and ZnTe- NRs.

ZnX-NR models show electronic structures very similar to those obtained for the corresponding QD. The passivation of the unsaturated atoms and the surface relaxation lead to the opening of the HOMO-LUMO gap. The HOMO is mainly localized at the borders of the nanorod and is therefore insensitive to quantum size effects (see Figure 4.22 (b)). For this reason, it can be probably considered as a trap state. On the contrary, the HOMO-1 is delocalized over the whole cluster and shifts upwards by increasing the length of the nanocluster (see Table 4.16); the LUMO, delocalized as well, (see Figure 4.22 (b)) moves to lower energies with the size of the rod.

Similar to QDs, the binding energy of the *d* peak has been also calculated. In this case, the HOMO-1 has been chosen as reference energy ($\triangle_d = E_{HOMO-1} - E_d$). In ZnO and ZnS, $\triangle_d$ opens only slightly with the wire length (see Table 4.16), about 0.04-0.07 eV. The trend is more pronounced for ZnSe- and ZnTe- NRs, about 0.2 eV for both. The widening of the $\triangle_d$ energy is mainly related to the upwards shift of the HOMO-1 along the chalcogen series. In our precedent work on ZnO and ZnS [300] we argued that the *3d* orbitals belonging to the semicore of the Zn atoms are assumed to be relatively stable with the size of the

nanostructure, whereas the valence band edge (HOMO-1 in this case) supposedly shifts to higher energies as the size of the material increases. Our calculations on ZnX-NRs (X = S, Se, Te) support this hypothesis.

Figure 4.22 (a) displays the computed TDDFT absorption spectra of the ZnS-NRs. Irrespective of the rod length, the first excited state is isolated from the rest in the spectra. This first transition is the result of a mixture of different singlet electron configurations, implying an electronic excitation from the HOMO to low-lying unoccupied molecular orbitals. Given that the HOMO is quite separated from the rest of the valence band, the energy difference with the rest of the excited states is reasonable. Being a defect surface state, no consistent shift of the first excitation is distinguished with the the size of the wire. This transition however has a low oscillator strength and is not relevant from an experimental point of view.

The most intense transitions involve excitations from occupied orbitals below the HOMO to the LUMO. These excited states are delocalized over the whole cluster (see Figure4.22 (b)) and are subject to quantum confinement. The transition energies are redshifted and their intensities are bigger by increasing the length of the rod. As shown in Figure 4.22 (c) and (d), similar absorption spectra have been obtained for ZnSe- and ZnTe- NRs.

Nanosheets

Two-dimensional (2D) nanostructures, called also surface slabs or nanosheets (NS), are relevant for the simulation of the surfaces of II-VI semiconductors. The intrinsic instability of the polar surfaces has been theoretically predicted [406, 411, 418]. Accordingly, nanostructures growing along the *c* direction and exposing apolar faces are the most common ones [441, 478]. Hence, we decided to focus our attention on these apolar slabs. The role of the quantum confinement on the electronic and optical properties has been addressed on $\sim$0.5 nm thick clusters by modifying the size of the slab along *a* and *c* directions.

The optimized 2D clusters obtained for ZnS are shown in Figure 4.21 (b). In brief, the dimensions of ZnS-NS1, -NS2 and -NS3, given as $a \times b \times c$, are 1.3 nm$\times$ 0.6 nm$\times$ 1.2 nm, 1.3 nm$\times$ 0.6 nm$\times$ 1.8 nm and 2.0 nm$\times$ 0.6 nm$\times$ 1.8 nm respectively. Accordingly, NS2 can be viewed as NS1 elongated along *c*, and NS3 as NS2 extended along *a*. The reconstruction of the apolar planes studied is very similar to that observed on the surface of the ZnX-QD models.

Valence band features observed in 0D and 1D models are again recognizable in 2D clusters. Figure 4.23 (a) displays the DOS obtained for the ZnS-NSs. In NS1 and NS2 models, the HOMO is quite separated from the rest of the valence band, and is mostly localized on atoms near the $(000\bar{1})$ plane. For this reason, it can be considered as a midgap state, similar to what we found in 1D NRs. The HOMO-1 is delocalized over the entire molecule and the energy difference with the LUMO decreases slightly when going from from NS1 to NS2 (5.12 *vs* 5.02 eV).

Interestingly, no midgap states have been found for NS3. The HOMO is quite delocalized over the whole cluster and is close to the rest of the occupied upper lying MOs. The HOMO-LUMO gap shrinks only slightly with respect to NS2 (5.02 *vs* 4.97 eV). This finding is in line with

a precedent work on ZnO nanostructures [416], where it was observed that the optical gaps were not particularly sensitive to the dimensions along the *a* axis. The binding energies of the *d* bands, remain quite unchanged with the size of the slab.

Figure 4.23 (b) shows TDDFT spectra of the ZnS-NSs. Analysis of the excited states reveals that, irrespective of the size of the model, the low-lying transitions occur from a high-lying occupied orbital to the LUMO. For NS1 and NS2, the HOMO→LUMO excitation is well separated from the rest of the excited states, as expected by the energy gap between HOMO and the rest of occupied states. The corresponding oscillator strength is quite small, meaning that the contribution of this first transition to the absorption spectrum is not significant. In this cases, it seems more appropriate to look at the HOMO-1→LUMO excitation, which has the largest oscillator strength for both NS1 and NS2. No significant shift of the excitation energy is noticeable upon increasing size of the slab along the *c* axis, although the intensity of the transition increases notably from NS1 to NS2. For NS3, no midgap states have been found, so that the most intense excitation corresponds to the HOMO→LUMO. This transition appears at 4.39 eV, at similar energies with respect to NS1 (4.42 eV) and NS2 (4.39 eV), but its oscillator strength is significantly larger.

All the properties that have been described above for ZnS-NS are found to appear also in ZnSe-NSs and ZnTe-NSs.

4.3.5 Summary and Conclusions

We have presented a computational study on the structural, electronic and optical properties of hexagonal ZnX (X = O, S, Se, Te) nanostructures of realistic size. We confirm that saturation of the polar surface with H_2X species is a powerful tool to quench unrealistic dipole moments, and has the effect of correctly minimizing the surface energy, and avoiding the intrusion of trap states.

TDDFT/B3LYP calculations on 0D quantum dots provide excitation energies that agree well with the experimental values. In all cases, the LUMO has been found to be rather separated from the rest of the conduction band, in such a way that all the low-lying excited states are mostly composed of transitions from high-lying occupied orbitals to the LUMO. Because hole cooling to the HOMO is known to be much faster than radiative recombination, emission bands of LUMO to HOMO type are expected to be narrow, like it has been actually found in the experiments. Computed binding energies for the *d* band are also quantitatively accurate, with just a systematic shift of 0.5 eV compared with the XPS measurements on bulk materials.

Analysis of anion vacancies on the surface of 0D ZnX quantum dots suggest that he defect-state recombination could be involved in the visible emission of Zn-based nanostructures. Computed TDDFT/B3LYP excitation energies agree fairly well with experimentally available emission bands.

Once checked the reliability of our computational strategy, we have focused on the characterization of ZnX 1D NRs and 2D NSs.

The surface reconstruction of ZnX 1D-NRs and its electronic structure are similar to those observed for their 0D counterparts, except for the fact that the HOMO is localized on the borders of the wire and can be considered as a midgap state.

The first TDDFT excitation, composed of a mixture of HOMO→LUMO+n single excited determinants, is quite separated from the rest of the excited states, and has a low oscillator strength. Despite its contribution to the absorption spectra is minimal, it might play a role in the emission. The binding energy of the *d* band decreases with the size of the model, mainly due to a shift to higher energies of the top of the valence band.

The geometrical reconstruction and the electronic structure of 2D-NS do not differ with respect to the 0D and 1D nanostructures. For the smallest models NS1 and NS2, the HOMO is again a trap state, further corroborating the fact that the stabilization of the clusters may imply the presence of localized states.

Table 4.10: Electronic and optical properties of ZnX-QDs (X = O, S, Se, Te), in eV, obtained at PCM-B3LYP/def2-SVP//PBE/DZ level of theory. ε_{HOMO-1}, ε_{HOMO}, ε_{LUMO}, and ε_{LUMO+1} are the HOMO-1, HOMO, LUMO and LUMO+1 KS eigenvalues, respectively. $\triangle_{HOMO-LUMO}$ is the HOMO-LUMO KS bandgap and $\triangle_{TD}$ refers to the TDDFT bandgap, *i.e.* the lowest excitation energy. Experimental optical bandgaps of similar size nanoparticles are also reported.

QD	ε_{HOMO-1}	ε_{HOMO}	ε_{LUMO}	ε_{LUMO+1}	$\triangle_{HOMO-LUMO}$	$\triangle_{TD}$	$\triangle_{Exp.}$
ZnO	-6.47	-6.46	-1.73	-1.06	4.73	3.97	3.7-3.8[a]
ZnS	-6.53	-6.53	-1.55	-0.97	4.98	4.28	4.3-4.4[b]
ZnSe	-6.31	-6.28	-1.76	-1.19	4.52	3.89	3.6-4.2[c]
ZnTe	-5.87	-5.85	-1.75	-1.37	4.10	3.52	3.2-3.8[d]

[a]From Refs [393–395], measured for 1.5-3.0 nm diameter ZnO QDs.
[b]From Refs [387,397,398], measured for 1.5-4.0 nm diameter ZnS QDs.
[c]From Refs [446,447], measured for 1.0-3.0 nm diameter ZnSe QDs.
[d]From Ref [454], measured for 1.5-2.5 nm diameter ZnTe QDs.

Table 4.9: Average geometric parameters of the ZnX-QDs (X = O, S, Se, Te) nanoclusters. Dimensions along the *a*, *b* and *c* crystallographic axes are given. The atoms in the central $(ZnX)_6$ unit belong to the core of the QD and are all four-fold coordinated –Zn(4)–. The atoms in the $(ZnX)_{42}$ shell are located in the surface. Depending on the number of surface attached molecules, their coordination number can vary from three to six –Zn(3), Zn(4) or Zn(>4)–. For clarity, surface-attached H_2X moieties have been excluded from the calculation of the averages.

				X			
Property	Crystallographic axis	Region	Coordination	O	S	Se	Te
Dimensions (nm)	*a*			1.04	1.26	1.32	1.42
	b			0.98	1.22	1.28	1.35
	c			0.95	1.12	1.18	1.30
Bond Length (Å)		Core	Zn(4)-X	2.082	2.465	2.578	2.775[a] (2.753)[b]
				(1.95)[c]	(2.35)[c]	(2.45)[c]	(2.65)[c]
		Surface	Zn(>4)-X	2.106	2.612	-	-
			Zn(4)-X	2.053	2.484	2.598	2.789[a] (2.770)[b]
			Zn(3)-X	1.950	2.381	2.493	2.691[a] (2.672)[b]
Bond Angle (Deg.)		Core	X-Zn(4)-X	109.4	109.4	109.3	109.4[a] (109.4)[b]
			Zn-X(4)-Zn	109.3	109.4	109.3	109.4[a] (109.4)[b]
		Surface	X-Zn(>4)-X	103.5	102.7	-	-
			X-Zn(4)-X	109.4	110.1	109.6	109.8[a] (109.9)[b]
			Zn-X(4)-Zn	109.0	108.8	109.4	108.3[a] (108.1)[b]
			X-Zn(3)-X	122.2	121.9	122.6	120.8[a] (120.8)[b]
			Zn-X(3)-Zn	105.0	95.7	95.8	95.1[a] (94.7)[b]

[a] Non-relativistic calculation.
[b] Relativistic calculation.
[c] Experimental bond lengths, reported for bulk materials.

Table 4.11: Valence excitation spectrum of the ZnX-QDs (X = O, S, Se, Te). Vertical excitation energy and corresponding oscillator strength are reported, along with the composition of the excited state. Among the low lying excitations, the first an those with $f > 0.1$ are shown. Energies in eV and oscillator strengths in a.u.. Calculations have been carried out at PCM-B3LYP/def2-SVP//PBE/DZ level of theory.

ZnO-QD					ZnS-QD				
# Transition	E(eV)	f	Main Monoexcitations	Weight (%)	# Transition	E(eV)	f	Main Monoexcitations	Weight (%)
1	3.97	0.1479	HOMO⟶LUMO	84	1	4.28	0.0409	HOMO⟶LUMO	78
7	4.17	0.2083	HOMO-6⟶LUMO	88	3	4.37	0.5063	HOMO-2⟶LUMO	66
8	4.20	0.2002	HOMO-7⟶LUMO	82				HOMO-1⟶LUMO	22
12	4.31	0.1310	HOMO-11⟶LUMO	68	5	4.45	0.2604	HOMO-3⟶LUMO	82
13	4.32	0.1102	HOMO-12⟶LUMO	70	6	4.47	0.4301	HOMO-4⟶LUMO	84
17	4.39	0.2480	HOMO-15⟶LUMO	60	7	4.53	0.1130	HOMO-6⟶LUMO	74
					8	4.54	0.1161	HOMO-7⟶LUMO	76
					16	4.71	0.1113	HOMO-14⟶LUMO	40
								HOMO-15⟶LUMO	28
					19	4.78	0.1094	HOMO-19⟶LUMO	54

ZnSe-QD					ZnTe-QD				
# Transition	E(eV)	f	Main Monoexcitations	Weight (%)	# Transition	E(eV)	f	Main Monoexcitations	Weight (%)
1	3.89	0.2998	HOMO⟶LUMO	88	1	3.52	0.3592	HOMO⟶LUMO	88
2	3.91	0.2288	HOMO-1⟶LUMO	88	2	3.55	0.3248	HOMO-1⟶LUMO	84
3	3.93	0.3546	HOMO-2⟶LUMO	86	3	3.58	0.2844	HOMO-2⟶LUMO	84
7	4.12	0.1593	HOMO-6⟶LUMO	58	4	3.61	0.3356	HOMO-3⟶LUMO	90
8	4.12	0.1884	HOMO-7⟶LUMO	62	5	3.68	0.1098	HOMO-4⟶LUMO	84
14	4.25	0.1569	HOMO-13⟶LUMO	50					
16	4.29	0.1039	HOMO-15⟶LUMO	46					
18	4.31	0.1100	HOMO-16⟶LUMO	58					
19	4.33	0.1543	HOMO-17⟶LUMO	52					
20	4.35	0.1673	HOMO-20⟶LUMO	38					

Table 4.12: Binding energies of characteristic valence-band features of the ZnX-QDs (X = O, S, Se, Te) with respect to the valence band maximum (VMB), given in eV. The binding energies reported are calculated as $\triangle_A = E_{HOMO} - E_A$. These results are obtained at the PCM-B3LYP/def2-SVP//PBE/DZ level of theory. Experimental results of the bulk are also provided.

		$\triangle_{P_{I,a}}$	$\triangle_{P_{I,b}}$	$\triangle_{P_{II}}$	$\triangle_{d}$	$\triangle_{P_{III,a}}$	$\triangle_{P_{III,b}}$
ZnO-QD	(Calc.)	0.70	-	3.26	7.04	17.28	19.93
Bulk ZnO	(Exp.)[a]	2.8-2.9		5.0-5.9	7.5-9.8	20.0-20.7	
ZnS-QD	(Calc.)	0.75	4.93	3.29	8.33	12.19	13.66
Bulk ZnS	(Exp.)[b]	2.6		4.9	9.0	12.4	
ZnSe-QD	(Calc.)	0.68	4.82	3.36	8.74	12.07	13.31
Bulk ZnSe	(Exp.)[c]	1.9		5.2	9.20	13.1	
ZnTe-QD	(Calc.)	0.75	4.52	3.47	9.30	11.14	12.03
Bulk ZnTe	(Exp.)[d]	1.7		5.1	9.84	11.9	

[a]From Ref [424–427].
[b]From Ref [424].
[c]From Ref [424].
[d]From Ref [424].

Table 4.13: Selected optimized bond distances (Å) calculated for the non-defective ZnX-QDs (X = O, S, Se, Te) and in the presence of a neutral X vacancy, optimized both in their ground state (S0). The values in parentheses correspond to the $[(ZnO)_{111}(H_2O)_{12}]$ quantum dot were previously characterized [416].

		No Vacancy (S0)		Neutral X Vacancy (S0)	
ZnO-QD	d(Zn-Zn)	3.142	(3.126)	2.707	(2.722)
	d(Zn-O)	2.010	(1.998)	2.032	(2.034)
ZnS-QD	d(Zn-Zn)	3.569		2.757	
	d(Zn-S)	2.415		2.479	
ZnSe-QD	d(Zn-Zn)	3.725		2.778	
	d(Zn-Se)	2.547		2.601	
ZnTe-QD	d(Zn-Zn)	3.965		2.813	
	d(Zn-Te)	2.708		2.779	

Table 4.14: Lowest singlet-singlet (S0→S1) and singlet-triplet (S0→T1) TDDFT excitation energies (eV) calculated at the S0 ground state geometries for the non-defective ZnX-QDs (X = O, S, Se, Te) and in the presence of a neutral X vacancy. Calculations have been carried out at PCM-B3LYP/def2-SVP//PBE/DZ level of theory. For comparison, experimental emission features of ZnX (X = O, S, Se) nanostructures are also provided.

		S0→S1	S0→T1	Exp. Emission
ZnO-QD	No vacancy	3.97	3.87	
	O vacancy	2.83	2.70	2.3-2.4[a]
ZnS-QD	No vacancy	4.28	4.18	
	S vacancy	3.29	2.92	2.8-3.1[b]
ZnSe-QD	No vacancy	3.89	3.81	
	Se vacancy	3.05	2.70	3.0[c]
ZnTe-QD	No vacancy	3.52	3.45	
	Te vacancy	2.79	2.24	2.2[d]

[a]From Refs [393–396], measured for 1.5-3.0 nm diameter ZnO QDs.
[b]From Refs [54, 398–402, 455, 456] , measured for a wide variety of ZnS nanostructures.
[c]From Ref [446], measured for 1.0 diameter ZnSe QDs.
[d]From Ref [457], measured for ZB-like ZnTe wires and ribbons.

Table 4.15: Composition of the frontier orbitals, in %, of the non-defective ZnX-QDs (X = O, S, Se, Te) and in the presence of neutral X vacancy. For Zn atoms, those located in the Zn triangle are distinguished from the rest. These results are obtained at the PCM-B3LYP/def2-SVP//PBE/DZ level of theory.

			No Vacancy				Neutral X Vacancy			
			ZnO	ZnS	ZnSe	ZnTe	ZnO	ZnS	ZnSe	ZnTe
%HOMO	Atom	Type								
	Zn	Triangle	-	-	-	-	53	52	47	41
		Rest	18	8	8	7	12	7	7	6
	X		82	92	92	93	35	41	47	53
	H		0	0	0	0	0	0	0	0
%LUMO	Atom	Type								
	Zn	Triangle	-	-	-	-	1	1	1	2
		Rest	59	44	42	45	57	45	42	44
	X		39	54	55	53	39	52	54	51
	H		2	2	3	2	2	2	3	2

Table 4.16: Electronic parameters calculated for the ZnX-NRs (X = O, S, Se, Te), in eV. d is the position of the d peak. ε_{HOMO-1} is the HOMO-1 KS eigenvalue. $\triangle_d$ refers to the binding energy of the d peak, taken with respect to the VBM (the HOMO-1 in our case). These results are obtained at the PCM-B3LYP/def2-SVP//PBE/DZ level of theory.

	ZnO			ZnS			ZnSe			ZnTe		
	d	ε_{HOMO-1}	$\triangle_d$	d	ε_{HOMO-1}	$\triangle_d$	d	ε_{HOMO-1}	$\triangle_d$	d	ε_{HOMO-1}	$\triangle_d$
NR1	$^{(a)}$	$^{(a)}$	$^{(a)}$	-14.80	-6.78	8.02	-14.97	-6.64	8.33	-15.10	-6.26	8.84
NR2	-13.64	-6.58	7.06	-14.76	-6.77	7.99	-14.93	-6.51	8.42	-15.06	-6.13	8.93
NR3	-13.61	-6.57	7.04	-14.75	-6.71	8.04	-14.91	-6.42	8.49	-15.05	-6.06	8.99
NR4	-13.60	-6.55	7.05	-14.73	-6.65	8.08	-14.90	-6.37	8.53	-15.04	-6.01	9.03
NR5	-13.58	-6.56	7.02	-14.72	-6.63	8.09	-14.89	-6.35	8.54	-15.03	-6.00	9.03

$^{(a)}$Geometry optimization does not converge.

Figure 4.16: Bulk wurtzite, seen along the *c* crystallographic axis ([0001]). The patterns employed in the construction of the nanostructures are highlighted, along with the resulting geometries (top of the colored panels, top view). For ZnS, the optimized structures of the passivated models are also shown (bottom of the colored panels, side view). Light blue = Zn, yellow = S and white = H atoms.

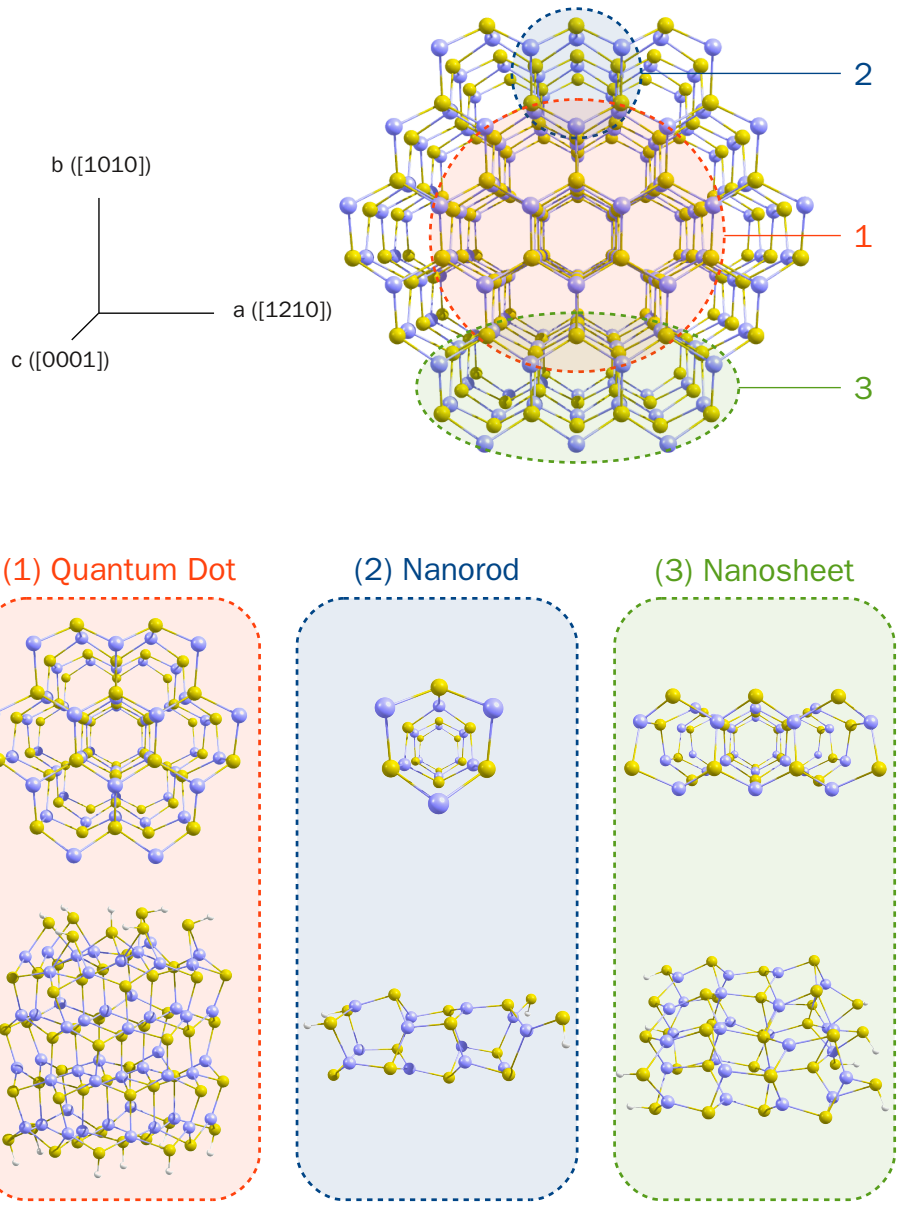


Figure 4.17: Isodensity plots of the frontier orbitals of the (a) ZnO-, (b) ZnS-, (c) ZnSe- and (d) ZnTe- QDs. These results are obtained at the PCM-B3LYP/def2-SVP//PBE/DZ level of theory. Light blue = Zn, red = O, yellow = S, orange = Se, green = Te and white = H atoms.

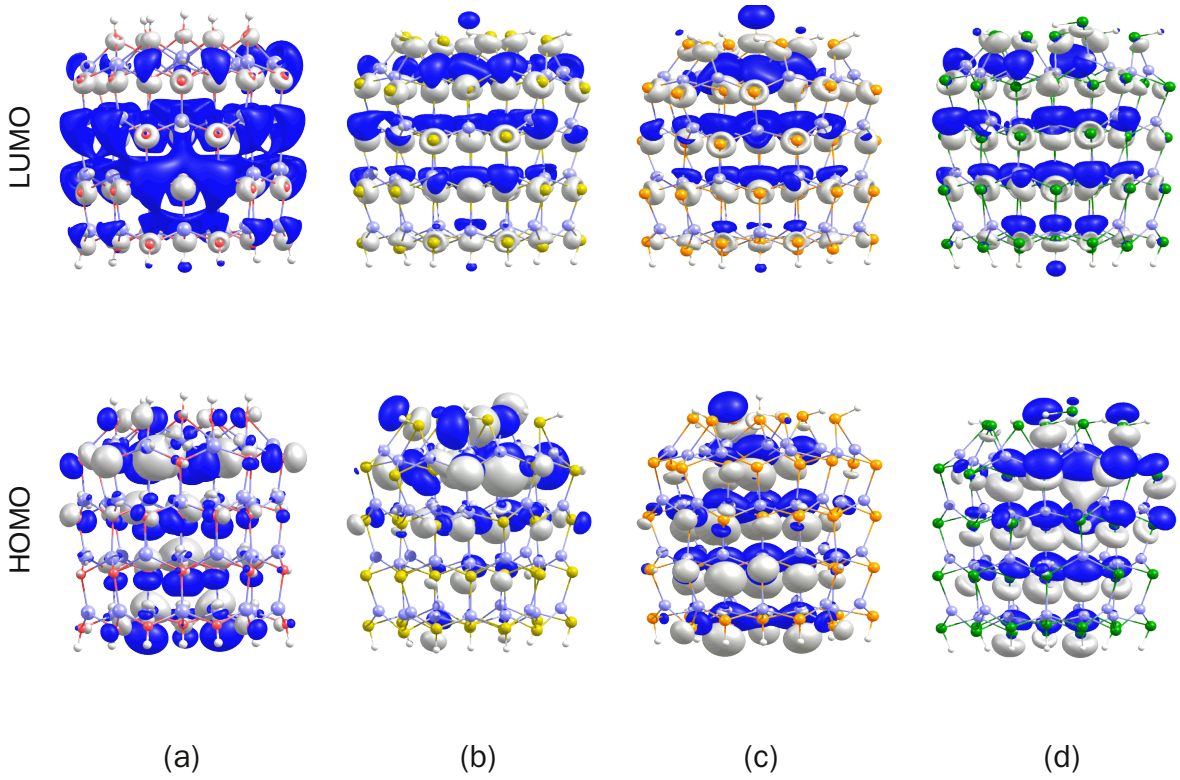


Figure 4.18: TDDFT absorption spectra of the ZnX-QDs (X = O, S, Se, Te), obtained by a Gaussian convolution with FWHM = 0.47 eV, calculated taking into account the lowest 20 electronic transitions. These results are obtained at the PCM-B3LYP/def2-SVP//PBE/DZ level of theory. The dots highlight the first transition for each QD.

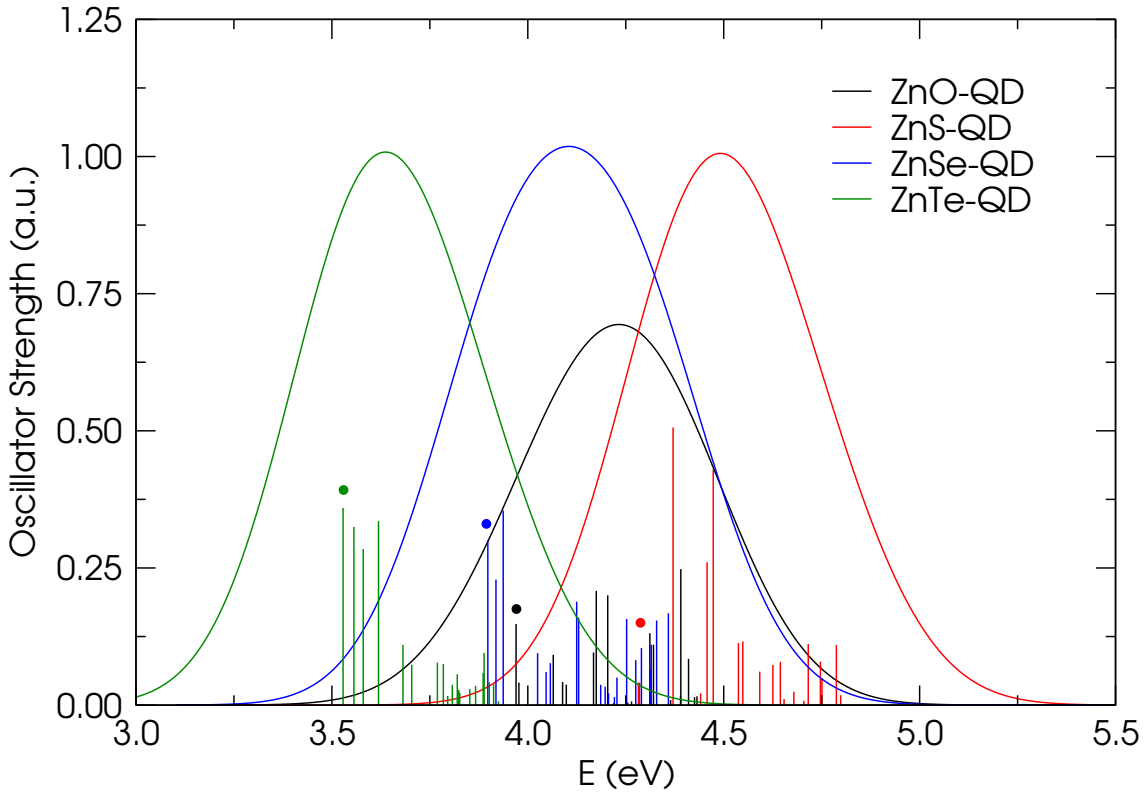


Figure 4.19: Total and Projected Density of States (DOS and PDOS) of (a) ZnO-, (b) ZnS-, (c) ZnSe- and (d) ZnTe-QDs, obtained by a Gaussian convolution of σ = 0.20 eV of the individual KS orbitals. The insets show a zoom of the regions close to the band edges (green = occupied and red = virtual orbitals). These results are obtained at the PCM-B3LYP/def2-SVP//PBE/DZ level of theory.

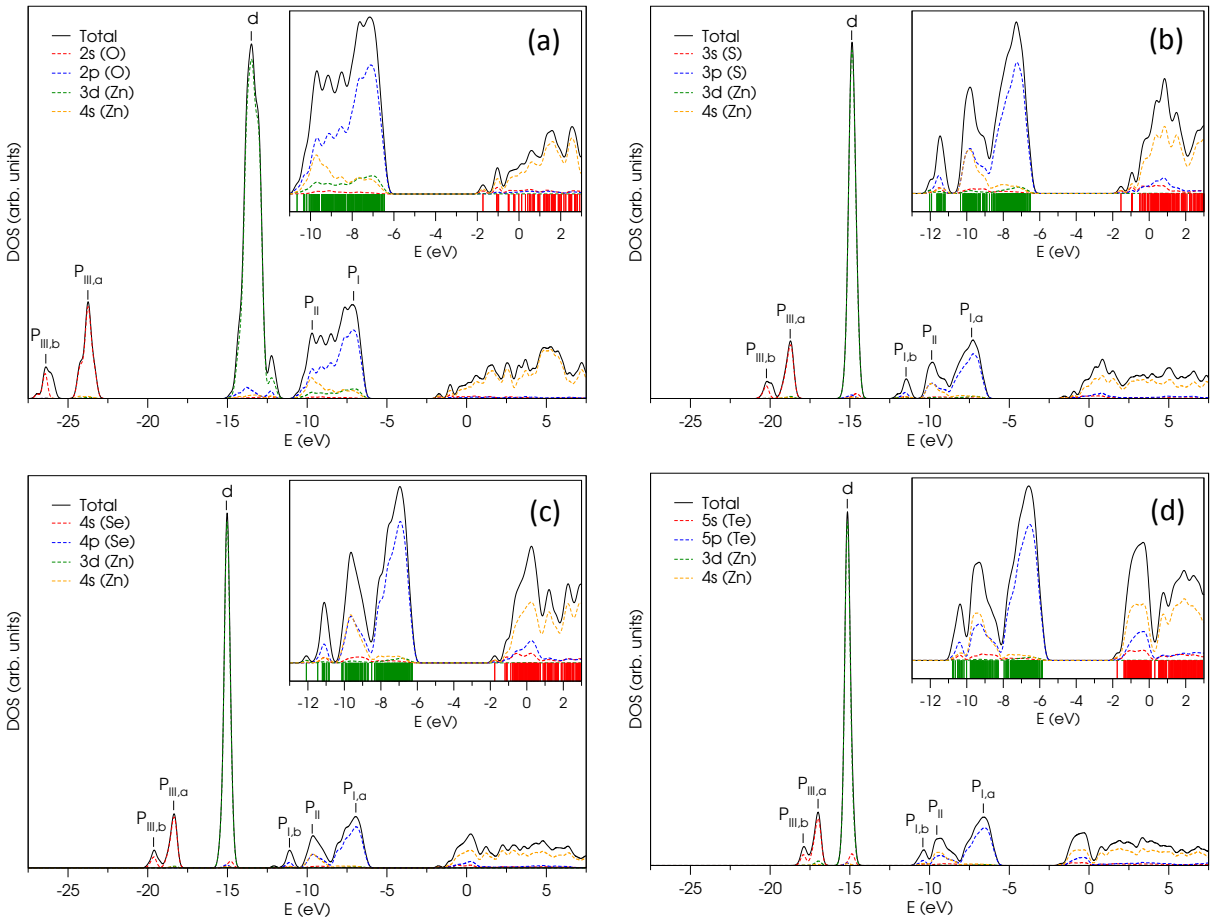


Figure 4.20: (a) Geometrical structure of the non-defective ZnO-QD, showing the site where an O vacancy is created (green) and the three Zn atoms to which the removed atom is bound (black). Light blue = Zn, red = O and white = H atoms. (b) Schematic representation of the energy levels for the ZnX-QDs (X = O, S, Se, Te) with a neutral X vacancy, optimized in their ground state (S0). The lowest TDDFT excitation energies (eV) for the singlet-singlet and the singlet-triplet (data in parentheses) are also reported. For the defective ZnO-QD the frontier orbitals involved in the lowest transition are shown. These results are obtained at the PCM-B3LYP/def2-SVP//PBE/DZ level of theory.

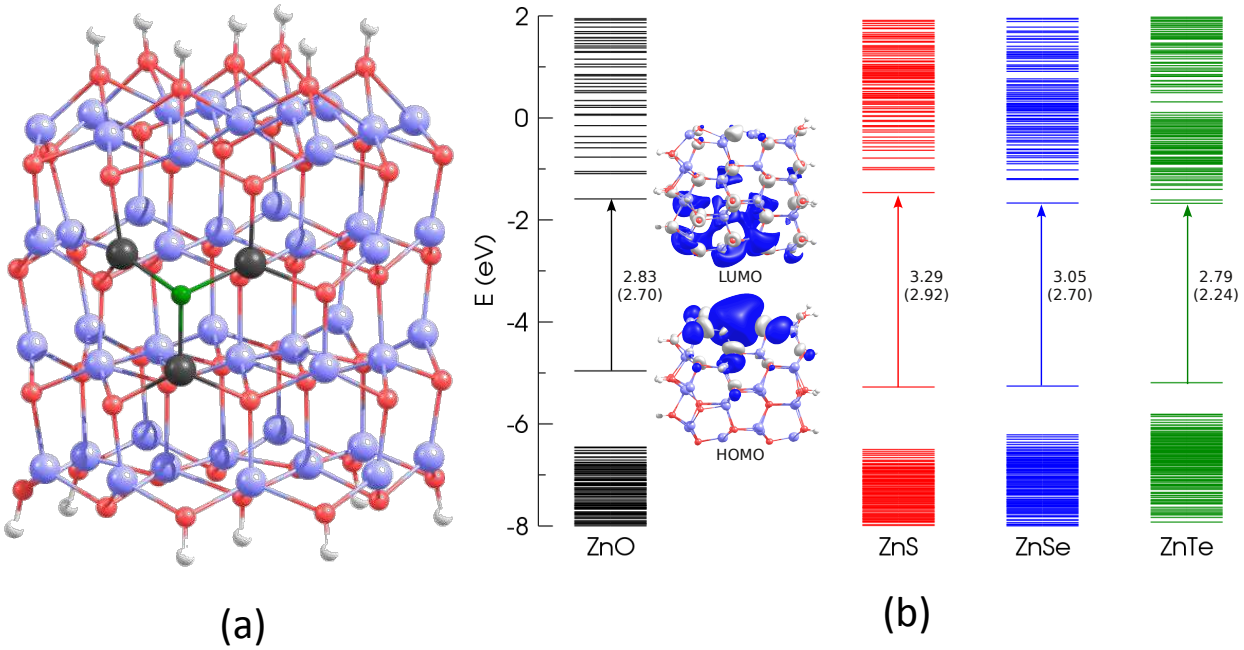


Figure 4.21: Optimized geometrical structures of the (a) ZnS-NRs and (b) ZnS-NSs. Light blue = Zn, yellow = S and white = H atoms. Similar structures have been obtained for ZnSe and ZnTe.

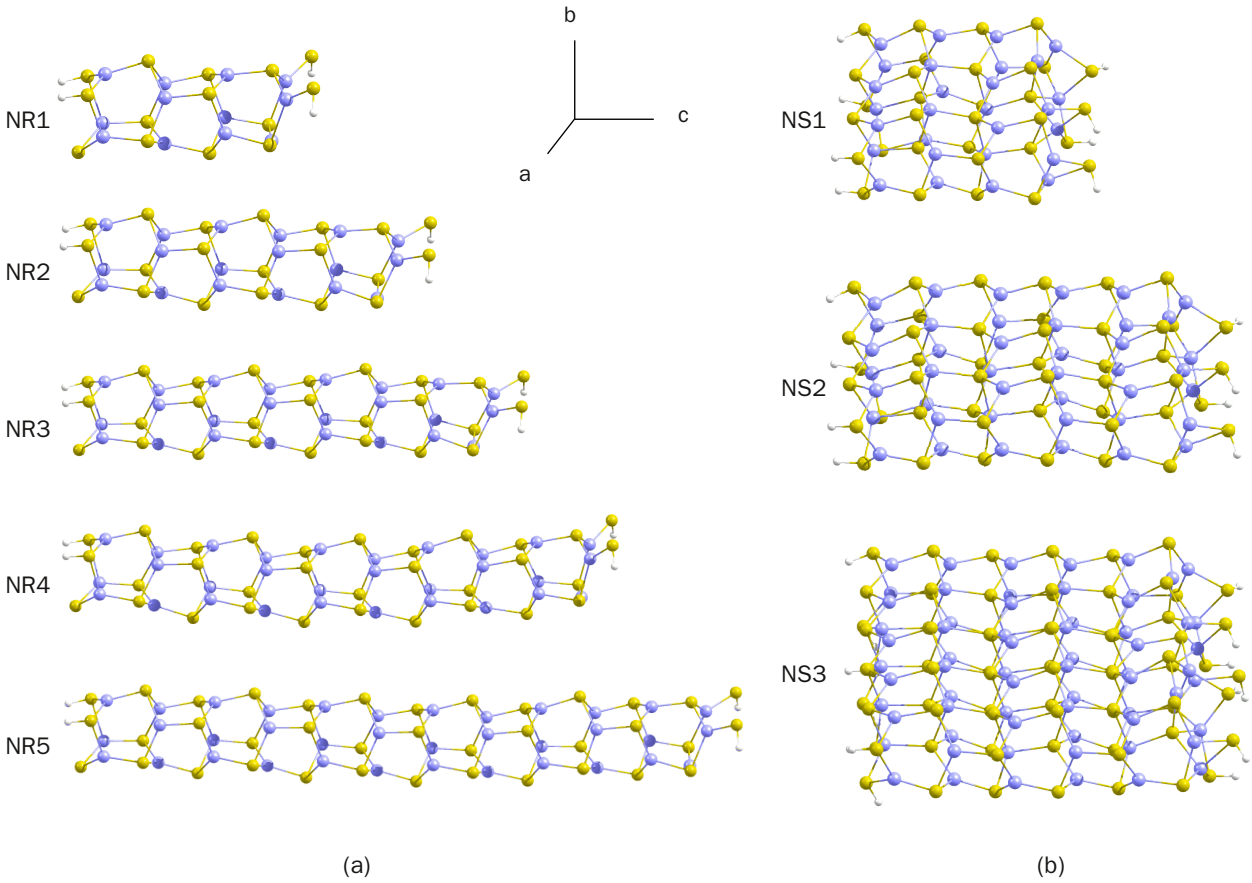


Figure 4.22: TDDFT absorption spectra of the (a) ZnS-, (c) ZnSe- and (d) ZnTe- NRs, obtained by a Gaussian convolution with FWHM = 0.47 eV, calculated taking into account the lowest 20 electronic transitions. The first transitions are highlighted in the insets. (b) Isodensity plots of the molecular orbitals involved in the first and the brightest transitions of ZnS-NR1. These results are obtained at the PCM-B3LYP/def2-SVP//PBE/DZ level of theory.

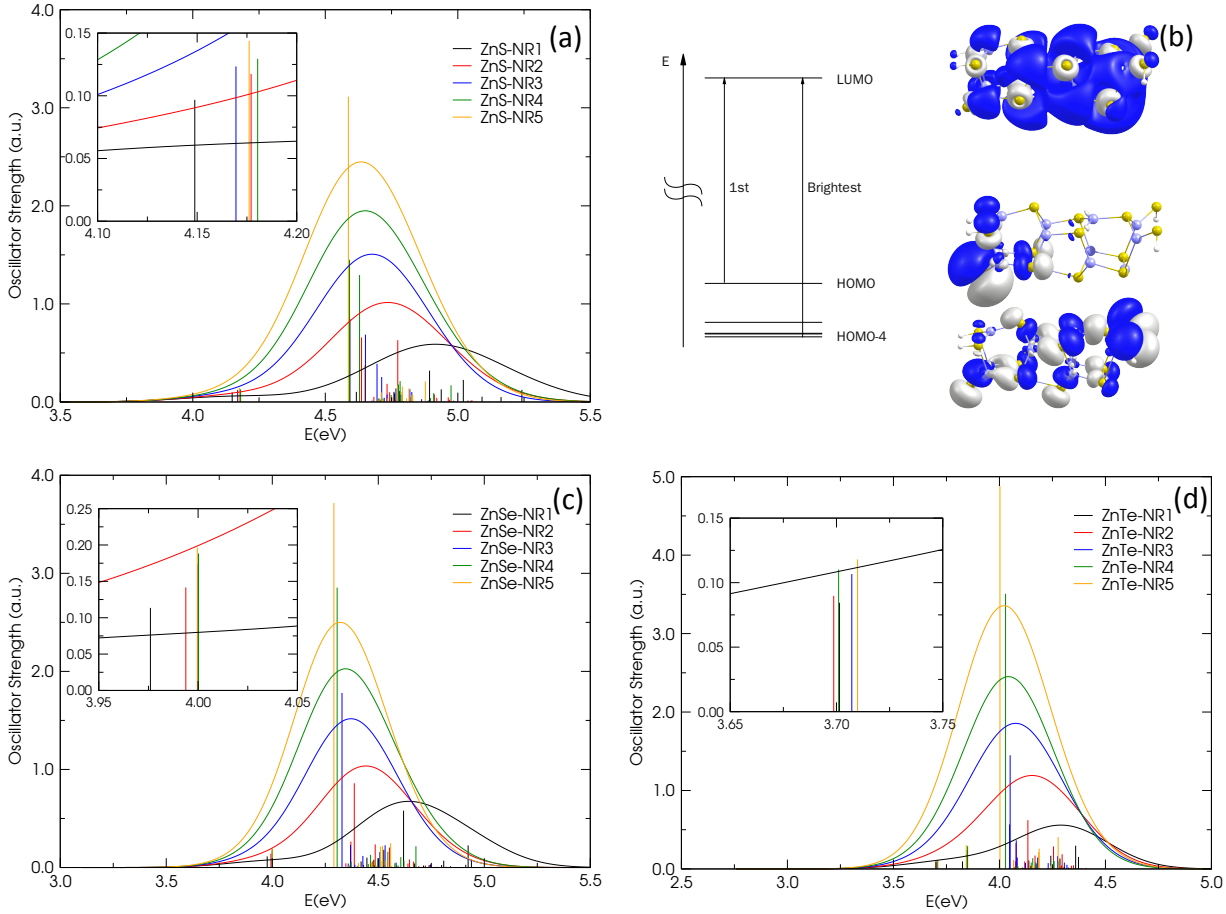
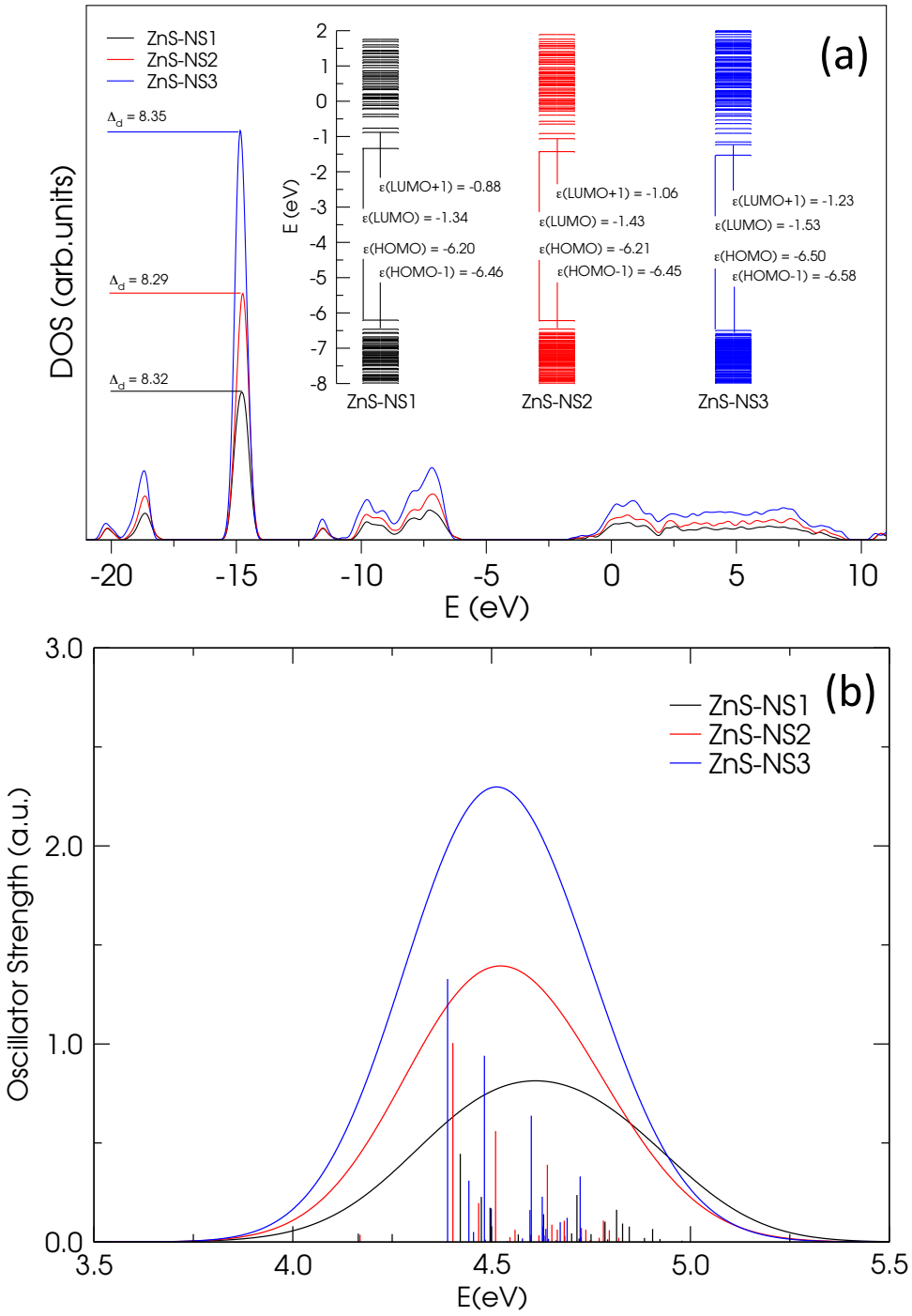


Figure 4.23: (a) Density of States (DOS) of ZnS-NSs, obtained by a Gaussian broadening of σ = 0.20 eV of the individual KS orbitals. For NS1 and NS2 HOMO-1 has been chosen as VBM, given that HOMO is a midgap state. (b) TDDFT absorption spectra of the ZnS-NSs, obtained by a Gaussian convolution with FWHM = 0.47 eV, calculated taking into account the lowest 20 electronic transitions. These results are obtained at the PCM-B3LYP/def2-SVP//PBE/DZ level of theory.



4.4 Modeling Surface Passivation of ZnS Quantum Dots

4.4.1 Abstract

We report on the interaction between ZnS quantum dots and several surface ligands by means of pure Quantum Mechanical (QM) and hybrid Quantum Mechanics/Molecular Mechanics (QM/MM) methods. To shed light on the nature of the interaction, we focus our discussion on the structural and energetic aspects. The $(ZnS)_6$ cluster has been chosen to model the quantum dot core, while trimethylamine (NMe_3), trimethylphosphine (PMe_3), trymethylphosphine oxide ($OPMe_3$), methanol (MeOH), methanethiol (MeSH), and methaneselenol (MeSeH) have been employed to model the passivating ligands. Our results concerning the interaction between the cluster and one ligand of each type reveal that NMe_3, PMe_3, and $OPMe_3$ show a significantly greater affinity to $(ZnS)_6$ than MeOH, MeSH, and MeSeH. We noticed that the softer the heteroatom of the ligand bonded to the cluster, the greater the interaction energy. A comparative study of different amines shows that the interaction is strengthened with the number and the length of the alkyl substituents in the ligand. We demonstrated that the interaction is mainly electrostatic, even if an important polarization of the charge density is observed. Fully passivated complexes have also been investigated, and our calculations point out that the bond is weaker than in the complexes with a single bonded ligand, suggesting that the repulsive interactions between the ligands and the diminished charge acceptor capacity of the cluster come into play.

4.4.2 Introduction

Semiconductor nanocrystals represent a class of quantum-confined objects in which the motion of the charge carriers can be restricted in one, two, or three spacial directions. When this confinement occurs in all three dimensions, the nanocrystal is called quantum dot (QD) and is characterized by a quantized structure of energy levels that can be tuned by varying the size and the shape of the nanostructure. QDs present broad absorption spectra, narrow emission bands, high extinction coefficients, unmatched photostability, and reasonably long photoexcited lifetimes [4]. These remarkable features substantially deviate from those of their bulk counterparts [4] and allow the QDs to be potentially useful in technological applications such as photooxidizers and photocatalysts [376,377], photovoltaic solar cells [378–381], quantum devices [382], optical sensitizers [383], or fluorescent probes [68].

Among the several routes devised for the production of semiconductor nanostructures, colloidal techniques by Bawendi and co-workers [90,114] have led to the preparation of a wide range of nanostructures. The synthesis of colloidal QDs occurs in solution in the presence of organic surfactant molecules, which control the growth and the geometry of the nanoparticle by dynamically adhering to it. The surfactant molecules passivate the QD, protect the surface from oxidation, and exert a strong influence on its photophysics [80], charge transport [479], catalysis [480] and magnetism [481]. In recent years, chemical functionalization

has been proven to be very helpful in designing materials with specific electrical and optical properties [183, 482–484]. In particular, the functionalization of inorganic clusters and QDs with organic ligands and biomolecules has been exhaustively investigated [485–487].

On the basis of these considerations, it is clear that a deep knowledge of the QD–ligand interface is fundamental. Much effort has been put forward to elucidate the passivated QD structure using modern experimental techniques, like X-ray diffraction, Transmission Electron Microscopy (TEM), Extended X-ray Absorption Fine Structure Spectroscopy (EXAFS), and Nuclear Magnetic Resonance (NMR). According to the most recent results, it is assumed that passivated semiconductor nanoparticles contain a bulk-like core, but the nature of the passivated surface remains unclear [13, 488–492]. Since the experiments suffer from significant restrictions, the integration of these techniques with theoretical models could provide valuable insight into the QD–ligand interaction [493].

Among the semiconductor nanomaterials developed to date, interest in II–VI (II: Zn, Cd, Hg and VI: O, S, Se, Te) QDs has increased notably due to their paramount technological potential. In particular, cadmium-based CdX (X = S, Se, Te) QDs have stimulated a great deal of research [94, 281, 488–490, 494, 495]. Consequently, seminal theoretical works focused on CdSe clusters. In a first approach, these systems were studied using a semiempirical tight binding approach to simulate the surface passivation by embedding the cluster in the potential generated by the ligands [496,497]. The optical band gaps were shown to be sensitive to the magnitude of the potential and the QD–ligand distance, meaning that any reliable theoretical model should explicitly reproduce the bond between the QD and the passivating ligand.

Among the whole set of Quantum Mechanical (QM) tools available for this purpose, DFT (DFT) [498] offers a reasonable level of accuracy. For the sake of computational efficiency, early DFT calculations employed hydrogen [289, 499] or oxygen [496, 500] atoms to saturate the surface Cd atoms of the CdSe nanostructures. However, the Cd–H (or Cd–O) bonds turned out to be too strong, and the effect of the surface reconstruction was poorly described. Indeed, subsequent works showed that H atoms tend to disrupt Cd–Se topology and can not represent the effects of more complex ligands [279]. Since then, several DFT studies have been published in which the surface passivation of small CdSe clusters with more realistic ligands has been assessed [279, 293, 325].

Ligands such as amines, phosphines, and phosphine oxides have been studied since they are commonly used as passivating agents in the synthesis of colloidal QDs. Yang and co-workers demonstrated that the binding energies of such ligands to the neutral $(CdSe)_2$ cluster decrease from phosphine oxides to phosphines [279]. In a subsequent study involving the much larger $(CdSe)_{33}$ structure, Kilina and co-workers observed a substantial polarization interaction on the surface of the passivated cluster due to the strong interaction between the surface and the ligands [293]. More recently, the role of ligand passivation on CdSe clusters of different shapes has been investigated [325]. It has been shown that for a given size of the cluster the computed bond energies do not follow a simple trend, suggesting that there are many effects underlying the ligand passivation. The bond strength decreases as

the cluster size increases, and the absorption spectra is blue-shifted upon ligation of surface molecules.

As demonstrated above, both bare and passivated CdSe QDs have been exhaustively investigated theoretically. Paradoxically, and regarding their potential application in biomedicine, recent *in vitro* and *in vivo* studies have revealed the cytotoxicity of CdSe QDs due to the release of free cadmium ions in the organic tissues [198, 199]. QD surface coating has been shown to reduce significantly its toxicity, but not enough to achieve a complete removal. As a consequence, the application of CdSe QDs *in vivo* must be critically reconsidered.

Zn-based QDs present a much lower toxicity and could be more appropriate for biological applications. Theoretical studies concerning the interaction of surfactant molecules with ZnS clusters are, however, rather scarce [315, 316]. Such investigations, carried out with DFT/BLYP, indicate that the interaction between the ligands and the cluster is mainly electrostatic and that the HOMO levels are affected upon ligand adsorption, whereas the LUMO remains practically unchanged.

In a previous work carried out by some of us, the structural, electronic, and optical properties of realistic ZnO and ZnS model structures were investigated by means of DFT/TDDFT [300]. In this paper, we report the results of DFT calculations to accurately describe the details of the interaction between ZnS clusters and several type of ligands. The minimal semispherical $(ZnS)_6$ cluster previously reported by our group [320] has been chosen to model the QD. Its existence in the gas phase has been proven experimentally by means of Time-Of-Flight Mass Spectrometry (TOF-MS) of ZnS clusters obtained by laser ablation of bulk ZnS [501]. More recently, the formation of such ultrasmall $(ZnS)_n$ (n = 1–9) clusters in solution using electroporation of unilamellar vesicles has been hypothesized [502]. Furthermore, the unrelaxed $(ZnS)_6$ cluster can be thought of as the unit cell of a wurtzite structure (Figure 4.24 (a)), which is reported to be the crystal structure of the bulk ZnS and the core structure of larger QDs. Hence, we believe that $(ZnS)_6$ is a reliable starting point to understand the chemical effects underlying the QD–ligand interaction. Moreover, it allows us to assess the theoretical model that will be used as a reference for further investigations concerning larger $(ZnS)_n$ clusters [300].

Apart from the core structure of the QD, another fundamental aspect of our calculations is the choice of the ligands. We decided to investigate the following moieties: trimethylamine (NMe_3), trimethylphosphine (PMe_3), trymethylphosphine oxide ($OPMe_3$), methanol (MeOH), methanethiol (MeSH), and methaneselenol (MeSeH). NMe_3, PMe_3, and $OPMe_3$ mimic large chain amines, phosphines, and phospine oxides, which are commonly employed as passivating ligands in the production of colloidal QDs. MeOH, MeSH, and MeSeH are often used not only in colloidal synthesis but also as typical polar moieties prone to interact with nanostructures and form bioconjugated systems. Furthermore, different amines have been studied to elucidate the role of the number and the length of the alkyl groups in the ligand.

4.4.3 Computational Details

All the QM calculations have been carried out using the exchange correlation (xc) Perdew – Burke – Ernzerhof (PBE) [238] functional within the Kohn–Sham framework of DFT (KS-DFT), as implemented in the ADF 2010.01 program [267]. A set of Slater-type orbitals (STO) of triple-ζ quality has been employed, including two sets of polarization functions on each atom (TZ2P). Full geometry optimizations have been performed, and no symmetry constraints have been imposed. Harmonic vibrational frequencies have been evaluated to verify whether the stationary points found are true minima. We carried out a preliminary benchmark study comparing PBE, PBE0 [359], and B3LYP [503] to check their performance. Our calculations showed that the choice of the functional has a minor influence on the geometry of the $(ZnS)_6$ cluster. Regarding the interaction between the $(ZnS)_6$ cluster and several ligands, our benchmark study showed that the geometries and bond energies obtained with PBE were satisfactorily close to those given by the hybrids PBE0 and B3LYP. These findings are in agreement with recently published results regarding CdSe clusters [280]. Consequently, we decided to proceed with the PBE functional because the computational acceleration techniques and the analysis tools supported by ADF and used in this article (*vide infra*) are more versatile.

To begin with, and for the sake of simplicity and computational saving, we have computed the interaction of the inorganic cluster with just one surface attached ligand at the PBE/TZ2P level. However, to describe the surface of the QD more realistically, we have decided on a sounder approach that includes the chemical interaction of the organic ligands on all the available sites of passivation.

To tackle these new extended systems in a more efficient manner, the performance of the hybrid QM/MM method developed by Woo et al. [269] has been assessed. Within this framework, the semiconductor cluster and its structural, electronic, and optical properties of interest have been treated with DFT-PBE/TZ2P. The surrounding layer of organic ligands, which is expected to modulate the properties of the inorganic core, is described using the AMBER95 [270] force field as implemented in ADF.

The complexity of the coordinate space of the system increases notably upon the attachment of surface ligands, with a large number of possible local minima on the potential energy surface. In this sense, the QM/MM module implemented in ADF shows several advantages: it implies a saving of the computational resources and also enables us to perform molecular dynamics simulations on the MM subsystem. These simulations, carried out at high temperature, allow the ligands to explore the conformational space. Once a large number of minima have been located, the stored structures are optimized and classified by their total QM/MM energy, in order to find the global minimum with more precision. In our study, the MM subsystem has been heated to a temperature of 700 K, and the simulations have been run for a total of 100 ps using a time step of 0.5 fs. Production snapshots have been taken every 0.1 ps, and a total of 1001 structures have been sampled. Finally, a minimization has been performed on each sampled structure.

The QM/MM method allows us to sample different structures of the coordinate space in a computationally efficient manner, therefore providing suitable starting points for further and more refined QM calculations. However, and to the best of our knowledge, this is the first work in which the QM/MM scheme is employed to shed light on the QD–ligand interaction so that the choice of the computational setup is not trivial. The main point of concern is how to treat the borders of the QM and MM regions. In a first approach, following our chemical intuition, we decided to include the cluster in the QM region and describe the ligands with MM. This partition, referred to as QM/MM(1), does not consider the orbital interaction between the QM and MM regions and poorly describes the geometry of the complexes. In a second approach, we have expanded the QM region to include the ligand atom X (X = N, P, O, S, Se) directly bonded to the cluster. This second partition, known as QM/MM(2), has shown to provide much better structures. Hence, we decided to focus our discussion on the results provided by QM/MM(2). For the sake of clarity, we will refer to it as QM/MM in the discussion of the results.

However, the QM/MM(2) partition implies that some covalent bonds cross the QM/MM boundaries. To tackle this drawback, we employed the Integrated Molecular Orbital and Molecular Mechanics (IMOMM) method developed by Maseras and Morokuma [269, 504]. Following their recipe, we cap the atoms with dangling bonds in the QM region to satisfy their valence requirements, so that a standard electronic structure calculation can be performed. For the sake of simplicity, we employed H as a capping atom. As an example, in the case of NMe_3 the N atom is included in the DFT along with the capping H atoms. Me groups are treated by MM and do not require capping.

Capping atoms introduce extra nuclear degrees of freedom that are not present in the real system. IMOMM alleviates this problem, defining the position of the MM atom involved in the truncated bond in terms of the QM atom it is bonded to and the capping atom that replaces it. In the particular case of NMe_3

$$X_{C(MM)} = \alpha X_{H(CAP)} + (1 - \alpha) X_{N(QM)} \tag{4.1}$$

where $X_{C(MM)}$, $X_{H(CAP)}$ and $X_{N(QM)}$ refer to the Cartesian coordinates of the subscripted atoms. α is a constant defined as the ratio of the truncated bond length to that of the length of the capping bond. In this case, $\alpha = \frac{d(N-C)}{d(N-H)}$. Therefore, the N–C bond is relaxed as well during the geometry optimization.

In a first step, MD simulations were carried out employing the QM/MM(1) partition, allowing the ligands to adopt different conformations with respect to the nanocluster. In a second step, QM/MM(2) was also checked. Since in the QM/MM(2) partition the ligand atom X bonded to the cluster is included in DFT, only the conformational space of the moieties bonded to X is explored. However, we realized that the bond between the nanocluster and the ligand is highly directional (notice that the coordination angles $\alpha(S - Zn - X)$ are close to the tetrahedral angle of 109° irrespective of the ligand, *vide infra*). Therefore, the inclusion of X in the MD simulation may not be crucial.

Although most of the MM parameters for the organic ligands could be taken from the default AMBER95, those that encompass the atoms of the cluster had to be evaluated explicitly. The stretching and bending parameters for the atoms of the ligands bonded directly to the Zn atoms of the cluster have been obtained using Badger's rules [271] taking as reference PBE/TZ2P calculation performed using a single ligand passivated on top of the cluster. All the torsional contributions involving cluster atoms have been set to zero. Multipole-derived charges [505] have been chosen to compute the electrostatic interaction between the ligand and the cluster, and have been allowed to be updated in a self-consistent way during the QM/MM geometry optimization.

Once the QM/MM structures have been fully optimized and the global minima have been found, we have run a geometry optimization at the PBE/TZ2P level to obtain the fully converged complexes and to benchmark them against both the QM/MM(1) and QM/MM(2) partitions. To reduce the computational cost, the length of the alkane chains of the ligands has been reduced. Previous studies on capped $(CdSe)_n$ demonstrated that substituting alkane chains by hydrogen atoms yields unphysical results [491]. They pointed out that modeling the alkane substituents with methyl groups was sufficient to accurately describe not only binding energies but also band edge states and the band gap observed for their large chain counterparts.

To analyze with greater detail the bond between the inorganic cluster and the organic ligands, we have performed a bond energy decomposition using the Ziegler and Rauk method [506–510] implemented in ADF. The overall bond energy $\triangle E$ is split into two main terms

$$\triangle E = \triangle E_{prep} + \triangle E_{int} \tag{4.2}$$

The first one, the so-called preparation energy $\triangle E_{prep}$, corresponds to the energy required to deform the separated fragments from their equilibrium structure to their geometry in the complex. The second one, $\triangle E_{int}$, accounts for the instantaneous interaction between the prepared fragments. The interaction energy is further decomposed into three contributions: the electrostatic interaction $\triangle V_{elst}$, the Pauli repulsion $\triangle E_{Pauli}$, and the orbital interaction $\triangle E_{oi}$.

$$\triangle E_{int} = \triangle V_{elst} + \triangle E_{Pauli} + \triangle E_{oi} \tag{4.3}$$

The latter term accounts for charge transfer and polarization effects, which are of crucial importance to characterize the QD–ligand interaction. To further discern between the charge transfer and the polarization contributions, we have made use of the Extended Transition State–Natural Orbitals for Chemical Valence scheme (ETS–NOCV) [511, 512]. Such an approach enables us to split the orbital interaction in several terms, each one arising from the chemically meaningful interactions between complementary pairs of molecular orbitals, which define the channels for transfer of electron density.

Recall that within this energy decomposition scheme the repulsive and the attractive interactions are positive and negative, respectively. Therefore, the more negative the energy term, the more attractive the corresponding interaction.

4.4.4 Results and Discussion

Bare $(ZnS)_6$

As shown in Figure 4.24 (b), the optimized Zn6S6 cluster can be envisioned as two bent hexagonal $(ZnS)_3$ rings stacked one on top of the other. The resulting prism possesses D_{3d} symmetry. Given such symmetry the cluster shows two types of d(Zn–S) bond distances. Within the $(ZnS)_3$ rings, the average bond length is 2.288 Å, while the distance between the parallel$(ZnS)_3$ units is 2.469 Å. Compared with respect to the ideal wurtzite structure (Figure 4.24(a)), Zn atoms move inward, while S atoms tend to relax outward. The ideal $(ZnS)_6$ wurtzite cluster shows three doubly coordinated Zn atoms on one of the $(ZnS)_3$ facets and three doubly coordinated S atoms on the other $(ZnS)_3$ facet. The optimized $(ZnS)_6$ exhibits flatter $(ZnS)_3$ rings. In the relaxed structure, all the surface atoms are 3-fold coordinated since the surface reconstruction brings the unsaturated ions closer. However, the bond distances aforementioned point out that the bond is slightly stronger within the $(ZnS)_3$ rings than between them. The shape and symmetry of the relaxed cluster are in good agreement with previously reported results.(49)

The frontier orbitals play a significant role in the chemical and optical properties of the cluster. The HOMO orbital consists mainly of S *3p* orbitals, whereas the LUMO is composed by Zn *4s/4p* hybrid orbitals (Figure 4.25). In the framework of a donor–acceptor picture of the bonding, the coordination of donor ligands is expected to occur through Zn since the low-lying unoccupied orbitals are mainly located in the metal atoms. The electrostatics of the interaction agree with this prediction since Zn atoms are positively charged, whereas ligands possess negatively charged heteroatoms. In line with this hypothesis, a couple of recent theoretical studies regarding the interaction between CdSe clusters and diverse molecules point out that the ligands do not bind to Se atoms [279, 332]. However, Puzder and co-workers reported that amines are expected to bind stronger with Se atoms than Cd atoms [491]. Therefore, we have also assessed the coordination of the ligands to the S atoms. Our geometry optimizations show that ligands do not link to S atoms and move onto nearby Zn atoms. Thus, we decided to focus our study simply on the passivation of Zn atoms.

$(ZnS)_6$-One-Ligand Complexes

We started by investigating the interaction between $(ZnS)_6$ and one ligand of each type. Recall that once the missing parameters have been calculated using the Badger's rules, the geometries have been fully optimized at the QM/MM level. The structures found have been further optimized at the pure QM level to obtain the fully converged complexes.

Geometry

Figure 4.26 displays the relevant geometric parameters considered for the structural characterization of the singly passivated complexes. The values of such parameters, corresponding to the structures optimized at QM/MM and QM levels, are shown in Table 4.17.

At first glance to the optimized complexes, a significant distortion of the cluster with respect to the bare $(ZnS)_6$ is noticeable. The distortion implies a relaxation of the passivated Zn atom toward the ligand.To quantify such pyramidalization, the average $\omega(S\text{–}Zn\text{–}S\text{–}S)$ dihedral angle (ω_{pyr}), formed by the passivated Zn atom (highlighted in blue in Figure 4.26) and its neighboring S atoms (highlighted in red in Figure 4.26), has been computed. Note also that the smaller the value of such an angle the greater the pyramidalization of the Zn atom.

Both QM/MM and QM structures exhibit an outer relaxation of the Zn atom with respect to the bare $(ZnS)_6$, as shown by the decrease of ω_{pyr} (Table 4.17). Accordingly, a slight elongation of the $d(Zn\text{–}S)_1$ bond length within the $(ZnS)_3$ units occurs due to the ligand attachment, while the $d(Zn\text{–}S)_2$ bond length remains nearly the same. The $d(Zn\text{–}S)_1$ distances are lengthened due to the donation of the electron density from the capping ligands to the Zn–S bonds.

The parameters shown in Table 4.17 reveal that the geometries provided by QM/MM and QM approaches are in quite good agreement. To further assess the performance of the QM/MM calculations, the Root Mean Square Deviation (RMSD) of the Zn and S atoms of the QM/MM complexes, calculated with respect to the reference QM structures, has been included in Table 4.17. The low RMSDs corroborate that QM/MM properly describes the geometry of the cluster.

The coordination bond length d(Zn–X) has shown to be strongly ligand dependent. At this point, and for the sake of clarity, we decided to split the set of the ligands studied in two subsets that group together the structurally similar molecules. On one side, NMe_3, PMe_3, and $OPMe_3$, and on the other, MeOH, MeSH, and MeSeH. Comparing NMe_3, PMe_3, and $OPMe_3$, we observe that d(Zn–X) varies in the order Zn–O < Zn–N < Zn–P. The trend is in line with the van der Walls radii of O (1.52 Å), N (1.55 Å), and P (1.80 Å). Comparing MeOH, MeSH, and MeSeH, we notice that d(Zn–X) increases as Zn–O < Zn–S < Zn–Se, also in agreement with the van der Walls radii of O (1.52 Å), S (1.80 Å), and Se (1.90 Å). We can conclude that irrespective of the method the coordination bond length increases with the size of the heteroatom X in the ligand.

The bond energies and the bond energy decomposition of the complexes with a single surface ligand are discussed in the following sections.

Bond Energies

The bond energies ($\triangle E$) of the structures optimized at the QM level are listed in Table 4.18. The negative values of the bond energies reveal that all complexes studied are stable. It is worth noting that NMe_3, PMe_3, and $OPMe_3$ show a significantly greater affinity than MeOH, MeSH, and MeSeH. Actually, long chain phosphines, amines, and phosphine oxides

are commonly employed ligands for the production of II–VI nanostructures. If we focus on comparable ligands bearing heteroatoms X of the same group, namely, NMe_3 *vs* PMe_3 and MeOH *vs* MeSH *vs* MeSeH, we notice that the softer the heteroatom, the greater the interaction energy, even if the d(Zn–X) distances are longer.

Zn^{2+} is a metal of borderline hardness in the framework of the Pearson's Hard and Soft Acids and Bases theory (HSAB), and it easily accommodates N, O (hard bases), and S (soft base) in its biological coordination sphere [285].

To explain the role of the number and the length of the alkyl groups of the ligand, complexes formed between the inorganic cluster and several amines have been optimized, and their interaction energies have been computed (Table 4.19). We decided to modify the nucleophilicity of the ligand by changing the number and the nature of the electron-donating groups of the ligand. The results reveal that, in general, as the number and the length of the alkyl groups increases, the interaction is strengthened. This finding is in line with previous works of Yang and co-workers regarding the interaction between $(CdSe)_n$ and several ligands. In an earlier study, they reported a stronger bond between the $(CdSe)_3$ and NMe_3, PMe_3 and $OPMe_3$ ligands compared to the corresponding bond between the cluster and NH_3, PH_3, and OPH_3.(41) The weaker interaction was attributed to their lower nucleophilicity, due to the lack of electron-donating methyl groups. More recently, they observed the same trend in the interaction energies computed between $(CdSe)_n$ (n = 6, 13) and several amines, phosphines, and phoshine oxides [332].

Bond Energy Decomposition

We employed the Ziegler and Rauk type energy decomposition scheme to analyze the interaction between $(ZnS)_6$ and the organic ligands. Table 4.18 shows a summary of the results obtained. Grimme's latest dispersion corrections [513] have also been computed ($\triangle E_{disp}$) to elucidate the role of the dispersion forces in the interaction. Such corrections have been calculated at the geometry obtained with the PBE functional since the molecular structures were not sensitive to the inclusion of dispersion.

As mentioned before, the energy decomposition analysis shows that all complexes assessed are stable. In terms of absolute values, the sum of the attractive interactions ($\triangle E_{attract} = \triangle V_{elst} + \triangle E_{oi} + \triangle E_{disp}$) is greater than the sum of repulsive terms ($\triangle E_{repul} = \triangle E_{Pauli} + \triangle E_{prep}$). Thus, the bond energy results are negative, *i.e.*, stabilizing. It is worth noting that the most important portion of the stabilization is electrostatic regardless of the ligand, covering as much as 60–65% of the attractive interaction. This observation is coherent with previous theoretical works [316, 514, 515]. Nevertheless, the orbital interaction is rather important as well.

The significance of the orbital term suggests an important polarization of the electron density in the surface of the cluster, in line with previous works regarding the surface passivation of CdSe clusters [293]. To quantify the charge redistribution induced by the adsorbed molecule, atomic charges have been computed with the Hirshfeld scheme [516].

As shown in Table 4.18, the cluster carries a significant net negative charge irrespective of

the ligand ($Q_{(ZnS)_6} < 0$), indicating a charge transfer from the adsorbed molecule, in agreement with recent theoretical results about the interaction between II–VI clusters and diverse surface attached molecules [316].

Comparing NMe_3 *vs* PMe_3 and MeOH *vs* MeSH *vs* MeSeH, we observe that the more polarizable the heteroatom X the greater the percentage of the orbital interactions at the expense of the electrostatic term. The $Q_{(ZnS)_6}$ charges reported in Table 4.18 are in agreement with this observation since the charge transferred increases with the polarizability of the heteroatom. These theoretical findings are in line with experimental works reporting a significant covalent character of the interaction between QDs and soft bases such as thiols [85].

Regarding the role of the alkyl groups of the ligands, the results shown in Table 4.19 reveal that as the number and the length of the alkyl chains increase, the weight of the orbital and dispersion terms augment at the expense of the electrostatic terms. Hirshfeld charges reported in Table 4.19 are in agreement with this observation; *i.e.*, the greater the contribution of the orbital and dispersion terms, the greater the charge transferred from the ligand to the cluster. The electron-donating effect of the alkyl groups is expected to be responsible of these findings.

ETS-NOCV

Even if the $Q_{(ZnS)_6}$ charges shown give an idea of the electron redistribution induced by the adsorbed molecule, the polarization of the charge density requires a more rigorous picture than the one given by the punctual charge approach. Indeed, the charges are not an observable, and there is an arbitrariness in their definition. Moreover, they provide an idea of the transfer of the charge density between the fragments, but they do not reflect the polarization occurring within each fragment. The above-mentioned ETS-NOCV scheme overcomes this deficiency and describes charge transfer and polarization effects on an equal foot. This method enables us to decompose the orbital interaction $\triangle E_{oi}$ into its several components $\triangle E^i_{oi}$, so that $\triangle E_{oi} = \sum_i \triangle E^i_{oi}$. The leading contributions to the orbital interaction are listed in Table 4.20. Each term$\triangle E^i_{oi}$ arises from the interaction of complementary pairs of NOCVs, namely, $NOCV^i_1$ and $NOCV^i_2$, which define the channels for charge transfer. The so-called deformation density $\triangle \rho^i_{oi}$ represents the change in the electron density associated to the charge transfer from $NOCV^i_1$ to $NOCV^i_2$. Figure 4.27 depicts $NOCV^1_1$ and $NOCV^1_2$, among which the leading contribution to the orbital interaction ($\triangle E^1_{oi}$) is computed. The associated deformation density ($\triangle \rho^1_{oi}$) is also shown.

Irrespective of the ligand, the deformation density reveals that the main contribution to the orbital interaction implies a polarization of the lone pair of the heteroatom X in the ligand toward the Zn atom. Therefore, a concentration of electron density is observed along the Zn–X bond. A closer inspection of the deformation density also shows a gain of electron density in the *3p* orbitals of the sulfur at the expense of the *4s* orbitals of the Zn. Overall, a flow of charge density occurs from the ligand to the cluster. This observation agrees with the $Q_{(ZnS)_6}$ charges reported in Table 4.18.

$(ZnS)_6$-Six-Ligand Complexes

As mentioned earlier, most of the studies regarding the surface passivated nanoparticles focus on the local interaction with a single ligand molecule [315,316,322,324,515]. The works in which the bonding of multiple ligands is investigated are rather scarce [279,293,298,332]. We believe that a proper description of the passivation phenomena should include at least a surrounding monolayer of ligands. On the one hand, the ligand–ligand interactions are taken into account. On the other hand, the way in which the properties of the cluster are modified due to the passivation depends on the number of surface attached molecules. Since our investigation of the complexes with a single-ligand molecule have shown that the methodology combining hybrid QM/MM optimization followed by QM reoptimization performs properly, we have employed it in the study of the fully passivated clusters. As mentioned before, the ideal $(ZnS)_6$ wurtzite cluster shows three 2-fold coordinated Zn atoms and three 3-fold coordinated Zn atoms. Therefore, at first glance, nine ligands would be required to remove all dangling bonds in the fully passivated $(ZnS)_6$. However, the optimized $(ZnS)_6$ cluster exhibits six 3-fold coordinated metal atoms since after the surface reconstruction the 2-fold coordinated Zn atoms become 3-fold coordinated. Thus, six ligands are enough to complete the coordination sphere of the unsaturated Zn atoms.

Geometry

Figure 4.28 displays the relevant geometric parameters considered for the structural characterization of the fully passivated complexes. The values of such parameters, corresponding to the structures optimized at QM/MM and QM levels, are shown in Table 4.21. To better describe the distortion of the cluster due to the ligands, the average distances of S and Zn atoms to the center of the cluster have been computed (hereafter referred to as r_S and r_{Zn}, respectively). In the bare cluster, the S atoms are placed outward with respect to the Zn atoms, as shown by r_S = 2.848 Å and r_{Zn} = 2.174 Å.

From previous studies [279, 316, 479] and the results reported for the cluster with a single surface ligand, an elongation of the Zn–S bonds is expected due to ligand bonding.

Both QM/MM and QM approaches reveal a relaxation of the Zn atoms outward the cluster. Since S atoms remain in their position, the Zn–S bonds elongate with respect to the bare cluster, in line with the above-mentioned studies. With the exception of the d(Zn–X) bond lengths, slightly overestimated, the geometries obtained with the QM/MM method are in good agreement with those obtained with pure QM.

Regardless of the method and the ligand, the coordination bond lengths d(Zn–X) are longer than the corresponding bond lengths of the complexes formed between $(ZnS)_6$ and one ligand. Again, the coordination bond length increases with the size of the heteroatom X in the ligand.

The bond energies and the bond energy decomposition of the fully passivated complexes are discussed in the following sections.

Bond Energies

The bond energies of the structures fully optimized at the QM level are given in Table 4.22. The bond energies listed are averaged bond energies for each ligand molecule. Comparing these with the corresponding values obtained for the singly passivated complexes, we notice that the average interaction energies per ligand are lower. This finding is in agreement with the longer d(Zn–X) distances observed for the fully covered cluster. Actually, the repulsion between neighbor ligands is expected to obstruct the adsorption. Moreover, the charge acceptor nature of the cluster will presumably diminish with the increasing number of donor ligands. As observed for the complexes with a single surface molecule, NMe_3, PMe_3, and $OPMe_3$ ligands show a significantly greater affinity than MeOH, MeSH, and MeSeH.

Table 4.22 reveals that MeSH and MeOH binding energies are the same despite S being significantly softer than O. It is likely that several factors interplay in the attachment of ligands to the surface of II–VI semiconductors so that the results could not be rationalized in light of the hardness/softness of the interacting molecules. Our results, together with previous theoretical works [279,293,325,332], suggest that the steric hindrance between ligand molecules, the charge acceptor nature of the cluster, and the occurrence of other interactions between the ligands and the cluster, etc., play an important role in the QD–ligand interaction.

Bond Energy Decomposition

The dispersion corrected energy decomposition analysis is shown in Table 4.22. In terms of absolute values, each contribution to the interaction energy is lower than in the case of a single ligand. As the d(Zn–X) bond lengths are longer, the Pauli repulsion between the electron densities is lower. Moreover, the preparation energies are smaller than those encountered for a single ligand. Nevertheless, the electrostatic and the orbital interaction are also weakened. The dispersion energy varies only slightly. Overall, the bond energies are lower. It is worth noting that the nature of the bond resembles the one observed for a single ligand. Even if the electrostatic contribution is the main term, the weight of the orbital interaction suggests a significant redistribution of the charge density. If we compare NMe_3 *vs* PMe_3 and MeOH *vs* MeSH *vs* MeSeH, we notice that the softer the heteroatom, the greater the percentage of the orbital interaction at the expense of the electrostatic term.

As in the case of a single ligand, the charges have been computed on the basis of the Hirshfeld scheme. The $Q_{(ZnS)_6}$ values reported in Table 4.22 show that the cluster carries a larger negative charge than in the case of a singly passivated cluster since the number of electron-donating ligands is greater, although the charge transferred per ligand is lower. As mentioned before, as the number of donor ligands increases, the charge acceptor nature of the cluster is expected to diminish. Finally, in line with the trends observed for a single ligand, the more polarizable the heteroatom X in the ligand, the greater the charge transferred to the cluster.

ETS-NOCV

To further clarify the charge transfer and polarization occurring due to the passivation, ETS-NOCV analysis has been performed. Table 4.23 shows that regardless of the ligand there are six terms that mainly contribute to the orbital stabilization. Figure 4.29 depicts the sum

of the deformation densities associated to such pairs ($\triangle\rho_{oi}^{1-6} = \sum_{i=1}^{6} \triangle\rho_{oi}^{i}$). The deformation density shows a significant polarization of the lone pair of the heteroatom X in the ligand toward the Zn atom. Therefore, there is a concentration of the electron density along the Zn–X bond. Moreover, sulfur atoms in the cluster are enriched in charge. These findings are in agreement with those reported in the case of a single ligand, supporting the idea that the nature of the interaction does not change as the number of surface attached molecules increases.

4.4.5 Summary and Conclusions

We have reported on the computational modeling of the interaction between ZnS QDs and surface attached ligands. $(ZnS)_6$ nanostructure has been chosen to model the QD core. Trimethylamine (NMe_3), trimethylphosphine (PMe_3), trymethylphosphine oxide (OPMev), methanol (MeOH), methanethiol (MeSH), and methaneselenol (MeSeH) have been studied as surface ligands.

To tackle these passivated systems in an efficient manner, the performance of the hybrid QM/MM method has been assessed. In a first approach, the cluster has been included in the QM region, and the ligands have been described by means of MM. However, the lack of orbital interaction between the QM and MM regions yields a poor description of the geometry of the complexes. The QM region has therefore been expanded to include the ligand atom X directly bonded to the cluster. We have taken advantage of the QM/MM method to sample different structures of the coordinate space in a computationally efficient manner and to obtain suitable starting points for further and more refined QM calculations.

To shed light on the nature of the QD–ligand interaction, we focused our investigation on the structural and energetic aspects. Regarding the former, an outer relaxation of the passivated Zn atoms has been observed. At the same time, an elongation of the Zn–S bonds is visible. The QD–ligand bond is highly directional, and its length increases with the size of the ligand atom X attached to the cluster.

Regarding the energetics, we can conclude that NMe_3, PMe_3, and $OPMe_3$ show a significantly greater affinity than MeOH, MeSH, and MeSeH. We have observed that the softer the heteroatom of the ligand bonded to the cluster, the greater the interaction energy. The comparative study of different amines reveals that, in general, as the number and the length of the alkyl chains increase, the interaction is strengthened. The interaction is mainly electrostatic regardless of the ligand, covering 60–65% of the attractive interaction. However, in view of the weight of the orbital interaction term, an important polarization of the electron density can be envisaged. Indeed, the Hirshfeld scheme suggest an important charge redistribution in the complexes, which implies a charge transfer from the ligand to the cluster. ETS-NOCV has shown that such a transfer occurs due to the polarization of the lone pair of the heteroatom X in the ligand toward the Zn atom. We noticed that the softer the heteroatom of the ligand bonded to the cluster, the greater both the percentage of the orbital

interaction and the charge transferred to the cluster. The comparative investigation of the amines shows that as the number and the length of the alkyl moieties increase, the weight of the orbital and dispersion terms augment at the expense of the electrostatic term. This finding has been ascribed to the electron-donating effect of the alkyl groups.

The study of the fully passivated complexes reveals that the bond energies for each ligand molecule are lower (in absolute value) than those encountered for a single ligand. In fact, the repulsion between neighbor ligands is expected to obstruct the adsorption. Moreover, the charge acceptor nature of the cluster will presumably diminish with the increasing number of electron-donating ligands.

We believe that this work paves the way for further studies on semiconductor quantum dots.

Table 4.17: Geometric parameters of the complexes formed between $(ZnS)_6$ and one ligand of each type. RMSD: Root Mean Square Deviation of the Zn and S atoms of the QM/MM complexes, calculated with respect to the reference QM structures; d(Zn-S)$_1$: average bond length within $(ZnS)_3$ units; d(Zn-S)$_2$: average bond length between Zn_3S_3 units; ω_{pyr}: average ω(S-Zn-S-S) dihedral angle formed by the passivated Zn atom and its neighboring S atoms; d(Zn-X): Zn-X coordination bond length; α(S-Zn-X): (S-Zn-X) angle. Distances in Å and angles in degrees.

	Level	d(Zn-S)$_1$	d(Zn-S)$_2$	ω_{pyr}
Bare $(ZnS)_6$	QM	2.288	2.469	136.3

Ligand	Level	RMSD	d(Zn-S)$_1$	d(Zn-S)$_2$	ω_{pyr}	d(Zn-X)	α(S-Zn-X)
NMe_3	QM/MM	0.034	2.295	2.464	123.6	2.101	105.1
	QM		2.299	2.466	119.8	2.120	109.0
PMe_3	QM/MM	0.060	2.292	2.479	125.2	2.407	93.1
	QM		2.301	2.466	116.3	2.396	108.7
$OPMe_3$	QM/MM	0.017	2.306	2.471	119.0	2.065	105.7
	QM		2.299	2.471	116.5	2.002	109.0
MeOH	QM/MM	0.010	2.294	2.467	126.2	2.163	104.1
	QM		2.299	2.470	124.4	2.126	109.3
MeSH	QM/MM	0.034	2.290	2.464	124.4	2.511	111.8
	QM		2.292	2.463	122.0	2.459	105.8
MeSeH	QM/MM	0.019	2.293	2.467	116.5	2.619	107.7
	QM		2.297	2.466	121.1	2.579	105.0

Table 4.18: Dispersion corrected energy decomposition analysis of the complexes formed between $(ZnS)_6$ and one ligand of each type. Energies given in Kcal/mol. Values in parentheses give the percentage of each attractive or repulsive term with respect to the sum of the attractive or repulsive terms, respectively. $Q_{(ZnS)_6}$, given in atomic units, indicates the charge carried by the $(ZnS)_6$ cluster. The values shown correspond to the structures optimized at pure QM level from QM/MM structures.

	NMe_3		PMe_3		$OPMe_3$		MeOH		MeSH		MeSeH	
$\triangle V_{elst}$	-71.2	(65%)	-81.5	(64%)	-63.5	(62%)	-42.0	(64%)	-46.5	(60%)	-45.8	(59%)
$\triangle E_{oi}$	-32.3	(29%)	-40.6	(32%)	-34.4	(33%)	-20.4	(31%)	-27.6	(35%)	-27.8	(36%)
$\triangle E_{disp}$	-6.5	(6%)	-5.2	(4%)	-4.9	(5%)	-3.1	(5%)	-3.8	(5%)	-3.9	(5%)
$\triangle E_{attrac}$	-110.1		-127.3		-102.8		-65.5		-77.9		-77.5	
$\triangle E_{Pauli}$	74.3	(95%)	87.4	(92%)	66.6	(92%)	45.1	(96%)	55.4	(96%)	54.2	(96%)
$\triangle E_{prep}$	3.9	(5%)	7.6	(8%)	5.8	(8%)	1.7	(4%)	2.3	(4%)	2.4	(4%)
$\triangle E_{repul}$	78.2		95.0		72.4		46.8		57.7		56.6	
$\triangle E$	**-31.9**		**-32.4**		**-30.4**		**-18.7**		**-20.2**		**-20.9**	
$Q_{Zn_6S_6}$	-0.19		-0.22		-0.18		-0.13		-0.17		-0.18	

Table 4.19: Dispersion corrected energy decomposition analysis of the complexes formed between $(ZnS)_6$ and one amine of each type. Energies given in Kcal/mol. Values in parentheses give the percentage of each attractive or repulsive term with respect to the sum of the attractive or repulsive terms, respectively. $Q_{(ZnS)_6}$, given in atomic units, indicates the charge of the $(ZnS)_6$ cluster. The values shown correspond to the structures optimized at pure QM level from QM/MM structures.

	NH_3		NH_2Me		$NHMe_2$		NMe_3		NEt_3		NPr_3	
$\triangle V_{elst}$	-62.9	(67%)	-68.2	(67%)	-70.8	(66%)	-71.2	(65%)	-73.4	(62%)	-71.9	(61%)
$\triangle E_{oi}$	-27.6	(30%)	-29.6	(29%)	-31.2	(29%)	-32.4	(29%)	-36.1	(30%)	-35.8	(31%)
$\triangle E_{disp}$	-2.7	(3%)	-3.8	(4%)	-5.1	(5%)	-6.5	(6%)	-9.2	(8%)	-9.9	(8%)
$\triangle E_{attrac}$	-93.2		-97.6		-107.1		-110.1		-118.7		-117.6	
$\triangle E_{Pauli}$	64.9	(97%))	69.5	(96%)	72.5	(96%)	74.2	(95%)	78.2	(92%)	76.5	(91%)
$\triangle E_{prep}$	2.2	(3%))	2.6	(4%)	3.3	(4%)	3.9	(5%)	7.2	(8%)	7.2	(9%)
$\triangle E_{repul}$	67.1		72.1		75.8		78.1		85.4		83.7	
$\triangle E$	**-26.1**		**-25.5**		**-31.3**		**-32.0**		**-33.3**		**-33.9**	
$Q_{Zn_6S_6}$	-0.17		-0.18		-0.19		-0.20		-0.21		-0.21	

Table 4.20: ETS-NOCV analysis of the complexes formed between $(ZnS)_6$ and a single ligand of each type. Energies given in Kcal/mol. Values in parentheses give the percentage of each term $\triangle E^i_{oi}$ with respect to the total orbital interaction $\triangle E_{oi}$. The values shown correspond to the structures optimized at pure QM level from QM/MM structures.

Ligand	NMe_3		PMe_3		$OPMe_3$		MeOH		MeSH		MeSeH	
$\triangle E_{oi}$	-32.4		-40.6		-34.4		-20.4		-27.3		-27.8	
$\triangle E^1_{oi}$(%)	-23.2	(72%)	-32.3	(79%)	-21.8	(64%)	-14.6	(72%)	-20.9	(77%)	-22.5	(81%)
$\triangle E^2_{oi}$(%)	-2.3	(7%)	-3.0	(7%)	-3.4	(10%)						
$\triangle E^3_{oi}$(%)					-3.2	(9%)						
$\triangle E^4_{oi}$(%)					-2.4	(7%)						

Table 4.21: Geometric parameters of the complexes formed between $(ZnS)_6$ and six ligand of each type. d(Zn-S)$_1$: average bond length within $(ZnS)_3$ units; d(Zn-S)$_2$: average bond length between $(ZnS)_3$ units; r_S and r_{Zn}: average distance of S and Zn atoms, respectively, with respect to the center of the cluster (values in parentheses indicate the difference with respect to the bare cluster). d(Zn-X): Zn-X bond length (values in parentheses indicate the difference with respect to the corresponding complexes formed between Zn_6S_6 and one ligand of each type); α(S-Zn-X): (S-Zn-X) angle (values in parentheses indicate the difference with respect to the corresponding complexes formed between Zn_6S_6 and one ligand of each type). Distances in Å and angles in degrees.

Cluster	d(Zn-S)$_1$	d(Zn-S)$_2$	r_S	r_{Zn}
Zn_6S_6	2.288	2.469	2.848	2.174

Ligand	Level	d(Zn-S)$_1$		d(Zn-S)$_2$		r_S		r_{Zn}		d(Zn-X)		α(S-Zn-X)	
NMe_3	QM/MM	2.343	(0.055)	2.449	(-0.020)	2.824	(-0.024)	2.386	(0.212)	2.220	(0.100)	115.5	(6.5)
	QM	2.337	(0.049)	2.460	(-0.009)	2.849	(0.001)	2.313	(0.139)	2.191	(0.071)	109.0	(0.0)
PMe_3	QM/MM	2.312	(0.024)	2.515	(0.046)	2.860	(0.012)	2.449	(0.275)	2.449	(0.053)	96.7	(-12.0)
	QM	2.352	(0.064)	2.469	(0.000)	2.844	(-0.004)	2.366	(0.192)	2.476	(0.080)	106.1	(-2.6)
$OPMe_3$	QM/MM	2.335	(0.047)	2.476	(0.007)	2.845	(-0.003)	2.323	(0.149)	2.234	(0.232)	104.0	(-5.0)
	QM	2.333	(0.045)	2.484	(0.015)	2.837	(-0.011)	2.347	(0.173)	2.126	(0.124)	105.0	(-4.0)
MeOH	QM/MM	2.316	(0.028)	2.461	(-0.008)	2.842	(-0.006)	2.280	(0.106)	2.235	(0.109)	106.5	(-2.8)
	QM	2.320	(0.032)	2.490	(0.021)	2.856	(0.008)	2.274	(0.100)	2.206	(0.203)	104.0	(-5.3)
MeSH	QM/MM	2.311	(0.023)	2.469	(0.000)	2.841	(-0.007)	2.268	(0.094)	2.595	(0.136)	103.2	(-2.6)
	QM	2.308	(0.020)	2.491	(0.022)	2.831	(-0.017)	2.283	(0.109)	2.540	(0.081)	92.8	(-13.0)
MeSeH	QM/MM	2.315	(0.027)	2.469	(0.000)	2.843	(-0.005)	2.275	(0.101)	2.706	(0.127)	102.7	(-2.3)
	QM	2.329	(0.041)	2.463	(-0.006)	2.841	(-0.007)	2.312	(0.138)	2.687	(0.108)	107.1	(2.1)

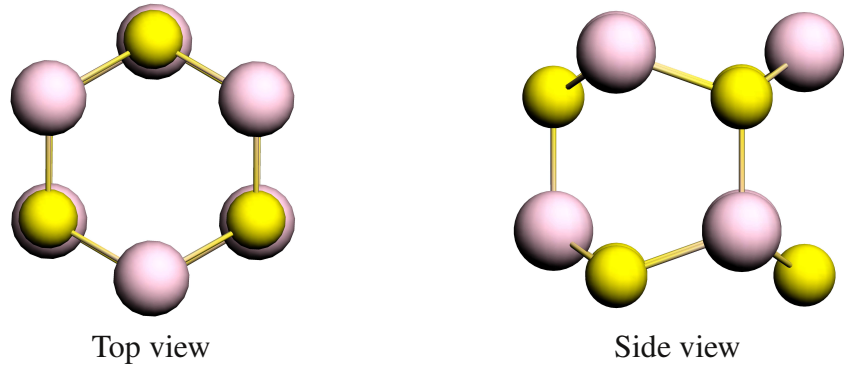
Table 4.22: Dispersion corrected energy decomposition analysis of the complexes formed between $(ZnS)_6$ and six ligand of each kind. Energies per ligand molecule given in Kcal/mol. Values in parentheses give the percentage of each attractive or repulsive term with respect to the sum of the attractive of repulsive terms, respectively. $Q_{(ZnS)_6}$, given in atomic units, indicates the charge carried by the $(ZnS)_6$ cluster. The values shown correspond to the structures optimized at pure QM level from QM/MM structures.

	NMe_3		PMe_3		$OPMe_3$		MeOH		MeSH		MeSeH	
$\triangle V_{elst}$	-58.8	(64%)	-60.9	(63%)	-47.8	(62%)	-37.3	(63%)	-39.0	(60%)	-35.9	(59%)
$\triangle E_{oi}$	-26.3	(29%)	-30.8	(32%)	-24.0	(31%)	-18.8	(32%)	-22.6	(34%)	-21.0	(35%)
$\triangle E_{disp}$	-6.6	(7%)	-5.1	(5%)	-5.3	(7%)	-3.0	(5%)	-3.8	(6%)	-3.9	(6%)
$\triangle E_{attrac}$	-91.7		-96.8		-77.1		-59.1		-65.4		-60.8	
$\triangle E_{Pauli}$	63.3	(97%)	68.0	(94%)	51.3	(95%)	41.9	(97%)	47.8	(97%)	42.5	(97%)
$\triangle E_{prep}$	2.0	(3%)	4.3	(6%)	2.6	(5%)	1.3	(3%)	1.4	(3%)	1.4	(3%)
$\triangle E_{repul}$	65.3		72.3		53.9		43.2		49.2		43.9	
$\triangle E$	**-26.4**		**-24.5**		**-23.2**		**-16.0**		**-16.2**		**-16.9**	
$Q_{Zn_6S_6}$	-0.69		-0.74		-0.55		-0.50		-0.62		-0.66	

Table 4.23: ETS-NOCV analysis of the complexes formed between $(ZnS)_6$ and six ligands of each type. Energies given in Kcal/mol. Values in parentheses give the percentage of each term with respect to the total orbital interaction. The values shown correspond to the structures optimized at pure QM level from QM/MM structures.

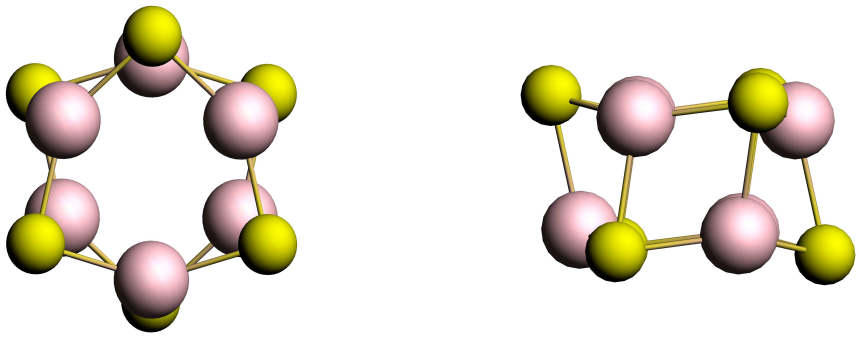
Ligand	NMe_3		PMe_3		$OPMe_3$		MeOH		MeSH		MeSeH	
$\triangle E_{oi}$	-157.5		-184.6		-143.7		-112.7		-135.4		-125.9	
$\triangle E^1_{oi}(\%)$	-21.0	(13%)	-27.9	(15%)	-17.8	(12%)	-15.4	(14%)	-19.6	(14%)	-21.0	(17%)
$\triangle E^1_{oi}(\%)$	-17.9	(11%)	-26.0	(14%)	-14.9	(10%)	-13.0	(12%)	-19.6	(14%)	-19.4	(15%)
$\triangle E^1_{oi}(\%)$	-16.6	(11%)	-21.3	(12%)	-14.6	(10%)	-11.9	(11%)	-14.6	(11%)	-14.8	(12%)
$\triangle E^1_{oi}(\%)$	-16.6	(11%)	-21.3	(12%)	-13.9	(10%)	-11.7	(10%)	-14.3	(11%)	-14.7	(12%)
$\triangle E^1_{oi}(\%)$	-16.5	(10%)	-21.1	(11%)	-13.7	(10%)	-11.3	(10%)	-14.1	(10%)	-14.5	(12%)
$\triangle E^1_{oi}(\%)$	-16.5	(10%)	-21.1	(11%)	-13.3	(9%)	-11.3	(10%)	-13.7	(10%)	-14.4	(11%)

Figure 4.24: Geometrical structure of (a) unrelaxed $(ZnS)_6$ cut from the bulk wurtzite and (b) relaxed $(ZnS)_6$. Pink = Zn and yellow = S atoms.



Top view Side view

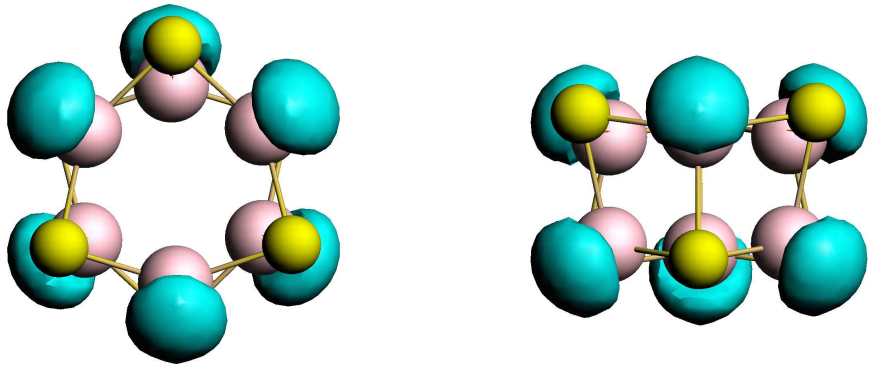
a



Top view Side view

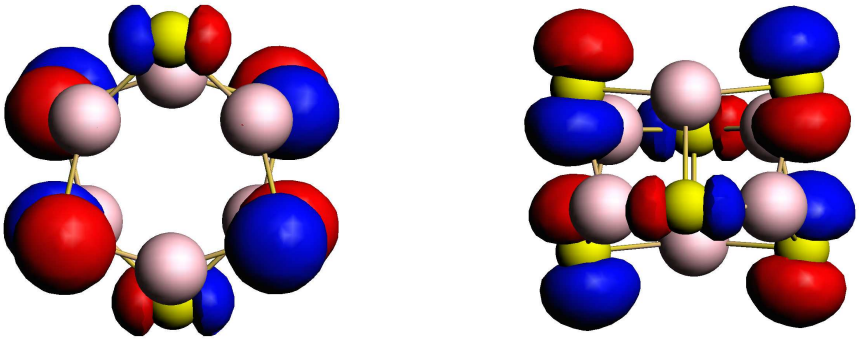
b

Figure 4.25: Frontier orbitals of the bare $(ZnS)_6$ cluster. Pink = Zn and yellow = S atoms.



Top view Side view

LUMO



Top view Side view

HOMO

Figure 4.26: Relevant geometric parameters of the complexes formed between $(ZnS)_6$ and one ligand of each type. Pink = Zn, yellow = S, blue = N, dark gray = C and white = H atoms.

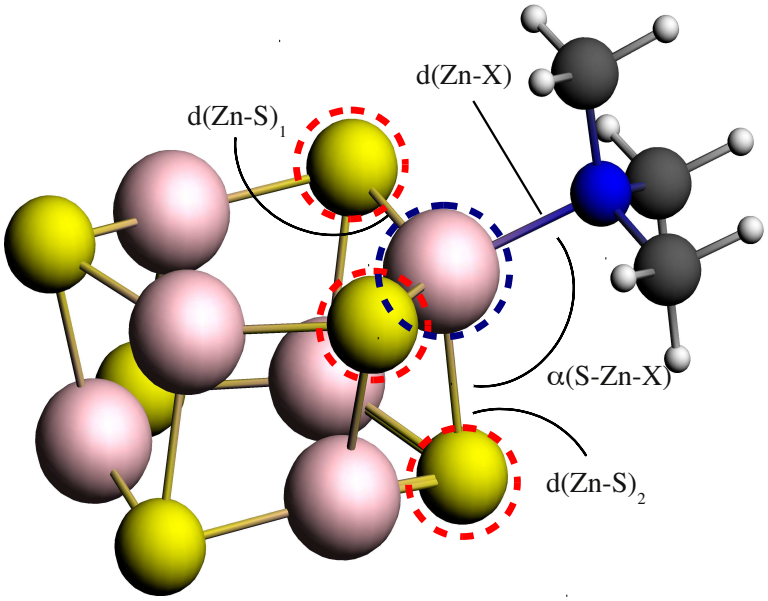


Figure 4.27: Contour plots of complementary $NOCV^1_1$ and $NOCV^1_2$ among which the leading contribution to the orbital interaction ($\triangle E^1_{oi}$) occurs. The associated deformation density ($\triangle \rho^1_{oi}$) is also shown. The contour values of the NOCV are ± 0.05 a.u.. The deformation densities are plotted with a smaller contour value of ± 0.001 a.u. for sake of visibility. The regions in which the deformation density is positive (meaning a concentration of electron density) are depicted in blue and those in which such deformation is negative (meaning a depletion of electron density) are colored in red. The pictures shown correspond to the structures optimized at pure QM level from QM/MM structures. Pink = Zn, yellow = S, blue = N, dark gray = C, white = H, orange = P, red = O and green = Se atoms.

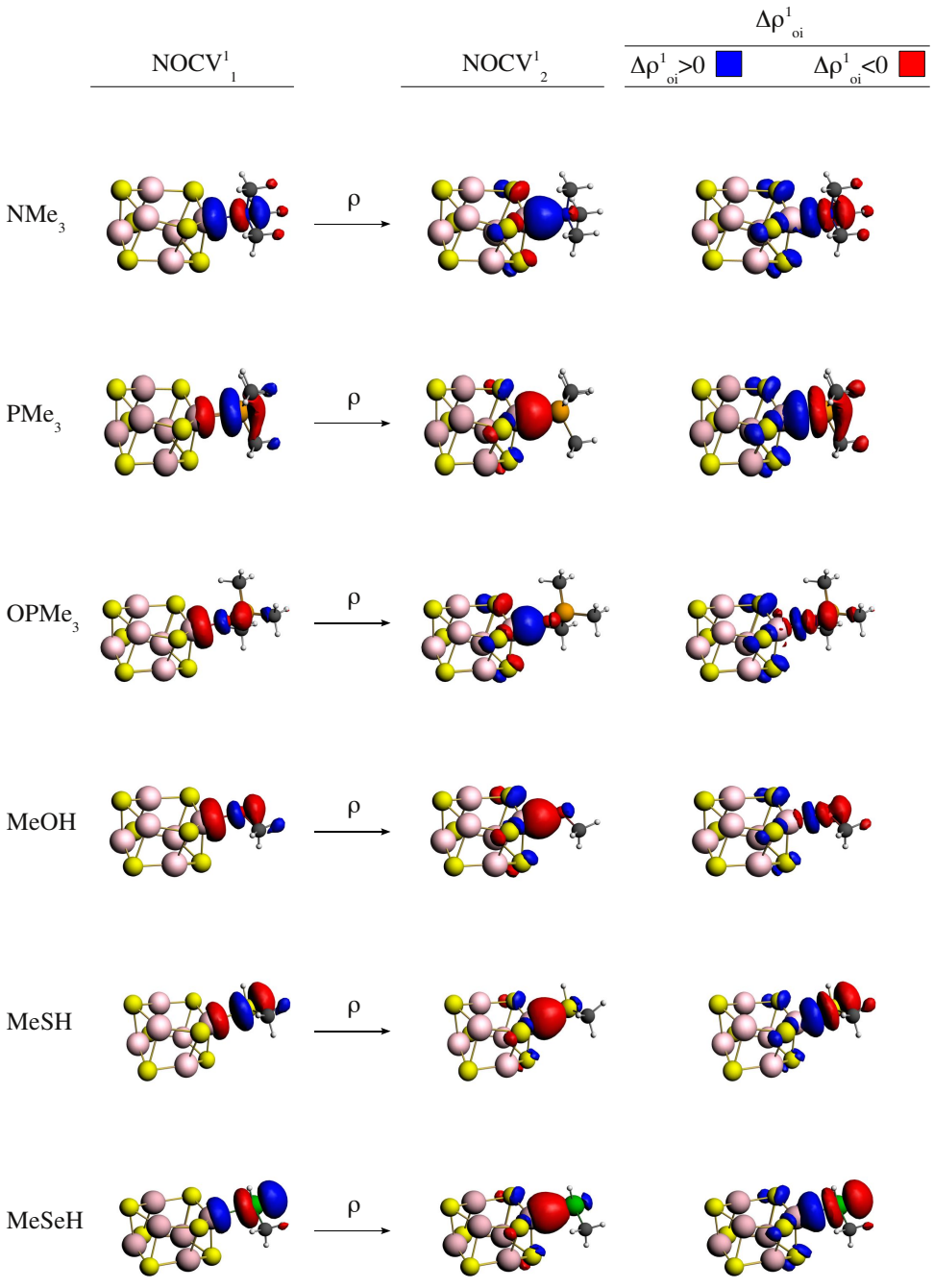


Figure 4.28: Relevant geometric parameters of the of the complexes formed between $(ZnS)_6$ and six ligands of each type. Pink = Zn, yellow = S, blue = N, dark gray = C and white = H atoms.

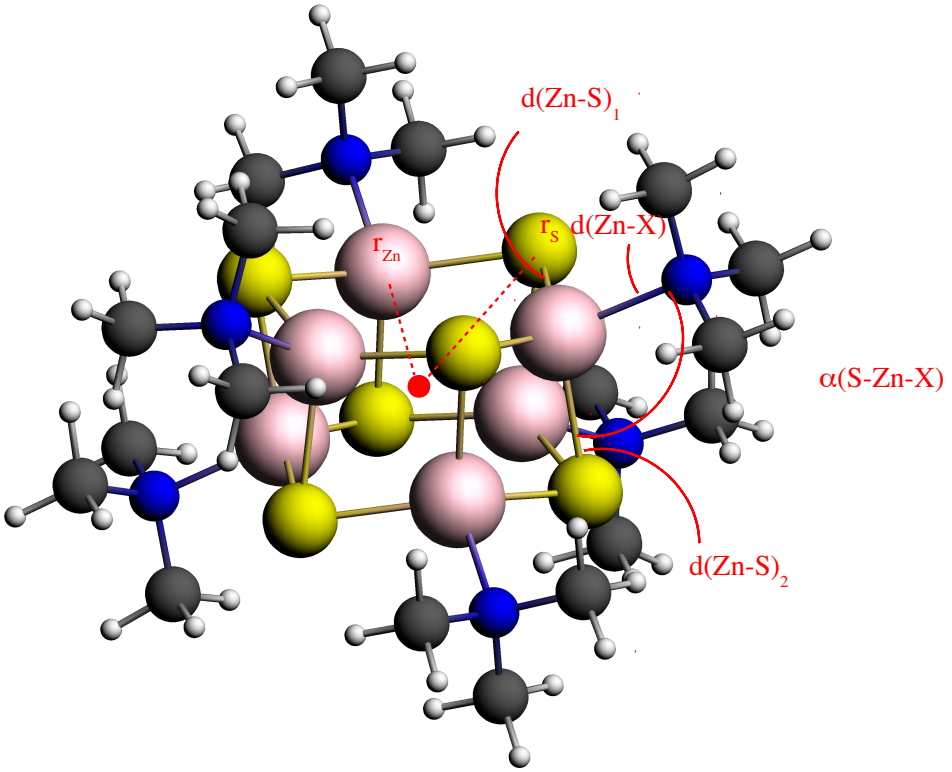
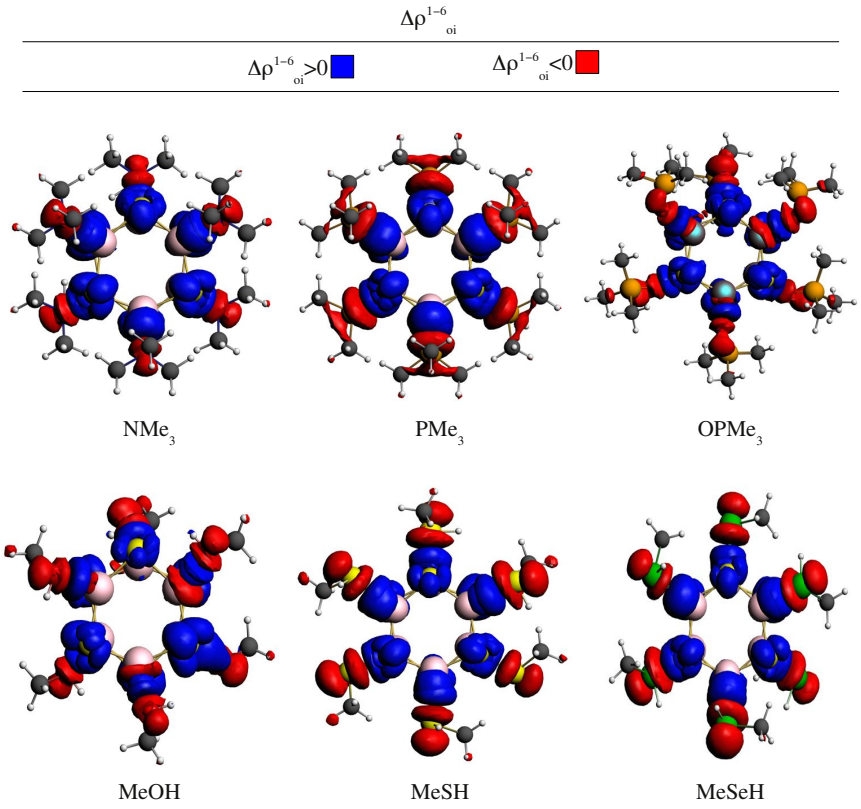


Figure 4.29: Contour plots of deformation density associated to the sum of the six leading contributions to the orbital interaction ($\triangle\rho_{oi}^{1-6} = \sum_{i=1}^{6} \triangle\rho_{oi}^{i}$). Such densities are plotted with a contour value of ± 0.0005 a.u. for sake of visibility. The regions in which the deformation density is positive (meaning a concentration of electron density) are depicted in blue and those in which such deformation is negative (meaning a depletion of electron density) are colored in red. The pictures shown correspond to the structures optimized at pure QM from QM/MM structures. Pink = Zn, yellow = S, blue = N, dark gray = C, white = H, orange = P, red = O and green = Se atoms.



4.5 A DFT/TDDFT Study on the Optoelectronic Properties of the Amine-Capped Magic $(CdSe)_{13}$ Nanocluster

4.5.1 Abstract

Motivated by the recent experiments by Wang et al. (*Angew. Chem. Int. Ed.* **2012**, *51*, 6154-6157), in which the alkylamine-capped magic-size $(CdSe)_{13}$ has been isolated for the first time, we report on the computational modeling of the putative low-lying isomers of $(CdSe)_{13}$, both bare and ligand-protected. According to DFT (DFT) calculations, the core@cage configuration $Se@Cd_{13}Se_{12}$, consisting in a Se atom incarcerated in the center of a puckered $Cd_{13}Se_{12}$ cage, lies lower in energy than fullerene- and wurtzite- like structures. Methylamine-capped nanoclusters present average bond energies per ligand of about 20 kcal/mol, while bond energy decomposition schemes show this interaction to be mostly electrostatically-driven. The computed Time-Dependent-DFT (TDDFT) spectrum of the low-lying methylamine-protected $(CdSe)_{13}$ isomer essentially coincides with the experiment, with a notable blueshift of the absorption features induced by the ligands. The LUMO has been found to be the acceptor orbital for all the lowest-lying electronic excitations, in both the bare and methylamine-capped clusters, which could explain the narrow emission profiles inherent in semiconductor nanostructures. In addition, the attachment of pyridine and aniline molecules has been evaluated. Interestingly, the molecular orbitals of these aromatic amines located on the edges of the valence and conduction bands may act as trap states, in agreement with experimental evidences. In the particular case of pyridine molecules, unoccupied orbitals intrude into the HOMO-LUMO gap of the cluster.

4.5.2 Introduction

In the last couple of decades, nanometric materials have been attracting a great deal of interest [273] due to their peculiar structural and electronic properties that deviate significantly from their bulk counterparts [4, 53, 272]. There are mostly two reasons responsible for this discrepancy. On one hand, the number of atoms forming nanostructure surface is a significant fraction of the total. These unsaturated atoms tend to reorganize in order to minimize the surface energy, favoring particular polymorphs and eventually leading to fancy atomic arrangements. Interestingly, the phase stability varies with size and shape. Due to the large surface-to-volume ratio inherent in nanometric materials, the environment (solvent and surface ligands) plays a pivotal role on the geometry of the nanostructure, which in turn determines its electronic and optical properties. On the other hand, charge carriers (electrons and holes) are confined to move in small regions of space. This confinement (also known as quantum confinement) results in the discretization of the electronic energy levels, in contrast to the continuous bands typical of macroscopic materials. As a consequence, the electronic and optical properties depend on the nanostructure size and shape. For instance, a characteristic blueshift of absorption/emission features is observed with the decreasing size of the

material. Again, surface attached ligands exert a strong influence on the properties of the nanomaterial.

In view of their paramount technological potential, a huge effort has been put forward to characterize II-VI semiconductor nanostructures (II = Zn, Cd; VI = O, S, Se, Te). Their outstanding properties like broad excitation bands, large extinction coefficient, tunable emission features, bright photoluminescence, non-linear optical properties, and high stability against photobleaching and chemicals, make them amenable for solar cell components [146, 147], optical sensors [133,274], and optoelectronic devices [275]. Recent advances in biofunctionalization have paved the way for the *in vivo* application of II-VI semiconductor nanostructures [68, 192]. The combined effect of their particular surface morphologies and quantum confinement allow these materials to be recurrently employed as catalysts [129–132].

Experimentally, the formation of nanostructures with well-defined numbers of constituent atoms has been reported. These aggregates, often referred to as magic-size clusters, exhibit exceptional stability relative to neighboring sizes. Interest on such magic nanostructures has increased notably in the last years for their promising feature of being used as building blocks for the bottom-up assembly of functional materials. Starting in 1984, when Knight et al. proved the existence of extremely stable stoichiometries for clusters of alkali metals [517], a myriad of magic nanostructures has been reported. $(ZnS)_n$ clusters with n = 13, 33, 34 and $(ZnSe)_n$ clusters with n = 6, 13, 19, 22, 23 were found to be particularly stable [518, 519]. More recently, laser ablation experiments have revealed that the stability of n = 13, 33 and 34 stoichiometries prevails for $(ZnTe)_n$, $(CdS)_n$, $(CdSe)_n$, and $(CdTe)_n$ [17, 18]. In the particular case of CdSe, n = 19 has been reported to be magic as well [17]. Interestingly, the formation of magic $(CdSe)_n$ clusters (n = 13, 19, 33, 34) has also been observed in solution, both in organic solvents [17, 469, 470, 520, 521] and in water [19, 20].

Unfortunately, the tiny space and time scales inherent in nanostructures make their experimental characterization challenging. Structure determination from the experiment is difficult and spectroscopic measurements provide indirect and often incomplete information. In this sense, computational modeling has emerged as a valuable tool for the understanding of nanometric materials. Among the II-VI semiconductor nanostructures, CdSe is probably the most extensively studied. Ultrasmall $(CdSe)_n$ clusters with n = 6-20 have been predicted to adopt cage-shaped structures [325, 522]. Calculations show that magic $(CdSe)_{13}$ and $(CdSe)_{19}$ clusters exhibit a core@cage arrangement [17, 325]. About the former, a C_3-symmetry $Se@Cd_{13}Se_{12}$ has been claimed to be the lowest-lying configuration, characterized by a puckered $Cd_{13}Se_{12}$ cage filled by a single tetra-coordinated Se atom bonded to four tetra-coordinated Cd atoms [17, 311, 313, 325]. Interestingly, ultrathin rods formed by the assembly of $(CdSe)_{13}$ clusters have been predicted to be particularly stable [311]. For the $(CdSe)_{19}$, Kasuya et al. claimed a low-symmetry $(CdSe)_{18}$ cage incarcerating a $(CdSe)_1$ monomer to be the optimal arrangement [17]. In a subsequent work a C_3-symmetry hollow cage was found to be lowest in energy [325]. From these results, the relative stability of the isomers considered strongly depends on the computational scheme adopted [523]. Likewise, two isomers have been proposed to explain the unmatched stability of the $(CdSe)_{33}$

stoichiometry, namely a core@cage cluster ($(CdSe)_5$@$(CdSe)_{28}$) [17] and a wurtzite-like arrangement [491]. However, the simple analysis of the energy differences can not be conclusive to determine the lowest-lying isomer [22]. Indeed, based on TDDFT calculations, the experimental formation of both has been inferred.

More recently, the interaction between CdSe nanoclusters and surface ligands have attracted a lot of computational research [293,298,313,332,335,491]. The ligands have been shown to play a crucial role in stabilizing bulk-like clusters [313]. The OPH_2Me-protected wurtzite-like $(CdSe)_{13}$ isomer has been calculated to lie 1.39 kcal/mol lower than the $Se@Cd_{13}Se_{12}$ cage, *i.e.* the lowest-lying configuration among the bare ones [332]. Ligand molecules have been calculated to produce a substantial charge redistribution and polarization effects on nanocluster surface, giving rise to hybridized states for which the electronic density is spread over the cluster and the ligands [293]. Moreover, the optoelectronic properties of the resulting complex depend on the nature of the surface ligand. Liu et al. have found SCH_3^- molecules to redshift the absorption onset of the $(CdSe)_6$, whereas NH_3 molecules are calculated to widen the HOMO-LUMO energy gap [298]. Accordingly, the TDDFT absorption features of the amine-protected $(CdSe)_{33}$ have been predicted to substantially differ from those calculated for the carboxylic acid-capped counterpart [313]. Quite recently, the molecular orbitals of aliphatic ligands have been calculated to lie deep inside the valence and conduction bands of the $(CdSe)_{33}$ cluster [335]. On the contrary, aromatic molecules such as pyridine have been predicted to introduce new state close to the conduction band edge.

The structural and optoelectronic properties of the bare and ligand-protected $(CdSe)_{13}$ isomer have already been investigated with DFT/TDDFT calculations [313,332]. Motivated by the recent experimental work by Wang et al. [524], where the magic $(CdSe)_{13}$ has been isolated for the first time, we further progress on the characterization of the putative isomers of $(CdSe)_{13}$ and of their amine-capped counterparts. As already made for $(ZnO)_{60}$ [523], energy calculations are combined with TDDFT spectra in order to identify the isomer found in the experiment. Our results are in excellent agreement with the experimental measurements recorded in toluene.

4.5.3 Model and Method

As displayed in Figure 4.30, three types of isomers have been considered for $(CdSe)_{13}$: (a) the allegedly more stable isomer, consisting of a Se atom encapsulated in the center of a puckered $Cd_{13}Se_{12}$ cage and exhibiting C_3 symmetry [17,311,313,325]; (b) a hollow $(CdSe)_{13}$ cluster with C_1 symmetry [311,325,522]; and (c) a $(CdSe)_{13}$ cluster with C_{3v} symmetry sliced from bulk wurtzite [311, 325]. We have taken advantage of the geometry proposed by Del Ben et al. [313], as carved out from bulk wurtzite, in order to reach the minimum energy configuration of isomer (a). Indeed, as recently stressed by Asara et al. [25], the appropriate cuts from bulk polymorphs can give rise to the configurations derived through bottom-up global optimization procedures. Two more isomers were initially considered stemming from (d)

bulk zinc-blende [525] and (e) a rod-like cluster [325]. However, these latter species present significantly higher energies than the first three and therefore have not been considered in the discussion that follows.

The n-octylamine and oleylamine ligands employed in the experiment [524] have been modeled using the methylamine molecule, $MeNH_2$. This approximation bears from the fact that alkane substituents replaced by methyl groups in the calculations have shown to appropriately reproduce binding energies, band edge states and bandgaps of large chain counterparts [304, 332, 491]. Aromatic amines like pyridine and aniline have also been considered in this work.

All geometries have been fully optimized using dispersion corrected (D3) [513] Perdew-Burke-Ernzerhof (PBE) [238] exchange correlation (xc) functional within the Kohn-Sham framework of DFT (KS-DFT), as implemented in the ADF 2012.01 program [267]. A double-valence set (DZ) of Slater-type orbitals (STO) have been employed on Cd and Se atoms. Atomic orbitals lying below the *3d/3p* shell have been treated with the frozen core approximation, as in previous works [313]. On the ligand atoms an all-electron DZP set has been selected, which includes extra polarization functions. Relativistic effects have been considered by means of the Zero-Order Regular Approximation (ZORA) [526]. As shown earlier [300, 303, 304, 416], GGA functionals appropriately reproduce the geometry of II-VI semiconductor nanostructures, at a fraction of the computational cost required by the hybrid functionals. The basis set size is consistent with previous studies on CdX nanostructures [293,313,325,335]. Geometry optimizations have been carried out both in the gas phase and in the presence of implicit solvent employing the COSMO scheme [459].

To gain insight into the interaction between the CdSe nanostructures and surface attached ligands, we have taken advantage of the bond energy decomposition scheme formulated by Ziegler and Rauk [507–510] and implemented in ADF. In this framework, the overall bond energy $\triangle E$ is decomposed into two main terms:

$$\triangle E = \triangle E_{prep} + \triangle E_{int} \tag{4.4}$$

The preparation energy $\triangle E_{prep}$ corresponds to the energy required to deform the separated fragments (*i.e.* cluster and ligand shell) from their equilibrium structure to their geometry in the supermolecular complex. The interaction energy $\triangle E_{int}$ accounts for the instantaneous interaction between the prepared fragments. This term is is further decomposed into four contributions, namely the Pauli repulsion $\triangle E_{Pauli}$, the electrostatic interaction $\triangle V_{elst}$, the orbital interaction $\triangle E_{oi}$ and the dispersion interaction $\triangle E_{disp}$:

$$\triangle E_{int} = \triangle E_{Pauli} + \triangle V_{elst} + \triangle E_{oi} + \triangle E_{disp} \tag{4.5}$$

Within this energy decomposition scheme the attractive and repulsive terms are negative and positive, respectively. Therefore, the more negative the energy term is, the more attractive is the corresponding interaction.

Despite being useful for geometry optimizations and relative energies, GGA functionals severely underestimate the bandgap of II-VI semiconductor nanostructure. We have opted, thus, to compute the excited states of the optimized clusters with the hybrid B3LYP [241] functional, in conjunction with the SBKJC-VDZ* basis set. However, there are several cases in which re-parameterization B3LYP with respect to the amount of the HF exchange has led to improved description of transition metal compounds. Consequently, the B3LYP functional has been modified to include 27.5% HF exchange (B3LYP* hereafter), as in our previous works about Zn-based II-VI nanostructures [300, 303, 416, 523]. The solvation effects have been included by means of the Polarizable Continuum Model (PCM) [462]. For sake of computational performance, calculations involving hybrid functionals have been conducted with the Gaussian09 software package [422].

X-Ray Diffraction patterns have been simulated by the Mercury software package. To do so, the optimized nanostructures have been placed in a 4 nm long cubic unit-cell, as in previous studies [333]. In order to reproduce the experimental measurements, the X-Ray wavelength has been set to the Cu kα value of 0.154056 nm. A FWHM of 2^{o} has been chosen for the convolution of the diffractogram.

4.5.4 Results and Discussion

Bare $(CdSe)_{13}$ Clusters

Relative Stability and Atomic Structure

The gas phase optimized structures of the three $(CdSe)_{13}$ isomers are displayed in Figure 4.30. Our calculations predict the core@cage $Se@Cd_{13}Se_{12}$ cluster to be the most stable [17, 311, 325]. The fullerene-like isomer (b) and the wurtzite-like isomer (c) are 26.3 and 28.5 kcal/mol higher in energy, respectively. In toluene, the energy ordering remains unchanged, while in water, the (a) structure is still the lowest-lying isomer, but isomer (c) is now more stable than (b) by about 2 kcal/mol.

As one may notice from Figure 4.30, in isomer (a) the encapsulated Se atom and the four Cd atoms to which it is bonded are four-fold coordinated (referred as Cd(4) from now on). This optimized cluster also displays three two-fold coordinated Cd atoms, Cd(2), and the remaining atoms as three-fold coordinated, Cd(3). On the other hand, isomer (b) presents all metal atoms as Cd(3). Conformer (c) also presents all Cd atoms as Cd(3), except for one Cd(4).

The average geometric parameters of the gas phase structures are summarized in Table 4.24. In case of isomers (a) and (c), the bonds of the four-fold coordinated atoms, Cd(4), are significantly longer than in the bulk material (2.74 *vs* 2.63 Å) [293, 300, 303, 313]. With the decreasing coordination number, a shortening of the Cd-Se bonds is also observed. The calculated Cd(3)-Se bonds are in fairly good accordance with the experiment, with reported distances of about 2.64-2.67 Å for ultrasmall CdSe nanoclusters [471]. Comparison with previous DFT calculations shows a substantial agreement [313, 325, 332], with the exception of

the B3LYP/LANL2DZ results that have been shown to overestimate Cd-Se bond distances, most probably to be attributed to the limited basis set size.

All four-fold coordinated atoms of isomer (a) display a tetrahedral conformation, with an average bond angle of 109^o , while the encapsulated four-fold Se atom presents a remarkably smaller angle of 96.8^o. Three-fold coordinated Cd atoms are pulled into the plane formed by their adjacent Se atoms, assuming in this way a planar trigonal coordination, with an average Se-Cd(3)-Se angle of $\sim$120^o. The Se(3) atoms are puckered out and adopt a pyramidal geometry, with an average Cd-Se(4)-Cd angle close to 90^o. All three isomers considered display similar surface reconstructions. Square $(CdSe)_2$ and hexagonal $(CdSe)_3$ are recognizable motifs, see Figure 4.30. The recurrence of such units have been attributed to the lowering of the surface strain [522]. The geometries of the bare $(CdSe)_{13}$ isomers remain quite unchanged upon the inclusion of implicit solvent.

To provide a direct comparison of the atomic structure with the experiment, XRD patterns have been simulated, see Figure 4.31. We focus on the part of the diffractogram most-likely attributable to intraparticle distances, *i.e.* $2\theta > 20^o$. Ultrasmall CdSe nanoclusters have been reported to display diffraction peaks at 2θ = 25, 40 and 50^o [281, 471]. The diffractogram of isomer (c) resembles the one reported by Jose et al. [471]. Isomers (a) and (b) better fit the findings by Wu et al. [281]. However, since the differences between isomers have been calculated to be rather subtle (in particular diffractograms of (a) and (b) are quite similar), XRD patterns could not be used as conclusive evidences in determining the structure of ultrasmall nanostructures. Experimentally, bulk-like arrangements have been proposed to explain the appearance of the diffraction peaks. However, XRD patterns can in principle be explained by models with amorphous looking structures such as isomer (b) [333].

Optoelectronic properties

Single point calculations at the B3LYP*/SBKJC-VDZ*//PBE/DZ level show that for the isomers considered the HOMO and the LUMO are rather delocalized over the entire cluster, see Figure 4.32. The HOMO arises mostly from Se *4p* orbitals, whereas the LUMO is mainly composed by Cd *5s* orbitals. Our models exhibit well opened bandgaps of about 4.0 eV, with no midgap states. Experimentally, the absence of trap states results in improved photoluminescence efficiencies. As one may notice from Figure 4.32, the HOMO is close in energy to the rest of the occupied states. The LUMO, despite having the same nature of the upper lying orbitals, is quite separated from the rest of the conduction band states [300,303,313,416,473]. The inclusion of the solvent produces an upward shift of both the valence and conduction band edges. The conduction band experiences a larger displacement, so that the HOMO-LUMO gaps open. Remarkably, the energy gap seems to rise with the increasing polarity of the solvent [280,335,336].

Figure 4.33 shows the Density of States (DOS) of the gas phase (a) isomer, along with the projection (PDOS) on the Cd and Se orbitals. The DOS calculated for (b) and (c) are roughly the same. As anticipated the highest lying occupied orbitals arise mainly from Se *4p* orbitals. Deeper in the valence band, the Cd *5s* and Se *4p* orbitals mix notably. The intense

peak at around -15.0 eV corresponds to the Cd *4d* orbitals. The deepest band in the valence band arises from Se *4s* orbitals. Similar DOS have been previously reported for CdSe nanoclusters [298]. The bands calculated coincide with those experimentally measured for bulk CdSe, referred as P_I, P_{II}, *d* and P_{III} in the literature [424]. Interestingly, the distance between the *d* peak and valence band maximum fairly agrees with the experiment (9.29 vs 10.04 eV [424]). The calculated number is 0.7 eV smaller than the experimental data, as in previous theoretical works regarding Zn-based II-VI nanostructures [300, 303] where quantum confinement effects were claimed to be responsible for such a deviation. The inclusion of the solvent plays a minor role on the overall picture of the electronic structure, except for the upward shift of the valence and the conduction bands.

We then performed TDDFT calculations to simulate the optical spectrum of the bare clusters. The optical gaps, *i.e.* the lowest electronic transitions with non-zero oscillator strength, are summarized in Figure 4.32 (values in bold). These are $\sim$0.7 eV smaller than the corresponding HOMO-LUMO gaps calculated from the Kohn-Sham eigenvalues. Figure 4.34 displays the simulated UV-vis spectra, obtained by a Lorentzian convolution of the 10 lowest electronic transitions. The first excitation of isomer (a) appears at 3.17 eV. The wurtzite-like isomer (c) exhibits the lowest energy absorption, with a calculated optical gap of 2.90 eV, while the fullerene-like isomer (b) absorbs below 3 eV as well, with a computed absorption onset of 2.98 eV. The low-lying excited states are composed of transition from high-lying occupied orbitals to the LUMO. Due to the wide gap between the LUMO and higher-lying unoccupied orbitals, small contribution of these latter to the lowest electronic transitions has been calculated [303, 313]. Since the cooling of the photogenerated hole to the HOMO by phonon coupling is expected to occur rapidly, our models are predicted to exhibit narrow emission bands, associated to the LUMO$\rightarrow$HOMO relaxation.

The inclusion of the solvent produces a blueshift of the entire absorption spectra. Apparently, the extent of the spectral displacement increases with the solvent polarity. Irrespective of the isomer, the intensity of the main transitions increases when solvent included.

Ligand-Capped $(CdSe)_{13}$ Clusters

In a previous theoretical work the cage-, wurtzite- and tube-like $(CdSe)_{13}$ clusters have been proposed to bear one amine ligand on each Cd atom on the surface [325]. More recently, $(CdSe)_{13}$ clusters passivated with 13 NH_3 molecules have been predicted to be unstable [332], *i.e.* 3 of the 13 ligands segregate from the cluster during geometry optimization. In the recent experimental work in which the $(CdSe)_{13}$ cluster has been isolated for the first time [524], the molecular formula $[(CdSe)_{13}(RNH_2)_{13}]$ has been proposed for the ligand-protected complex. We therefore decided to perform a set of calculations on our $(CdSe)_{13}$ models including explicitly 13 methylamine molecules. The binding of aromatic amines like pyridine and aniline has also been considered.

Relative Stability and Atomic Structure

The gas phase optimized geometries of the methylamine- and pyridine- protected $(CdSe)_{13}$ are shown in Figure 4.30. We decided to saturate each Cd atom on the surface to achieve a four-fold coordination: each Cd(3) has been passivated with a single ligand molecule, Cd(2) with two, and the remaining ligand molecule has been placed on top of one of the Cd(4). For comparison, a second configuration was also considered, where a single amine molecule was placed on each surface Cd atom, regardless of its coordination. This latter system was found to lie higher in energy (+41.0 kcal/mol for methylamine), but no ligand detachment was observed for the Cd(4) atoms [332]. From our findings, a higher nucleophilicity of the Cd(2) can be inferred as compared to Cd(4). Indeed, for the bare cluster (a) Hirshfeld charges of 0.31 and 0.18 $|e|$ have been calculated for Cd(2) and Cd(4), respectively. For the isomers (b) and (c) a single amine molecule has been placed on each surface Cd atom.

For the methylamine-protected complexes, the isomer (a) is again the most stable configuration. The wurtzite-like (c) is the second lowest-lying isomer, 21.6 kcal/mol higher in energy. Compared to the bare clusters, where (c) was 28.5 kcal/mol less stable than (a), the ligand shell stabilizes (c) by 6.90 kcal/mol with respect to (a). A similar stabilization of the wurtzite-like $(CdSe)_{13}$ nanocluster has been previously reported upon ligand adsorption [332]. The fullerene-like (b) is the least stable among the complexes studied, 34.9 kcal/mol higher than (a). Regarding the pyridine-capped clusters, (a) stays as the most stable isomer, with (c) and (b) 35.7 and 49.9 kcal/mol higher, respectively.

The values of the relative energies remain almost the same for the complexes optimized in implicit solvent.

The main geometric parameters of the gas phase complexes are summarized in Table 4.24. Irrespective of the isomer and the surface ligand, Cd-Se bonds are lengthened as compared to the bare clusters, due to the donation of electron density from the capping ligands to the Cd-Se bonds. For isomer (a), such lengthening produces the disruption of the bond between the encapsulated Se atom and the surface Cd(4) atoms in which a ligand has been placed. In the case of methylamine, the Cd-N bonds vary from 2.42 to 2.51 Å , in good agreement with numbers previously reported for amine-protected $(CdSe)_{13}$ [313, 332]. The nanocluster-pyridine bonds are slightly longer, with calculated values between 2.43 and 2.54 Å. Regardless of the ligand, the length of the bond increases with the the coordination number of the Cd atom, *i.e.* the Cd-N bond weakens with the increased saturation of the Cd atom.

In previous theoretical works on II-VI semiconductor nanoclusters a puckering of the metal atom has been observed upon the ligand attachment [304]. Consistently, the Se-Cd(2)-Se angles shrinks by about 15º for isomer (a). However, the Cd(3) retain their planar trigonal coordination [313]. Similarly, the Se-Cd(4)-Se remain almost unchanged. Our findings coincide with results provided in Ref. [336], where amine molecules were predicted to produce only minor changes in the geometry of Cd-based clusters.

The geometries of the inorganic cluster are almost unaffected by the inclusion of implicit solvent. On the contrary, a significant shortening of the Cd-N bond is observed both in

toluene and water relative to gas phase geometries.

Bond Energy and Bond Energy Decomposition

The bond energies calculated for gas phase and solvent complexes are summarized in Table 4.25. For gas phase structures, bond energy decomposition is provided by taking the $(CdSe)_{13}$ cluster and ligand molecules as separated moieties.

Regardless of the $(CdSe)_{13}$ isomer, our calculations provide bond energies of about 20 kcal / mol for both methylamine-capped clusters. Our numbers are in line with previous theoretical results on alkylamine-protected CdSe nanoclusters. Puzder et al. calculated a bond energy of 21.0 kcal/mol for a single Me_3N molecule on top of a $(CdSe)_{15}$ cluster [491]. For the $(CdSe)_{33}$ cluster fully covered with 21 $MeNH_2$ molecules, values of about 15.5 kcal/mol have been provided [293, 335]. Del Ben et al. reported a bond energy of 19.4 kcal/mol for the $(CdSe)_{33}$ cluster bearing 9 $MeNH_2$ molecules on its surface [313]. Nguyen et al. calculated values lying in the range 13.6-17.7 kcal/mol for $MeNH_2$ capped $(CdSe)_n$ cluster (n = 6, 9, 12) [325]. For the pyridine-capped models, bond energies are similar to those obtained for methylamine, with numbers ranging between 19.85-21.72 kcal/mol. Compared with previous works where calculate values of about 10-15 kcal/mol have been reported for the CdSe-pyridine bond [335], we predict the interaction to be stronger. The inclusion of the dispersion may explain the discrepancy. Quite recently, the inclusion of the dispersion has been shown to be mandatory in order to properly describe interaction of pyridine derivatives with gold (111) surfaces [527].

In the case of methylamine, isomer (c) presents greater affinity towards ligand bonding, followed by (a) and (b). Irrespective of the type of cluster, the bonding interaction is mainly electrostatic, covering as much as 64-66 % or the attractive interaction. However, the importance of the orbital interaction term (27-29 %) suggests an important polarization of the electron density on the surface of the cluster [293]. To quantify the electron redistribution occurring upon ligand bonding, atomic charges have been computed within the Hirshfeld scheme. As shown in Table 4.25, the $(CdSe)_{13}$ cluster bears a negative charge of about -1.40 $|e|$, indicating a significant charge transfer from the surface-adsorbed ligands of about 0.1 $|e|$ per molecule. Regarding the dispersion, it absorbs 7% of the attractive interaction. The bond energy decomposition nicely agrees with previous works on ligand-protected ZnS nanoclusters, where the electrostatic, orbital and dispersion terms were calculated to comprise 67, 29 and 4% for the $MeNH_2$ ligand [304].

Among the pyridine-passivated models, isomer (a) presents the largest interaction bond energy with the ligand, followed by (c) and (b). As one may notice from Table 4.25, the Pauli repulsion between the electron densities of the two moieties is lower than for methylamine, most likely to an increased Cd-N bond length. The electrostatic and the orbital interaction are also diminished. On the contrary, the dispersion term increases, revealing that weak attractive interactions might exist between nanoparticles and aromatic ligands. Compared to methylamine-capped models, the contribution of the orbital and dispersion terms increases at the expense of the electrostatic term, meaning that the ionic character of the bond de-

creases. Remarkably, the pyridine-pyridine interactions further stabilize the complexes, as shown by the negative preparation energies of the ligand shell.

The bond energies calculated for the structures optimized in solvent are slightly weaker than in gas phase, by about 5%. In previous theoretical works an implicit solvent model has been reported to screen the interaction between CdSe clusters and surface attached ligands [279,280,335]. Yang et al. have also shown chloroform to produce an uniform weakening of 10% of the coordination bonds in $(CdSe)_2$ in fair agreement with our results [279]. Albert et al., however, found the bond energies towards $(CdSe)_{33}$ to diminish by about 70% relative to gas phase results [280]. The reduced dipole of the fully covered $(CdSe)_2$ and $(CdSe)_{13}$ models as compared to the singly passivated $(CdSe)_{33}$ cluster could explain the disagreement, as already suggested in Ref [280].

Regarding charge transfer, and irrespective of the isomer, the $(CdSe)_{13}$ cluster in toluene carries a smaller negative charge relative to gas phase results. On the contrary, in water the charge transferred to $(CdSe)_{13}$ increases.

Optoelectronic Properties

The electronic structure of the gas phase ligand-capped $(CdSe)_{13}$ isomers is shown in Figure 4.32.

Regarding the methylamine-protected clusters, surface ligands destabilize both the valence and the conduction band edges. A larger upward shift has been calculated for the latter, with the concomitant opening of the HOMO-LUMO gap. Similar results have already been reported for CdSe and CdTe cluster with amine and phosphine oxide molecules on their surface [298,323,336], and also for ultrasmall hydrated ZnS clusters [334]. About the latter, the electrostatic field induced by the adsorbed water molecules was calculated to be responsible for the blueshift of the energy gap. In addition, we believe the surface ligands to destabilize the lowest-lying unoccupied states by charge transfer [298]. Accordingly, the clusters develops a significant negative charge upon ligation.

As observed for the uncapped species, the LUMO is quite separated from the rest of the conduction band states. The valence band of the bare cluster is still recognizable in the methylamine-capped cluster, see Figure 4.33 (b), and the position of the main peaks remains almost unchanged. More importantly, the ligand-associated states lie deep inside the valence and the conduction band. These states display hybridized character, spreading also over the nanocluster atoms. The highest occupied and the lowest unoccupied molecular orbitals of the capped complexes are composed of atomic Se and Cd orbitals, respectively. As a consequence, the low-lying electronic excitations involve molecular orbitals localized on the inorganic $(CdSe)_{13}$ core.

Covering the cluster with pyridine molecules results on the shrinkage of the HOMO-LUMO gap. Again, the valence and the conduction band edges are destabilized relative to the bare cluster, but now the former occurs to a greater extent, see Figure 4.32. Inspection of the frontier orbitals reveals the lowest-lying unoccupied orbitals to be localized on the aromatic rings of the surface ligands, see Figure 4.32. In agreement with previous theoretical works

on the $(CdSe)_{33}$ cluster [335], pyridine ligands are predicted to introduce orbitals just below the conduction band of the nanocluster, which could act as trap states for excited electrons. Pyridine molecules also contribute to the high-lying occupied states, as shown by ligand-localized states ∼2.5 eV below the valence band edge, see Figure 4.33 (c). Such states could explain hole acceptor capacity of pyridine [85, 528].

Unlike the bare structures, the inclusion of the solvent stabilizes both the valence and the conduction band edges of the capped clusters. The slightly larger shift to lower energies of the former induces the opening of the HOMO-LUMO gap relative to the gas phase results. The extent of such a solvatochromic effect increase with the polarity of the solvent. However, the impact of the solvent on the optoelectronic properties is weaker than in the bare cluster, because ligands screen the nanocluster states from the solvent [335].

As one may notice from Figure 4.34, the adsorption of methylamine molecules results in a significant blueshift of the TDDFT spectra. As found for the bare clusters, the implicit solvent produces a even larger hypsochromic shift of the absorption spectra and increases the intensity of the main transitions.The most stable methylamine-protected isomer (a) displays two low-lying bands at 3.56 and 3.60 eV. The third absorption feature appears at 3.96 eV. When dielectric constant of toluene is included, such main bands slightly move to higher energies, with calculated values of 3.59, 3.63 and 4.02 eV (shaded spectrum in Figure 4.34). Our number esentially coincide with the experimental UV peaks assigned to the $[(CdSe)_{13}(MeNH_2)_{13}]$, located at 3.55, 3.68 and 3.99 eV as measured in toluene [524] (dashed lines in Figure 4.34). The other two isomers (b) and (c) present a different pattern of excitations, with several peaks falling in the region between 3.7 and 4.0 eV, where the experimental spectrum is optically inactive. On the basis of our calculations, we can therefore conclude that the core@cage $Se@Cd_{13}Se_{12}$ is presumably the configuration present in the experiment. Irrespective of the isomer, the calculated excited states imply transitions from high-lying occupied orbitals to the LUMO, as found for the bare counterparts. Similarly, for the pyridine complexes the LUMO is the orbital accepting the photoexcited electrons. Due to the localized nature of the acceptor orbital, pyridine-protected complexes display low-intensity excitations in the low-energy region of the UV spectrum. However, since TDDFT often fails describing such charge-transfer excitations, results concerning pyridine-capped models should be taken with caution.

To better understand the effect of aromatic ligands on the photoelectronics of semiconductor nanostructures, aniline-protected (a) isomer has also been studied. As one may notice from Figure 4.35, the aniline-protected cluster displays a clean HOMO-LUMO gap, with no ligand-related midgap states. The LUMO is now delocalized over the inorganic core, as it is the HOMO. As a consequence, the main absorption features of the aniline-capped complex lay between 3.5 and 4.0 eV, see Figure 4.35, as found for the methylamine-protected models. However, the contribution of the aniline states to the band-edge states is remarkable. Importantly, the ligand-related occupied states appear only ∼1.5 eV below the top of the valence band. Therefore, our calculations predict aniline ligands to be effective hole scavengers, in agreement with recent experimental works where the photoluminescence of CdSe QDs have

been found to drastically decrease upon aniline adsorption [529].

4.5.5 Summary and Conclusions

Inspired by the recent experiments by Wang et al. [524], in which the primary amine derivatives of the $(CdSe)_{13}$ cluster have been prepared for the first time, we report on the computational modeling of such magic cluster, both bare and ligand-protected. A core@cage-like $Se@Cd_{13}Se_{12}$ configuration has been predicted to be the most stable isomer, regardless of being bare or ligand-capped, with fullerene- and wurtzite-like arrangements lying higher in energy. The calculated valence band features of the bare $(CdSe)_{13}$ clusters are in nice agreement with the XPS measurements on bulk CdSe. From TDDFT calculations, all the three $(CdSe)_{13}$ clusters studied show an absorption onset of about 3.0 eV. However, each isomer displays unique absorption features, which could enable their experimental identification. The inclusion of the solvent produces a notable blueshift of the whole absorption spectrum. Irrespective of the isomer, the LUMO has been found to be rather separated from the rest of the conduction band states, in such a way that the lowest electronic excitations are composed of transitions from high-lying occupied orbitals to the LUMO. Since the phonon-assisted cooling of the photogenerated hole is known to be much faster than the radiative recombination, the emission bands of such ultrasmall clusters can be envisioned as LUMO→HOMO relaxations. This finding might explain the narrow absorption features inherent to semiconductor quantum dots.

Methylamine, pyridine and aniline ligands have been shown to strongly interact with the $(CdSe)_{13}$ cluster, with calculated bond energies of about 20 kcal/mol. The interaction is mainly electrostatic irrespective of the ligand, covering about 65% of the attractive interactions. However, in view of the contribution of the orbital interaction term, an important polarization of the electron density can be envisaged. Accordingly, Hirshfeld charges reveal an important charge redistribution in the complexes, which implies a charge transfer from the ligand to the cluster. Dispersion interactions contribute notably to the stabilization of the capped complexes. This kind of weak interaction is particularly important in the case of aromatic ligands such as pyridine and aniline. For all the models studied, the inclusion of the implicit solvent weakens the nanocluster-ligand bond by about 5%, as in previous computational works [279,280].

The geometry of the $(CdSe)_{13}$ isomers remains almost unchanged upon ligand bonding, as previously found for amine-capped CdSe nanoclusters [313,336]. However, surface ligands exert a strong influence on the optoelectronic properties of the inorganic cluster. The adsorption of methylamine molecules produces a significant blueshift of the absorption spectra, due to the destabilization of the conduction states. As found for the bare clusters, the implicit solvent moves the absorption bands to higher energies. However the solvatochromic effect is weaker, since ligands screen the nanocluster states from the solvent. The optical features of the methylamine-capped $Se@Cd_{13}Se_{12}$ isomer esentially coincide with the experimental spectrum, suggesting that it might be the configuration found in the experiment, in

agreement with the relative stabilities calculated.

Remarkably, the methylamine-related states lie deep inside the valence and the conduction bands. On the contrary, pyridine and aniline molecules introduce ligand-localized states close to the band edges, which may act as hole scavengers, in agreement with experimental evidences. In the particular case of pyridine molecules, unoccupied orbitals intrude into the HOMO-LUMO gap of the cluster.

In conclusion, we predict the core@cage-like $Se@Cd_{13}Se_{12}$ configuration to be the experimentally detected isomer, based on calculated relative stabilities and TDDFT spectra. The effect of aliphatic and aromatic amines on the electronic and optical properties have been examined and experimental findings have been reproduced. In view of the encouraging results obtained, we believe this work to provide the required computational framework for the investigation of ligand adsorption on II-VI nanostructures and the optoelectronic characteristics of the resulting hybrid compounds.

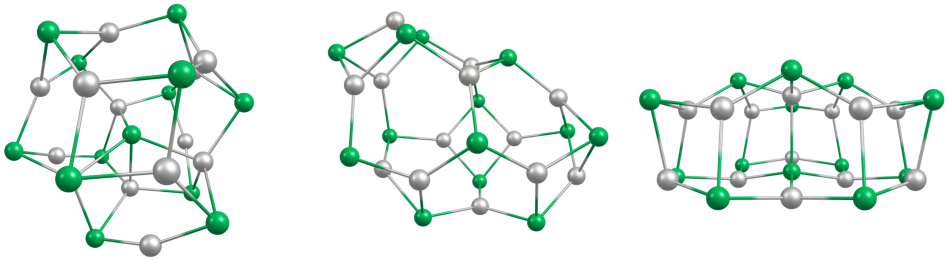
Table 4.24: Average geometric parameters of bare and ligand-capped $(CdSe)_{13}$ isomers, optimized in the gas phase. Results obtained at the PBE-D3/DZ level of theory. Bond lengths in Å and bond angles in degrees.

$(CdSe)_{13}$	(a)			(b)			(c)		
Ligand	Bare	$MeNH_2$	Pyr	Bare	$MeNH_2$	Pyr	Bare	$MeNH_2$	Pyr
d(Cd(2)-N)	-	2.416	2.428	-	-	-	-	-	-
d(Cd(3)-N)	-	2.471	2.539	-	2.457	2.530	-	2.452	2.473
d(Cd(4)-N)	-	-	-	-	-	-	-	2.511	-
d(Cd(2)-Se)	2.526	2.610	2.589	-	-	-	-	-	-
d(Cd(3)-Se)	2.658	2.677	2.674	2.643	2.666	2.656	2.651	2.671	2.662
d(Cd(4)-Se)	2.752	2.710	2.697	-	-	-	2.736	2.773	-
α(Se-Cd(2)-Se)	161.5	145.6	147.8	-	-	-	-	-	-
α(Se-Cd(3)-Se)	119.8	119.0	118.8	118.6	118.2	117.8	117.4	116.7	116.5
α(Se-Cd(4)-Se)	108.7	109.5	109.5	-	-	-	109.4	107.7	-
α(Cd-Se(3)-Cd)	85.5	89.9	90.1	91.2	94.1	94.7	88.1	89.3	91.2
α(Cd-Se(4)-Cd)	96.8	-	-	-	-	-	109.0	109.4	-

Table 4.25: Gas phase energy decomposition analysis of the amine-protected $(CdSe)_{13}$ nanoclusters. Resuls obtained at the PBE-D3/DZ level of theory. Energies per ligand molecule given in kcal/mol. Values in parentheses give the percentage of each attractive (repulsive) term with respect to the sum of the attractive (repulsive) terms. $Q\left[(CdSe)_{13}\right]$, given in a.u., indicates the charge carried by the $(CdSe)_{13}$ cluster, computed on the basis of the Hirshfeld scheme. Bond energies and charges have also been computed for solvent calculations.

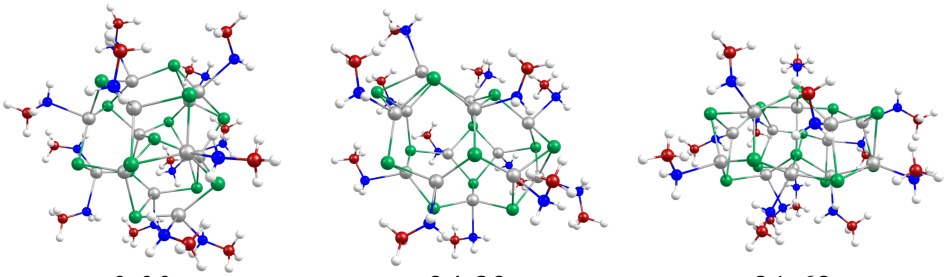
	$(CdSe)_{13}$	(a)				(b)				(c)			
	Ligand	$MeNH_2$		Pyr		$MeNH_2$		Pyr		$MeNH_2$		Pyr	
Vacuo	$\triangle E$	-20.19		-21.72		-19.50		-19.85		-20.69		-21.12	
	$\triangle E_{prep}$	1.15		-2.41		1.10		-2.12		1.95		-2.44	
	$\triangle E_{int}$	-21.34		-19.31		-20.59		-17.73		-22.65		-18.68	
	$\triangle E_{Pauli}$	49.31		44.48		45.96		40.69		50.71		43.56	
	$\triangle V_{elst}$	-45.18	(64%)	-39.87	(62%)	-43.75	(66%)	-36.51	(62%)	-47.01	(64%)	-39.70	(64%)
	$\triangle V_{oi}$	-20.81	(29%)	-18.32	(29%)	-18.21	(27%)	-16.13	(28%)	-21.23	(29%)	-17.34	(28%)
	$\triangle E_{disp}$	-4.66	(7%)	-5.60	(9%)	-4.59	(7%)	-5.78	(10%)	-5.11	(7%)	-5.19	(8%)
	$Q\left[(CdSe)_{13}\right]$	-1.39		-1.07		-1.36		-0.97		-1.43		-1.13	
Toluene	$\triangle E$	-19.36		-20.23		-18.57		-18.60		-19.84		-19.91	
	$Q\left[(CdSe)_{13}\right]$	-1.17		-0.87		-1.21		-0.95		-1.11		-0.85	
Water	$\triangle E$	-19.39		-19.97		-18.50		-18.18		-19.48		-19.94	
	$Q\left[(CdSe)_{13}\right]$	-1.78		-1.29		-1.64		-1.22		-1.52		-1.13	

Figure 4.30: Gas phase optimized structures of the three $(CdSe)_{13}$ isomers, both bare (top row) and ligand-protected (methylamine = middle and pyridine = bottom rows). Results obtained at the PBE/DZ(P) level of theory. Relative stabilities in kcal/mol. Grey = Cd, green = Se, blue = N, red = C and white = H atoms.

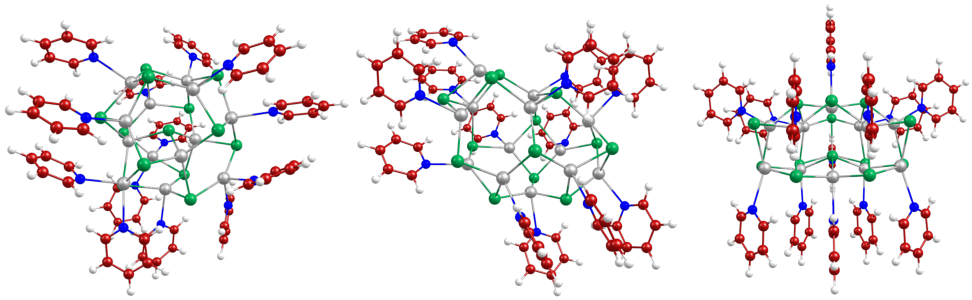


a b c

Vacuo	0.00	26.32	28.52
Toluene	0.00	25.52	26.74
Water	0.00	25.66	24.94



Vacuo	0.00	34.89	21.62
Toluene	0.00	35.88	20.59
Water	0.00	37.28	23.77



Vacuo	0.00	49.93	35.68
Toluene	0.00	46.77	30.91
Water	0.00	48.93	25.35

Figure 4.31: Simulated XRD pattern of the $(CdSe)_{13}$ isomers considered. In the inset, a zoom of the region between 20 and 60º is shown.

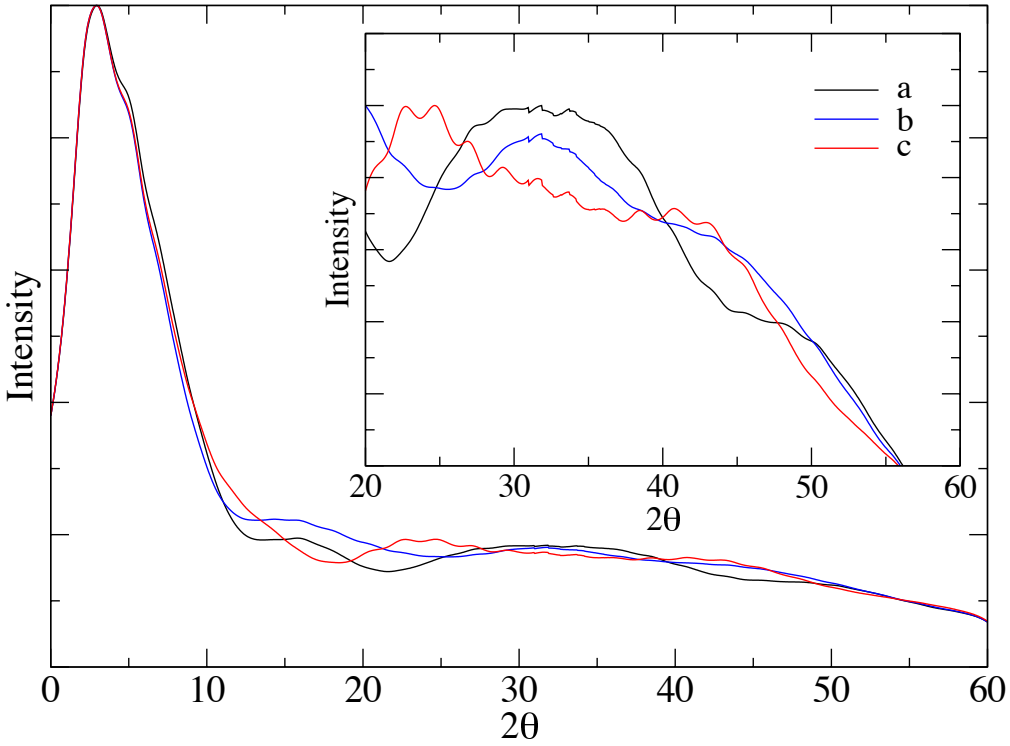


Figure 4.32: Gas phase electronic structure of the $(CdSe)_{13}$ isomers, both bare (B) and ligand-protected (M = methylamine and P = pyridine). Results obtained at the B3LYP*/SBKJC-VDZ* level. KS HOMO-LUMO differences and TDDFT optical gaps, in bold, are shown. For isomer (a), HOMO-1, HOMO, LUMO and LUMO+1 orbitals are also depicted. For clarity, a contour value of 0.015 e/a.u.^{3} has been chosen.

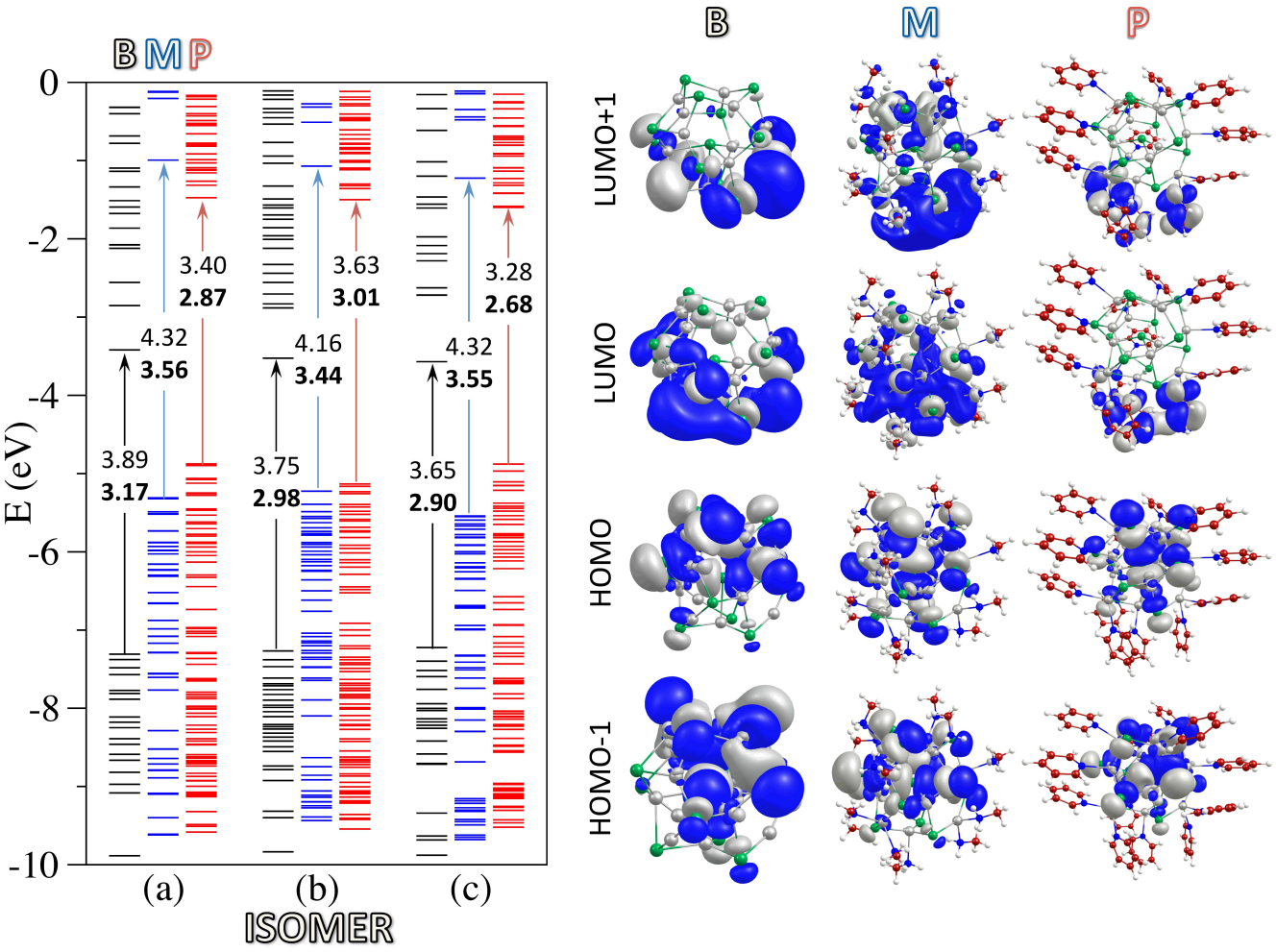


Figure 4.33: Gas phase Density of States of the $(CdSe)_{13}$ isomer (a), bare (a) and methylamine- and pyridine-capped (b and c), drawn by a Gaussian convolution of $\sigma = 0.2$ eV of the individual Kohn-Sham orbitals. Results obtained at the B3LYP*/SBKJC-VDZ* level.

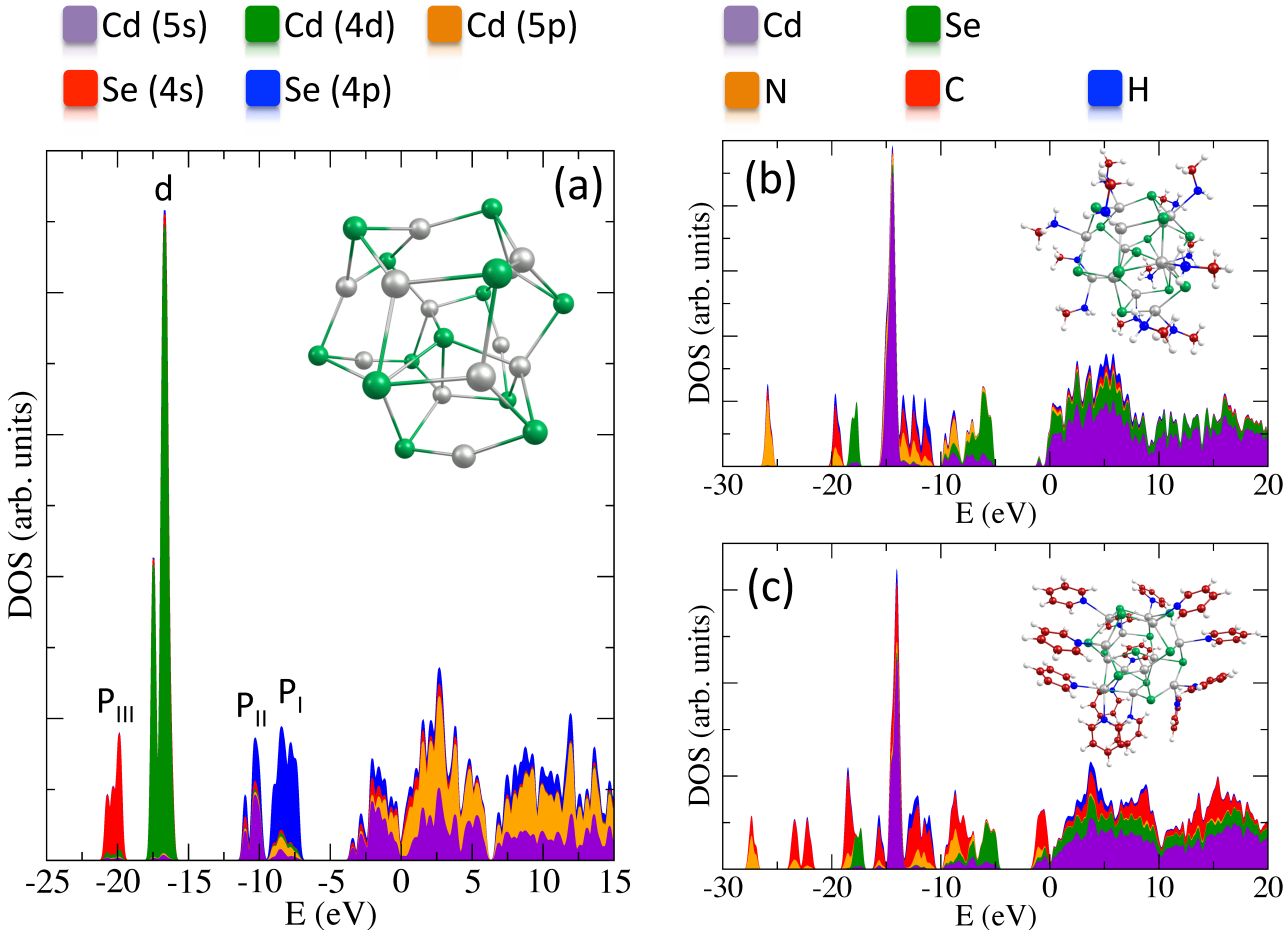


Figure 4.34: Gas phase simulated absorption spectra of the $(CdSe)_{13}$ isomers, both bare and ligand-protected, drawn by a Lorentzian convolution with FWHM = 0.2 eV, calculated taking into account the lowest 10 electronic transitions. Results obtained at the B3LYP*/SBKJC-VDZ* level. Black = (a), blue = (b) and, red = (c) isomers. For the methylamine-capped clusters, the TDDFT spectrum of isomer (a) in toluene is also provided (shaded spectrum), along with the experimentally reported bands (dashed vertical lines).

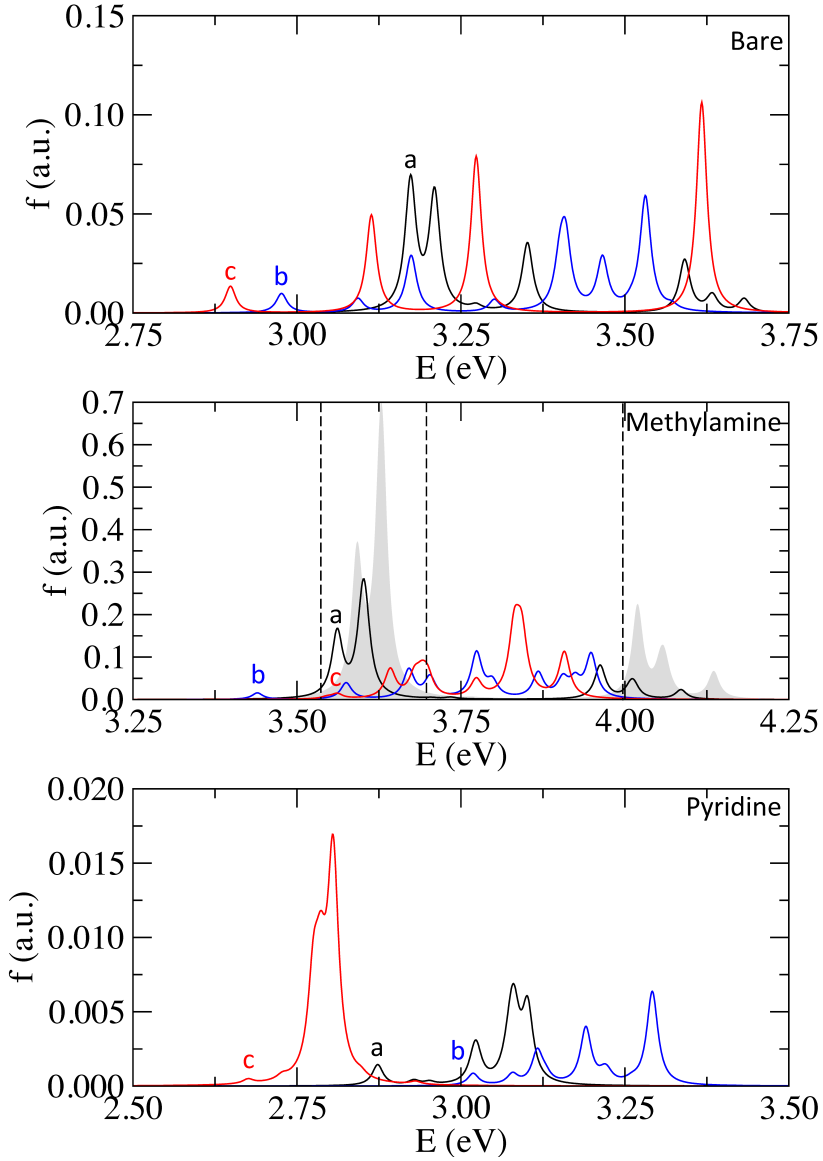
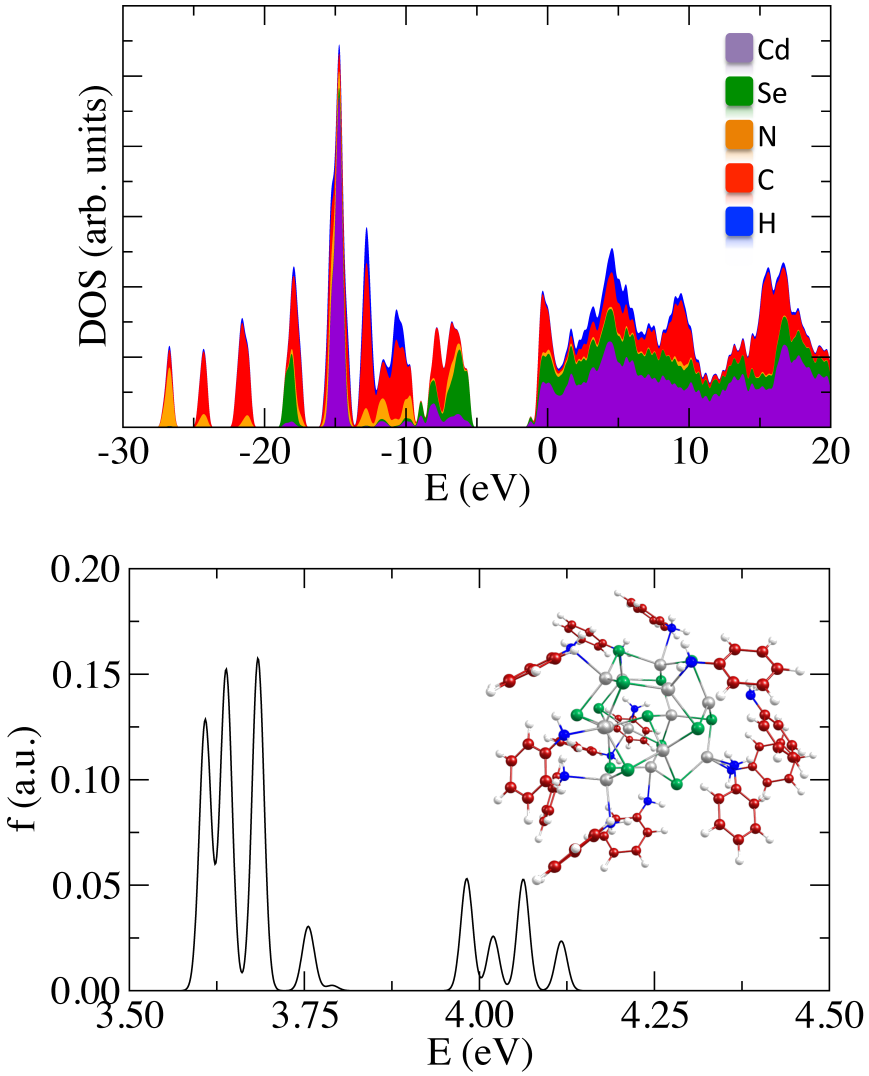


Figure 4.35: Gas phase Density of States of the aniline-capped $(CdSe)_{13}$ isomer (a), drawn by a Gaussian convolution of σ = 0.2 eV of the individual Kohn-Sham orbitals (top). Gas phase simulated absorption spectra of the aniline-capped $(CdSe)_{13}$ isomer (a), drawn by a Lorentzian convolution with FWHM = 0.2 eV, calculated taking into account the lowest 10 electronic transitions (bottom). Results obtained at the B3LYP*/SBKJC-VDZ* level.



4.6 Quantum Dot Photoactivation of Pt(IV) Anticancer Agents: Evidence of an Electron Transfer Mechanism Driven by Electronic Coupling

4.6.1 Abstract

Herein we elucidate the mechanism of photoreduction of the Pt(IV) *cis,cis,trans* - [$Pt(NH_3)_2(Cl)_2(O_2CCH_2CH_2CO_2H)_2$] (**1**) complex into Pt(II) species (among which is cisplatin) by quantum dots (QDs), a process which holds potential for photodynamic therapy. Density functional theory (DFT) and time-dependent density functional theory (TDDFT) methodologies, integrated by selected experiments, were employed to study the interaction and the light-induced electron transfer (ET) process occurring between two QD models and **1**. Direct adsorption of the complex on the nanomaterial surface results in large electronic coupling between the LUMO (lowest unoccupied molecular orbital) of the excited QD* and the LUMO+1 of **1**, providing the driving force to the light-induced release of the succinate ligands from the Pt derivative. As confirmed by photolysis experiments performed a posteriori, DFT highlights that QD photoactivation of **1** can favor the formation of preferred photoproducts, paving the way for the design of novel hybrid Pt(IV)-semiconductor systems where photochemical processes can be finely tuned.

4.6.2 Introduction

Semiconductor quantum dots [272] (QDs) have become in recent years one of the most fascinating and promising type of materials with technological applications ranging from photovoltaics [145–149] and optoelectronic devices [275] to biosensors [192] and bioimaging agents [68]. The attractiveness of QDs lies in their high optical extinction coefficients, sharp emission spectrum, carrier multiplication ability and high photo and thermal stability [4,5], features which can be tuned by varying QD size and shape. A key ubiquitous process in QD chemistry is electron transfer (ET). For example, efficient charge separation at the interface between a QD (or a film of QDs) and an oxide semiconductor material, *e. g.* TiO_2, is mandatory to obtain highly performing photovoltaic cells [148], while field-effect transistor devices engineered from thin-film of QDs rely on efficient charge hopping between adjacent QD units [530]. QDs are also being explored as light-induced ET activators with very promising results in other research areas, as for example photoactivatable protein inhibitors, photodynamic therapy (PDT) [531,532], and photocatalysis [45,533].

Thorough understanding of the ET mechanism in these systems, in particular the role played by parameters such as reorganization energy, Gibbs free energies and electronic coupling, is therefore paramount for researchers involved in the advance of QD-based applications.

Density functional theory (DFT) is a powerful tool to achieve such goal as recently demonstrated in the ET mechanism elucidation of QD-metal oxide [534] and QD-fullerene systems [535]. Indeed DFT is able to provide a good description of QDs electronic structure

and model their interaction with molecules and material surfaces, ultimately providing useful insights in the thermodynamic and kinetic factors ruling ET.

In this work we present a combination of DFT calculations and selected experiments in the context of rationalizing the ET process from a core-shell CdSe@ZnS QD into a Pt(IV) anticancer agent, namely *cis,cis,trans* - $[Pt(NH_3)_2(Cl)_2(O_2CCH_2CH_2CO_2H)_2]$ (**1**). Pt(IV) complexes have been extensively studied as prodrugs whose activity can be switched on *in vitro* and *in vivo* by biological reductants [536–541] or by light excitation [542–544]. Nanoparticle-mediated photoactivation of anticancer complexes is now becoming a hot topic as demonstrated by several ground-breaking results reported recently [545–547].

Earlier, Mareque and coworkers have employed core-only and core-shell QDs to control Pt(IV) $\rightarrow$ Pt(II) reduction and deliver cisplatin [38, 548]. In particular, they have recently synthesized a QD-Pt composite with potential use as a theranostic agent for cancer therapy and multimodal imaging [38, 549]. In such system, a core-shell CdSe@ZnS QD (*ca.* 5 nm diameter), complex **1**, and the γ-emitter radioactive *fac* - $[^{99m}Tc(H_2O)_3(CO)_3]^+$ complex are transported by a high stability micelle to the target site. The ^{99m}Tc compound gives SPECT (single-photon emission computed tomography) imaging capability while the Pt(IV) and the QDs are exploited for therapy, with QDs being suitable for optical imaging as well. In such composite, QDs can efficiently photoactivate the Pt(IV) complex *via* ET using visible light up to 630 nm, a wavelength currently in use for clinical PDT. These hybrid systems have the potential to overcome the poor absorption properties of metal complexes in the visible, particularly in the therapeutic window (630-700 nm).

In this study, we initially investigate the behavior of **1** under UV light irradiation and elucidate how dicarboxylato Pt(IV) prodrugs are transformed under chemically reducing conditions. Successively, modeling QD-**1** adducts we show how the energy alignment between the QD and **1** favors the injection of the photoexcited electron from the former to the latter, with the concomitant reduction of the Pt(IV) complex into Pt(II). In particular, DFT indicates that QD injects electrons not only to the LUMO (lowest unoccupied molecular orbital) level of **1**, but also and more efficiently to the LUMO+1, favoring the release of selected ligands and the formation of the preferred photoproducts (among which is cisplatin). Photolysis experiments performed a posteriori support such outcome, highlighting that QD surfaces can be tailored for photoactivation of specific target states of metal complexes, potentially opening new opportunities to control a wide range of photochemical processes for different applications. Structures of all the models investigated in our study are reported in Figure 4.36.

4.6.3 Computational Section

All calculations were performed with the Gaussian 09 program [422]. Ground- and excited-state properties of all the systems employed in this work were analyzed with DFT and time-dependent DFT (TDDFT), using the PBE0/def2-SVP combination. Such functional and basis set was chosen after careful benchmarking against available experimental data of **1 [550]** and

because it has been recently demonstrated to perform extremely well for the QDs studied here [551]. Calculation on **1** and its derivatives were performed using the polarized continuum model (PCM) with water as implicit solvent [552] (as this is the environment in which their photophysical and photochemical properties were studied), while calculations including the QD alone and the QD with complex **1** were performed using as implicit solvent hexane, to approximate the micelle environment. The nature of all stationary points was confirmed by normal mode analysis. For the QD-1 complexes, the Basis Set Superposition Error (BSSE) was considered by means of the counterpoise (CP) method [553, 554]. TDDFT calculations on a reduced space (*vide infra*) were carried out with Q-Chem 4.0 [555].

For analysis and visualization of computational results the software packages GAUSSSUM 2.2 [556], AOMix [557, 558], and Chimera [559] were employed.

4.6.4 Results and Discussion

Complex 1: Photochemistry and Redox Properties

Ground- and excited-state structure and electronic properties of *cis,cis,trans* - $[Pt(NH_3)_2(Cl)_2(O_2CCH_2CH_2CO_2H)_2]$ (**1**) and related species (*vide infra*) were investigated by DFT and TDDFT to characterize the photochemical and redox behavior of the complex (Table 4.26 and Figure 4.37). The DFT ground-state (GS) geometry of **1** displays bond distances in good agreement with the X-ray values. Similarly, the TDDFT simulated spectrum (Figure 4.37a) correctly reproduces the experimental absorption in the 275–450 nm range. Electron density difference maps (EDDMs), which graphically describe changes in electron density (Figure 4.37b), indicate the singlet-singlet low-energy transitions in the UV region are mixed d–d/LMCT and have dissociative nature due to significant contributions from the σ-antibonding orbitals LUMO and LUMO+1 [560].

Optimization of excited state structures (singlet with TDDFT method and triplet with unrestricted Kohn-Sham method) was performed to obtain snapshots of transient species and characterize the excited-state dynamics of **1** upon UV light excitation. In the S1 excited state, **1** shows significantly elongated Pt–O distances (*ca.* 0.25 Å) compared to the GS, while the other Pt–L bond lengths are only slightly changed (Table 4.26). It is reasonable that population of S1, which has major contributions from the LUMO+1 orbital, leads to succinate release, whereas S2 and S3, mainly involving the LUMO orbital, should promote the formation of free Cl^- and NH_3. Triplet state optimizations gave similar results affording two lowest-lying triplet geometries, ll-T and ll-T2 ($\triangle E$ = 0.29 eV), suggesting dissociation of succinate as well as Cl^- and NH_3 ligands could take place. In particular, ll-T geometry resembles the S1 geometry with elongated Pt–O bond lengths (*ca.* 0.3 Å) with respect to the GS, whereas ll-T2 shows elongated Pt–Cl (2.384 Å) and Pt–N (2.488 Å) bond lengths. In principle, photosubstitution *via* these excited-state species can involve a single monodentate ligand as well as the simultaneous release of two ligands. Furthermore, subsequent isomerization reactions should not be ruled out, indicating the formation of several photoproducts

is likely to occur under light irradiation.

Photolysis experiments on **1** (Figure 4.38a) clearly show appearance of the free succinate signal in the NMR spectrum within few minutes of UV light irradiation (385 nm, $\sim$40mW·cm^{-2}). Furthermore, the NH_3 multiplet of **1** ($^1J_{14N-1H}$ = 54 Hz, $^2J_{195Pt-1H}$ = 27 Hz) at 6.3 ppm decreases in intensity while peaks corresponding to free NH_3 ($^1J_{14N-1H}$ = 52 Hz) and a number of Pt(IV) photoproducts appears nearby, consistently with the possibility of multiple photochemical pathways. However, it is significant that XPS measurements performed on UV irradiated solution of **1** (Figure 4.38b) show little or no formation of Pt(II) species compared to the dark control (a fraction of Pt(II) is present due to direct reduction of the metal under the X-ray beam as visible in the control spectrum). Consistently with the prevalent photogeneration of inert Pt(IV), binding experiments with GMP (guanosine 5'-monophosphate) exclude the formation of Pt(II)-GMP adduct and the presence of cisplatin-like complexes. One of the most likely photoproduct formed upon release of the succinate could be the complex *cis*,*cis*,*trans* - $[Pt^{IV}(NH_3)_2(Cl)_2(OH)_2]$ in agreement with the NMR data and the *in vitro* activity observed for solutions of **1** in the dark and after UV irradiation.

For the sake of comparison with the excited state computational characterization and to gain further insights, the first step in the reduction of **1** was investigated by performing geometry optimization calculation on the complex *cis*,*cis*,*trans* - $[Pt(NH_3)_2(Cl)_2(O_2CCH_2CH_2CO_2H)_2]^-$, which results from the addition of 1 electron (1e) to **1**. Chemical reduction of Pt(IV) complexes is a fundamental process in the biological mechanism of action of this family of prodrugs [539,541,561]. Conversion of octahedral Pt(IV) to square planar Pt(II) can be promoted by endogenous reducing agents and occur through simultaneous ligand dissociation pathways [541, 561, 562]. Two geometries were obtained corresponding to electronic structures where the extra electron is localized either on the LUMO+1 (**1a**) or on the LUMO (**1b**) ($\triangle E$ = 0.15 eV). Consistently with the shape of the orbitals hosting the unpaired electron (see spin density surface in Figure 4.37c), **1a** is characterized by elongated Pt–O bonds (Table 4.26), similarly to S1 and ll-T. Instead **1b** shows one longer Pt–Cl and Pt–N distance compared to **1** (Table 4.26), in agreement with the ll-T2 geometry of **1**. Plausibly, release of succinate occurs from **1a**, while Cl^- and NH_3 can dissociate from **1b**.

Adopting **1a**, **1b** and the GS structures as starting point, the 2e-reduced structure of **1** was also optimized employing the aforementioned approach. As shown in Figure 4.37c, two different Pt(II) reduction products were obtained: *cis* - $[Pt^{II}(NH_3)_2(Cl)_2]$ (**2**, cisplatin) + 2 $O_2CCH_2CH_2CO_2H$ from **1a**, and *trans* - $[Pt^{II}(NH_3)(Cl)(O_2CCH_2CH_2CO_2H)_2]$ (**3**) + Cl^- and NH_3 from **1b** and the GS.

Such result suggests the presence of distinct reductive pathways and formation of different Pt(II) species [541,561,562] and is in agreement with cell toxicity tests [38].

QD-1: The Model and the Interaction

As shown earlier for complex **1** and other related compounds [38,548], an efficient approach to promote Pt(IV) to Pt(II) reduction using (more penetrating and less harmful) visible light

is by excitation of a tailored-synthesized QD in the proximity of the Pt complex. In such a way, the photoactivated QD* can transfer the excited electron from its conduction band to the Pt(IV) complex, (*e.g.* **1**) which rapidly undergoes ligand dissociation and formation of Pt(II) toxic species at the target cancer cells.

Full modeling of the interaction between **1** and the QD is not straightforward due to the complexity and heterogeneity of the system (even more when the composite is designed to reach the target site inside water soluble poly(ethylene glycol) micelles). Nevertheless, QD-**1** models where the complex is directly anchored on the surface of the nanomaterials are a valid approximation, able to provide a satisfactory description of the electronic phenomena, taking place on the QD surface. This is supported by recent results showing that Ru metal complexes bearing COOH-functionalized ligands can directly be attached onto QD surface despite the presence of bulky organic ligands [45,329,563]. Indeed, photoluminescence (PL) quenching experiments were carried out (Figure 4.39) and indicate that **1** is adsorbed on the on the QD surface ($K \sim 5{\cdot}10^4\ M^{-1}$) as demonstrated by the better fitting to the Langmuir isotherm (surface adsorption) compared to the Stern-Volmer expression (collisional dynamic quenching).

On the bases of such experimental findings we explored QD-**1** models where the complex is direct anchored to the surface of the nanomaterial. Furthermore, the composites developed by Mareque and coworkers employed core-shell CdSe@ZnS QDs of about 5 nm (*ca.* 2000–3000 atoms) [38], a size untreatable by current theoretical approaches like DFT. Therefore, QD dimensions were scaled down the as much as possible but still keeping them large enough to reflect the instantaneous interactions between the QD and complex **1**. At first, we chose a small bare CdSe composed of 24 atoms, *i.e.* a $(CdSe)_{12}$ (Figure 4.36), then we have added a ZnS layer to provide a model for the core-shell system. The final QD is composed by a $(CdSe)_{12}$ core covered by a shell of $(ZnS)_{48}$, for a size of approximately 1.5 nm (Figure 4.36).

Structural optimization for the $(CdSe)_{12}$-**1** and $(CdSe)_{12}$@$(ZnS)_{48}$-**1** adducts shows that in both cases complex **1** is attached to the QD with three anchoring groups, the two carboxylates and one of the chlorine atoms. The chlorine and the oxygen of the carboxyl groups are directly adsorbed on the Cd atoms (or Zn atoms in the core-shell adduct), while the O–H group of the succinates form hydrogen bonds with the Se atoms (or S atoms in the core-shell). The instantaneous interaction energy between complex **1** and the QD is stabilizing of about 32.5 kcal/mol in $(CdSe)_{12}$-**1** and 78.4 kcal/mol in $(CdSe)_{12}$@$(ZnS)_{48}$-**1**. When the CP (counterpoise) correction is applied, the interaction energies are 22.6 and 60.0 kcal/mol, respectively. If also preparation energies are included (*i.e.* the energy required to deform the fragments from their equilibrium structure to the geometry they adopt in the interacting complex) the interaction energies reduce further to 12.3 and 32.1 kcal/mol, respectively. The larger stabilization in the core-shell complex is most likely associated to the larger surface area of adsorption with respect to the much smaller $(CdSe)_{12}$ complex, where the strain forces to accommodate complex **1** are augmented. Bond decomposition analysis reveals that the nature of QD-**1** interaction is about 60% electrostatic and 40% covalent for both the

bare and core-shell QDs. In particular, complex **1** transfers about 0.09 electrons to the bare $(CdSe)_{12}$ and 0.29 electrons to $(CdSe)_{12}@(ZnS)_{48}$. Such charge transfer has important effects on the electronic structure of $(CdSe)_{12}$-**1** and $(CdSe)_{12}@(ZnS)_{48}$-**1**. In Figure 4.40, the density of states (DOS) and molecular orbital (MO) energy levels of both adducts are plotted.

As it is immediately clear, the charge donation from complex **1** to any of the two QDs raises the MOs energy levels of the QDs and lowers those of complex **1**. The latter indeed becomes slightly more cationic, with the consequence of increasing its ionization energy (IP), roughly approximated to the negative value of the HOMO (highest occupied molecular orbital) energy [564]. Theoretically, there is still some debate whether Koopmans Theorem hold within DFT. However, in this context, it provides useful information on IP trends. The HOMO (or IP) of **1** passes from –7.62 eV in the isolated conformation to –7.77 eV in $(CdSe)_{12}$-**1** and to –8.28 eV in $(CdSe)_{12}@(ZnS)_{48}$-**1**. The larger IP of the latter is a consequence of the larger charge transfer to the core-shell complex. On the other hand, the QD becomes more negative and more prone to ionization (HOMO level raised). The HOMO of the isolated $(CdSe)_{12}$ is indeed shifted from –6.46 eV to –6.39 eV, whereas that of $(CdSe)_{12}@(ZnS)_{48}$ moves from –6.25 eV to –6.02 eV. One might think that these effects on the MO energy levels are dampened in a much larger QD than the one employed in the calculation, however in a realistic system is also more likely that each QD absorbs more than one molecule of complex **1**, maintaining in this way the trend shown here.

Moreover, it is well known that ligands affect the QD absorption spectrum by shifting their excitation energies. For this reason, the first excitation energy of $(CdSe)_{12}$-**1**, associated to the HOMO-LUMO transition within the bare $(CdSe)_{12}$, is blue-shifted of about 0.1 eV, from 3.27 to 3.38 eV upon bond formation at the TDDFT level of theory. Note that the TDDFT HOMO-LUMO gap localized in the QD has been computed within a reduced single-excitation subspace to avoid the interference of low-lying charge transfer states induced by the Pt complex. Remarkably, the HOMO-LUMO gap estimation taken from the MO energies (Kohn-Sham KS orbitals) provides the same trend, with a similar blue-shift, from 4.00 to 4.09 eV. From these numbers, it is however clear that the absolute value of the HOMO-LUMO gap within the QD, is not a good approximation to the actual excitation energy, as it does not take into account relaxation effects induced by the formation of the electron-hole pair. This effect is however included in the TDDFT calculation which gives a value for the first excitation energy of $(CdSe)_{12}$ much lower than the HOMO-LUMO gap of 4.00 eV. For the larger $(CdSe)_{12}@(ZnS)_{48}$, the first excitation energy decreases to 3.00 eV with respect to 3.27 eV of the $(CdSe)_{12}$ QD. Considering that the core has the same size as the bare $(CdSe)_{12}$ cluster, the effect can be attributed largely to the ZnS shell. In this case, TDDFT could not be employed to compute the HOMO-LUMO excitation energy of the QD in the$(CdSe)_{12}@(ZnS)_{48}$-**1** complex due to its large size. However, assuming that the trends are well reproduced by the simple KS orbitals energy level, we can estimate a red-shift of only 0.03 eV upon interaction with complex **1**.

QD-1: The ET Mechanism

Under the assumption the electron donor is the excited QD* and the acceptor is complex **1**, two mechanisms for the QD-mediated photoactivation of **1** are possible: (a) electronic energy transfer (EET) or (b) direct electron transfer (ET). EET processes (Dexter and Forster) can be ruled out since no donor-acceptor spectral overlap is present, thus leaving direct ET as the only valid alternative. The standard theoretical framework for ET processes is the Marcus theory [565], which in the non-adiabatic and high temperature limits assumes the form:

$$k_{ET} = \sqrt{\frac{\pi}{\hbar^2 \lambda k_b T}} |H_{DA}|^2 exp\left[\frac{-(\triangle G + \lambda)^2}{4\lambda k_b T}\right] \tag{4.6}$$

where k_B is the Boltzmann constant, T is the temperature, and $\hbar$ is the reduced Planck constant. According to Eq. 4.6, the k_{ET} depends on three tunable variables: (i) the electron coupling term H_{DA}; (ii) the driving force $\triangle G$ for the charge separation process; and (iii) the reorganization energy λ, which quantifies the deformation energy of the donor and acceptor upon electron transfer. This latter term is usually decomposed in internal reorganization energy, λ_{INT}, which reflects the response of the molecular donor and acceptor systems to ET and external reorganization energy, λ_{EXT}, associated instead to the rearrangement of the solvent upon ET. Because an excess of organic ligands is present inside the micelle, we can assume that this shell behaves as a solvent with a very low dielectric, and therefore λ_{EXT} can be expected to be negligible. The ET activation energy is thus expressed as:

$$\triangle G^{\ddagger} = \frac{(\triangle G + \lambda_{INT})^2}{4\lambda_{INT}} \tag{4.7}$$

Notably, λ_{INT} and $\triangle G$ have opposite sign, hence the largest ET rate is reached at values of $\triangle G \sim \lambda_{INT}$. For values of $\triangle G < \lambda_{INT}$ the Marcus theory predicts that the ET rate increases with the driving force, while for $\triangle G > \lambda_{INT}$ a decrease of ET rate occurs at increased driving forces (inverted regime). In Table 4.27 we present all the computed parameters of Eq. 4.6 for two processes, one associated to the electron injection from the excited QD* (bare and core-shell) to complex **1**, to form QD^+ and **1a** and the other to form complex **1b.**

Internal Reorganization Energy

In the weak interaction limit the reorganization energy is computed as:

$$\lambda_{INT} = \lambda_{INT}^{QD^* \rightarrow QD^+} + \lambda_{INT}^{1 \rightarrow 1^-} = \frac{\lambda_{QD^+}^{QD^*} + \lambda_{QD^*}^{QD^+}}{2} + \frac{\lambda_{1^-}^{1} + \lambda_{1}^{1^-}}{2} \tag{4.8}$$

where $\lambda_{INT}^{QD^* \rightarrow QD^+}$ and $\lambda_{INT}^{1 \rightarrow 1^-}$ are the reorganization energies of the excited QD* and complex **1** (whether as **1a** or **1b**), respectively, during the ET mechanism, and λ_B^A indicates the deformation energy of adduct A (QD^*, QD^+, **1**, $\mathbf{1}^-$) to attain the geometry of B (QD^+, QD*,

1, **1**$^{-}$). As shown in Table 4.27, the $(CdSe)_{12}$ and $(CdSe)_{12}$@$(ZnS)_{12}$ QDs present deformation energies $\lambda_{INT}^{QD^* \rightarrow QD^+}$ of 0.33 eV and of 0.50 eV, respectively. These values are likely overestimated because in the real environment the QDs are passivated by ligands that dampen the structural rearrangements. However, the structural deformations of complex **1a** and **1b** are well described and show larger values due to the population of the σ-antibonding Pt–X orbitals (*vide supra*). The elongation of the Pt–O bond distances is more effective and leads to a deformation energy of 1.64 eV for the **1a** complex, as compared to 1.21 eV for the **1b**, where the Pt–Cl bond is stretched.

Overall, the total reorganization energies λ_{INT} after electron injection, computed from Eq. 4.8, are therefore quite large, ranging from 2.17 eV in $(CdSe)_{12}$-**1a** to 1.71 eV in $(CdSe)_{12}$-**1b**.

Gibbs Free Energy Difference

The formula to evaluate $\triangle G$ is the following:

$$\triangle G = -\left[\left(\omega_{(QD-1)}^{QD-1 \rightarrow QD^*-1} - \lambda_{QD}^{QD^*}\right) - \left(\omega_{(QD-1)}^{QD-1 \rightarrow QD^+-1^-} - \left(\lambda_{QD}^{QD^+} + \lambda_1^{1^-}\right)\right)\right] \tag{4.9}$$

where $\omega_{(QD-1)}^{QD-1 \rightarrow QD*-1}$ is the TDDFT vertical excitation energy of the QD-**1a** (or QD-**1b**) complex associated to a localized QD→QD* HOMO-LUMO excitation; $\omega_{(QD-1)}^{QD-1 \rightarrow QD^+-1^-}$ is the TDDFT vertical excitation energy associated to the charge-separation process, and is usually the lowest computed excited state. The choice of the PBE0 functional is supposed to minimize the statistical error inherent in TDDFT for the estimation of charge transfer states.

From Table 4.27, we can infer that the computed $\triangle G$ are smaller than λ_{INT} and, therefore, the ET process occurs always in the normal regime of Marcus theory. For the smaller $(CdSe)_{12}$ QD, the $\triangle G$ of injection to form complex **1a** (1.46 eV) is larger of about 0.50 eV to form **1b** (0.98 eV). However, the corresponding activation energy $\triangle G^{\ddagger}$ is more favorable for the creation of the **1b** complex, thanks to a lower reorganization energy to rearrange the QD*-**1** complex (see Eq. 4.7 above). The same trend is found for the core-shell QD, which shows a larger $\triangle G$ value of injection to form 1a, but lower activation energy. Interestingly, the absolute $\triangle G$s of injection from $(CdSe)_{12}$@$(ZnS)_{48}$ to **1** are higher than in the smaller cluster: 1.82 (**1a**) and 1.34 (**1b**) eV against 1.46 (**1a**) and 0.98 (**1b**) eV. The consequence is that the overall ET activation energies are smaller for the core-shell systems, with the effect that the larger QD might inject electrons more rapidly to the Pt complex than $(CdSe)_{12}$.

Electronic Coupling and Kinetics of Charge Separation

The most significant results obtained in this work involve the electronic coupling (H_{DA}). H_{DA} is computed by evaluating the charge transfer integrals between the LUMO of the QD, corresponding to the donor orbital of QD*, and the LUMO+1 (for the **1a** complex) or LUMO (for **1b**) of complex **1**, both representing the acceptor orbitals. The H_{DA} is calculated on the geometry of the supermolecular complex QD-1. According to Table 4.27, in both types of QDs, the electron coupling is *ca.* 2 times larger when the ET induces the release of the succinate ligands to form the **1a** complex. The electronic coupling enters the Marcus equation

with the square of its value, therefore, only according to the Fermi's golden rule, the kinetic of ET to form the **1a** complex is 4 times larger than to form **1b**. Furthermore, the electronic coupling is much smaller than the reorganization energy, validating the weak interaction limit of the Marcus equation. Table 4.27 provides estimates for the kinetic of ET calculated as in Eq. 4.6. In absolute values, these terms might be far from the experiment because of the high sensitivity of the Marcus equation to an exponential term. Nevertheless, trends are qualitatively well described and show how electron injection from both types of QD to the Pt complex more favorably leads to **1a** than **1b**, *i.e.* to release the succinate ligand and form Pt(II) species, among which cisplatin. To verify this DFT result we followed by ^{1}H NMR the photolysis (λ_{exc} = 630 nm) of **1** in the presence of CdSe@ZnS core-shell QDs. NMR shows that the photoreduction is much cleaner under such conditions compared to UV-light irradiation (Figure 4.41). In particular, dissociation of succinate appears to be favored compared to formation of the Pt(IV) photoproducts responsible for the set of peaks at 5.5–7 ppm. The presence of cisplatin and cisplatin-like species was confirmed by GMP binding experiments and previously by XPS [38]. Calculations and experiments point out that interaction of **1** with the semiconductor surface can affect the photochemical and redox behavior of this Pt(IV) derivative. Selection of photochemical pathways through thermodynamic and kinetic control of the QD-metal complex interaction has the potential to create new fascinating scenarios for future developments on hybrid nanosystems coupled with metal complexes for a range of application (*e.g.* phototherapy, photocatalysis).

4.6.5 Conclusions

In summary, combination of DFT/TDDFT with selected experiments was used to gain new insights into the photochemistry and reduction behavior of **1**, and to investigate the QD-mediated photoactivation of the complex, a precursor of cisplatin. Our study allows to draw the following key conclusions:

1. Excitation of **1** with UV light leads to the generation of dissociative singlet and triplet excited states which can evolve towards the formation of different Pt(IV) photoproducts, among which likely the cytotoxic *cis*,*cis*,*trans* - [PtIV$(NH_3)_2(Cl)_2(OH)_2$]. As confirmed by XPS data, direct UV light excitation does not seem to efficiently promote Pt(IV) $\rightarrow$ Pt(II) conversion. On the contrary, **1** can be transformed into at least two distinct Pt(II) complexes upon chemical reduction, including cisplatin.

2. QDs-mediated light activation can promote the formation of Pt(II) photoproducts as a result of the interaction between **1** and the surface of the material. Fitting of quenching data shows that the complex is adsorbed onto the QD surface. Consistently, DFT calculations on two different QD-**1** models gives strong stabilization energies for such adducts.

3. The electron transfer (ET) occurring from the QD to **1** falls in the normal regime of Marcus theory ($\triangle G < \lambda_{INT}$) where increase in driving force favors the process. Ir-

respective of the QD model, the ΔGs calculated predict the formation of **1a** to be favored with respect to **1b**, however a higher activation energy $\triangle G^{\ddagger}$ needs to be surmounted due to an increased reorganization energy. ET appears to be favored in the core-shell model, as shown by the increase of $\triangle G$ and the decrease of $\triangle G^{\ddagger}$ relative to the core-only model. Crucially, computation of the electronic coupling H_{DA} highlights that electrons are better transferred from the QD to the LUMO+1 of **1** to generate a transient intermediate such as **1a**, hence the release of the succinate ligands. The second possible pathway involving the LUMO and leading to **1b** is indeed less probable, consistently with a cleaner photolysis reaction in the presence of QDs with respect to UV excitation. Such findings suggests that activation through QDs might also drive the formation of preferred photoproduct (*e.g.* cisplatin) compared to simple chemical reduction or direct light excitation, a fine prospect for developing anticancer agents acting through novel and selected mechanisms of actions.

Table 4.26: Selected bond distances (Å) for the X-ray and DFT-optimized geometries of **1**, **1a** and **1b**.

PBE0/def2-SVP						
Complex **1**	Pt-O4	Pt-O9	Pt-N14	Pt-N18	Pt-Cl2	Pt-Cl3
X-ray	1.992	2.008	2.050	2.066	2.311	2.319
GS	2.014	2.016	2.057	2.049	2.344	2.333
S1*	2.278	2.291	2.081	2.043	2.291	2.322
ll-T	2.301	2.320	2.078	2.071	2.308	2.319
ll-T2	1.998	1.996	2.384	2.065	2.353	2.488
Complex $\mathbf{1}^{-}$	Pt-O4	Pt-O9	Pt-N14	Pt-N18	Pt-Cl2	Pt-Cl3
1a	2.380	2.386	2.059	2.045	2.369	2.363
1b	2.048	2.045	2.372	2.046	2.378	2.669

*S1 geometry was obtained using the CAM-B3LYP functional. All attempts to optimize the structure of S1 with PBE0 functional failed.

Table 4.27: Reorganization energies, Gibbs free energy differences (absolute values), and electronic couplings calculated for the QD-**1** nanocomposites studied, along with the corresponding electron transfer rates calculated by means of the Marcus equation. All energies are expressed in eV.

	$\lambda_{QD}^{QD^+}$	$\lambda_{QD^*}^{QD*}$	$\lambda_{QD*}^{QD^+}$	λ_{QD}^{QD*}	$\lambda_{1^-}^{1}$	$\lambda_{1}^{1^-}$
$(CdSe)_{12}$	0.22	0.33	0.89	0.59		
$(CdSe)_{12}@(ZnS)_{48}$	0.23	0.50	0.82	0.58		
1a					1.64	1.48
1b					1.21	1.00
	Marcus Parameters					
	$\triangle G$	$\triangle G^{\ddagger}$	λ_{INT}	H_{DA}	k_{ET}	
$(CdSe)_{12}$-**1a**	1.46	0.27	2.17	0.235	$6.7{\cdot}10^{13}$	
$(CdSe)_{12}$-**1b**	0.98	0.23	1.71	0.064	$2.5{\cdot}10^{12}$	
$(CdSe)_{12}@(ZnS)_{48}$-**1a**	1.82	0.09	2.22	0.227	$2.9{\cdot}10^{14}$	
$(CdSe)_{12}@(ZnS)_{48}$-**1b**	1.34	0.08	1.77	0.134	$8.3{\cdot}10^{13}$	

Figure 4.36: DFT optimized structures of the models investigated in this study (PBE0/def2-SVP level).

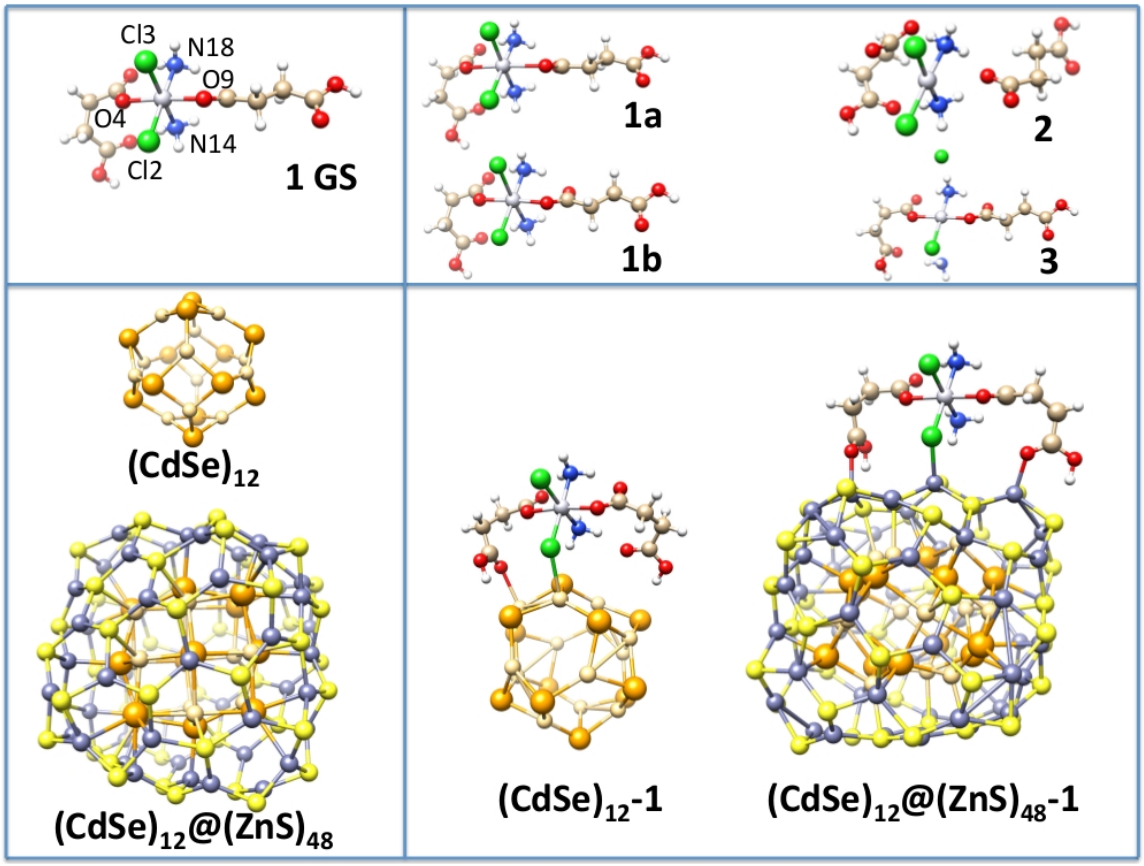


Figure 4.37: (a) Comparison between experimental (black) and calculated (blue) absorption spectra for **1** in water (PCM) calculated at the PBE0/def2-SVP level. Singlet-singlet transitions are shown as vertical bars with heights equal to their oscillator strengths. The theoretical curves were obtained using GAUSSSUM 2.2 (FWHM = 3000 cm^{-1}). Inset: photoluminescence spectrum of QDs used in this work. (b) Selected EDDMs of singlet-singlet electronic transitions and molecular orbitals for **1** in water (PCM) calculated at the PBE0/def2-SVP ground-state geometry. In the EDDMs, green indicates a decrease in electron density, while orange indicates an increase. (c) Energy diagram for complexes **1**, **1a**, **1b**, **2** and **3** calculated at the PBE0/def2-SVP level in water (PCM). For complexes **1a** and **1b** the spin density surface is re-ported in the figure (isovalue 0.0005).

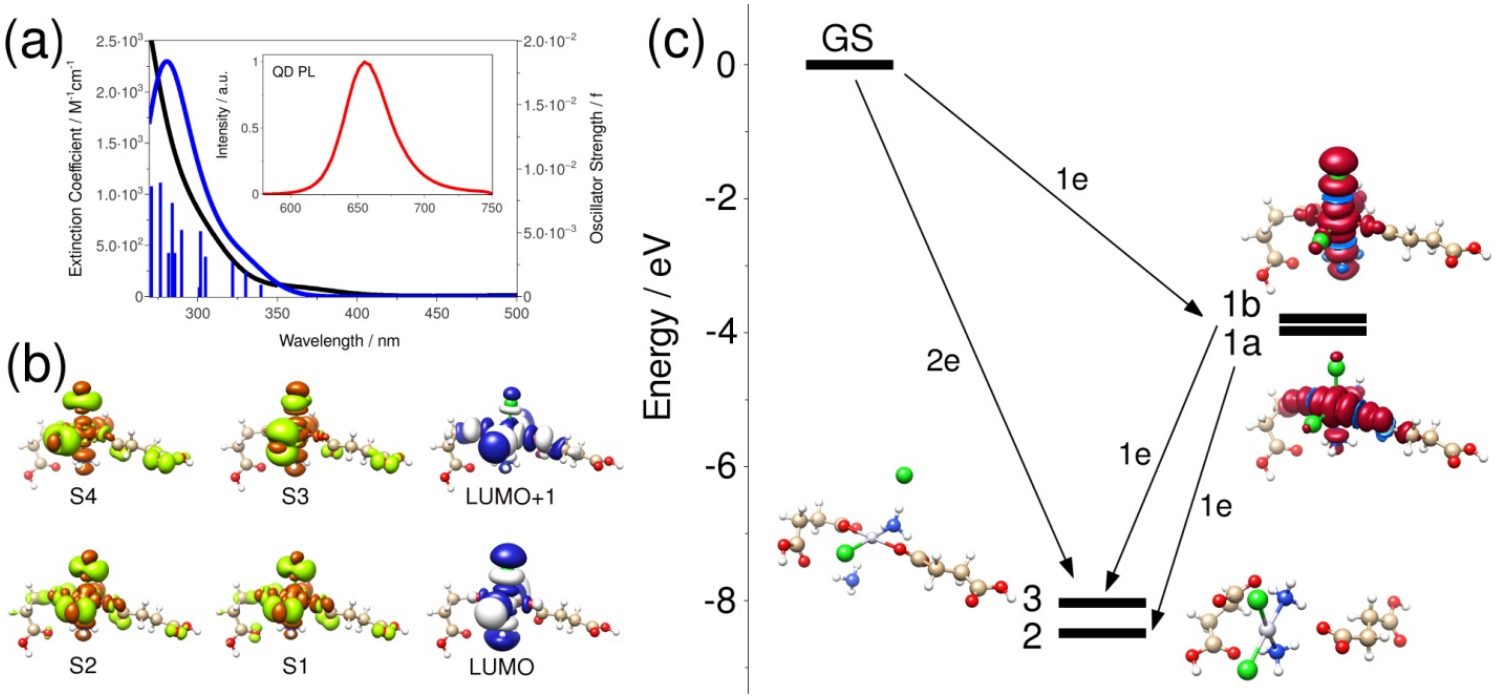


Figure 4.38: (a) Selected regions of the ^{1}H NMR spectrum of **1** in H_2O/D_2O (5:1, [**1**] = 1 mM) in the dark (bottom) and after irradiation with 385 nm light (top, 2 min., ~40mW·cm^{-2}); Pt 4f XPS spectra of **1** in the dark (bottom) and after irradiation (top) with 385-nm light (15 min., ~40mW·cm^{-2}).

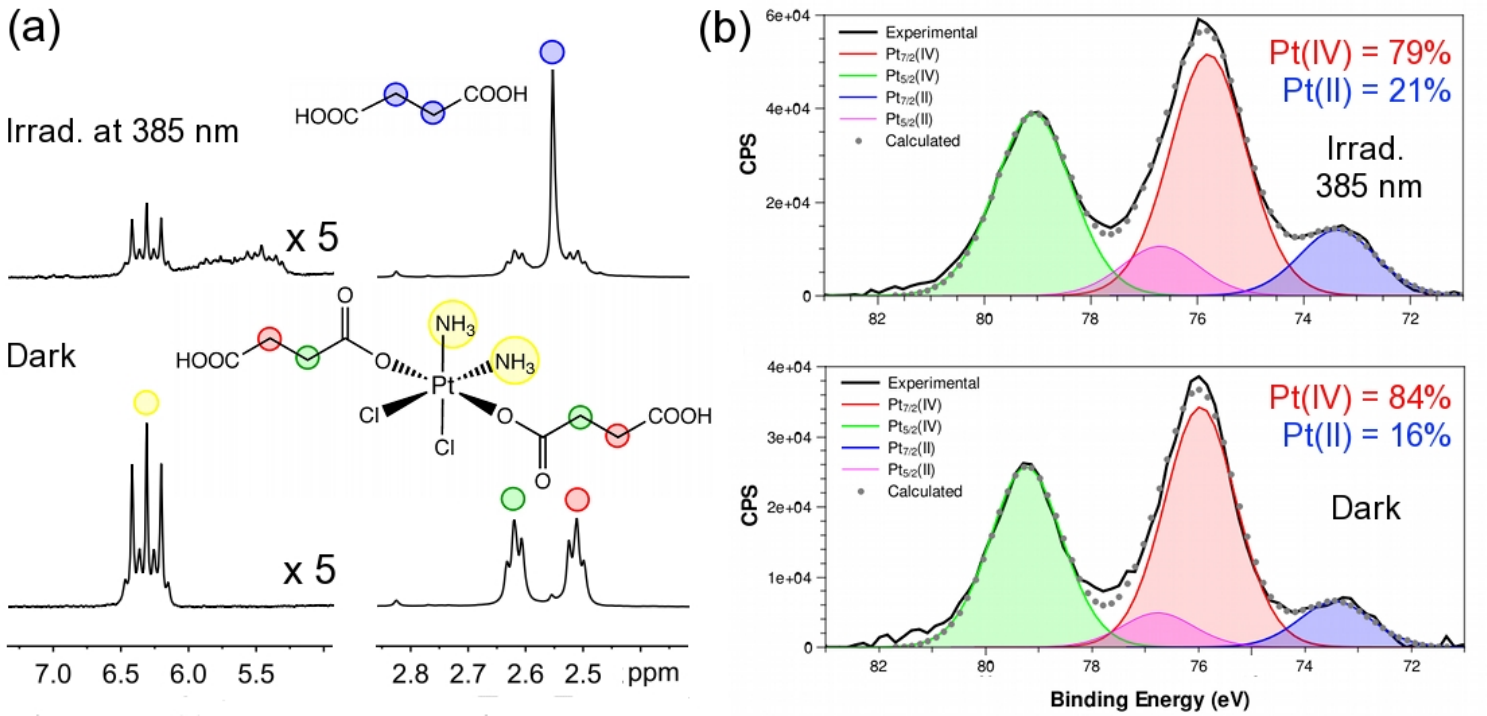


Figure 4.39: Core-shell CdSe@ZnS PL quenching plots as a function of the concentration of **1**. (a) Data fitting with the Langmuir absorption isotherm (R-Square = 0.99) and (b) with the Stern-Volmer model for dynamic collisional quenching (R-Square = 0.83). Error bars were determined by comparing three PL spectra for each point and propagating the error in an additive fashion.

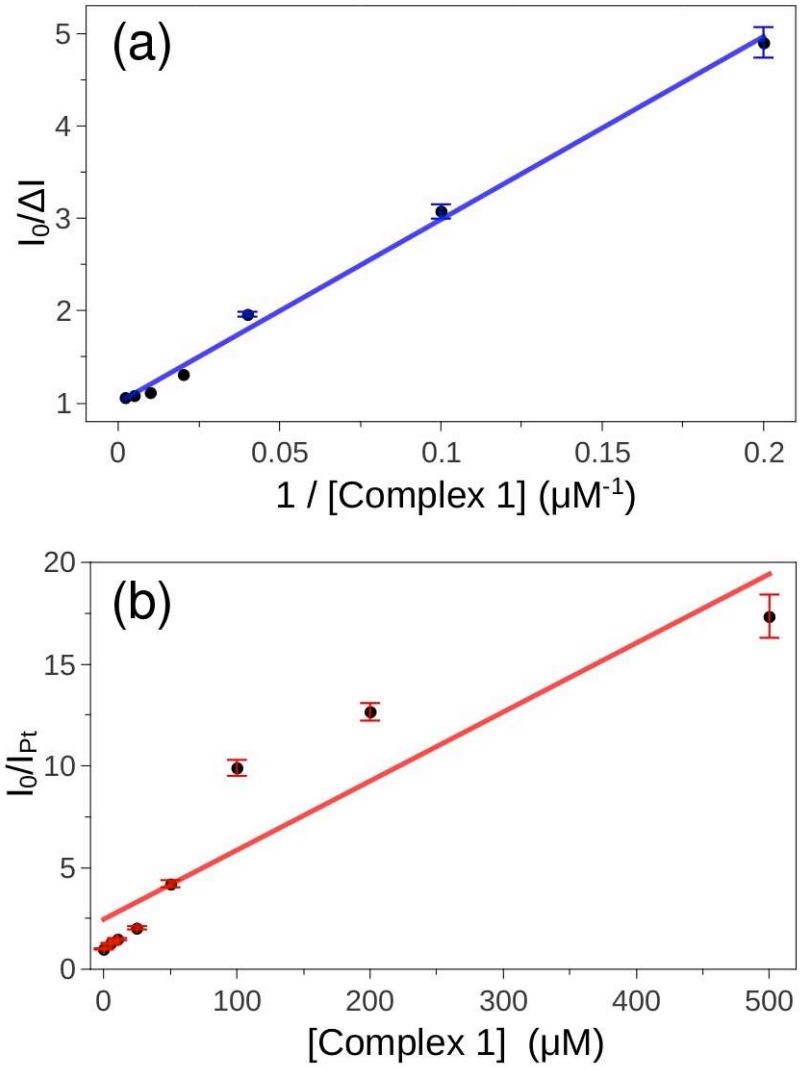


Figure 4.40: MOs energy levels and density of states for the $(CdSe)_{12}$-**1** (a) and $(CdSe)_{12}@(ZnS)_{48}$-**1** (b) compounds. The MOs for the QDs are always depicted in black, while the MOs of **1** are in red. The MOs of the final complex are shown in the center and are split in those mostly localized on the QD (in black) and those mostly localized on **1** (in red). Solid (dashed) arrows refer to HOMO-LUMO (TDDFT) gaps. For the core-shell model, the shaded region corresponds to the projection of the DOS on the core atoms.

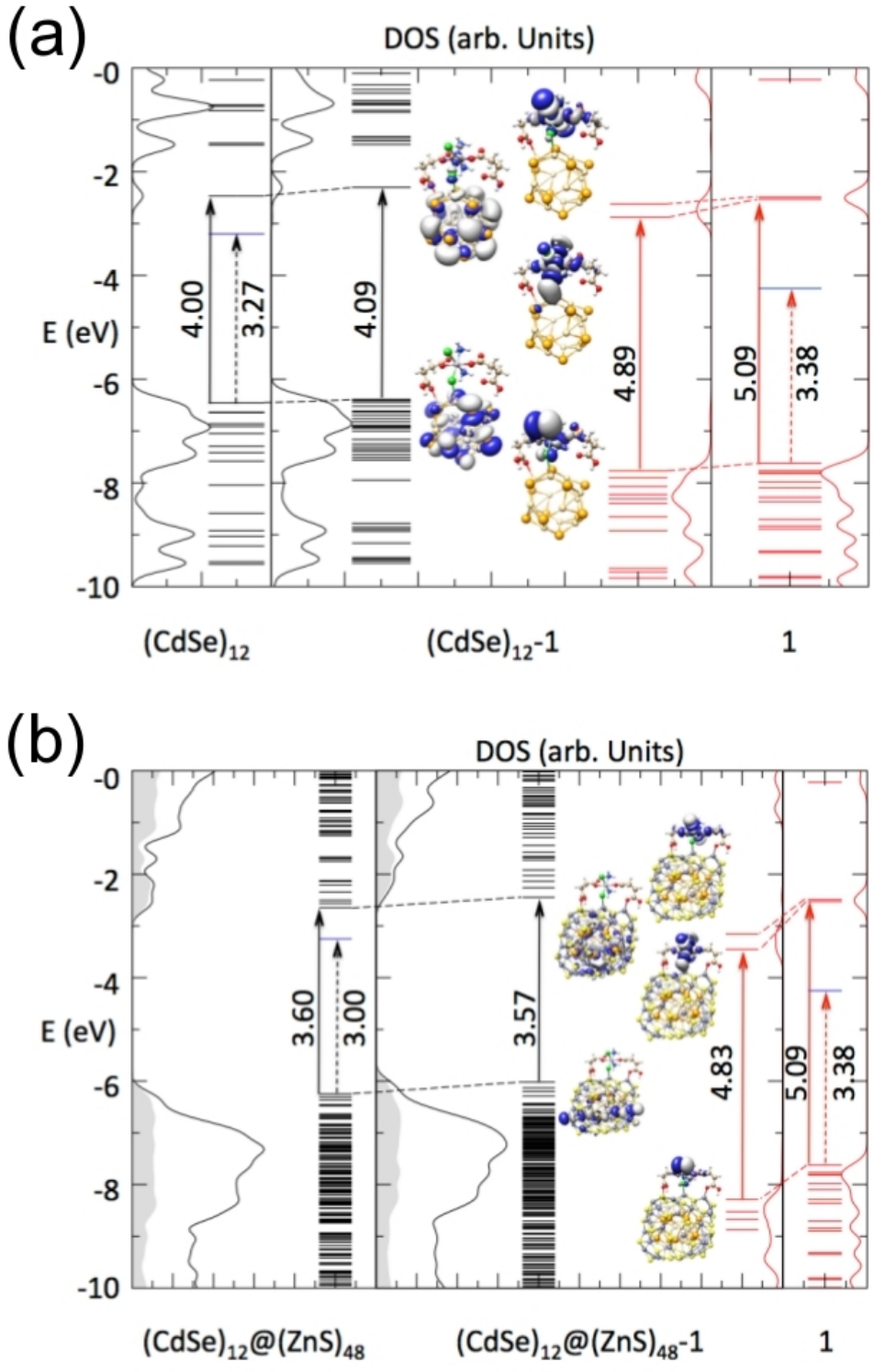
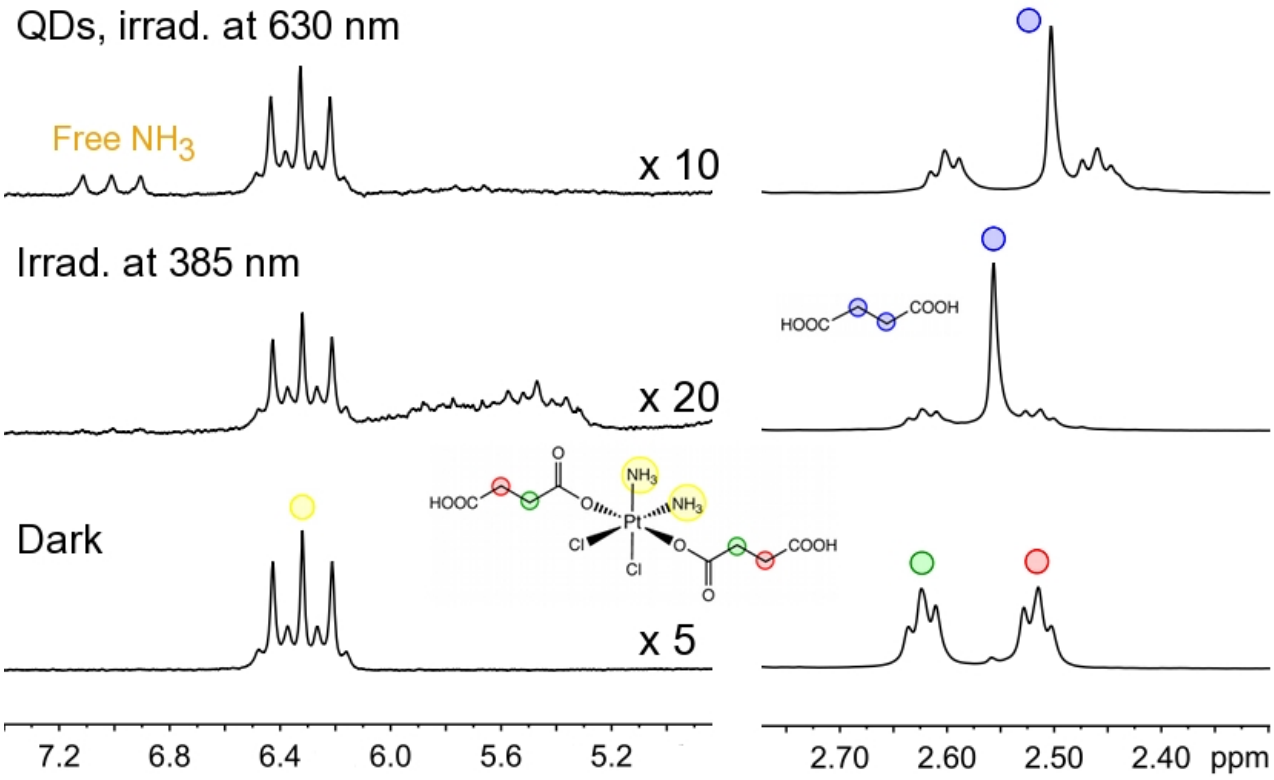


Figure 4.41: Selected regions of the ^{1}H NMR spectrum of **1** in H_2O/D_2O (5:1, [**1**] = 1 mM) in the dark (bottom), under irradiation at 385 nm (middle, 2 min., ∼40mW·cm^{-2}) and under irradiation at 630 nm in the presence of PEGylated CdSe/ZnS QDs (top, [QD] = 100 nM, 3 h, ∼20mW·cm^{-2}).



4.7 Effect of Structural Dynamics on the Opto-Electronic Properties of Bare and Hydrated ZnS QDs

4.7.1 Abstract

Quantum mechanical calculations on the structural and optoelectronic features of two realistic wurtzite-like ZnS quantum dot (QD) models, namely, $(ZnS)_{33}$ and $(ZnS)_{116}$, are presented both in vacuo and in an explicit water solution environment. Car–Parrinello molecular dynamics (CPMD) simulation and excited-state, Time-Dependent DFT (DFT/TDDFT) calculations on extended models are combined to unravel hitherto inaccessible atomistic features of the investigated systems. Ultrasmall QDs are predicted to exhibit strong dynamical fluctuations. Accordingly, the bare $(ZnS)_{33}$ model undergoes a drastic structural rearrangement and evolves from the starting bulk-like structure to an amorphous phase. The geometrical changes occurring over the time are reflected on the opto-electronic properties. The band-edge states and the optical absorption onset both sizably vary along the CPMD trajectory. Eventually, the optical gap decreases due to the emergence of high-lying occupied orbitals. These midgap states are mainly localized in undercoordinated S sites and could act as trap states for the photogenerated holes. Water molecules are predicted to form strong Zn–OH_2 bonds with the surface Zn atoms. Hydration seems to lower the surface energy, stabilize the wurtzite polymorph, hinder the Zn–S bond breaking, and largely prevent the appearance of trap states. Besides, adsorbed water molecules produce a notable blue-shift of the optical gap. The electrostatic field induced by the solvent shell and the electron-donor properties of the water molecules are supposed to be responsible for the opening of the gap. Moreover, capping the QDs with water molecules increases the intensity of the lowest-lying electronic excitations. This study sheds light on the important opto-electronic modifications occurring for realistic QD in water solution and offers at the same time the methodological framework to investigate photocatalytic reactions mediated by ZnS.

4.7.2 Introduction

Over the last years, interest on II–VI (II: Zn, Cd, Hg; VI: O, S, Se, Te) semiconductor quantum dots (QDs) has grown notably due to their novel properties [4, 5]. Their unique behavior, which often differs from the bulk material, lies on the combined effect of their large surface-to-volume ratio and quantum confinement. Due to their outstanding properties, they are recurrently employed as solar cell components [146, 147], optical sensors [133, 274], opto-electronic devices [275], and photocatalysts [129–132].

Among the II–VI materials, ZnS nanostructures have earned lots of attention. ZnS QDs, typically absorbing/emitting in the UV–vis, have found application in opto-electronics [384] and catalysis [566]. Besides, since ZnS is an abundant, highly stable, and environmentally friendly material, ZnS nanoparticles are amenable for biological applications [68].

Due to the high surface-to-volume ratio inherent in nanomaterials, surface ligands and solvent molecules may play an important role on the properties of QDs [9]. Capping molecules are known to modify the surface energy of QDs and determine, to some extent, the atomic arrangement of the nanomaterial. Moreover, surface adsorbed molecules tailor the opto-electronics of QDs. In this context, interest on hydrated ZnS QDs has increased notably [28,30–33]. Indeed, most of the QDs operate in water or, at least, immersed in a solvent. The understanding of ZnS–water interaction is thus particularly important with a view to their (bio)medical application. Even if ZnS QDs have been employed themselves in biology, ZnS is also commonly used as protective shell for CdSe QDs to avoid the release of toxic Cd^{2+} ions. Therefore, for a safe application of ZnS nanostructures *in vivo*, their behavior in water solution should be precisely investigated. From a different perspective, the study of the ZnS–water interaction may pave the way to understand the photocatalytic water splitting reaction occurring at the semiconductor surfaces. Recently, ZnS QDs have proven to be an efficient catalyst for H_2 generation from water [567,568].

Most of the works published so far on hydrated ZnS QDs have focused on the effect of water (and other capping ligands) on the structure of the QDs [28,30–33]. In these studies, the uncapped ZnS QDs are reported to undergo a drastic rearrangement driven by the unsaturated atoms on the surface. Surface ligands are known to cap undercoordinated atoms, minimize surface energy, and stabilize the QD structure. These conclusions are based on various experimental techniques but also assisted by classical molecular dynamics simulations. *Ab initio* molecular dynamics, which provide an accurate framework for the description of intermolecular forces, have been limited to minimal models such as $(ZnS)_4$ [31]. For this kind of small clusters, $(ZnS)_n$, with n = 4, 6, 12, the effect of the surrounding water molecules on the opto-electronic properties have been investigated by means of DFT/TDDFT calculations [334,338]. So far computational modeling has provided valuable insights of the effect of hydration on the structural and the optoelectronic properties of ZnS QDs. Realistic models have however been analyzed only by means of classical molecular dynamics simulations. Then, accurate DFT/TDDFT calculations have been reported for realistic $(ZnS)_{116}$ clusters of nanometric size but the effect of the water solvent was described by an implicit solvation model [300]. Furthermore, previous studies have been carried out on optimized minimum energy structures, thus not accounting for the dynamic behavior of solvated QDs. Experimentally, however, QDs may display a marked dynamical character and structural changes are reflected on the absorption and emission features, which change over time [14]. The interplay between the structure and the ligands in relation to the presence of trap states (hole or electron) is also of particular interest [26,301].

The present work represents a step forward in the characterization of hydrated ZnS QDs. It tries to unveil the role of structural fluctuations and solvent effects on the opto-electronic properties of realistic QDs. With that goal, two wurtzite-like QD models of increasing size have been selected, $(ZnS)_{33}$ and $(ZnS)_{116}$, surrounded by shells of 207 and 341 explicit water molecules, respectively, see Figure 4.42. *Ab initio* molecular dynamics simulations in the Car–Parrinello framework have been performed to capture the dynamic fluctuations of the

bare and hydrated QDs. Furthermore, the ground and excited state of an ensemble of configurations sampled along the dynamics have been characterized by hybrid DFT/TDDFT calculations.

Water has been predicted to stabilize wurtzite bulk-like structures, even for small ZnS QDs, which would otherwise be disordered in nature. Furthermore, the presence of surrounding water molecules sizably affects the electronic and optical features of the models studied, leading to a strong reduction in the number of midgap states, which could act as charge trapping sites. This work sheds light on the important opto-electronic modifications occurring for realistic QD in water solution and provides the methodological framework to investigate photocatalytic reactions mediated by ZnS.

4.7.3 Model and Computational Details

To unravel the behavior of hydrated ZnS nanostructures two realistic models of increasing size have been chosen, namely $(ZnS)_{33}$ and $(ZnS)_{116}$. With an approximate diameter of 1 nm, the $(ZnS)_{33}$ cluster is a recurrent product of both gas and condensed phase synthesis of ZnS nanostructures [17]. To explain the abundance of the so-called magic $(ZnS)_{33}$ stoichiometry, found for other II–VI materials like ZnSe, CdS, and CdSe [17], two kind of models have been proposed: (1) core@cage [17, 21, 22] and (2) wurtzite-like [288, 293]. In this work, the latter has been chosen. However, as one may notice from Figure 4.42, the relaxed structure (b) significantly differs from the pristine cluster (a) cleaved from the bulk wurtzite. Such reconstruction (or self-healing, as named by Puzder et al. [288]) minimizes the number of dangling bonds on the surface. To provide a direct comparison with the experimentally accessible ZnS QDs, the 1.5 nm size $(ZnS)_{116}$ model has also been considered. Sliced from the bulk wurtzite, Zn and S adatoms have been placed on its S- and Zn-rich polar faces, leading to the saturation of the undercoordinated atoms, the minimization of the dipole along the c axis, and the stabilization of the pristine bulk-like nanoparticle [300]. The gas phase optimized structures of the $(ZnS)_{33}$ and $(ZnS)_{116}$ clusters, obtained by means of the PBE functional [238] in combination with a STO valence DZ basis set, as implemented in the ADF 2012.10 software [267], have been immersed in a periodic box of water molecules, and *ab initio* Car–Parrinello molecular dynamics (CPMD) have been performed on the resulting fully solvated systems. For comparison, the dynamics of the bare $(ZnS)_{33}$ cluster have also been studied.

CPMD simulations [262] have been carried out using the GGA-PBE exchange-correlation functional [238] in conjunction with a plane wave basis set (25/240 Ry cutoff for wave functions and augmented charge density) and ultrasoft pseudopotentials [420], as implemented in the Quantum-Espresso package [419]. Dynamic simulation have been performed at finite temperature (350 K), in a cubic supercell of side 16.78, 19.71, and 24.83 Å for the bare $(ZnS)_{33}$, the hydrated $(ZnS)_{33}(H_2O)_{207}$, and the hydrated $(ZnS)_{116}(H_2O)_{341}$ models, respectively. The number of water molecules included in the simulation has been evaluated by considering the volume encumbrance of the cluster. In particular, starting from a preliminary simulation

of bulk water, a cavity is created removing a number of water molecules equivalent to the volume of the cluster, and finally, the cluster is placed into the cavity. In order to equilibrate the systems, they are allowed to evolve for 1 ps to check their actual temperature and then a Nosé thermostat is applied for about 2 ps. Once the thermalization is achieved, the thermostat is removed and the systems are allowed to evolve naturally in time.

The total simulation time was about 12 ps for the bare $(ZnS)_{33}$ cluster and about 6 ps for the hydrated $(ZnS)_{33}$ model, composed by 687 atoms. For the hydrated $(ZnS)_{33}$ cluster, comprising a total of 1255 atoms, the atomic motion was evolved for about 4 ps. Interestingly, for the hydrated $(ZnS)_{33}$ cluster the statistics at 4 and 6 ps are almost indistinguishable, validating the shorter simulation time for the $(ZnS)_{116}$ model.

For the bare and hydrated $(ZnS)_{33}$ models, snapshots were taken each 200 time steps (*ca.* 0.05 ps) and DFT/TDDFT calculations were performed on top of them employing the modified form of the B3LYP functional, including 27.5% of HF exchange (B3LYP* hereafter), in conjunction with the LANL2DZ [341–343] basis set. Due to the very large size of the hydrated $(ZnS)_{116}$ model, only single point calculations were conducted on a few representative snapshots taken from the dynamics. In previous works on II–VI semiconductor nanostructures, the parametrization of B3LYP has led to a better description of the optoelectronic properties [300, 303, 416]. Regarding the basis set, LANL2DZ is probably the most popular choice to model realistic II–VI nanoclusters because it reproduces the results of larger sets at a fraction of the computational cost. Quite recently, however, it has been shown to perform quite disappointingly for II–VI QDs [325, 551]. To check the reliability of LANL2DZ for our purposes, it has been benchmarked against other basis sets such as SDD [569, 570], def2-SVP [348, 349], and the reference def2-TZVP [348, 349], see Figure 4.43. The conductor-like polarizable continuum model of solvation (CPCM) has also been employed [460–462]. All the DFT/TDDFT calculations have been conducted by means of the Gaussian09 program package [422].

Radial distribution functions have been calculated using the Virtual Molecular Dynamics (VMD) software [571]. The X-ray diffraction patterns have been simulated by means of the Mercury software package [572]. To do so, the models have been placed in a 10 nm long cubic unit cell. In order to reproduce the experimental conditions, the X-ray wavelength has been set to the Cu Kα value of 0.154056 nm. A FWHM of 0.1° has been chosen for the convolution of the diffractogram.

4.7.4 Results and Discussion

Structural Features

The CPMD simulations reveal that the B-$(ZnS)_{33}$ model undergoes a significant reconstruction. Along the dynamics it evolves from the wurtzite-like geometry to an amorphous structure. After local geometry optimization, the amorphous structure was calculated to lie about 20 kcal/mol lower than the optimized bulk-like geometry [573]. It appears that ultrasmall

nanoclusters are intrinsically disordered, in agreement with the experimental evidence [14]. So far, such small QDs have been predicted to adopt ordered structures such as bulk- or core@shell-like.

With the increasing size of the nanostructure (and the decreasing surface-to-volume ratio), bulk-like geometries are expected to be favored. In this sense, based on CPMD calculations, the bare $(ZnS)_{116}$ model was predicted to preserve the wurtzite structure, though surface atoms were found to rearrange during the dynamics [300]. Apparently, the inclusion of explicit solvent stabilizes the bulk-like structure. For the W-$(ZnS)_{33}$ model, the characteristic pattern of the wurtzite structure is recognizable along the whole trajectory.

To further characterize the structure of our models, the Zn–S radial distribution function (RDF) has been calculated, see Figure 4.44. For comparison, the Zn–S RDF of the perfect $(ZnS)_{33}$ model (WZ-$(ZnS)_{33}$), as cleaved from the bulk wurtzite, has been also considered. For the latter, Zn–S bond distances are set to the experimental bulk value of 2.35 Å. As one may notice from Figure 4.44, the time-averaged Zn–S RDFs (gZn–S(r)) of the B-$(ZnS)_{33}$ and W-$(ZnS)_{33}$ models substantially deviate from the pristine WZ-$(ZnS)_{33}$ model. For the latter, the Zn–S RDF displays sharp peaks at well-determined distances, such as the eye-catching feature at 2.35 Å, which corresponds to adjacent Zn and S atoms. According to the CPMD simulations, both models in the gas phase and in water solution exhibit broader peaks due to surface reconstruction and the thermal fluctuations. The first peak is centered at 2.30 and 2.32 Å for B-$(ZnS)_{33}$ and W-$(ZnS)_{33}$, respectively, slightly shorter than in the bulk ZnS. The longer average Zn–S distance observed for W-$(ZnS)_{33}$ suggests that water adsorption relaxes the shrunk Zn–S bonds in B-$(ZnS)_{33}$. Remarkably, B-$(ZnS)_{33}$ displays a wider distribution of Zn–S distances, indicative of a lower short-range ordering as compared to W-$(ZnS)_{33}$. From the area under the peak, an average Zn–S coordination number of about 3.3 has been obtained for both B-$(ZnS)_{33}$ and W-$(ZnS)_{33}$. A similar coordination number of 3.2 has been reported for magic-size $(CdSe)_n$ clusters (n = 33, 34) [17]. For r > 3 Å, the B-$(ZnS)_{33}$ model displays a broad profile of Zn–S pair distances, meaning little long-range ordering. On the contrary, the W-$(ZnS)_{33}$ model displays three well-resolved peaks, representing a higher degree of ordering. This finding reveals that the atomic ordering of the cluster increases upon hydration, in agreement with the experimental observations and previous classical MD simulations [28, 31].

For comparison, the Zn–S RDF of the W-$(ZnS)_{116}$ is also reported in Figure 4.44. The main features already observed for W-$(ZnS)_{33}$ are recognizable. However, the sharpening of the bands mirrors the highly ordered structure of the W-$(ZnS)_{116}$ cluster relative to the small model. Apart from the crystallinity imposed by the solvent, the pristine $(ZnS)_{116}$ undergoes a modest structural distortion upon relaxation, whereas the $(ZnS)_{33}$ model requires a drastic atomic rearrangement to saturate the undercoordinated atoms on the surface. An average bond distance of 2.33 Å is calculated for adjacent Zn and S atoms (vs 2.32 Å in W-$(ZnS)_{33}$), with an average coordination number of 3.4 (vs 3.3 Å in W-$(ZnS)_{33}$). The Zn–S bond length and coordination number increase with the size of the hydrated model, as the surface-to-volume ratio decreases, and swiftly approach the bulk values of 2.35 Å and 4, respectively.

To deepen on the dynamics of the investigated models, the number of 2-, 3-, and 4-fold Zn and S atoms have been computed along the CPMD trajectories, see Figure 4.45. To provide a direct comparison with B-$(ZnS)_{33}$, Zn–OH_2 and S–H_2O bonds have not been considered for the hydrated models. Zn and S atoms are assumed to be coordinated if the distance between them is smaller than 3.2 Å (the first minimum in the Zn–S RDF, see Figure 4.44). As one may notice from Figure 4.45, the Zn atoms are mainly 3-fold coordinated in B-$(ZnS)_{33}$, due to the large surface-to-volume ratio of the model. However, the number of 3-fold and 4-fold Zn atoms oscillates notably, reflecting the significant dynamical fluctuations of the bare QD. S atoms tend to be 3-coordinated. Nevertheless, the number of 3- and 4-fold S atoms fluctuates to a much lesser extent than variations in Zn coordination. In fact, transition metal atoms are obviously more versatile and can better accommodate different coordination environments. For the W-$(ZnS)_{33}$ model, 3-fold coordinated atoms are again more likely, but the differences with the 4-fold atoms are smaller. More importantly, the number of 3- and 4-fold oscillates to a lesser extent. Similar results have been obtained for the large W-$(ZnS)_{116}$ cluster. From this data, the structure of the bare cluster fluctuates notably, with several Zn–S bond breaking/forming over the time. Capping QDs surface with water molecules seems to lower the surface energy, stabilize the bulk-like geometry, and avoid Zn–S bond breaking events, which ultimately could lead to electronically localized midgap states.

Let us now focus on the interaction between the QDs and the surrounding water solvent. There are presumably three ways for water adsorption on ZnS-QD surface [31]: (a) through Zn–O interactions; (b) through S–H interactions; or (c) through concomitant Zn–O and S–H interactions. To unravel the binding mode of water to the ZnS QDs, the Zn–O and S–H RDFs have been calculated, see Figure 4.46. Irrespective of the cluster size, average Zn–O and S–H distances of 2.08 and 2.28 Å have been obtained. These values commensurate with previous CPMD results for the hydrated $(ZnS)_4$ cluster [31], with computed distances of 2.0 and 2.3 Å, respectively. Remarkably, the position of the first Zn–O peak essentially coincides with that measured experimentally for the hydrated Zn^{2+} cation (2.078 Å, as derived from EXAFS data analysis) [574]. Regardless of the model, the Zn–O bond seems to be stronger than the S–H bond. The slightly shorter Zn–O distance for the smaller $(ZnS)_4$ cluster (2.0 [31] vs 2.08 Å) could mean a stronger QD–water interaction, due to the enhanced nucleophilicity of the 2-fold coordinated Zn atoms in $(ZnS)_4$ compared to the 3-fold coordinated atoms on the surface of the $(ZnS)_{33}$ cluster. More recently, B3LYP/def2-TZVP results on hydrated $(ZnS)_4$ and $(ZnS)_6$ have also been reported, with calculated Zn–O distances increasing from 2.16 to 2.22 Å with increasing adsorption of water [334].

The first feature in the Zn–O RDF represents the first layer of tightly bound water. For the W-$(ZnS)_{116}$ model, the area under the peak provides an average coordination number of 0.4 water molecules per Zn atom. The W-$(ZnS)_{33}$ model delivers a higher value of 0.5, meaning that the water coverage increases with the decreasing QD size, presumably due to the increased surface curvature of small QDs, which increases the surface reactivity and possibly minimizes the repulsion between adjacent adsorbed molecules [31]. In agreement with previous MD calculations regarding Zn^{2+} microsolvation [574], our simulations discard the

exchange of water molecules between the first and the second solvation shells. The minimum between the first and the second hydration spheres, located at r ∼3.0 Å, is in agreement with previous MD simulations on the hydrated Zn^{2+} cation with a reported value of 2.85 Å [575]. The depth of this minimum is quite pronounced, implying a sizable energy penalty that prevents water exchange between the first and the second solvation shells. Our results are consistent with the long residence times reported for the microhydrated Zn^{2+} cation both experimentally and theoretically [575].

In summary, ultrasmall bare clusters are predicted to exhibit large dynamic fluctuations at room temperature, and to undergo substantial structural rearrangements over time. Water molecules strongly interact with the QD surface by means of Zn–OH_2 bonds. Hydration lowers the surface energy and stabilizes the wurtzite-like geometry. Besides, bulk-like structures appear to be stabilized with the increasing size of the model, due to the decreased surface-to-volume ratio.

Electronic Properties

To model the optoelectronic properties of the investigated bare and hydrated QDs, single point DFT and excited state TDDFT calculations have been carried out on top of selected snapshot geometries taken from the CPMD simulation. As one may notice from Figure 4.47, where the Density of States (DOS) of the first production snapshot (t = 0 ps) is shown for each system, the B-$(ZnS)_{33}$ model displays a clear HOMO–LUMO gap of 3.59 eV, as calculated in the gas phase. Surface reconstruction leads to the saturation of the undercoordinated surface atoms, stabilizing the QD and, in principle, avoiding the occurrence of midgap states. The atomic orbitals projection of the DOS reveals that the high-lying occupied states (*i.e.*, those constituting the valence band edge) arise mainly from S *3p* orbitals, whereas the lowest-lying unoccupied states (*i.e.*, those contributing the conduction band edge) are mainly composed by Zn *4s* orbitals, see Figure 4.48. Four main features are recognizable in the valence band of the B-$(ZnS)_{33}$ model, referred to as P_I, P_{II}, d, and P_{III} according to the notation proposed in the literature [424]. From the projected DOS, P_I and P_{III} are due to the S *3p* and *3s* orbitals, respectively. P_{II} arises from Zn *4s* orbitals, with a notable participation of the S *3p* states. Finally, the *d* feature is composed by Zn *3d* orbitals. Our calculations qualitatively reproduce the valence band structure reported for the bulk material [424]. Notable differences are however found, that is, the calculated *d* band is located 13.09 eV below the top of the valence band, to be compared with the experimental value of about 9.0 eV. These differences are likely to be due to the small size of the QD, as they tend to be lifted by increasing the QD size [300].

The inclusion of implicit water produces an upward shift of both the valence and the conduction band edges. The unoccupied states experience a larger solvent-induced energy displacement, so that the HOMO–LUMO gap sizably widens (4.60 eV). Implicit solvent stabilizes the outermost valence band states relative to the gas phase, thus, placing HOMO close to the other valence band orbitals. The LUMO, despite having a similar nature to the upper

lying virtual orbitals, appears separated in energy from the rest of unoccupied orbitals. This observation coincides with our previous studies on Zn-based nanostructures [300, 303, 416] and with other theoretical works regarding CdSe [313, 473], revealing that this isolated LUMO might be an intrinsic property of the nanometric II–VI semiconductor materials.

For the hydrated clusters, calculations including CPCM as an additional implicit solvent layer improve the position of the valence band features as compared to gas phase results so, unless otherwise stated, the CPCM results will be presented hereafter.

Moving to the hydrated W-$(ZnS)_{33}$ system, a wide HOMO–LUMO gap of 4.87 eV is calculated, see Figure 4.47e. The adsorption of explicit water molecules produces an upward displacement of both the valence and the conduction band edges, as recently found for anatase TiO_2 nanocrystals [158]. In our case, the conduction band experiences a larger shift, so that the HOMO–LUMO gaps opens by about 0.3 eV. Covering $(CdX)_n$ (X = Se, Te; n = 6, 9) nanoclusters with NH_3 and OPH_3 molecules has been calculated to cause a similar effect [336]. As observed for the B-$(ZnS)_{33}$ model, the HOMO is close to the rest of the occupied states and the LUMO is quite separated from the higher-lying unoccupied orbitals. The valence band features of ZnS are still recognizable in the W-$(ZnS)_{33}$ structure. Remarkably, the position of the bands remains almost unchanged. Water introduces occupied states between the P_I and the d bands. The molecular orbitals at about −10 eV reveal a significant hybridization between the Zn on the cluster surface and the O atoms of the water molecules, in line with the Zn–O adsorption mode proposed. The molecular orbitals at the edges of the valence and conduction bands are composed by S and Zn orbitals, respectively, as in the bare model. Consequently, the lowest-lying electronic transitions involve states localized in the $(ZnS)_{33}$ core, in agreement with previous results on hydrated $(ZnS)_n$ (n = 4, 6) clusters [334].

To check whether the blue-shift of the band gap in the hydrated model arises from the geometry imposed by the solvation shell, the electronic structure of W-$(ZnS)_{33}$ after the removal of water molecules has also been calculated, see Figure 4.47d. The shape of the valence and conduction band edges remains almost unchanged. However, the structural distortion is predicted to produce a significant reduction of the HOMO–LUMO, with a computed value by CPCM of 4.35 eV. Zwijnenburg et al. observed a similar effect in their work regarding small hydrated ZnS clusters, where the electrostatic field induced by the absorbed water molecules was proven to be responsible for the opening of the gap [334]. Not only the electric field, but also the electron-donor properties of the H_2O molecules may however play a role. Indeed, the W-$(ZnS)_{33}$ has been calculated to bear a formal charge of about −4 $|e|$ due to the charge transfer from the solvent molecules to the QD. For completeness, gas phase results of the W-$(ZnS)_{33}$ after the removal of water molecules are also reported. Calculations deliver a HOMO–LUMO gap of 2.00 eV, due to the appearance of occupied midgap states.

Figure 4.49 shows the evolution of the band-edge state density along the dynamics for the B-$(ZnS)_{33}$ and W-$(ZnS)_{33}$ models. Irrespective of the model, the LUMO remains almost constant along the whole CPMD trajectory. On the contrary, the HOMO energy oscillates notably. Such fluctuations are particularly important for B-$(ZnS)_{33}$. As one may notice from Figure 4.50, the bare model exhibits wide HOMO–LUMO gaps of about 4.5–5.0 eV. How-

ever, eventually the band gap shrinks due to the appearance of high-lying HOMOs, separated from the rest of the valence band states. To elucidate the nature of such midgap states, the projection of the band edges orbitals on the basis functions of the individual atoms have been calculated. From our calculations, the low-lying unoccupied orbitals are much more delocalized than the high-lying occupied orbitals, irrespective of the model and of the considered snapshot. The HOMOs are particularly localized in the case of the bare B-$(ZnS)_{33}$ model. To better illustrate this point, the B-$(ZnS)_{33}$ structure with the highest HOMO (and lowest band gap) has been analyzed in detail, see **1** in Figure 4.50. For comparison, the snapshot with the lowest HOMO (and highest band gap) has also been considered, see **2** in Figure 4.50. As it appears, the frontier orbitals of structures **1** and **2** show significant differences, see Figure 4.51. For structure **2**, both the HOMO and the LUMO are delocalized over the entire cluster. For structure **1**, the LUMO is also spread over the whole QD, whereas the HOMO is mainly concentrated on two S atoms, that is, a 2-fold coordinated core atom and a three-coordinated surface atom. For structure **1**, the S atoms highlighted in Figure 4.51a comprise 48 and 15% of the HOMO, respectively. On the contrary, the HOMO of structure **2** is distributed over all the 33 S atoms in the nanostructure, with no individual contribution larger than 10%. From our calculations, the break-up of Zn–S bonds and the formation of under-coordinated S atoms may thus result in the appearance of midgap states above the valence band edge, with the concomitant shrinkage of the band gap. The inclusion of the explicit solvent has important consequences, limiting bond breaking phenomena and consequently hindering the emergence of high-lying localized states.

Regarding the W-$(ZnS)_{116}$ model, the average DOS of representative snapshots has been calculated, along with the projection on the water molecules, see Figure 4.52. This hydrated model displays a HOMO–LUMO gap of 4.38 eV, 0.5 eV smaller than W-$(ZnS)_{33}$. However, the shape of the valence band is almost the same. Remarkably, the highest-lying occupied orbitals are quite separated from the rest of the valence band states. Such states have been found to arise from S atoms in the polar surfaces of the $(ZnS)_{116}$ cluster. Therefore, the solvent cannot totally avoid the occurrence of localized states on the ZnS polar surfaces. For comparison, the DOS of the same structure after the removal of the solvent molecules is also shown. The shape of the valence and conduction band edges does not change significantly. However, the band gap slightly decreases with respect to the hydrated model (4.13 vs 4.38 eV) due to the downward shift of the LUMOs. From Figure 4.52, the water-related states are predicted to intrude between the P_{II} and d features of the ZnS QD, as calculated for the W-$(ZnS)_{33}$ model.

Optical Properties

Even if the Kohn–Sham (KS) eigenvalues provide reasonable values for the band gap transition energies of bulk II–VI semiconductors, the description of the excitons in nanostructures requires a more rigorous groundwork, as that supplied by TDDFT [410]. Therefore, Figure 4.53 the simulated absorption onset of B-$(ZnS)_{33}$ and W-$(ZnS)_{33}$, obtained by a Gaussian con-

volution of the lowest TDDFT transition calculated for each system, sampled along the dynamics trajectory. For the bare model the optical gap emerges at 4.0 eV, in line with the experimental results reported for small ZnS nanoparticles [387, 397, 398]. As previously noticed, water adsorption leads to a slight absorption blue-shift of 0.1–0.2 eV. Furthermore, the intensity of the lowest transition is found to increase, in agreement with previous works [334]. Irrespective of the model, the LUMO is the final state of the lowest-lying TDDFT excitations. Since the cooling of the photogenerated hole to the HOMO is expected to occur rapidly by virtue of the large effective mass of the hole and the high valence band DOS, our models are predicted to display sharp emission bands, related to the LUMO – HOMO relaxation. Eventually, the B-$(ZnS)_{33}$ model displays low-intensity absorption features in the low-energy region of the spectrum. These signatures are related to the localized HOMOs, as discussed above, and tend to disappear upon hydration.

4.7.5 Summary and Conclusions

The effect of structure and solvent dynamics on the optoelectronic properties of realistic ZnS QDs has been studied. Inclusion of explicit water molecules in our simulations plays an important role on the structure of the investigated QDs by lowering the surface energy and stabilizing a bulk-like geometry, thus, avoiding the occurrence of Zn–S bond breaking events [28]. Hydration produces in all cases an upward shift of both the valence and the conduction band edges, which ultimately leads to a blue-shift of about 0.3 eV of the absorption onset. The electrostatic field induced by the solvent shell and the electron-donor properties of the water molecules are supposed to be responsible for the opening of the gap. Besides, covering the QD with water increases the intensity of the low-lying electronic excitations.

The dynamic behavior of the ZnS QDs is reflected in their optoelectronic properties. The band-edge states vary continuously along the CPMD trajectory. For the bare $(ZnS)_{33}$ model, eventually the band gap shrinks due to the appearance of high-lying HOMOs, segregated from the rest of the valence band states. These high-lying states have been shown to be localized in nature. From our simulations, the continuous Zn–S bond breaking observed in the bare model leads to such midgap states, which could act as trap states. The inclusion of the explicit solvent appears to stabilize the wurtzite-like geometry, prevent the bond disruption and hinder the emergence of S-localized high-lying states.

This study sheds light on the important optoelectronic modifications occurring for realistic QDs in water solution and further provides the methodological framework to investigate photocatalytic reactions mediated by ZnS.

Figure 4.42: (a) Geometry of the pristine WZ-$(ZnS)_{33}$ cluster as cleaved out from bulk wurtzite. (b) Optimized geometry of the bare B-$(ZnS)_{33}$. (c) Starting geometry of the hydrated W-$(ZnS)_{33}$ for the CPMD simulation. (d) Optimized geometry of the bare B-$(ZnS)_{116}$. (e) Starting geometry of the hydrated W-$(ZnS)_{116}$ for the CPMD simulation. Light blue = Zn, yellow = S, red = O, and white = H atoms.

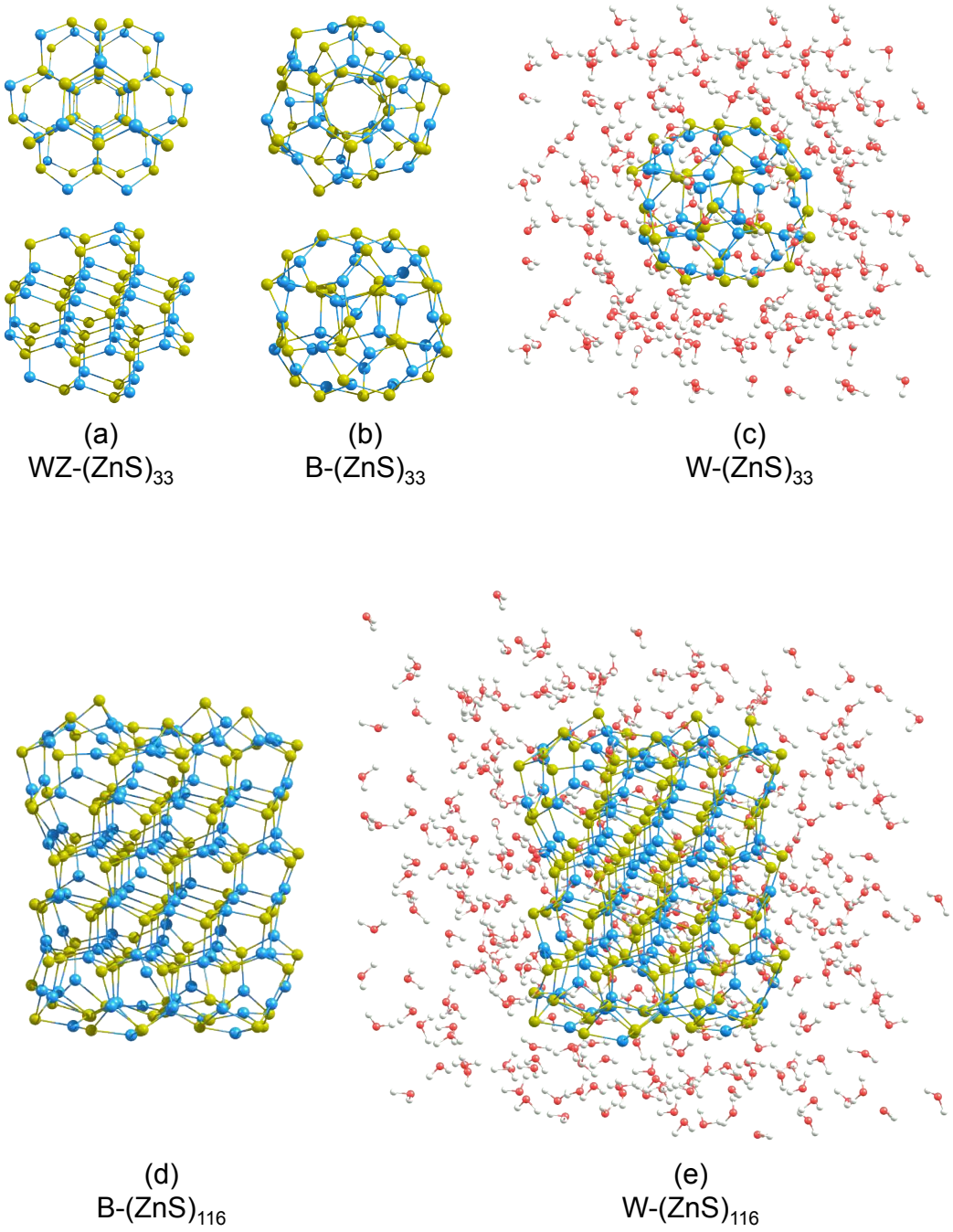


Figure 4.43: Projected Density of States (PDOS) of the bare B-$(ZnS)_{33}$ and the hydrated W-$(ZnS)_{33}$ models, obtained by a Gaussian convolution of σ = 0.20 eV of the individual KS orbitals. Results obtained with the modified B3LYP functional (B3LYP*) in conjunction with different basis sets. Note that the contribution of each orbital type is proportional to the colored area and not its height.

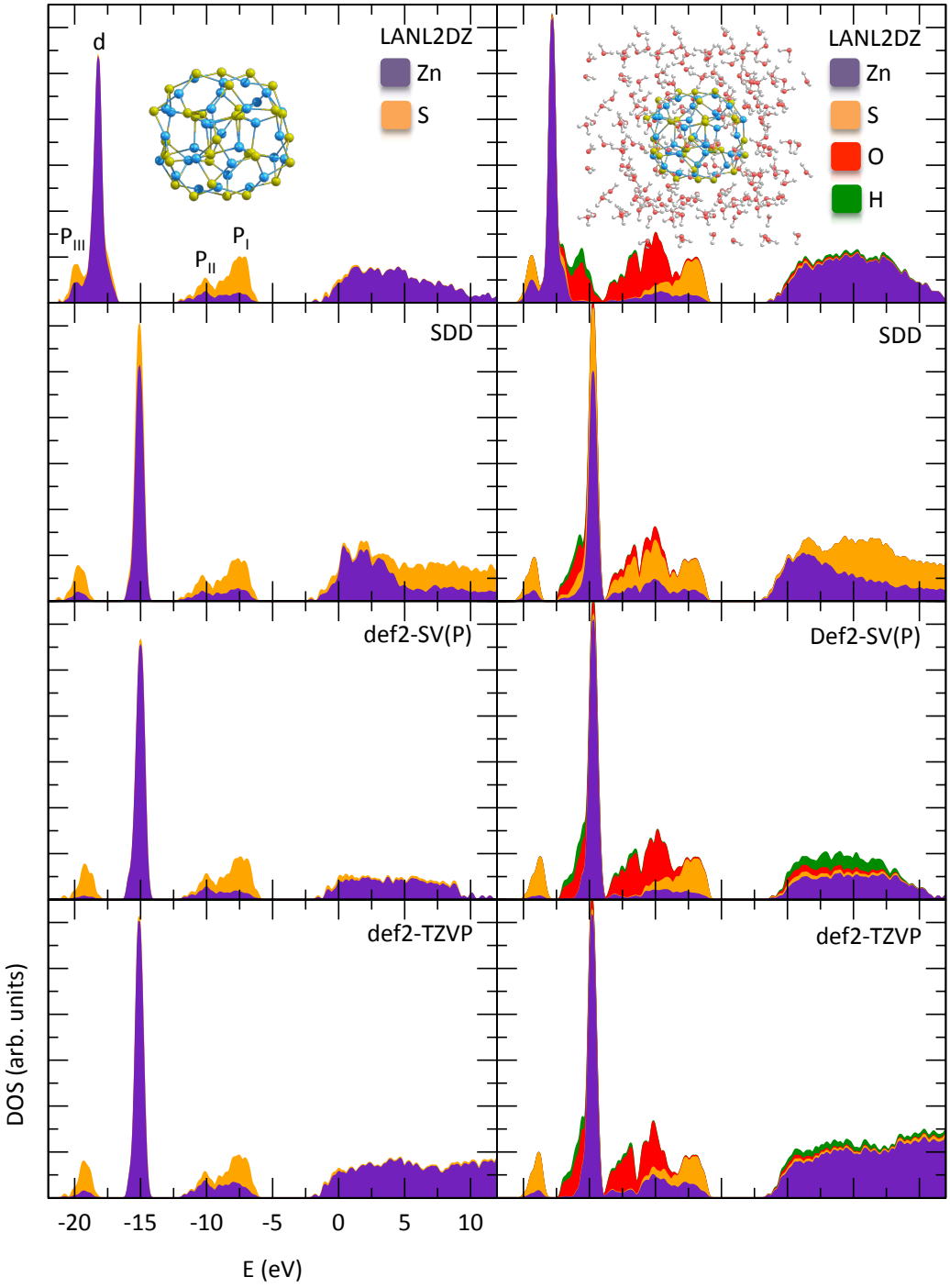


Figure 4.44: Zn–S radial distribution functions ($g_{Zn-S}(r)$) and coordination numbers ($n_{Zn-S}(r)$) of the B-$(ZnS)_{33}$ (in black), W-$(ZnS)_{33}$, and W-$(ZnS)_{116}$ models (in red), averaged along the CPMD trajectory. For sake of comparison, the RDF of the optimized B-$(ZnS)_{33}$ cluster (in gray) and the RDF of bulk wurtzite ZnS (in blue) are provided.

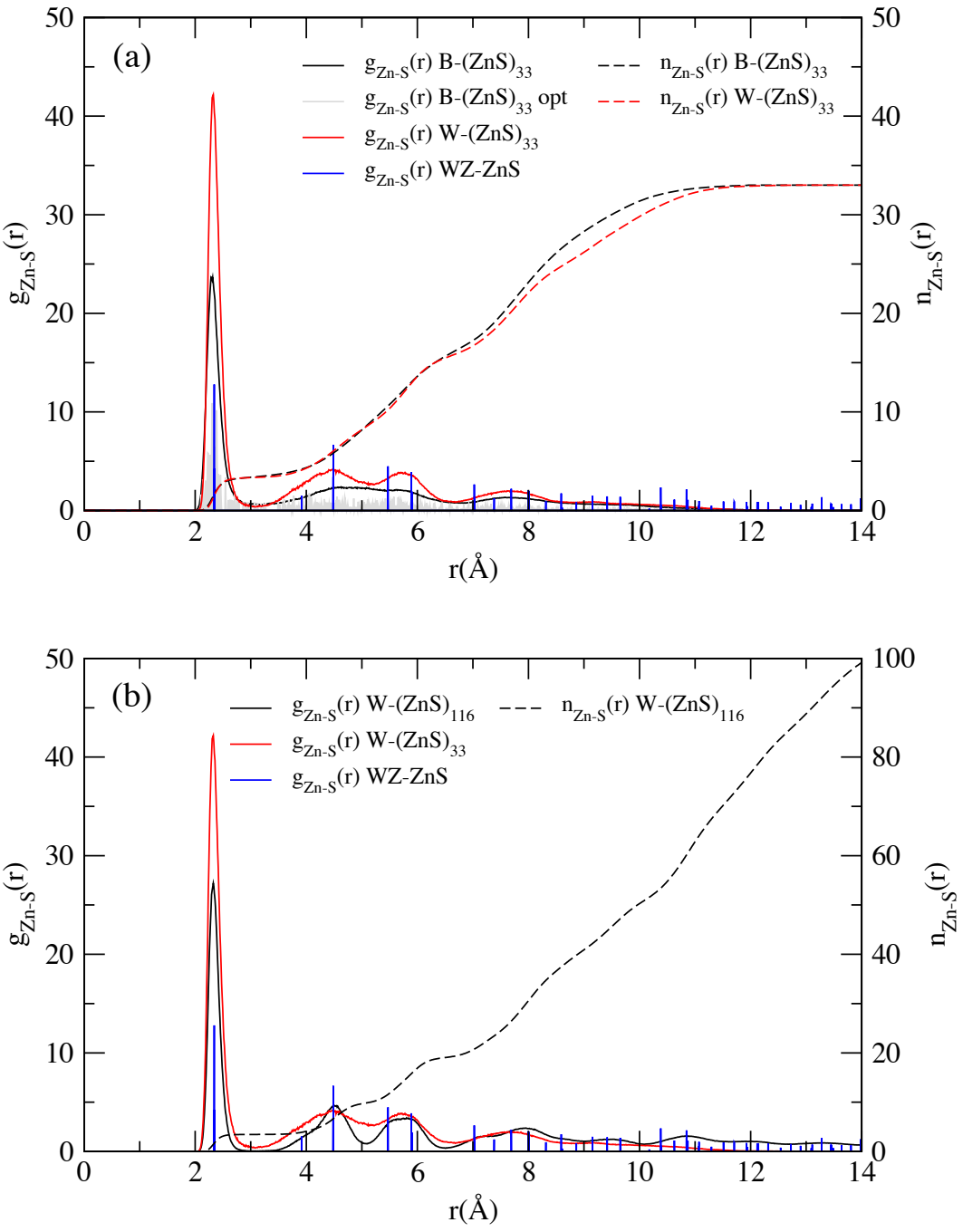


Figure 4.45: Number of 2-fold (black), 3-fold (red), and 4-fold (blue) Zn (top panels) and S (bottom panels) atoms during the simulation, calculated for B-$(ZnS)_{33}$ (left), W-$(ZnS)_{33}$ (middle) and W-$(ZnS)_{116}$ (right). "Av" refers to the average coordination number.

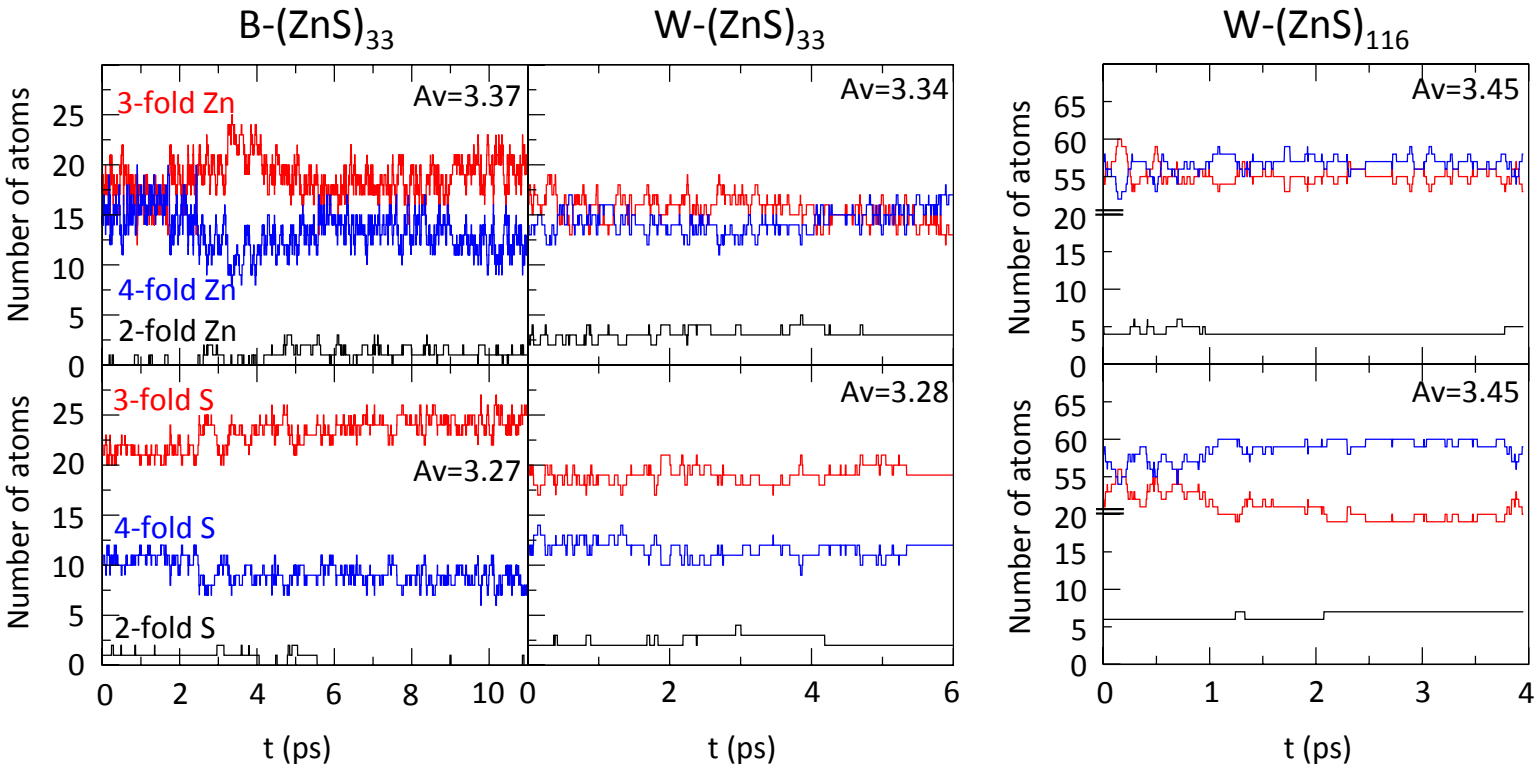


Figure 4.46: Zn–O and S–H radial distribution functions ($g_{Zn–O}(r)$ and $g_{S–H}(r)$) and coordination numbers ($n_{Zn–O}(r)$ and $n_{S–H}(r)$) of the hydrated W-$(ZnS)_{33}$ (a) and W-$(ZnS)_{116}$ models (b).

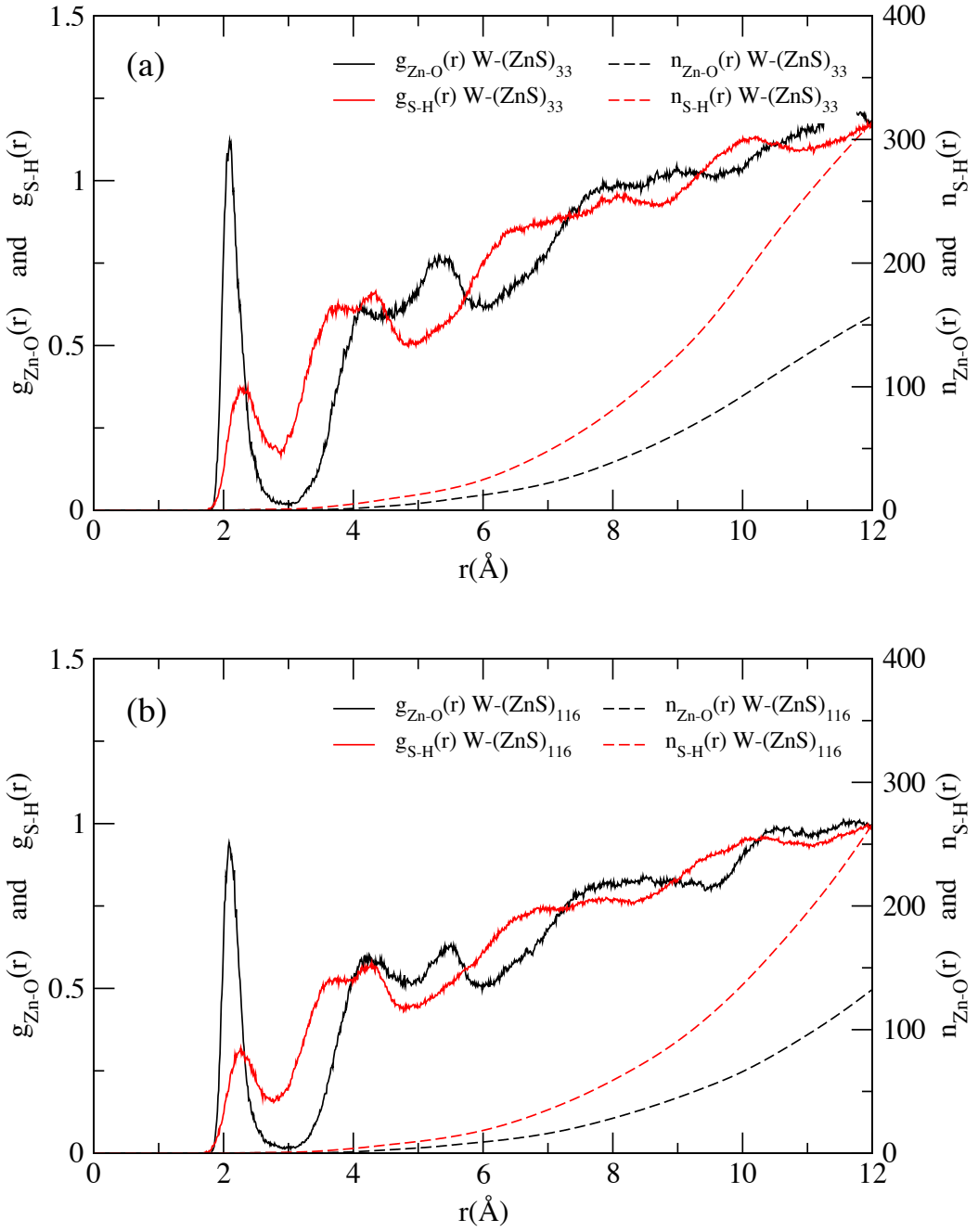


Figure 4.47: Total and projected density of states (DOS and PDOS) of B-$(ZnS)_{33}$ (a, b) and W-$(ZnS)_{33}$ (c, d, and e) obtained by a Gaussian convolution of σ = 0.20 eV of the individual KS orbitals. The insets display a zoom of the bandgap region. Results obtained at the B3LYP*/LANL2DZ level, calculated on top of the first equilibrated snapshot. Note that the contribution of each atom type is proportional to the colored area and not its height.

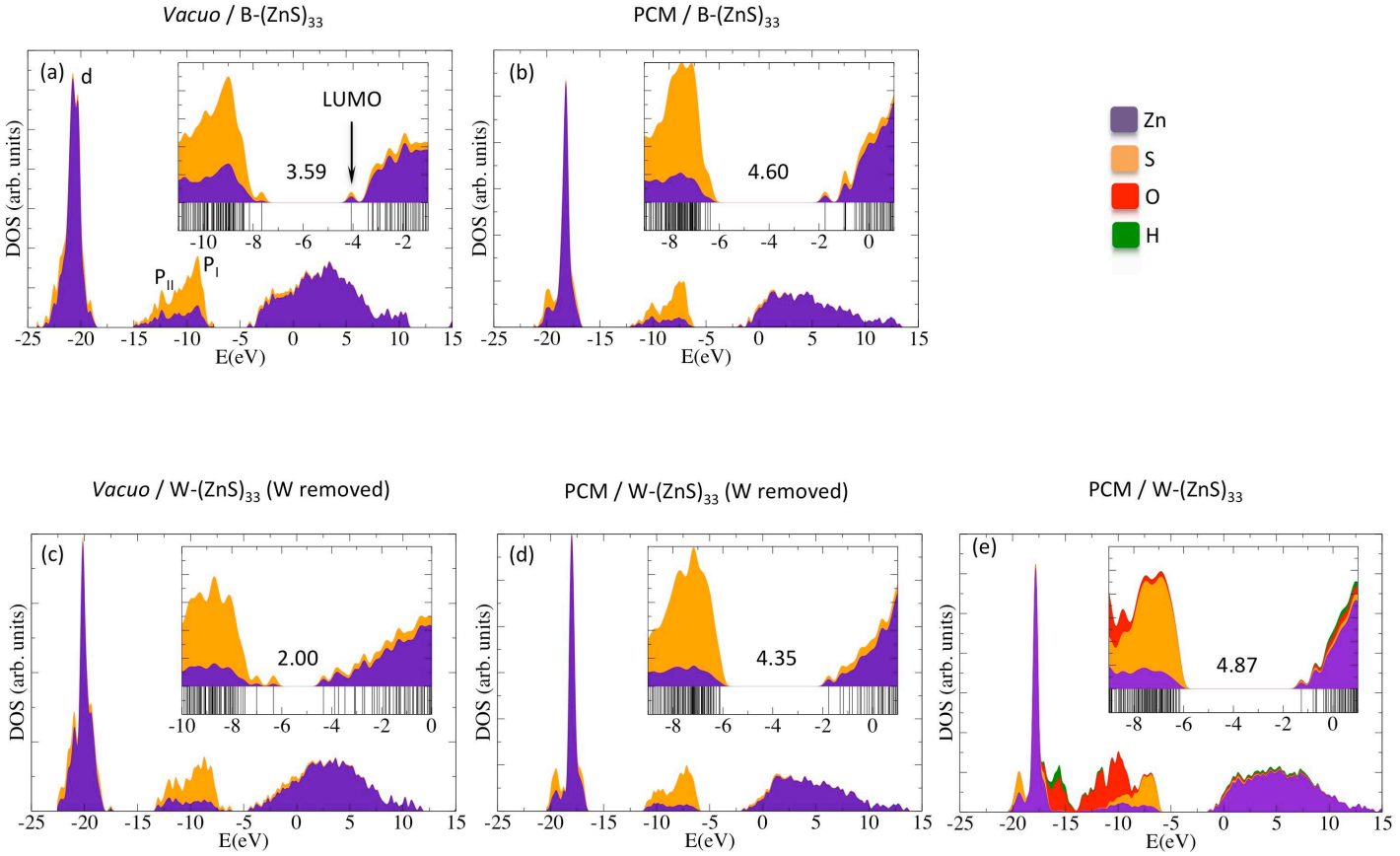


Figure 4.48: Projected Density of States (PDOS) of the bare B-$(ZnS)_{33}$ obtained by a Gaussian convolution of σ = 0.20 eV of the individual KS orbitals. Results obtained at the B3LYP*/LANL2DZ level of theory. Note that the contribution of each orbital type is proportional to the colored area and not its height.

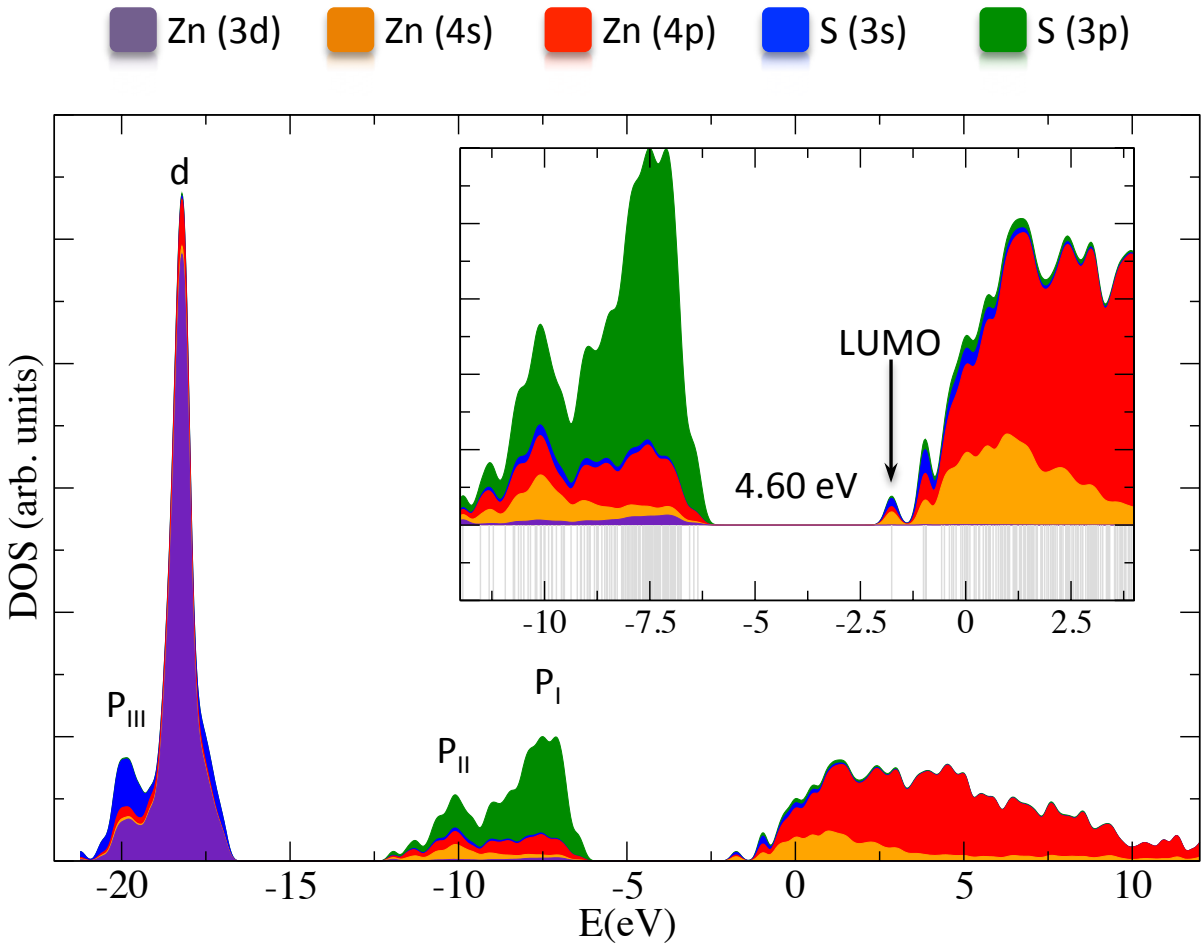


Figure 4.49: Density of states of B-$(ZnS)_{33}$ and W-$(ZnS)_{33}$, obtained by a Gaussian convolution of σ = 0.20 eV of the individual KS orbitals, along the dynamics. HOMO and LUMO levels highlighted in red.

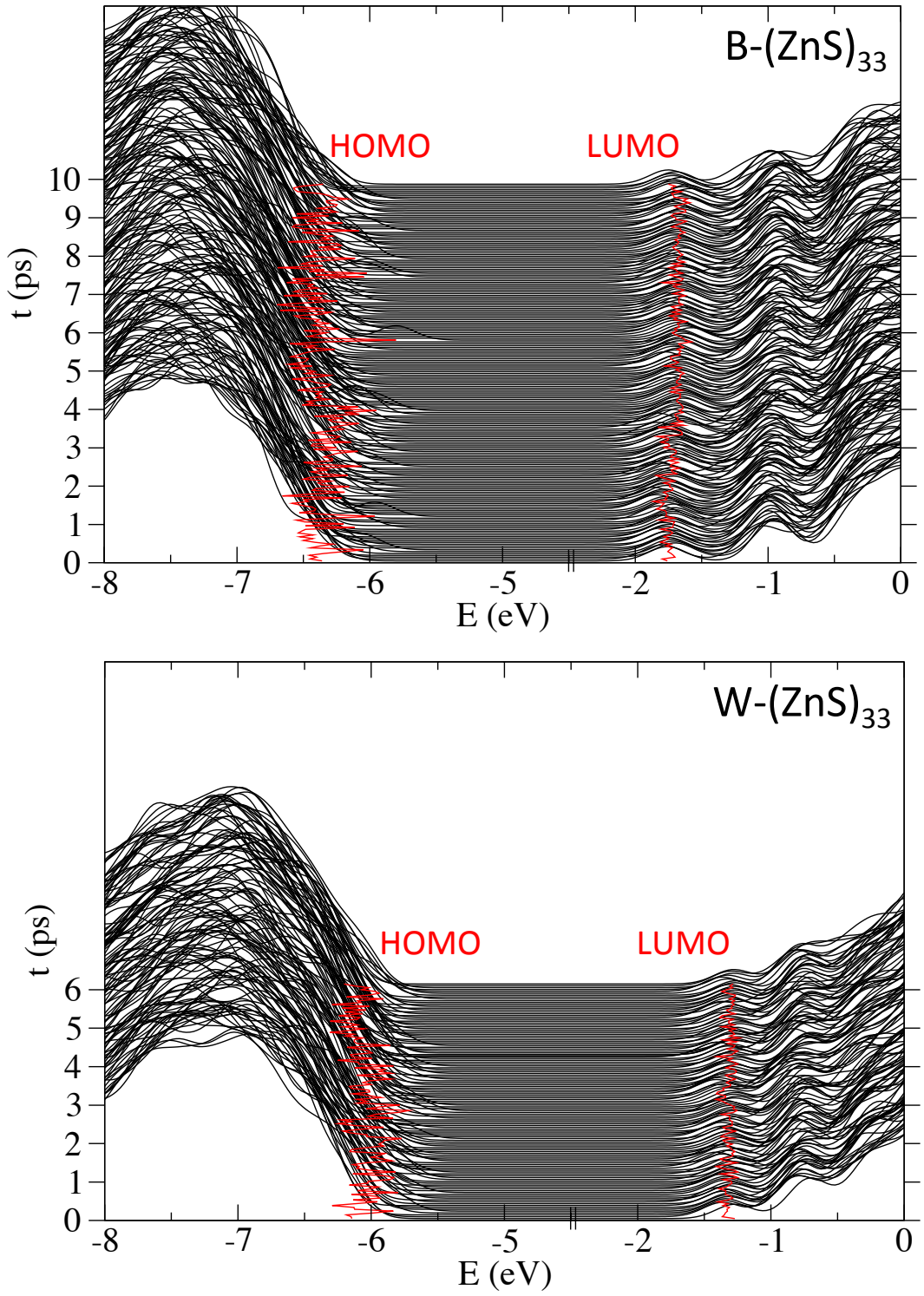


Figure 4.50: Top panels: KS energies of the frontier orbitals as a function of time for (a) B-$(ZnS)_{33}$, (b) W-$(ZnS)_{33}$, and (c) W-$(ZnS)_{33}$ after the removal of water molecules. Green and red lines stand for the occupied and virtual states, respectively. Bottom panels: Calculated HOMO–LUMO gaps, in black. The first TDDFT excitation energy is also provided, in red. Running averages in blue. Results obtained at the B3LYP*/LANL2DZ level.

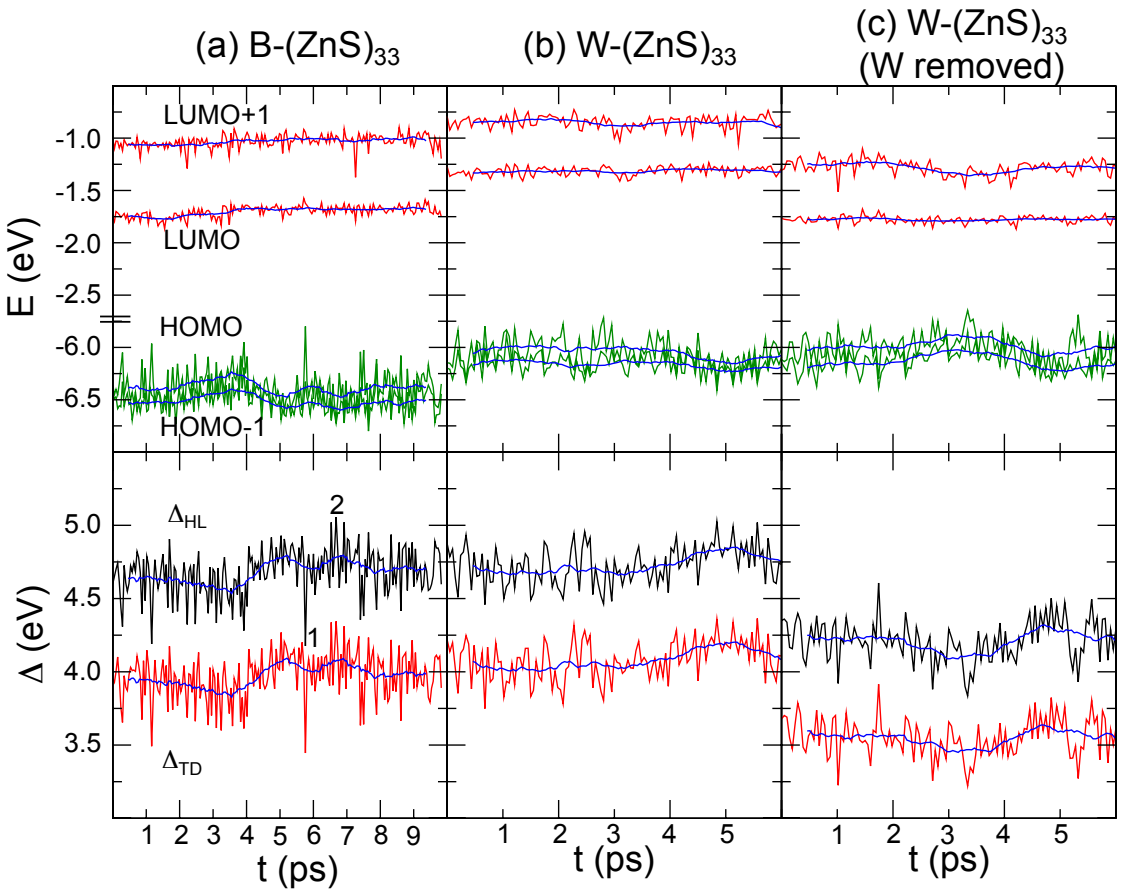


Figure 4.51: Isodensity plots of the frontier orbitals of two representative B-$(ZnS)_{33}$ structures, referred to as **1** and **2** in Figure 4.50. For visibility, contour value of 0.013 has been chosen. Light blue = Zn and yellow = S atoms.

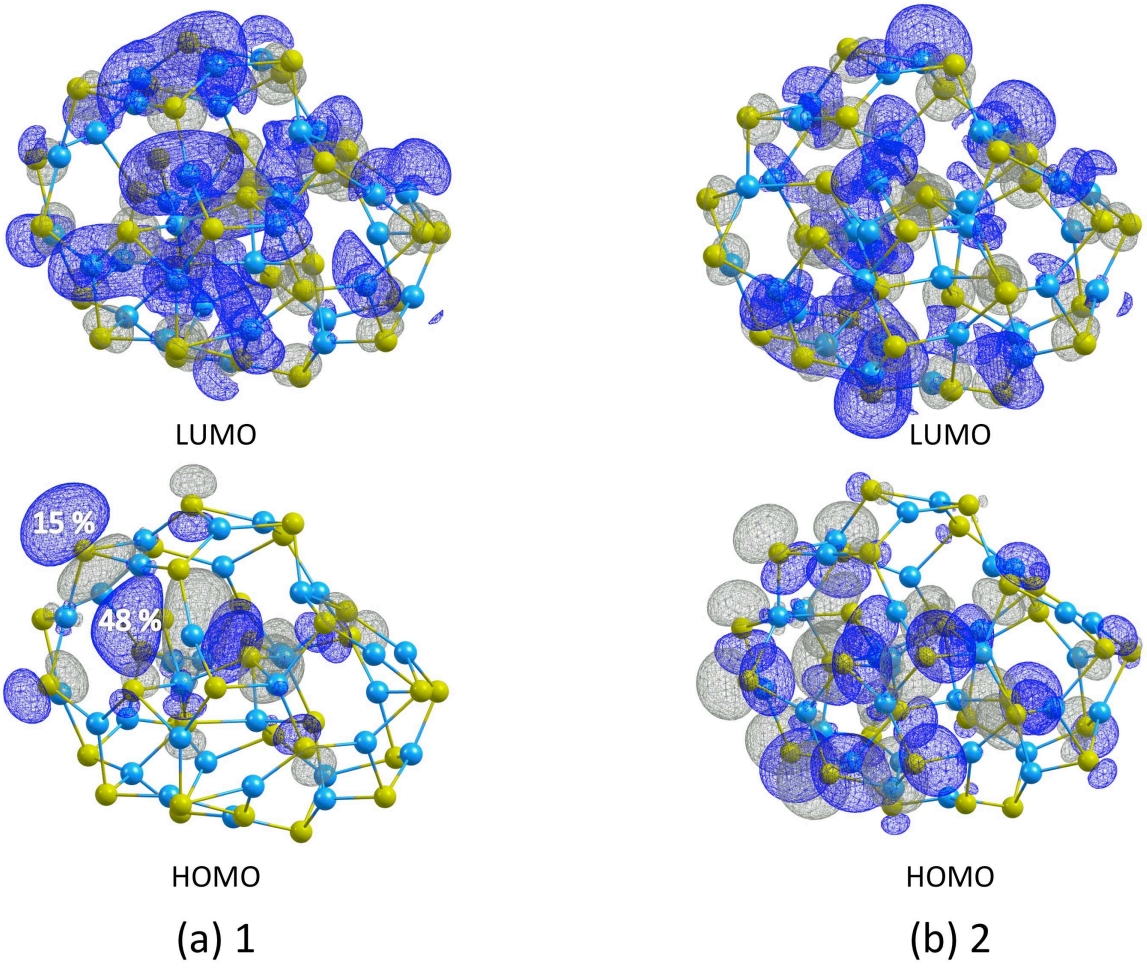


Figure 4.52: (a) Total (black line) and water-projected (red line) density of states of the W-$(ZnS)_{116}$, obtained by a Gaussian convolution of σ = 0.20 eV of the individual KS orbitals. For comparison, the DOS of the W-$(ZnS)_{116}$ after the removal of water molecules have been included (red, shaded). Results obtained at the B3LYP*/LANL2DZ level, averaged over four representative snapshots taken from the molecular dynamics. (b) Detail of the polar (0001) and (000$\bar{1}$) surfaces of the first equilibrated snapshot of W-$(ZnS)_{116}$. For clarity, water molecules are not shown. Light blue = Zn and yellow = S atoms.

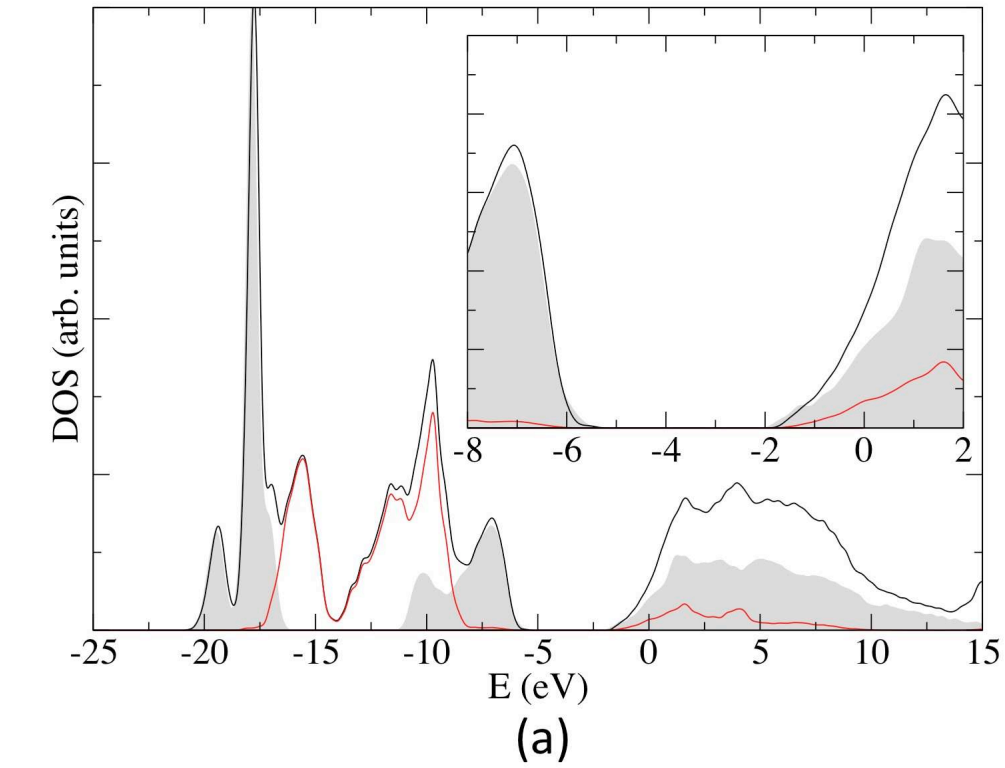
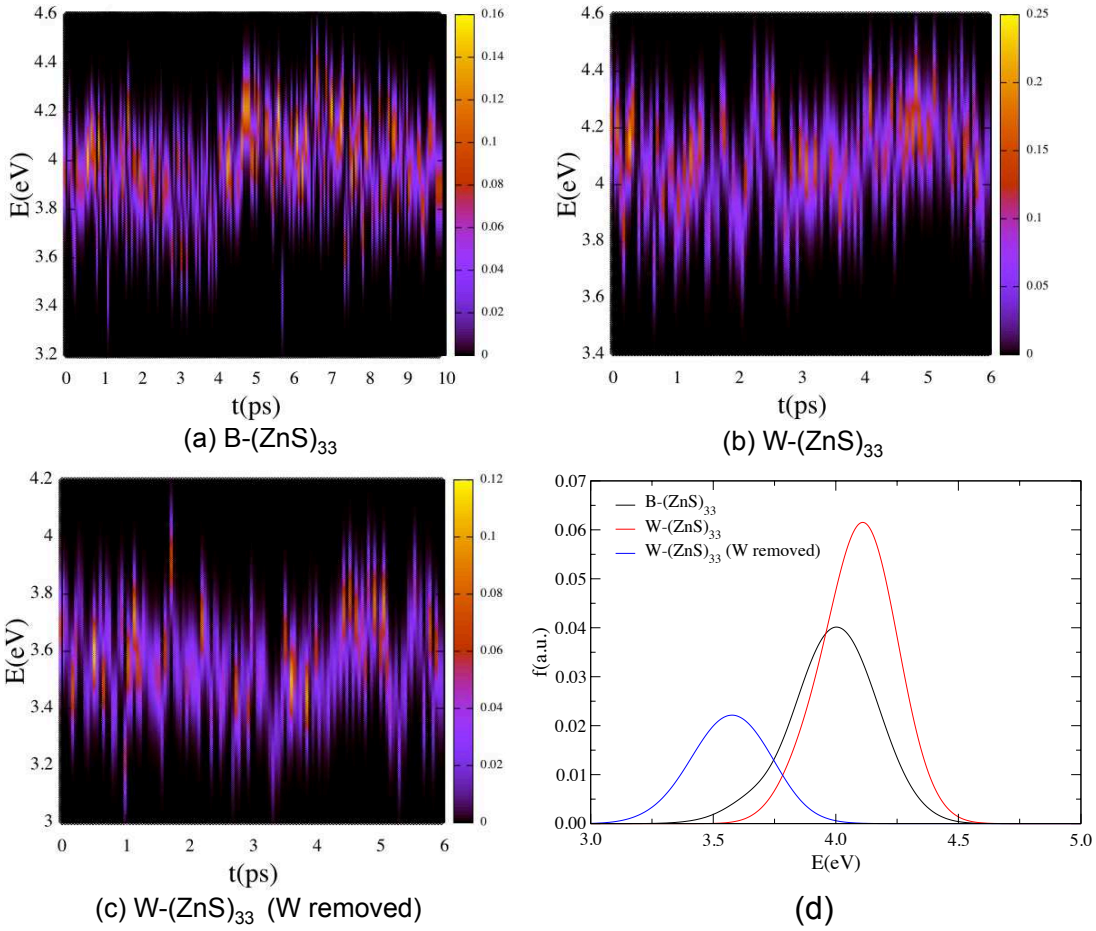


Figure 4.53: Absorption onset of (a) B-$(ZnS)_{33}$ and (b) W-$(ZnS)_{33}$ along the dynamics, drawn by a Gaussian convolution of the lowest TDDFT transition. X and Y axes correspond to the simulation time (in ps) and the excitation energy (in eV), respectively. Color scale refers to the oscillator strength, in a.u.. For completeness, the calculated onset of W-$(ZnS)_{33}$ structures after the removal of the water molecules is also shown in (c). Time-averaged spectra in (d). Results obtained at the B3LYP*/LANL2DZ level.



4.8 DFT/TDDFT Study of the Adsorption of N3 and N719 Dyes on ZnO $(10\bar{1}0)$ Surfaces

4.8.1 Abstract

ZnO has attracted a great deal of research as a potential replacement of TiO_2 for Dye Sensitized Solar Cells (DSSCs), owing to the unique combination of interesting electronic properties (*i.e.* high electron mobility) and structural richness. Here we present a DFT/TDDFT study about the interaction between the prototypical N3 and N719 Ru(II)-sensitizers and a ZnO $(10\bar{1}0)$ surface model, to understand some of the atomistic details which are crucial to the dye/semiconductor interaction. We pay particular attention to the adsorption mode of the sensitizer and to the effect of the complexation on the electronic structure of the dye. Both N3 and N719 are calculated to strongly interact with the ZnO surface. In particular, the interaction is strengthened when three dye carboxylic groups are involved in the adsorption. Moreover, if the anchoring group bears a proton, the adsorption is predicted to be dissociative. The charge density donation from the dye to the semiconductor rises the valence and conduction band edges of the latter, in such a way that the optical gap of ZnO widens. Proton transfer from the dye to the semiconductor balances the charge donation effect and restores the electronic levels of the non-interacting fragments. The impact of dye/semiconductor interaction on the adsorbed dye optical properties are then discussed.

4.8.2 Introduction

Over the last decades the depletion of fossil fuels and the serious environmental concerns associated to their combustion have triggered the development of new energy sources. In particular, solar energy has emerged as a clean, efficient, renewable, and sustainable alternative. The dye-sensitized solar cells (DSSC) firstly developed by O'Regan and Grätzel represented a key breakthrough for the efficient light conversion at low cost [576]. DSSCs consist of a mesoporous wide-gap semiconductor layer, typically TiO_2, grafted with a monolayer of sensitizing dye, which absorbs solar radiation and injects the photoexcited electrons into the conduction band of the semiconductor [37]. The concomitant hole is then usually trapped by an electrolyte, closing the circuit.

Ruthenium (II) polypyridyl complexes are among the most popular light harvesters within the solar cell community. In particular, the prototype [*cis*-(dithiocyanato)-Ru-bis(2,2'-bipyridine-4,4'- dicarboxylato)] complex (N3) and its doubly protonated tetrabutylammonium salt (N719) have maintained a clear lead due to their efficiency [577, 578]. In this type of compounds, the bipyridine ligands ensure stable anchoring to the semiconductor surface through the carboxylic groups, allowing for the strong electronic coupling required for efficient excited-state electron injection. On the other hand, the thiocyanate ligands guarantee fast regeneration of the oxidized dye [579].

Regarding the semiconductor, TiO_2 is probably the most widely employed compound in DSSC devices. However, a significant deal of research is being devoted to other metal oxides such as SnO_2, ZnO, Nb_2O_5, and WO_3 [580–585]. SnO_2 and ZnO are particularly interesting materials, because the electron mobility in their bulk phases is over two orders of magnitude higher than that of TiO_2 [585–589]. As a consequence, the charge recombination losses should be minimized in SnO_2- and ZnO-based DSSCs. Moreover, ZnO is particularly amenable for DSSCs because it possesses virtually identical band energetics as TiO_2 in their bulk form [580–583, 585]. Furthermore, ZnO has been reported to crystalize in a plethora of nanometric shapes, ranging from nanorods and nanowires to tetrapods [384, 396], depending on the experimental conditions. Such structural richness has received a considerable interest because it introduces a new variable for the on-purpose modification of the electronic properties of the DSSC photoanode. Elongated nanostructures are particularly attractive for photovoltaic applications, because they offer a directional charge-carrier pathway toward electrodes and prevent recombination events during transport across the semiconductor [590].

Despite their paramount technological potential, ZnO-based devices have performed quite disappointingly so far, with record efficiencies of $\sim$8% [591], whereas for TiO_2 DSSCs efficiencies exceeding 12% have been reported [592]. The reasons underlying this efficiency gap remain unclear. The electronic structure of the semiconductor might play a role, because bulk ZnO and TiO_2 possess similar band gaps and conduction band energies, but a quite different band structure. In particular, ZnO shows a much smaller density of states than TiO_2 at the edge of the conduction band, making the electron injection from the dye excited state less favorable [593, 594]. Moreover, the lowest-lying unoccupied states of TiO_2 arise from Ti *3d* t_{2g} orbitals, whereas the conduction band edge (CBE) of ZnO is comprised primarily of Zn *4s* states. As a consequence, different coupling with the excited dye states can be anticipated.

Besides, when approaching the nanoscale, quantum confinement effects are known to largely influence the band edges of ZnO [393–395]. With the decreasing structure size the conduction band experiences a significant upward shift and the probability of electron injection from the photoexcited dye decreases [595]. On the contrary, the band edge states and the bandgap of TiO_2 appear to be quite insensitive to particle size above a minimum threshold [594]. Moreover, nanostructures often develop midgap states that could act as traps for the photogenerated electrons, thus lowering the performance of the device. ZnO nanostructures in particular are known to bear a dense distribution of intraband defect states [585,596]. Therefore, even if bulk ZnO produces better transport of charge carriers than TiO_2, in current DSSC nanocomposites both metal oxides perform basically the same because charge diffusion is limited by electronic trap states [597].

The functioning of DSSCs is not determined solely by the semiconductor nature, but the interface with the sensitizer plays a pivotal role. Electron injection from the photoexcited dye is a complex process and a great deal of research is being devoted to it. For the typical sensitizers used with TiO_2, slow electron injection rates have been found for ZnO [598],

presumably due to the formation of interface-bound charge-separate pairs, which play the role of intermediate states preceding the generation of free electrons [599–601]. These long-lived pairs, not found for TiO_2, have been ascribed to the low dielectric constant of ZnO ($\sim$8 vs. $\sim$30-170 for TiO_2 [602]).

From a different perspective, the chemical interaction between the dye and the semiconductor is also very important. In this respect the interface between different sensitizers and TiO_2 has been investigated thoroughly. Prototypical dyes bearing carboxylic groups seem to be unsuitable to ZnO sensitization due to the poor chemical stability of ZnO electrodes in the presence of acids, with the concomitant release of Zn^{2+} ions [603]. Dyes containing complexating groups could also remove Zn^{2+} from the ZnO lattice [604]. As a consequence dye/Zn-complexes are often formed in ZnO DSSCs, resulting in a poor performance of the device. To circumvent this drawback, other dyes are being checked. Indoline sensitizers, in particular, have been successfully tested.36 The lower interaction with ZnO surfaces prevents the complex formation, but it also gives rise to a weak and unstable sensitization effect.

Computational simulations rooted in DFT (DFT) and time-dependent DFT (TDDFT) have become a crucial tool to understand the detailed atomistic features governing the performance of TiO2-DSSCs [37, 578, 579, 605–609]. Studies on dye sensitized ZnO models are however scarce, see e.g. Refs. [428, 610–614], and to the best of our knowledge the interaction of the prototypical N3/N719 Ru(II) dyes with ZnO has never been reported. In order to fill this void, here we present a DFT/TDDFT study about the interaction between the prototypical dyes N3/N719 and a model ZnO nanostructure. We pay particular attention to the adsorption modes, geometries, and energies. The role of the proton transfer from the dye to the semiconductor surface is also tested. Besides, we study the effect of interaction on the electronic and optical properties of the dye and the semiconductor.

4.8.3 Computational Details

Figure 4.54 depicts the optimized geometries of the semiconductor and dye models employed throughout this work. To reproduce the $(10\bar{1}0)$ facets often found in ZnO nanostructures, a $(ZnO)_{54}$ slab has been built up from an underlying wurtzite structure. To minimize the dipole along the $[000\bar{1}]$ axis and stabilize the cluster, we saturate the polar Zn- and O-terminated surfaces with dissociated water molecules [300,303,416]. The ZnO model, which has 1.4×1.5 nm dimensions along the $[11\bar{2}0] \times [000\bar{1}]$ directions, is large enough to accommodate the N3 and N719 molecules and it allows us to explore the different adsorption modes of the sensitizers. Regarding the N3 dye, no simplifications were made in its structure. For the N719 dye, however, we did not consider the counterions, because their effect on the ground and excited state energy levels is predicted to be marginal [578]. As one may notice from Figure 4.54, three isomers of N719 have been considered: **1** and **2**, where the protonated carboxyls are *cis* and *trans*, respectively, to the NCS ligands; and **3**, in which the protonated groups are one in *cis* and the other in *trans*. As one may notice from Figure 4.54,

1 and **2** are almost degenerated in energy, with **3** lying 2.10 kcal/mol higher [606].39 Our values are consistent with NMR data, which rule out the existence of isomer **3** [578]. Accordingly, only isomers **1** and **2** have been considered to investigate the adsorption of N719 on ZnO.

All the models have been fully optimized without any symmetry constraint by means of the BP86 [237, 242] xc functional within the Kohn-Sham framework of DFT (KS-DFT), as implemented in the ADF 2012.01 software package [267]. A double-zeta basis set (DZ) of Slater-type orbitals (STO) have been employed. For simplicity, geometry optimizations have been conducted in gas phase. To characterize the interaction between the dyes and the ZnO surface, we have taken advantage of the bond energy decomposition scheme developed by Ziegler and Rauk [508] and implemented in ADF. Under this scheme, the overall bond energy between two fragments $\triangle E$ is broken down into two main terms:

$$\triangle E = \triangle E_{prep} + \triangle E_{int} \tag{4.10}$$

The preparation energy $\triangle E_{prep}$ accounts for the energy required to deform the separated fragments from their equilibrium structure to their geometry in the complex. The interaction energy $\triangle E_{int}$ refers to the instantaneous interaction between the prepared fragments. This term is further decomposed into four contributions, namely the Pauli repulsion $\triangle E_{Pauli}$, the electrostatic interaction $\triangle V_{elst}$, the orbital interaction $\triangle E_{oi}$, and the dispersion interaction $\triangle E_{disp}$

$$\triangle E_{int} = \triangle V_{elst} + \triangle E_{Pauli} + \triangle E_{oi} \tag{4.11}$$

Recall that within this energy decomposition scheme the attractive and repulsive terms are negative and positive, respectively. Therefore, the more negative the energy term is, the more attractive is the corresponding interaction.

GGA functionals have shown to properly reproduce the geometries and the energetics of DSSC models, at a fraction of the computational cost required by their hybrid counterparts. However, they severely underestimate the HOMO-LUMO gap of both the dyes and the semiconductor. Therefore the B3LYP [241] functional has been used, in conjunction with the DGDZVP basis set, to perform the ground and excited state TDDFT calculations on the optimized structures. For computational performance, calculations involving B3LYP have been carried out by means of Gaussian09 package [422]. The effect of water solvation has been included by means of the Conductor-like Polarizable Continuum Model (CPCM) [462].

4.8.4 Results and Discussion

Adsorption Modes

The adsorption of the dye on the semiconductor surface is known to play a crucial role on DSSCs [606]. Indeed, the strength of the dye-semiconductor interaction determines the sta-

bility of the nanocomposite lying at the heart of the solar cell. From a different perspective, the electronic levels of both the sensitizer and the semiconductor may be modified due to their mutual interaction.

A correct prediction of the adsorption geometry is an essential prerequisite to properly capture the intricate electronic structure of the dye@ZnO nanocomposites. Therefore, different adsorption modes have been studied for the interacting system, see Figure 4.55. Regarding N719, we started by placing isomer **1** with the two carboxylate groups facing the ZnO slab (N719-A). Upon optimization, the carboxylate groups adopt a bridging bidentate geometry. A second geometry was also checked, where a third acidic group was allowed to interact with the semiconductor (N719-B). Along the optimization, a proton transfer from this group a neighboring surface oxygen is observed, suggesting that dissociative adsorption is favored on ZnO surfaces, as found for TiO_2 [608]. To check this hypothesis, two additional geometries were considered (N719-A' and N719-B') by adsorbing isomer **2** with the protonated carboxylic groups facing the ZnO cluster. As expected, the most stable complexes imply proton transfer to the oxide surface. Note that N719-A' and N719-B' closely resemble N719-A and N719-B, with the two acidic protons initially carried by the dye being transferred to the ZnO cluster. This allows us to investigate the dye/ZnO protonation effects separately. For the N3@ZnO model, two adsorption modes have been considered: (1) N3-A', where the dye interacts by means of two of the acidic groups; and (2) N3-B', where three carboxylic groups are involved in the anchoring of the dye. Based on the geometry found for N719-B, dissociative adsorption has been considered for N3-A' and N3-B'.

The N719 dye is predicted to strongly interact with the ZnO surface, with a computed binding energy of -97.2 kcal/mol for the N719-A model, see Figure 4.55. The ZnO cluster undergoes an important distortion to enhance the interaction with N719, with a calculated preparation energy of 30.0 kcal/mol. Regarding the dye, the departure from the optimized geometry implies an energy penalty of only 9.1 kcal/mol. The interaction is electrostatically driven, covering 66% of the attractive terms. The importance of the orbital interaction (34%), however, means that the polarization effects are important on the surface of this kind of complexes. Accordingly, a charge donation of *ca.* 0.5 e is found from the dye to the ZnO surface. This charge transfer is expected to modify the electronic structure of both the sensitizer and the semiconductor (*vide infra*) [615]. The N719-B model, where a third acid group interacts with the ZnO slab, lies slightly lower in energy than N719-A, with a calculated binding energy of -101.7 kcal/mol. The N719-A' geometry is 32 kcal/mol less stable than N719-A. On the other hand, the N719-B' isomer lies 12 kcal/mol lower than N719-B.

From our results, N719 sticks better on the ZnO surface when three carboxylic groups are involved than when only two of them are exploited. Furthermore, if the anchoring group carries a proton, the adsorption is predicted to be dissociative. Our results are in agreement with previous works on N719 sensitized TiO_2 anatase (101) surfaces [607, 616]. In these studies, the configuration where two protons were transferred from the carboxylic groups to the surface was found to lie 37 kcal/mol higher in energy than if the sensitizer was adsorbed exploiting the deprotonated carboxylate groups and the protons were retained in the

dye. From our data, however, N719-A' is predicted to be energetically unfavorable by 32 kcal/mol.

Regarding the protonated N3 dye, binding energies of -65.5 and -89.6 kcal/mol have been found for N3-A' and N3-B'. Again, the adsorption by means of three anchoring groups is not only possible but energetically favored by *ca.* 25 kcal/mol.

Electronic and Optical Properties

We start by investigating the electronic structure of the isolated dyes. As one may notice from Figure 4.56, for N719 in solution we find HOMO and LUMO values of -5.59 and -3.13 eV respectively, in good agreement with reference theoretical results [607]. Regarding the N3 dye, the HOMO is stabilized compared to N719, presumably due to diminished charge donation to the metal, where the high-lying occupied orbitals are mainly localized. The LUMO, localized on the bipyridine ligands bearing the protonated acid groups, is also stabilized, but to a larger extent, in such a way that the HOMO-LUMO narrows from N719 (2.47 eV) to N3 (2.28 eV).

Regarding the ZnO model, the calculated bandgap of 3.63 eV reasonably compares with the experimental values for ultrasmall ZnO nanoparticles, with reported numbers between 3.4 and 3.8 eV [393–395]. As it is evident from Figure 4.56, however, the valence band edge (VBE) at -5.58 eV essentially coincides with the HOMO levels of N719 and N3, whereas the conduction band edge, at -1.95 eV, lies *ca.* 1.2 eV higher than the LUMO levels of the sensitizers. The band edges are in agreement with our previous results on small ZnO models [613]. Recently, Hedrick et al. found a similar alignment of electronic levels for the magic $(ZnO)_{33}$ nanoparticle sensitized with ruthenium (II) polypyridine molecules [614]. Notably, the dye/semiconductor alignment of energy levels is not correctly reproduced by our models, in particular the gap between the dye's LUMO and the semiconductor's CBE is probably overestimated in our calculations. The limited size of the model is expected to artificially shift the CBE of ZnO upwards [613]. Also, the VBE is too high in energy compared to the dye HOMO, which is placed correctly. This imbalance in dye/semiconductor electronic structure still represents a challenge for current DFT methods.

Having the limitation of our model and computational framework in mind, we mainly focus on the effect of the complexation on the electronic structure of both the dye and the semiconductor, which are expected to be reasonably independent from the employed model. As one may notice from Figure 4.56, the conduction band edge of ZnO, comprised primarily of Zn *4s* states, rises by 0.2 eV in the N719-A complex due to the interaction with the dye. Such an upward shift of the lowest-lying unoccupied states, already reported other II-VI materials and TiO_2 [306, 334, 338, 607], has been attributed to the electrostatic field induced by the sensitizer and the charge density transferred from the dye to the semiconductor upon the interaction. The VBE of ZnO arising from the O *2p* orbitals also rises, but to a lesser extent (0.1 eV). As a consequence, the HOMO-LUMO gap of ZnO widens by *ca.* 0.1 eV with respect to the non-interacting cluster. Concomitant with the upward shift of the band edges

of ZnO and the opening of the gap, is the stabilization of the HOMO level of N719 by 0.1 eV, possibly due to the lowered charge transfer to the Ru center. The LUMO lowers similarly and the HOMO-LUMO gap remains unchanged relative to the isolated dye.

Regarding the protonation effects, the electronic structure of N719-A' reveals that the semiconductor levels are restored when protons are transferred from the dye to the ZnO. Apparently, the charge donation from the dye to the semiconductor is compensated by the protons adsorbed on the surface of the latter. Regarding the sensitizer, the HOMO level is destabilized, since the charge donation from the bipyridine ligands to the Ru metal increases upon deprotonation. The upward shift of the LUMO levels is even larger, in such a way that the HOMO-LUMO gap widens by *ca.* 0.3 eV.

A similar situation is found for the N719-B complex, where N719 exploits three carboxylic groups to sensitize the ZnO surface and a proton has already been transferred to semiconductor. Charge donation from the dye to the semiconductor stabilizes the frontier orbitals of the former, whereas the band edges of the latter rise. The proton transferred to the ZnO slab, however, somehow balances the charge donation effect and recovers the electronic levels of the isolated fragments. Upon a second proton transfer (N719-B') , the dye levels rise and the ZnO band edges move downwards (or remain almost the same), as found for N719-A and N719-A'.

The results calculated for N3 are consistent with those found for N719. The band edges of ZnO remain almost constant relative to the isolated cluster. Again, the surface protonation seems to counterbalance the charge density donation from the sensitizer. Regarding the N3 molecule, the HOMO and the LUMO levels rise upon the interaction, but the latter undergoes a larger shift, so the HOMO-LUMO gap opens by *ca.* 0.1 eV. N3-A' and N3-B' display a similar electronic structures, meaning that the adsorption mode (two *vs* three anchoring groups) plays a minor role on the electronic structure of the dye@ZnO nanocomposite, as one might anticipate from the data retrieved for N719@ZnO complexes.

Even if the KS molecular orbitals and their eigenvalues may deliver a reasonable picture for the electronic excitation energies of the systems studied here, the accurate description of the excited states requires a more rigorous framework, as the one provided by TDDFT. Figure 4.57 displays the simulated absorption spectra of the dye@ZnO models considered.

Regarding the isolated fragments, the simulated TDDFT spectra are in line with the experimental data available. As one may notice from Figure 4.57, the N719 sensitizer displays two absorption bands in the low-lying region of the spectrum, at 2.22 and 2.85 eV respectively, in fairly good agreement with the experimental values of 2.35 and 3.22 eV.3 Regarding N3, we find a single band at 2.52 eV, with a shoulder at 2.05 eV. Experimentally, the lowest-lying absorption band of N3 (in ethanol) appears at 2.30 eV.64 Regarding ZnO, our model displays a broad feature centered at 3.5 eV, with similarly small ZnO nanoparticles absorbing at 3.4-3.8 eV.23-25

As it is immediately clear from Figure 4.57, there is no spectral overlap between the sensitizers and the ZnO, in line with the energy levels mismatch discussed above. The lowest-lying

electronic excitations of the interacting complexes are mainly localized on the dye. Accordingly, the simulated absorption spectra of the dye@ZnO models mimic the optical spectra of the isolated dyes. In this respect, our results may resemble those obtained with an embedding scheme in which the semiconductor only produces a perturbation on the dye energy levels. Similar results were recently reported for the $(ZnO)_{33}$ nanoparticle sensitized with Ru (II) polypyridine ligands, with the first band at 2.7-3.2 eV belonging to the dye transitions [614].

To better characterize the lowest-lying transitions, their associated charge density differences have been computed. In Figure 4.58, the Electron Density Difference Maps (EDDMs) related to the first and the brightest excitations are collected. As one may notice from Figure 4.58, the electron localizes on the dye's bipyridine ligands, irrespective of the sensitizer and the adsorption mode. In fact, as already discussed above, the LUMOs of both N719 and N3 lie below the CBE of ZnO. Accordingly, there is no admixture of the dye/ZnO states in the lowest-lying unoccupied states of the interacting complexes.42 The hole localizes on the Ru center and the NCS ligands, but often there is a sizable contribution from the semiconductor. From Figure 4.58, it seems that the hole localization on the ZnO cluster is favored when the sensitizer exploits three carboxylic groups to anchor the semiconductor surface. We notice, however, that this is an unphysical situation, which is driven by the improper alignment of energy levels.

4.8.5 Summary and Conclusions

Recently ZnO has earned lots of attention as an interesting alternative to TiO_2 for DSSCs, due to a better electron mobility and a fascinating structural diversity. However, ZnO-based devices have worked quite disappointingly so far, for reasons that remain unclear. Here we have presented a DFT/TDDFT study on the interaction between the prototypical Ru(II) bypyridyl sensitizers N3/N719 and ZnO, aimed at understanding some of the atomistic details governing the performance of DSSCs. We have explored different adsorption modes for the sensitizers, because a correct prediction of the interacting geometry is an essential prerequisite to properly reproduce the complex electronic structure of dye@ZnO compounds. Then, we have investigated the effect of the complexation on the electronic structure of the sensitizers and the semiconductor.

From our results, N719 adsorbs better on the ZnO surface when three carboxylic groups are exploited than when only two are involved. Moreover, if the anchoring group bears a proton, the adsorption is predicted to be dissociative. On the contrary, proton transfer from distal carboxylic moieties to the ZnO surface is energetically unfavorable. The interaction is mainly electrostatic, covering 66% of the attractive terms. Nevertheless, the orbital contribution is also sizable, meaning that the polarization effects on the semiconductor surface are also important. N3 shows a slightly weaker affinity than N719 towards the ZnO nanoparticle, but the interaction is still strong enough (*ca.* -66 kcal/mol) to ensure an stable anchoring of the dye.

We have found the sensitizers' LUMOs to lie ca. 1.2 eV below the CBE of the ZnO nanoparticle. This unphysical alignment of electronic levels is due to two combined effects, *i.e.* the reduced size of the considered ZnO cluster and to some extent to an non-optimal description of the ZnO energy levels by standard DFT functionals. On the contrary, the dye energy levels are nicely accounted for by standard DFT. In spite of these model limitations, the considered systems allowed us to qualitatively evaluate the effect of the interaction on the electronic structure of the sensitizer and the semiconductor.

If the acidic protons are retained on the dye, the adsorption of the sensitizer rises the CBE of the ZnO, due to the electrostatic field induced by the Ru (II) complex and the charge density transferred to the semiconductor. The VBE also rises, but to a lesser extent, so the semiconductor gap widens. Proton transfer from the dye to the semiconductor balances the charge donation effects and restores the electronic levels of the non-interacting fragments. The adsorption mode (two *vs* three anchoring groups) seems to play a minor role on the electronic structure of the dye@ZnO complex.

The TDDFT calculations reveal that the sensitizer's optical features appear at 1.5-3.5 eV, with the ZnO model absorbing at 3.0-4.0 eV. Due to the small spectral overlap between the sensitizers and the semiconductor, the lowest-lying electronic excitations of the interacting complexes are mainly localized on the dyes. The photoexcited electrons are predicted to localize on the bipyridine ligands, with negligible contribution from the ZnO states.

This study confirms the difficulty of simulating ZnO/dye interactions in a proper theoretical framework, *i.e.* including a TDDFT description of the excited states of the joint system along with the effect of a surrounding solvation. Probably post-DFT methods will be needed to encompass such difficulty.

Figure 4.54: Optimized geometrical structures of the (a) N719, (b) N3, and (c) ZnO models considered in this work. For N719, values in parentheses indicate the relative stability, in kcal/mol, of each isomer wrt the lowest-lying **2**. For ZnO, views along the [1010] (left), [1210] (right, top), [0001] (right, bottom) axes are provided.

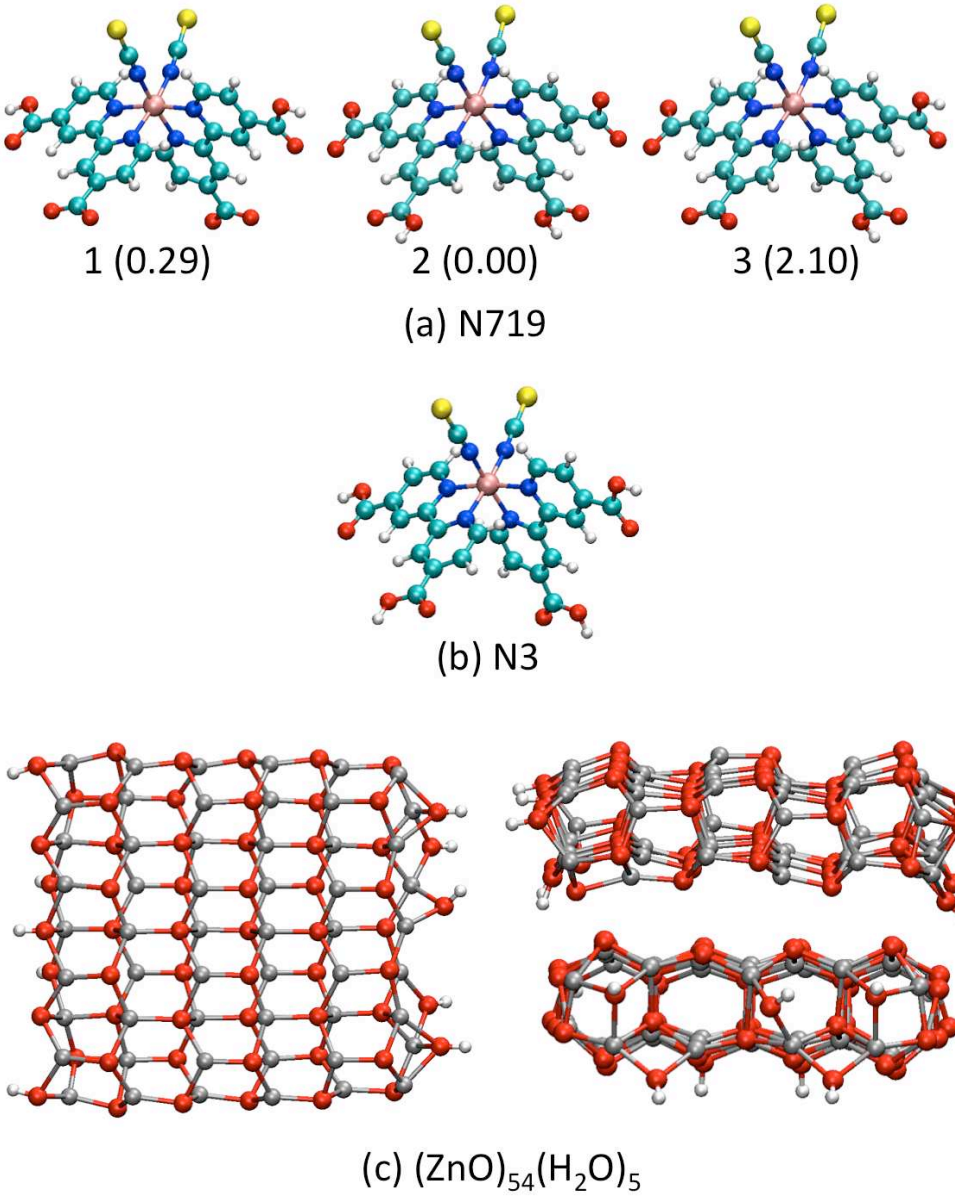


Figure 4.55: Optimized geometrical structures of the N719@ZnO ((a), (b), (c), and (d)) and N3@ZnO ((e) and (f)) models considered in this work. Protons are highlighted in blue. BE stands for the binding energy, given in kcal/mol.

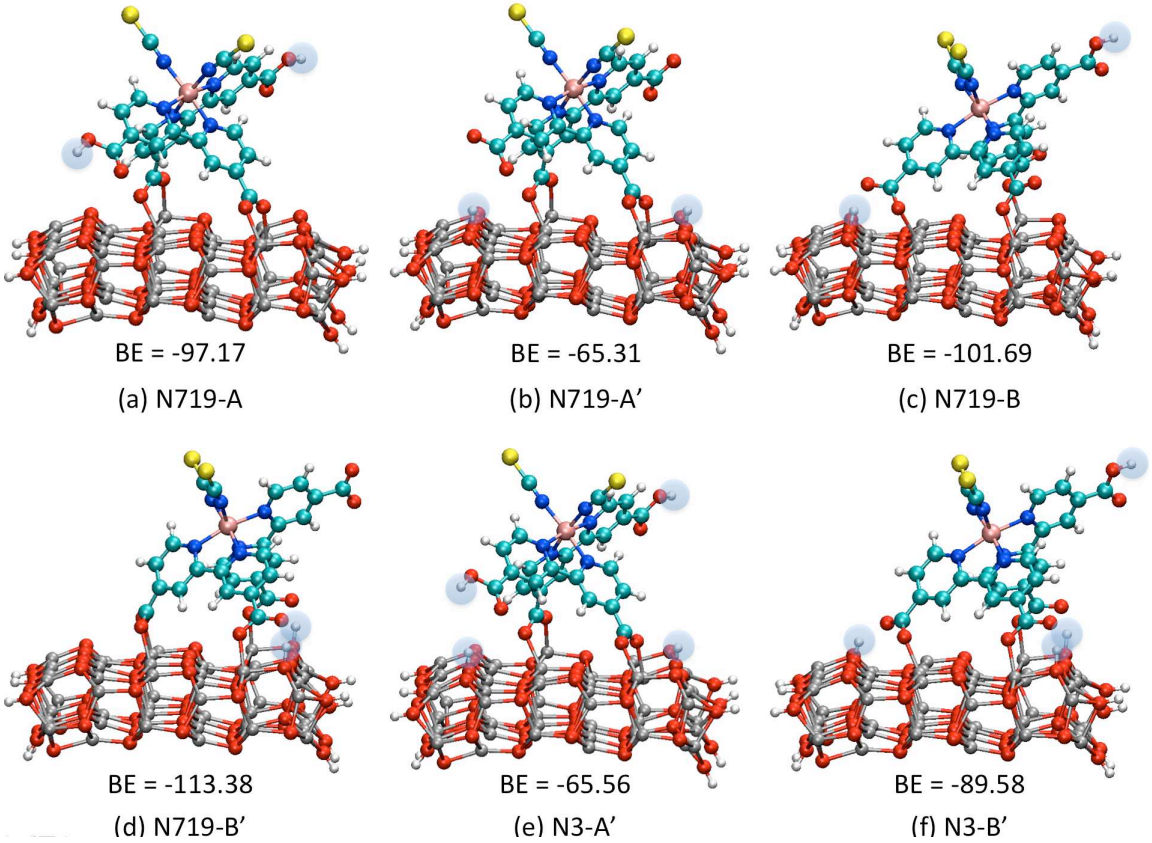


Figure 4.56: Electronic structure of the (a) N719@ZnO and (b) N3@ZnO models considered in this work (right panels), along with the electronic structure of the isolated fragments (left panels). Red (grey) bars represent the Kohn-Sahm orbitals mostly localized on the sensitizer (ZnO). Horizontal red (grey) arrows highlight the HOMO and LUMO levels of the sensitizer (ZnO). Vertical red (grey) arrows highlight the Kohn-Sham gaps of the sensitizer (ZnO). Red (black) lines represent the Density of States, drawn by a Gaussian convolution of σ = 0.20 eV of the individual electronic levels, and projected on the sensitizer (ZnO).

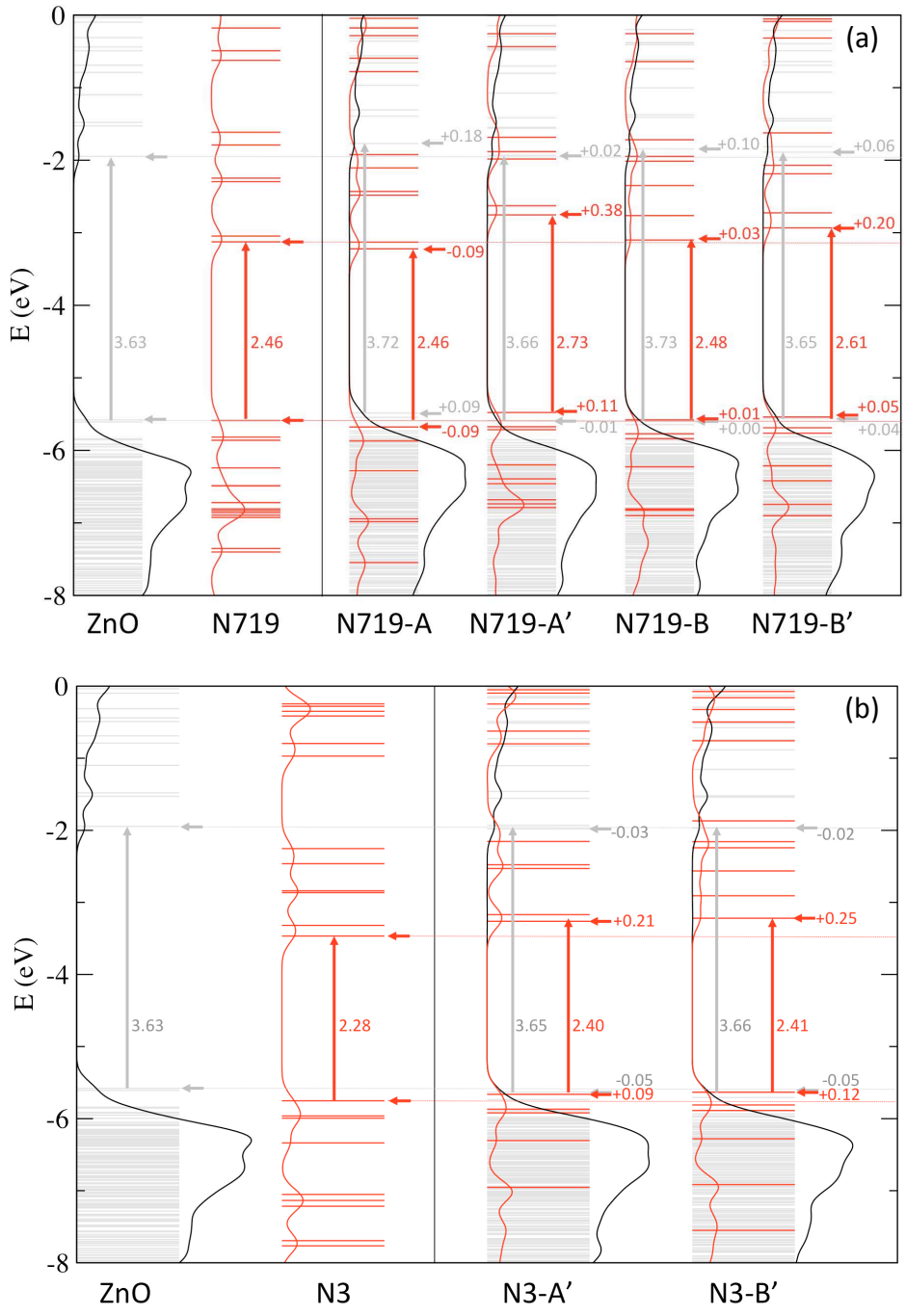


Figure 4.57: TDDFT absorption spectra of the (a) N719@ZnO and (b) N3@ZnO models considered in this work, obtained by a Gaussian convolution with FWHM = 0.37 eV, calculated taking into account the lowest 20 singlet-singlet electronic transitions. For comparison, the spectra of the isolated dyes/ZnO are also shown.

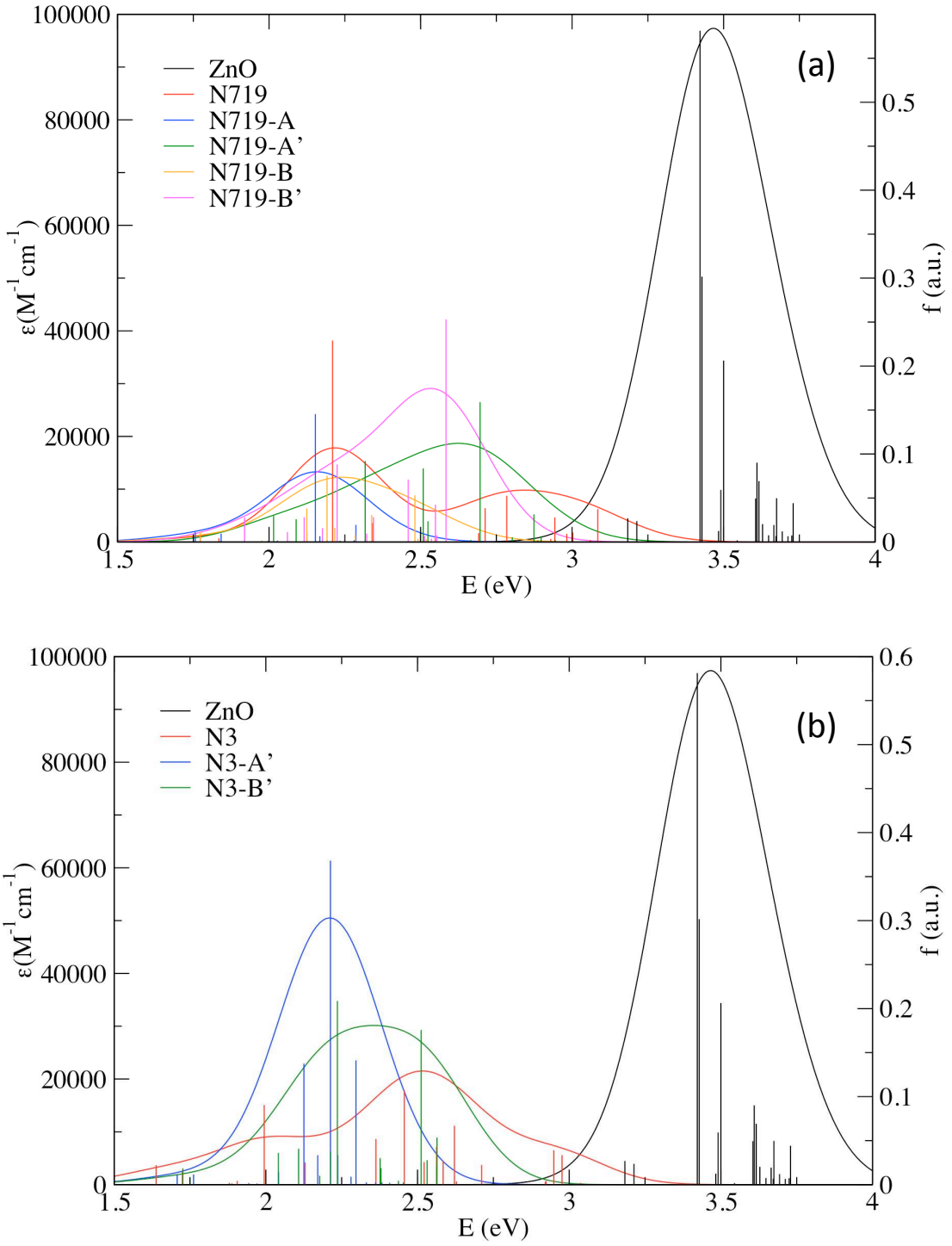
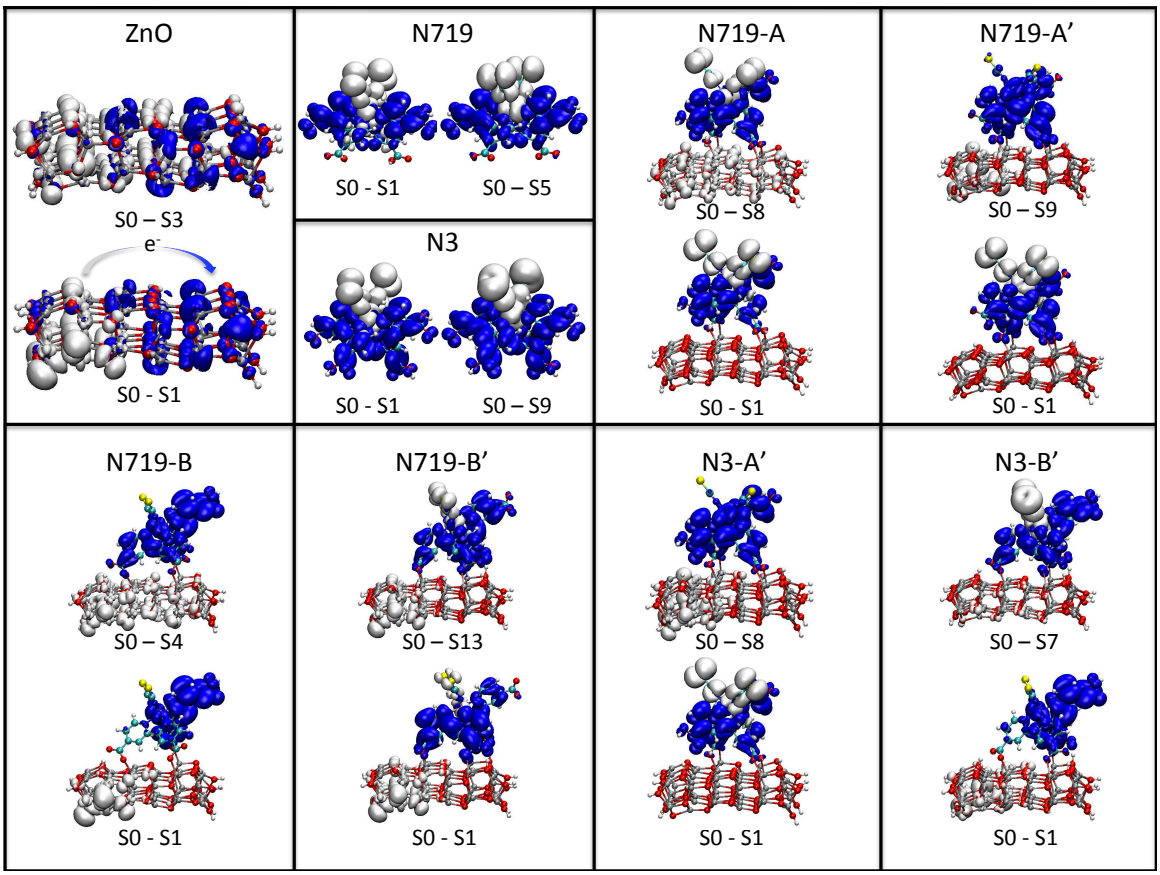


Figure 4.58: Selected Electron Density Difference Maps (EDDMS) of the singlet-singlet electronic transitions for the N719@ZnO N3@ZnO models considered in this work. For comparison, the EDDMs of the isolated dyes/ZnO are also shown. Isocontour value of 0.0002 a.u..



4.9 PbS Quantum Dot Sensitized Solar Cells: Insights from First Principles

4.9.1 Abstract

We present a DFT/TDDFT study aimed at understanding the atomistic features of PbS quantum dot sensitized solar cells (QDSSCs). With that goal, and in a first step, we investigate the structural, electronic, and optical properties of PbS QDs of increasing size. In a second step, we study the sensitization of two prototypical anatase TiO_2 surfaces, namely (101) and (001), with a 1.7 nm size QD model. With regard to the standalone PbS QDs, they are predicted to undergo a significant geometrical distortion with respect to the rock salt structure. Such an atomic rearrangement stabilizes the QD and opens the bandgap. All the models studied exhibit wide bandgaps, with no midgap states that could deteriorate the performance of the solar cell. Compared to II-VI QDs, the PbS models studied here display a large density of unoccupied states, which could trigger electron injection to the TiO_2 substrate. However, such orbitals are mostly localized on the QD core, which might block the charge transfer due to the small coupling between the donor and acceptor states. The 1.7 nm size QD model is predicted to adsorb on the TiO_2 slabs through the S-rich (111) facets. The adsorption is particularly strong on the TiO_2 (101) surface. Irrespective of the TiO_2 model, the occupied states of the QD intrude into the HOMO-LUMO gap of the oxide, whereas the unoccupied orbitals appear immersed in the conduction band of the oxide. The LUMO of the QD (the LUMO+5 in the interacting complex) is the arriving state of the lowest-lying electronic excitations. It is an almost pure state, since the contribution of the TiO_2 nanoparticle is less than 6%, suggesting a non-adiabatic electron injection mechanism in this kind of systems.

4.9.2 Introduction

In the last decades solar energy has emerged as an environmentally clean, efficient, cost-effective, renewable, and sustainable alternative to solid fuels. In this context, dye sensitized solar cells (DSSC) are embodying a significant leap forward to efficient light conversion at low cost [576]. DSSCs consist of a mesoporous wide gap oxide layer, usually TiO_2 or ZnO, grafted with a monolayer of sensitizing dye, which absorbs the solar radiation and injects the photogenerated electrons into the manifold of unoccupied states (conduction band or CB) of the oxide [37]. These electrons are then collected on an external load, while holes on the dyes are scavenged by an electrolyte and transported to the cathode where they close the circuit.

More recently, semiconductor quantum dots (QDs) have gained a lot of attention as efficient light harvesters due to their attractive properties [4, 5]. They present high extinction coefficients and large dipole moments, and their absorption spectrum can be tuned by changing their size and morphology. In addition, QDs provide the opportunity to increase solar cell photocurrent by either extracting hot carriers or taking advantage of the Multiple Carrier

Generation (MCG) phenomenon, which can potentially overcome the Shockley-Queisser limit of 33% power conversion efficiency (PCE) [155]. Along with these outstanding optoelectronic properties, QDs nanocrystals are characterized by versatile and low-cost synthetic routes, and unmatched photostability that make them amenable for photovoltaic applications.

In particular, PbS QDs, which belong to the IV-VI family of compounds, have attracted a great deal of research in photovoltaics. They present a relatively large Bohr radius (18 nm) that allows tuning their bandgap in the 0.5 to 5.5 eV [617–622] range (*i.e.* in the NIR and visible), covering most of the solar emission spectrum. PbS QDs also present large absorption cross section ($\sim$10-15 cm^{-2}), long excitonic lifetime ($\sim$200-800 ns), exceptionally high quantum efficiency (80%), and carrier multiplication [623–625].

In view of their technological potential, several PbS QD solar cells architectures have been engineered, ranging from sensitized solar cells (QDSSCs) that have reached a PCE of 5.6% [626], to thin films assemblies of QDs, which attained a record of 8.5% [627]. Despite these promising results, PbS QDSSCs however have performed quite disappointingly if we compare them to their dye sensitized counterparts that hold a record PCE of 12.3% and the more recent perovskite solar cells with 15.4%. The reasons why QDSSCs still present low efficiencies have been investigated thoroughly and boil down to the following facts: (a) QDs display localized surface states (trap states) that block the flow of charge carriers into the circuit [26,157,158]; (b) the interfacial electron injection from the QD to the metal oxide competes with several deleterious fast recombination pathways [41,44,159,160]; (c) the polysulphide electrolyte couple employed in sensitized QDSC present a high redox potential that lower the open-circuit voltage [628] and therefore the overall PCE.

In this framework, computational modeling has emerged as a valuable tool to shed light on aspects hardly accessible experimentally. Seminal works on PbS QDs have been focused on the characterization of the energetic, structural, and optical properties of small nanoclusters [629–631]. More recently, realistically large PbS QDs models have been employed to provide a direct comparison with the experiments and guide the design of improved photovoltaic devices [632–634]. Particular attention has been paid to the variation of the electronic structure with the size of the QD [632] as it is of prime importance to predict the relative position of the band-edge states of the QD and the oxide substrate, which determine the probability of interfacial electron/hole transfer in QDSSCs. These challenging computational simulations of QDSSCs have been limited to only a couple of works. Dong et al. have found that the high-lying occupied electronic states of a very small $(CdSe)_2$ model intrude in the bandgap of TiO_2 nanotubes, whereas the unoccupied states of the adsorbate lie deep inside the CB of TiO_2, thus favoring the interfacial electron transfer from the QD to the oxide [635]. Later on Long et al. have modeled the photoinduced electron transfer from the $(PbSe)_{16}$ QD model into the rutile TiO_2 (100) surface by means of *ab initio* nonadiabatic molecular dynamics [534]. They reported that electron injection occurs in the ultrafast timescale, as found in the experiments, as a consequence of the strong coupling between the QD and the TiO_2 surface.

This work represents a contribution to this computational endeavor, aimed at understanding QDSSCs. With that goal, and in a first step, we report on the structural, electronic, and optical properties of PbS QDs of increasing size, with particular attention to the properties relevant for the functioning of QDSSCs. In a second step, we investigate the sensitization of two prototypical anatase surfaces, namely TiO_2(101) and TiO_2(001), with a PbS QD model of 1.7 nm.

4.9.3 Methodology

QD Models

Stoichiometric QD models of spherical shape have been cleaved from the underlying rock salt structure of bulk PbS. The origin of each model cluster has been set at the center of a $(PbS)_4$ unit [290, 313]. The newly generated models expose non-stoichiometric (111) and stoichiometric (100) facets, in line with the experiments [633, 636]. Figure 4.59 displays the optimized structures of the nanoclusters studied. Some of the models have already been reported in the literature for PbS and PbSe [82, 83, 534, 629–631, 637].

TiO_2 Models

The TiO_2 slab exposing the (101) facets has been built from bulk TiO_2. It is stoichiometric and composed by 82 TiO_2 units: $(TiO_2)_{82}$ or TiO_2(101) hereafter. The TiO_2 slab exposing the (001) facets is non-stoichiometric and we have added 24 OH- groups to compensate the Ti excess of the pristine slab: $(Ti_{143}O_{274})(OH)_{24}$ or TiO_2 (001) hereafter.

Computational Approach

All the models have been fully optimized without any symmetry constraint with the dispersion corrected (D) [513] Perdew-Burke-Ernzerhof (PBE) [238] xc functional within the Kohn-Sham framework of Density Functional Theory (KS-DFT), as implemented in the ADF 2012.01 software package [267]. PbS QDs were relaxed in vacuum until the maximum norm of the Cartesian gradients was smaller than $1{\cdot}10^{-3}$ Hartree/Angstrom. For the PbS@TiO_2 nanocomposites, a looser convergence criterion of $5{\cdot}10^{-3}$ Hartree/Angstrom has been chosen. To take account for relativistic effects, we employed the Zero-Order Regular Approximation (ZORA) [526]. The choice of the PBE functional to optimize geometries has been followed because it reproduces well the geometry of semiconductor nanostructures at a fraction of the computational cost required by the hybrid functionals [551].

The clusters studied in this work comprise up to 600 atoms, therefore for some elements the size of the basis set has been reduced. A double-zeta basis set (DZ) of Slater-type orbitals (STO) have been added for Pb, S, O, and H atoms, while a single-zeta set (SZ) has been chosen for Ti. In addition, inner lying atomic orbitals (core) have been frozen for all atoms.

Despite being useful for geometry optimizations and energetics, the PBE, and more in general the GGA functionals, severely underestimate the bandgap of semiconductor nanostructures [551]. Therefore, we decided to use the B3LYP [241] functional in conjunction with the LANL2DZ (Pb and S atoms) and 3-21G* (Ti, O, and H atoms) basis sets, to perform ground (DFT) / excited state (TDDFT) calculations on the PBE optimized structures. The choice of this functional / basis set combination has been followed because it reproduces correctly the CB offsets of both TiO_2 and PbS clusters. These calculations have been carried with Gaussian09 package [422]. To reproduce the effect of the electrolyte environment, solvent effects have been included using the Conductor-like Polarizable Continuum Model (CPCM) with the water dielectric constants [460–462].

Radial Distribution Functions have been calculated using the Virtual Molecular Dynamics (VMD) software [571]. Theoretical UV-Vis curves were obtained by means of the GAUSSSUM 2.2 program [556]. The electronic structure of the compounds considered was analyzed using the AOMix software [557, 558].

4.9.4 Results and Discussion

Bare PbS QDs

Energetic and Structure

The binding energy $E_b(n)$ 84 of each QD is given by

$$E_b(n) = nE(1) - E(n) \tag{4.12}$$

where $E(n)$ is the total energy of the composed structure made of n formula units and $E(1)$ is the energy of the smallest unit, *i.e.* $(PbS)_1$. From Figure 4.59, all the QD studied here are stable, as shown by the positive binding energies (in red). Moreover, the stability increases with the size of the QD. Our results are in accordance with previous works on II-VI semiconductor nanostructures and predict the crystal growth to be thermodynamically favorable [24]. This process is expected to be driven by the minimization of the surface-to-volume ratio with the increasing size of the nanostructure. In this sense, surface ligands, solvent molecules, and the environment play a pivotal role in lowering the surface energy and stabilizing the nanostructure [24, 304, 306, 638].

As one may notice from Figure 4.59, the optimized PbS QDs preserve the bulk-like structure. However, our models experience a significant distortion upon relaxation. In contrast to II-VI cluster models, where the atomic reconstruction is mainly concentrated on the surface [300,303], the optimization affects also the core. To better characterize the optimized models, the Pb-S, Pb-Pb and S-S Radial Distribution Functions (RDF) have been calculated for each QD (Figure 4.60). The relaxed models display a broad distribution of Pb-S distances in the range of 2.75 and 3.75 Å. However, two features are recognizable: (a) a narrow distribution of Pb-S distances corresponding to shortened Pb-S bond lengths, and (b) a wider profile

at elongated Pb-S bond distances. Regardless of a particular atomic rearrangement, Pb-S bonds shorten when moving away from the center of the QD. A lower coordination number on the surface atoms seems to be the driving force for the shrinkage of the bonds in the outer region [300,303]. Concerning Pb-Pb and S-S RDFs, a wide distribution of distances has been found for each model, and the trend is again bimodal. Interestingly, the nearest S-S pairs are closer than the corresponding Pb-Pb pairs. This finding is in contrast with previous works on II-VI QDs, where metal atoms form short M-M contacts [300,303,629].

Electronic Structure

Figure 4.61 shows the energy of the band edge states for the bare PbS QDs, along with their corresponding Density of States (DOS). All QDs studied display HOMO-LUMO gaps with no midgap states and both HOMO and the LUMO are delocalized over each system. QD1 shows the largest band-gap (4.02 eV), which shrinks monotonically with the size of the QD model (2.27 eV in QD5), mainly due to the downward shift of the CB states.

Moving from QD1 to QD5, the DOS becomes denser, as it is evident from the increased curvature at the top of the valence band (VB) and also in the CB. Overall, PbS QDs display a higher density of unoccupied states as compared to II-VI QDs where the top of the VB is much denser than the bottom of the CB [300, 303, 306]. As known from literature and evident here, PbS present a more symmetric DOS, although far from being mirrorlike, with a VB denser than the CB, in agreement with recent calculations on PbSe QDs [637].

To get a deeper insight into the electronic structure of PbS QDs, we focused on the QD5 model ($\sim$1.7 nm), which closely resembles experimental PbS QDs. As expected, the VB edge displays spreads *ca.* 4 eV below the HOMO and consists mainly of S 3p orbitals, with a sizable contribution of Pb 6s and 6p orbitals (Figure 4.62a). The CB edge is comprised primarily of Pb 6p states. Localized surface states could act as trap states for the photogenerated electrons and hinder the electron injection to the TiO_2. To unveil the spatial localization of the band edge states, we analyzed the composition of the frontier molecular orbitals. We found each atom contributes with no more than 7%. Interestingly, as one may notice from Figure4.62b, the high-lying occupied orbitals are mostly spread over the surface, whereas the LUMOs are primarily concentrated on the core, in agreement with results reported for PbSe QDs [637].

Optical Properties

Even if the ground state DFT molecular orbitals deliver fair energy values of the HOMO-LUMO gap, the accurate description of the electronic excitations in these QDs is attained within the more accurate time-dependent TDDFT framework. As shown in Figure 4.61, for the smallest QD1 the computed bandgap is 4.02 eV, which has to be compared with the more reasonable TDDFT value of 3.15 eV. This same trend holds for the rest of the models, but with a discrepancy that lowers with the size of the model.

Figure 4.63 displays the simulated absorption spectra of the PbS QDs, drawn by a Gaussian convolution of the 10 lowest singlet-singlet TDDFT excitations. With the increasing size of the QD, a significant redshift of the optical spectrum is observed. However, the intensity

of the transitions does not seem to follow a trend. QD2 displays two strong absorption features, at 2.46 and 2.85 eV. The absorption bands of QD3, QD4, and QD5 appear to be more symmetric and locate at 2.29. 1.97 and 1.82 eV, respectively.

In our previous works on II-VI QDs, the LUMO was calculated to lie quite separated from the rest of the CB states, in such a way that the lowest electronic excitations were composed from high-lying occupied orbitals to the LUMO [303, 306]. For the PbS QDs considered here, where a greater number of unoccupied orbitals is available in the excitation window explored, LUMO+n up to n = 3 have been found to participate. The lowest-lying TDDFT transitions imply an important mixing of monoelectronic excitations.

QD@TiO_2 Complexes

To properly simulate PbS QDSC devices, models of realistic size have to be chosen. For this reason we considered the QD5@TiO_2(101) and QD5@TiO_2(001) molecular systems. The QD5 moiety presents a calculated first excited state (TDDFT) at 1.79 eV, which is in good agreement with the first experimental band at 1.7 eV [636, 639]. The TiO_2(001) and TiO_2(101) slabs have a calculated bandgap (TDDFT) of 3.42 and 3.15 eV, which match well the experimental value of 3.2-3.3 eV for standard TiO_2 nanoparticles [640, 641]. These preliminary results ensure a fair analysis of the interface between a PbS QD and the metal oxide substrate.

Energetic and Structure

As stated earlier, the QD5 model exposes Pb-rich (111), S-rich (111), and stoichiometric (100) facets. Consequently, three interaction modes can be envisioned where each of the QD planes face the TiO_2 slab (see Figure 4.64). We will call them as QD5(Pb-111)@TiO_2, QD5(S-111)@TiO_2, and QD5(100)@TiO_2. In Table 4.28, the bond energies of the interacting compounds are summarized, along with their energy decomposition analysis.

All QD5@TiO_2 models considered here are stable, as shown by the (negative) binding energy $\triangle E_{bond}$ between QD5 and TiO_2. This term is most likely overestimated for several reasons: (a) the DFT functional employed (*e.g.* pure GGA functionals tend to over bind), (b) the absence of solvent effects, and (c) the limited size of the basis set. In any case, they provide interesting clues about the QD/TiO_2 interaction.

Irrespective of the adsorption mode, the QD5 model is predicted to adsorb more strongly on the TiO_2(101) surface, with binding energies ranging from -85.2 to -187.4 kcal/mol. When the same QD5 model is adsorbed on the TiO_2(001) facet, the interactions are much weaker, from -13.5 to a maximum of -112.5 kcal/mol. Regardless of the TiO_2 facets, the most stable complex is always obtained when the QD is adsorbed from the S-rich (111) side. Therefore, and unless otherwise stated, the rest of the discussion will focus on this particular adsorption mode.

To get a deeper insight into the interaction, the bonding energy has been broken down into several terms using the Ziegler and Rauk decomposition scheme [507–510]. In this frame-

work, the binding energy between two moieties (in our case QD5 and TiO_2) is expressed as:

$$\triangle E = \triangle E_{prep} + \triangle E_{int} \tag{4.13}$$

The preparation energy $\triangle E_{prep}$ accounts for the energy required to deform the separated fragments from their isolated equilibrium structure to their geometry in the supercomplex. The interaction energy $\triangle E_{int}$ refers to the instantaneous interaction between the two fragments at the supercomplex configuration. This latter term is further decomposed into four contributions with a physical meaning: the Pauli repulsion $\triangle E_{Pauli}$, the electrostatic interaction $\triangle V_{elst}$, the orbital interaction $\triangle E_{oi}$ (accounting for charge transfer and polarization effects) and the dispersion (long-range) interaction $\triangle E_{disp}$

$$\triangle E_{int} = \triangle V_{elst} + \triangle E_{Pauli} + \triangle E_{oi} \tag{4.14}$$

Recall that within this energy decomposition scheme the attractive and repulsive terms are negative and positive, respectively. Therefore, the more negative the energy term is, the more attractive is the corresponding interaction.

Inspection of Table 4.28 show that the QD5 undergoes a great distortion to enhance the interaction in QD5(S-111)@TiO_2(001), with a huge (destabilizing) preparation energy of 80.3 kcal/mol *vs* the 54.2 kcal/mol in QD5(S-111)@TiO2(001). In addition, irrespective of the oxide facets, the interaction energy $\triangle E_{int}$ is mostly electrostatic, covering as much as 54-57% of the attractive terms. The orbital interaction, $\triangle E_{oi}$, contributes with 32%, revealing an important polarization of the electron density of both moieties upon interaction. More in detail, the QD5 transfers about 0.20 e and 0.14 e to the TiO_2(101) and TiO_2(001) nanoparticles, respectively. These polarization effects affect the band edges of both the sensitizer and the oxide as we will see in the next sections. Finally, the dispersion energy represents about 11-14% of the attractive terms, meaning that even weak interactions may play an important role on defining the conformation of these interfaces, where the contact between the fragments are overall not very strong.

Looking at the geometry of these nanocomposites, there are presumably two types of bonds taking place at the interface, Pb-O and S-Ti. On this regard, we have thus computed the Pb-O and the S-Ti RDFs as shown in Figure 4.65. Irrespective of the slab, the S-Ti bonds are shorter (*ca.* 2.6 Å and narrowly distributed compared to the Pb-O distances. The binding S(111) facet on the QD, however, undergoes a sizable distortion upon complexation. It adopts a planar configuration, and the inner Pb atoms move towards the oxide surface driven by attractive Pb-O interactions (either electrostatic or orbital). Pb and O atoms are closer in the QD5(S-111)@TiO_2(101) nanocomposite (2.62 Å) *vs* the 2.90 Å in QD5(S-111)@TiO_2(001)), suggesting that the TiO_2(101) surface indeed better accommodates the QD. On this respect, also the S-Ti bond lengths are on average smaller, even though in this case difference is rather subtle (2.55 Å *vs* 2.57 Å). Consistent with this findings, the integrated Pb-O and S-Ti RDFs reveal a

higher coordination between the QD5 and the TiO_2(001) surface.

Electronic Structure

Figure 4.66 displays the DOS of the QD5(S-111)@TiO_2(101) and QD5(S-111)@TiO_2(001) systems. Both models show a similar pattern. In brief, the VB of the QD5 isolated fragment, the high-lying occupied states of the QD are located about 2.5 eV above the top of the VB of the TiO_2 slab, whereas the unoccupied orbitals are *ca.* 0.3 eV higher in energy than the CB edge of the oxide substrate. This kind of type II alignment, where the unoccupied orbitals of the QD are immersed in the manifold of the conduction states of the TiO_2, favors the injection of the photoexcited electron from the QD to the oxide. Upon complexation, the QD and the TiO_2 slab undergo a sizable structural distortion, which in turn affects the position of the band edge states. In particular, the VB edges experience an upward shift and, as a consequence, the bandgaps of the isolated fragments shrink by about 0.2-0.3 eV.

The central panel of Figure 4.66 depicts the DOS of the interacting complexes, along with the projection into the QD5 and the TiO_2 moieties. As one may anticipate, the valence and the CB edges belong to the QD and the TiO_2 slab, respectively. The PDOS esentially coincide with the DOS of the isolated fragments. However, the charge density transfer from the QD to the TiO_2 slab aforementioned produces an upward shift of the CB edge of the latter, relative to the isolated TiO_2. Concomitantly, the VB edge of the (distorted) QD is stabilized by *ca.* 0.1 eV.

To unveil the nature of the band edge states, the contribution of the interacting fragments to the complex molecular orbitals has been computed. From the bottom panel of Figure 4.66, high-lying occupied orbitals are (almost) pure QD states. Deeper in the VB, a notable mixing between the QD and the TiO_2 states is observed. The contribution of the QD decreases until -8.5 eV, where the orbitals localize in the TiO_2 slab. Regarding the virtual states, the CB edge belongs mainly to the TiO_2. However, the unoccupied orbitals of the QD appear immersed in the manifold of the conduction states of the oxide. Irrespective of the TiO_2 model, the LUMO+5 orbital of the interacting system is mainly localized in the QD. It is almost a pure state, since the contribution of the TiO_2 to the orbital is *ca.* 5%. Deeper in the CB, the mixing of the QD-related orbitals with the TiO_2 conduction states increases.

Optical Properties

To simulate the optical absorption of the QDSSC models, TDDFT calculations have been performed. Figure 4.67 displays the simulated spectrum of the QD5(S-111)@TiO_2(101) complex. Compared to the bare QD5, the absorption band is redshifted by *ca.* 0.3 eV, in agreement with the DOS presented in Figure 4.66. Such a spectral displacement, already reported experimentally, has been attributed the redistribution of the electronic density in the interacting complex [639]. From Figure 4.66, however, it appears to be also related to the atomic rearrangement occurring in the QD upon interaction with the oxide surface. Consistently, we observe the TDDFT spectrum of the distorted QD to be already redshifted by about 0.2 eV with respect to that of the optimized QD, see Figure 4.67. The absorption band of the interacting complex is further displaced to lower energies, but just by *ca.* 0.1 eV. The small

impact of the complexation in the absorption spectrum suggests a weak coupling between the QD and the TiO_2 band edge states. To clarify this point, the composition of the lowest-lying TDDFT excitations is shown in Table 4.29. Notably, the brightest transitions imply excitations from the QD-related high-lying occupied states to the LUMO+5, which is also localized in the QD. Excitations from the QD-localized states to TiO_2-related orbitals are dark, due probably to the small spatial overlap.

4.9.5 Conclusions

Semiconductor QDs lie at the heart of several nanostructure architectures for solar energy conversion, including heterojunction and QDSSCs. On the latter, QDs have gained ground as light harvesters against the classical organic dyes due to their outstanding properties, including the tunability of the absorption features and the possibility of MEG. However, QDSSCs have performed quite disappointingly so far and the reasons underlying remain unclear. Here we present a DFT/TDDFT study on PbS QDSSCs, aimed at understanding their atomistic features. With that goal, and in a first step, we study the structural, electronic, and optical properties of PbS QDs of increasing size. Then, we investigate the interaction of a 1.7 nm PbS QD with two prototypical anatase facets, namely (101) and (001)

The bare QDs, cut from an underlying rock salt lattice, are predicted to undergo a significant distortion upon optimization. The structural relaxation is not limited to the surface, as found for II-VI cluster models, but affects also the core. The departure from the bulk-like geometry stabilizes the cluster and opens the bandgap. Accordingly, the QDs studied exhibit wide HOMO-LUMO gaps and no surface states. Compared to II-VI QDs, our QD models displays a high DOS at the edge of the CB, which could facilitate electron injection to the TiO_2 nanoparticle. However, the LUMOs are mostly localized on the core and the injection process could therefore be hindered due to the small coupling between the donor and acceptor states.

The 1.7 nm QD model is predicted to firmly adsorb on the TiO_2 surfaces through S-rich (111) facets. The interaction is particularly strong on the TiO_2(101) facet, with a a calculated binding energy of -187.46 kcal/mol. The adsorption of the QD on the TiO_2(001) facet is looser, with longer S-Ti and Pb-O bonds and a computed binding energy of -112.50 kcal/mol. The interaction is mainly electrostatic. However the orbital interaction contributes notably, suggesting that the polarization effects are important at the QD/TiO_2 interface. Accordingly, charge transfer from the QD to the TiO_2 is observed, which in turn perturbs the band edges of both the constituents of the nanocomposite. The dispersion forces are also sizable, meaning that weak interactions might play a role on this kind of nanocomposites.

Upon interaction, both the QD and the TiO_2 nanoparticle undergo a significant distortion, which in turn rises the VB edges by 0.2-0.3 eV. The polarization effects at the QD/TiO2 interface rise the CB edge of TiO_2 and restore the VB edge of the QD. The HOMOs of the interacting complex are pure QD states. Deeper in the VB a significant mixing between the QD and the TiO_2 orbitals is observed, until *ca.* 3 eV below the band edge, where the

orbitals localize on TiO_2. Regarding the CB edge, it belongs to TiO_2. However, the LUMOs of the QD appear immersed in the manifold of the unoccupied states of the oxide, therefore favoring electron injection. In particular, the LUMO of the isolated QD is the LUMO+5 in the interacting system. The brightest TDDFT excitations in the interacting system imply transitions from the HOMOs to the LUMO+5, from where electron injection is supposed to occur. It is an almost pure state, since the contribution of the TiO_2 nanoparticle is less than 6%, suggesting a non-adiabatic electron injection mechanism in this kind of systems. Higher in the CB, the QD/TiO_2 mixing increases, a crucial requirement for adiabatic injection.

Table 4.28: Energy decomposition analysis of the QD5@TiO_2(101) and QD5@TiO_2(001) complexes, calculated at the D-PBE/SZ(Ti)DZ(H,O,Pb,S). Energies written in kcal/mol. Values in parentheses give the percentage of each attractive term with respect to the sum of the attractive terms. Q(QD5), given in a.u., indicates the charge developed by the PbS QD5 upon interaction, computed by means of the Hirshfeld scheme.

	QD5(Pb-111)@TiO_2(101)		QD5(Pb-111)@TiO_2(101)		QD5(Pb-111)@TiO_2(101)	
$\triangle E$	-85.19		-187.36		-71.94	
$\triangle E_{prep}$	14.98		150.80		53.65	
QD5	5.86		80.34		34.05	
TiO_2	9.12		70.46		19.60	
$\triangle E_{int}$	-100.17		-338.16		-125.59	
$\triangle E_{Pauli}$	200.03		722.12		265.47	
$\triangle V_{elst}$	-142.5	(47%)	-605.15	(57%)	-204.28	(52%)
$\triangle E_{oi}$	-96.67	(32%)	-342.93	(32%)	-127.05	(32%)
$\triangle E_{disp}$	-61.03	(20%)	-112.21	(11%)	-59.73	(15%)
Q(QD5)	0.00		0.20		-0.10	
	QD5(Pb-111)@TiO_2(001)		QD5(Pb-111)@TiO_2(001)		QD5(Pb-111)@TiO_2(001)	
$\triangle E$	-13.54		-112.50		-52.03	
$\triangle E_{prep}$	5.12		127.96		16.66	
QD5	5.10		53.84		11.00	
TiO_2	0.02		74.12		5.66	
$\triangle E_{int}$	-18.66		-240.46		-68.69	
$\triangle E_{Pauli}$	1.21		463.41		75.84	
$\triangle V_{elst}$	-3.44	(17%)	-379.10	(54%)	-66.97	(46%)
$\triangle E_{oi}$	-2.72	(14%)	-223.38	(32%)	-31.26	(22%)
$\triangle E_{disp}$	-13.70	(69%)	-101.39	(14%)	-46.30	(32%)
Q(QD5)	0.00		0.14		-0.22	

Table 4.29: Valence excitation spectra of the QD5@TiO_2(101) nanocomposite. Vertical excitation energy (in eV) and the corresponding oscillator strength (in a.u.) are reported, along with the composition of the excited states. Only monoexcitations with % > 10% are reported. Results obtained at B3LYP/LANL2DZ.

# Excitation	E (eV)	f (a.u.)	Composition
1	1.40	0.0014	69% H – L+5
			19% H-1 – L+5
2	1.47	0.0000	53% H-2 – L
			32% H-3 – L
3	1.49	0.0000	97% H – L
4	1.51	0.0050	66% H-1 – L+5
			22% H – L+5
5	1.54	0.0000	88% H-1 – L
6	1.55	0.0001	58% H-3 – L
			37% H-2 – L
7	1.59	0.0001	56% H-2 – L+1
			19% H-3 – L+1
8	1.60	0.0000	95% H – L+1
9	1.61	0.0009	39% H-5 – L
			27% H-9 – L
10	1.62	0.0001	62% H-7 – L
			16% H-5 – L

Figure 4.59: Optimized geometries of the PbS QD (top) and the TiO_2 slab (bottom) models used in this work. Binding energies (red) and size (black) are expressed in kcal/mol and nm, respectively.

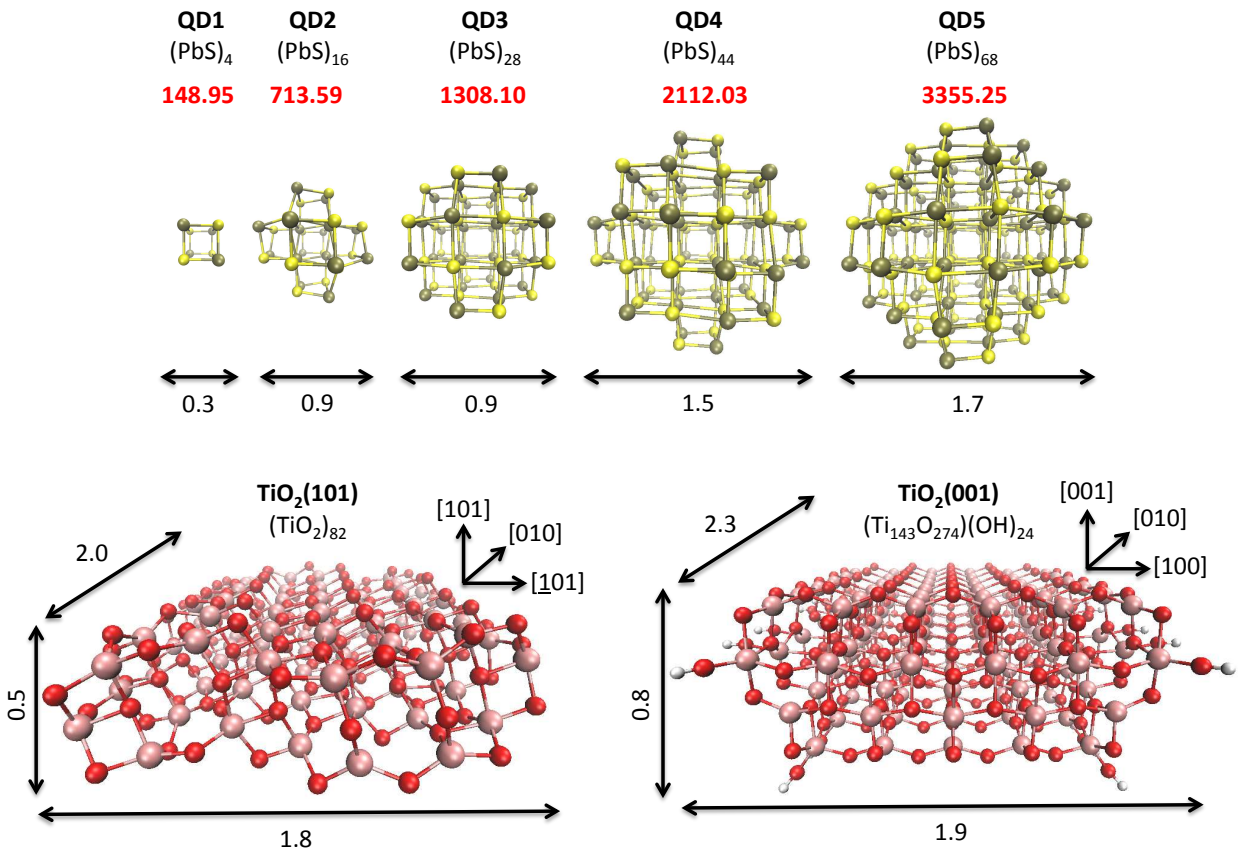


Figure 4.60: Pb-S (solid black), Pb-Pb (solid red), and S-S (solid blue) Radial Distribution Functions (RDFs) of the PbS QD models studied. For comparison, the bulk Pb-S (dashed black) and Pb-Pb / S-S (dashed red) distances are also shown.

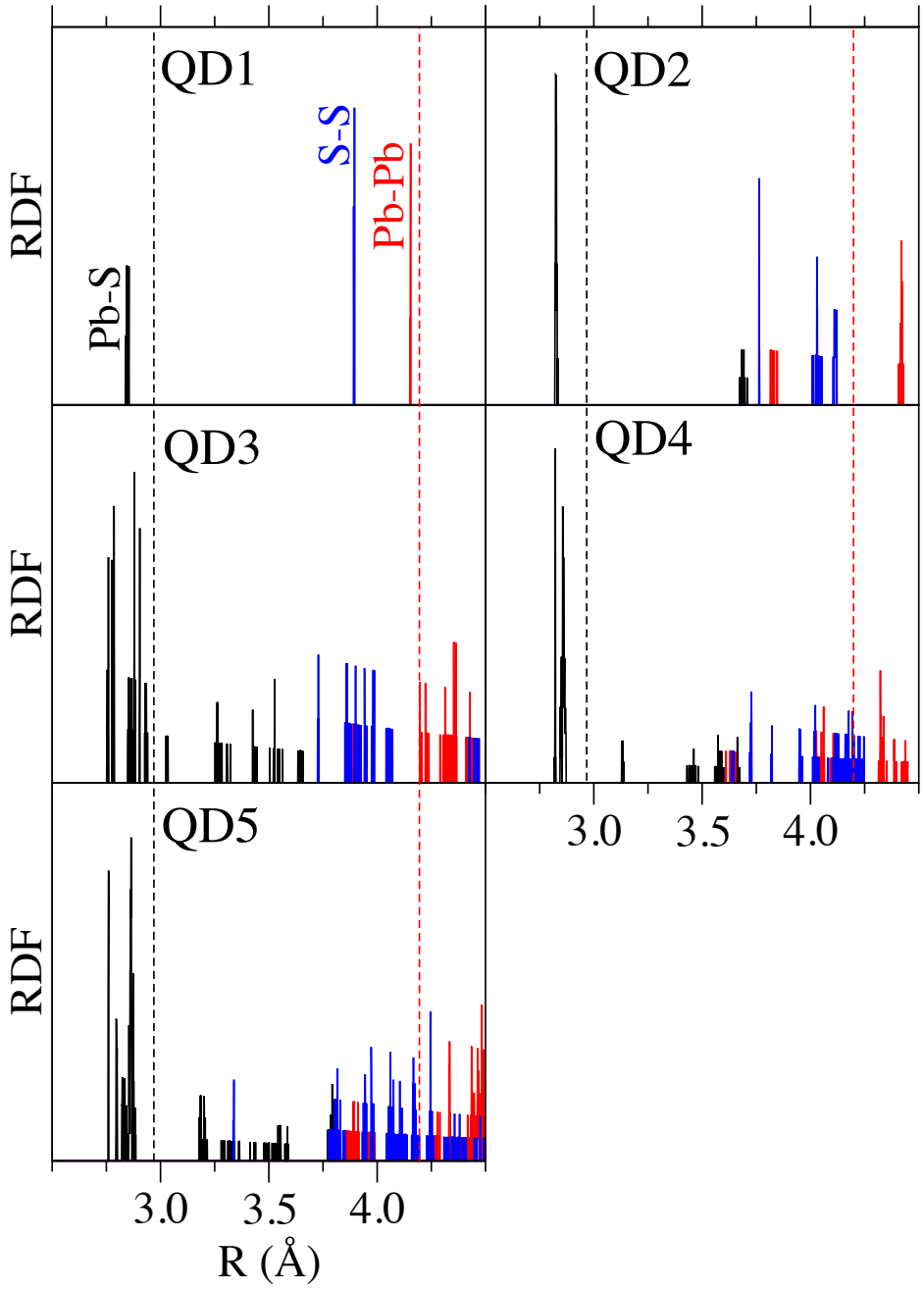


Figure 4.61: Energy diagram of the band edge orbitals, along with their corresponding DOS, obtained by a Gaussian convolution of σ = 0.2 eV of the individual orbitals. DOS have been normalized to fit the scale. For each QD, the Kohn-Sham bandgap is provided (in normal style), along with the first TDDFT electronic transition (in bold). Numbers in blue refer to the number of nearly degenerated molecular states at the band edges. Results obtained at the B3LYP/LANL2DZ level.

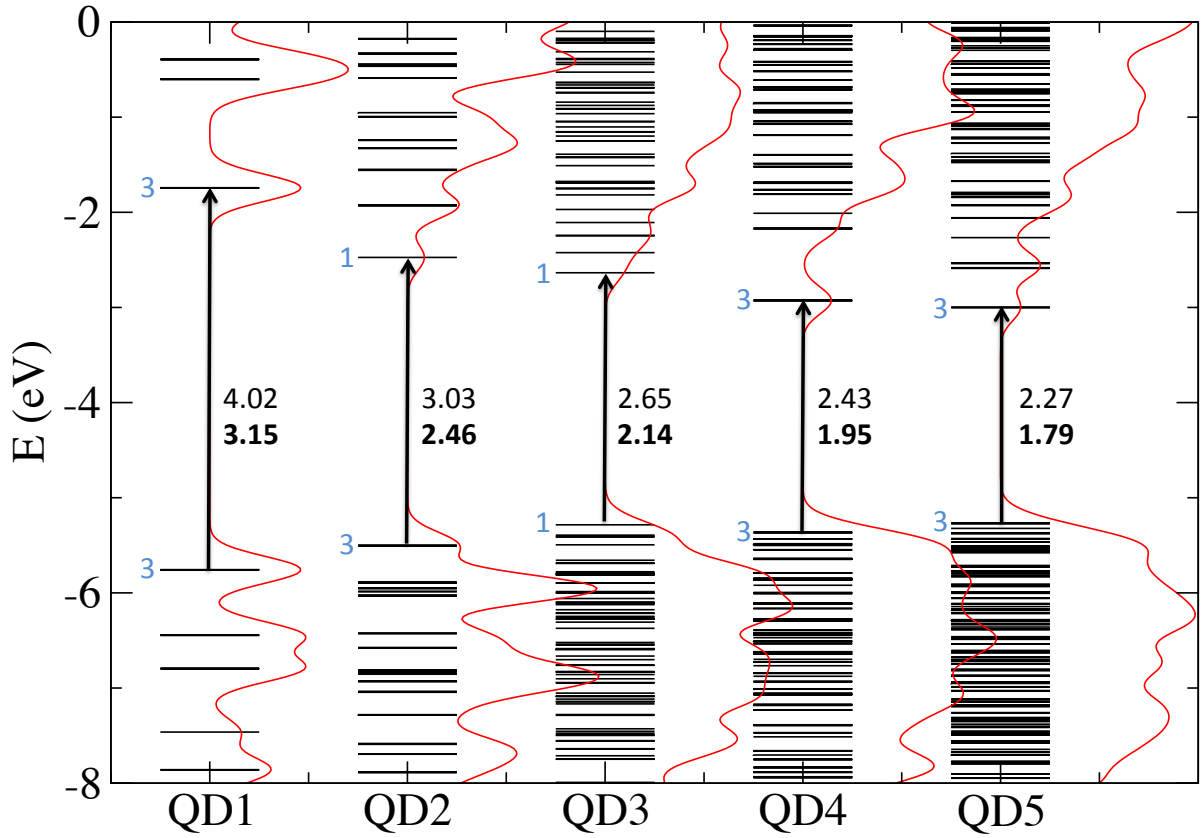


Figure 4.62: DOS of the QD5 model, obtained by a Gaussian convolution of σ = 0.2 eV of the individual orbitals, along with the projection into the atomic orbitals (a) and into the core/surface atoms (b). Results obtained at the B3LYP/LANL2DZ level.

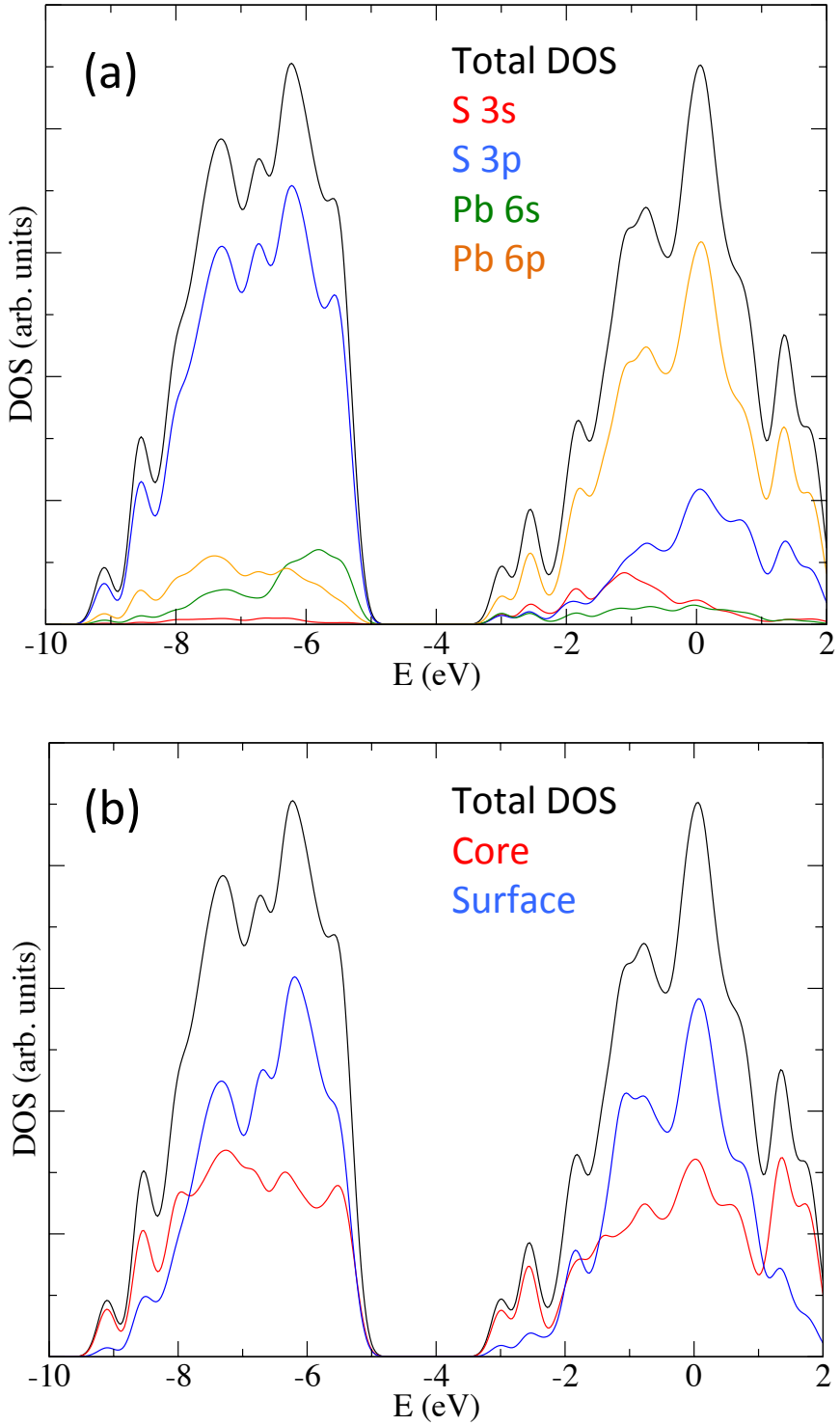


Figure 4.63: Simulated absorption spectra of the PbS QD models, drawn by a Gaussian convolution with FWHM = 3000 cm^{-1}, calculated taking into account the lowest 10 electronic transitions. Results obtained at the B3LYP/LANL2DZ level.

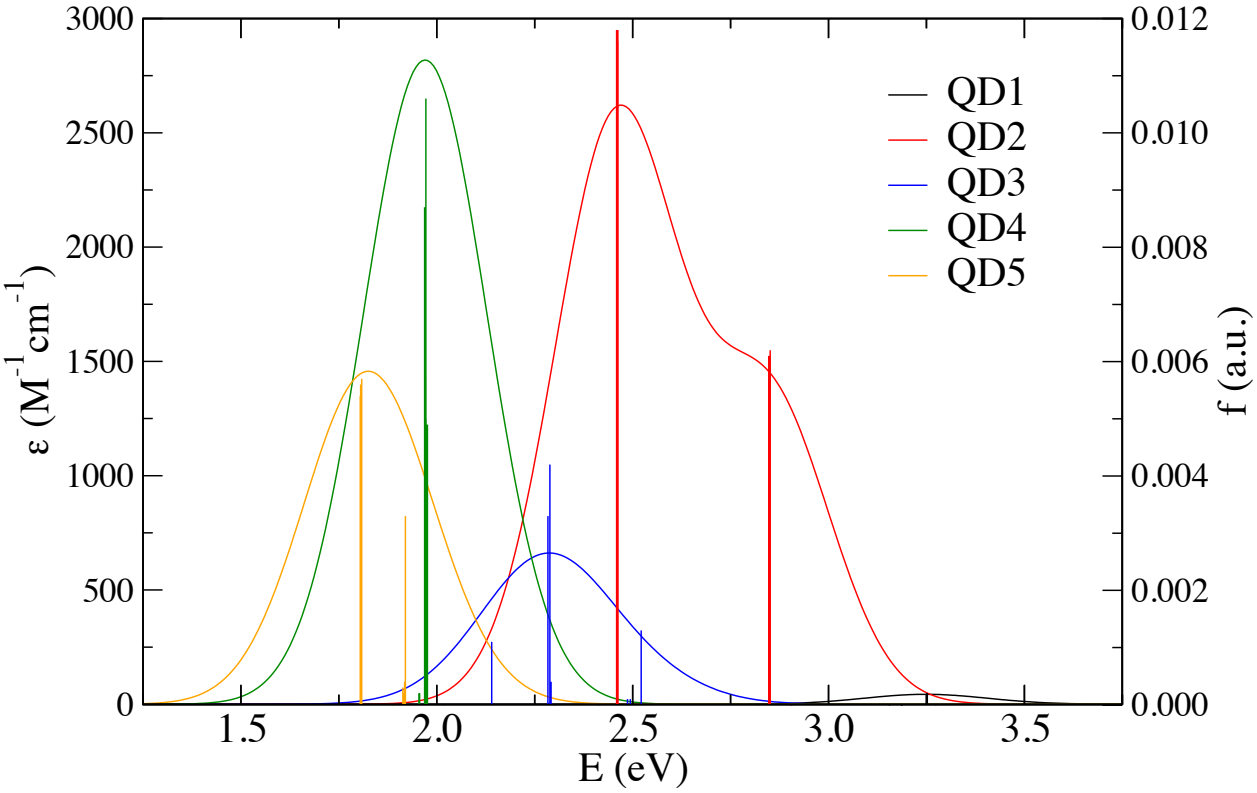


Figure 4.64: Side (left) and top (right) views of the optimized geometries of the QD5@TiO_2(101) (a-c) and QD5@TiO_2(001) (d-f) nanocomposites studied.

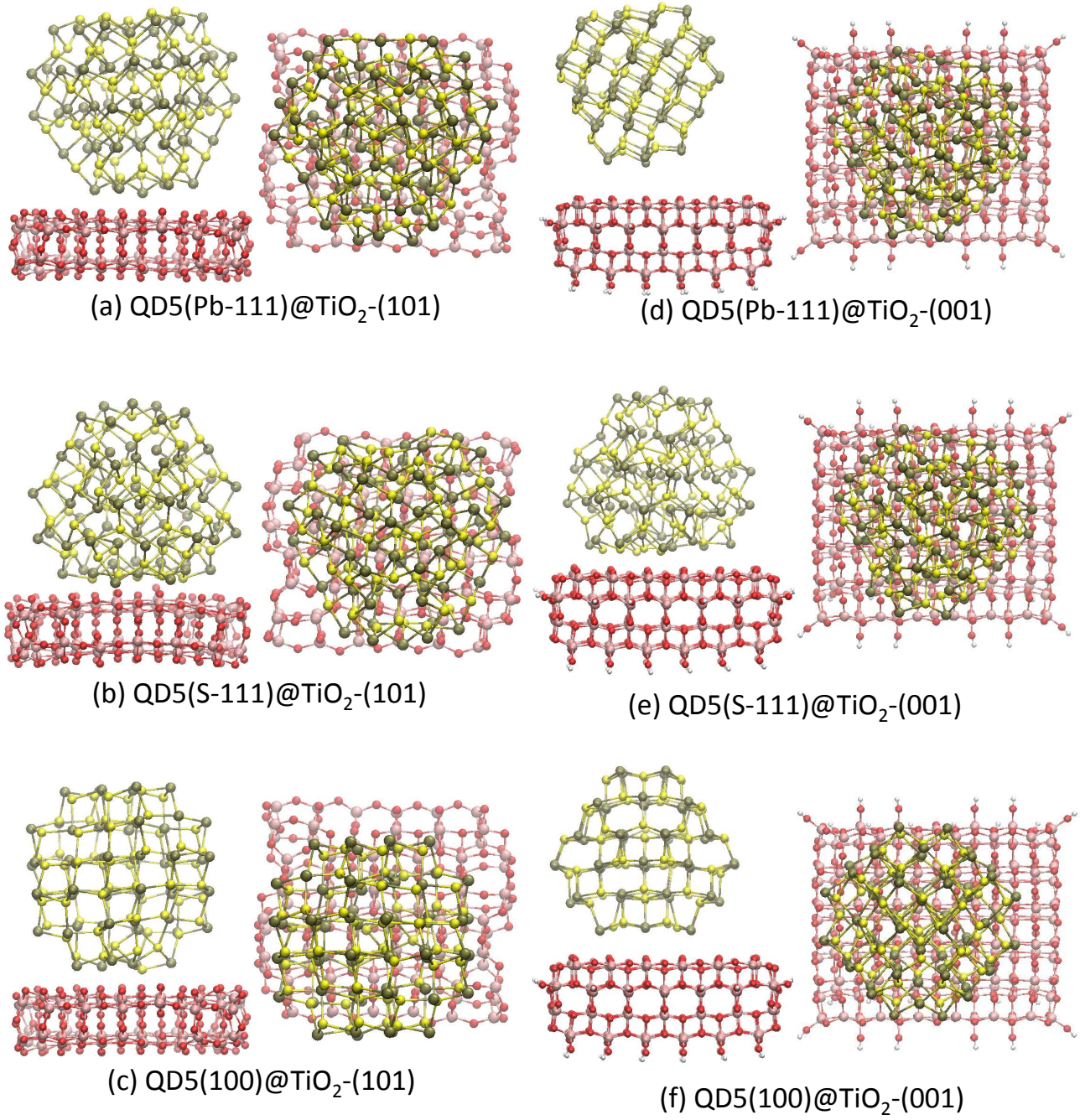


Figure 4.65: O-Pb (top panel) and Ti-S (bottom panel) RDF (left axes) of the optimized QD5(S-111)@TiO_2(101) (black) and QD5(S-111)@TiO_2(001) (red) nanocomposites, along with the corresponding integrated RDF (right axes). Geometries obtained at the PBE/SZ(Ti)DZ(H,O,Pb,S) level.

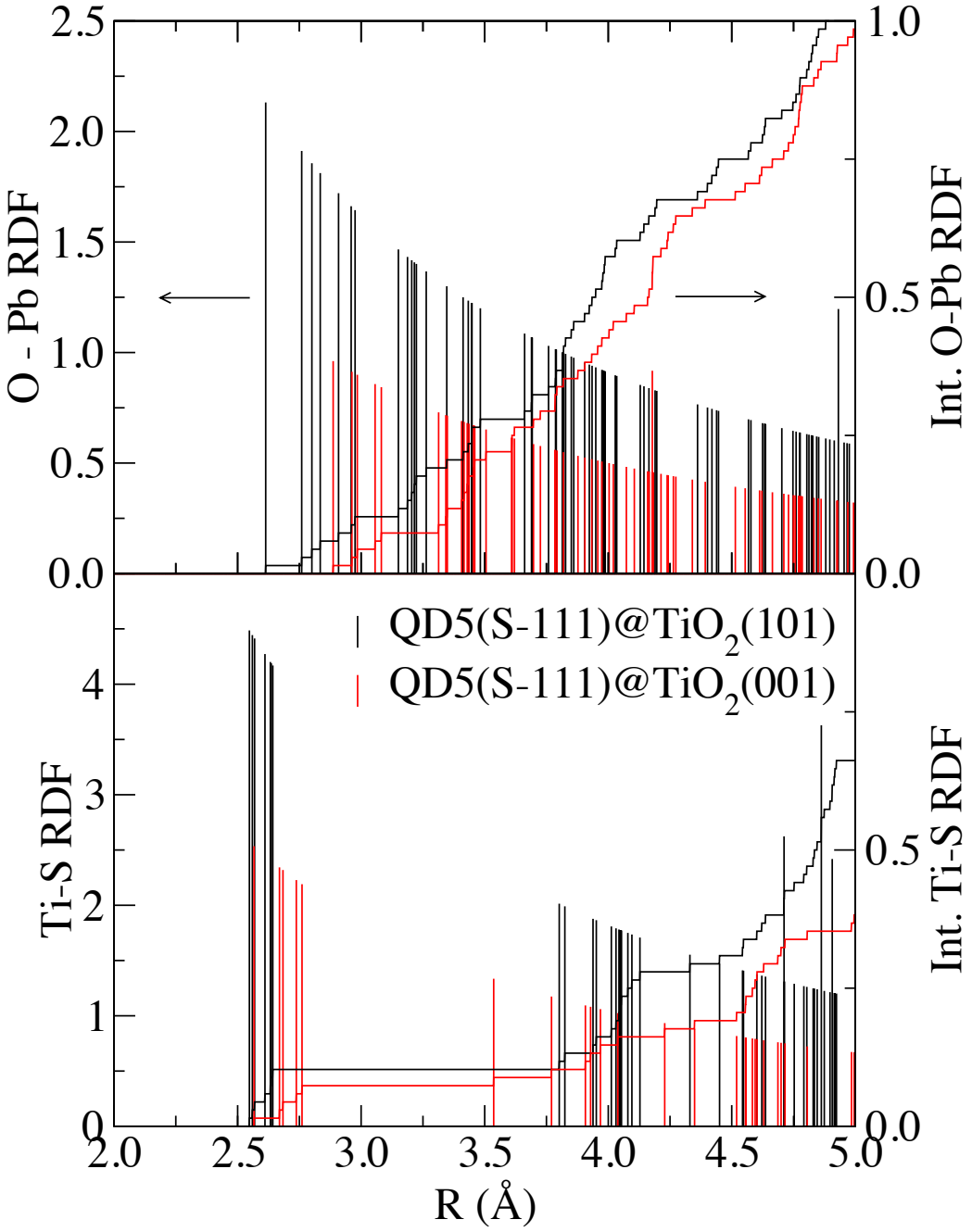


Figure 4.66: Top panel: DOS of the PbS QD5 (red) and the TiO_2 (blue) models calculated at their equilibrium geometries (solid lines) and at the structure they have in the interacting complex (dashed lines). Middle panel: DOS of the interacting complex, along with the projection into the QD5 and the TiO_2 fragments. Bottom panel: molecular orbitals of the interacting complex with contributions from the QD5 (red) and the TiO_2 (blue) fragments. The height of the stick represents the % of the orbital localized in each corresponding fragment. Results are obtained at the B3LYP/LANL2DZ level of theory.

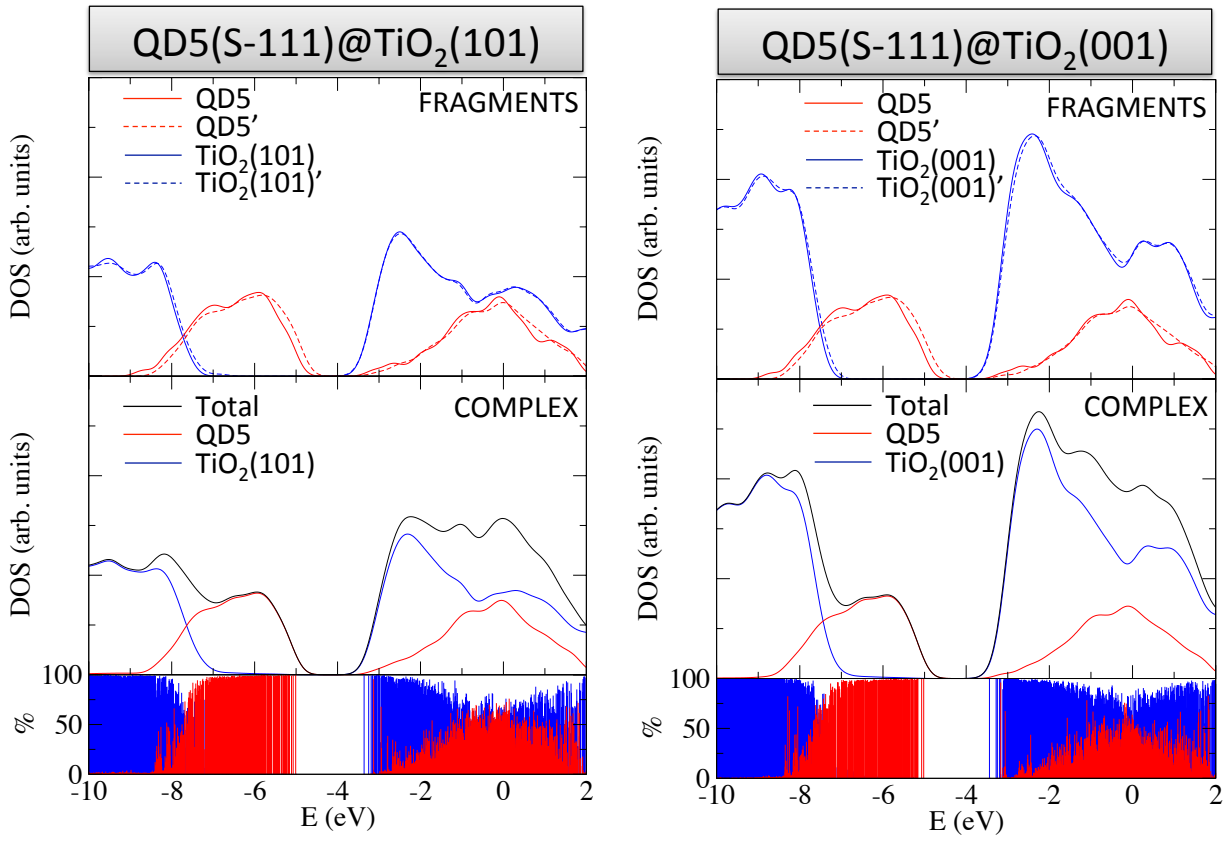
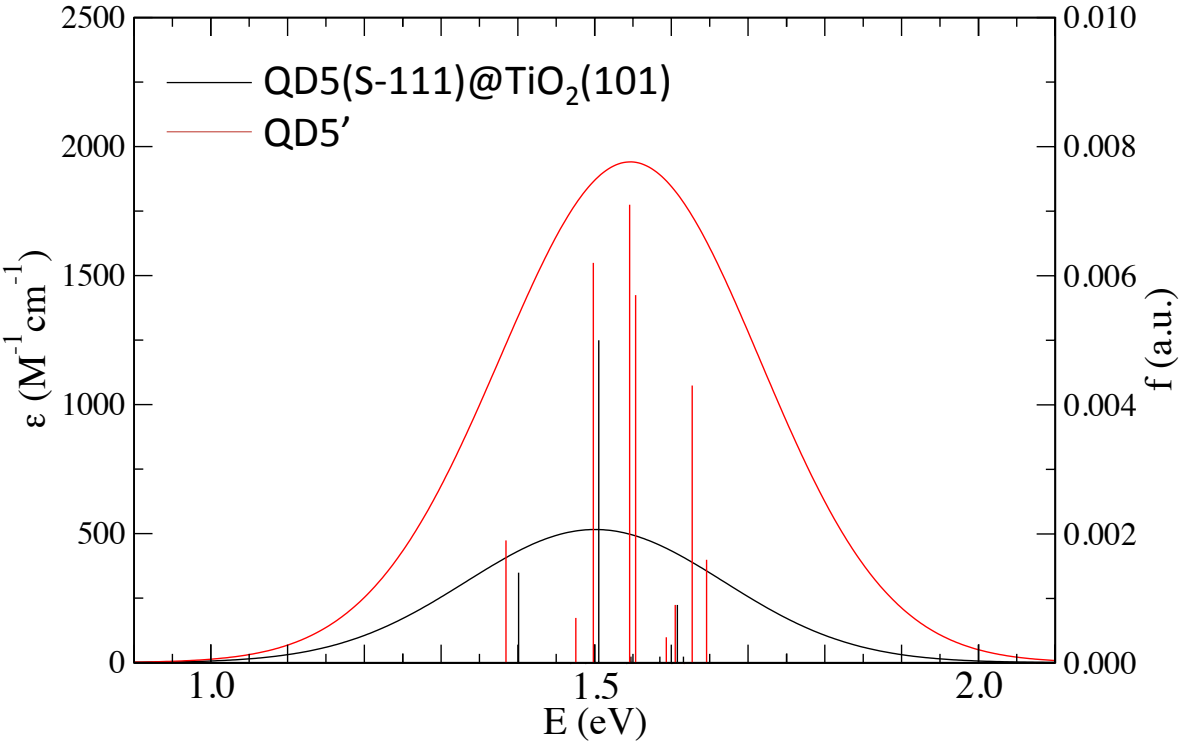


Figure 4.67: Simulated absorption spectrum of the QD5(S-111)@TiO_2(101) model (black), drawn by a Gaussian convolution with FWHM = 3000 cm^{-1}, calculated taking into account the lowest 10 electronic transitions. For comparison, the spectrum of the isolated QD5 is also shown (red), calculated in the geometry adopted in the interacting complex. Results obtained at the B3LYP/LANL2DZ level.



Chapter 5

Final Conclusions

Now this is not the end. It is not even the beginning of the end. But it is, perhaps, the end of the beginning.

Winston Churchill

The growing interest on semiconductor QDs has triggered a great deal of theoretical effort, aimed at unraveling their atomistic features, which are hardly accessible by experiment. DFT methods have gained momentum in the nano community because they represent a balanced compromise between accuracy and computational cost. Most of the computational works reported so far are based on a widespread standard combination of DFT functional and basis set. However, as shown in Section 4.1, the proper description of the structural, vibrational, electronic, and optical properties of QDs requires a careful selection of the actual DFT approach. Among the 26 functionals checked, PBE0 emerges as the best performing one. Other well-behaved functionals include certain degree of HF exchange, but imply an increased computational cost. Cheaper GGA and MGGA functionals properly reproduce the structural and vibrational properties, but they suffer from the well known underestimation of the electronic excitation energies. However, this drawback can be pragmatically fixed by a rigid energy shift of the whole spectrum, because the shape of the absorption features is almost insensitive to the functional. Alternatively, one could characterize the ground state of the QD model by means of a GGA/MGGA functional, followed by a single-point TDDFT calculation using a well-performing hybrid functional. Indeed, this is the approach adopted throughout this Thesis. With regard to the basis set, def2-SV(P) and SBKJC are the best ones in terms of computational efficiency and accuracy.

Armed with this sound computational scheme, Sections 4.2 and 4.3 deepen on the structural, electronic, and optical properties of bare ZnX (X = O, S, Se, Te) nanostructures of hexagonal crystal structure. This kind of wurtzite-like models undergo a drastic structural

rearrangement, driven by the saturation of the dangling bonds on the surface and the minimization of the dipole along the *c* axis. The saturation of the polar surfaces with dissociated H_2X molecules of Zn/X adatoms is shown to saturate the dangling bonds, minimize the dipole, and stabilize the wurtzite crystal structure, typically found in the experiments. The calculated absorption onsets are in nice agreement with the experiment. The lowest-lying electronic excitations imply transitions from the edge of the valence band to the LUMO exclusively, which could explain the characteristic broad/narrow absorption/emission spectra of semiconductor QDs. Anion vacancies are predicted to introduce localized orbitals into the bandgap, which could act as trap states for the photogenerated charge carriers and therefore explain the visible light emission typical in ZnX nanostructures.

As shown in Sections 4.2 and 4.3, nude bulk-like models undergo drastic structural reconstruction, driven by the unsaturated atoms on the exposed facets. Surface ligands are known to cap the dangling atoms, lower the surface energy, and stabilize the whole nanostructure. In Section 4.4 we report on the interaction between the $(ZnS)_6$ QD model and capping molecules, among which NMe_3, PMe_3, $OPMe_3$, MeOH, MeSH, and MeSeH. NMe_3, PMe_3, and $OPMe_3$ display a significantly greater affinity towards $(ZnS)_6$ than MeOH, MeSH, and MeSeH. The interaction is strengthened (i) with the decreasing hardness of the heteroatom bound to the QD surface and (ii) with the number and the length of the alkyl substituents in the ligand. The adsorption is predicted to be electrostatic, even if an important polarization of the charge density is observed. The QD-ligand bond is weakened with the increasing number of capping molecules on the surface, due presumably (i) to the repulsive interactions between adjacent ligands and (ii) to the diminished charge acceptor ability of the QD.

Due to the large surface-to-volume ratio inherent in nanomaterials, surface ligands often govern the nanostructure properties. Section 4.5 is devoted to the characterization of the $(CdSe)_{13}$ nanocluster, which has been recently isolated for the first time, and the effect of capping molecules on the electronic and optical properties. With regard to the bare cluster, a core@cage configuration, consisting of a Se atom incarcerated in the center of a puckered $Cd_{13}Se_{12}$, has been predicted to be the most stable isomer, with fullerene- and wurtzite-like structure lying higher in energy. Aliphatic and aromatic amines strongly interact with the nanocluster, with calculated binding energies of *ca.* 20 kcal/mol. Interestingly, the core@cage is still the lowest-lying isomer for the ligand-protected models, but the wurtzite geometry is stabilized with respect to the fullerene-like structure, confirming that the choice of the capping ligands determine the nanostructure shape. The interaction is mainly electrostatic, with an important orbital contribution, which in turn modifies the nanocluster frontier orbitals. The adsorption of alkylamines produces a significant blueshift of the absorption features of $(CdSe)_{13}$, due to the destabilization of the unoccupied states. However, the ligand-localized orbitals lie deep inside the valence and conduction bands of the nanocluster, and do not contribute to the lowest-lying electronic excitations. In contrast, aromatic amines introduce ligand-related states close to the band edges, which may act as trap states for the photogenerated charge carriers.

Indeed, appropriate alignment of electronic levels might promote charge transfer processes between QDs and capping ligands, which in turn could initiate chemical reactions in the surface attached molecules. This is the strategy recently exploited by Mareque et al. [38] to photoreduce Pt(IV) prodrugs on the CdSe@ZnS QD surface and generate Pt(II) species, among which cisplatin, with anticancer activity. In Section 4.6 we try to disentangle the mechanism underneath. The *cis*,*cis*,*trans*- $[Pt(NH_3)_2(Cl)_2(O_2CCH_2CH_2CO_2H)_2]$ prodrug is predicted to firmly adsorb on the surface of our $(CdSe)_{12}$ and $(CdSe)_{12}@(ZnS)_{48}$, in agreement with photoluminescence quenching data. The interaction is particularly strong with the $(CdSe)_{12}@(ZnS)_{48}$ model, due presumably to the smaller strain required to accommodate the Pt(IV) complex on the flatter surface of the core@shell cluster. Irrespective of the QD model, the valence band edge intrudes into the HOMO-LUMO gap of the Pt(IV) complex, and the conduction band edge lies slightly above the LUMO and the LUMO+1 of the prodrug. This alignment of electronic levels facilitates electron transfer from the QD to the Pt(IV) compound upon photoexcitation. Such a transfer is particularly favored to the LUMO+1 of the Pt(IV) compound, which in turn triggers the release of succinate ligands and the formation of cisplatin. The second pathway, involving the LUMO of the Pt(IV) species and leading to the secretion of NH_3 and Cl^-, is predicted to be less probable. This finding implies that QD-mediated photoactivation might drive the formation of preferred photoproducts compared to the simple chemical reduction or direct photoexcitation, which opens new avenues for developing anticancer agents.

However, for a safe application of semiconductor QDs *in vivo*, their behavior in water environment needs to be examined. Therefore, in Section 4.7 we investigate the effect of hydration on ZnS QDs. Bare QDs are predicted to undergo deep structural rearrangements, and evolve from the starting bulk-like geometry to an amorphous phase. These geometrical changes are reflected on the optoelectronic properties. In particular, the disruption of the Zn-S bonds in the QD lead to undercoordinated S atoms on the surface, which in turn develop localized midgap states that could act as trap states for the photogenerated holes. Water molecules are predicted to form strong H_2O-Zn bonds, lower the surface energy, stabilize the wurtzite-like structure of our clusters, and prevent the appearance of trap states.

In Section 4.6 we saw that electron transfer processes between QDs and ligands is a key process in photocatalysis. It is also of prime importance in Dye Sensitized Solar Cells, in which photoexcited electrons are injected from an organic molecule into a wide gap nanostructure material. On the latter, TiO_2 is the typical compound in the construction of this kind of nanocomposites, but ZnO nanomaterials have gained ground due to their interesting electronic properties and structural richness. In Section 4.8, we study the adsorption of N3 and N719 dyes on ZnO nanostructures. The sensitizers are predicted to adsorb firmly on the (1010) surface of ZnO. The interaction is particularly strong when three dye carboxylic groups are involved. Furthermore, if the anchoring group bears a proton, the adsorption is predicted to be dissociative. The sensitizers' LUMO are calculated to lie below the conduction band edge of the ZnO model, due to the reduced size of the considered ZnO model and to some extent to a non-optima description of the ZnO energy levels by standard DFT

functionals. In spite of these model limitations, the electron density donation from the dye to the ZnO is predicted to rise the band edges of the latter, in such a way that the optical gap of ZnO widens. Proton transfer seems to balance this effect, restoring the electronic levels of the non-interacting fragments.

More recently, QDSSCs have earned lots of attention, due to the paramount potential of QDs as light harvesters. However, this kind of nanocomposites have performed quite disappointingly so far, for reasons that remain unknown. In Section 4.9 we present a DFT/TDDFT work aimed at understanding the atomistic features of PbS quantum dot sensitized solar cells (QDSSCs). In a first step, we study the structural, electronic, and optical properties of PbS QDs of increasing size. In a second step, we investigate the sensitization of two prototypical anatase TiO_2 surfaces, namely (101) and (001), with a 1.7 nm size QD model. Regarding the standalone PbS QDs, they are predicted to undergo a significant geometrical distortion with respect to the rock salt structure. Such an atomic rearrangement stabilizes the QD and opens the bandgap. All the models studied exhibit wide bandgaps, with no midgap states that could deteriorate the performance of the solar cell. Compared to II-VI QDs, the PbS models studied here display a large density of unoccupied states, which could trigger electron injection to the TiO_2 substrate. However, such orbitals are mostly localized on the QD core, which might block the charge transfer due to the small coupling between the donor and acceptor states. The 1.7 nm size QD model is predicted to firmly adsorb on the TiO_2 slabs through the S-rich (111) facets. The adsorption is particularly strong on the TiO_2 (101) surface. Irrespective of the TiO_2 model, the occupied states of the QD intrude into the HOMO-LUMO gap of the oxide, whereas the unoccupied orbitals appear immersed in the conduction band of the oxide. The LUMO of the QD (the LUMO+5 in the interacting complex) is the arriving state of the lowest-lying electronic excitations. It is an almost pure state, since the contribution of the TiO_2 nanoparticle is less than 6%, suggesting a non-adiabatic electron injection mechanism in this kind of systems.

Chapter 6

List of Publications

The results presented in this Thesis have left their sequel in 8 publications in international peer-reviewed scientific journals, along with a 9th manuscript in preparation:

Benchmark Assessment of Density Functional Methods on Group II-VI MX (M = Zn, Cd; X = S, Se, Te) Quantum Dots

Jon M. Azpiroz, Jesus M. Ugalde, Ivan Infante

J. Chem. Theory. Comput., **2014**, *10*, 76-89

Modeling ZnS and ZnO Nanostructures: Structural, Electronic, and Optical Properties

Jon M. Azpiroz, Edoardo Mosconi, Filippo De Angelis

J. Phys. Chem. C, **201**1, *115*, 25219-25226

A First-Principles Study of II-VI (II = Zn; VI = O, S, Se, Te) Semiconductor Nanostructures

Jon M. Azpiroz, Ivan Infante, Xabier Lopez, Jesus M. Ugalde, Filippo de Angelis

J. Mater. Chem., **2012**, *22*, 21453-21465

Modeling Surface Passivation of ZnS Quantum Dots

Jon M. Azpiroz, Xabier Lopez, Jesus M. Ugalde, Ivan Infante

J. Phys. Chem. C, **2012**, *116*, 2740-2750

A DFT/TDDFT Study on the Optoelectronic Properties of the Amine-Capped Magic $(CdSe)_{13}$ Nanocluster

Jon M. Azpiroz, Jon M. Matxain, Ivan Infante, Xabier Lopez, Jesus M. Ugalde

Phys. Chem. Chem. Phys., **2013**, *15,* 10996-11005

Quantum Dot Photoactivation of Pt(IV) Anticancer Agents: Evidence of an Electron Transfer Mechanism Driven by Electronic Coupling

Ivan Infante, Jon M. Azpiroz, Nina Gomez Blanco, Emmanuel Ruggiero, Jesus M. Ugalde, Juan C. Mareque-Rivas, Luca Salassa

J. Phys. Chem. C , **2014**, *118*, 8712-8721

Effect of Structural and Solvent Dynamics on the Opto-Electronic Properties of Bare and Hydrated ZnS Quantum Dots

Jon M. Azpiroz, Edoardo Mosconi, Jesus M. Ugalde, Filippo de Angelis

J. Phys. Chem. C, **2014**, *118*, 3274-3284

DFT/TDDFT Study of the Adsorption of N3 and N719 Dyes on ZnO $(10\bar{1}0)$ *Surfaces*

Jon M. Azpiroz, Filippo De Angelis

J. Phys. Chem. A, **2014**, DOI: 10.1021/jp501058x

PbS Quantum Dot Sensitized Solar Cells: Insights from First Principles

Jon M. Azpiroz, Jesus M. Ugalde, Ivan Infante, Filippo De Angelis

Manuscript in preparation

Besides, during the Thesis, I have co-authored other 4 articles:

Heavy Periodane

Jon M. Azpiroz, Diego Moreno, Alonso Ramirez-Manzanares, Jesus M. Ugalde, Miguel Angel Mendez-Rojas, Gabriel Merino

J. Mol. Model., **2013**, *19*, 1953-1958

CdS Nanoclusters Doped with Divalent Atoms

Elisa Jimenez-Izal, Jon M. Azpiroz, Riti Gupta, Jon M. Matxain, Jesus M. Ugalde

Accepted for publication in *J. Mol. Model.*

Carbo-Cages: A Computational Study

Jon M. Azpiroz, Rafael Islas, Diego Moreno, Maria Fernandez-Herrera, Sudip Pan, Pratim Chattaraj, Gerardo Martinez-Guajardo, Jesus M. Ugalde, G. Merino

Accepted for publication in *J. Org. Chem.*

Multiple-Time-Stepping Generalized Hybrid Monte Carlo Methods

Bruno Escribano, Elena Akhmatskaya, Sebastian Reich, Jon M. Azpiroz

Submitted to *J. Comput. Phys.*

Chapter 7

Bibliography

Bibliography

[1] R. F. Service, *Science*, **2000**, *290*, 1526–1527.

[2] N. Lane, *J. Nanopart. Res.*, **2001**, *3*, 95–103.

[3] R. P. Feynmann; Perseus Books, 1999.

[4] A. P. Alivisatos, *J. Phys. Chem.*, **1996**, *100*, 13226–13239.

[5] A. P. Alivisatos, *Science*, **1996**, *271*, 933–937.

[6] A. N. Goldstein, C. M. Echer, and A. P. Alivisatos, *Science*, **1992**, *256*, 1425–1427.

[7] S. H. Tolbert and A. P. Alivisatos, *Annu. Rev. Phys. Chem.*, **1995**, *46*, 595–626.

[8] C. C. Chen, A. B. Herhold, C. S. Johnson, and A. P. Alivisatos, *Science*, **1997**, *276*, 398–401.

[9] C. Feigl, S. P. Russo, and A. S. Barnard, *J. Mater. Chem.*, **2010**, *20*, 4971–4980.

[10] A. S. Barnard, C. A. Feigl, and S. P. Russo, *Nanoscale*, **2010**, *2*, 2294–2301.

[11] C. A. Feigl, A. S. Barnard, and S. P. Russo, *Phys. Chem. Chem. Phys.*, **2012**, *14*, 9871–9879.

[12] S. Li and G. W. Yang, *J. Phys. Chem. C*, **2010**, *114*, 15054–15060.

[13] B. Gilbert, F. Huang, H. Z. Zhang, G. A. Waychunas, and J. F. Banfield, *Science*, **2004**, *305*, 651–654.

[14] T. J. Pennycook, J. R. McBride, S. J. Rosenthal, S. J. Pennycook, and S. T. Pantelides, *Nano Lett.*, **2012**, *12*, 3038–3042.

[15] A. Burnin and J. J. Belbruno, *Chem. Phys. Lett.*, **2002**, *362*, 341–348.

[16] A. Burnin, E. Sanville, and J. J. BelBruno, *J. Phys. Chem. A*, **2005**, *109*, 5026–5034.

[17] Atsuo Kasuya, Rajaratnam Sivamohan, Yurii a Barnakov, Igor M Dmitruk, Takashi Nirasawa, Volodymyr R Romanyuk, Vijay Kumar, Sergiy V Mamykin, Kazuyuki Tohji, Balachandran Jeyadevan, Kozo Shinoda, Toshiji Kudo, Osamu Terasaki, Zheng Liu, Rodion V Belosludov, Vijayaraghavan Sundararajan, and Yoshiyuki Kawazoe, *Nat. Mater.*, **2004**, *3*, 99–102.

[18] V. R. Romanyuk, I. M. Dmitruk, Yu. a. Barnakov, R. V. Belosludov, and A. Kasuya, *J. Nanosci. Nanotechnol.*, **2009**, *9*, 2111–2118.

[19] Y. S. Park, A. Dmytruk, I. Dmitruk, A. Kasuya, M. Takeda, N. Ohuchi, Y. Okamoto, N. Kaji, M. Tokeshi, and Y. Baba, *ACS Nano*, **2010**, *4*, 121–128.

[20] Y. S. Park, A. Dmytruk, I. Dmitruk, A. Kasuya, Y. Okamoto, N. Kaji, M. Tokeshi, and Y. Baba, *J. Phys. Chem. C*, **2010**, *114*, 18834–18840.

[21] A. Kasuya, Y. Noda, I. Dmitruk, V. Romanyuk, Y. Barnakov, K. Tohji, V. Kumar, R. Belosludov, Y. Kawazoe, and N. Ohuchi, *Eur. Phys. J. D*, **2005**, *34*, 39–41.

[22] Silvana Botti and Miguel Marques, *Phys. Rev. B*, **2007**, *75*, 035311(1–6).

[23] S. Hamad, S. M. Woodley, and C. R. A. Catlow, *Mol. Simulat.*, **2009**, *35*, 1015–1032.

[24] C R A Catlow, S T Bromley, S Hamad, M Mora-Fonz, A A Sokol, and S M Woodley, *Phys. Chem. Chem. Phys.*, **2010**, *12*, 786–811.

[25] G. G. Asara, A. D. Lewoczko, A. Burnin, J. J. Belbruno, and S. T Bromley, *J. Phys. Chem. C*, **2012**, *116*, 20625–20632.

[26] O. Voznyy, S. M. Thon, A. H. Ip, and E. H. Sargent, *J. Phys. Chem. Lett.*, **2013**, *4*, 987–992.

[27] R. Long, N. J. English, and O. V. Prezhdo, *J. Am. Chem. Soc.*, **2013**, *135*, 18892–18900.

[28] Hengzhong Zhang, Benjamin Gilbert, Feng Huang, and Jillian F Banfield, *Nature*, **2003**, *424*, 1025–1029.

[29] Hengzhong Zhang, Feng Huang, Benjamin Gilbert, and Jillian F. Banfield, *J. Phys. Chem. B*, **2003**, *107*, 13051–13060.

[30] Benjamin Gilbert, Hengzhong Zhang, Feng Huang, Jillian F Banfield, Yang Ren, Daniel Haskel, J C Lang, George Srajer, Astrid Jürgensen, and Glenn a Waychunas, *J. Chem. Phys.*, **2004**, *120*, 11785–11795.

[31] Hengzhong Zhang, James R Rustad, and Jillian F Banfield, *J. Phys. Chem. A*, **2007**, *111*, 5008–5014.

[32] C.M. Goodell, B. Gilbert, S.J. Weigand, and J.F. Banfield, *J. Phys. Chem. C*, **2008**, *112*, 4791–4796.

[33] Benjamin Gilbert, Feng Huang, Zhang Lin, Carmen Goodell, Hengzhong Zhang, and Jillian F Banfield, *Nano Lett.*, **2006**, *6*, 605–610.

[34] D. V. Talapin, J. S. Lee, M. V. Kovalenko, and E. V. Shevchenko, *Chem. Rev.*, **2010**, *110*, 389–458.

[35] Douglas A. Hines and Prashant V. Kamat, *J. Phys. Chem. C*, **2013**, *117*, 14418–14426.

[36] B. O. Dabbousi, J. Rodriguez-Viejo, F. V. Mikulec, J. R. Heine, H. Mattoussi, R. Ober, K. F. Jensen, and M. G. Bawendii, *J. Phys. Chem. B*, **1997**, *101*, 9463–9475.

[37] M. Pastore, S. Fantacci, and F. De Angelis, *J. Phys. Chem. C*, **2013**, *117*, 3685–3700.

[38] C. R. Maldonado, N. Gomez Blanco, M. Jauregui-Osoro, V. G. Brunton, L. Yate, and J. C. Mareque-Rivas, *Chem. Commun.*, **2013**, *49*, 3985–3987.

[39] S. Ruhle, M. Shalom, and A. Zaban, *Chem. Phys. Chem.*, **2010**, *11*, 2290–2304.

[40] I. Mora-Sero and J. Bisquert, *J. Phys. Chem. Lett.*, **2010**, *1*, 3046–3052.

[41] I. Hod, V. Gonz, Z. Tachan, F. Fabregat-Santiago, I. Mora-Sero, J. Bisquert, and A. Zaban, *J. Phys. Chem. Lett.*, **2011**, *2*, 3032–3035.

[42] I. Mora-Sero, T. Dittrich, A. S. Susha, A. L. Rogach, and J. Bisquert, *Thin Solid Films*, **2008**, *516*, 6994–6998.

[43] I. Mora-Sero, V. Likodimos, S. Gimenez, E. Martinez-Ferrero, J. Albero, E. Palomares, A. G. Kontos, P. Falaras, and J. Bisquert, *J. Phys. Chem. C*, **2010**, *114*, 6755–6761.

[44] I. Mora-Seró, D. Gross, T. Mittereder, A. A. Lutich, A. S. Susha, T. Dittrich, A. Belaidi, R. Caballero, F. Langa, J. Bisquert, and A. L. Rogach, *Small*, **2010**, *6*, 221–225.

[45] H. W. Tseng, M. B. Wilker, N. H. Damrauer, and G. Dukovic, *J. Am. Chem. Soc.*, **2013**, *135*, 3383–3386.

[46] I. L. Medintz, M. H. Stewart, S. A. Trammell, K. Susumu, J. B. Delehanty, B. C. Mei, J. S. Melinger, J. B. Blanco-Canosa, P. E. Dawson, and H. Mattoussi, *Nat. Mater.*, **2010**, *9*, 676–684.

[47] O. V. Prezhdo, *Acc. Chem. Res.*, **2009**, *42*, 2005–2016.

[48] A. I. Ekimov, A. A. Onushchenko, and V. A. Tzehomskii, *Sov. Phys. Chem. Glass.*, **1980**, *6*, 511–512.

[49] A. Henglein, *Ber. Bunsenges. Phys. Chem.*, **1982**, *86*, 301–305.

[50] D. J. Norris, A. L. Efros, and S. C. Erwin, *Science*, **2008**, *319*, 1776–1779.

[51] V. Chikan, *J. Phys. Chem. Lett.*, **2011**, *2*, 2783–2789.

[52] P. Reiss, M. Protière, and L. Li, *Small*, **2009**, *5*, 154–168.

[53] A. M. Smith and S. Nie, *Acc. Chem. Res.*, **2010**, *43*, 190–200.

[54] S. Sapra, A. Prakash, A. Ghangrekar, N. Periasamy, and D. D. Sarma, *J. Phys. Chem. B*, **2005**, *109*, 1663–1668.

[55] N. Pradhan, D. Goorskey, J. Thessing, and X. Peng, *J. Am. Chem. Soc.*, **2005**, *127*, 17586–17587.

[56] L. E. Brus, *J. Chem. Phys.*, **1983**, *79*, 5566–5571.

[57] J. D. Bryan and D. R. Gamelin, *Progress in Inorganic Chemistry;* John Wiley and Sons, Inc., 2005.

[58] D. J. Norris, N. Yao, F. T. Charnock, and T. A. Kennedy, *Nano Lett.*, **2001**, *1*, 3–7.

[59] K. M. Hanif, R. W. Meulenberg, and G. F. Strouse, *J. Am. Chem. Soc.*, **2002**, *124*, 11495–11502.

[60] C. A. Stowell, R. J. Wiacek, A. E. Saunders, and B. A. Korgel, *Nano Lett.*, **2003**, *3*, 1441–1447.

[61] S. B. Orlinskii, J. Schmidt, P. G. Baranov, D. M. Hofmann, C. de Mello Donegá, and A. Meijerink, *Phys. Rev. Lett.*, **2004**, *92*, 047603(1–4).

[62] M Fujii, Y. Yamaguchi, Y. Takase, K. Ninomiya, and S. Hayashi, *Appl. Phys. Lett.*, **2005**, *87*, 211919(1–3).

[63] L. P. Balet, S. A. Ivanov, A. Piryantinski, M. Achermann, and V. I. Klimov, *Nanot Lett.*, **2004**, *4*, 1485–1488.

[64] S. Kim, B. Fisher, H. J. Eisler, and M. Bawendi, *J. Am. Chem. Soc.*, **2003**, *125*, 13559–13563.

[65] S. Kumar, M. Jones, S. S. Lo, and G. D. Scholes, *Small*, **2007**, *3*, 1633–1639.

[66] P. Kambhampati, *Acc. Chem. Res.*, **2011**, *44*, 1–13.

[67] M. Nirmal, B. Dabbousi, M. G. Bawendi, J. J. Macklin, J. K. Trautman, T. D. Harris, and L. E. Brus, *Nature*, **1996**, *383*, 802–804.

[68] I. L. Medintz, H. T. Uyeda, E. R. Goldman, and H. Mattoussi, *Nat. Mater.*, **2005**, *4*, 435–446.

[69] D. E. Gomez, M. Califano, and P. Mulvaney, *Phys. Chem. Chem. Phys.*, **2006**, *8*, 4989–5011.

[70] B. Mahler, P. Spinicelli, S. Buil, X. Quelin, J. P. Hermier, and B. Dubertret, *Nat. Mater.*, **2008**, *7*, 659–664.

[71] Y. F. Chen, J. Vela, H. Htoon, J. L. Casson, D. J. Werder, D. A. Bussian, V. I. Klimov, and J. A. Hollingsworth, *J. Am. Chem. Soc.*, **2008**, *130*, 5026–5027.

[72] A. L. Efros, V. A. Kharchenko, and M. Rosen, *Solid State Commun.*, **1995**, *93*, 281–284.

[73] R. R. Cooney, S. L Sweall, K. E. H. Anderson, E. A. Dias, and P. Kambhampati, *Phys. Rev. Lett.*, **2007**, *98*, 177403(1–4).

[74] R. D. Schaller, J. M. Pietryga, S. V. Goupalov, M. A. Petruska, S. A. Ivanov, and V. I. Klimov, *Phys. Rev. Lett.*, **2005**, *95*, 196401(1–4).

[75] A. J. Nozik, *Annu. Rev. Phys. Chem.*, **2001**, *52*, 193–231.

[76] R. D. Schaller and V. I. Klimov, *Phys. Rev. Lett.*, **2004**, *92*, 186601(1–4).

[77] R. J. Ellingson, M. C. Beard, J. C. Johnson, P. R. Yu, O. I. Micic, A. J. Nozik, A. Shabaev, and A. L. Efros, *Nano Lett.*, **2005**, *5*, 865–871.

[78] J. A. McGuire, J. Joo, J. M. Pietryga, R. D. Schaller, and V. I. Klimov, *Acc. Chem. Res.*, **2008**, *41*, 1810–1819.

[79] R. R. Cooney, S. L. Sewall, E. A. Dias, D. M. Sagar, K. E. H. Anderson, and P. Kambhampati, *Phys. Rev. B*, **2007**, *75*, 245311(1–14).

[80] A. Pandey and P. Guyot-Sionnest, *Science*, **2008**, *322*, 929–932.

[81] E. Hendry, M. Koeberg, F. Wang, H. Zhang, C. de Mello Donegá, D. Vanmaekelbergh, and M. Bonn, *Phys. Rev. Lett.*, **2006**, *96*, 057408(1–4).

[82] S. V. Kilina, D. S. Kilin, C. F. Craig, and O. V. Prezhdo, *J. Phys. Chem. C*, **2007**, *111*, 4871–4878.

[83] S. V. Kilina, D. S. Kilin, and O. V. Prezhdo, *ACS Nano*, **2009**, *3*, 93–99.

[84] V. I. Klimov, A. A. Mikhailovsky, S. Xu, A. Malko, J. A. Hollingsworth, C. A. Leatherdale, H. J. Eisler, and M. G. Bawendi, *Science*, **2000**, *290*, 314–317.

[85] P. Guyot-Sionnest, B. Wehrenberg, and D. Yu, *J. Chem. Phys.*, **2005**, *123*, 074709(1–7).

[86] S. Kilina, K. A. Velizhanin, S. Ivanov, O. V. Prezhdo, and S. Tretiak, *ACS Nano*, **2012**, *6*, 6515–6524.

[87] H. M. Jaeger, K. Hyeon-Deuk, and O. V. Prezhdo, *Acc. Chem. Res.*, **2013**, *46*, 1280–1289.

[88] V. I. Klimov, *J. Phys. Chem. B*, **2006**, *110*, 16827–16845.

[89] B. Cho, W. K. Peters, R. J. Hill, and T. L. Courtney, *Nano Lett.*, **2010**, *10*, 2498–2505.

[90] M. G. Bawendi C. B. Murray, D. J. Norris, *J. Am. Chem. Soc.*, **1993**, *115*, 8706–8715.

[91] Y. Yin and A. P. Alivisatos, *Nature*, **664-670**, *437*, 2005.

[92] D. V. Talapin, A. L. Rogach, A. Kornowski, M. Haase, and H. Weller, *Nano Letters*, **2001**, *1*, 207.

[93] B. Blackman, D. M. Battaglia, T. D. Mishima, M. B. Johnson, and X. Peng, *Chem. Mater.*, **2007**, *19*, 3815–3821.

[94] Z. A. Peng and X. J. Peng, *J. Am. Chem. Soc.*, **2002**, *124*, 3343–3353.

[95] G. Morello, M. De Giorgi, S. Kudera, L. Manna, R. Cingolani, and M. Anni, *J. Phys. Chem. C*, **2007**, *111*, 5846–5849.

[96] K. T. Yong, Y. Sahoo, M. T. Swihart, and P. N. Prasad, *J. Phys. Chem. C*, **2007**, *111*, 2447–2458.

[97] O. I. Micic, C. J. Curtis, K. M. Jones, J. R. Sprague, and A. J. Nozik, *J. Phys. Chem.*, **1994**, *98*, 4966–4969.

[98] D. V. Talapin, A. L Rogach, E. V. Shevchenko, A. Kornowski, M. Haase, and H. Weller, *J. Am. Chem. Soc.*, **2002**, *124*, 5782–5790.

[99] D. Battaglia and X. Peng, *Nano Lett.*, **2002**, *2*, 1027–1030.

[100] S. M. Lee, Y. W. Jun, S. N. Cho, and J. J. Cheon, *J. Am. Chem. Soc.*, **2002**, *124*, 11244–11245.

[101] M. A. Hines and G. D. Scholes, *Adv. Mater.*, **2003**, *15*, 1844–1849.

[102] W. Lin, K. Fritz, G. Guerin, G. R. Bardajee, S. Hinds, V. Sukhovatkin, E. H. Sargent, G. D. Scholes, and M. A. Winnik, *Langmuir*, **2008**, *24*, 8215–8219.

[103] L. Cademartiri, J. Bertolotti, R. Sapienza, D. S. Wiersma, G. von Freynmann, and J. Ozin, *J. Phys. Chem. B*, **2006**, *110*, 671–673.

[104] K. A. Abel, J. Shan, J. C. Boyer, F. Harris, and F. C. J. M. van Veggel, *Chem. Mater.*, **2008**, *20*, 3794–3796.

[105] D. V. Talapin and C. B. Murray, *Science*, **2005**, *310*, 86–89.

[106] J. J. Urban, D. V. Talapin, E. V. Shevchenko, and C. B. Murray, *J. Am. Chem. Soc.*, **2006**, *128*, 3248–3255.

[107] N. Gaponik, D. V. Talapin, A. L. Rogach, K. Hoppe, E. V. Shevchenko, A. Kornowski, A. Eychmüller, and H. Weller, *J. Phys. Chem. B*, **2002**, *106*, 7177–7185.

[108] A. Shavel, N. Gaponik, and A. Eychmüller, *J. Phys. Chem. B*, **2006**, *110*, 19280–19284.

[109] A. L. Rogach, T. Franzl, T. A. Klar, J. Feldmann, N. Gaponik, V. Lesnyak, A. Shavel, A. Eychmüller, Y. P. Rakovich, and J. F. Donegan, *J. Phys. Chem. C*, **2007**, *111*, 14628–14637.

[110] B. L. Cushing, V. L. Kolesnichenko, and C. J. O'Connor, *Chem. Rev.*, **2004**, *104*, 3893–3946.

[111] C. Burda, X. Chen, R. Narayanan, and M. A. El-Sayed, *Chem. Rev.*, **2005**, *105*, 1025–1102.

[112] J. A. Dahl, B. L. S. Maddux, and E. James, *Chem. Rev.*, **2007**, *107*, 2228–2269.

[113] M. Kuno, J. K. Lee, B. O. Dabbousi, F. V. Mikulec, and M. G. Bawendi, *J. Chem. Phys.*, **1997**, *106*, 9869–9882.

[114] C. B. Murray, C. R. Kagan, and M. G. Bawendi, *Annu. Rev. Mater. Sci.*, **2000**, *30*, 545–610.

[115] G. Konstantatos, I. Howard, A. Fischer, S. Hoogland, J. Clifford, E. Klem, L. Levina, and E. H. Sargent, *Nature*, **2006**, *442*, 180.

[116] N. Gaponik, D. V. Talapin, A. L. Rogach, A. Eychmüller, and H. Weller, *Nano Lett.*, **2002**, *2*, 803–806.

[117] J. S. Owen, J. Park, P. E. Trudeau, and A. P. Alivisatos, *J. Am. Chem. Soc.*, **2008**, *130*, 12279–12281.

[118] M. J. Hostetler, S. J. Green, J. J. Stokes, and R. W. Murray, *J. Am. Chem. Soc.*, **1996**, *118*, 4212–4213.

[119] I. S. Liu, H. H. Lo, C. T. Chien, Y. Y. Lin, C. W. Chen, Y. F. Chen, W. F. Su, and S. C. Liou, *J. Mater. Chem.*, **2008**, *18*, 675–682.

[120] M. J. Hostetler, A. C. Templeton, and R. W. Murray, *Langmuir*, **1999**, *15*, 3782–3789.

[121] E. E. Foos, A. W. Snow, M. E. Twigg, and M. G. Ancona, *Chem. Mater.*, **2002**, *14*, 2401–2408.

[122] X. Peng, M. C. Schlamp, A. V. Kadavanich, and A. P. Alivisatos, *J. Am. Chem. Soc.*, **1997**, *119*, 7019–7029.

[123] U. Woggon, E. Herz, O. Schops, M. V. Artemyev, C. Arens, N. Rousseau, D. Schikora, K. Lischka, D. Litvinov, and D. Gerthsen, *Nano Lett.*, **2005**, *5*, 483–490.

[124] M. V. Kovalenko, D. V. Talapin, M. A. Loi, F. Cordella, G. Hesser, M. I. Bodnarchuk, and W. Heiss, *Angew. Chem. Int. Ed.*, **2008**, *47*, 3029–3033.

[125] G. H. Woehrle, L. O. Brown, and J. E. Hutchison, *J. Am. Chem. Soc.*, **2005**, *127*, 2172–2183.

[126] M. Law, J. M. Luther, Q. Song, B. K. Hughes, C. L. Perkins, and A. J. Nozik, *J. Am. Chem. Soc.*, **2008**, *130*, 5974–5985.

[127] J. S. Liu, T. Tanaka, K. Sivula A. P. Alivisatos, and J. M. Frechet, *J. Am. Chem. Soc.*, **2004**, *126*, 6550–6551.

[128] H. Skaff, K. Sill, and T. Emrick, *J. Am. Chem. Soc.*, **2004**, *126*, 11322–11325.

[129] C. Harris and P. V. Kamat, *ACS Nano*, **2009**, *3*, 682–690.

[130] C. Harris and P. V. Kamat, *ACS Nano*, **2010**, *4*, 7321–7330.

[131] C. Wang, R. L. Thompson, J. Baltrus, and C. Matranga, *J. Phys. Chem. Lett.*, **2010**, *1*, 48–53.

[132] T. P. A. Ruberu, N. C. Nelson, I. I. Slowing, and J. Vela, *J. Phys. Chem. Lett.*, **2012**, *3*, 2798–2802.

[133] D. Jimenez de Aberasturi, J. M. Montenegro, I. Ruiz de Larramendi, T. Rojo, T. A. Klar, R. Alvarez-Puebla, L. M. Liz-Marzan, and W. J. Parak, *Chem. Mater.*, **2012**, *24*, 738–745.

[134] F. Zhang, Z. Ali, F. Amin, A. Feltz, M. Oheim, and W. J. Parak, *Chem. Phys. Chem.*, **2010**, *11*, 730–735.

[135] A. Reidinger, F. Zhang, F. Dommershuasen, C. Röcker, S. Brandholdt, G. U. Nienhaus, U. Koert, and W. J. Parak, *Small*, **2010**, *6*, 2590–2597.

[136] R. V. Benjaminsen, H. Sun, J. R. Henriksen, N. M. Christensen, K. Almdal, and T. L. Andresen, *ACS Nano*, **2011**, *5*, 5864–5873.

[137] I. L. Medintz, R. Aaron, H. Mattoussi, E. R. Goldman, B. Fisher, and J. M. Mauro, *Nat. Mater.*, **2003**, *2*, 630–638.

[138] M. T. Fernandez-Argüelles, A. Yakovlev, R. A. Sperling, C. Luccardini, S. Gaillard, A. S. Medel, J. M. Mallet, J. C. Brochon, A. Feltz, M. Oheim, and W. J. Parak, *Nano Lett.*, **2007**, *7*, 2613–2617.

[139] A. S. Susha, J. A. Munoz, W. J. Parak, and A. L. Rogach, *Colloids Surf.*, **2006**, *281*, 40–43.

[140] Y. Chen and Z. Rosenzweig, *Anal. Chem.*, **2002**, *74*, 5132–5138.

[141] M. J. Ruedas-Rama and E. A. H. Hall, *Anal. Chem.*, **2008**, *80*, 8260–8268.

[142] R. Freeman, T. Finder, and I. Willner, *Angew. Chem. Int. Ed.*, **2009**, *48*, 7818–7821.

[143] X. R. He, H. B. Liu, Y. L. Li, S. Wang, Y. J. Li, N. Wang, J. C. Xiao, X. H. Xu, and D. B. Zhu, *Adv. Mater.*, **2005**, *17*, 2811–2815.

[144] C. C. Huang and H. T. Chang, *Anal. Chem.*, **2006**, *78*, 8332–8338.

[145] P. V. Kamat, *J. Phys. Chem. C*, **2007**, *111*, 2834–2860.

[146] P. V. Kamat, *J. Phys. Chem. C*, **2008**, *112*, 18737–18753.

[147] F. Hetsch, X. Xu, H. Wang, S. V. Kershaw, and A. L. Rogach, *J. Phys. Chem. Lett.*, **2011**, *2*, 1879–1887.

[148] P. V. Kamat, *Acc. Chem. Res.*, **2012**, *45*, 1906–1915.

[149] E. H. Sargent, *Nat. Photonics*, **2012**, *6*, 133–135.

[150] W. U. Huynh, J. J. Dittmer, and A. P. Alivisatos, *Science*, **2002**, *295*, 2425–2427.

[151] S. Dayal, N. Kopidakis, D. C. Olson, D. S. Ginley, and G. Rumbles, *Nano Lett.*, **2010**, *10*, 239–242.

[152] W. W. Yu, L. Qu, W. Guo, and X. Peng, *Chem. Mater.*, **2003**, *15*, 2854–2860.

[153] A. J. Nozik, *Physica E*, **2002**, *14*, 115–120.

[154] J. B. Sambur, T. Novet, and B. A. Parkinson, *Science*, **2010**, *330*, 63–66.

[155] W. Shockley and H. J. Queisser, *J. Appl. Phys.*, **1961**, *32*, 510–519.

[156] V. Gonzalez-Pedro, C. Sima, G. Marzari, P. P. Boix, S. Gimenez, Q. Shen, T. Dittrich, and I. Mora-Sero, *Phys. Chem. Chem. Phys.*, **2013**, *15*, 13835–13843.

[157] O. Voznyy, D. Zhitomirsky, P. Stadler, Z. Ning, S. Hoogland, and E. H. Sargent, *ACS Nano*, **2012**, *6*, 8448–8455.

[158] F. Nunzi, E. Mosconi, L. Storchi, E. Ronca, A. Selloni, M. Grätzel, and F. De Angelis, *Energy Environ. Sci.*, **2013**, *6*, 1221–1229.

[159] H. Choi, M. Kuno, G. V. Hartland, and P. V. Kamat, *J. Mater. Chem. A*, **2013**, *1*, 5847–5491.

[160] M. Planells, L. X. Reynolds, U. Bansode, S. Chhatre, S. Ogale, N Robertson, and S. A. Haque, *Phys. Chem. Chem. Phys.*, **2013**, *15*, 7679–7684.

[161] T. Franzl, T. A. Klar, S. Schietinger, A. L. Rogach, and J. Feldmann, *Nano Lett.*, **2004**, *4*, 1599–1603.

[162] A. Kongkanand, K. Tvrdy, K. Takechi, M. Kuno, and P. V. Kamat, *J. Am. Chem. Soc.*, **2008**, *130*, 4007–4015.

[163] Y. L. Lee and Y. S. Lo, *Adv. Funct. Mater.*, **2009**, *19*, 604–609.

[164] C. Luan, A. Vaneski, A. S. Susha, X. Xu, H. E. Wang, X. Chen, W. Zhang, A. L. Rogach, and J. A. Zapien, *Nanoscale Res. Lett*, **2011**, *6*, 340(1–8).

[165] A. Braga, S. Gimenez, I. Concina, A. Vomiero, and I. Mora-Sero, *J. Phys. Chem. Lett.*, **2011**, *2*, 454–460.

[166] M. Shalom, J. Albero, Z. Tachan, E. Martinez-Ferrero, A. Zaban, and E. Palomares, *J. Phys. Chem. Lett.*, **2010**, *1*, 1134–1138.

[167] Q. Shen, J. Kobayashi, L. J. Diguna, and T. Toyoda, *J. Appl. Phys.*, **2008**, *103*, 084304.

[168] H. H. Lee, M. Wang, P. Chen, D. R. Gamelin, S. M. Zakeeruddin, M. Grätzel, and M. K. Nazeeruddin, *Nano Lett.*, **2009**, *9*, 4221–4227.

[169] V. Gonzalez-Pedro, X. Xu, I. Mora-Sero, and J. Bisquert, *ACS Nano*, **2010**, *4*, 5783–5790.

[170] B. R. Hyun, A. C. Bartnik, L. Sun, T. Hanrath, and F. W. Wise, *Nano Lett.*, **2011**, *11*, 2126–2132.

[171] N. Gaponik and A. L. Rogach, *Phys. Chem. Chem. Phys.*, **2010**, *12*, 8685–8693.

[172] Y. Tachibana, H. Y. Akiyama, Y. Ohtsuka, T. Torimoto, and S. Kuwabata, *Chem. Lett.*, **2007**, *36*, 88–89.

[173] Y. L. Lee and C. H. Chang, *J. Power Sources*, **2008**, *185*, 584–588.

[174] S. A. Sapp, C. M. Elliott, C. Contado, S. Caramori, and C. A. Bignozzi, *J. Am. Chem. Soc.*, **2002**, *124*, 11215–11222.

[175] H. J. Lee, J. H. Yum, H. C. Leventis, S. M. Zakeeruddin, S. A. Haque, P. Chen, S. I. Seok, M. Grätzel, and M. K. Nazeeruddin, *J. Phys. Chem. C*, **2008**, *112*, 11600–11608.

[176] J. H. Bang and P. V. Kamat, *ACS Nano*, **2009**, *3*, 1467–1476.

[177] I. Robel, M. Kuno, and P. V. Kamat, *J. Am. Chem. Soc.*, **2007**, *129*, 4136–4137.

[178] A. Miyawaki, *Dev. Cell*, **2003**, *4*, 295–305.

[179] C. M. Niemeyer, *Angew. Chem. Int. Ed.*, **2001**, *40*, 4128–4158.

[180] C. J. Murphy, *Anal. Chem.*, **2002**, *74*, 520–526.

[181] W. J. Parak, D. Gerion, T. Pellegrino, D. Zanchet, C. Micheel, S. C. Williams, R. Boudreau, M. A. Le Gros, C. A. Larabell, and A. P. Alivisatos, *Nanotechnology*, **2003**, *14*, 15–27.

[182] A. P. Alivisatos, *Nat. Biotechnol.*, **2004**, *22*, 47–52.

[183] H. Mattoussi, J. M. Mauro, E. R. Goldman, G. P. Anderson, V. C. Sundar, F. V. Mikulec, and M. G. Bawendi, *J. Am. Chem. Soc.*, **2000**, *122*, 12142–12150.

[184] D. Gerion, F. Pinaud, S. C. Williams, W. J. Parak, D. Zanchet, S. Weiss, and A. P. Alivisatos, *J. Phys. Chem. B*, **2001**, *105*, 8861–8871.

[185] G. P. Mitchell, C. A. Mirkin, and R. L. Letsinger, *J. Am. Chem. Soc.*, **1999**, *121*, 8122–8123.

[186] E. R. Goldman, E. D. Balighian, H. Mattoussi, M. K. Kuno, J. M. Mauro, P. T. Tran, and G. P Anderson, *J. Am. Chem. Soc.*, **2002**, *124*, 6378–6382.

[187] H. T. Uyeda, I. L. Medintz, J. K. Jaiswal, S. M. Simon, and H. Mattoussi, *J. Am. Chem. Soc.*, **2005**, *127*, 3870–3878.

[188] M. Bruchez, M. Moronne, P. Gin, S. Weiss, and A. P. Alivisatos, *Science*, **1998**, *281*, 2013.

[189] B. Dubetret, P. Skourides, D. J. Norris, V. Noireaux, A. H. Brivanlou, and A. Libchaber, *Science*, **2002**, *298*, 1759–1762.

[190] T. Pellegrino, L. Manna, S. Kudera, T. Liedl, D. Koktysh, A. L. Rogach, S. Keller, J. Rädler, G. Natile, and W. J. Parak, *Nano Lett.*, **2004**, *4*, 703–707.

[191] X. Gao, Y. Cui, R. M. Levenson, L. W. K. Chung, and S. Nie, *Nat. Biotechnol.*, **2004**, *22*, 4103–4104.

[192] N. Hildebrandt, *ACS Nano*, **2011**, *5*, 5286–5290.

[193] F. Chen and D Gerion, *Nano Lett.*, **2004**, *4*, 1827–1832.

[194] A. M. Derfus, W. C. W. Chan, and S. N. Bhatia, *Adv. Mater.*, **2004**, *16*, 961–966.

[195] E. B. Voura, J. K. Jaiswal, H. Mattoussi, and S. M. Simon, *Nat. Med.*, **2004**, *10*, 993–998.

[196] M. Dahan, S. Lévi, C. Luccardini, P. Rostaing, B. Riveau, and A. Triller, *Science*, **2003**, *302*, 442–445.

[197] D. S. Lidke, P. Nagy, R. Heintzmann, D. J Arndt-Jovin, J. N. post, H. E. Grecco, E. A. Jares-Erijman, and T. M. Jovin, *Nat. Biotechnol.*, **2004**, *22*, 198–203.

[198] A. M. Derfus, W. C. W. Chan, and S. N Bhatia, *Nano Lett.*, **2004**, *4*, 11–18.

[199] N. Lewinski, V. Colvin, and R. Drezek, *Small*, **2008**, *4*, 26–49.

[200] S. Pathak, S. K. Choi, N. Arnheim, and M. E. Thompson, *J. Am. Chem. Soc.*, **2001**, *123*, 4103–4104.

[201] Y. Xiao and P. E. Barker, *Nucl. Acids Res.*, **2004**, *32*, E28(1–5).

[202] D. Gerion, F. Chen, B. Kannan, A. Fu, W. J. Parak, D. J. Chen, A. Majumdar, and A. P. Alivisatos, *Anal. Chem.*, **2003**, *75*, 4766–4772.

[203] E. R. Goldman, A. R. Clapp, G. P. Anderson, H. T. Uyeda, J. M. Mauro, I. L. Medintz, and H. Mattoussi, *Anal. Chem.*, **2004**, *76*, 684–688.

[204] A. L. Efros and M Rosen, *Annu. Rev. Mater. Sci.*, **2000**, *30*, 475–521.

[205] D. J. Norris and M. G. Bawendi, *Phys. Rev. B*, **1996**, *53*, 16338–16346.

[206] D. J. Norris, A. L. Efros, M. Rosen, and M. G. Bawendi, *Phys. Rev. B*, **1996**, *53*, 16347–16354.

[207] L. W. Wang and A. Zunger, *J. Phys. Chem. B*, **1998**, *102*, 6449–6454.

[208] A. Franceschetti and A. Zunger, *Phys. Rev. Lett.*, **1997**, *78*, 915–918.

[209] L. W. Wang, M. Califano, A. Zunger, and A. Franceschetti, *Phys. Rev. Lett.*, **2003**, *91*, 056404(1–4).

[210] A. Franceschetti, J. M. An, and A. Zunger, *Nano Lett.*, **2006**, *6*, 2191–2195.

[211] J. M. An, M. Califano, A. Franceschetti, and A. Zunger, *J. Chem. Phys.*, **2008**, *128*, 164720(1–7).

[212] M. Born and J. R. Oppenheimer, *Ann. Physik*, **1927**, *44*, 455.

[213] D. R. Hartre, *Proc. Cambridge Philos. Soc.*, **1928**, *24*, 89–110.

[214] J. C. Slater, *Phys. Rev.*, **1929**, *34*, 1293–1322.

[215] A. Szabo and N. S. Ostlund, *Modern Quantum Chemistry;* McGraw-Hill, 1992.

[216] C. C. J. Roothaan, *Rev. Mod. Phys.*, **1951**, *23*, 69–89.

[217] G. G. Hall, *Proc. R. Soc. A*, **1951**, *205*, 541–552.

[218] B. O. Roos and P. R. Taylor, *Chem. Phys.*, **1980**, *48*, 157–173.

[219] K. Andersson, P. A. Malmqvist, B. O. Roos, A. J. Sadlej, and K. Wolinski, *J. Phys. Chem.*, **1990**, pages 5483–5488.

[220] K. Andersson, P. A. Malmqvist, and B. O. Roos, *J. Chem. Phys.*, **1992**, *96*, 1218–1226.

[221] J. Olsen, B. O. Roos, P. Jørgensen, and H. J. A. Jensen, *J. Chem. Phys.*, **1988**, *89*, 2185–2192.

[222] K. Raghavachari and G. W. Trucks, *Chem. Phys. Lett.*, **1989**, *157*, 479–483.

[223] C. Hattig and F. Weigend, *J. Chem. Phys.*, **2000**, *113*, 5154–5161.

[224] E. Fermi, *Z. Phys.*, **1926**, *36*, 902–912.

[225] P. A. M. Dirac, *Proc. R. Soc. A*, **1926**, *112*, 661–677.

[226] J. C. Slater, *Quantum Theory of Molecules and Solids. Vol. 4. The Self-Consistent Field for Molecules and Solids;* McGraw-Hill, 1974.

[227] K. Schwarz, *Phys. Rev. B*, **1972**, *5*, 2466–2468.

[228] P. Hohenberg and W. Kohn, *Phys. Rev.*, **1964**, *136*, B864.

[229] W. Kohn and L. J. Sham, *Phys. Rev.*, **1965**, *140*, A1133.

[230] O. Gunnarsson, B. I. Lundqvist, and J. W. Wilkens, *Phys. Rev. Lett.*, **1974**, *10*, 1319–1327.

[231] R. Stowasser and R. Hoffmann, *J. Am. Chem. Soc.*, **1999**, *121*, 3414.

[232] T. Kar, J. G: Angyan, and A. B. Shannigrahi, *J. Phys. Chem. A*, **2000**, *104*, 9953.

[233] S. H. Vosko, L. Wilk, and M. Nusair, *Can. J. Phys.*, **1980**, *58*, 1200.

[234] J. P. Perdew and Y. Wang, *Phys. Rev. B*, **1992**, *45*, 13244–13249.

[235] A. D. Becke, *Phys. Rev. A*, **1988**, *38*, 3098–3100.

[236] A. D. Becke, *J. Chem. Phys.*, **1986**, *84*, 4524–4529.

[237] J. P. Perdew, *Phys. Rev. B*, **1986**, *33*, 8822–8824.

[238] J. P. Perdew, K. Burke, and M. Ernzerhof, *Phys. Rev. Lett.*, **1996**, *77*, 3865–3868.

[239] C. T. Lee, W. T. Yang, and R. G. Parr, *Phys. Rev. B*, **1988**, *37*, 785–789.

[240] R. Colle and O. Salvetti, *Theor. Chim. Acta*, **1975**, *37*, 329–334.

[241] A. D. Becke, *J. Chem. Phys.*, **1993**, *98*, 5648–5652.

[242] A. D. Becke, *J. Chem. Phys.*, **1988**, *88*, 1053–1062.

[243] E. K. U. Gross and W. Kohn, *Ad. Quant. Chem.*, **1990**, *21*, 255.

[244] M. E. Casida, *Recent Advances in Density Functional Methods;* World Scientific, 1995.

[245] M. E. Casida, *Recent Developments and Applications of Modern Density Functional Theory, Theoretical and Computational Chemistry;* Elsevier, 1996.

[246] E. Runge and E. K. U. Gross, *Phys. Rev. Lett.*, **1984**, *52*, 997.

[247] G. Vignale, P. Skudlarski, and M. Rasolt, *Phys. Rev. B*, **1992**, *45*, 8494–8497.

[248] S. J. A. van Gisbergen, J. A. Groeneveld, A. Rosa, J. G. Snijders, and E. J. Baerends, *J. Phys. Chem. A*, **1999**, *103*, 6835–6844.

[249] A. Rosa, E. J. Baerends, S. J. A. Gisbergen, E. van Lenthe, J. A. Groeneveldt, and J. G. Snijders, *J. Am. Chem. Soc.*, **1999**, *121*, 10356–10365.

[250] P. Boulet, H. Chermette, C. Daul, F. Gilardoni, F. Rogemond, J. Weber, and G. Zuber, *J. Phys. Chem. A*, **2001**, *105*, 885–894.

[251] S. Hirata and M. Head-Gordon, *Chem. Phys. Lett.*, **1999**, *302*, 375–382.

[252] S. Hirata, T. J. Lee, and M. Head-Gordon, *J. Chem. Phys.*, **1999**, *111*, 8940–8912.

[253] N. N. Matsuzawa, A. Ishitani, D. A. Dixon, and T. Uda, *J. Phys. Chem. A*, **2001**, *105*, 4953–4962.

[254] Z. L. Cai and J. R. Reimers, *J. Chem. Phys.*, **2000**, *112*, 527–530.

[255] R. Bauernschmitt, R. Alhrichs, F. Henrich, and M. M. Kappes, *J. Am. Chem. Soc.*, **1998**, *120*, 5052–5059.

[256] S. Hirata, M. Head-Gordon, and R. J. Bartlett, *J. Chem. Phys.*, **1999**, *111*, 10774–10786.

[257] D. J. Tozer N. C. Handy, *Phys. Chem. Chem. Phys.*, **2000**, *2*, 2117–2121.

[258] J. C. Shieh, J. L. Chang, J. C. Wu, R. Li, A. M. Mebel, N. C. Handy, and Y. T. Chen, *J. Chem. Phys.*, **2000**, *112*, 7384–7393.

[259] A. Dreuw, J. L Weisman, and M. Head-Gordon, *J. Chem. Phys.*, **2003**, *119*, 2943–2946.

[260] P. R. T. Schipper, O. V. Gritsenko, S. J. A. van Gisbergen, and E. J. Baerends, *J. Chem. Phys.*, **2000**, *112*, 1344–1352.

[261] M. Grüning, O. V. Gritsenko, S. J. A. van Gisbergen, and E. J. Baerends, *J. Chem. Phys.*, **2001**, *114*, 652–660.

[262] R. Car and M. Parrinello, *Phys. Rev. Lett.*, **1985**, *55*, 2471–2474.

[263] D. R. Hamann, M. Schliüter, and C. Chiang, *Phys. Rev. Lett.*, **1979**, *43*, 1494.

[264] D. Vanderbilt, *Phys. Rev. B*, **1990**, *41*, 7892.

[265] G. Kresse and J. Hafner, *J. Phys.: Condens. Matter*, **1994**, *6*, 8245.

[266] E. J. Baerends, D. E. Ellis, and P. Ros, *Chem. Phys.*, **1973**, *2*, 41–51.

[267] G. te Velde, F. M. Bickelhaupt, E. J. Baerends, C. Fonseca Guerra, S. J. A. van Gisbergen, J. G. Snijders, and T. Ziegler, *J. Comput. Chem.*, **2001**, *22*, 931–967.

[268] H. M. Senn and W. Thiel, *Angew. Chem. Int. Ed.*, **2009**, *48*, 1198–1229.

[269] T.K. Woo, L. Cavallo, and T. Ziegler, *Theor. Chem. Acc.*, **1998**, *100*, 307–313.

[270] W. D. Cornell, P. Cieplak, C. I. Bayly, I. R. Gould, K. M. Merz, D. M. Ferguson, D. C. Spellmeyer, T. Fox, J. W. Caldwell, and P. A. Kollman, *J. Am. Chem. Soc.*, **1995**, *117*, 5179–5197.

[271] R. M. Badger, *J. Chem. Phys.*, **1934**, *2*, 128–131.

[272] C. J. Murphy and J. L. Coffer, *Appl. Spectrosc.*, **2002**, *56*, 16–27.

[273] S. E. Lohse and C. J. Murphy, *J. Am. Chem. Soc.*, **2012**, *124*, 15607–15620.

[274] A. Z. Abbasi, F. Amin, T. Niebling, S. Friede, M. Ochs, S. Carregal-Romero, J. M. Montenegro, P. Rivera Gil, W. Heimbrodt, and W. J. Parak, *ACS Nano*, **2011**, *5*, 21–25.

[275] T. Nann and W. M. Skinner, *ACS Nano*, **2011**, *5*, 5291–5295.

[276] F. Malet and P. Gori-Giorgi, *Phys. Rev. Lett.*, **2012**, *109*, 246402(1–5).

[277] C. Yannouleas and U. Landman, *Rep. Prog. Phys.*, **2007**, *70*, 2067–2148.

[278] F. Malet, A. Mirtschink, J. C. Cremon, S. M. Reimann, and P Gori-Giorgi, *Phys. Rev. B*, **2013**, *87*, 115146(1–10).

[279] P. Yang, S. Tretiak, A. E. Masunov, and S. Ivanov, *J. Chem. Phys.*, **2008**, *129*, 74709(1–12).

[280] V. V. Albert, S. A. Ivanov, S. Tretiak, and S. V. Kilina, *J. Phys. Chem. C*, **2011**, *115*, 15793–15800.

[281] S. Wu, H. Liu, H. Liu, Z. Wu, Z. Du, and Z. A. Schelly, *Nanotechnology*, **2007**, *18*, 485607(1–6).

[282] J. A. Pople, M. Headgordon, and K. Raghavachari, *J. Chem. Phys.*, **1987**, *87*, 5968–5975.

[283] D. E. Bernholdt and R. J. Harrison, *J. Chem. Phys.*, **1998**, *109*, 1593–1600.

[284] K. Eichkorn, O. Treutler, H. Ohm, M. Haser, and R. Ahlrichs, *Chem. Phys. Lett.*, **1995**, *240*, 283–289.

[285] E. A. Amin and D. G. Truhlar, *J. Chem. Theory Comput.*, **2008**, *4*, 75–85.

[286] J. O. Joswig, M. Springborg, and G. Seifert, *J. Phys. Chem. B*, **2000**, *104*, 2617–2622.

[287] P. Sarkar and M. Springborg, *Phys. Rev. B*, **2003**, *68*, 235409(1–7).

[288] A. Puzder, A. J. Williamson, F. Gygi, and G. Galli, *Phys. Rev. Lett.*, **2004**, *92*, 217401(1–4).

[289] M. Lopez del Puerto, M. L. Tiago, and J. R. Chelikowsky, *Phys. Rev. Lett.*, **2006**, *97*, 096401(1–4).

[290] M. Yu, G. W. Fernando, R. Li, F Papadimitrakopoulos, N. Shi, and R. Ramprasad, *Appl. Phys. Lett.*, **2006**, *88*, 231910(1–3).

[291] J. Schrier, D. O. Demchenko, L. W. Wang, and A. P. Alivisatos, *Nano Lett.*, **2007**, *7*, 2377–2382.

[292] S. P. Nanavati, V. Sundararajan, S. Mahamuni, V. Kumar, and S. V. Ghaisas, *Phys. Rev. B*, **2009**, *80*, 245417(1–9).

[293] S. Kilina, S. Ivanov, and S. Tretiak, *J. Am. Chem. Soc.*, **2009**, *131*, 7717–7726.

[294] S. K. Bhattacharya and A. Kshirsagara, *Eur. Phys. J. D*, **2008**, *48*, 355–364.

[295] X. Zhang, M. Zhao, S. Yan, T. He, W. Li, X. Lin, Z. Xi, Z. Wang, X. Liu, and Y. Xia, *Nanotechnology*, **2008**, *19*, 305708(1–6).

[296] X. Zhang, M. Zhao, T. He, W. Li, X. Lin, Z. Wang, Z. Xi, X. Liu, and Y. Xia, *Solid State Commun.*, **2008**, *147*, 165–168.

[297] H. Chen, D. Shi, J. Qi, J. Jia, and B. Wang, *Phys. Lett. A*, **2009**, *373*, 371–375.

[298] C. Liu, S. Y. Chung, S. Lee, S. Weiss, and D. Neuhauser, *J. Chem. Phys.*, **2009**, *131*, 174705(1–8).

[299] J. G. Vilhena, S. Botti, and M. A. L. Marques, *Appl. Phys. Lett.*, **2010**, *96*, 123106(1–3).

[300] J. M. Azpiroz, E. Mosconi, and F. De Angelis, *J. Phys. Chem. C*, **2011**, *115*, 25219–25226.

[301] O. Voznyy, *J. Phys. Chem. C*, **2011**, *115*, 15927–15932.

[302] M. A. Zwijnenburg, C. Sousa, F. Illas, and S. T. Bromley, *J. Chem. Phys.*, **2011**, *134*, 064511(1–8).

[303] J. M. Azpiroz, I. Infante, X. Lopez, J. M. Ugalde, and F. De Angelis, *J. Mater. Chem.*, **2012**, *22*, 21453–21465.

[304] J. M. Azpiroz, X. Lopez, J. M. Ugalde, and I. Infante, *J. Phys. Chem. C*, **2012**, *116*, 2740–2750.

[305] J. R. I. Lee, H. D. Whitley, R. W. Meulenberg, A. Wolcott, J. Z. Zhang, D. Prendergast, D. D. Lovingood, G. F. Strouse, T. Ogitsu, E. Schwegler, L. J. Terminello, and T. van Buuren, *Nano Lett.*, **2012**, *12*, 2763–2767.

[306] J. M. Azpiroz, J. M. Matxain, I. Infante, X. Lopez, and J. M. Ugalde, *Phys. Chem. Chem. Phys.*, **2013**, *15*, 10996–11005.

[307] E. Spano, S. Hamad, and C. R. A. Catlow, *J. Phys. Chem. B*, **2003**, *107*, 10337–10340.

[308] S. Hamad, C. R. A. Catlow, E. Spano, J. M. Matxain, and J. M. Ugalde, *J. Phys. Chem. B*, **2005**, *109*, 2703–2709.

[309] S. Hamad and C. R. A. Catlow, *J. Cryst. Growth*, **2006**, *294*, 2–8.

[310] D. S. Kilin, K. Tsemekhman, O. V. Prezhdo, E. I. Zenkevich, and C. von Borczyskowski, *J. Photochem. Photobiol. A*, **2007**, *190*, 342–351.

[311] W. Sangthong, J. Limtrakul, F. Illas, and S. T. Bromley, *Nanoscale*, **2010**, *2*, 72–77.

[312] X. Zhang, H. Zhang, T. He, and M. Zhao, *J. Appl. Phys.*, **2010**, *108*, 064317(1–6).

[313] M. Del Ben, R. W. A. Havenith, R. Broer, and M. Stener, *J. Phys. Chem. C*, **2011**, *115*, 16782–16796.

[314] N. Krainara, J. Limtrakul, F. Illas, and S. T. Bromley, *Phys. Rev. B*, **2011**, *83*, 233305.

[315] T. Huang, K. Tan, and M. Lin, *J. Mol. Struct.*, **2007**, *821*, 101–105.

[316] Y. Gu, K. Tan, and M. Lin, *J. Mol. Struct.*, **2010**, *961*, 62–65.

[317] D. Zhang, L. Chen, J. Zhang, and X. Miao, *J. Am. Ceram. Soc.*, **2011**, *94*, 759–764.

[318] P. Deglmann, R. Ahlrichs, and K. Tsereteli, *J. Chem. Phys.*, **2002**, *116*, 1585–1597.

[319] G. Malloci, L. Chiodo, A. Rubio, and A. Mattoni, *J. Phys. Chem. C*, **2012**, *116*, 8741–8746.

[320] J. M. Matxain, J. E. Fowler, and J. M. Ugalde, *Phys. Rev. A*, **2000**, *61*, 053201(1–8).

[321] J. M. Matxain, J. M. Mercero, J. E. Fowler, and J. M. Ugalde, *Phys. Rev. A*, **2001**, *64*, 054201(1–8).

[322] S. Y. Chung, S. Lee, C. Liu, and D. Neuhauser, *J. Phys. Chem. B*, **2009**, *113*, 292–301.

[323] T. M. Inerbaev, A. E. Masunov, S. I. Khondaker, A. Dobrinescu, A. V. Plamada, and Y. Kawazoe, *J. Chem. Phys.*, **2009**, *131*, 044106(1–6).

[324] H. S. Kim, S. W. Jang, S. Y. Chung, S. Lee, Y. Lee, B. Kim, C. Liu, and D. Neuhauser, *J. Phys. Chem. B*, **2010**, *114*, 471–479.

[325] K. A. Nguyen, P. N. Day, and R. Pachter, *J. Phys. Chem. C*, **2010**, *114*, 16197–16209.

[326] C. Wang, S. Xu, L. Ye, W. Lei, and Y. Cui, *Struct. Chem.*, **2010**, *21*, 1215–1219.

[327] S. Xu, C. Wang, and Y. Cui, *J. Mol. Model.*, **2010**, *16*, 469–473.

[328] S. Xu, C. Wang, and Y. Cui, *Struct. Chem.*, **2010**, *21*, 519–525.

[329] A. Y. Koposov, T. Cardolaccia, V. Albert, E. Badaeva, S. Kilina, T. J. Meyer, S. Tretiak, and M. Sykora, *Langmuir*, **2011**, *27*, 8377–8383.

[330] A. Mohajeri and M. Alipour, *Int. J. Quant. Chem.*, **2011**, *111*, 3888–3896.

[331] S. Xu, C. Wang, and Y. Cui, *Int. J. Quant. Chem.*, **2011**, *111*, 156–164.

[332] P. Yang, S. Tretiak, and S. Ivanov, *J. Cluster Sci.*, **2011**, *22*, 405–431.

[333] M. A. Zwijnenburg, *Nanoscale*, **2011**, *3*, 3780–3787.

[334] M. A. Zwijnenburg, F. Illas, and S. T. Bromley, *Phys. Chem. Chem. Phys.*, **2011**, *13*, 9311–9317.

[335] S. A. Fischer, A. M. Crotty, S. V. Kilina, S. A. Ivanov, and S. Tretiak, *Nanoscale*, **2012**, *4*, 904–914.

[336] A. E. Kuznetsov, D. Balamurugan, S. S. Skourtis, and D. N. Beratan, *J. Phys. Chem. C*, **2012**, *116*, 6817–6830.

[337] E. Lim, A. E. Kuznetsov, and D. N. Beratan, *Chem. Phys.*, **2012**, *407*, 97–109.

[338] M. A. Zwijnenburg, *Nanoscale*, **2012**, *4*, 3711–3717.

[339] J. M. Matxain, A. Irigoras, J. E. Fowler, and J. M. Ugalde, *Phys. Rev. A*, **2001**, *64*, 013201(1–7).

[340] J. M. Matxain, L. A. Eriksson, J. M. Mercero, J. M. Ugalde, E. Spano, S. Hamad, and C. R. A. Catlow, *Nanotechnology*, **2006**, *17*, 4100–4105.

[341] P. J. Hay and W. R. Wadt, *J. Chem. Phys.*, **1985**, *82*, 270–283.

[342] P. J. Hay and W. R. Wadt, *J. Chem. Phys.*, **1985**, *82*, 299–310.

[343] W. R. Wadt and P. J. Hay, *J. Chem. Phys.*, **1985**, *82*, 284–298.

[344] J. S. Binkley, J. A. Pople, and W. J. Hehre, *J. Am. Chem. Soc.*, **1980**, *102*, 939–947.

[345] W. J. Stevens, M. Krauss, H. Basch, and P. G. Jasien, *Can. J. Chem.*, **1992**, *70*, 612–630.

[346] T. R. Cundari and W. J. Stevens, *J. Chem. Phys.*, **1993**, *98*, 5555–5565.

[347] J. P. Perdew, J. A. Chevary, S. H. Vosko, K. A. Jackson, M. R. Pederson, D. J. Singh, and C. Fiolhais, *Phys. Rev. B*, **1992**, *46*, 6671–6687.

[348] D. Andrae, U. Haussermann, M. Dolg, H. Stoll, and H. Preuss, *Theor. Chim. Acta*, **1990**, *77*, 123–141.

[349] F. Weigend and R. Ahlrichs, *Phys. Chem. Chem. Phys.*, **2005**, *7*, 3297–3305.

[350] P. M. W. Gill, *Mol. Phys.*, **1996**, *89*, 433–445.

[351] C. Adamo and V. Barone, *J. Comput. Chem.*, **1998**, *19*, 418–429.

[352] C. Adamo and V. Barone, *J. Chem. Phys.*, **1998**, *108*, 664–675.

[353] E. van Lenthe and E. J. Baerends, *J. Comput. Chem.*, **2003**, *24*, 1142–1156.

[354] N. C. Handy and A. J. Cohen, *Mol. Phys.*, **2001**, *99*, 403–412.

[355] W. M. Hoe, A. J. Cohen, and N. C. Handy, *Chem. Phys. Lett.*, **2001**, *341*, 319–328.

[356] C. Adamo and V. Barone, *Chem. Phys. Lett.*, **1997**, *274*, 242–250.

[357] P. J. Wilson, T. J. Bradley, and D. J. Tozer, *J. Chem. Phys.*, **2001**, *115*, 9233–9242.

[358] A. J. Cohen and N. C. Handy, *Mol. Phys.*, **2001**, *99*, 607–615.

[359] C. Adamo and V. Barone, *J. Chem. Phys.*, **1999**, *110*, 6158–6170.

[360] X. Xu and W. A. Goddard, *Proc. Natl. Acad. Sci. U. S. A.*, **2004**, *101*, 2673–2677.

[361] S. Grimme, *J. Comput. Chem.*, **2006**, *27*, 1787–1799.

[362] F. A. Hamprecht, A. J. Cohen, D. J. Tozer, and N. C. Handy, *J. Chem. Phys.*, **1998**, *109*, 6264–6271.

[363] A. D. Boese, N. L. Doltsinis, N. C. Handy, and M. Sprik, *J. Chem. Phys.*, **2000**, *112*, 1670–1678.

[364] A. D. Boese and N. C. Handy, *J. Chem. Phys.*, **2001**, *114*, 5497–5503.

[365] Y. Zhao and D. G. Truhlar, *J. Chem. Phys.*, **2006**, *125*, 194101(1–18).

[366] Y. Zhao, N. E. Schultz, and D. G. Truhlar, *J. Chem. Phys.*, **2005**, *123*, 161103(1–4).

[367] Y. Zhao, N. E. Schultz, and D. G. Truhlar, *J. Chem. Theory Comput.*, **2006**, *2*, 364–382.

[368] Y. Zhao and D. G. Truhlar, *Theor. Chem. Acc.*, **2008**, *120*, 215–241.

[369] Y. Zhao and D. G. Truhlar, *J. Phys. Chem. A*, **2006**, *110*, 5121–5129.

[370] Y. Zhao and D. G. Truhlar, *J. Phys. Chem. A*, **2006**, *110*, 13126–13130.

[371] J. M. Tao, J. P. Perdew, V. N. Staroverov, and G. E. Scuseria, *Phys. Rev. Lett.*, **2003**, *91*, 146401(1–4).

[372] T. Yanai, D. P. Tew, and N. C. Handy, *Chem. Phys. Lett.*, **2004**, *393*, 51–57.

[373] O. A. Vydrov and G. E. Scuseria, *J. Chem. Phys.*, **2006**, *125*, 234109(1–9).

[374] O. A. Vydrov, G. E. Scuseria, and J. P. Perdew, *J. Chem. Phys.*, **2007**, *126*, 154109(1–9).

[375] J. D. Chai and M. Head-Gordon, *Phys. Chem. Chem. Phys.*, **2008**, *10*, 6615–6620.

[376] A. J. Hoffman, G. Mills, H. Yee, and M. R. Hoffmann, *J. Phys. Chem.*, **1992**, *96*, 5546–5552.

[377] S. Kuwabata, K. Nishida, R. Tsuda, H. Inoue, and H. Yoneyama, *J. Electrochem. Soc.*, **1994**, *141*, 1498.

[378] T. L. Chu and S. S. Chu, *Solid State Electron.*, **1995**, *38*, 533–549.

[379] P. R. Edwards, S. A. Gallogay, and K. Durose, *Thin Solid Films*, **2000**, *361*, 364–370.

[380] R. Chakrabarti, J. Dutta, S. Bandyopadhyay, D. Bhattacharyya, S. Chaudhuri, and A. K. Pal, *Sol. En. Mat. Sol. Cells*, **2000**, *61*, 113–126.

[381] G. Contreras, O. Vigil, M. Ortega, A. Morales, J. Vidal, and M. L. Albor, *Thin Solid Films*, **2000**, *361-362*, 378.

[382] E. Corcoran, *Sci. Am.*, **1990**, *263*, 74.

[383] P. J. Sebastian and M. Ocampo, *Sol. Energy Mater. Sol. Cells*, **1996**, *44*, 1–10.

[384] X. Fang, Y. Bando, U. K. Gautam, T. Zhai, H. Zeng, X. Xu, M. Liao, and D. Golberg, *Crit. Rev. Solid State Mater. Sci.*, **2009**, *34*, 190–223.

[385] Z. W. Wang, L. L. Daemen, Y. S. Zhao, C. S. Zha, R. T. Downs, X. D. Wang, Z. L. Wang, and R. J. Hemley, *Nat. Mater.*, **2005**, *4*, 922–927.

[386] K. Murakoshi, H. Hosokawa, and S. Yanagida, *Jpn. J. Appl. Phys.*, **1999**, *38*, 522–527.

[387] Y. W. Zhao, Y. Zhang, H. Zhu, G. C. Hadjipianayis, and J. Q. Xiao, *J. Am. Chem. Soc.*, **2004**, *126*, 6874–6875.

[388] F. Huang and J. F. Banfield, *J. Am. Chem. Soc.*, **2005**, *127*, 4523–4529.

[389] W. Liu, *Mater. Lett.*, **2006**, *60*, 551–554.

[390] H. Tong, Y. J. Zhu, L. X. Yang, L. Li, L. Zhang, J. Chang, L. Q. An, and S. W. Wang, *J. Phys. Chem. C*, **2007**, *111*, 3893–3900.

[391] J. Q. Sun, X. P. Shen, K. M. Chen, Q. Liu, and W. Liu, *Solid State Commun.*, **2008**, *147*, 501–504.

[392] S. B. Qadri, E. F. Skelton, A. D. Dinsmore, J. Z. Hu, W. J. Kim, C. Nelson, and B. R. Ratna, *J. Appl. Phys.*, **2001**, *89*, 115–119.

[393] S. Monticone, R. Tufeu, and A. V. Kanaev, *J. Phys. Chem. B*, **1998**, *102*, 2854–2862.

[394] A. van Dijken, E. A. Meulenkamp, D. Vanmaekelbergh, and A. Meijerink, *J. Phys. Chem. B*, **2000**, *104*, 1715–1723.

[395] M. L. Kahn, T. Cardinal, B. Bousquet, M. Monge, V. Jubera, and B. Chaudret, *Chem. Phys. Chem.*, **2006**, *7*, 2392–2397.

[396] A. B. Djurisic and Y. H. Leung, *Small*, **2006**, *2*, 944–961.

[397] A. H. Souici, N. Keghouche, J. A. Delaire, H. Remita, and M. Mostafavi, *Chem. Phys. Lett.*, **2006**, *422*, 25–29.

[398] S. Biswas and S. Kar, *Nanotechnology*, **2008**, *19*, 045710(1–11).

[399] S. Kar and S. Chaudhuri, *Chem. Phys. Lett.*, **2005**, *414*, 40–46.

[400] S. Kar and S. Chaudhuri, *J. Phys. Chem. B*, **2005**, *109*, 3298–3302.

[401] S. Kar, S. Biswas, and S. Chaudhuri, *Nanotechnology*, **2005**, *16*, 737–740.

[402] H. Tang, G. Y. Xu, L. Q. Weng, L. J. Pan, and L. Wang, *Acta Mater.*, **2004**, *52*, 1489–1494.

[403] A. F. Kohan, G. Ceder, D. Morgan, and C. G. Van de Walle, *Phys. Rev. B*, **2000**, *61*, 15019–15027.

[404] J. Muscat, A. Wander, and N. M. Harrison, *Chem. Phys. Lett.*, **2001**, *342*, 397–401.

[405] B. Meyer, D. Marx, O. Dulub, U. Diebold, M. Kunat, D. Langenberg, and C. Woell, *Angew. Chem. Int. Ed.*, **2004**, *43*, 6641–6645.

[406] B. Meyer, *Phys. Rev. B*, **2004**, *69*, 045416(1–10).

[407] S. Lany and A. Zunger, *Phys. Rev. B*, **2005**, *72*, 035215(1–13).

[408] C. H. Patterson, *Phys. Rev. B*, **2006**, *74*, 144432(1–13).

[409] A. Janotti and C. G. Van de Walle, *Phys. Rev. B*, **2007**, *76*, 165202(1–22).

[410] J. M. Matxain, J. M. Mercero, J. E. Fowler, and J. M. Ugalde, *J. Am. Chem. Soc.*, **2003**, *125*, 9494–9499.

[411] C. Li, W. Guo, Y. Kong, and H. Gao, *Appl. Phys. Lett.*, **2007**, *90*, 205604(1–6).

[412] X. Shen, P. B. Allen, J. T. Muckerman, J. W. Davenport, and J. C. Zheng, *Nano Lett.*, **2007**, *7*, 2267–2271.

[413] B. Wang, S. Nagase, J. Zhao, and G. Wang, *J. Phys. Chem. C*, **2007**, *111*, 4956–4963.

[414] E. Spano, S. Hamad, and C. R. A. Catlow, *Chem. Commun.*, **2004**, *XX*, 864–865.

[415] S. Pal, B. Goswami, and P. Sarkar, *J. Chem. Phys.*, **2005**, *123*, 044311(1–9).

[416] F. De Angelis and L. Armelao, *Phys. Chem. Chem. Phys.*, **2011**, *13*, 467–475.

[417] S. Hamad, S. Cristol, and C. R. A. Callow, *J. Phys. Chem. B*, **2002**, *106*, 11002–11008.

[418] A. Wander and N. M. Harrison, *J. Chem. Phys.*, **2001**, *115*, 2312–2316.

[419] P. Giannozzi, S. Baroni, N. Bonini, M. Calandra, R. Car, C. Cavazzoni, D. Ceresoli, G. L. Chiarotti, M. Cococcioni, I. Dabo, A. Dal Corso, S. de Gironcoli, S. Fabris, G. Fratesi, R. Gebauer, U. Gerstmann, C. Gougoussis, A. Kokalj, M. Lazzeri, L. Martin-Samos, N. Marzari, F. Mauri, R. Mazzarello, S. Paolini, A. Pasquarello, L. Paulatto, C. Sbraccia, S. Scandolo, G. Sclauzero, A. P. Seitsonen, A. Smogunov, P. Umari, and R. M. Wentzcovitch, *J. Phys. Condens. Matter*, **2009**, *21*, 395502(1–19).

[420] P. Giannozzi, F. De Angelis, and R. Car, *J. Chem. Phys.*, **2004**, *120*, 5903–5915.

[421] A. Pasquarello, K. Laasonen, R. Car, C. Y. Lee, and D. Vanderbilt, *Phys. Rev. Lett.*, **1992**, *69*, 1982–1985.

[422] M. J. Frisch, G. W. Trucks, H. B. Schlegel, G. E. Scuseria, M. A. Robb, J. R. Cheeseman, G. Scalmani, V. Barone, B. Mennucci, G. A. Petersson, H. Nakatsuji, M. Caricato, X. Li, H. P. Hratchian, A. F. Izmaylov, J. Bloino, G. Zheng, J. L. Sonnenberg, M. Hada, M. Ehara, K. Toyota, R. Fukuda, J. Hasegawa, M. Ishida, T. Nakajima, Y. Honda, O. Kitao, H. Nakai, T. Vreven, J. A. Montgomery Jr., J. E. Peralta, F. Ogliaro, M. Bearpark, J. J. Heyd, E. Brothers, K. N. Kudin, V. N. Staroverov, R. Kobayashi, J. Normand, K. Raghavachari, A. Rendell, J. C. Burant, S. S. Iyengar, J. Tomasi, M. Cossi, N. Rega, J. M. Millam, M. Klene, J. E. Knox, J. B. Cross, V. Bakken, C. Adamo, J. Jaramillo, R. Gomperts, R. E. Stratmann, O. Yazyev, A. J. Austin, R. Cammi, C. Pomelli, J. W. Ochterski, R. L. Martin, K. Morokuma, V. G. Zakrzewski, G. A. Voth, P. Salvador, J. J. Dannenberg, S. Dapprich, A. D. Daniels, Ö. Farkas, J. B. Foresman, J. V. Ortiz, J. Cioslowski, and D. J. Fox; Gaussian 09 revision b.01; Gaussian Inc. Wallingford CT 2009.

[423] K. Leung, S. Pokrant, and K. B. Whaley, *Phys. Rev. B*, **1998**, *57*, 12291–12301.

[424] L. Ley, R. A. Pollak, F. R. McFeely, Kowalczy.Sp, and D. A. Shirley, *Phys. Rev. B*, **1974**, *9*, 600–621.

[425] R. A. Powell, W. E. Spicer, and McMenami J. C., *Phys. Rev. B*, **1972**, *6*, 3056–3065.

[426] C. J. Vesely, R. L. Hengehol, and D. W. Langer, *Phys. Rev. B*, **1972**, *5*, 2296–2301.

[427] G. Zwicker and K. Jacobi, *Solid State Commun.*, **1985**, *54*, 701–704.

[428] F. Labat, I. Ciofini, and C. Adamo, *J. Chem. Phys.*, **2009**, *131*, 044708(1–11).

[429] P. Rinke, A. Qteish, J. Neugebauer, C. Freysoldt, and M. Scheffler, *New J. Phys.*, **2005**, *7*, 126(1–35).

[430] M. Shishkin and G. Kresse, *Phys. Rev. B*, **2007**, *75*, 235102(1–9).

[431] R. Passler, E. Griebl, H. Riepl, G. Lautner, S. Bauer, H. Preis, W. Gebhardt, B. Buda, D. J. As, D. Schikora, K. Lischka, K. Papagelis, and S. Ves, *J. Appl. Phys.*, **1999**, *86*, 4403–4411.

[432] A. Slobodskyy, C. Gould, T. Slobodskyy, C. R. Becker, G. Schmidt, and L. W. Molenkamp, *Phys. Rev. Lett.*, **2003**, *90*, 246601(1–4).

[433] J. F. Holzman, F. E. Vermeulen, S. E. Irvine, and A. Y. Elezzabi, *Appl. Phys. Lett.*, **2002**, *81*, 2294–2296.

[434] T. Tanaka, K. Saito, M. Nishio, Q. Guo, and H. Ogawa, *Appl. Phys. Express*, **2009**, *2*, 122101(1–3).

[435] Q. Wu, M. Litz, and X. C. Zhang, *Appl. Phys. Lett.*, **1996**, *68*, 2924–2926.

[436] S. Kaniyankandy, S. Rawalekar, S. Verma, and H. N. Ghosh, *J. Phys. Chem. C*, **2011**, *115*, 1428–1435.

[437] X. Fang, T. Zhai, U. K. Gautam, L. Li, L. Wu, Y. Bando, and Dmitri Golberg, *Prog. Mater. Sci.*, **2011**, *56*, 175–287.

[438] M. V. R. Krishna and R. A. Friesner, *J. Chem. Phys.*, **1991**, *95*, 8309–8322.

[439] L. Jin, W. C. H. Choy, Y. P. Leung, T. I. Yuk, H. C. Ong, and J. B. Wang, *J. Appl. Phys.*, **2007**, *102*, 044302(1–6).

[440] L. Chai, J. Du, S. Xiong, H. Li, Y. Zhu, and Y. Qian, *J. Phys. Chem. C*, **2007**, *111*, 12658–12662.

[441] L. W. Yin, Y. Bando, J. H. Zhan, M. S. Li, and D. Golberg, *Adv. Mater.*, **2005**, *17*, 1972–1977.

[442] S. H. Yu and M. Yoshimura, *Adv. Mater.*, **2002**, *14*, 296–300.

[443] Y. Jiang, X. M. Meng, W. C. Yiu, J. Liu, J. X. Ding, C. S. Lee, and S. T. Lee, *J. Phys. Chem. B*, **2004**, *108*, 2784–2787.

[444] S. L. Xiong, J. M. Shen, Q. Xie, Y. Q. Gao, Q. Tang, and Y. T. Qian, *Adv. Func. Mater.*, **2005**, *15*, 1787–1792.

[445] W. C. H. Choy, C. F. Guo, Y. P. Leung, G. Z. Wang, and T. I. Yuk, *Appl. Phys. A: Mater. Sci. Process.*, **2006**, *83*, 301–304.

[446] P. Kumar and K. Singh, *J. Optoelectron. Biomed. Mater.*, **2009**, *1*, 59–69.

[447] L. J. Zhang, X. C. Shen, H. Liang, and J. T. Yao, *J. Phys. Chem. C*, **2010**, *114*, 21921–21927.

[448] S. Xu, C. Wang, Q. Xu, H. Zhang, R. Li, H. Shao, W. Lei, and Y. Cui, *Chem. Mater.*, **2010**, *22*, 5838–5844.

[449] J. Zhang, S. Jin, H. C. Fry, S. Peng, E. Shevchenko, G. P. Wiederrecht, and T. Rajh, *J. Am. Chem. Soc.*, **2011**, *133*, 15324–15327.

[450] B. Goswami, S. Pal, and P. Sarkar, *Phys. Rev. B*, **2007**, *76*, 045323(1–7).

[451] J. M. Matxain, J. E. Fowler, and J. M. Ugalde, *Phys. Rev. A*, **2000**, *62*, 053201(1–10).

[452] B. Wang, X. Wang, G. Chen, S. Nagase, and J. Zhao, *J. Chem. Phys.*, **2008**, *128*, 144710(1–6).

[453] H. S. Chen, B. Lo, J. Y. Hwang, G. Y. Chang, C. M. Chen, S. J. Tasi, and S. J. J. Wang, *J. Phys. Chem. B*, **2004**, *108*, 17119–17123.

[454] E. Groeneveld, S. van Berkum, A. Meijerink, and C. de Mello Donega, *Small*, **2011**, *7*, 1247–1256.

[455] J. F. Suyver, S. F. Wuister, J. J. Kelly, and A. Meijerink, *Nano Lett.*, **2001**, *1*, 429–433.

[456] X. Wang, J. Shi, Z. Feng, M. Li, and C. Li, *Phys. Chem. Chem. Phys.*, **2011**, *13*, 4715–4723.

[457] Q. Meng, C. Jiang, and S. X. Mao, *J. Cryst. Growth*, **2008**, *310*, 4481–4486.

[458] J. G. Snijders and E. J. Baerends, *Mol. Phys.*, **1978**, *36*, 1789–1804.

[459] A. Klamt, *J. Phys. Chem.*, **1995**, *99*, 2224–2235.

[460] M. Cossi and V. Barone, *J. Phys. Chem. A*, **2000**, *104*, 10614–10622.

[461] M. Cossi and V. Barone, *J. Chem. Phys.*, **2001**, *115*, 4708–4717.

[462] M. Cossi, N. Rega, G. Scalmani, and V. Barone, *J. Comput. Chem.*, **2003**, *24*, 669–681.

[463] H. F. Qian, L. Li, and J. C. Ren, *Mater. Res. Bull.*, **2005**, *40*, 1726–1736.

[464] H. Li, W. Y. Shih, and W. H. Shih, *Nanotechnology*, **2007**, *18*, 205604(1–6).

[465] Z. Deng, F. L. Lie, S. Shen, I. Ghosh, M. Mansuripur, and A. J. Muscat, *Langmuir*, **2009**, *25*, 434–442.

[466] P. Dagtepe, V. Chikan, J. Jasinski, and V. J. Leppert, *J. Phys. Chem. C*, **2007**, *111*, 14977–14983.

[467] M. Li, J. Ouyang, C. I. Ratcliffe, L. Pietri, X. Wu, D. M. Leek, I. Moudrakovski, Q. Lin, B. Yang, and K. Yu, *ACS Nano*, **2009**, *3*, 3832–3838.

[468] Q. Yu and C. Y. Liu, *J. Phys. Chem. C*, **2009**, *113*, 12766–12771.

[469] A. D. Dukes III, J. R. McBride, and S. J. Rosenthal, *Chem. Mater.*, **2010**, *22*, 6402–6408.

[470] B. M. Cossairt and J. S. Owen, *Chem. Mater.*, **2011**, *23*, 3114–3119.

[471] R. Jose, N. U. Zhanpeisov, H. Fukumura, Y. Baba, and M. Ishikawa, *J. Am. Chem. Soc.*, **2006**, *128*, 629–636.

[472] A. Zunger, *Appl. Phys. Lett.*, **2003**, *83*, 57–59.

[473] L. W. Wang and A. Zunger, *Phys. Rev. B*, **1996**, *53*, 9579–9582.

[474] Y. N. Xia, P. D. Yang, Y. G. Sun, Y. Y. Wu, B. Mayers, and B. Gates, *Adv. Mater.*, **2003**, *15*, 353–389.

[475] C. M. Lieber and Z. L. Wang, *Mater. Res. Soc. Bull.*, **2007**, *32*, 99–108.

[476] E. Comini, C. Baratto, G. Faglia, M. Ferroni, A. Vomiero, and G. Sberglieri, *Prog. Mater. Sci.*, **2009**, *54*, 1–67.

[477] T. Y. Zhai, X. S. Fang, M. Y. Liao, and X. J. Xu, *Sensors*, **2009**, *9*, 6504–6529.

[478] Z. Zhang, H. Yuan, D. Liu, L. Liu, J. Shen, Y. Xiang, W. Ma, W. Zhou, and S. Xie, *Nanotechnology*, **2007**, *18*, 145607(1–5).

[479] D. Yu, C. Wang, and P. Guyot-Sionnest, *Science*, **2003**, *300*, 1277–1280.

[480] Hyunjoo Lee, Susan E. Habas, Sasha Kweskin, Derek Butcher, Gabor A. Somorjai, and Peidong Yang, *Angew. Chem. Int. Ed.*, **2006**, *45*, 7824–7828.

[481] C. B. Murray, S. H. Sun, H. Doyle, and T. Betley, *Mater. Res. Soc. Bull.*, **2001**, *26*, 985–991.

[482] R. Gill, I. Willner, I. Shweky, and U. Banin, *J. Phys. Chem. B*, **2005**, *109*, 23715–23719.

[483] J. B. Delehanty, I. L. Medintz, T. Pons, F. M. Brunel, P. E. Dawson, and H. Mattoussi, *Bioconjugate Chem.*, **2006**, *17*, 920–927.

[484] J. M. Tsay, S. Doose, and S. Weiss, *J. Am. Chem. Soc.*, **2006**, *128*, 1639–1647.

[485] X. Gao and S. Nie, *Nature*, **2001**, *413*, 450–452.

[486] T. M. Jovin, *Nat. Biotechnol.*, **2003**, *21*, 32–33.

[487] M. A. Stroscio and M. Dutta, *Biological Nanostructures and Applications of Nanostructures in Biology;* Springer, 2004.

[488] L. R. Becerra, C. B. Murray, R. G. Griffin, and M. G. Bawendi, *J. Chem. Phys.*, **1994**, *100*, 3297–3300.

[489] J. E. B. Katari, V. L. Colvin, and A. P. Alivisatos, *J. Phys. Chem.*, **1994**, *98*, 4109–4117.

[490] L. Manna, L. W. Wang, R. Cingolani, and A. P. Alivisatos, *J. Phys. Chem. B*, **2005**, *109*, 6183–6192.

[491] A. Puzder, A. J. Williamson, N. Zaitseva, G. Galli, L. Manna, and A. P. Alivisatos, *Nano Letters*, **2004**, *4*, 2361–2365.

[492] Knut W. Urban, *Science*, **2008**, *321*, 506–510.

[493] S. Hamad, S. M. Woodley, and C. R. A. Catlow, *Mol. Simul.*, **2009**, *35*, 1015–1032.

[494] Z. A. Peng and X. G. Peng, *J. Am. Chem. Soc.*, **2001**, *123*, 1389–1395.

[495] L. Qu and X. Peng, *J. Am. Chem. Soc.*, **2002**, *124*, 2049–2055.

[496] K. Leung and K. B. Whaley, *J. Chem. Phys.*, **1999**, *110*, 11012–11022.

[497] S. Pokrant and K. B. Whaley, *Eur. Phys. J. D*, **1999**, *6*, 255–267.

[498] J. M. Mercero, J. M. Matxain, X. Lopez, D. M. York, A. Largo, L. A. Eriksson, and J. M. Ugalde, *Int. J. Mass Spectrom.*, **2005**, *240*, 37–99.

[499] G. M. Dalpian, M. L. Tiago, M. L. del Puerto, and J. R. Chelikowsky, *Nano Lett.*, **2006**, *6*, 501–504.

[500] N. A. Hill and K. B. Whaley, *J. Chem. Phys.*, **1994**, *100*, 2831–2837.

[501] A. Burnin, E. Sanville, and J. J. BelBruno, *J. Phys. Chem. A*, **2005**, *109*, 5026–5034.

[502] X. Wang, H. Xu, H. Liu, Z. A. Schelly, and S. Wu, *Nanotechnology*, **2007**, *18*, 155604(1–5).

[503] P. J. Stephens, F. J. Devlin, C. F. Chabalowski, and M. J. Frisch, *J. Phys. Chem.*, **1994**, *98*, 11623–11627.

[504] F. Maseras and K. Morokuma, *J. Comput. Chem.*, **1995**, *16*, 1170–1179.

[505] M. Swart, P. T. Van Duijnen, and J. G. Snijders, *J. Comput. Chem.*, **2001**, *22*, 79–88.

[506] K. Morokuma, *J. Chem. Phys.*, **1971**, *55*, 1236–1244.

[507] K. Kitaura and K. Morokuma, *Int. J. Quantum Chem.*, **1976**, *10*, 325–340.

[508] T. Ziegler and A. Rauk, *Theor. Chim. Acta*, **1977**, *46*, 1–10.

[509] T. Ziegler and A. Rauk, *Inorg. Chem.*, **1979**, *18*, 1558–1565.

[510] T. Ziegler and A. Rauk, *Inorg. Chem.*, **1979**, *18*, 1755–1759.

[511] M. P. Mitoraj, A. Michalak, and T. Ziegler, *J. Chem. Theory Comput.*, **2009**, *5*, 962–975.

[512] M. P. Mitoraj, A. Michalak, and T. Ziegler, *Organometallics*, **2009**, *28*, 3727–3733.

[513] S. Grimme, J. Antony, S. Ehrlich, and H. Krieg, *J. Chem. Phys.*, **2010**, *132*, 154104(1–19).

[514] P. Schapotschnikow, B. Hommersom, and T. J. H. Vlugt, *J. Phys. Chem. C*, **2009**, *113*, 12690–12698.

[515] P. Joshi, V. Shewale, R. Pandey, V. Shanker, S. Hussain, and S. P. Karna, *Phys. Chem. Chem. Phys.*, **2011**, *13*, 476–479.

[516] F. L. Hirshfeld, *Theor. Chim. Acta*, **1977**, *44*, 129–138.

[517] W. D. Knight, K. Clemenger, W. A. Deheer, W. A. Saunders, M. Y. Chou, and M. L. Cohen, *Phys. Rev. Lett.*, **1984**, *52*, 2141–2143.

[518] A. Burnin and J. J. BelBruno, *Chem. Phys. Lett.*, **2002**, *362*, 341–348.

[519] L. M. Kukreja, A. Rohlfing, P. Misra, F. Hillenkamp, and K. Dreisewerd, *Appl. Phys. A: Mater. Sci. Process.*, **2004**, *78*, 641–644.

[520] S. Kudera, M. Zanella, C. Giannini, A. Rizzo, Y. Li, G. Gigli, R. Cingolani, G. Ciccarella, W. Spahl, W. J. Parak, and L. Manna, *Adv. Mater.*, **2007**, *19*, 548–552.

[521] J. C. Newton, K. Ramasamy, M. Mandal, G. K. Joshi, A. Kumbhar, and R. Sardar, *J. Phys. Chem. C*, **2012**, *116*, 4380–4389.

[522] J. M. Matxain, J. M. Mercero, J. E. Fowler, and J. M. Ugalde, *J. Phys. Chem. A*, **2004**, *108*, 10502–10508.

[523] C. Caddeo, G. Malloci, F. De Angelis, L. Colombo, and A. Mattoni, *Phys. Chem. Chem. Phys.*, **2012**, *14*, 14293–14298.

[524] Y. Wang, Y. H. Liu, Y. Zhang, F. Wang, P. J. Kowalski, H. W. Rohrs, R. A. Loomis, M. L. Gross, and W. E. Buhro, *Angew. Chem. Int. Ed.*, **2012**, *51*, 6154–6157.

[525] T. P. Martin, *Phys. Rep.*, **1996**, *273*, 199–241.

[526] E. van Lenthe, A. Ehlers, and E. J. Baerends, *J. Chem. Phys.*, **1999**, *110*, 8943–8953.

[527] D. Mollenhauer, N. Gaston, E. Voloshina, and B. Paulus, *J. Phys. Chem. C*, **2013**, *117*, 4470–4479.

[528] P. Guyot-Sionnest, M. Shim, C. Matranga, and M. Hines, *Phys. Rev. B*, **1999**, *60*, 2181–2184.

[529] K. E. Knowles, D. B. Tice, E. A. McArthur, G. C. Solomon, and E. A. Weiss, *J. Am. Chem. Soc.*, **2010**, *132*, 1041–1050.

[530] I. Mora-Sero, L. Bertoluzzi, Gonzalez-Pedro V., S. Gimenez, F. Fabregat-Santiago, K. W. Kemp, E. H. Sargent, and J. Bisquert, *Nat. Commun.*, **2013**, *4*, 2272(1–8).

[531] C. R. Maldonado, L. Salassa, N. Gomez Blanco, and J. C. Mareque-Rivas, *Coord. Chem. Rev.*, **2013**, *257*, 2668–2688.

[532] A. Garaikoetxea Arguinzoniz, E. Ruggiero, A. Habtemariam, J. Hernandez-Gil, L. Salassa, and J. C. Mareque-Rivas, *Part. Part. Syst. Charact.*, **2014**, *31*, 46–75.

[533] M. D. Peterson, R. J. Holbrook, T. J. Meade, and E. A. Weiss, *J. Am. Chem. Soc.*, **2013**, *135*, 13162–13167.

[534] R. Long and O. V. Prezhdo, *J. Am. Chem. Soc.*, **2011**, *133*, 19240–19249.

[535] V. V. Chaban, V. V. Prezhdo, and O. V. Prezhdo, *J. Phys. Chem. Lett.*, **2013**, *4*, 1–6.

[536] S. Dhar, Z. Liu, J. Thomale, H. Dai, and S. J. Lippard, *J. Am. Chem. Soc.*, **2008**, *130*, 11467–11476.

[537] S. Mukhopadhyay, C. M. Barnés, A. Haskel, S. M. Short, K. R. Barnes, and S. J. Lippard, *Bioconjugate Chem.*, **2008**, *19*, 39–49.

[538] S. Dhar, W. L. Daniel, D. A. Giljohann, C. A. Mirkin, and S. J. Lippard, *J. Am. Chem. Soc.*, **2009**, *131*, 14652–14653.

[539] P. Gramatica, E. Papa, M. Luini, E. Monti, M. Gariboldi, M. Ravera, E. Gabano, Gaviglio L., and D. Osella, *J. Biol. Inorg. Chem.*, **2010**, *15*, 1157–1169.

[540] N. Graf, D. R. Bielenberg, N. Kolishetti, C. Muus, J. Banyard, O. C. Farokhzad, and S. J. Lippard, *ACS Nano*, **2012**, *6*, 4530–4539.

[541] H. P. Varbanov, M. A. Jakupec, A. Roller, F. Jensen, M. Galanski, and B. K. Keppler, *J. Med. Chem.*, **2013**, *56*, 330–344.

[542] N. J. Farrer, L. Salassa, and P. J. Sadler, *Dalton Trans.*, **2009**, *0*, 10690–10701.

[543] N. J. Farrer, J. A. Woods, L. Salassa, Y. Zhao, K. S. Robinson, G. Clarkson, F. S. Mackay, and P. J. Sadler, *Angew. Chem. Int. Ed.*, **2010**, *49*, 8905–8908.

[544] A. F. Westendorf, J. A. Woods, K. Korpis, N. J. Farrer, L. Salassa, K. Robinson, V. Appleyard, K. Murray, R. Gruenert, A. M. Thompson, P. J. Sadler, and P. J. Bednarski, *Mol. Cancer Ther.*, **2012**, *11*, 1894–1904.

[545] Y. Dai, H. Xiao, J. Liu, Q. Yuan, P. Ma, D. Yang, C. Li, Z. Cheng, Z. Hou, P. Yang, and J. Lin, *J. Am. Chem. Soc.*, **2013**, *135*, 18920–18929.

[546] Y. Min, J. Li, F. Liu, E. K. L. Yeow, and B. Xing, *Angew. Chem. Int. Ed.*, **2014**, *53*, 1012–1016.

[547] E. Ruggiero, A. Habtemariam, L. Yate, J. C. Mareque-Rivas, and L. Salassa, *Chem. Commun.*, **2014**, *50*, 1715–1718.

[548] N. Gomez Blanco, C. R. Maldonado, and J. C. Mareque-Rivas, *Chem. Commun.*, **2009**, *0*, 5257–5259.

[549] N. Gomez Blanco, M. Jauregui-Osoro, M. Cobaleda-Siles, C. R. Maldonado, M. Henriksen-Lacey, D. Padro, S. Clark, and J. C. Mareque-Rivas, *Chem. Commun.*, **2012**, *48*, 4211–4213.

[550] M. R. Reithofer, S. M. Valiahdi, M. A. Jakupec, V. B. Arion, A. Egger, M. Galanski, and B. K. Keppler, *J. Med. Chem.*, **2007**, *50*, 6692–6699.

[551] J. M. Azpiroz, J. M. Ugalde, and I. Infante, *J. Chem. Theory Comput.*, **2014**, *10*, 76–89.

[552] D. M. York and M. Karplus, *J. Phys. Chem. A*, **1999**, *103*, 11060–11079.

[553] S. F. Boys and F. Bernardi, *Mol. Phys.*, **1970**, *19*, 553–566.

[554] S. Simon, M. Duran, and J. J. Dannenberg, *J. Chem. Phys.*, **1996**, *105*, 11024–11031.

[555] A. I. Krylov and P. M. W. Gill, *WIREs Comput. Mol. Sci.*, **2013**, *3*, 317–326.

[556] N. M. O'Boyle, A. L. Tenderholt, and K. M. Langner, *J. Comput. Chem.*, **2008**, *29*, 839–845.

[557] S. I. Gorelsky, *AOMix: Program for Molecular Orbital Analysis; version 6.8*, **2013**, *University of Ottawa, http://www.sg-chem.net*.

[558] S. I. Goreslky and A. B. P. Lever, *J. Organomet. Chem.*, **2001**, *635*, 187–196.

[559] E. F. Pettersen, T. D. Goddard, C. C. Huang, G. S. Couch, D. M. Greenblatt, E. C. Meng, and T. E. Ferrin, *J. Comput. Chem.*, **2004**, *25*, 1605–1612.

[560] C. Garino and L. Salassa, *Phil. Trans. R. Soc. A.*, **2013**, *371*, 20120134.

[561] A. Nemirovski, I. Vinograd, K. Takrouri, A. Mijovilovich, A. Rompel, and D. Gibson, *Chem. Commun.*, **2010**, *46*, 1842–1844.

[562] J. Z. Zhang, E. Wexselblatt, T. W. Hambley, and D. Gibson, *Chem. Commun.*, **2012**, *48*, 847–849.

[563] M. Sykora, M. A. Petruska, J. Alstrum-Acevedo, I. Bezel, T. J. Meyer, and V. I. Klimov, *J. Am. Chem. Soc.*, **2006**, *128*, 9984–9985.

[564] T. Koopmans, *Physica*, **1934**, *1*, 104–113.

[565] R. A. Marcus, *J. Chem. Phys.*, **1956**, *24*, 966–978.

[566] D. Chen, F. Huang, G. Ren, D. Li, M. Zheng, Y. Wang, and Z. Lin, *Nanoscale*, **2010**, *2*, 2062–2064.

[567] H. M. Chen, C. K. Chen, R. S. Liu, C. C. Wu, W. S. Chang, K. H. Chen, T. S. Chan, J. F. Lee, and D. P. Tsai, *Adv. Energy Mater.*, **2011**, *1*, 742–747.

[568] Y. Tachibana, L. Vayssieres, and J. R Durrant, *Nat. Photonics*, **2012**, *6*, 511–518.

[569] M. Dolg, U. Wedig, H. Stoll, and H. Preuss, *J. Chem. Phys.*, **1987**, *86*, 866–872.

[570] T. H. Dunning and P. J. Hay, *Modern Theoretical Chemistry;* Plenum, 1976.

[571] W. Humphrey, A. Dalke, and K. Schulten, *J. Molec. Graphics*, **1996**, *14*, 33–38.

[572] C. F. Macrae, P. R. Edgington, P. McCabe, E. Pidcock, Shields. G. P., R. Taylor, M. Towler, and J. van de Streek, *J. Appl. Cryst.*, **2006**, *39*, 453–457.

[573] C. Junkermeier, J. Lewis, and G. Bryant, *Phys. Rev. B*, **2009**, *79*, 125323(1–8).

[574] P. D'Angelo, V. Barone, G. Chillemi, N. Sanna, W. Meyer-Klaucke, and N. V. Pavel, *J. Am. Chem. Soc.*, **2002**, *124*, 1958–1967.

[575] J. C. Wu, J. P. Piquemal, R. Chaudret, P. Reinhardt, and P. Ren, *J. Chem. Theory Comput.*, *6*.

[576] B. O'Regan and M. Grätzel, *Nature*, **1991**, *353*, 737–740.

[577] M. K. Nazeeruddin, A. Kay, I. Rodicio, R. Humphry-Baker, E. Mueller, P. Liska, N. Vlachopoulos, and M. Grätzel, *J. Am. Chem. Soc.*, **1993**, *115*, 6382–6390.

[578] M. K. Nazeeruddin, F. De Angelis, S. Fantacci, A. Selloni, G. Viscardi, P. Liska, S. Ito, B. Takeru, and M. Grätzel, *J. Am. Chem. Soc.*, **2005**, *127*, 16835–16847.

[579] F. De Angelis, S. Fantacci, E. Mosconi, M. K. Nazeeruddin, and M. Grätzel, *J. Phys. Chem. C*, **2011**, *115*, 8825–8831.

[580] R. W. Fessenden and P. V. Kamat, *J. Phys. Chem.*, **1995**, *99*, 12902–12906.

[581] J. B. Asbury, E. Hao, Y. Wang, H. N. Ghosh, and T. Lian, *J. Phys. Chem. B*, **2001**, *105*, 4545–4557.

[582] M. Grätzel, *Nature*, **2001**, *414*, 338–344.

[583] R. Katoh, A. Furube, T. Yoshihara, K. Hara, G. Fujihashi, S. Takano, S. Murata, H. Arakawa, and M. Tachiya, *J. Phys. Chem. B*, **2004**, *108*, 4818–4822.

[584] Y. Fukai, Y. Kondo, S. Mori, and E. Suzuki, *Electrochem. Commun.*, **2007**, *9*, 1439–1443.

[585] P. Tiwana, P. Docampo, M. B. Johnston, H. J. Snaith, and L. M. Herz, *ACS Nano*, **2011**, *5*, 5158–5166.

[586] Z. M. Jarzebski and J. P. Marton, *J. Electrochem. Soc.*, **1976**, *123*, 299–310.

[587] E. Shanthi, V. Dutta, A. Banerjee, and K. L. Chopra, *J. Appl. Phys.*, **1980**, *51*, 6243–6251.

[588] D. Jousse, C. Constantino, and I. Chambouleyron, *J. Appl. Phys.*, **1983**, *54*, 431–434.

[589] D. C. Look, D. C. Reynolds, J. R. Sizelove, R. L. Jones, C. W. Litton, G. Cantwell, and W. C. Harsh, *Solid State Commun.*, **1998**, *105*, 399–401.

[590] M. Law, L. E. Greene, J. C. Johnson, R. Saykally, and P. Yang, *Nat. Mater.*, **2005**, *4*, 455–459.

[591] N. Memarian, I. Concina, A. Braga, S. M. Rozati, A. Vomiero, and G. Sberveglieri, *Angew. Chem. Int. Ed.*, **2011**, *123*, 12529–12533.

[592] A. Yella, H. W. Lee, H. N. Tsao, C. Yi, A. K. Chandiran, M. K. Nazeeruddin, E. W. G. Diau, C. Y. Yeh, S. M. Zakeeruddin, and M. Grätzel, *Science*, **2011**, *334*, 629–634.

[593] J. M Szarko, A. Neubauer, A. Bartelt, L. Socaciu-Siebert, F. Birkner, K. Schwarzburg, T. Hannappel, and R. Eichberger, *J. Phys. Chem. C*, **2008**, *112*, 10542–10552.

[594] J. E. Moser, *Dye-Sensitized Solar Cells;* EPFL Press, 2010.

[595] R. Viswanatha, S. Sapra, B. Satpati, P. V. Satyam, B. N. Dev, and D. D. Sarma, *J. Mater. Chem.*, **2004**, *14*, 661–668.

[596] E. Guillen, E. Azaceta, L. M. Peter, A. Zukal, R. Tena-Zaera, and J. A. Anta, *Energy Environ. Sci.*, **2011**, *4*, 3400–3407.

[597] J. A. Anta, E. Guillen, and R. Tena-Zaera, *J. Phys. Chem. C*, **2012**, *116*, 11413–11425.

[598] J. B. Asbury, Y. Wang, and T. Lian, *J. Phys. Chem. B*, **1999**, *103*, 6643–6647.

[599] A. Furube, R. Katoh, K. Hara, S. Murata, H. Arakawa, and M. Tachiya, *J. Phys. Chem. B*, **2003**, *107*, 4162–4166.

[600] A. Furube, R. Katoh, T. Yoshihara, K. Hara, S. Murata, H. Arakawa, and M. Tachiya, *J. Phys. Chem. B*, **2004**, *108*, 12583–12592.

[601] D. Stockwell, Y. Yang, J. Huang, C. Anfuso, Z. Huang, and T. Lian, *J. Phys. Chem. C*, **2010**, *114*, 6560–6566.

[602] G. Oskam, Z. Hu, R. Penn, N. Pesika, and P. Searson, *Phys. Rev. E*, **2002**, *66*, 011403(1–4).

[603] H. M. Nguyen, R. S. Mane, T. Ganesh, S. H. Han, and N. Kim, *J. Phys. Chem. C*, **2009**, *113*, 9206–9209.

[604] R. Gonzalez-Moreno, P. L. Cook, I. Zegkinoglou, X. Liu, P. S. Johnson, W. Yan, R. E. Ruther, R. J. Hamers, R. Tena-Zaera, F. J. Himpsel, J. E. Ortega, and C. Rogero, *J. Phys. Chem. C*, **2011**, *115*, 18195–18201.

[605] F. De Angelis, S. Fantacci, A. Selloni, M. K. Nazeeruddin, and M. Grätzel, *J. Am. Chem. Soc.*, **2007**, *129*, 14156–14157.

[606] F. De Angelis, S. Fantacci, A. Selloni, M. Grätzel, and M. K. Nazeeruddin, *Nano Lett.*, **2007**, *7*, 3189–3195.

[607] F. De Angelis, S. Fantacci, and A. Selloni, *Nanotechnology*, **2008**, *19*, 424002(1–7).

[608] C. Anselmi, E. Mosconi, M. Pastore, E. Ronca, and F. De Angelis, *Phys. Chem. Chem. Phys.*, **2012**, *14*, 15963–15974.

[609] M. Pastore and F. De Angelis, *Phys. Chem. Chem. Phys.*, **2012**, *14*, 920–928.

[610] P. Persson and L. Ojamäe, *Chem. Phys. Lett.*, **2000**, *231*, 302–308.

[611] P. Persson, S. Lunell, and L. Ojamäe, *Int. J. Quantum. Chem.*, **2002**, *89*, 172–180.

[612] F. Labat, I. Ciofini, H. P. Hratchian, M. Frisch, K. Raghavachari, and C. Adamo, *J. Am. Chem. Soc.*, **2009**, *131*, 14290–14298.

[613] A. Amat and F. De Angelis, *Phys. Chem. Chem. Phys.*, **2012**, *14*, 10662–10668.

[614] M. M. Hedrick, M. L. Mayo, E. Badaeva, and S. Kilina, *J. Phys. Chem. C*, **2013**, *117*, 18216–18224.

[615] E. Ronca, M. Pastore, L. Belpassi, F. Tarantelli, and F. De Angelis, *Energy Environ. Sci.*, **2013**, *6*, 183–193.

[616] F. De Angelis, S. Fantacci, A. Selloni, M. K. Nazeeruddin, and M. Grätzel, *J. Phys. Chem. C*, **2010**, *114*, 6054–6061.

[617] R. Reiche, R. Thielsch, S. Oswald, and K. Wetzig, *J. Electron Spectrosc. Relat. Phenom.*, **1999**, *104*, 131–149.

[618] Z. Zeng, S. Wang, and S. Yang, *Chem. Mater.*, **1999**, *11*, 3365–3369.

[619] K. K. Nanda and S. N. Sahu, *Adv. Mater.*, **2001**, *13*, 280–283.

[620] M. Kowshik, W. Vogel, J. Urban, S. K. Kulkarni, and K. M. Paknikar, *Adv. Mater.*, **2002**, *14*, 815–818.

[621] Y. Zhou, H. Itoh, T. Uemura, K. Naka, and Y. Chujo, *Langmuir*, **2002**, *18*, 5287–5292.

[622] S. Wu, H. Zeng, and Z. A. Schelly, *Langmuir*, **2005**, *21*, 686–691.

[623] L. Etgar, J. Park, C. Barolo, M. K. Nazeeruddin, G. Viscardi, and M Grätzel, *ACS Appl. Mater. Interfaces*, **2011**, *3*, 3264–3267.

[624] L. Etgar, T. Moehl, S. Gabriel, S. G. Hickey, A. Eychmüller, , and M Grätzel, *ACS Nano*, **2012**, *6*, 3092–3099.

[625] L. Etgar, W. Zhang, S. Gabriel, S. G. Hickey, M. K. Nazeeruddin, A. Eychmüller, B. Liu, and M Grätzel, *Adv. Mater.*, **2012**, *24*, 2202–2206.

[626] J. W. Lee, D. Y. Son, T. K. Ahn, H. W. Shin, I. Y. Kim, S. J. Hwang, M. J. Ko, S. Sul, H. Han, and N. G. Park, *Sci. Rep.*, **2013**, *3*, 1050(1–8).

[627] P. Maraghechi, A. J. Labelle, A. R. Kirmani, X. Lan, M. M. Adachi, S. M. Thon, S. Hoogland, A. Lee, Z. Ning, A. Fischer, A. Amassian, and E. H. Sargent, *ACS Nano*, **2013**, *7*, 6111–6116.

[628] H. Lee, H. C. Leventis, S. J. Moon, P. Chen, S. Ito, S. A. Haque, T. Torres, F. Nüesch, T. Geiger, S. M. Zakeeruddin, M. Grätzel, and M. K. Nazeeruddin, *Adv. Func. Mater.*, **2009**, *19*, 2735–2742.

[629] H. Zeng, Z. A. Schelly, K. Ueno-Noto, and D. S. Marynick, *J. Phys. Chem. A*, **2005**, *109*, 1616–1620.

[630] J. He, C. Liu, F. Li, R. Sa, and Wu. K., *Chem. Phys. Lett.*, **2008**, *457*, 163–168.

[631] P. Koirala, B. Kiran, Kandalam A. K., Fancher C. A., Li X. de Clercq, H. L., and K. H. Bowen, *J. Chem. Phys.*, **2011**, *135*, 13431(1–12).

[632] R. S. Kane, R. E. Cohen, and R. Silbey, *J. Phys. Chem.*, **1996**, *100*, 7928–7932.

[633] H. Choi, J. H. Ko, Y. H. Kim, and S. Jeong, *J. Am. Chem. Soc.*, **2013**, *135*, 5278–5281.

[634] D. Kim, D. H. Kim, J. H. Lee, and J. C. Grossman, *Phys. Rev. Lett.*, **2013**, *110*, 196802(1–5).

[635] C. Dong, X. Li, and J. Qi, *J. Phys. Chem. C*, **2011**, *115*, 20307–20315.

[636] A. H. Khan, U. Thupakula, A. Dalui, S. Maji, A. Debangshi, and S. Acharya, *J. Phys. Chem. C*, **2013**, *117*, 7934–7939.

[637] A. Franceschetti, *Phys. Rev. B*, **2008**, *78*, 075418(1–6).

[638] J. M. Azpiroz, E. Mosconi, J. M. Ugalde, and F. De Angelis, *J. Phys. Chem. C*, **2014**, *118*, 3274–3284.

[639] B. R. Hyun, Y. W. Zhong, A. C. Bartnik, L. Sun, H. D. Abrun, F. W. Wise, J. D. Goodreau, J. R. Matthews, T. M. Leslie, and N. F. Borrelli, *ACS Nano*, **2008**, *2*, 2206–2212.

[640] M. Khoudiakov, A. R. Parise, and B. S Brunschwig, *J. Am. Chem. Soc.*, **2003**, *125*, 4637–4632.

[641] Y. X. Weng, Y. Q. Wang, J. B. Asbury, H. N. Ghosh, and T. Lian, *J. Phys. Chem. B*, **2000**, *104*, 93–104.